Assessing the Impact of Biofouling on the Hydraulic Efficiency of Pipelines

By

Matthew William Cowle

BEng

This thesis is submitted in partial fulfilment of the requirements for the degree of

Doctor of Philosophy (PhD)

School of Engineering, Cardiff University,

Cardiff, Wales, UK

2015

Declaration

This work has not previously been accepted in substance for any degree and is not being concurrently submitted in candidature for any degree.

Signed…….... (candidate)

Date……

Statement 1

This thesis is being submitted in partial fulfilment of the requirements for the degree of Doctor of Philosophy (PhD)

Signed…….... (candidate)

Date……

Statement 2

This thesis is the result of my own interrogations, except where otherwise stated.

Other sources are acknowledged by footnotes giving explicit references. A biography is appended

Signed…….... (candidate)

Date……

Statement 3

I hereby give consent for my thesis, if accepted, to be available for photocopying and for inter-library loan, and for the title and summary to be made available to outside organisations

Signed…….... (candidate)

Date……

Assessing the Impact of Biofouling on the Hydraulic Efficiency of Pipelines
Matthew William Cowle

Abstract

Pipeline distribution systems account for the vast majority of the physical infrastructure in the water industry. Their effective management represents the primary challenge to the industry, from both an operational and public health standpoint. Biofouling has a ubiquitous presence within these systems, and it can significantly impede their efficiency, through an increase in boundary shear caused by characteristic changes in surface roughness dynamics. Nonetheless, conventional pipeline design practices fail to take into account such effects, partially because research findings that could contribute to upgraded and optimised design practices appear inconsistent in the literature. The overall aim of this study was to improve the current scientific understanding of biofouling within water and wastewater pipelines; for the purpose of instigating a step-change in pipeline design theory by incorporating biofouling, thereby enabling future pipelines to be as sustainable as possible. The nature of the problem, necessitated the need for a multidisciplinary approach, based upon engineering and microbiological principles and techniques.

The primary focus of this study was to investigate the impact of biofouling on surface roughness, mean flow structure and sediment transport within wastewater systems. To this effect biofilms were incubated with a synthetic wastewater on a High Density Polyethylene pipe, within a purpose built pipeline facility for 20 days, at three steady-state flow regimes, including the average freestream velocities of 0.60, 0.75 and 1.00 m/s. The physico-chemical properties of the synthetic wastewater were purposely designed to be equivalent to the properties associated with actual wastewater found within typical European sewers. The impact of biofouling on flow hydrodynamics was comprehensively identified using a series of static pressure tappings and a traversable Pitot probe. Molecular and image analysis was also undertaken to support the observations derived from the aforementioned measurements, particularly with regards to the structural composition and mechanical stability of the biofouled surfaces. The study has confirmed that the presence of a low-form gelatinous biofilm can cause a significant increase in frictional resistance and equivalent roughness, with increases in friction factor of up to 85% measured over the non-fouled values. The reported increases in frictional resistance resulted in a reduction in flow rate of up to 22% and increased the pipe's self-cleansing requirements. The structural distribution of a biofilm was shown to play a key role in its overall frictional capacity and strength, which in turn was found to be a function of the biofilms conditioning shear. In particular, it was found that a biofilm conditioned at higher shear will have less of an impact on a pipe's overall frictional resistance, although, will be stronger and more difficult to remove than a biofilm conditioned at lower shear. The biofilm's impact on frictional resistance was found to be further compounded by the fact that traditional frictional relationships and their derivatives are not applicable to biofouled surfaces in their current manifestation. In particular, the von Kármán constant, which is an integral aspect of the Colebrook-White equation is non-universal and dependent on Reynolds Number for biofouled surfaces. It was found that the most suitable manner to deal with the dynamic and case-specific nature of a biofouled surface was to quantify it using a series of dynamic roughness expressions, the formulation of which were the culmination of this study, and should be the focus for further research.

The influence of different plastic based pipe materials and flow regimes on biofilm development within drinking water distribution systems was also briefly investigated using a series of flow cell bioreactors and molecular analysis techniques.

Keywords: Biofilm; biofouling; pipe; hydraulic efficiency; equivalent roughness; von Kármán constant; Colebrook-White equation; drainage network; wastewater; drinking water.

Dedicated to Amie

For her unconditional love and support

Acknowledgements

I would like to thank all the people who have helped me throughout the four years it's taken to complete this thesis. Firstly, I would like to thank my academic supervisors Dr Bettina Bockelmann-Evans and Dr Akintunde Babatunde for their continued support, for pushing me to achieve, allowing me the freedom to think independently and kind words of encouragement when needed. In addition, I would like to extend my sincerest gratitude to Dr Vasilios Samaras (Asset International Ltd) and Mr Simon Thomas (Asset International Ltd), for their vast knowledge of the water sector, input and understanding not only during my industry placement, within your Newport office, but throughout the entire process. Furthermore, Dr William Rauen (Universidade Positivo, Brazil) and Prof Binliang Lin (Tsinghua University, China) must be acknowledged and accredited for the initial research concept and for championing and encouraging me to take up the position. Your combined wealth of knowledge and selfless time and care have been greatly appreciated throughout my time at Cardiff University. I would like to thank the UK Engineering and Physical Sciences Research Council (EPSRC) in combination with Asset International Ltd for their funding, without which this research would not have been possible.

In addition to those aforementioned individuals, I am greatly appreciative of the input from Dr Andrew Barton (Federation University Australia, Australia) whose unsurpassed knowledge of the area of biofouling has been invaluable to this study. In addition, Dr Gordon Webster (Cardiff University, Wales) whose contribution of both time and expertise to the microbiological aspects of this study have gone beyond the requirements of his role. The experimental work which formed the basis of this study would not have been possible without the School of Engineering technical staff, and in particular, Mr Len Czekaj and Mr Paul Leach, Mr Harry Lane, Mr Steffan Jones and Mr Des Sanford. Your practical knowledge and ability to build something out of nothing is unrivalled. I would also like to extend my gratitude to the wider School of Engineering staff, including those working within the research office, library and IT support teams. I would also like to thank Dr Prasad Tumula (Salford University) and Dr Shunqi Pan, for examining and reviewing this thesis.

I would like to thank my family and friends, especially my parents, for their continued support, encouragement and most importantly patience. I would like to reserve my greatest thanks to my partner Amie, without your constant support and encouragement I would never have completed this thesis.

List of Publications

Journal Publications

Cowle, M.W, Babatunde, A.O, Rauen, W.B, Bockelmann-Evans, B.N. and Barton, A.F. (2014). Biofilm development in water distribution and drainage systems: dynamics and implications for hydraulic efficiency. Environmental Technology Reviews, 4(1), pp. 31-47.

Conference Publications

Cowle, M. W., Vasilios, S. and Rauen, W. B. (2012). A comparative analysis of the carbon footprint of large diameter concrete and HDPE pipes. In Paper Presented to the XVI International Plastic Pipes Conference Barcelona, Spain, Hotel Arts.

Table of Contents

List of Tables

List of Figures

Nomenclature

Symbols

A	Cross-sectional area
B	Nikuradse's roughness function
C	Smooth wall Log-Law Constant = 5.60
C'	Smooth wall Log-Law Constant = 1.20
C_1	Boundary layer development constant 1 = 0.50
C_2	Boundary layer development constant 1 = 5.00
c	Chezy friction coefficient
c_f	Local skin friction coefficient
D	Pipe diameter (typically, taken as the internal diameter)
d_c	Diameter of the pressure transducer connection tube
d_g	Geometric mean grain size
d_h	Wall tapping hole diameter
d_n	Grain diameter for which n% of the grans by mass is finer
d_p	Pitot Probe diameter
d_{50}	Grain diameter for which 50% of the grans by mass is finer
g	Gravity acceleration constant = 9.81 m/s^2
H	Boundary layer shape factor = δ^*/θ
h	Hydraulic head = $P/\rho g$
H_f	Hydraulic headloss
H_{Pitot}	Dynamic pressure head recorded by the Pitot Probe
H_{Static}	Static pressure head
k	Absolute surface roughness height (mm)
k_{av}	Mean roughness height (mm)
k_{max}	Maximum roughness height (mm)
k_{min}	Minimum roughness height (mm)
k_s	Nikuradse-type equivalent sandgrain roughness (mm)
$k_{s(E)}$	Values of k_S for a mature biofilm

k_{rms}	Root-mean square roughness height (mm)
k_t	Maximum peak-to-tough roughness height (mm) = $r_{max} - r_{min}$
L	Streamwise Length
L_0	Initial boundary layer transition length
L_1	Turbulent boundary layer development length
L_2	Turbulence quantities development length
L_E	Entrance length or overall boundary development length = $L_0 + L_1 + L_2$
n	Manning's friction coefficient
P_w	Wetted perimeter
P	Hydraulic gauge pressure
ΔP	Pressure drop
P_E	Pressure error
Q	Volumetric flow rate = $\bar{U}A$
R	Pipe radius = $D/2$
R^2	Coefficient of determination
R_h	Hydraulic radius = A/P
Re	Reynolds Number
Re_x	Reynolds Number based on $x = \bar{U}x/\nu$
Re_D	Reynolds Number based on $D = \bar{U}D/\nu$
Re_L	Reynolds Number based on $L = \bar{U}L/\nu$
SG	Specific gravity
S_o	Pipe invert slope
S_f	Friction slope = dH_f/dL
T	Temperature
t	Time
T_{Tank}	Tank temperature
T_{Pipe}	Pipe temperature
U	Maximum freestream velocity
$\bar{U}$	Average freestream velocity = Q/A
u	Local freestream velocity = $f(x,y)$
U^+	Normalised velocity = u/u^*
u^*	Wall shear velocity = $(\tau_w / \rho)^{0.5}$

u^*_{cr}	Critical frictional velocity for sediment transport
ΔU^+	Hama's (1954) roughness function
V	Volume
W	Wake strength
X^*	Preston probe calibration parameter 1
Y^*	Preston probe calibration parameter 2
w_s	Settling velocity
x	Characteristic length scale
$\bar{x}$	Statistically average
y	Distance from the wall
y^+	Normalised distance from the wall yu^*/ν
α	Non-dimensional velocity gradient
Δ	Change in a variable
δ	Boundary layer thickness at 99% of the fresstream velocity (mm)
δ'	Viscous sublayer thickness
δ^*	Boundary layer momentum thickness (mm)
ε	Wall origin error (mm)
ζ	Minor loss coefficient
θ	Boundary layer displacement thickness (mm) or actual Shields parameter for sediment transport
θ_{cr}	Critical Shields parameter for sediment transport
κ	von Kármán constant = 0.42
λ	Darcy-Weisbach friction factor
λ_A	Lag-time (bacterial growth)
μ	Dynamic viscosity of fluid
Ξ	von Kármán constant diagnostic function
Π	Wake strength parameter
ρ	Density of fluid
σ_x	Standard deviation in x
σ_g	Geometric standard deviation of sediment sizes
τ_w	Wall shear stress
τ_{cr}	Critical wall shear stress
ν	Kinematic viscosity of fluid

ϕ	Angle
ψ	*C* constant diagnostic function
$^+$	Normalised by u^* or u^*/ν

Abbreviations

A	Acrylic
ADV	Acoustic Doppler velocimetry
AOC	Assimilable organic carbon
BSA	Bovine serum albumin
B	Bradshaw (1959)
C	Carbon or conditioning stage (biofilm development)
CAM	Combined Average Method
Cl	Chlorine
COD	Chemical oxygen demand
C/P	Carbohydrate to protein ratio
C-W	Colebrook-White
d	Days
DN	Drainage network
DNS	Direct Numerical Simulation
DOC	Dissolved organic carbon
DGGE	Denaturing gradient gel electrophoresis
DPD	N,N-Diethyl-p-phenylenediamine
D-W	Darcy-Weisbach
DWDS	Drinking water distribution system
E	Equilibrium stage (biofilm development)
EDTA	Ethylenediaminetetraacetic acid
EPS	Extracellular polymer substances
ESEM	Environmental scanning electron microscope
Fe	Iron
HDPE	High Density Polyethylene
HRT	Hydraulic retention time
IC	Inorganic carbon

LLS	Log-Law Slope
Mn	Manganese
N	Nitrogen
NH_4^+	Ammonium
NO_3^-	Nitrate
OECD	Organisation for Economic Cooperation and Development
PAN	1-(2-Pyridylazo)-2-naphthol
P	Phosphorous
PL	Perry and Li (1990)
PP	Preston Probe or Poypropylene
PBS	Phosphate buffer saline
PE	Polyethylene
PG	Pressure gradient
PIV	Particle image velocimetry
PJ	Perry and Joubert (1964)
PVC	Polyvinyl chloride
RRS	Root-square-sum
T	Transitional stage (biofilm development)
S-HDPE	Solid wall HDPE
Str-HDPE	Structured wall HDPE
SFM	Slope Fit Method
TAE	Tris-acetate EDTA
TC	Total carbon
TN	Total nitrogen
TOC	Total organic carbon
TP	Total phosphorus

Chapter 1 Introduction

"Biofouling is a biofilm reactor in the wrong place" (Flemming and Wingender 2010)

Population growth, urbanisation and climate change will undoubtedly put increasing pressure on pipeline infrastructure over the next century (Astaraie-Imani et al. 2012; Mikovits et al. 2014; Kharin et al. 2014). It is widely acknowledged that the magnitude and intensity of precipitation in extreme events will increase as a direct result of climate change (Kharin et al. 2013). The resultant increase in runoff and storm water discharge will increase the likelihood of surcharge and flooding, particularly in highly populated urban areas. Global population growth will further exacerbate the impact of climate change on combined sewage and stormwater systems, especially in urbanised areas, where it is forecast that the majority of the growth will be absorbed (United Nations, 2012). Urbanisation will also cause changes in land use and the sealing of surfaces (Astaraie-Imani et al. 2012; Mikovits et al. 2014), and as a consequence, areas which had not been previously deemed at risk from flooding will become endangered (Ashley et al. 2005). Therefore, the effective management of Drainage Networks (DNs), including sewage, stormwater water and combined systems is one of the most important challenges to the water industry from both an operational and public health standpoint. This challenge is exacerbated by the environmental complexities of DNs, which are characterised by highly diverse and variable flow rates, temperatures and their contents. Fouling mechanisms (individually and cumulatively, see Figure 1.1) both contribute to and are governed by these inherent complexities.

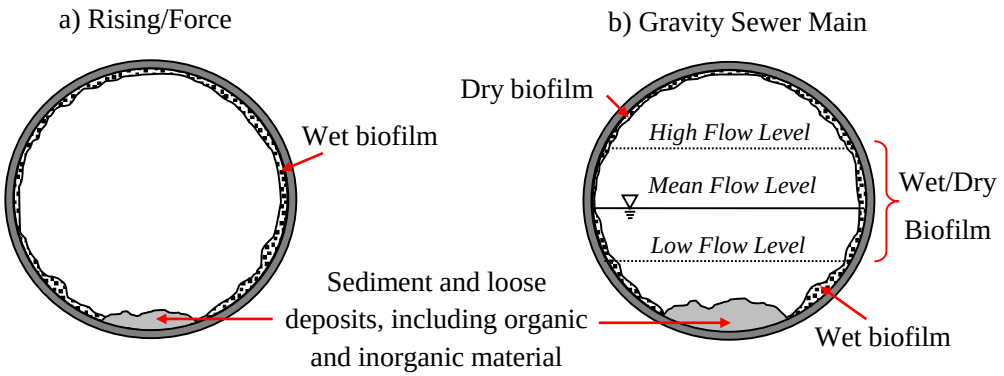

Figure 1.1 Typically fouled water and wastewater pipes, including a) rising/force wastewater main, and b) traditional gravity fed wastewater main.

Of particular concern is pipeline biofouling which refers to the natural, albeit sometimes undesirable process through which a complex microbiological slime layer, composed of microbial cells and colonies embedded within a highly hydrated, protective polymer matrix – referred to as a biofilm – forms upon the surface of a pipeline (for example, see Figure 1.2). The term biofouling also includes the physico-chemical interaction of the biofilm with the pipe surface and the external environment, such as scaling and corrosion.

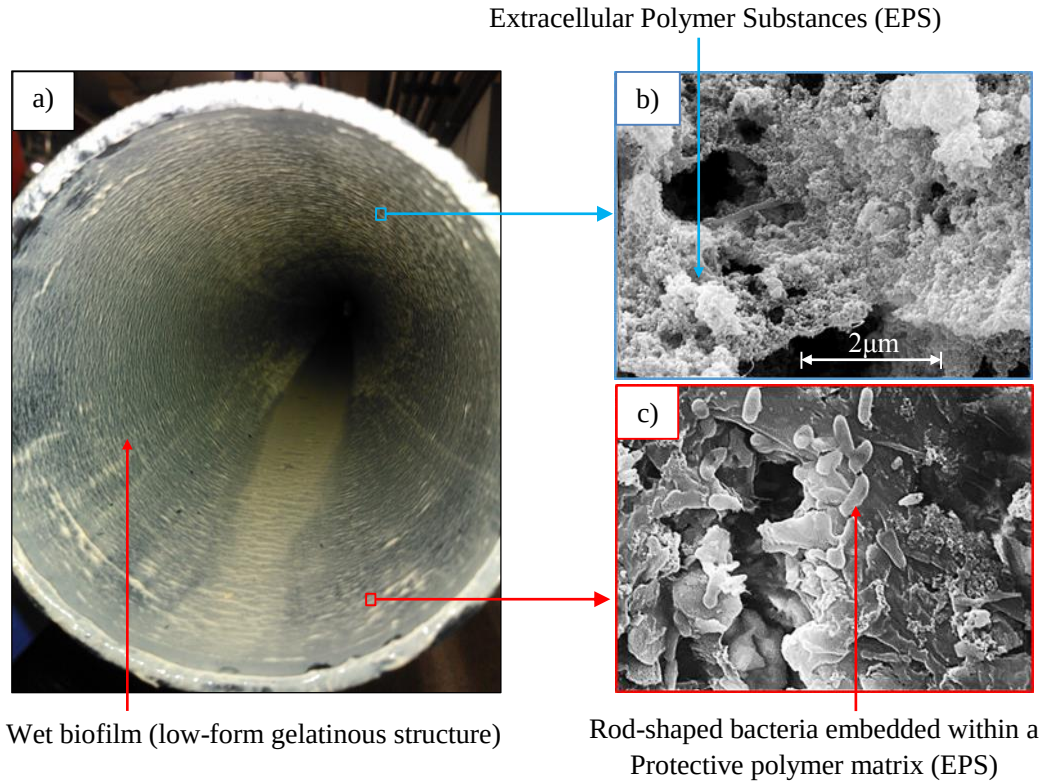

Figure 1.2 Biofouling within a full bore pipe (Diameter = 0.1 m) on the macro- and micro- scale (the photomicrographs in b) and c) were captured using Environmental scanning electron microscope (ESEM) at x 20000 magnification).

The presence of a biofilm can significantly alter the pipeline's solid-liquid interface, typically resulting in increased boundary shear stresses and associated flow resistance, thereby affecting the pipe's hydraulic efficiency over time. For instance, the primary cause of energy losses and thus flow capacity reductions within pipelines is due to friction along the solid-liquid interface which tends to increase with increasing surface roughness and interface instabilities (Shockling et al. 2006). This is illustrated by Figure 1.3, which shows the impact of biofouling on the performance of a range of concrete pipelines with internal diameters

from 50-200 mm. The flow within the pipes was full bore and assumed to be uniform and therefore, friction slope, S_f was to be equal to invert slope, S_i, which was S_i = 1:150. The increase in flow resistance resulting from an increase in equivalent roughness (namely the Nikuradse-type equivalent sandgrain roughness, k_s), as estimated using the widely applied Colebrook-White (C-W) equation (Nikuradse 1933; Colebrook 1939) illusrates the potential impact of biofouling. From Figure 1.3, it can be seen that an increase in k_s from the "clean" pipe value of 0.06mm to the UK's recommended k_s range for fouled pipes of 0.6 mm < k_s < 1.5 mm (Wallingford and Barr 1994) reduces the pipe's average flow capacity by between 28-50%.

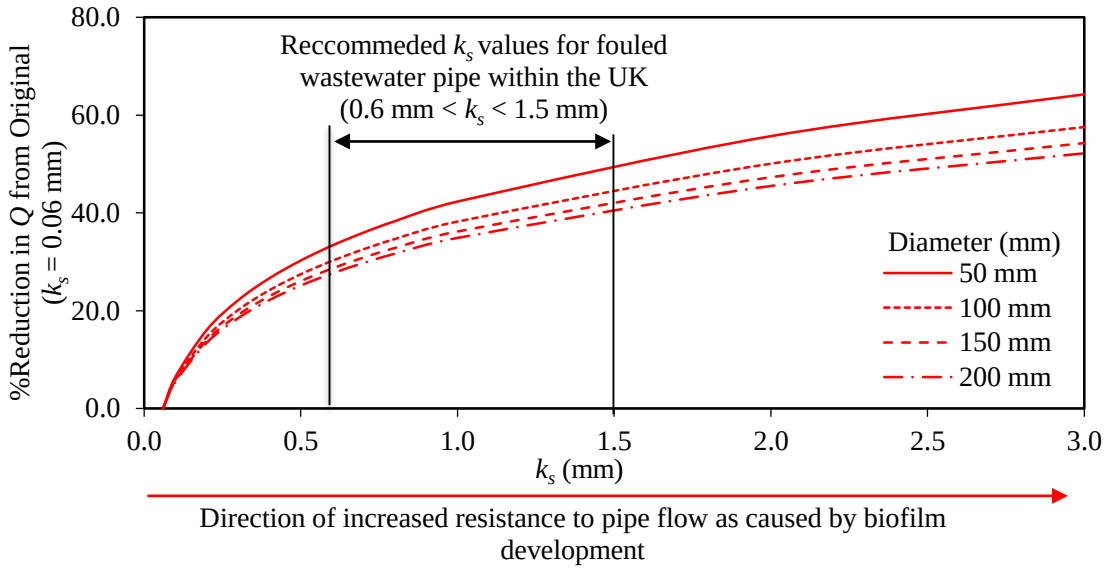

Figure 1.3 Estimated percentage reduction in flow rate, Q caused by an increase of the effective roughnes (k_s) due to biofouling for a range of pipe diameters (50-200 mm) relative to a non-fouled concrete pipe.

The magnitude of the change in surface roughness caused by biofouling is a function of the physical nature of the biofouled surface (Stoodley et al. 1998b; Schwartz et al. 1998; 2003; Barton 2006; Andrewartha et al. 2008), and therefore, it is not solely based upon an absolute parameter such as the roughness height. Consequently, the effective roughness of a biofouled surface can be significantly higher than predicted based upon the roughness height and wall similarity hypothesis alone (i.e. using the classical equivalent sandgrain roughness) (Characklis 1973; 1981; Picologlou et al. 1980; Stoodley et al. 1998b; Schultz 2000; Andrewartha et al. 2008). For instance, Schultz and Swain (1999) observed increases in flow resistance of between 33-68% following the development of biofilms with mean thicknesses as low as 160-350 μm.

The variations in roughness caused by biofouling can affect the duty point of a given pumped system (Lambert et al. 2008), increase maintenance costs (Barton et al. 2008) and decrease the operational efficiency, potentially resulting in system failures. The change in surface roughness dynamics caused by biofouling will also affect the conveyance of sediments and loose deposits, which is an essential aspect of an efficient DN, as failure to do so could result in clogging, surcharge and ultimately flooding issues (Guzmán et al. 2007; Chughtai and Zayed 2008). All of which, could have significant financial and environmental implications to asset holders.

It should be noted that other mechanisms beyond biofouling, such as the accumulation of sediments, loose deposits and FOGs (fats, oils and greases) (see Figure 1.1) can also contribute to fouling within DNs and subsequently impair their ability to convey flow (Ackers et al. 1963; Guzmán et al. 2007). However, relatively speaking the constituents of these mechanisms only cover a small percentage of the overall pipe's wetted perimeter, and are local to one area (typically at the invert, Figure 1.1) and although, their impact on hydraulic efficiency can sometimes be extreme, they are not investigated in detail as part of the current study. The primary focus of the current study is based upon the global impact of biofouling and in particular, that of biofilm development, which typically affects and covers the whole wetted perimeter of a pipe. Though, the influence of biofilm development on a pipe's ability to convey non-cohesive sediment is briefly evaluated as part of the current study.

The presence of a biofilm within DNs is realistically unavoidable, and consequently its surface dynamics, as opposed to the characteristics of the underlying "clean" engineered surface, should represent the "true" effective roughness of all pipelines in service. Therefore, the accurate evaluation of a biofouled surface is imperative for both efficient pipeline design (i.e. optimum flow rate) and effective fouling control strategies (both in terms of controlling biofouling itself and other fouling mechanisms). However, this is not possible through the application of conventional design approaches, such as British Standard BS EN 752 (2008) and *Sewer for Adoption* (Water Research Centre (Great Britain) 2006), which utilise traditional frictional relationships and constant surface roughness scales. In particular, the C-W equation and k_s have been deemed inadequate for biofouled surfaces in their current form (Schultz and Swain 1999; Schultz 2000; Barton et al. 2004; Barton 2006; Lambert et al. 2009; Perkins et al. 2012; 2014). Consequently, current design practices inadvertently fail to design a system as efficiently as it could be, which could have both financial and environmental implications in the long term. The inadequacies of current design practices is a reflection of the current state of scientific understanding on the topic of biofouling within DNs, which is fundamentally sparse and lacking in assessment of the key interacting processes over a wide

range of conditions, as highlighted by the literature review presented within Chapter 2 and by Cowle et al. (2014). Furthermore, the current prevailing understanding on biofilm-flow interaction is predominantly based upon observations within hydropower systems (Barton et al. 2004; Barton 2006; Andrewartha 2010; Perkins et al. 2013; 2014; Walker et al. 2013) and marine environments (Schultz and Swain 1999; Schultz 2000), which have inherently different ecologies to that expected within DNs. This would be reflected in the respective system's biofilms. The increasing awareness and emphasis on sustainability within the water industry with respect to both the capacity and efficiency of existing networks and future installations means it is now more important than ever to change the perception of biofouling and address the inadequacies in current pipe design approaches.

The overall aim of the current study was to contribute to a significantly improved scientific understanding on the hydraulic efficiency of wastewater pipelines; for the purpose of instigating a step-change in pipeline design theory through the incorporation of the dynamic and case-specific nature of biofouling. This was achieved using a multidisciplinary approach, based principally on experimental measurements and observations recorded in a controlled laboratory environment. Biofilms were incubated with a representative, albeit synthetic wastewater on a High Density Polyethylene (HDPE) surface within a purpose built pilot-scale pipeline for 20 d (or 480 h). The frictional resistance of the cultivated biofilms was comprehensively established using both boundary layer and head loss measurements. The biofilms molecular composition, which was determined using polymerase Chain Reaction-Denaturing Gradient Gel Electrophoresis, DNA and Extracellular Polymer Substances quantification was used to support the hydrodynamic measurements.

The pipeline facility, which was designed for the sole purpose of evaluating biofilms within DNs is comprehensively outlined in Chapter 3. The physico-chemical composition of the synthetic wastewater used within the current study is also presented within Chapter 3. The synthetic wastewater was purposely designed to be equivalent to that of naturally occurring wastewater found within DNs in Europe. The suitability of the pipeline to facilitate the intended boundary layer and biofouling investigation was determined under non-fouled conditions and is outlined in Chapter 4. The conventional approaches for assessing turbulent pipe flow were also evaluated experimentally within Chapter 4; for the purpose of contributing to knowledge on the topic of smooth pipe flow.

The primary ecological factor under review within the current study was flow hydrodynamics. Three different steady state flow regimes including, the average freestream velocities of 0.60, 0.75 and 1.00 m/s were assessed discretely. The discrete nature of the

investigation allowed for a clear interpretation on how each of the respective flow regimes affected the biofilms frictional resistance over time. The results of this phase, which is referred to as the incubation phase are outlined in Chapter 5. A biofilms influence on the von Kármán constant, which is an integral aspect in the determination of frictional resistance from boundary layer and head loss data was also established within the incubation phase.

Arguably, given the highly variable nature of a typical DN the influence of changing conditions on mature biofilms has a more industrial relevance than the discrete flow evaluations outlined in the incubation phase (in Chapter 5). The prevailing conditions within DNs ensure that the development period for a wastewater biofilm is relatively short, which also highlights the need to understand biofilms in their mature state as it will represent the most frequently occurring condition. Consequently, once the biofilms had reached a state of equilibrium in terms of their frictional resistance they were then subject to varying flow regimes. The results of this phase of testing, which also incorporates all the molecular analysis undertaken within the study are outlined in the mature phase and are presented within Chapter 6. A brief discussion on the impact of mature biofilms on sediment transport in pipes is also outlined within Chapter 6.

A brief and independent investigation on the impact of biofouling within drinking water distribution systems is presented at the end of this thesis in Chapter 7. The purpose of this investigation was to determine the influence of different pipe materials and flow regimes on biofilms incubated with drinking water. In this investigation biofilms were incubated on four different pipe materials, under two steady state flow regimes within purpose built flow cell styled biofilm reactors. Despite, the limited nature of this aspect of the study considerable contributions to knowledge were established.

The main conclusions and industrial applications of the current study are given in Chapter 9. The recommendations for further research on the topic are also outlined within Chapter 9.

Chapter 2 Literature review

2.1 Introduction

A review of the current scientific literature on biofilms and biofouling is presented in this chapter. The overall aim of review was to critically review biofouling impact on the hydraulic efficiency of pipelines used within water management projects; and identify the current gaps in knowledge which will inform the research direction of the current study. Though the primary emphasis of this study was on DNs, the impact of biofouling within drinking water distribution systems (DWDSs) is also reviewed within this chapter. The chapter begins by outlining the practical implications of biofouling to asset holders. The discrete aspects of a biofilm are presented and the key processes involved within biofouling are then reviewed. The influence of pipe ecology on biofilms and biofouled surfaces are highlighted and discussed. An overview of the governing equations and key parameters required to investigate the effects of biofouling within pipelines is then presented within this chapter. The chapter ends by providing rational suggestions of how biofouling should be treated in an engineering context. The chapter finishes with a short summary.

2.2 Nature of biofouling

Any pipe conveying a liquid is potentially susceptible to biofilm development and thus biofouling to some degree, as bacteria, fungi, mosses and invertebrates seek to exploit the desirable growth conditions that the pipe surface provides. Such ecological advantages include: a constant source of nutrients, sufficient aeration and removal of waste products (Batté et al. 2003; Costerton and Lewandowski 1995). The resulting microbial system, typically dominated by *Bacteria*, and in particular members of the phylum *Proteobacteria* (namely *Betaproteobacteria* and *Gammaproteobacteria*) are prevalent within DWDSs. Biofilms are generally classified in terms of their structure (on the macro-scale) as either low-form gelatinous or filamentous (or both), with the former being more common within pipeline systems, especially within DNs (LeChevallier et al. 1987; Callow 1993; Barton et al. 2008; Santo Domingo et al. 2011; Douterelo et al. 2013). The presence of these complex microbial structure on the surface of a pipeline can significantly increase its frictional resistance (Seifert

and Kruger 1950; Sharp 1954; Minkus 1954; Picologlou et al. 1980; Barton et al. 2008; Lambert et al. 2008; 2009; Perkins et al. 2013; 2014). For instance, Seifert and Kruger (1950) and Sharp (1954) reported that a 0.66 mm "ripple-like slime" layer and a 9.4 mm "slime" layer reduced the flow capacity of standard and rising water main by 55% and 22%, respectively. In the case of the rising main, this consequently resulted in a 13% increase in pumping costs over a period of 8 years (Sharp 1954). Similarly, Minkus (1954) reported that a biofilm layer of between 0.8-1.6 mm reduced the flow capacity of a 0.9 m diameter concrete and 1.1 m diameter iron water pipelines by 23% (in 5 years) and 12% (in 2 years), respectively. Therefore, biofouling is a major concern to the water and wastewater industries, where efficient and sustainable systems are a priority.

The ecology of a pipeline is predominantly governed by the application in which it is employed. Typical conditions within DWDSs and DNs are inherently different, and this is reflected in the resultant biofilm incubated within the each of the respective environments. The prevailing conditions within DWDS (i.e. high turbulent flow velocities, low nutrient contents) generally inhibit biofilm development (Stoodley et al. 1998a). In contrast, conditions within DNs (i.e. low velocities, high nutrient content and microbial diversity) are likely to significantly favour biofilm development (Stoodley et al. 1998a), therefore, the resultant effective roughness of the system would be considerably higher when compared to its initial "clean" condition. For example, biofilms within DNs have been reported to cause the Manning's roughness coefficient, *n* to increase up to 0.043, which is the equivalent of the drag imparted by large stones and cobbles in rivers (Guzmán et al. 2007). Such an increase in frictional resistance within DNs is likely to contribute and/or exaggerate other fouling mechanisms, namely the accumulation of more cohesive sediments and loose deposits (Guzmán et al. 2007, Vignaga 2012). Moreover, the lack of comprehensive frictional resistance information (including an accurate means of evaluation) for biofouled surfaces would make it difficult to adequately account for the impact of sediment accumulation in the future. For instance, in order to ensure a drainage pipeline operates at a minimum self-cleaning velocity (typically > 0.60 m/s), whereby sediments and other loose deposits remain suspended within the water column or at least deposited in areas and amounts which can be re-suspended during the next flow event (Guzmán et al. 2007), an accurate wall roughness must be known. Otherwise, the deposits will accumulate upon the surface, further impeding the flow and potentially resulting in clogging, surcharge and ultimately flooding issues (Chughtai and Zayed 2008).

Moreover, an accurate underlying wall roughness is also required in the modelling of effective flushing strategies for DNs (Creaco and Bertrand-Krajewski 2009; Shirazi et al.

2013). Within DNs, biofilms also contribute to the production of unwelcome gases, namely hydrogen sulphide and methane, which present their own problems for the industry, ranging from odour and corrosion issues, to potentially endangering maintenance crews (Guisasola et al. 2008; Nielsen et al. 2008).

Hence, biofouling is likely to be more substantial and have a more significant impact in DNs than in DWDSs. This is the general perception within the water and wastewater industries. Nevertheless, greater emphasis within the industry and in literature is put on DWDSs, due to: i) the greater pumping requirements of the application and ii) the detrimental impact that biofilms can have on water quality. Such water quality issues include impaired taste, odour and colour; in addition to causing potential health problems to consumers, ranging from viral and bacterial gastro-enteric diseases, to infections such as hepatitis A and giardiasis (Prévost et al. 1998; Momba et al. 2000; Husband et al. 2008; Douterelo et al. 2013). From an engineering standpoint, biofilm development within DWDSs would also likely contribute to undesirable corrosion and nitrification issues within the system. Furthermore, biofilms can contribute and/or exaggerate the accumulation of Iron and Manganese, which like biofouling can affect the whole wetted perimeter of a DWDS. Iron and Manganese accumulation represent a major problem to the water industry as it can significantly affect a pipe's hydraulic efficiency. Consequently, within DWDSs, the impact of biofouling on surface roughness is generally considered to be of secondary importance, especially with regards to the aforementioned water quality issues. This is because poor water quality will generally result in more customer complaints. Furthermore, water quality is usually compromised by a very thin biofilm (i.e. < 30 μm), therefore, it is the general practice of asset holders to make use of disinfectants and flushing techniques to minimise biofouling within DWDSs. However, biofilms are known to have a high resilience to these control measures (Douterelo et al. 2013) and in any case, even a relatively thin biofilm (i.e. < 160 μm) can potentially cause a considerable increase in frictional resistance (Schultz and Swain 1999), particularly in long pipe runs. The early observations within water mains by Seifert and Kruger (1950), Sharp (1954) and Minkus (1954), also highlight the potential impact that biofouling can have on DWDSs, in spite of the reported biofilm thicknesses (i.e. the order of 1.0 to 9.4 mm) being unrepresentative of biofilm typically found within modern, well maintained DWDSs (which seldom exceed 1 mm). Furthermore, the resultant decreases in flow capacity within DWDSs as a result of biofouling, will also increase the planktonic (free-floating) bacteria concentrations; through an increase in the pipelines hydraulic retention time (HRT) (Eisnor and Gagnon 2003). Consequently, the water quality is impaired and the likelihood of further fouling and fouling issues (i.e. public health problems) is increased.

Both water and wastewater industries have expressed concerns over hydraulic efficiency, although the concerns within the former are arguably superseded by concerns relating to biofilm induced water issues. Furthermore, despite the magnitude of growth between the two applications being significantly different the impact will nonetheless be considerable in both cases for different reasons, e.g. in terms of operational performance/costs and public health.

The industry's perception on biofouling as outlined within this section was established from private conversations with some of the leading members of the water industry and practicing engineers.

2.3 Process of biofouling

The majority of all biofilm development occurs within a thin layer located near the solid-liquid interface, and which coincides with the boundary layer as defined in fluid mechanics (Schlichting 1979). The boundary layer thickness, δ is generally defined as the distance normal to wall where the velocity differs by 1% from the maximum freestream velocity, U. Typically, biofilm development involves four stages, (see Figure 2.1), namely: conditioning stage; initial cell attachment stage; main development stage; and equilibrium stage.

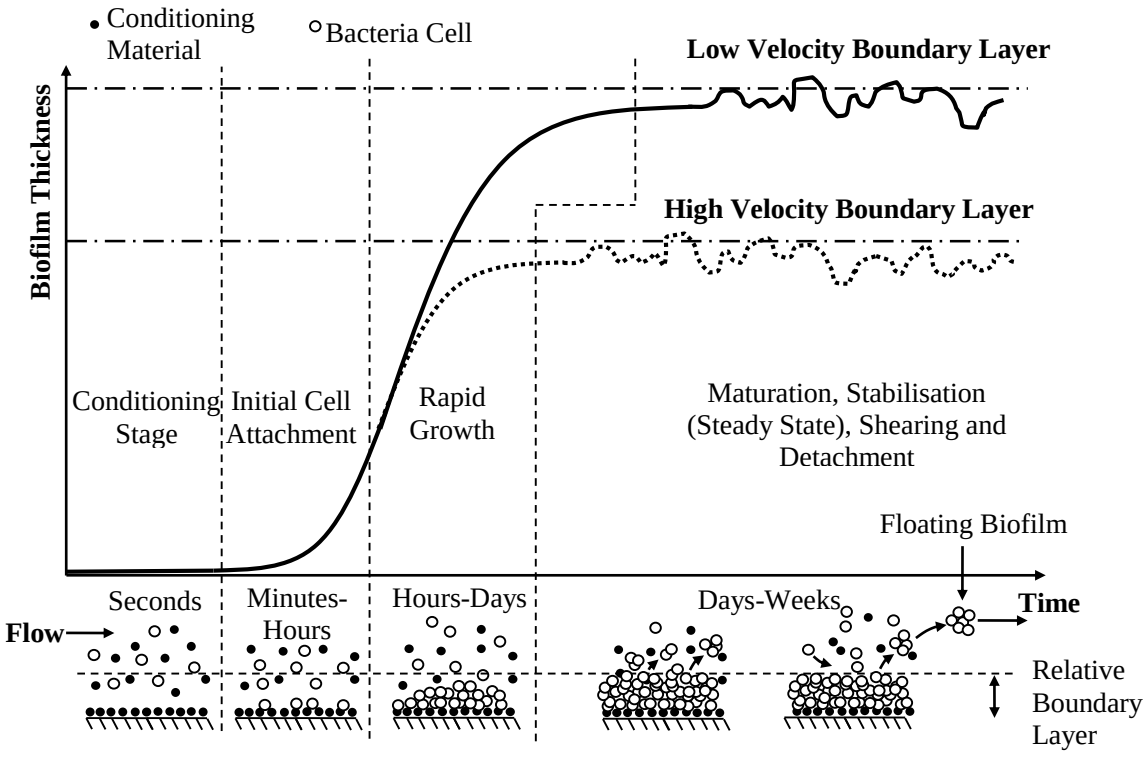

Figure 2.1 Idealised biofilm development for a high and low flow velocity scenarios (Characklis 1981; Melo and Bott 1997; Flemming 2002).

2.3.1 Conditioning stage

The conditioning stage is initiated within seconds of the biological matter entering the pipeline, with the spontaneous adsorption and formation of a conditioning layer or film. The conditioning film is formed mainly by organic molecules, however, films consisting of inorganic materials such as metallic oxides and fine clays or slit particles have also been documented (Chamberlain 1992; Callow 1993). The duration of the conditioning stage is commonly referred to as the lag-time, λ_A and is a function of the operational conditions of the pipeline including fluid viscosity, flow hydrodynamics and surface roughness (see Figure 2.1 and Table 2.1).

2.3.2 Initial cell attachment stage

Initial microbiological adhesion occurs during the initial cell attachment stage, this is predominately encouraged by the conditioning film, owing to: i) neutralisation of the surface charge, ii) provision of nutrients and iii) polarisation of the forces between the film and the microorganisms. Therefore, the conditioning film is essentially the catalyst in the initial attraction and attachment of the discrete planktonic bacterium, and is therefore a vital component in the successful development of biofilms within pipelines (Callow 1993; Callow and Callow 2000). For instance, it has been stated that the interactions between the substrate and the conditioning film is the key to subsequent attachment, and so an improved understanding of the physico-chemical properties of the conditioning material is crucial to the development of effective control strategies (Callow 1993; Callow and Callow 2000). Initially, the surface will only consist of a few randomly distributed cells (or initial colonisers), adhered to the surface via weak, reversible forces known as Van-der-Waals forces (Vigeant et al. 2002). Cell division and Extracellular Polymer Substances (EPS) secretion then follows, along with the formation of substantially stronger bonds, which anchor the now densely packed cell matrix to the pipe surface (Melo and Bott 1997).

2.3.3 Rapid growth stage

This stage is characterised by further colonisation and growth which takes place over time. This results in an increasingly thicker and denser structure, which protrudes further into the flow. Within the boundary layer, viscous effects cause the flow velocity to decrease steadily to zero at the wall (i.e. no-slip conditions), as shown by Figure 2.2. In the near wall region the turbulent fluctuations of the flow are considerably reduced (Schlichting 1979). Therefore, as the biofilm structure grows in the direction normal to the wall, different parts of the biofilm will be subject to different conditions, which become gradually more hostile as the distance from the wall increases (as shown in Figure 2.2). This stage of development continues until a point of equilibrium is reached between the favourable and adverse growth conditions.

Typically, under idealised conditions (i.e. sufficient nutrient availability) which would be representative of the environment within many drainage networks, a state of equilibrium would occur when the biofilm has extended through the boundary layer and into the outer flow region. At this point the biofilm's internal cohesion is significantly impaired by the numerous adverse conditions associated with the outer flow region, predominantly by increased flow shear.

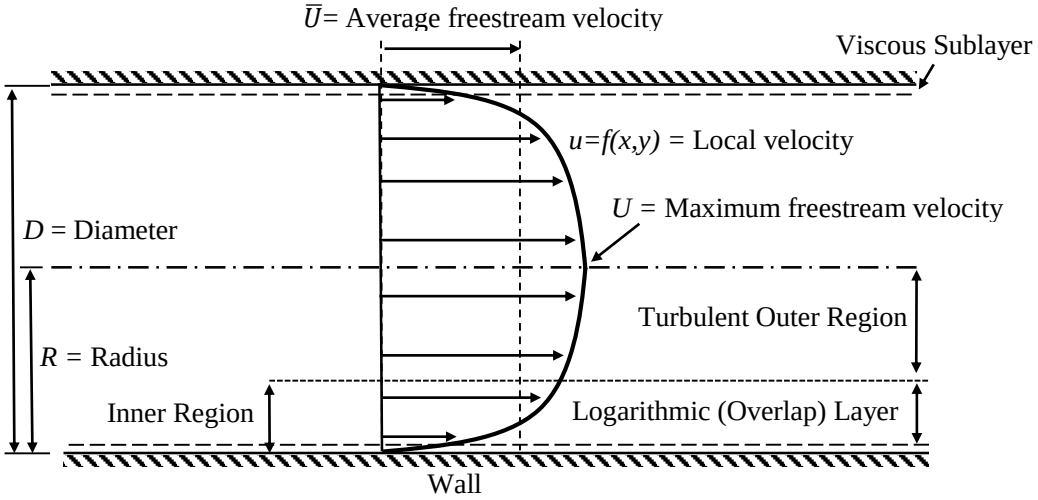

Figure 2.2 The velcoity profile in fully developed turbulent pipe flow.

2.3.4 Equilibrium stage

Provided that the environmental and operational conditions (e.g. flow velocity, boundary layer structure, nutrient content etc.) remain reasonably constant, the biofilm thus formed tends to reach a pseudo-steady state. Dependant on the conditioning it can take between 10 to 385 d for a biofilm to reach structural maturity (Hallam et al. 2001; Boe-Hansen et al. 2002**)**, with the latter typically associated with low nutrient and DWDS conditions (i.e. Assimilable Organic Carbon, AOC in the order of 5.0 µg/L). In contrast, in terms of a biofilm's frictional behaviour, studies have shown that in favourable nutrient conditions, it can take a biofilm between 100-420 h to reach a state of equilibrium (Picologlou et al. 1980; Lambert et al. 2008; 2009; Andrewartha 2010). For instance, Andrewartha (2010) found that the drag induced by a biofouled plate was the same after 2 weeks of cultivation as to that observed after 16 weeks of cultivation.

Once a biofilm has formed on a section of a pipe under favourable conditions and locations (i.e. at joints and bends), it may quickly spread through the entire pipeline system and induce

colonisation in other areas that were not initially favourable to growth. This happens as cells and/or whole clusters are "sloughed off" the surface and are carried by the flow as floating biofilms which then settle downstream (Kjelleberg and Givskov 2007; Stewart 2012). Further growth can be fostered downstream by the waste generated by the upstream biofilms, which can be utilised as either a conditioning material or as a direct source of nutrients. Therefore, the attainment of a pseudo-steady state in a region of a pipeline is not necessarily indicative of equilibrium throughout the entirety of the system.

It should be noted that in any given pipeline, the properties of the mature biofilm such as its overall structure; surface topography; thickness; morphology and microbial composition (Characklis 1981; Barton 2006; Douterelo et al. 2013) will change over time. This is due to competition between biofilm species, the relatively short term survival of biofilm species (the life and death cycle), and the varying (seasonal and daily) operational and environmental dynamics of the pipeline Table 2.1.

Table 2.1 Key aspects and perceived impacts on i) substrate accumulation ii) biofilm structural composition and iii) biofilm dynamic behaviour due to flow interaction, within pipelines

Factor(s)	***Impacts upon Growth***			***References***
	(i)	***(ii)***	***(iii)***	
Residual Disinfectant Concentration*		✓		Cloete et al. (1998), Hallam et al. (2001), Tsvetanova (2006), Zhou et al. (2009)
Flow hydrodynamics	✓	✓	✓	Pedersen (1990), Stoodley et al. (1998a), Stoodley et al. (1998b), Cloete et al. (2003), Lauchlan et al. (2005), Tsvetanova (2006), Lambert et al. (2008; 2009)
Nutrient and biological content		✓		Costerton and Lewandowski (1995), Melo and Bott (1997), Stoodley et al. (1998a), Gjaltema et al. (2004)
Surface Material	✓			Pedersen (1990), Van der Kooij et al. (1995), Niquette et al. (2000), Hallam et al. (2001), Manuel et al. (2007), Zhou et al. (2009)
Seasonal/Daily Variations in Conditions		✓	✓	Cloete et al. (1998), Hallam et al. (2001), Tsvetanova (2006), Zhou et al. (2009)

Only applicable within certain drinking water distribution systems

2.4 Causes of biofouling

A number of factors impact upon biofilm development within pipelines and the resultant growth interacts with the system hydraulics. This section focus on a review of the key factors as listed in Table 2.1 with the exception of disinfectant concentration which has been comprehensively reviewed over the years, most notably by Bridier et al. (2011).

2.4.1 Flow hydrodynamics and nutrient availability

There is an inherent link between flow hydrodynamics and nutrient availability on biofilm development, owing to their influence on mass transfer and diffusion rates. The mass transfer and diffusion rates of a system are predominantly governed by the level of turbulence in the flow, which is usually estimated by the dimensionless parameter, Reynolds number, *Re*. The *Re* represents the balance between the magnitude of inertial and viscous forces:

$$Re_x = \frac{\rho \bar{U} x}{\mu} \qquad \textit{Equation 2.1}$$

where x is a characteristic length scale (i.e. pipe diameter, D), $\bar{U}$ is the average freestream velocity, ρ is the Density of fluid and μ is the dynamic viscosity of the fluid.

Using D as the characteristic length scale flows within pipes generally conforms to the following patterns; for $Re_D \leq 2000$, laminar flow exits; for $2000 < Re_D < 4000$, the flow is transitional; for $Re_D > 4000$, the flow is turbulent. Since high *Re* values are associated with high velocity flows, it follows that viscous effects are less important in establishing the flow condition in the turbulent flow regime. Conversely low *Re* values indicate that viscous effects significantly influence the flow condition under relatively low velocites. The flow within most DWDSs and DNs is typically turbulent in nature. However, laminar flow conditions can be observed in areas of low water consumption (i.e. rural areas) and/or towards the end of long branches and the network periphery, where flow can be very low or periodically stagnant.

Conceptually, the boundary layer of turbulent flows can be divided into two regions, namely the inner and outer regions, as shown in Figure 2.2. The inner region of the boundary layer generally consists of two layers namely; (i) the viscous or laminar sublayer and (ii) the logarithmic sublayer (Schlichting 1979). The viscous sublayer is closest to the pipe wall and its thickness δ' is given by;

$$\delta' = \frac{5v}{u^*} \qquad \textit{Equation 2.2}$$

where v is the kinematic viscosity of the fluid and u^* is the shear velocity.

The shear velocity is given by;

$$u^* = \sqrt{\frac{\tau_w}{\rho}} \qquad \textit{Equation 2.3}$$

where τ_w is wall shear stress.

Hence, the value of δ' is a function of the type of fluid and the flow condition. For example, an increase in flow rate, Q leads to an increase in u^* and a decrease in δ' for the same fluid, i.e. it causes a reduction of the boundary layer thickness. Beyond the logarithmic layer lies the outer flow region, where the mean flow velocity is that of the free stream. As illustrated in Figure 2.3, there are three types of boundary layers, namely hydraulically smooth (Figure 2.3a), transitional (Figure 2.3b) and hydraulically rough (Figure 2.3c and Figure 2.3d). The classification depends upon the thickness of the absolute surface roughness height (k) relative to δ'. A boundary layer is classed as hydraulically smooth for $k < \delta'$ and it is classed as hydraulically rough for $k > \delta'$. For $k \approx \delta'$, the boundary layer is classified as transitional. Furthermore, in terms of the k_s, Nikuradse (1933) found that for a surface consisting of closely packed, nearly mono-disperse sandgrain roughness (i.e. k_s) the flow was smooth for k_s^+ ($=k_s v/u^*$) ≤ 5, transitionally rough for $5 < k_s^+ < 70$, and fully rough for $k_s^+ \geq 70$. The average sandgrain height was used to represent k_s (Nikuradse 1933). For each of these classifications, the influence of the surface roughness on biofilm development is inherently different, with the greatest impact occurring under hydraulically rough conditions and the least impact under hydraulically smooth conditions.

Previous studies have shown that the boundary layer structure is altered by the presence of a biofilm (Schultz 2000; Andrewartha and Sargison 2011). Andrewartha and Sargison (Andrewartha and Sargison 2011) found that biofilms altered both the turbulent structure and thickness of the boundary layer. The altered boundary layer then impacts upon further biofilm development, thereby establishing a dynamic two-way (symbiotic) feedback relationship. This process has a subsequent effect on flow resistance and Q. Such changes in the operating conditions affect δ' further, as well as its relationship to k, and so on until a point of equilibrium can be reached. This complex matrix of interacting causes and effects is illustrated in Figure 2.4. If these conditional changes are significant, then they can be considered as influential upon the resulting biofilm development as flow hydrodynamics.

The degree of influence that flow hydrodynamics can have upon biofilm development is highly dependent on the system's flow classification (Lewandowski and Stoodley 1995; Stoodley et al. 1998a).

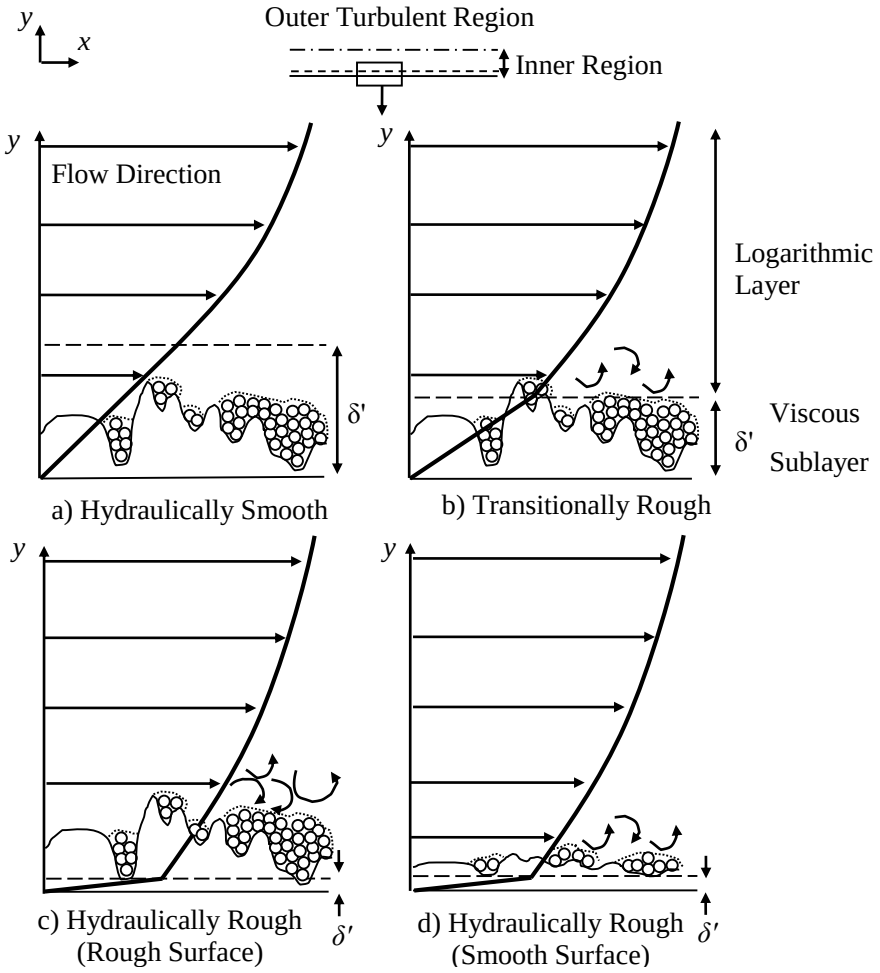

Figure 2.3 Boundary layer classifications, including; a) hydraulically smooth, b) transitionally rough, and c)-d) hydraulically rough, for a smooth and rough surface (Barton 2006).

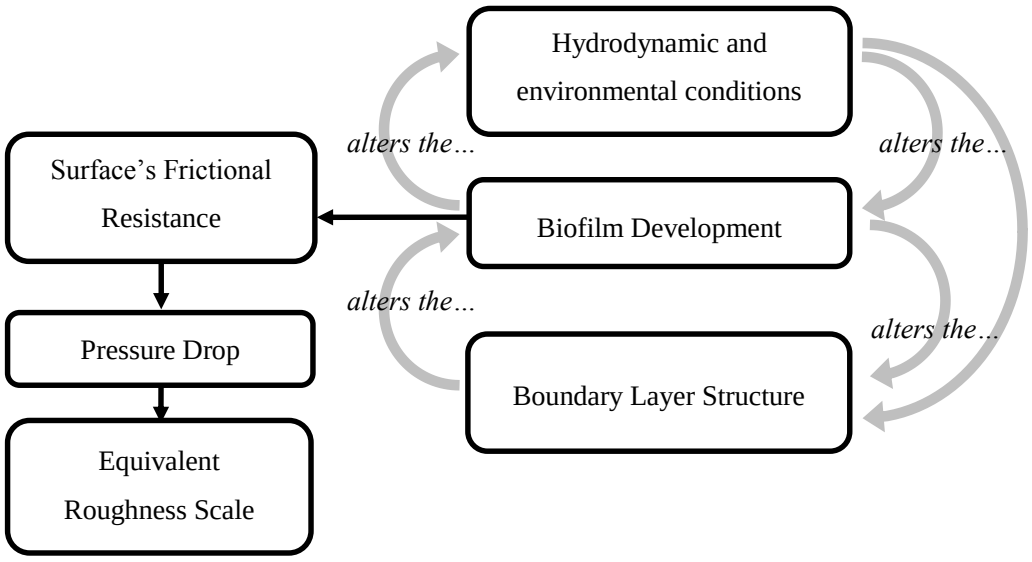

Figure 2.4 Schematic representation of the dynamic feedback relationship that exists between the boundary layer hydrodynamics, biofilm development, operational and environmental conditions.

In laminar flow conditions there is a relatively thick boundary layer. The ample boundary layer and the low near wall shear forces are in theory conducive to successful biofilm development (Stoodley et al. 1998a). However, such a large boundary layer combined with the inherent lack of mixing within laminar conditions is non-conducive to successful mass transfer, as it is likely to retard the influx and diffusion of microorganisms, dissolved oxygen and nutrients to the surface, thus potentially impairing overall biofilm growth rate. On the other hand, within DWDSs which utilise disinfectants, the retarded diffusion rates are likely to reduce the disinfectant's effectiveness, which is of benefit to the biofilm. However, in reality and in most cases this is not likely to be a factor, as laminar conditions are most prevalent within DWDSs at the network periphery, where disinfectant levels are typically at their lowest.

Low flow velocities in laminar conditions promote planktonic growth, through an increase in HRT, which would subsequently increase the likelihood growth on the surface (Eisnor and Gagnon 2003). Ultimately, laminar conditions provide numerous benefits for successful and significant biofilm growth, although, its overall growth rate would be impaired by the low diffusion rates. Consequently, the resultant biofilm coverage under laminar conditions is generally irregular and isolated across the surface (De Beer et al. 1994; Lewandowski and Stoodley 1995; Stoodley et al. 1998a).

The overall effect of a biofilm on frictional resistance under laminar conditions has been found to follow the traditional smooth pipe friction law relationship (Lambert et al. 2008). Whereby, the overall pressure drop is primarily influenced by skin friction and hence by the total surface area of the biofilm as opposed to the shape or structure of the fouled surface (Stoodley et al. 1998b).

In fully turbulent flow conditions, the laminar sublayer is reduced significantly in thickness. In such situations, the frictional resistance of the biofouled surface is known to increase dramatically with *Re* (Lambert et al. 2008, Perkins et al. 2013; 2014). The overall pressure drop in turbulent conditions is influenced to a greater extent by surface roughness, which produces form drag when sufficiently great (i.e. from transitional to fully rough). Therefore, the structure, shape and nature of a fouled surface have an influence the overall pressure drop in turbulent flow conditions (Stoodley et al. 1998b). In turn, these characteristics are significantly affected by the turbulence. The considerably reduced laminar sublayer and increased turbulent mixing in the near proximity of the wall (induced by the presence of the roughness element within the logarithmic region) greatly increases the influx and diffusion of microorganisms, dissolved oxygen and nutrients to the surface. The resultant biofilm

coverage is likely to be more dense and compact than in laminar conditions (Dumbleton 1995; Percival et al. 1999). The additional turbulence will also result in more efficient waste removal. The favourable mass transfer and diffusion rates will likely increase the degree of fouling, and the inherent link between turbulent flow and surface roughness will significantly accentuate its overall impact. For instance, Percival et al. (1999) found more rapid and extensive biofilm growth at relatively high *Re* (including Re_D = 1.90x10^4 and 3.50x10^4), which was followed by a statistically steady-state. However, the inherently high shear forces associated with high *Re* will also reduce the likelihood of the material adhering to the surface. For instance, Stoodley et al. (1998a) found that although, a biofilm grown under high turbulent conditions reached a statistically steady state earlier than a biofilm grown under low flow conditions its growth rate was higher under the low flow conditions. The increased accumulation rate at low flow conditions was a result of the lower detachment rate relative to the growth rate, as defined by the following mass balance relationship: accumulation rate = attachment rate + growth rate – detachment rate (Bryer and Characklis 1981). This would also explain why Lambert et al. (2008) observed a significant decrease in the biofilm thickness as a result of the increased turbulence in the vicinity of a pipe bend. Flow shear is therefore, a key controlling factor on biofilm development within pipelines, and its resultant equivalent roughness scale.

The favourable mass transfer and diffusion rates associated with turbulent flow conditions will also amplify the overall impact of nutrient loading, providing the overall shear force remains below the critical levels for biofilm detachment (which is typically equal to the conditioning shear). For example, Melo and Bott (1997) reported a 400% increase in biofilm thickness when nutrient levels increased from 4.0 to 10.0 mg/l, within a system in which the average streamwise velocity remained constant at 1.20 m/s. Similarly, for *Pseudomonas aeruginosa* it has been documented that high nutrient concentrations foster its formation as a biofilm within DWDSs (Peyton 1996). Lambert et al. (2008; 2009) found that an increase in nutrient loading significantly increased biofilm development both in terms of its physical thickness and equivalent roughness scale. Conversely, irrespective of the favourable mass transfer conditions, if the nutrient loading is reduced or is originally relatively low, the opposite is likely to occur, and the overall growth and development will tend to be more restricted and sparse, i.e. similar to that in laminar conditions (Melo and Bott 1997; Stoodley et al. 1998a; Volk and LeChevallier 1999; Gjaltema et al. 2004). For instance, Volk and LeChevallier (1999) found that overall density of a biofilm decreased with decreasing nutrient loading. Naturally, the starvation of a biofilm will lead a reduction in growth and ultimately, biofilm detachment (Hunt et al. 2004).

The typically dense and compact coverage inherent within turbulent conditions (with sufficient nutrient loading) may lead to "skimming flow", i.e. the relocation of the velocity profile to the top of the roughness element – which is, in this case, the top of the biofilm layer (Stoodley et al. 1998b). Skimming flow has been documented to cause significantly higher flow resistance, and can be triggered by as little as an 8.3% surface coverage (Nowell and Church 1979). Other factors contributing to form drag, namely the biofilm's shape and thickness, are likely to have a greater impact upon the overall pressure drop under turbulent flow conditions after the onset of skimming flow (Stoodley et al. 1998b).

Another important hydrodynamic aspect is that of the formation of elongated cell clusters in the downstream direction (known as streamers) which have been documented to occur under high flow conditions (Lewandowski and Stoodley 1995; Stoodley et al. 1998a; 1998b; Percival et al. 1999). However, such filamentous biofilms can also develop irrespective of the hydrodynamic conditions, provided that certain bacteria species, such as *Hyphomicrobium sp., Spharotilus sp.* and *Beggiatoa sp.* are present. The resulting cell formation will further aid cell adhesion by providing a greater attachment and shelter area, in addition to providing the embedded microorganisms with a greater access to essential nutrients and dissolved oxygen within the flow (Percival et al. 1999). Consequently, systems and areas of high turbulence (i.e. contractions, expansions and bends) are likely to foster substantial and dynamic biofilm growth, but the maximum biofilm thickness is limited by the inherently high shear conditions. Therefore, unlike within laminar conditions, current design practices and theories cannot accurately evaluate the resultant growths' frictional behaviour. This, coupled with the complex growth patterns inherent within turbulent conditions makes the task of accurately designing an efficient pipeline challenging, if not impossible.

2.4.2 Pipe material

Microorganisms have been found to adhere and thrive upon a wide variety of pipe materials, ranging from concrete and metal, to plastic-based materials, such as HDPE and Polyvinyl Chloride (PVC) (Kerr et al. 1999; Niquette et al. 2000; Momba and Makala 2004). The properties of these materials have been shown to have a significant impact upon microbial attachment and subsequent biofilm development include surface roughness, chemical composition and resistance to corrosion and abrasion.

2.4.2.1 Surface roughness

Typically, all microbial material found within pipelines are likely to be significantly smaller than the gaps and crevices that make up the overall surface roughness. Therefore, they will often find shelter and protection from turbulent flow and shear forces within these roughness

elements. This type of protection is only required within the logarithmic region, and consequently surface roughness is only likely to affect microbial accumulation and biofilm development when the boundary layer is classified as either transitional (see Figure 2.3b) or fully rough (Figure 2.3c). However, when the system is classified as hydraulically smooth (see Figure 2.3a), the surface roughness is unlikely to have any significant impact upon the degree of microbiological material attachment, other than providing a greater surface area. This is because the relatively low velocities occurring in the laminar sublayer are less likely to dislodge deposited materials. Moreover, in situations of low resistance to attachment, biofilms may fixate upon the roughness peaks or high points to gain an ecological advantage within the flow regime. In such situations, traditional hydraulic theory is likely to apply irrespective of the presence of a biofilm.

Within transitional or hydraulically rough conditions the magnitude of the absolute surface roughness will either promote or hinder microbial attachment and development by providing (or not) sufficient attachment area and protection. This implies that microbial adhesion is likely to be slower upon smooth pipe materials, compared to rough materials (Lauchlan et al. 2005; Barton 2006; Tsvetanova 2006). Furthermore, smoother surfaces will generally induce higher near wall velocities and provide less protection and attachment areas than rougher materials. In contrast, the rougher the material, the greater the area of protective and attachment potential, both of which favour greater microbial accumulation (Pedersen 1990; Verran et al. 1991; Costerton and Lewandowski 1995; Percival et al. 1999; Gjaltema et al. 2004; Kurth 2008; Yu et al. 2010). By favouring initial biofilm development when internal cohesive forces are relatively weak, rough surfaces are likely to accommodate more mature biofilms, as a biofilm can propagate out of the numerous roughness crevices, following the formation of strong and permanent internal bonds (see Figure 2.5). Naturally, the opposite is true for relatively smooth materials. It should be noted, that roughness is a relative concept; all materials will appear rough under sufficient magnification. In the current study a material is considered to be smooth if the material conforms to the smooth flow criteria (i.e. $k_s v/u^* \leq 5$). The concept that smoother surfaces foster less growth is supported by the findings of several authors who have found that plastic- and copper- based materials (which are typically very smooth), inhibit biofilm growth over both the short and long term (Pedersen 1990; Kerr et al. 1999; Niquette et al. 2000; Yu et al. 2010). In particular, Niquette et al. (2000) found that the density of fixed biomass on a cement-based surface (typically rough) was 2.63 times greater than on PVC. However, this may not always be the case, as shown by Momba and Makala (2004) where it was reported that concrete-based materials supported less fixed biomass than plastic-based materials.

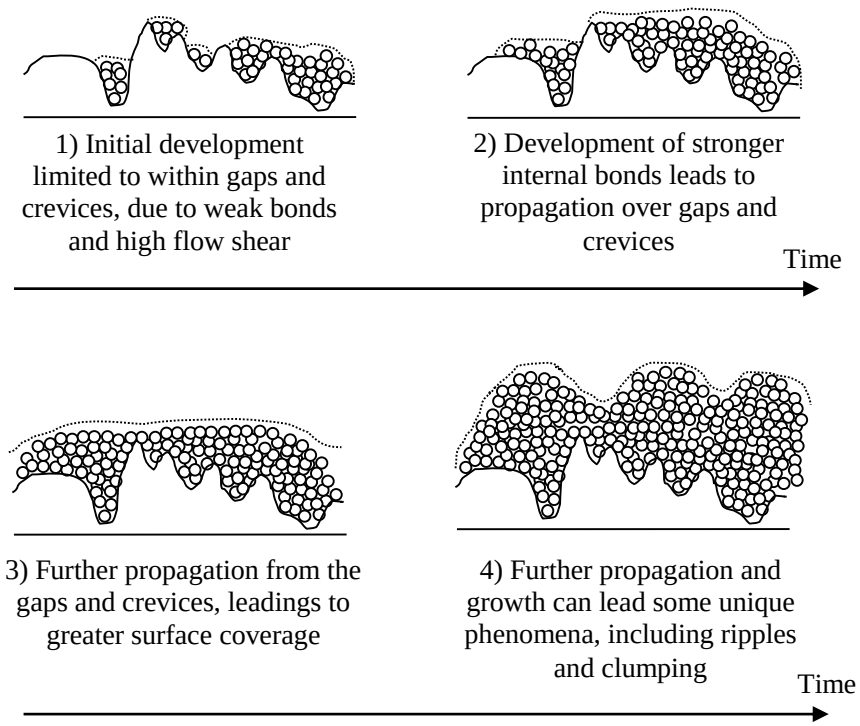

Figure 2.5 Biofilm propagation over time on a rough surface and some unique growth phenomena. Adapted from Barton (2006).

Interestingly, Barton (2006) and Andrewartha (2010) suggested that certain growth practices could potentially smoothen the initial roughness of a pipe surface, and therefore reduce its associated frictional resistance. Such growth practices are common with low level fouling, which can be common within DWDSs due to their low nutrient content. Therefore, there is a high potential that within DWDSs, biofilm development could in fact improve the hydraulic performance for an initially rough surface. However, this may not always be the case, as shown by Barton (2006) who noted that under low fouling conditions biofilms formed upon the peaks of roughness elements to gain a competitive advantage over the biofilms growing within roughness elements. This growth behaviour was also observed Nikora et al. (2002). This, combined with the typically isolated growth patterns associated with low nutrient loading will likely have the opposite effect. Whereby, the overall frictional resistance of the pipeline will be significantly impaired, via an accentuation in the absolute roughness and induce wake interactions.

When a biofilm layer only covers a small proportion of the surface an ‘isolated roughness flow’ will occur, whereby the discrete cell clusters experience essentially the same shear forces. When the cell clusters are closer together, ‘wake interaction flow’ occurs, in which

the vortices shed from upstream clusters may not dissipate before interacting with the downstream clusters, resulting in increased drag (Nowell and Church 1979; Santos et al. 1991; Viera et al. 1993; Dumbleton et al. 1995; Pecival 1999; Liu and Tay 2001; Stoodley et al. 2002; Celmer et al. 2008).

2.4.2.2 Chemical Composition, Resistance to Corrosion and Abrasion

In certain situations, surface roughness could be considered to be a key aspect in microbial accumulation and potential biofilm growth. Therefore, any factor that can potentially affect it should be assessed. For example, cement-based materials, are particularly susceptible to one of the most well-known and documented corrosive processes within DNs, namely corrosion via microbial production of acids (in particular sulphuric acid) (Sand and Bock 1991; Gaylarde and Morton 1999; Nielsen et al. 2005). In such situations, hydrogen sulphide, a commonly found compound within DNs, is oxidised by sulphur-oxidising bacterium (such as *Thiobacillus Thiooxidans*) to form sulphuric acid, which attacks the surface of the pipe, increasing its internal roughness and impairing structural integrity. Moreover, iron and steel based DWDSs have also been found to be impaired by microbial corrosion (Niquette et al. 2000). Recently water authorities (particularly within the UK) have stop recommending the use of such materials and as a consequence, plastic materials, and in particular HDPE have become increasingly prevalent within modern water management projects. The increased prevalence also comes as a result of increased market availability, a diverse range of sizes and inherent benefical material properties, such as their lightweight nature. There is also compelling evidence to suggest that plastic materials are more environmentally sustainable than traditional pipe materials, such as concrete (Samaras 2011; Cowle et al. 2012). As a result, of the increase use of plastics the potential impact of microbial corrosion within future DWDSs will be significantly reduced. However, most pipelines in service within the UK are fabricated from concrete and iron, and as a consequence, microbial corrosion should not be completely dismissed.

The additional roughness caused by corrosion can also promote further attachment of microorganisms and nutrients (Niquette et al. 2000). This leads to further microbiological corrosion in a positive feedback mechanism with negative consequences for the pipe structure. It is generally understood that the increased magnitude of fouling within pipes made of traditional materials, compared to plastic-based materials can ultimately be linked to their susceptibility to corrosion (Niquette et al. 2000). This problem has been addressed by manufacturers through the lining of susceptible pipes with corrosion-resistant materials, such as plastics and resins. However, this may add to the cost and carbon footprint of the fabrication process.

The surface topography and roughness of a pipe may also be affected by abrasion caused by debris impacting upon the surface during operation. Abrasion resistance refers to the ability to withstand mechanical erosion. The extent of the problem depends on the type of abrasive event, frequency, flow velocity and pipe material. Abrasion is particularly high in areas of high turbulence. Any selected pipe material used in DNs requires a significantly high abrasion resistance, as it is not uncommon in such applications for grit and other suspended solids to be present.

2.4.3 Seasonal effects – Temperature

The internal temperature of a pipeline can also have a significant impact upon the resultant biofilm development. As temperature is generally considered to be a significant controlling factor in biological growth, it has the potential to offset other factors, especially if high enough. This is highlighted by the use of high disinfectant levels within DWDSs in summer months (Lehtola et al. 2004). Furthermore, it has been reported that an increase in fluid temperature from 30 ºC to 35 ºC resulted in a 70% increase in biofilm biomass (Bott and Pinheiro 1977). Similarly, it has been shown that a biofilm's microbial activity can be significantly affected by temperature (Hallam et al. 2001). For instance, Hallam et al. (2001) found that a biofilm's microbial activity was 50% lower at a temperature of 7 ºC relative to 17 ºC. It has also been observed that large temperature deviations can encourage filamentous-type growth, which otherwise would not have been expected (Barton 2006).

2.4.4 Discussion on interacting conditions

In natural systems the aforementioned factors would be continuously interacting with each other. By assessing these interactions, the factor deemed most influential and controlling of biofilm development can be determined. Such information is vital in the development of improved design considerations. There is compelling evidence in the literature to suggest that flow hydrodynamics and residual disinfectants (if utilised) are the two most influential factors governing biofilm development within pipelines, due to their potential to remove existing biofilm and/or counteract further growth (Hallam et al. 2001; Tsvetanova 2006; Zhou et al. 2009). This is highlighted by their common use in pipeline cleaning for biofilm control and maintenance strategies (Douterelo et al. 2013). The influential impact of flow shear has been reported e.g. by Percival et al. (1999) and Perkins et al. (2013; 2014), who inferred that high freestream velocities (> 1.77 m/s) limited biofilm development in the pipelines investigated. Perkins et al. (2013; 2014) further reported that such a control measure tended to reduce the overall pressure drop within a hydropower pipeline. A comparison of the relative impact of flow hydrodynamics and residual disinfectant treatments was made by Tsevtanova (2006), who found that the latter, which is usually only applicable in certain DWDSs, was the most

influential of the two. However, nutrient content and fluid temperature were not examined within these studies, despite their inherent importance to biological growth. Thus, flow hydrodynamics (particularly in terms of boundary layer diffusion and flow shear) and residual disinfectants (if used) are likely to have an impact upon biofilm growth, although ultimately, it is the nutrient content (or lack of it) that is the underlying limiting factor in DWDSs. On the other hand, within DNs where it is more likely that sufficient nutrients would be available, flow hydrodynamics will be the primary controlling factor. However, if nutrient levels are high enough, they can potentially offset any hydrodynamic effects (Stoodley et al. 1998a). Although, the nutrient levels documented within the study were particularly high even for DNs.

The impact of material properties, as reported in the literature is seemingly conflicting. A number of studies have suggested that different pipe materials can have a considerable impact upon biofilm formation (Pedersen 1990; Percival et al. 1998; Niquette et al. 2000; Schwartz et al. 2003; Momba and Makala 2004; Abdel-Monim et al. 2005; Zhou et al. 2009), while other studies suggest that any potential impact from the pipe material is offset by other factors, namely flow hydrodynamics, nutrient availability and disinfectant levels (Bland et al. 1975; Bott and Miller 1983; Melo and Bott 1997; Hallam et al. 2001; Cloete et al. 2003; Lauchlan et al. 2005,). Therefore, materials which are relatively smooth, such as plastics and metals are not necessarily less rough when fouled than materials with a higher natural roughness, such as concrete. For example, in an investigation involving different wastewater pipeline materials and flow velocities, Lauchlan et al. (2005) found that the magnitude of the material effect was indistinguishable from the standard deviation of the whole data set obtained under similar flow conditions. On the other hand, flow velocity was found to have a significant impact on the resultant roughness scale value. A relationship between the two variables was obtained however, the data scatter was large and in some cases, of several orders of magnitude. In agreement with the findings of Lauchlan et al. (2005), Cloete et al. (2003) reported notable changes in the biofilm growth rate as a result of varying flow velocities, and no significant difference in growth between the pipe materials assessed. The materials assessed included asbestos-cement, coated cast iron, galvanized steel, and PVC, all of which are representative of those typically used within both DNs and DWDSs. Within this particular study the average streamwise velocities used, were particularly high, ranging from between 3.0 and 4.0 m/s, and therefore unrepresentative of most field conditions (particularly within the UK). For example, in the UK, DWDSs are usually operated at average freestream velocities of between 0.04 to 2.00 m/s, with most tending towards the lower end of the spectrum, with 0.06 m/s being the average (Husband et al. 2008).

Appraising the aforementioned studies critically, it may be concluded that the material properties undoubtedly have an impact upon initial attachment, both in terms of protection and induced turbulent mixing. Whether this promotion of initial attachment can be linked to future growth will likely depend on the favourability of other factors. In the situations where material properties were considered more influential, factors such as flow velocity and disinfectant residuals, were seemingly low (i.e. $\overline{U}$ < 0.3 m/s and 0.10 < mgCl/l < 0.20l) (Pedersen 1990; Niquette et al. 2000). Such conditions can occur in many DWDSs, particularly at the end of long runs and branches, and are prevalent in DNs, where disinfectants are not used and flow rates are naturally low.

In reality, there is no absolute controlling factor to biofilm development (shown in Table 2.1) and thus to the effective roughness of a biofouled surface. Ultimately, which factor is considered most controlling depends upon the specific condition of the pipeline in question, as appraised in this section. Such understanding is not yet reflected in current pipeline design practices, namely in the UK by British Standard BS EN 752 (2008) and *Sewer for Adoption* (Water Research Centre (Great Britain) 2006).

2.5 Extracellular Polymer Substances

The EPS are vital to a biofilm and thus contribute significantly to biofilm- and biofouling-related problems within pipelines: *"Put simply, there is no biofilm without an EPS matrix"* (Flemming and Wingender 2010). These highly hydrated "slime-like" substances (see Figure 2.6), in which the biofilm cells are embedded, are mostly produced and secreted by the cells themselves (Flemming and Wingender 2010; Flemming 2002).

a) HDPE b) PVC

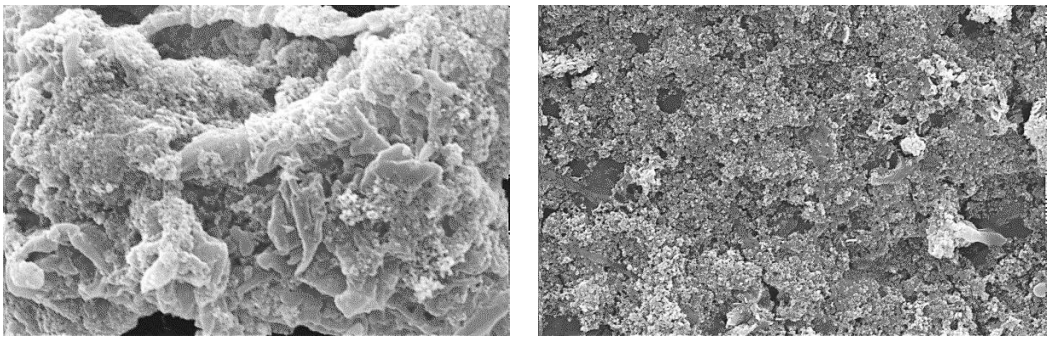

Figure 2.6 Photomicrographs of biofilm EPS captured by ESEM at x 20000 magnification (the presented biofilms were incubated on a) HDPE and b) PVC in drinking water for 100 d).

The EPS are essentially the "glue" which holds the microorganisms and biological matter together, and to the surface. The stronger these bonds, the stronger the structural integrity of the biofilm, both internally and externally (Kalmokoff et al. 2001). The EPS can also trap free-floating organic (e.g. carbon, nitrogen and phosphate) and inorganic (e.g. iron and manganese) materials, and can protect the individual components of the biofilm from the negative influence of their surrounding environment, such as flow shear and residual disinfectants (LeChevallier et al. 1988; Srinivasan et al. 1995; Cochran et al. 2000; Boe-Hansen et al. 2002; Simes et al. 2006; Flemming and Wingender 2010; Bridier et al. 2011). For example, it has been documented that even a relatively high shear stress ($\geq$ 3.0 N/m^2) caused by a flushing event, did not completely remove a biofilm from the pipe wall (Douterelo et al. 2013). As a consequence of the EPS, biofilms are one of the most successful forms of life on the planet (Flemming 2002).

The EPS also contributes to many of the commonly associated properties and characteristics of biofilms and biofouled surfaces, such as their: i) "slimy" or gelatinous appearance, ii) visco-elastic and filamentous nature, and iii) adsorptive nature (Picologlou et al. 1980; Barton 2006). Therefore, EPS contributes significantly to the additional energy dissipation mechanisms associated with biofouled surfaces and the inherent difficulties of their frictional evaluation. The higher the EPS fraction of the biofilm biomass, the more visco-elastic the biofilm layer becomes, and as a result more energy the biofilm can potentially remove from the flow, leading to a higher effective roughness (Picologlou et al. 1980).

The EPS matrix can account for over 90% of the dry biomass (Flemming and Wingender 2010) and commonly consists of a variety of biopolymers, including polysaccharides, proteins, nucleic acids, lipids and deoxyribonucleic acid (DNA) (Goodwin and Forster 1985; Horan and Eccles 1986; Flemming and Wingender 2010). However, the exact proportions of each are highly variable both in space and time, as they are influenced significantly by environmental conditions. The type of microbial community present, also influences the overall EPS composition ratios. Environmental factors such as flow shear stress and nutrient content, in addition to the biofilm age and growth rates, have been shown to influence the EPS production rate and exact composition, both directly and indirectly through changing microbial community structure (Donlan and Costerton 2002; Prakash et al. 2003; Qi et al. 2008; Douterelo et al. 2013). It has also been reported that the slower the biofilm growth rate, the more energy is available for EPS production (Kreft and Wimpenny 2001). Furthermore, as biofilm growth rate is greatly influenced by nutrient availability, so also is EPS content and production rate (Sutherland 2001). For example, the introduction of additional phosphates (commonly used to prevent corrosion within DWDSs) of the order of 3 to 300

µg/l was found to promote biofilm growth (both in terms of thickness and coverage) and inhibit EPS production (Fang et al. 2009). Similarly, it has been documented that in wastewater treatment processes, reduced phosphate levels caused increased carbohydrate levels in the EPS (Hoa et al. 2004). Phosphorus released from plastics such as polyethylene (PE) was also documented to promote growth, although EPS production was not monitored (Lehtola et al. 2004).

It has also been documented that flow shear impacts upon the structure and composition of the EPS matrix and thus the biofilm itself. Generally, high shear and turbulent conditions favour the production of more dense and compact biofilms; as such conditions encourage EPS production and higher cohesiveness (Stoodley et al. 2002). Consequently, under low shear conditions the resultant biofilm is likely to be less stable. Biofilm growth under favourable EPS production conditions will have a high resistance to external detachment forces (Manuel et al. 2007). Consequently, when EPS is inhibited, the resultant biofilm (although, maybe thicker) is likely to be less stable and more susceptible to flow shear and residual disinfectant. The flow conditions in DWDs and DNs are likely to vary, and therefore, the cohesive forces of the EPS will vary as a result.

Polysaccharides and in some cases proteins, are generally reported as the predominant component of the EPS matrix, representing over 50% of the overall EPS fraction (Horan and Eccles 1986; Flemming and Wingender 2010). The mechanical stability of the EPS matrix comes from a multitude of relatively weak physicochemical forces, the majority of which are supplied by the polysaccharides due to their filamentous nature (Wloka et al. 2004). Polysaccharide concentration can therefore be considered a useful measure of overall stability and resilience. However, as EPS composition also depends on microbial community structure, and thus differing among discrete biofilms (Molobela and Ilunga 2011), a more robust EPS quantification should incorporate multiple EPS components, in addition to polysaccharide concentration.

2.6 Quantifying pipeline hydraulic efficiency

2.6.1 Traditional approach

Pipe flow has been comprehensively studied over the years (Darcy 1857; Colebrook and White 1937; Colebrook 1939; Moody 1944; Zagarola and Smits 1998; McKeon and Smits 2002; Guo and Julien 2003; McKeon et al. 2003; 2004a; 2004b; Morrison et al. 2004; McKeon and Zagarola 2005; Shockling et al. 2006; Allen et al. 2007). As a result, it is reasonably well understood. Nevertheless, there is still a significant reliance on experimental

data and empirical relations for most fluid flow problems, with the exception of very simple cases, such as laminar flow, where closed-form analytical solutions are applicable. Even under controlled laboratory conditions, no two systems are exactly alike, which particularly true of investigations involving biofilms.

Figure 2.7 presents the coordinate system used within the current study. The *x*-direction is the streamwise direction and corresponds to the streamwise velocity, *u*. The *y*-direction is the wall-normal direction (from invent to soffit). The *z*-direction is the spanwise direction.

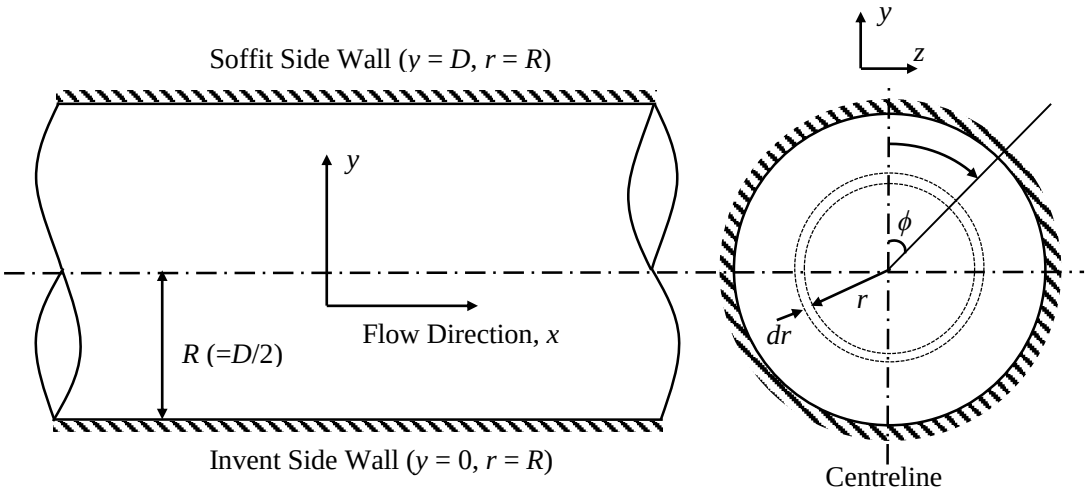

Figure 2.7 Diagram of the coordinate system used in the current study.

2.6.1.1 Pressure Drop in Pipelines

A vital area of interest in the analysis of pipe flow within the general engineering community is the pressure drop ΔP ($=P_1-P_2$; where P is the hydraulic gauge pressure). A pipeline's ΔP can be established using the conservation of energy principle (i.e. the modified Bernoulli equation), as given by Equation 2.4.

$$\frac{P_1}{\rho g} + \frac{\overline{U}_1^{\,2}}{2g} + z_1 = \frac{P_2}{\rho g} + \frac{\overline{U}_2^{\,2}}{2g} + z_2 + \Delta P \qquad \textit{Equation 2.4}$$

where g is the acceleration due to gravity (i.e. 9.81 m/s^2), and z is the vertical elevation above the arbitrary datum.

For laminar flow ΔP along a specific streamwise length, L is given by:

$$\Delta P = \frac{8\mu L\overline{U}}{R^2} = \frac{32\mu L\overline{U}}{D^2} \qquad \textit{Equation 2.5}$$

Equation 2.5, illustrates that for laminar flow, the pressure drop is proportional to the viscosity of the fluid, and ΔP would be zero if there was no friction. In other words the pressure drop between two points is a function of viscous effects.

A pipeline's pressure drop is typically expressed by the Darcy-Weisbach (D-W) equation, which is vaild for both laminar and turbulent flows, as given by;

$$\Delta P = \frac{\lambda \rho L \bar{U}^2}{2D} \qquad \textit{Equation 2.6}$$

where λ is the Darcy-Weisbach friction factor, given by:

$$\lambda = \frac{8\tau_w}{\rho \bar{U}^2} \qquad \textit{Equation 2.7}$$

Equation 2.6 is more commonly expressed in terms of hydraulic headloss, H_f (=$\Delta P/\rho g$);

$$H_f = \frac{\lambda L \bar{U}^2}{2gD} \qquad \textit{Equation 2.8}$$

or

$$S_f = \frac{\lambda \bar{U}^2}{2gD} \qquad \textit{Equation 2.9}$$

where S_f is the friction slope or pressure gradient (=dH_f/dL)

2.6.1.2 Solving for laminar flow in pipes (i.e. $Re_D \leq 2000$)

Hagen-Poiseuille's law, which is derived analytically from Equation 2.5 and Equation 2.6 is generally used to express λ for fully developed laminar flow in pipes, as given by:

$$\lambda = \frac{64\mu}{v\bar{U}D} = \frac{64}{Re_D} \qquad \textit{Equation 2.10}$$

2.6.1.3 Solving for Smooth Turbulent Flow in Pipes (i.e. $Re_D > 4000$, $k_s^+ \leq 5$)

The evaluation of λ for fully developed turbulent flow is more complicated. The lack of an exact solution for a turbulent velocity field precludes the determination of an all-encompassing λ relation. Consequently, only approximate solutions have been documented.

The friction factor for a smooth pipe subject to fully developed turbulent flow is a a unique function of Re_D as wall roughness is insignificant;

$$\lambda = \frac{4\tau_w}{0.5\rho \bar{U}^2} = \frac{-H_f g D}{0.5\bar{U}^2} = 8\left(\frac{u^*}{\bar{U}}\right)^2 \qquad \textit{Equation 2.11}$$

Nikuradse (1933) and Prandtl (see Durand 1935) proposed the following equation for turbulent flow in smooth pipes:

$$\frac{1}{\sqrt{\lambda}} = 2\log\left(Re_D\sqrt{\lambda}\right) - 0.8 \qquad \textit{Equation 2.12}$$

The values of λ derived from Equation 2.12 have been found to be within ±3% of actual experimental data, for the range $1.0\text{x}10^4 < Re < 3.2\text{x}10^6$ (Zagarola 1996). Consequently, Equation 2.12 is used to define smooth pipe flow on the traditional Moody Diagram, as shown by Figure 2.11. However, in more recent years turbulent flow within smooth pipes, for the range $3.10\text{x}10^4 \leq Re_D \leq 3.50\text{x}10^6$ has been expressed more accurately (i.e. to within ±1.25% of experimental data) by (McKeon and Zagarola 2005):

$$\frac{1}{\sqrt{\lambda}} = 1.93\log\left(Re_D\sqrt{\lambda}\right) - 0.537 \qquad \textit{Equation 2.13}$$

Both Equation 2.12 and Equation 2.13 are implicit for λ, and thus, iteration is required, which is fundamentally inefficient as a process. Consequently, the Blasius (1913) equation and the Filoneko equation are more widely used in the expression of turbulent flow in smooth pipes.

The Blasius (1913) equation is given by;

for $Re_D \leq 2.0\text{x}10^4$ $$\lambda = \frac{0.316}{{Re_D}^{1/4}}; \qquad \textit{Equation 2.14}$$

for $Re_D > 2.0\text{x}10^4$ $$\lambda = \frac{0.184}{{Re_D}^{1/5}} \qquad \textit{Equation 2.15}$$

The Filoneko equation is applicable for the range $3000 \leq Re_D \leq 5\text{x}10^6$ and is given by:

$$\lambda = [0.79\ln(Re_D - 1.64)]^{-2} \qquad \textit{Equation 2.16}$$

An explicit equation for fully developed turbulent flow in smooth pipes was also proposed by Guo and Julien (2003);

$$\lambda = \frac{0.316}{{Re_D}^{1/4}}\left(1 + \frac{Re_D}{4.31 \times 10^5}\right)^{1/8} \qquad \textit{Equation 2.17}$$

Equation 2.17 has a stronger correlation with the smooth pipe data outlined by Nikuradse (1932) and Zagarola (1996) than the Blasius (1913) equation.

In order to evaluate the mean-velocity distribution in fully developed turbulent flow in smooth pipes, the boundary layer structure requires further examination. A turbulent boundary layer conceptually consists of an inner and outer region. The length scale for the inner region is typically taken as the viscous length (i.e. $\delta'=\nu/u^*$) and the boundary layer thickness (i.e. $\delta = R$) is generally taken outer region length scale. The main component of the outer region, where turbulent stresses dominate, is the wake region, which is loacted at 300-500 < y^+ < R^+ ($=Rv/u^*$). The inner region of a turbulent boundary layer, which covers the innermost 10-20% of the overall boundary layer (see Figure 2.8), consists of: i) a viscous sublayer for $y^+(=yu^*/\nu) \leq 5$, where the inner scaled $u^+(=u/u^*)$ varies linearly with y^+ (i.e. $u^+=y^+$) and ii) a buffer region for 5 ≤ y+ ≤ 30-50, where the velocity profile is neither linear nor logarithmic; rather it is a smooth transition between the respective layers. The mean-velocity distribution in the inner region for smooth surfaces is given by (Spalding 1961);

$$y^+ = U^+ + e^{-\kappa C}\left(e^{\kappa u^+} - 1 - \kappa u^+ - \frac{(\kappa u^+)^2}{2!} - \frac{(\kappa u^+)^3}{3!} - \frac{(\kappa u^+)^4}{4!}\right)$$

for $y^+ > 100$ *Equation 2.18*

where C is an empirical constant and κ is the von Kármán Constant.

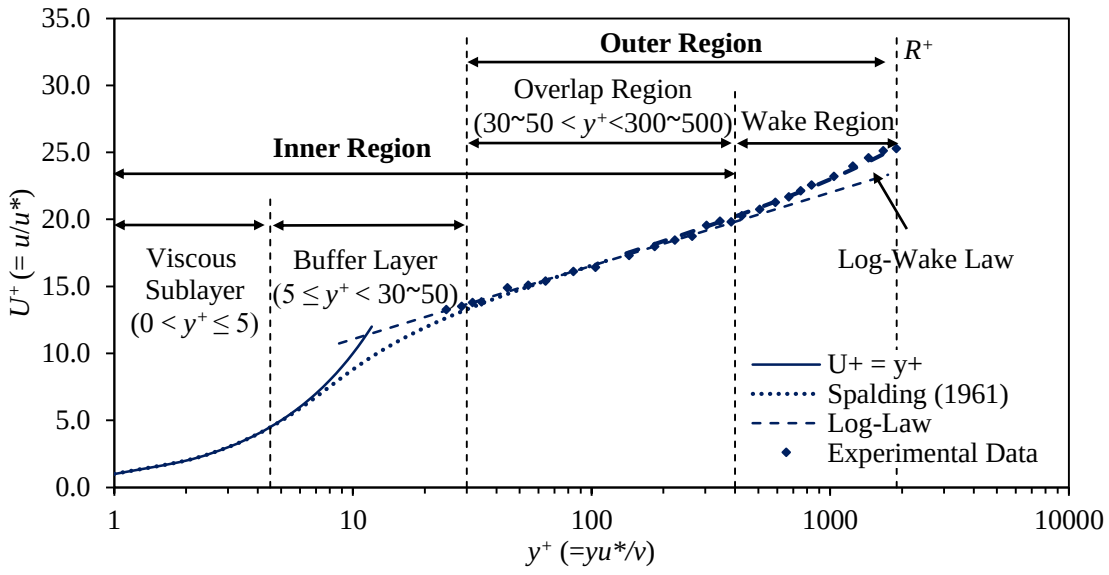

Figure 2.8 Smooth wall turbulent boundary layer, highlighting the viscous sublayer, buffer layer, overlap region and the wake region.

The von Kármán Constant, which relates the mean-velocity profile to the shear stress at the wall is considered to be universal and independent of *Re* in the classical theory. That is to say the same value of κ is used for all wall bounded flows, including pipes. Reynolds (1974) suggested a values of κ = 0.4 ± 15% and C = 5 ± 15%. The high variability is due to differences in channel geometry, wall roughness effects, and non-idealised flow, among other factors. Therefore, ranges of $0.38 < \kappa < 0.45$ and $5.3 < C < 5.85$ have been documented within the literature for smooth and rough walls **(**Krogstad et al. 1992; Zagorala and Smits 1998; McKeon et al. 2004b; George 2007; Walker 2014). George (2007) suggested that an appropriate value of κ for fully developed turbulent pipe flow is 0.43. Similarly, McKeon et al. (2004b) found that values of κ and C associated with smooth pipe flow were 0.421 ± 0.002 and 5.60 ± 0.08, respectively.

At sufficiently large *Re*, the mean-velocity distribution in the inner and outer regions of fully developed smooth turbulent pipe flow are given by Equation 2.19 and Equation 2.20, respectively;

$$U^+ = \frac{u}{u^*} = f(y^+); \quad y^+ = \frac{yu^*}{\nu} \qquad \textit{Equation 2.19}$$

$$\frac{U-u}{u^*} = F(\eta); \quad \eta = \frac{y}{\delta} = \frac{y}{R} \qquad \textit{Equation 2.20}$$

where R is the pipe radius (=D/2).

Millikan (1938) proposed that for $\nu/u^* < y < \delta$ (=R), an overlap region between the inner and outer layers exist. In this region – traditionally referred to as the logarithmic overlap region – the law of the wall (i.e. Equation 2.19) and the defect law (i.e. Equation 2.20) are both valid. The logarithmic overlap region typically exists at 30~50 < y^+ < 300~500 (or 0.15~0.2R^+). Millikan (1938) proposed, by combining Equation 2.19 and Equation 2.20 that the logarithmic overlap region in the inner and outer variables for smooth turbulent flow is given by Equation 2.21 and Equation 2.22, respectively;

$$U^+ = \frac{1}{\kappa}\ln(y^+) + C \qquad \textit{Equation 2.21}$$

$$\frac{U-u}{u^*} = -\frac{1}{\kappa}\ln\left(\frac{y}{R}\right) + C' \qquad \textit{Equation 2.22}$$

where C' is an empirical constant, given by McKeon et al. (2004b) as 1.20 ± 0.1.

Equation 2.21 is the common manifestation of the Log-Law in classical theory (George 2007) and all references herein to the Log-Law will be in reference to Equation 2.21. It is evident

from Figure 2.8, which shows the regions of a smooth wall turbulent boundary layer that the Log-Law sufficiently represents the mean-velocity structure of a turbulent boundary layer, excluding for the regions very close to the wall and near the pipe centreline. Consequently, the Log-Law is typically applied universally to a turbulent boundary layer. However, caution should be taken when using Equation 2.52 to estimate the maximum freestream velocity, *U* (i.e. the velocity to the pipe's centreline). The law of the wake was proposed by Coles (1956) for smooth turbulent flow to compensate for the disparities of the Log-Law in the wake region (including, the underestimation of the maximum freestream velocity). Laufer (1954) found that the Log-Law starts to deviate from experimental data when $y/D > 0.1$~0.2. The law of the wake or wake function, *W* is given by;

$$W = \frac{2\Pi}{\kappa}\sin^2\frac{\pi\left(\frac{y}{R}\right)}{2} \qquad \textit{Equation 2.23}$$

where Π is the wake strength parameter. The wake strength is typically a function of the pressure gradient and *Re*. Coles (1956) suggested Π is constant and equal to 0.55 for zero pressure gradients.

By combining Equation 2.21 and Equation 2.23, a modified Log-Law – referred to as the Log-Wake Law is derived, and is given by:

$$\frac{u}{u^*} = \left(\frac{1}{\kappa}\ln\left(\frac{yu^*}{v}\right) + C\right) + \frac{2\Pi}{\kappa}\sin^2\frac{\pi\left(\frac{y}{R}\right)}{2} \qquad \textit{Equation 2.24}$$

In light of an improved physical interpretation of the wake region Guo and Julien (2002) further modified the Log-Wake Law of pipe flow. The Modified Log-Wake Law proposed by Guo and Julien (2002) is given by:

$$\frac{u}{u^*} = \left(\frac{1}{\kappa}\ln\left(\frac{yu^*}{v}\right) + C\right) + \frac{2\Pi}{\kappa}\sin^2\frac{\pi\left(\frac{y}{R}\right)}{2} - \frac{1}{\kappa}\frac{\left(\frac{y}{R}\right)^3}{3} \qquad \textit{Equation 2.25}$$

or

$$\frac{U-u}{u^*} = -\frac{1}{\kappa}\left(\ln\left(\left(\frac{y}{R}\right) - \frac{1-\left(\frac{y}{R}\right)^3}{3}\right)\right) + \frac{2\Pi}{\kappa}\cos^2\frac{\pi\left(\frac{y}{R}\right)}{2} \qquad \textit{Equation 2.26}$$

Guo and Julien (2002) found that the log, sine-squared and cubic terms in Equation 2.25 respectively better reflected the restriction of the wall, contribution of the pressure gradient

and the axial symmetrical conditions, within smooth turbulent pipe flow. Guo and Julien (2002) found that the value of $\Pi = \kappa$ (≈ 0.42) fitted the Modified Log-Wake Law well with experimental data. The Modified Log-Wake Law proposed by Guo and Julien (2002) will herein be referred to as the Log-Wake Law. Theoretically determined mean-velocity profiles established from the Log-Law (Equation 2.21) and Log-Wake Law (Equation 2.25) are presented within Figure 2.9. Experimentally determined mean-velocity data is also presented within Figure 2.9.

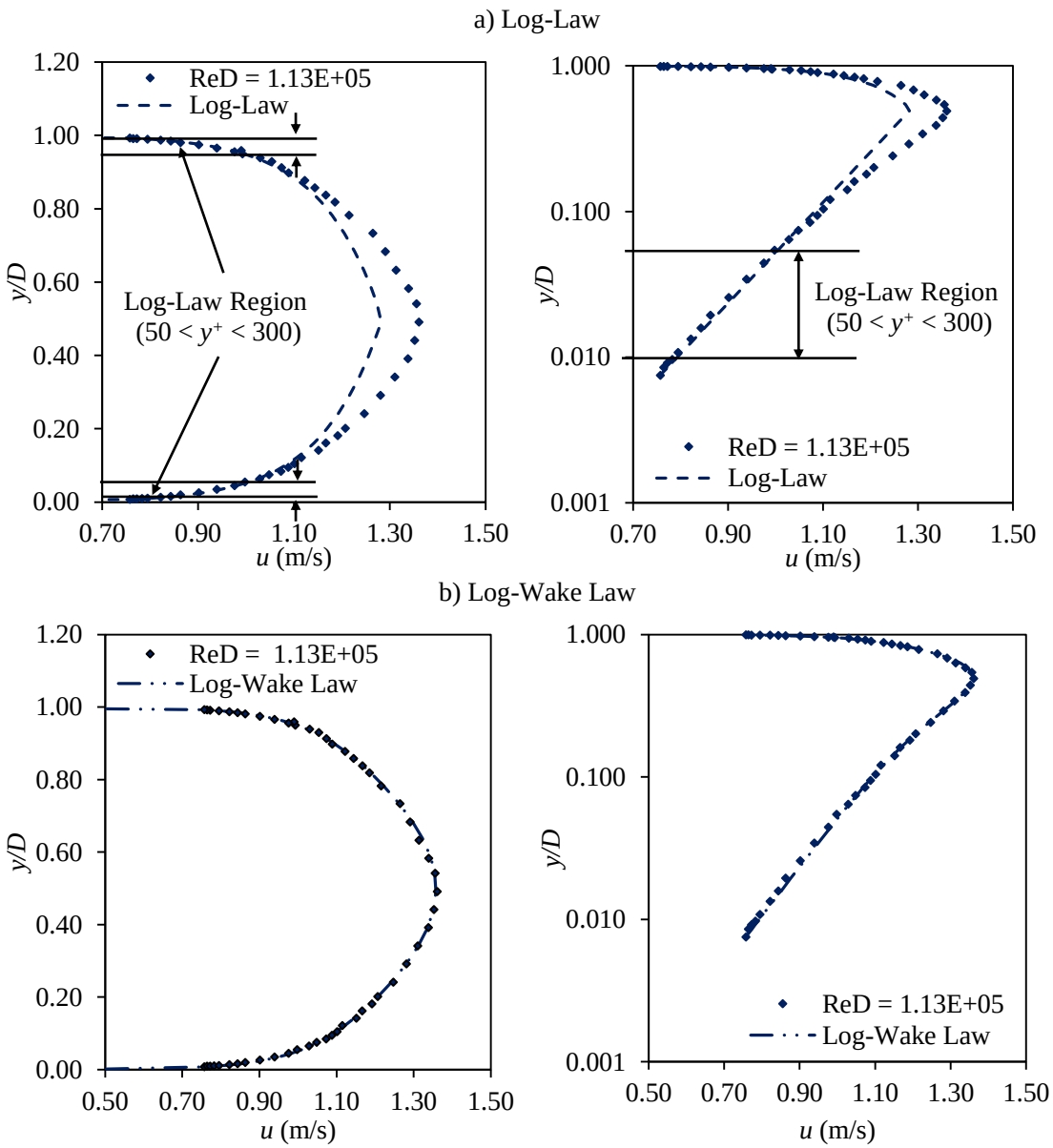

Figure 2.9 Comparison of the a) Log-Law and b) Log-Wake Law with experimentally determined data (where $\kappa = 0.42$, $C = 5.59$ and $\Pi = 0.46$).

As expected, the Log-Law fits the experimental data well in the logarithmic overlap region (i.e. $50 < y^+ < 300$), though fails in the outer wake region. It is evident that the Log-Wake Law fits the experimental data extremely well for all wall-normal positions. Consequently, all theoretically determined logarithmic-based velocity profiles within the current study will include a Law of the Wake component.

Numerous other empirical relations have been documented within the literature to express the mean-velocity distribution. The most notable is the power-law, which is given by;

$$\frac{u}{U} = \left(\frac{y}{R}\right)^{1/n} \qquad \textit{Equation 2.27}$$

where the exponent *n* is a *Re* depended constant. The value of *n* is proportional to *Re*, although, the value of 7 (i.e. one-seventh power-law) generally applicable to most flows in practice. There has been considerable debate in recent years to whether the mean-velocity distribution in fully developed turbulent flow is best represented by a power-law relationship (Milikan 1938; Wosnik et al. 2001; Oberlack 2001) or by a logarithmic relationship (Österlund et al. 2000; Saleh 2005; Zanoun et al. 2003; 2007).

2.6.1.4 Solving for Rough Turbulent Flow in Pipes (i.e. $Re_D > 4000$, $k_s^+ > 70$)

Surface roughness starts to have an impact on flow characteristics when either *Re* and *k/D* are sufficiently large. For instance, an increase in *Re* or *k* for a fixed pipe diameter will increase the *k*:*δ'* ratio through a reduction in *δ'*.

For transitional turbulent flow (i.e. $5 < k_s^+ < 70$), the velocity distribution in the inner region of the boundary layer is given by:

$$U^+ = f(y^+, k^+); \quad y^+ = \frac{yu^*}{v},\ k^+ = \frac{ku^*}{v} \qquad \textit{Equation 2.28}$$

According to Townsend (1976), roughness will only manifest itself in the outer region of the boundary layer by modulating the wall stress. Consequently, the velocity distribution in the outer region is unaffected by roughness, assuming that *k* remains small compared to *D* (Shockling et al. 2006). Townsend's (1976) outer region hypothesis – referred to herein as Townsend's Wall Similarity Hypothesis has been validated for both engineered and biofouled surfaces (Bakken et al. 2005; Flack et al. 2005; Shocking et al. 2006; Wu and Christensen 2007; Walker et al. 2013). Assuming that Townsend's Wall Similarity Hypothesis applies the velocity distribution in the overlap region, as given by the Log-Law is still applicable for transitional turbulent flow as given by Equation 2.31.

$$U^+ = \frac{1}{\kappa}\ln(y^+) + C - \Delta U^+ \qquad \textit{Equation 2.29}$$

where ΔU^+ is Hama's (1954) roughness function, which is governed solely k^+.

The roughness function represents the shift in the velocity profile from the Log-Law, and increases with increasing surface roughness, as shown by Figure 2.10, which represents surface roughness as k_s.

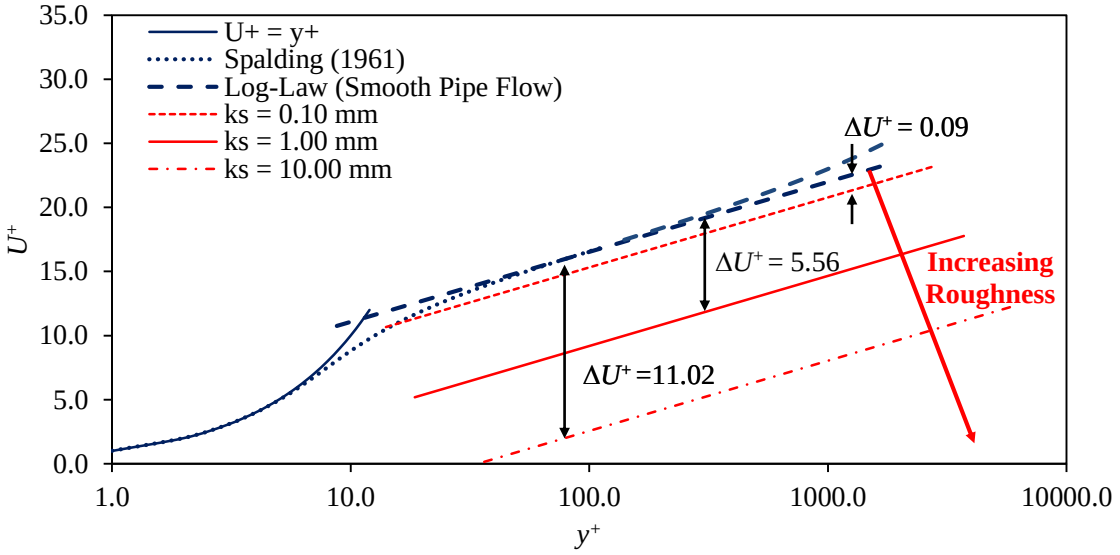

Figure 2.10 Impact of surface roughness on mean-velocity data (highlighting impact of k_s on ΔU^+).

For fully rough turbulent flow (i.e. $k_s^+ > 70$), the velocity distribution in the inner region is no longer dependent on just viscosity, as given by;

$$U^+ = f\left(\frac{y}{k}\right) \qquad \textit{Equation 2.30}$$

Therefore:

$$U^+ = \frac{1}{\kappa}\ln\left(\frac{y}{k}\right) + B \qquad \textit{Equation 2.3132}$$

where B is Nikuradse's roughness function, which assumes determine values depending on the flow conditions. For fully rough flow B is typically equal to 8.48 for conventional surfaces. For the smooth-to-rough transition the relationship proposed by Ligrani & Moffat (1986) was used to determined B, as given by Eqaution 3.32.

$$B = C + \frac{1}{\kappa}\ln\left(k_s{}^{+}\right) + \left[8.5 - C - \frac{1}{\kappa}\ln\left(k_s{}^{+}\right)\right]\sin\left(\frac{\pi}{2}M\right) \qquad \textit{Equation 2.33}$$

where;

for $k_s{}^{+} < 5$ $\quad M = 0;$

for $5 < k_s{}^{+} < 70$ $\quad M = \dfrac{\ln\left(k_s{}^{+}/5\right)}{\ln(70/5)};$ *Equation 2.34*

for $k_s{}^{+} > 70$ $\quad M = 1$

From Equation 2.29 and Equation 2.31, Hama's (1954) roughness function can be given by:

$$\Delta U^{+} = \frac{1}{\kappa}\ln(k^{+}) + C - B \qquad \textit{Equation 2.35}$$

Equation 2.31, which will be referred to herein as the Rough Wall Log-Law is generally expressed in terms of k_s, as given by:

$$U^{+} = \frac{1}{\kappa}\ln\left(\frac{y}{k_s}\right) + B \qquad \textit{Equation 2.36}$$

Solving the Rough Wall Log-Law for k_s yields:

$$k_s = \frac{y}{e^{(U^{+}-B)\kappa}} \qquad \textit{Equation 2.37}$$

Historically, the C-W equation (Colebrook 1939) and the Moody Diagram (Moody 1944) (see Figure 2.11) have been used to determine λ for turbulent flow over a rough boundary. In actual fact, the C-W equation is valid for the range of $4000 \leq Re_D \leq 10^8$ and $0 \leq k_s/D \leq 10^8$, and as a consequence, can be applied to all turbulent flow regimes, i.e. from hydraulically smooth to fully rough. The C-W equation is given by:

$$\frac{1}{\sqrt{\lambda}} = -2.00\log\left(\frac{k_s}{3.7D} + \frac{2.51}{Re_D\sqrt{\lambda}}\right); \qquad \textit{Equation 2.38}$$

or

$$\frac{1}{\sqrt{\lambda}} = -0.88\ln\left(\frac{k_s}{3.7D} + \frac{2.51}{Re_D\sqrt{\lambda}}\right) \qquad \textit{Equation 2.39}$$

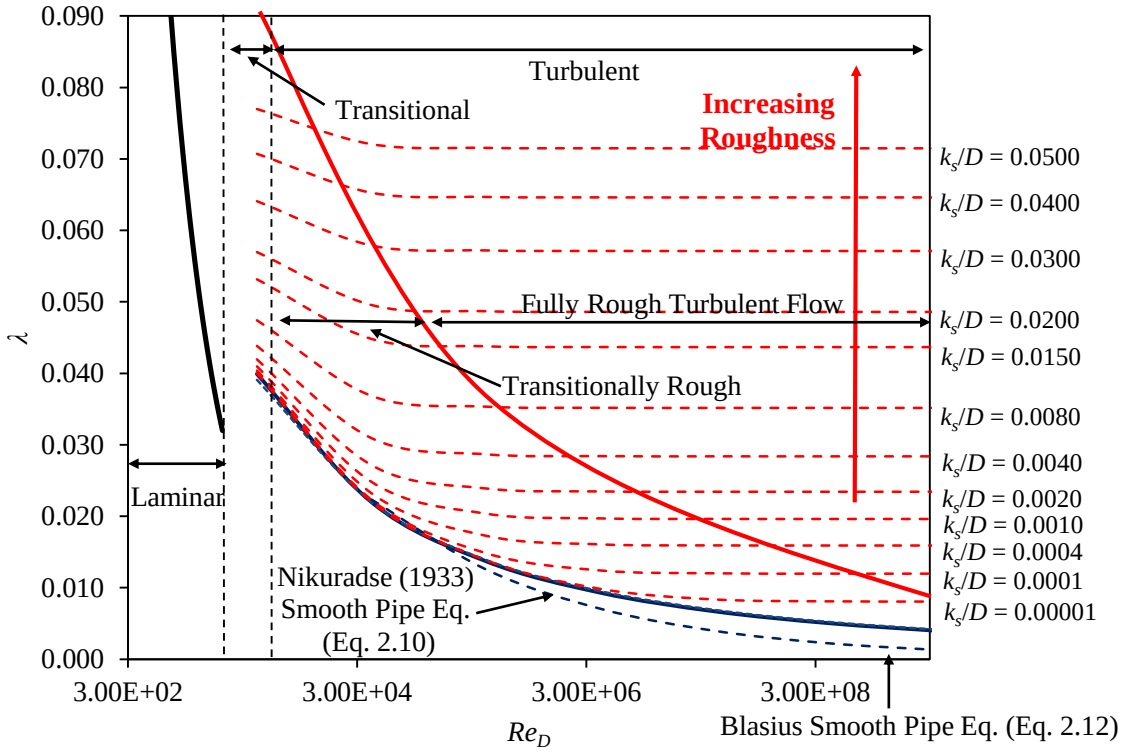

Figure 2.11 An example of a modified Moody Diagram.

A more practical arrangement of the C-W equation, is given by the combined C-W and D-W equation (i.e. Equation 2.8), as given by:

$$\overline{U} = -2.00\sqrt{2gDS_f}\log\left(\frac{k_s}{3.7D} + \frac{2.51\nu}{D\sqrt{2gDS_f}}\right); \qquad \textit{Equation 2.40}$$

or

$$\overline{U} = -0.88\sqrt{2gDS_f}\ln\left(\frac{k_s}{3.7D} + \frac{2.51\nu}{D\sqrt{2gDS_f}}\right) \qquad \textit{Equation 2.41}$$

Solving Equation 2.38 and Equation 2.40 for k_s yields Equation 2.43 and Equation 2.44, respectively:

$$k_s = 3.7D\left(10^{\frac{-1}{2\sqrt{\lambda}}} - \frac{2.51}{Re_D\sqrt{\lambda}}\right) \qquad \textit{Equation 2.42}$$

$$k_s = 3.7D\left(10^{\frac{-\overline{U}}{2\sqrt{2gDS_f}}} - \frac{2.51\nu}{D\sqrt{2gDS_f}}\right) \qquad \textit{Equation 2.43}$$

The transitional function proposed by Colebrook (1939) is based upon empirical information and geometric similarity considerations, and was derived from the laboratory experiments on rough pipes performed by Colebrook and White (1937). Colebrook and White (1937) collected a vast amount of λ data from pipes in commercial use at the time. Surface roughness characteristics, such as height, orientation, geometric arrangement and spacing are defined globally within the C-W equation by the one-dimensional roughness scale of k_s.

Due to its wide applicability, the C-W equation, along with the Moody Diagram have become the accepted relationship for evaluating the frictional resistance of turbulent flow in pipes systems, especially within the UK. For instance, in the UK the C-W equation is included in design documents, such as British Standard BS EN 752 (2008) and *Sewer for Adoption* (Water Research Centre (Great Britain) 2006). However, the expression of λ in the C-W equation is implicit in nature, and as a result, it is not convenient to use. Typically, 7 iterations are required for a convergence of 0.01% (Brkic 2011). Iteration as a process is fundamentally inefficient, which is unacceptable in an environment driven by the requirements to improve the performance of all associated processes. Despite this, the implicit nature of the C-W equation is generally seen as a minor drawback, to what is one of the most cited and useful equations in the vast literature on pipe friction (Matthew 1990). In any respect, the Moody Diagram, which graphically depicts the C-W equation can be used to solve for λ more conveniently, although, the estimated values of λ should be used with caution as they can have an associated error of up to 21.49% (Brkic 2011). For this reason, a number of approximate explicit equations have been proposed over the years, using the traditional C-W equation as the starting point (Jain 1976; Barr 1977; Zigrang and Sylvester 1982; Chen 1979; Romeo et al. 2001; Sonnad and Goudar 2006; Brkic 2011, Danish et al. 2011). The explicit relationship proposed by Romeo et al. (2001) is considered to be highly accurate for all flow regimes (Brkic 2011) and is given by:

$$\frac{1}{\sqrt{\lambda}} \approx -2\,log\left(\frac{k_s}{3.7065D} - \frac{5.0272}{Re_D}log\left(\frac{k_s}{3.827D} - \frac{4.567}{Re_D}log\left(\left(\frac{k_s}{7.7918D}\right)^{0.9924} + \left(\frac{5.3326}{208.815 + Re_D}\right)^{0.9345}\right)\right)\right)$$

Equation 2.44

Surface roughness is also defined in terms of the *n* and Chezy roughness coefficients as given in the Manning (1980) equation (Equation 2.44) and Chezy equation (Equation 2.25).

$$\bar{U} = \frac{1}{n} {R_h}^{2/3} \sqrt{S_f} \qquad \textit{Equation 2.45}$$

$$\bar{U} = c\left(S_f R_h\right)^{1/2} \qquad \textit{Equation 2.46}$$

where R_h is the hydraulic radius (=A/P_W, where A is the cross-section area, and P_W is the wetted perimeter).

Both the Manning and Chezy equations are conventionally used to define the surface roughness of an open channel, as opposed to a closed conduit. However, a pipe is defined as an open channel when it is not operating at full bore, which is typically the case within most DNs, with the exception of rising/force mains. The Hazen-Williams frictional relationship and roughness coefficient are also commonly employed to express flow within a pipe, despite, its documented limitations, which are particularly notable when simulating large-diameter pipelines (Christensen et al. 2000; Bennett and Glaser 2011). Fundamentally, the C-W equation can more accurately represent a wider range of pipe diameters and flow conditions. The reason why the Hazen-Williams relationship is widely used within the industry, is due to instrumentation limitations, which typically result in high measurement errors. For instance, global positioning systems, which are only accurate to within 1-3 m are widely used to estimate headloss within pipelines. The benefits of using the C-W equation, in terms of improved accuracy are superseded by such instrumentation errors. Terefore, the Hazen-Williams relationship can provide a reasonable estimation of the flow within a pipeline. Nevertheless, unless stated otherwise the C-W equation and k_s were predominately used in the evaluation of frictional resistance, within the current study.

2.6.2 Accounting for biofouling

The traditional approach of adopting the C-W equation to simulate pipeline hydraulics has been proven to be inadequate in evaluating the frictional resistance of biofouled pipelines (Schultz 2000; Schultz and Swain 1999; Barton 2006; Lambert et al. 2009). However, under certain situations this is proven not to be the case, namely at the polar extremes of the Moody diagram (i.e. very low and very high flow), where traditional approaches are valid irrespective of the presence of a biofilm (Picologlou et al. 1980; Lambert et al. 2009). For example, Lambert et al. (2009) documented that a 25 mm diameter biofouled pipe followed a smooth pipe law frictional relationship at $Re_D < 5000$. This is attributable to the larger boundary layer associated with such conditions and thus the onset of hydraulically smooth flow. Similarly at the other extreme, high detachment inducing shear forces are likely to limit the extent of biofilm growth. However, such situations are generally uncommon within most DNs and DWDSs. The application, therefore, of traditional practices in most cases can lead to under-

or over- estimated pipeline flow capacities, which will result in unforeseen efficiency issues. For example, if the flow capacity of a pipeline is underestimated (i.e. undersized), it may fail to achieve the design velocity required for self-cleansing and as a result, the likelihood of future fouling and fouling issues will increase. Furthermore, if a pipeline is oversized (i.e. overestimated) it could add unnecessarily to the cost of the project, both financially and environmentally (i.e. in terms of the projects carbon footprint (Cowle et al. 2012)). As it would lead to additional pipe material and ground excavations being required.

Lambert et al. (2009) used experimental observations to obtain a modified C-W equation, which is aimed at addressing the inadequacy of the original equation for relating frictional resistance and equivalent roughness for biofouled pipes. Lambert et al. (2009) found that the von Kármán constant of biofouled surfaces was non-universal, and was lower than the conventional value (i.e. κ = 0.42). Lambert et al. (2009) expressed the non-universal κ as a function of Re_D, as given by:

$$\kappa = 1.00 \times 10^{-6} Re_D + 0.26 \qquad \textit{Equation 2.47}$$

The C-W equation (i.e. Equation 2.38 and Equation 2.39) was derived from a logarithmic velocity distribution (Matthew 1990; Lambert et al. 2009). In particular, it is based upon a universal κ. The von Kármán constant is integrated in to the logarithmic multiplier, which is traditionally given as either -0.88 or -2.00 determining the logarithmic form of the equation.

Expressing Equation 2.38 and Equation 2.39 in their natural forms produces:

$$\frac{1}{\sqrt{\lambda}} = -\frac{1}{\sqrt{8.08\kappa}} \ln\left(\frac{k_s}{3.7D} + \frac{2.51}{Re_D\sqrt{\lambda}}\right) \qquad \textit{Equation 2.48}$$

$$\frac{1}{\sqrt{\lambda}} = -\frac{1}{\sqrt{1.56\kappa}} \log\left(\frac{k_s}{3.7D} + \frac{2.51}{Re_D\sqrt{\lambda}}\right) \qquad \textit{Equation 2.49}$$

These representations of the C-W equation, namely Equation 2.48 were the basis of the modified C-W equation proposed by Lambert et al. (2009). Lambert et al. (2009) found that Equation 2.48 overestimated the value of k_s applied to biofouled surfaces, to correct this error the dimensionless constant multiplier for D was altered from 3.70 to 0.85. The modified C-W equation proposed by Lambert et al. (2009) is given by Equation 2.49.

$$\frac{1}{\sqrt{\lambda}} = -\frac{1}{\sqrt{8.08\kappa}} \ln\left(\frac{k_s}{0.85D} + \frac{2.51}{Re_D\sqrt{\lambda}}\right) \qquad \textit{Equation 2.50}$$

Solving the modified C-W equation (namely Equation 2.48) for k_s yields:

$$k_s = 0.85D\left(e^{\frac{-1\sqrt{8.08\kappa}}{\sqrt{\lambda}}} - \frac{2.51}{Re_D\sqrt{\lambda}}\right) \qquad \textit{Equation 2.51}$$

A more practical form of Equation 2.50 is Equation 2.52, which combines the modified C-W equation of Lambert et al. (2009) with the D-W equation, such as:

or

$$\overline{U} = -\frac{\sqrt{2gDS_f}}{\sqrt{8.08\kappa}} \ln\left(\frac{k_s}{0.85D} + \frac{2.51\nu}{D\sqrt{2gDS_f}}\right) \qquad \textit{Equation 2.52}$$

Figure 2.12 illustrates the detrimental impact of applying the traditional C-W equation as opposed to the modified C-W equation proposed by Lambert et al. (2009) for biofouled pipes, in terms of Q estimations. For example, the Q estimated for pipe of D = 100 mm with k_s = 0.60 mm, using Equation 2.38 and Equation 2.50 are 5.0 and 4.3 l/s, respectively. The disparity between these two estimates is 14%, which highlights the potential error that could arise through the application of the traditional C-W equation for biofouled pipes.

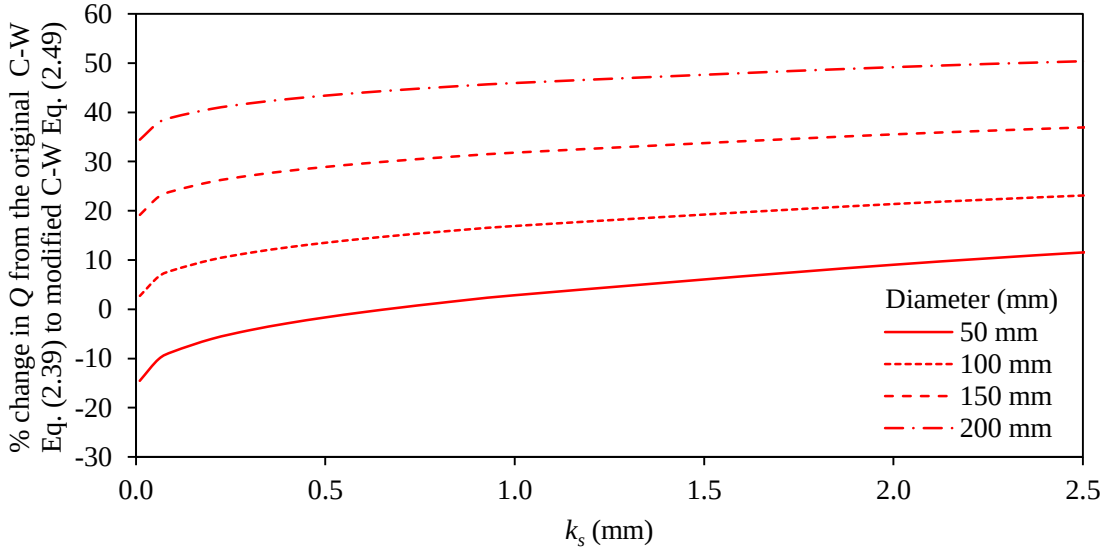

Figure 2.12 Percentage change in Q from the application of the original C-W equation (2.39) to the modified C-W equation (2.49) for a range of pipe diameters from 50-200 mm, each flowing full and with a pipe invert slope of 1:150. The flow within them was assumed to be uniform and hence S_f = invert slope.

Equation 2.50 and/or Equation 2.52 are recommended in principle for use in simulating pipelines at the pseudo-equilibrium biofouling stage, in that it presupposes the use of a constant k_s value. It was recently shown that the modified equation presented by Lambert et al. (Lambert et al. 2009) had good correlation with experimental results obtained below the critical shearing velocity of 1.77 m/s (Perkins et al. 2013). It should be noted however, that Lambert et al. (2009) assessed a relatively small range of environmental and hydrodynamic conditions. For example, only three different mean-velocities, namely 1.15 m/s, 0.89 m/s and 0.22m/s were assessed. Furthermore, only two very unique water sources were employed (Myponga Reservoir and River Murray water, South Australia), which again limits the broader application of the equations, particularly the derived κ relationships. Since the roughness characteristics of biofilms are highly dependent upon the conditions they are subjected to, further experimentation is required to confirm the validity or obtain a refined equation for use under a range of environmental conditions and flow regimes (Lambert et al. 2009).

2.6.3 Gaps in the quantification of unsteady effects

Under relatively constant operational conditions in a pipeline with a mature biofilm, i.e. one that has reached the pseudo-equilibrium stage of development, the use of a constant roughness scale value in Equation 2.50 and/or Equation 2.52 may represent well the actual conditions, provided that the correct k_s value is used. For example, Andrewartha (2010) found that the frictional behaviour of a hydropower channel, covered by freshwater low-form gelatinous biofilms, supported the rigid wall similarity hypothesis normally used in pipeline modelling studies. However, errors can arise from applying a generic global k_s value for biofouled pipes, such as k_s = 0.6 or 1.5 mm, as also recommended in practical guidelines (Wallingford and Barr 1994), without further verification of the actual conditions. In particular, these guidelines were derived from seemingly limited datasets and they were based on work carried out between 1966 and 1979. Considerable advances have since been made within the industry, especially with regards to the use of different pipe materials. All such design advances will be considerably negated by the use of these out-dated design guideline parameters.

The traditional approach of using a constant roughness scale value in a one-dimensional hydraulics model has been found to fail under highly unsteady conditions (Schultz 2000; Schultz and Swain 1999; Barton 2006; Guzmán et al. 2007; Lambert et al. 2008). This is typically due to the biofilm's vibrating and oscillating behaviour (Characklis 1973; Stoodley et al. 1998a; 1998b; Andrewartha et al. 2008; 2010; Andrewartha 2010; Barton 2006; Lambert et al. 2008; 2009; Walker et al. 2013). For example, the effective roughness scale of a thin low-form gelatinous biofilm has been found to be up to three times higher under normal

flow conditions than its dimensions would initially suggest, due to vibration-induced drag and pressure drop (Barton 2006). In the case of filamentous biofilms (or streamers), the resultant increase in drag is a function of the resonant/oscillating frequency of the streamer and is, therefore, governed by its length and diameter, as well as the flow velocity (Stoodley et al. 1998b; Andrewartha et al. 2008). The effect of filamentous formation on effective roughness can be significant, and far greater than non-filamentous biofilms (Picologlou et al. 1980; Lewandowski and Stoodley 1995; Stoodley et al. 1998a; 1998b; Schultz and Swain; 1999; Schultz 2000). Furthermore, flow induced biofilm oscillation and vibration behaviour will result in temporal fluctuations onto the structure of the boundary layer and cause a phenomenon known as vortex shedding (Stoodley et al. 1998b; Andrewartha et al. 2008; 2010; Andrewartha 2010; Walker et al. 2013). In theory, the periodical nature of such fluctuating phenomena allows for a time-averaged analysis approach of the net effects of processes on the energy dissipation in a biofouling pipeline, although such an approach has not been reported in the literature.

Biofilms have also been documented to compress themselves under pressure, which tends to confer an increased ability to resist the effects of flow shear (Percival et al. 1999; Douterelo et al. 2013). Such effects have been shown to occur even when the surface is classified as hydraulically smooth (Stoodley et al. 1998b). In addition, significantly increased turbulent parameters (namely turbulence intensities and Reynolds stresses) within the outer region of the boundary layer have also been associated with the occurrence of biofouling, further indicating the potential to cause large-scale motion and pressure drops (Schwartz et al. 1998; 2003; Andrewartha 2010). It follows that even if a given k_s value is representative of space-averaged conditions, it cannot include the dynamic temporal effects of biofouling which can occur due to biofilm growth and/or varying operational and environmental configurations (Lauchlan et al. 2005; Barton 2006; Andrewartha et al. 2008). As such, factors, either individually or cumulatively, are likely to cause significant changes both in space and time to all aspects of the biofouled surface, including its frictional characteristics (i.e. over the length and operational life of the pipeline and from pipeline to pipeline). This was observed within operational pipelines by Lauchlan et al. (2005), who reported varying k_s values for different pipelines operating under similar conditions and which were in some cases, different by over an order of magnitude.

2.7 The way forward

This Chapter has provided an overview of the current understanding of biofilms and biofouling in pipelines used within DWDSs and DNs. The detrimental effect of biofouling on frictional resistance has been well documented over the last century, through both field and laboratory investigations. The increase in frictional resistance caused by a biofilm is typically far beyond that expected based upon its physical roughness. Though, the impact of biofouling is well known, the mechanisms behind the increase in frictional resistance induce by the biofilm-flow interaction are not well understood, particularly in water and wastewater systems. The current prevailing understanding of biofilm-flow interaction is predominantly based on observations within hydropower applications (Barton 2006; Barton et al. 2007; 2010; Andrewartha et al. 2007; 2008; Andrewartha 2010; Perkins et al. 2013; 2014; Walker et al. 2013) and marine environments (Schultz and Swain 1999; Schultz 2000), which have inherently different ecologies to those typical within water and wastewater systems. Furthermore, at present, most literature on biofouling is fundamentally sparse and lacking in assessment of the key interacting processes under a wide range of conditions. The observed gaps in scientific literature are reflected within the industry, whereby biofouling is not independently acknowledged in its own right within current design practices. As a result, current design methods to deal with the problem of biofouling have little theoretical basis and are geared more towards immediate cost savings, rather than longer term improvements in efficiency and the benefits that would result. The fundamental lack of comprehensive information and data on biofouling within DNs and DWDSs, over a wide range of conditions, means that the current task of improving design practices to incorporate biofouling is exceptionally challenging, particularly given the highly complex nature of biofouling and biofilms.

Further research is therefore essential to better understand and evaluate the true nature of biofouling, and its inevitable impact on pipeline flow resistance. A proposed direction of how such research should be based is outlined herein. The proposal is applicable to any system, including both DNs and DWDSs, although, it is only applied to wastewater systems within the current study.

2.7.1 Dynamic k_s formulations

If an equation such as Equation 2.52 is used to predict the hydraulic performance of a pipeline operated under highly unsteady conditions, then the variation of k_s with time should be taken into account by using a separate formulation, namely a dynamic k_s approach. One way to achieve this would be by describing the variation of such a parameter with respect to multiple ecological factors. Due to the considerable complexity of this task, an indirect approach may

be preferred, in which the unknowns are the steady state k_s value and the trend of variation of k_s with respect to time. This has been achieved in sediment transport applications involving bedform development (Rauen et al. 2008; 2009). If the impact of biofilm development on flow resistance variation can be represented in such a way, then a predictive tool might become available to aid the design and operation control of pipelines, which could be used, for example, to determine the frequency of cleaning interventions. Such time-varying biofilm development models are presented within the literature (Sharp and Walski 1988; Melo and Bott 1997; Manuel et al. 2007; Lambert et al. 2008). However, only Lambert et al. (2008) and Sharp and Walski (1988) related the growth to a time-varying equivalent roughness-scale for steady state conditions. The model proposed by Sharp and Walski (1988) employed a growth rate constant expressed in mm/year to represent the combined impact of biofilm development, internal corrosions and tuberculation (in terms of Hazen-Williams coefficient) over time. The steady state model proposed by Lambert et al. (2008) for k_s (in mm) is given by;

$$k_s = k_{s(e)} \frac{1 - e^{-\frac{t}{40}}}{1 + 200e^{-\frac{t}{40}}} \qquad \textit{Equation 2.53}$$

where t is time and $k_{s(e)}$ is equilibrium stage k_s. Lambert et al. (2008) found that $k_{s(e)}$ = 6.80 mm for a biofilm cultivated within a 25.0 mm diameter pipe at $\overline{U}$ = 0.30 m/s.

Further studies on this topic centred on DWDSs and DNs could lead to the refinement of existing formulae and/or the development of new ones. Nonetheless, design practices could benefit from the inclusion of a calibrated dynamic roughness computation routine in the estimation of pipeline carrying capacity over its lifecycle or between cleaning operations. By doing this, Equation 2.52 would be used to calculate a time series of mean flow velocity and, thus, discharge values for the pipeline during the period considered. This could lead to more realistic design and operation planning measures being developed.

Chapter 3 Materials and methods

3.1 Introduction

The most challenging phase of the current study was the design, development, procurement and construction of the pilot-scale pipeline facility, which is discussed in detail in this chapter. In particular, a comprehensive description of the facility is provided, which details its fundamental components and instrumentation. The results of a comprehensive sensitivity analysis on the C-W equation and k_s are also provided; for the purpose of validating the facility's instrumentation for the intended study. The composition of the synthetic wastewater, which was used to cultivate all biofilms also is outlined. The experimental programs undertaken within the pipeline, including relevant sampling protocols and operating conditions are outlined in detail at the end of this chapter.

3.2 Experimental facility

3.2.1 General description

The pilot-scale pipeline facility (Figure 3.1 and Figure 3.2) was located within the Hydraulics Laboratory at Cardiff University School of Engineering. It was designed based upon the strict guidelines and principles outlined by Zagarola and Smits (1998) and Eisnor and Gagnon (2003); for the specific purpose of studying biofilm-flow interaction within DNs, over a wide range of Re_D. The facility was an open loop, recirculating system, which allowed high Re_D to be investigated with minimal daily water waste (Teodósio et al. 2011). The system, which was mostly fabricated from HDPE consisted of a storage tank (350 l), working part and recirculation part. The working part of the facility had an internal diameter of 102 mm, a length of 9.5 m and included a test pipe and visualisation pipe. The test pipe was a Solid Wall High Density Polyethylene (S-HDPE) pipe, which is commercially referred to as *PE100*. This pipe was selected due to its ubiquitous presence within the water management industry, which is particularly the case within the UK and especially within modern projects (Lauchlan et al. 2005; Nielsen et al. 2005; Douterelo et al. 2013). The recirculation part of the system, which was located directly underneath the S-HDPE pipe comprised of a flexible reinforced pipe of

D = 76.2 mm and a PVC pipe of $D \approx 100$ mm. A standpipe of length 0.3 m was located at the downstream end of the working part of the system.

The global and local frictional conditions of the S-HDPE pipe with and without fouling were accurately measured using a series of static pressure tappings and a traversable Pitot probe.

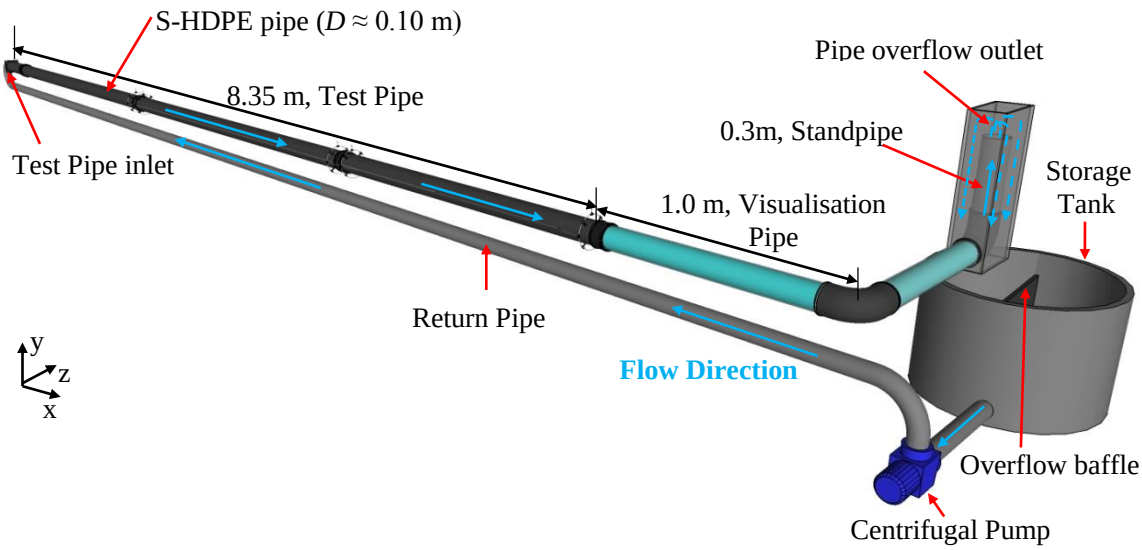

Figure 3.1 Perspective 3-D view of pilot-scale pipeline (the flow direction is clockwise).

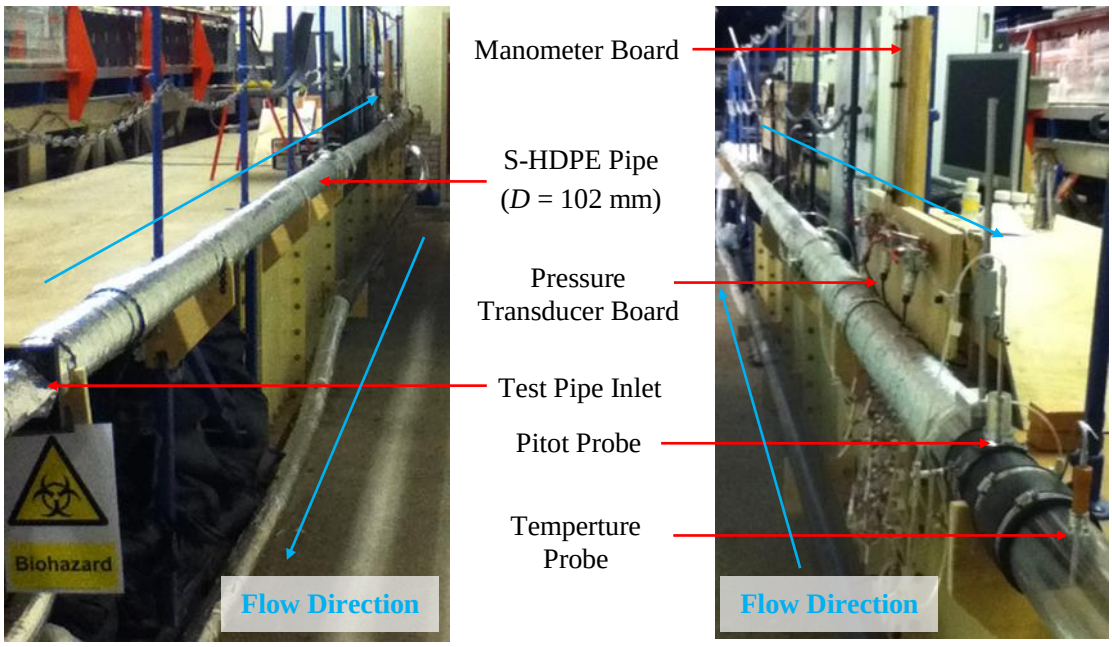

Figure 3.2 The pilot-scale pipeline in the hydraulic laboratory at Cardiff University School of Engineering.

3.2.2 Components

The water within the pipeline was recirculated by a 2.25kW single centrifugal pump (*Clarke* CPE30A1), which had a maximum design flow rate of approximately 13.3 l/s. The internal components of the pump were fabricated predominantly from cast iron. Therefore, in order to prevent rusting, the internal components were coated with anti-corrosive ceramic paint (*Devcon* Brushable Ceramic paint). Rusting would have had a negative impact on water chemistry and pump performance.

The maximum achievable system Q, which was based upon the pump, system geometry and surface conditions with and without fouling was 12.5 l/s (as shown by the pump performance plot presented in Appendix A.1 in Figure A.1). However, following extensive testing in the facility it was found that the pump could comfortably exceed 10 l/s, especially for prolonged periods. Furthermore, the minimum Q that the pump could maintain without causing significant and uncontrollable over heating issues (both within the pump and fluid) was approximately 2.5 l/s. Consequently, the achievable average freestream velocity range within the S-HDPE pipe was 0.3 m/s < $\overline{U}$ < 1.3 m/s, which equates to a Re_D range of $3.0x10^4 < Re_D < 1.30x10^5$ (based on a fluid temperature of 20ºC). Figure 3.3 illustrates relative location of this operational range within the Moody Diagram.

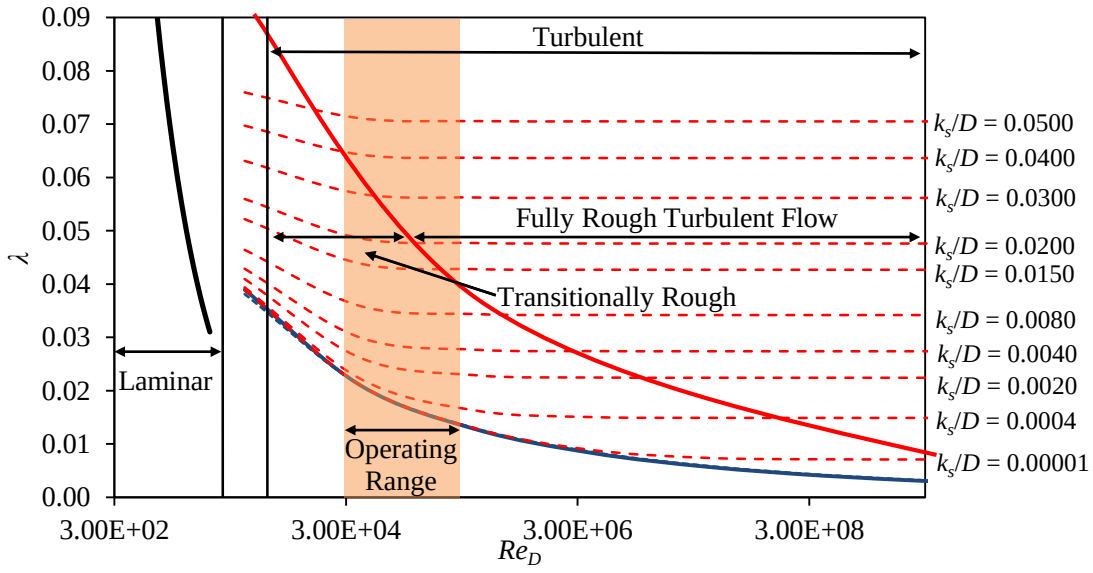

Figure 3.3 Moody Diagram, highlighting achievable operational within the pilot-scale pipeline (i.e. $3.00x10^4 < Re_D < 1.30x10^5$).

The flow rate within the pipeline was manually controlled and regulated using a gate valve, which was attached to the outlet side of the pump.

A honeycomb styled flow conditioner designed to encourage flow homogeneity within the test pipe was trialled. However, the difference between discrete measurements namely, local pressures and velocities with and within the flow conditioner, were negligible and within experimental uncertainties. Consequently, the flow conditioner was not used in any of the biofouling investigations outlined within the current study.

The standpipe (see Figure 3.4), induced a positive pressure throughout the system. Despite, the fact that negative pressures can be easily compensated for through standard numerical calculations, their presence was not desirable within the current study, as areas of negative pressure would likely draw in surrounding air, which if not dealt with correctly (i.e. by air bleeding) would cause anomalous pressure readings. A shroud was installed around the stand pipe to direct the flow back into the storage tank. The outlet arrangement (i.e. the overflow and drop) induced high aeration and as a result, promoted aerobic conditions within the system. Aerobic conditions were beneficial from a safety point of view, as the production of hydrogen sulphide and methane is limited in contrast to anaerobic conditions (Guisasola et al. 2008; Nielsen et al. 2008).

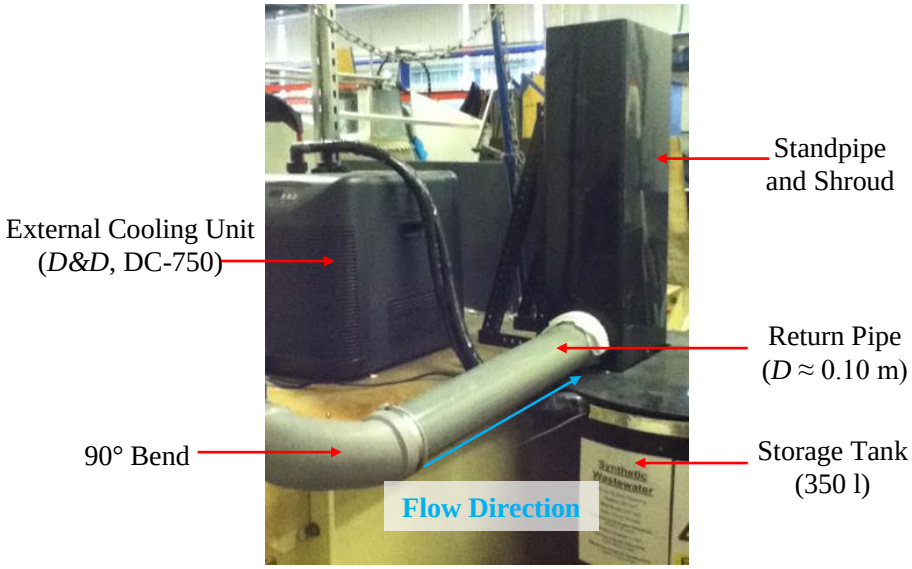

Figure 3.4 Outlet arrangement for the pilot-scale pipe, including the standpipe and external cooling unit.

Efforts were made to incorporate a temperature control system within the pipeline facility. Temperature control is essential in biofilm and boundary layer investigations; for the purpose of environmental and Re_D control. The water temperature in the facility could not be maintained at a constant level without control due to the significant heat input from the 2.25

kW pump and gate valve. The high ambient air temperature within the hydraulics laboratory (which could exceed 25°C in the summer) also made it difficult to maintain a constant temperature within the system without control.

Inability to maintain a constant temperature would have had the following impacts on the current stsudy:

1. The fluid properties, namely density and viscosity would vary with time and as a result, so to would Re_D. It is imperative that a constant Re_D is maintained during a boundary layer traverse to ensure that the near-wall boundary layer conditions are maintained (Andrewartha 2010). It is also essential that Re_D remains constant during different test scenarios for comparison purposes.
2. Temperature variations would have an influence on the biofilm development within the facility (Bott and Pinheiro 1977; Hallam et al. 2001; Lehtola et al. 2004; Barton 2006). Temperature is known to significantly influence bacterial growth and it has the potential to offset the impact of other ecological factors, such as those being investigated, i.e. flow hydrodynamics. Barton (2006) reported that large temperature deviations encourage filamentous- type growth. Filamentous- type growth is typical at high *Re* and can significantly increase the overall frictional resistance (Picologlou et al. 1980; Lewandowski and Stoodley 1995; Schultz and Swain 1999; Schultz 2000; Stoodley et al. 1998a; 1998b). Consequently, without appropriate temperature control, it would have been impossible to drawn reliable conclusions on the overall impact of discrete flow regimes being investigated within the current study.
3. Significant temperature variations would impacted on the effectiveness and accuracy of the ultrasonic flow meter (details to follow).

A constant fluid temperature within the system was maintained using an external cooling unit (*D&D*, DC-750), which was capable of cooling volumes of between 200-600 l to within ± 1°C, over the temperature, T range of 4°C < T < 28°C. A submersible pump (*Aqua Medic*, OR2500) was used to the divert storage tank water into the cooling unit, which then cooled the fluid to the required temperature, before returning it to the storage tank. The pump operated at a flow rate of 0.5 l/s. In addition to the cooling unit, the whole system was comprehensively insulated using high grade pipe insulation; to further prevent heat loss and reduce temperature variations within the system.

3.2.3 Test pipe

The S-HDPE test pipe was 8.5 m in length and was manufactured from a high density copolymer resin (referred to as *Carbon Black*). As illustrated in Figure 3.5 the test pipeline

composed of a Run-in Section and Test Section. The Run-in was 3.35 m (or 34 *D*) long and corresponded to the region 0.00 m < *x* < 3.35 m. The Test Section, which was were all the frictional measurements were recorded was 5.0 m in length and was located between 3.35 m < *x* < 8.35 m. Pressure tappings, in ring formation were located at five different streamwise locations (designated P_1 to P_5) along the Test Section. A traversable Pitot probe was also located at the downstream end of Test Section i.e. at P_5 (see Figure 3.5).

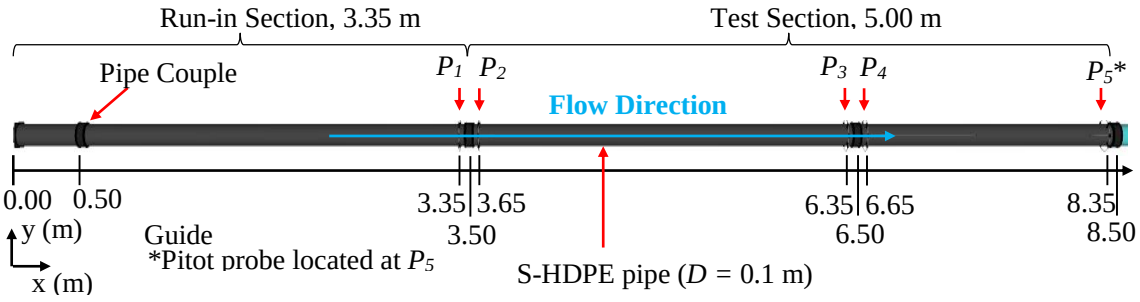

Figure 3.5 Schematic of the 8.5m test pipe of the pilot-scale pipeline, highlighting pressure tapping and Pitot probe location(s) (the flow direction is from left to right).

The test pipe had a measured outer diameter of 110.30 ± 0.28 mm and a wall thickness of 4.19 ± 0.28 mm. The inner diameter of the pipe was measured at 6 different locations along the length of the pipeline. In total 8 axial measurements were recorded at each of the 6 locations. The inner diameter at each location was at worst within ±0.68 mm of the average diameter at a given location, with the average being within ±0.44 mm. This tolerance was independent of angular and longitudinal location although, the measurements were limited to the pipe connection regions. The internal diameter of the S-HDPE pipe within the Test Section measured at 102.08 ± 0.44 mm.

The 8.5 m test pipeline consisted of four individual pipe segments, as shown in Figure 3.5. The four discrete segment lengths measured 0.5, 3.0, 3.0 and 2.0 m respectively. The discrete pipe segments were carefully aligned and connected by flexible pipe coupling in such a manner to ensure a smooth transition between the segments. Nevertheless, it was inevitable that the joints would cause some disruption to the velocity fields in the system. Consequently, pressure tappings were positioned either side of the joints, at 0.15 m from the leading edge. This allowed the frictional impact of the joints to be established. The pressure tappings located at the downstream end of each segment (i.e. P_1, P_3, and P_5) were at worst 1.85 m (19 *D*) downstream from the nearest joint, with most being 3.35 m (34 *D*) downstream from a

joint. The Pitot probe was 1.85 m downstream from the nearest joint. These lengths were deemed sufficient to ensure that any disruptions caused by the respective joints had a negligible impact on the respective pressure measurements.

The flexible nature of the S-HDPE pipe meant it was unlikely that the pipe was perfectly round along its longitudinal length. Consequently, the velocity fields within the system may have been influenced by potential variations in diameter and roundness along its longitudinal length, which could have implications of on the established frictional data recorded. Due to the nature of the pipe material it was not possible to correct this anomaly, and thus any potential errors arising from it were accepted. However, it should be stated that these errors would likely have been negligible. Furthermore, the frictional data determined is likely to be more representative of the material in its natural state if these anomaly remained uncorrected.

The straightness of the pipeline was confirmed to be within acceptable limits by a basic visual interception.

The test pipe was laid at a slight positive gradient (0.18%) in the upstream to downstream direction to allow for drainage back into the storage tank. As the system was pressurised this gradient had no effect on the experimental measurements and observations documented within the current study.

3.2.3.1 Surface finish

The test pipe had an extremely smooth surface finish. The equivalent Nikuradse-styled roughness scale typically associated with a S-HDPE pipe is between 0.003-0.015 mm (based on a survey of pipe manufacturers, results not shown). However, more often than not, the k_s value of solid wall HDPE pipes is taken as 0.012 mm (Grann-Meyer 2010). A Manning's roughness coefficient of n = 0.009 and Chezy roughness coefficient of c = 150 are also commonly used to define the effective roughness of a a S-HDPE pipe.

A surface is considered to be hydraulically smooth if k_s^+ is less than five viscous lengths. Based on a k_s of 0.012 mm the maximum value of k_s^+, which coincides with the maximum Re_D investigated (i.e. 1.30×10^5) would be $k_s^+ = 0.71$. Therefore, theoretically the pipe can be considered to be hydraulically smooth for the full range of Re_D assessed. For $Re_D = 3.0 \times 10^4$ and $Re_D = 1.30 \times 10^5$ the maximum allowable value of k_s to satisfy the smooth flow criteria would be k_s = 0.314 mm and k_s = 0.084 mm, respectively.

Figure 3.6 illustrates a typical three-dimensional micro-topography of the surface of the S-HDPE test pipe. This image was captured using a Veeco FEI (*Philips*) XL30 ESEM in the Gaseous Secondary Electron (GSE) detection mode, at x200 magnification. The image

analysis software, commercially known as MountainsMap (developed by *Digital Surf*, version 7), was used to process and profile the raw ESEM image.

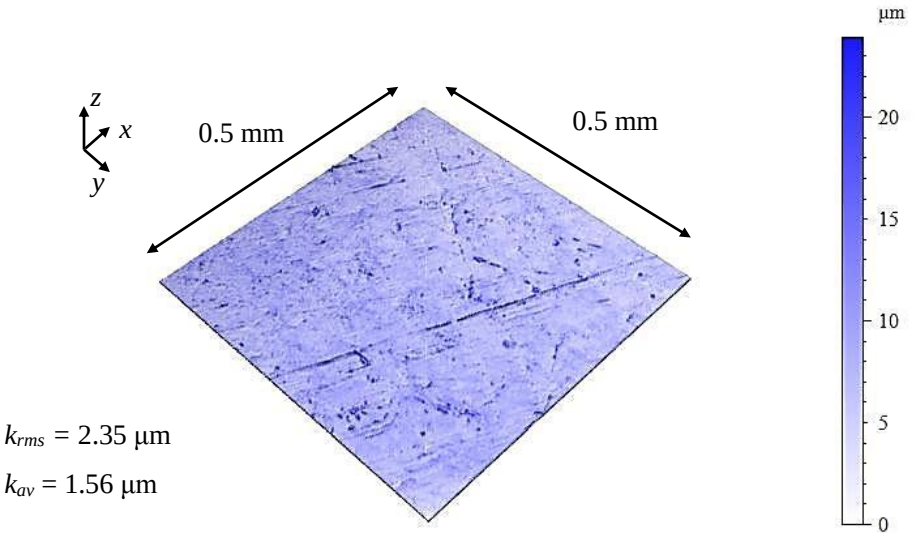

Figure 3.6 3-D surface topography map of the S-HDPE test pipe (Sample Size: 0.5 x 0.5 mm^2, Magnification: x200).

The surface roughness of a material can be defined by a number of different statistical parameters, including: mean roughness height, k_{av}; maximum peak-to-trough height, k_t (= $r_{masx} - r_{min}$ where r is the distance from the mean roughness height); root-mean-square roughness height, k_{rms} (=$\sqrt{1/\sum_{i=1}^{N} r^2}$; where N is the sample number); skewness of the roughness distribution, s_{kl} (= $\left(1/N \sum_{i=1}^{N} r_i^3 \left[(1/N) \sum_{i=1}^{N} r_i^2\right]^{3/2}\right)$ and kurtosis of the roughness distribution, k_u (= $(1/N \sum_{i=1}^{N} r_i^4 \left[(1/N) \sum_{i=1}^{N} r_i^2\right]^2)$. The aforementioned parameters have been related to equivalent roughness scales, namely k_s, with varying degrees of success (Hama 1954; Zagarola and Smits 1998; Shockling et al. 2006; Barton 2006; Barton et al. 2010; Andrewartha 2010; Flack and Schultz 2010). It has been documented, that an engineered surface can be related to k_s using k_{rms} and s_{kl} (Flack and Schultz 2010) or using k_{rms} on its own (Hama 1954; Zagarola and Smits 1998). However, the relationship reported by Flack and Schultz (2010) which combined both k_{rms} and s_{kl} (namely, $k_s \approx 4.43 k_{rms} (1 + s_k)^{1.37}$) is only applicable for surfaces with relatively high k_s values (k_s > 500 µm). For an engineered material with a small k_s value (i.e. k_s < 10 µm) the following relationships are typically applied (Hama 1954; Zagarola and Smits 1998):

$$k_s \approx 5 k_{rms}; \qquad \textit{Equation 3.1}$$

or

$$k_s \approx 3 k_{rms} \qquad \textit{Equation 3.2}$$

However, which relationship is used is dependent on the surface finish of the material in question. For instance, Hama (1954) suggested Equation 3.1 should be used for machine finished surfaces with an approximate Gaussian roughness distribution. Whereas, Equation 2.15 was suggested by Zagarola and Smits (1998) for materials, such as aluminium or steel which have been honed and polished. Based on Equation 3.1 and Equation 2.15 and the k_s value of 0.012 mm, the k_{rms} of the test pipe was estimated to be between 2.4-4μm.

The actual physical roughness of the test pipe was determined using ESEM imaging and the MountainsMap software. The software estimated the surface topography using a "single four image scan" approach as per the manufacturer's specification. ESEM images captured at 8 different axial locations along the test pipe were assessed, as shown in Appendix A.2 in Figure A.2. The sample area was 0.5x0.5 mm^2. The results of the physical roughness evaluation are presented in Table 3.1, which presents the average values determined from the 8 images. Prior to imaging the material samples were sterilised in an 80% ethanol solution for 12 h; for the purpose of eliminating any errors casued by foreign bodies on the surface, which would distort the measured surface roughness. For improved image resolution the samples were coated with gold before imaging.

Table 3.1 Physical and Equivalent surface roughness parameters of the S-HDPE pipe.

Material	k_{av} ***(μm)***	k_t ***(μm)***	k_{rms} ***(μm)***	S_{kl}	k_s ***(μm) (Predicted)***[1]	k_s ***(μm) (Actual)***[2]
S-HDPE Pipe	1.82±0.34	28.41±3.99	2.73±0.60	2.33±0.54	12.00	8.86±5.00

[2] As outlined by Grann-Meyer (2010), [1] See Chapter 4 for full details on actual k_s

The analysis indicated that the k_{av} and $\boldsymbol{k_{rms}}$ of the S-HDPE pipe was 1.82 ± 0.60 μm and 2.73 ± 0.60 μm, respectively.

A hydrodynamic evaluation of the test pipe over the range of $3.15x10^4 < Re_D < 1.23x10^5$ indicated that it had a k_s = 8.86 ± 5.00 (for full details see Chapter 4). Therefore, the relationship between k_{rms} and k_s for the S-HDPE pipe was found to be $k_s = 3.25\ k_{rms,}$ which is approximately equal to the relationship proposed by Zagarola and Smits (1998) (i.e. Equation 3.2).

The effective roughness of the 100 mm diameter, S-HDPE test pipe was found to be hydraulically equivalent to a 400 mm diameter, Structural Wall High polyethylene (Str-HDPE) pipe, as shown by Moody Diagram presented in Figure 3.7. This is despite the

inherent differences in physical roughness of the two materials. Full details of this comparative analysis are presented in in Appendix A.3.

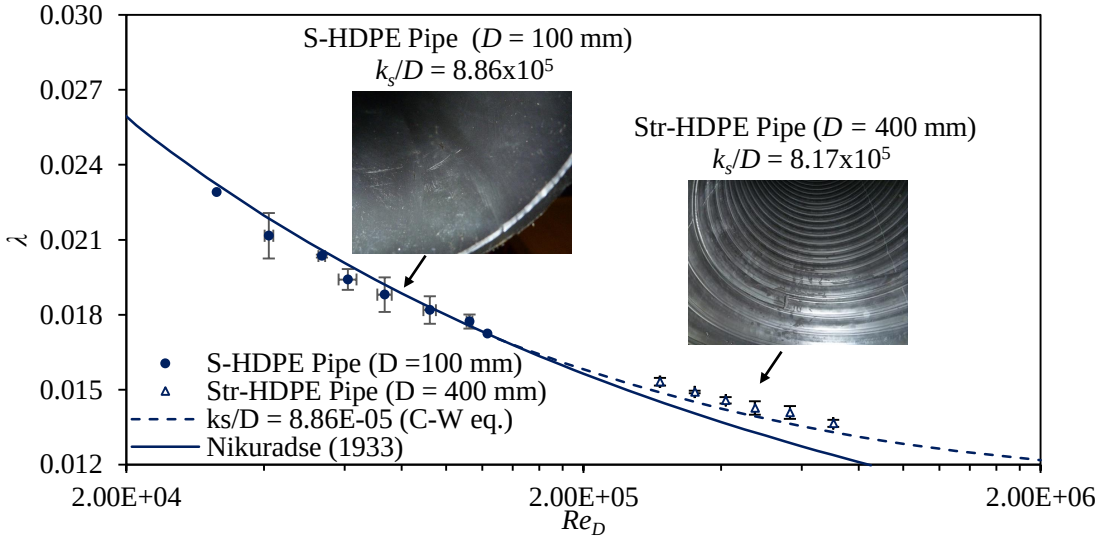

Figure 3.7 Moody Diagram illsurating the determined friction factors for the 100 and 400 mm internal diameter HDPE pipes.

3.2.3.2 Flow development length

In order to accurately determine the test pipe's frictional resistance, it was important to establish whether the flow in the Test Section was fully developed. A flow is considered to be fully developed to the highest criteria when all mean flow quantities (namely, velocity and pressure gradient) and all turbulence quantities are constant, independent of streamwise location. Boundary layer growth, as a result of viscous friction between the fluid and wall will commence at the entrance of the system (i.e. the pipe inlet), as shown by Figure 3.8. The development will continue in a streamwise direction until a critical threshold or thickness is reached. Typically, under idealised conditions within a pipe this coincides with the pipe's centreline, as shown in Figure 3.8. After this point the boundary layer is considered to be fully developed. The overall development length or entrance length, L_e for a zero-pressure gradient system is given as (Zagarola and Smits 1998);

$$L_e \approx L_0 + L_1 + L_2 \qquad \textit{Equation 3.3}$$

where L_0 is the initial boundary layer development length, L_1 is the turbulent boundary layer development length and L_2 is the turbulent quantities development length.

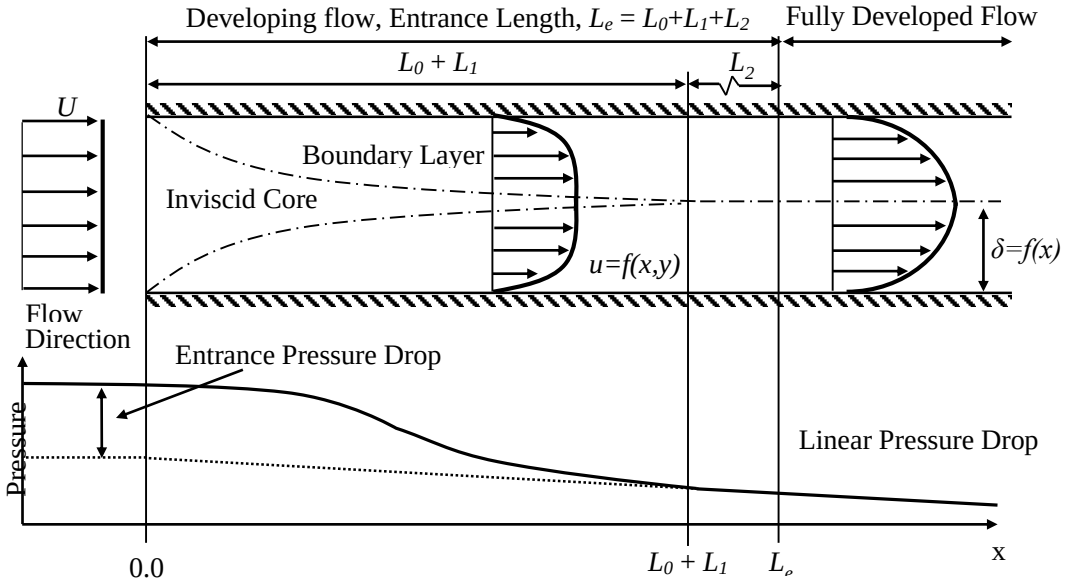

Figure 3.8 Flow development within a typical pipe, highlighting development lengths and the fully developed flow region.

The initial boundary layer development length is dependent on the streamwise length Reynolds number, Re_l. For systems with low levels of freestream turbulence a reasonable estimate of Re_l is $2x10^5$. On this basis L_0 is given by:

$$\frac{L_0}{D} \approx \frac{Re_l}{Re_D} \approx \frac{2 \times 10^5}{Re_D} \qquad \textit{Equation 3.4}$$

The maximum value of L_0 coincides with the lowest Re_D investigated and as a result, in high turbulent investigations (i.e. in the order of 10^6) it is typically ignored. However, based on the Re_D range investigated within the current study (i.e. $3.0x10^4 < Re_D < 1.30x10^5$), L_0 was included in summation of the overall development length.

If the mild favourable pressure gradient and the transverse curvature of the pipe wall are neglected, then L_1 is inversely proportional to the skin-friction coefficient and is given by;

$$\frac{L_1}{D} \approx \frac{C_1}{\lambda} \qquad \textit{Equation 3.5}$$

where C_1 is an empirical constant, taken as 0.5 for Re_D in the order of 10^5 (Dean and Bradshaw 1976.

A more general estimate of L_1 for turbulent flow is given as a function of Re_D:

$$\frac{L_1}{D} \approx 4.44(Re_D)^{1/6} \qquad \textit{Equation 3.6}$$

The development length required to satisfy fully developed turbulence quantities is given by;

$$\frac{L_2}{D} \approx \frac{C_2}{\lambda^{1/2}} \qquad \textit{Equation 3.7}$$

where C_2 is empirical constant, estimated as 5.0 (Dean and Bradshaw 1976).

Previous investigations in pipes and channels have shown that for Re_D in the order of 10^5, the required overall entrance length is typically within the range of $60\ D < L_e < 100\ D$ (Perry and Abell 1975). Notwithstanding, in most practical engineering cases entrance affects are typically deemed negligible after a length of 10 D (Chadwick et al. 2004). The maximum value of L_e for the system, which coincides with the maximum Re_D investigated (i.e. $Re_D = 1.30\text{x}10^5$) was found to be 6.82 m (or 69 D), as shown by Figure 3.9a. This length represents the total length required to attain fully developed flow in terms of both mean flow and turbulence quantities. For the purpose of the current study only the mean flow needs to be fully developed (i.e. $L_0 + L_1$). The maximum development length required to attain fully developed flow in terms of mean flow structure was 3.03 m (or 31 D), as shown by Figure 3.9b. Consequently, the 3.35 m Run-in Section provided sufficient length to ensure fully developed mean flow within the Test Section. Furthermore, it can be stated that the flow was fully developed to the highest criteria prior to P_5, which was where local velocity data was recorded.

The boundary layer development relationship proposed by Schlichting (1979), as given by Equation 3.8 was also used to illustrate that Run-Section was sufficient in attaining fully developed flow. Figure 3.10 illustrate the results of application of Equation 3.8. In Figure 3.10a the fully developed boundary layer thickness was taken as the pipe radius (i.e. 0.05 m), whereas in Figure 3.10b, the experimentally determined values of δ were used (as given in Section 4.4 in Table 4.2).

$$\delta = 0.37x\ (Re_x)^{-1/5} \qquad \textit{Equation 3.8}$$

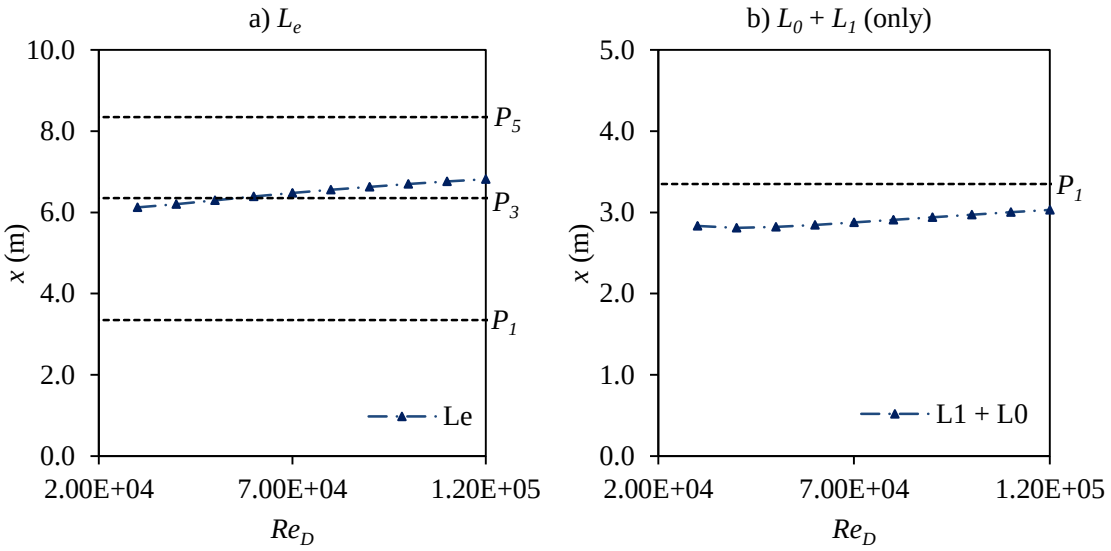

Figure 3.9 The flow development lengths of a) L_e and b) L_0+L_1 (only) for the pilot-scale pipeline.

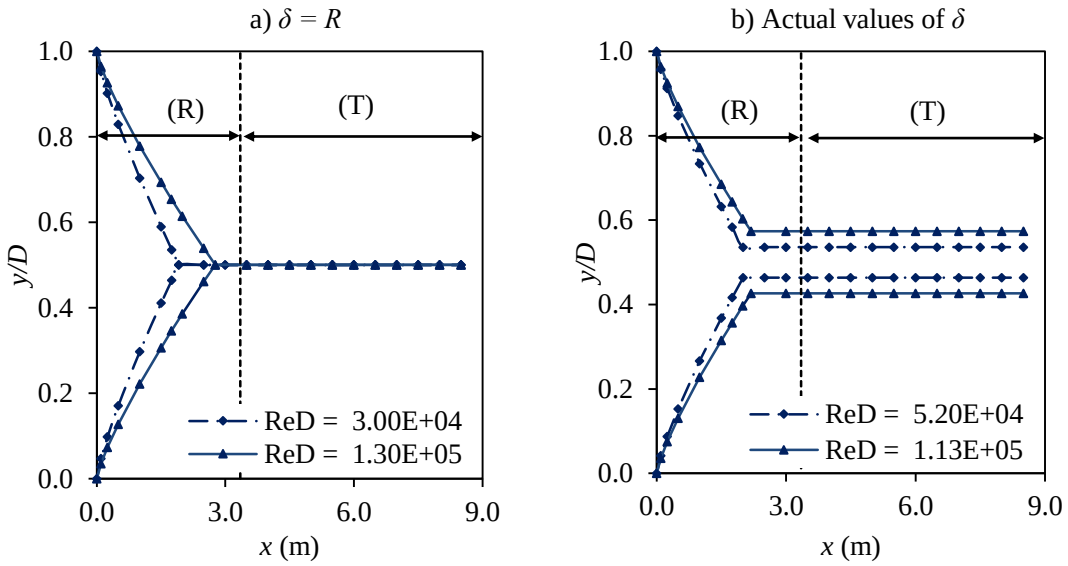

Figure 3.10 Boundary layer development within the pilot-scale pipeline using a) $\delta = R$ and b) actual values of δ. Highlighting the Run-in (R) and Test (T) Sections.

3.2.4 Visualisation pipe

The visualisation pipe, which was completely transparent had an internal diameter of $D \approx 100$ mm and an overall length of 1.0 m. It was located within the region of 8.5 m < x < 9.5 m. The purpose of the pipe was to allow for real-time visual analysis of biofilm development. A high definition web camera (*HP* HD 2300), along with a high resolution camera (*Braumer* TXG 14F) were used to capture stills and videos of the biofilms incubated within the current study.

Both camera were positioned on the invert side of the pipe. The web camera could capture a 0.3 m length of the pipe, whereas the high resolution camera was traversable and as a result, could capture a 0.5 m length. Each traverse typically composited of three images and included a 10% overlap, as shown in Figure 3.11.

It should be noted that the visualisation pipe was covered with high grade blackout material when images were not being captured.

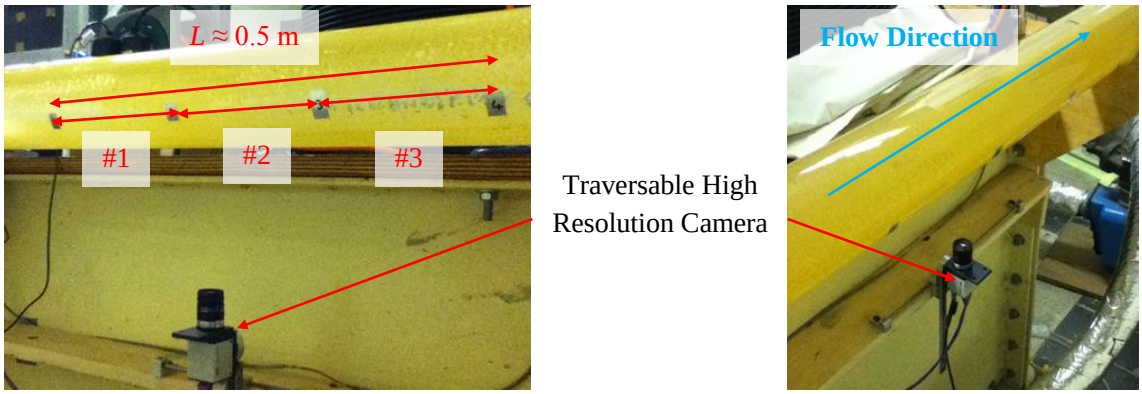

Figure 3.11 Traversable high resolution camera arrangement within the pilot-scale pipe facility.

3.3 Measurements and instrumentation

The following sections detail the measurements that were recorded and instrumentation that was installed on the pilot-scale pipeline. Where necessary, the methodology used to determine the dependent variables, such as mean-velocity is also provided.

3.3.1 Static wall pressure and headloss

As the flow within the test pipe was fully developed pipe flow, the frictional resistance of the pipe can be accurately determined directly from the system's Pressure Gradient (PG) by applications of simple equilibrium considerations (i.e. Equation 2.4). In the current study, static wall tappings located at various circumferential and longitudinal locations were used to measure the system's PG. A wall tapping is essentially a small hole drilled in the wall, which is connected to a pressure gauge.

Four wall tappings located at 45°, 135°, 225° and 315° from the vertical centreline, were linked in a pressure arrangement (see Figure 3.12 and Figure 3.13) long along the Test Section. The pressure ring arrangement allowed a circumferential average pressure to be determined at each location, which reduced potential errors caused by uneven and unstable flow distributions (Barton 2006).

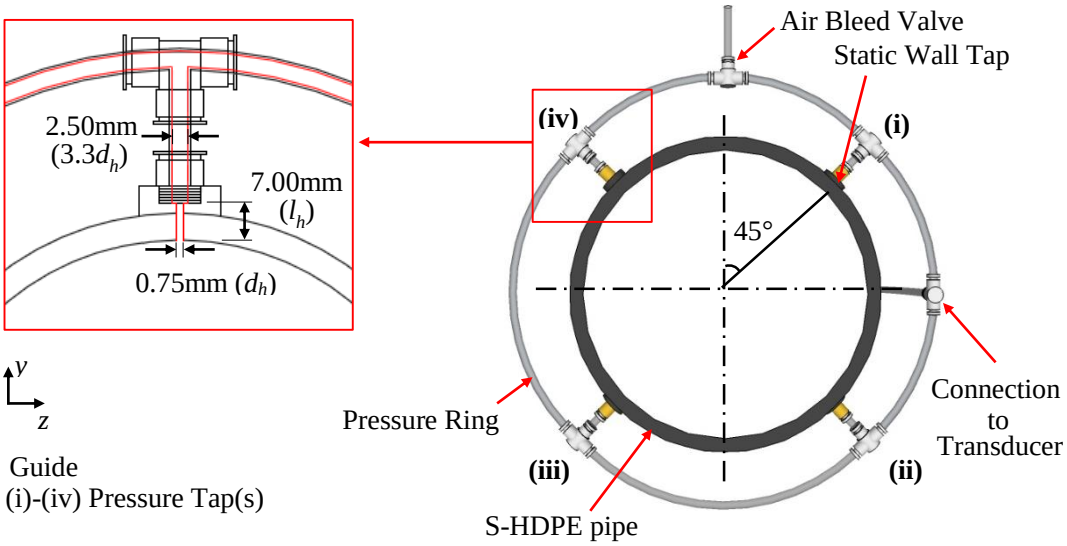

Figure 3.12 Schematic of a standard wall tapping arrangement within the pilot-scale pipeline.

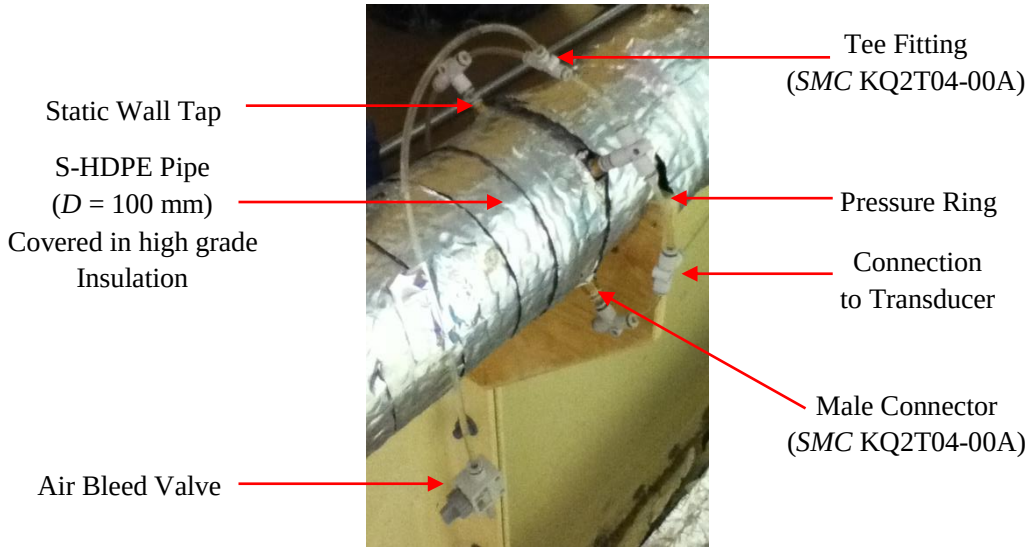

Figure 3.13 Photograph of a standard wall tapping arrangement within the pilot-scale pipeline.

A connection pipe fitted to each pressure ring relayed the static pressure to the pressure transducer. The pressure ring and connection pipe were fabricated from a 2.5 mm internal diameter clear Neylon tube (*SMC* TUS0425N-20), and connected together by high performance grade pipe fittings (namely, *SMC* KQ2T04-00A and KQ2H04-02AS).

The presence of the wall tapping disrupts the surface characteristics and thus affects the flow structure. Typically, streamlines are deflected into the hole causing eddies and vortices form within the cavity of the tapping, as shown by Figure 3.14.

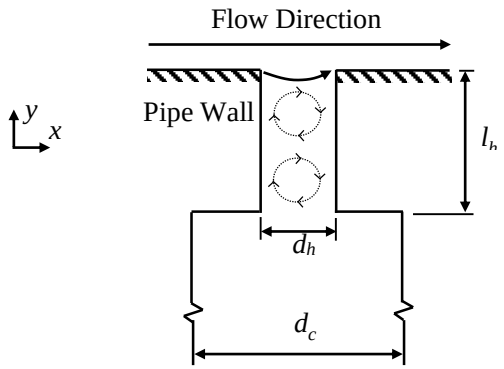

Figure 3.14 Wall tapping geometry and flow structure, adapted from McKeon and Smits (2002).

As a result, the pressure recorded from the tapping is generally higher than the true or actual value associated with the boundary. The error induced by the wall tapping – referred to as the pressure error, P_E – is a function of the hole diameter d_h, the hole depth l_h, the diameter of the connection to the manometer d_c, the wall shear stress, the fluid density and the dynamic viscosity. For large d_h/D ratios, i.e. $d_h/D > 0.1$ pipe diameter is also important. Therefore, the pressure error caused by a wall tapping can be expressed non-dimensionally by (Shaw 1960; McKeon and Smits 2002):

$$\Pi_p = \frac{P_E}{\tau_w} = f\left(\frac{d_h u^*}{\nu}, \frac{d_h}{D}, \frac{l_h}{d_h}, \frac{d_c}{d_h}\right) \qquad \textit{Equation 3.9}$$

where Π_P is the non-dimensional pressure error.

It is generally suggested that in order to ensure a wall tapping has minimal impact on the pipe's flow structure ratio of d_h to D should be as small as physically possible, as ΔP approaches zero as d_h approaches zero (Shaw 1960; McKeon and Smits 2002). However, it has been documented that even a very small hole can introduce a considerable pressure error (Kistler and Tan 1967). In the current study d_h = 0.75 mm (i.e. d_h/D = 0.0075), as shown in Figure 3.12. Therefore, the wall tapping diameter Reynolds numbers, d_h^+ ($=d_h u^*/\nu$) was at worst 44.63 (i.e. for $Re_D = 1.30\text{x}10^5$). The ratio of l_h/d_h dictates the vortex structure and flow development within the cavity. The ratio of l_h/d_h used in the current study was constant and equal to 9.3 (i.e. l_h = 7.0 mm), which was sufficient ensured fully developed flow within the

cavity, independent of *Re* (Shaw 1960; McKeon and Smits 2002). The diameter of the connection pipe is also a salient design consideration. For instance, when $d_c > d_h$, the pressure error can be negative (Chue 1975) and the overall pressure reading at the gauge is more stable, due to viscous damping. Typically, if d_c is not equal to d_h, then the ratio of d_c/ d_h should be at least 2 (Shaw 1960). In the current study the ratio of d_c/ d_h was 3.3 (i.e. d_c = 2.50 mm) and was therefore deemed acceptable. The length of the connection pipe, which at its maximum was approximately 5.0 m (i.e. for P_1) was found to have a negligible impact on the measured pressures. In particular, it was found that under non-flow conditions all recorded pressure discrepancies between respective streamwise measurement locations were within experimental uncertainty. This also suggested that any potential damping effects induced by the flexible nature of the (Neylon) connection pipe, were also negligible.

For accurate pressure readings the hole edge of the tapping should be square and free from any hole burrs (Shaw 1960; McKeon and Smits 2002). In order to achieve minimal hole edge burring and/or rounding, all tappings were drilled inwards from the internal surface. However, some degree of burring and/or rounding was unavoidable, particularly due to the very small nature of the tapping. Sanding was avoided as this is likely to round the edge of the tapping and would compromise the internal surface finish of the pipe in the vicinity of the tapping. Nevetheless, any rounding and burring was considered to have a minimal effect on pressure measurements. For instance, McKeon and Smits (2002), who examined tappings, which had been prepared in the same manner as those within the current study of diameters between 0.254-2.381 mm, found that only the largest d_h had burring issues, and even then the impact was negligible.

Based upon the current study's pressure tapping arrangement and the recommendations outlined by McKeon and Smits (2002) and Shaw (1960) the pressure error was at worst P_E/τ_w = 0.09 (i.e. for d_h^+ = 44.63 and $Re_D = 1.30\text{x}10^5$). Zagarloa (1996) reported that a P_E/τ_w of 0.10 only caused a ±0.03% error in the average freestream velocity established from the mean-velocity data. Consequently, the maximum pressure error reported within the current study would have likely had negligible effect on the recorded headloss and velocity measurements. Notwithstanding, the greatest source of pressure error and measurement instability within the current study was attributed to trapped air within the connection tubes and pressure transducers. In order to neutralise trapped air's overall impact, the connection tubes were periodically drained of air bubbles. Each pressure tapping ring had its own air bleed valve, located at the top of the ring, as shown in Figure 3.12. Trapped air within the pressure transducers, which was a particular problem was resolved by attaching a "de-airing block" to each pressure transducer, as shown in Figure 3.15. The "de-airing block" allowed the air

bubbles trapped at the dead end of the transducer (i.e. at its diaphragm) to be released, with minimal disruption to the main system.

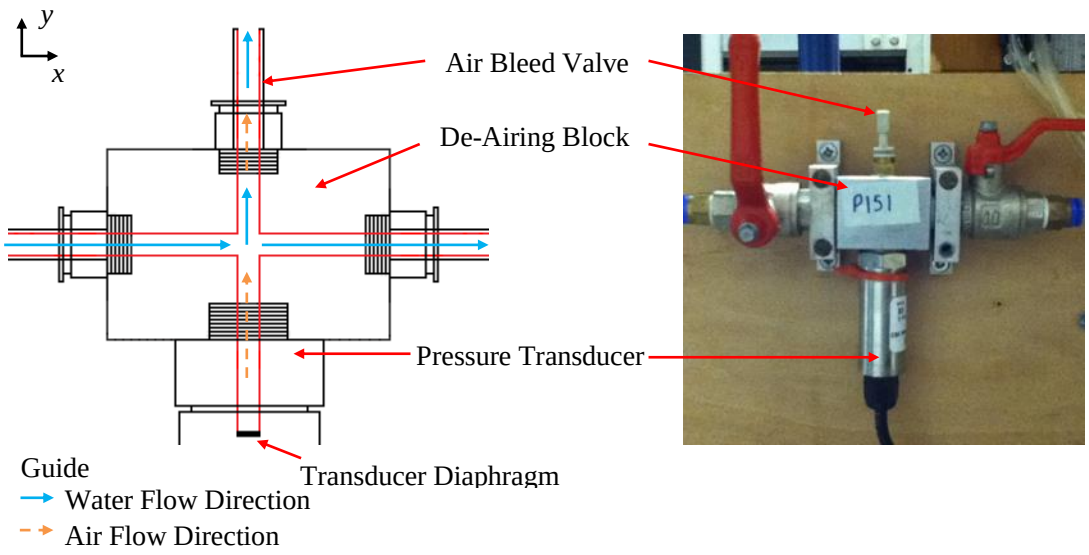

Figure 3.15 De-airing block arrangement used within the pilot-scale pipeline (highlighting idealised water and air flow directions).

3.3.2 Local velocity

The purpose built Pitot probe, which was used to obtain all time-averaged velocity profiles within the current study is presented within Figure 3.16. A Pitot probe was selected, as its presence within the test pipe causes minimal disruptions to the flow structure and/or the biofilm development. Pitot probes have also been widely used in biofouling investigations (Andrewartha 2010; Barton 2006; Barton et al. 2008, Perkins et al. 2013; Walker et al. 2013). A standard sized Acoustic Doppler Velocimeter (ADV) probe was initially considered, however, the probes size relative to the cross-sectional area of the test pipe meant its use was unfeasible.

As the Pitot probe was positioned permanently at P_5, it recorded the local vertical velocity profile across for the P_5 (i.e. x =8.35 m) plane. The Pitot probe had a circular, 1.0 mm diameter cross-section and a square end. The selected probe diameter provided adequate spatial resolution within the near wall near (Zagorola 1996). Furthermore, Andrewartha (2010) found when comparing Pitot probes of varying geometries and sizes that a circular 1.0 mm probe gave acceptable results, which collapsed well onto expected curves, across a range of *Re*. Interestingly, Andrewartha (2010) found that a 1.0 mm diameter probe out performed a 0.7 mm diameter probe. The 1.0 mm diameter probe was attached to a 10.0 mm diameter stiff

strut, which provided rigidity and prevented flow induced movement. Though, the probe's aperture was located in the same plane as the wall tapping at P_5, the main body of the probe was offset from the plane by 30 mm in a downstream direction. This minimised potential distributions to the pressure measurements caused by the presence of the Pitot probe.

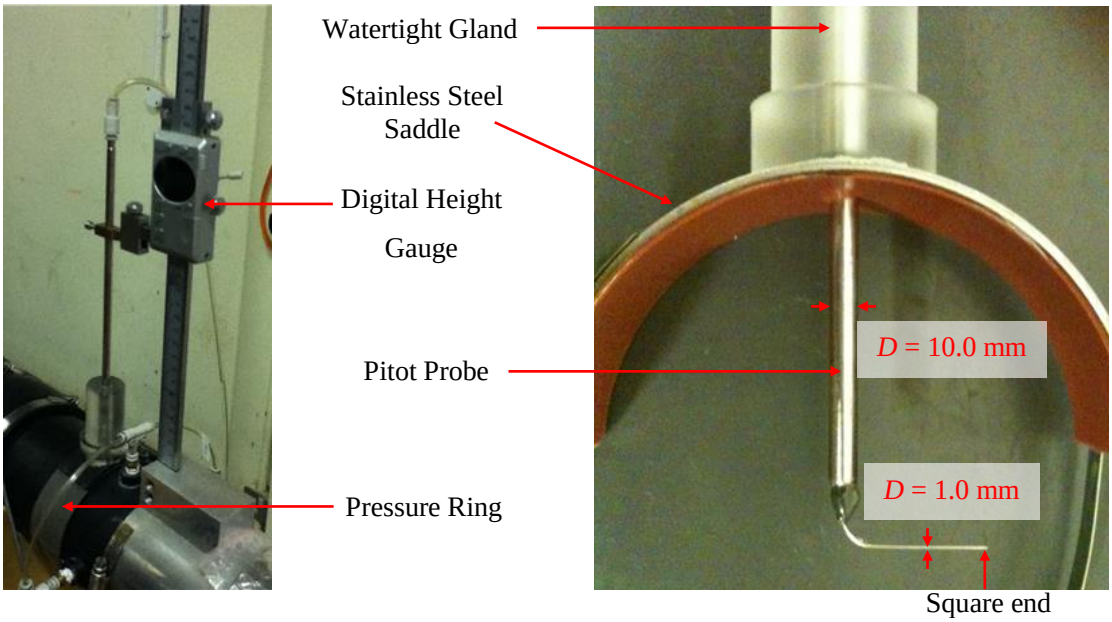

Figure 3.16 Purpose built pitot probe used to measure boundary layer velocity profile within the pilot-scale pipeline.

A watertight gland, consisting of two 'O' ring-type seals, allowed the probe to freely traverse 93% of the pipe's vertical plane or *y*-axis. A stainless steel watertight saddle securely fastened and held the Pitot probe along the pipe's vertical centreline. This arrangement allowed the entire assembly to be removed from the test pipe for maintenance. The Probe was manually aligned with the flow direction to at least ±1º. This tolerance has been found to cause an insignificant error in the Pitot probe pressure (Zagarola 1996). The distance along the *y*-axis at any particular transverse, relevant to the wall was accurately determined using a digital height gauge (*Rapid* AK9636D). The height gauge had an accuracy of ±0.01 mm, and was manually zeroed by positioning the Pitot probe parallel to the pipe's invert.

The local velocity, *u* can be determined at any given normal-wall position from the dynamic or stagnation pressure head measured by the Pitot probe, H_{Pitot} and the static pressure head, H_{Static} measured by wall tappings using the Bernoulli equation:

$$u = \sqrt{2g(H_{Pitot} - H_{Static})} \qquad \textit{Equation 3.10}$$

To accurately determine streamwise velocity using a Pitot probe and static wall tapping, several corrections were required to account for the effects of viscosity, velocity gradient, the presence of the wall, and turbulence (McKeon and Smits 2002; McKeon et al. 2003; Bailey et al. 2013). The viscous correction is only required when the Pitot probe's aperture diameter Reynolds number, d_p^+ ($=d_p v/u^*$; where d_p is the diameter of Pitot probe's aperture) was less than 100. Since, d_p^+ seldom exceed 50 within the current study the viscous correction was disregarded. The use of a Pitot probe at the wall, introduces additional adverse effects through nonlinear averaging of pressure variation across the probe aperture and asymmetric deflection of the streamlines. Typically, the impact of spatial averaging across the probe aperture is small, relative to the streamlines deflection. The streamlines are deflected towards the region of lower velocity. Consequently, the probe registers a higher dynamic pressure than the actual dynamic pressure of the given location. This error is most commonly addressed by applying a virtual shift to the location of the measurement recorded by the Pitot probe in the normal to wall direction by an amount Δy. The required Δy was determined by the method proposed by McKeon et al. (2003) and will be referred to herein as the McKeon Method. The McKeon Method states that when $y > 2d_p$, Δy is given by;

$$\frac{\Delta y}{d_p} = 0.15 \tanh\left(4\sqrt{\alpha}\right) \qquad \textit{Equation 3.11}$$

where α is a non-dimensional velocity gradient given by:

$$\alpha = \frac{d_p}{2u}\frac{du}{dy} \qquad \textit{Equation 3.12}$$

A near-wall correction is required when $y < 2d_p$ to account for the blockage effects in the vicinity of a wall, where the presence of the probe causes a reduction in the aforementioned shear-induced streamline deflections.

In the near-wall region and for $8 < d_p^+ < 110$, the McKeon Method states that Δy is given by:

$$\frac{\Delta y}{d_p} = 0.12 \qquad \textit{Equation 3.13}$$

A separate turbulence correction is not required when the McKeon Method is utilised.

3.3.3 Pressure

All static and dynamic pressure measurements were obtained using three industrial high accuracy pressure transducers (*Omega* PXM409-070HG10V), designated 1 to 3 (see Figure 3.17).

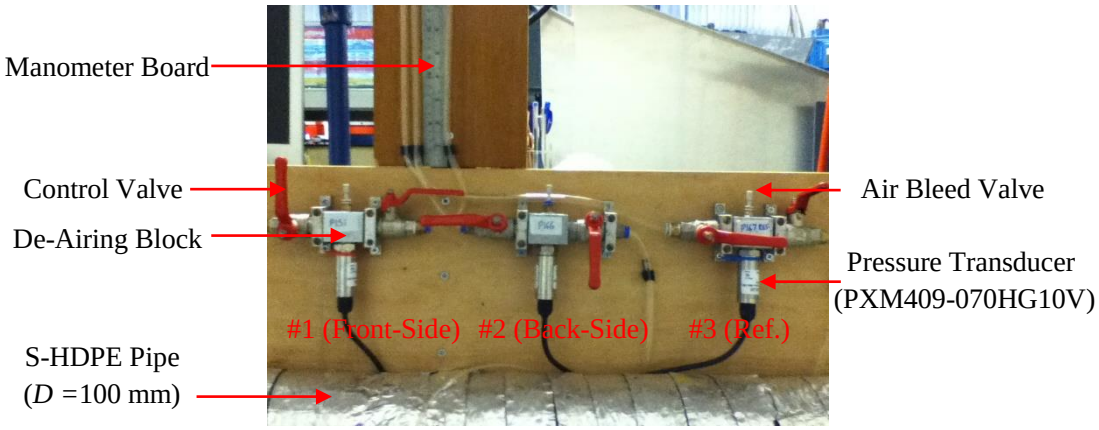

Figure 3.17 Photograph of the three pressure transducers used to record all static and dynamics pressure measurements within the study.

The pressure transducers had an operation range of 0 to 70 mbar (or 0 to 71.2 cmH_2O, at 20ºC) and full scale accuracy (including effects of linearity, hysteresis and repeatability) of ±0.08%, which equates to 0.06 mbar or 0.57 mmH_2O (at 20ºC). A measurable k_s accuracy of ±0.128 mm < k_s < ±0.002 mm can be estimated for Re_D range of $3.0x10^4 < Re_D < 1.30x10^5$ using defined instrumentation accuracy (and L = 5.0 m). The response time of the transducer was 1 ms, which made it suitable for unsteady measurements. A bench top power supply (*Rapid* SMPS 25A) supplied the required 15-30 Volts to energise the pressure transducers.

Each H_f measurement within the current study consisted of two sets of pressure readings. The two sets of readings were designated the "front-side" and "back-side" measurement sets. Each of the "front-side" and "back-side" sets consisted of three discrete pressure readings, recorded simultaneously by the three pressure transducers. The pressure readings recorded by transducers 1 and 2 within each set, related to either an upstream or downstream static pressure, depending on the respective measurement set. For instance, in the case of the "front-side" measurement set, transducers 1 and 2 recorded the static pressure at a particular upstream and downstream location, respectively. Alternatively, in the case of the "back-side" measurement set, the same location was recorded, although, transducers 1 and 2 recorded the opposite location to that recorded during the "front-side" set (i.e. downstream and upstream, respectively). When determining the local velocity profile, transducers 1 and 2 recorded H_{Pitot}

and H_{Static} for the "front-side" measurement set. Whereas for the "back-side" measurement set, transducers 1 and 2 recorded H_{Static} and H_{Pitot}, respectively. An average reading was established from the "front-side" and "back-side" measurement sets. Transducer 3, in both sets always recorded the static pressure at location P_1, and was designated the reference pressure. The reference pressure was used to remove any temporal variations, observed during the testing period.

A series of control valves were used to deviate required pressure to the relative transducer, as shown schematically by Figure 3.18 and Figure 3.17.

The pressure transducers were regularly calibrated using individual wall mounted water manometers. The voltage output was recorded against the water level in the relative manometer. The reading accuracy of the manometer was ± 0.5 mm. Typical calibration curves for the three transducers are presented in Appendix A.4 in Figure A.8. The transducers were calibrated prior to every measurement series within the current study. A minimum h of 5.0 cmH_2O was required when calibrating, to provide sufficient hydro-static pressure to seal the control valves, and thus provide a stable reading.

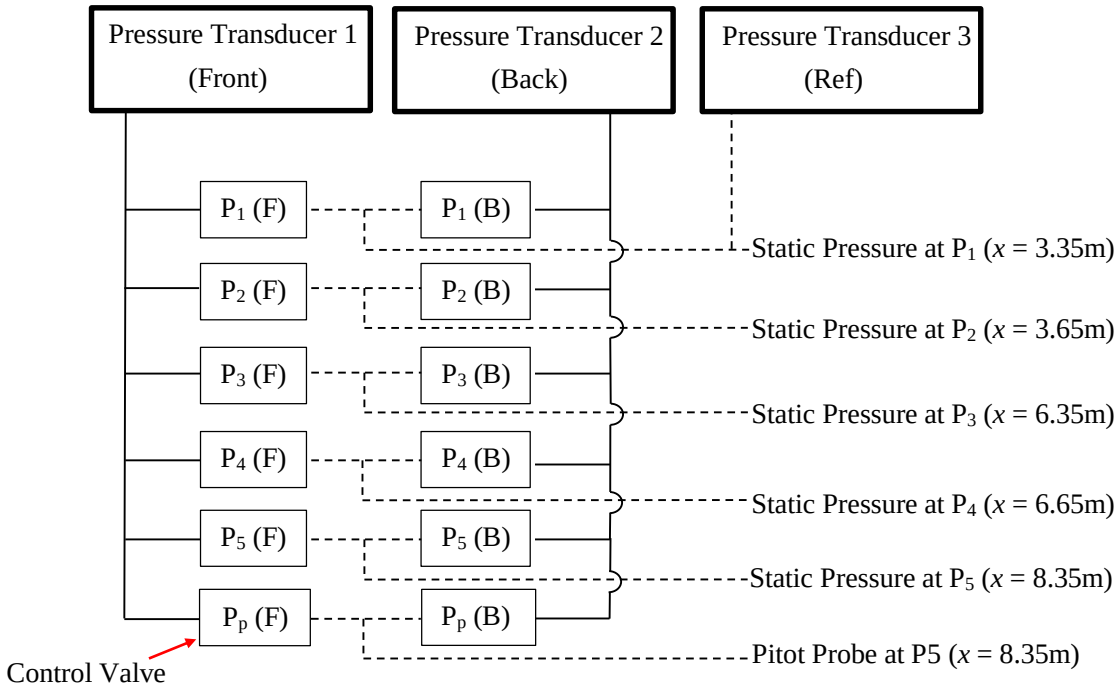

Figure 3.18 Pressure connection schematic diagram for the pilot-scale pipeline.

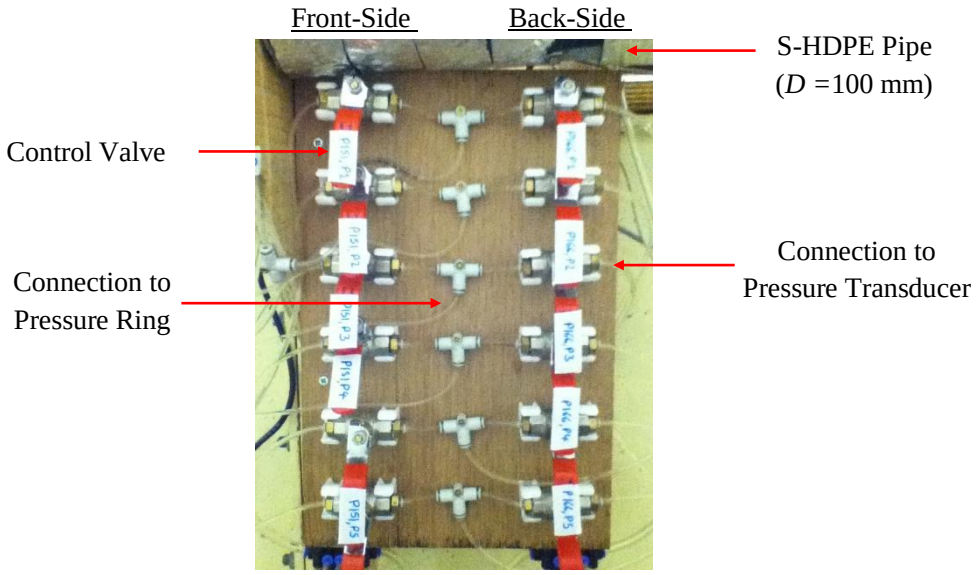

Figure 3.19 Pressure connection relay board for the pilot-scale pipeline.

3.3.4 Flow rate

The average volumetric flow rate was recorded using a "time of fight" ultrasonic flowmeter (*Nixon* CU100), which had a reading accuracy of ±1.5%, and an operational range of 0.2 m/s < $\overline{U}$ < 12.0 m/s. An ultrasonic flowmeter was selected due to its non-intrusive nature and ability to measure clean and dirty fluids (providing suspended solids are < 2%). Ultrasonic flowmeters have been widely used in biofouling investigations (Barton 2006; Barton et al. 2008, Perkins et al. 2013). Potential alterations to the attachment pipe's surface characteristics and/or to internal diameter as a result of biofilm development were found to have a minimal affect on the flowmeter operational performance. Furthermore, any impact was easily compensated through accurate re-calibration (as shown in Figure 3.21).

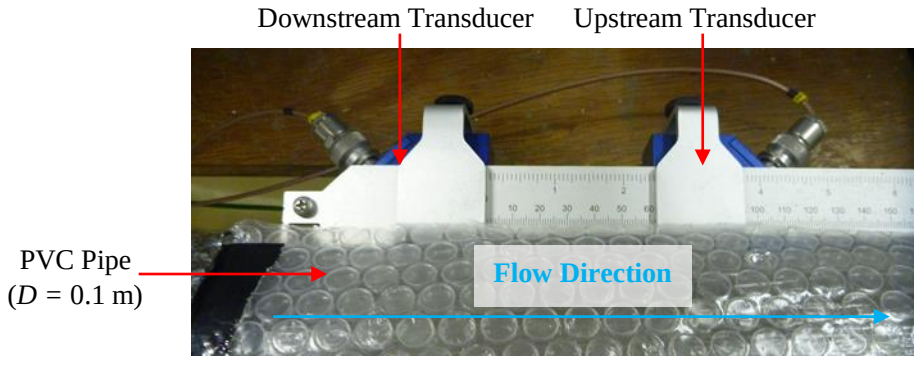

Figure 3.20 Ultrasonic flowmeter attached to the recirculation PVC pipe of the pilot-scale pipeline.

The flowmeter was attached to a 5.0 m long (undisrupted), PVC pipe, which was located within the recirculation part of the facility. A PVC pipe was selected in accordance to the manufacturer's recommendation for improved accuracy and performance. The flowmeter's ultrasonic transducers were positioned longitudinally along the PVC pipe at 90° from the vertical centreline. For maximum reading stability and accuracy the flowmeter's transducers were located 3.8 m (38 *D*) and 1.0 m (10 *D*) from the PVC pipe's inlet and outlet, respectively.

The ultrasonic flowmeter was verified and calibrated against values of Q independently established from the mean-velcoity measured using the Pitot probe. Flow rate can be determined from the velocity profile at any streamwise location using the conservation of mass principle, as given by:

$$Q = \bar{U}A = 2\pi \int_0^R u\, dr \qquad \textit{Equation 3.14}$$

For a 1.0 mm diameter Pitot probe, the spatial resolution near the wall was limited to approximately 0.5 mm. Consequently, the Q needed to be corrected to account for this unresolved region near the wall (i.e. $y < 0.5$ mm), especially for high Re_D were it is likely that the mass flux in the region between wall and the first wall-normal measurement position would be significant. The simplest method to account for the near wall region was to assume a linear velocity variation from the point closet to the wall (Zagarola 1996). Typical calibration data for the fouled and non-fouled pipe is presented in Figure 3.21.

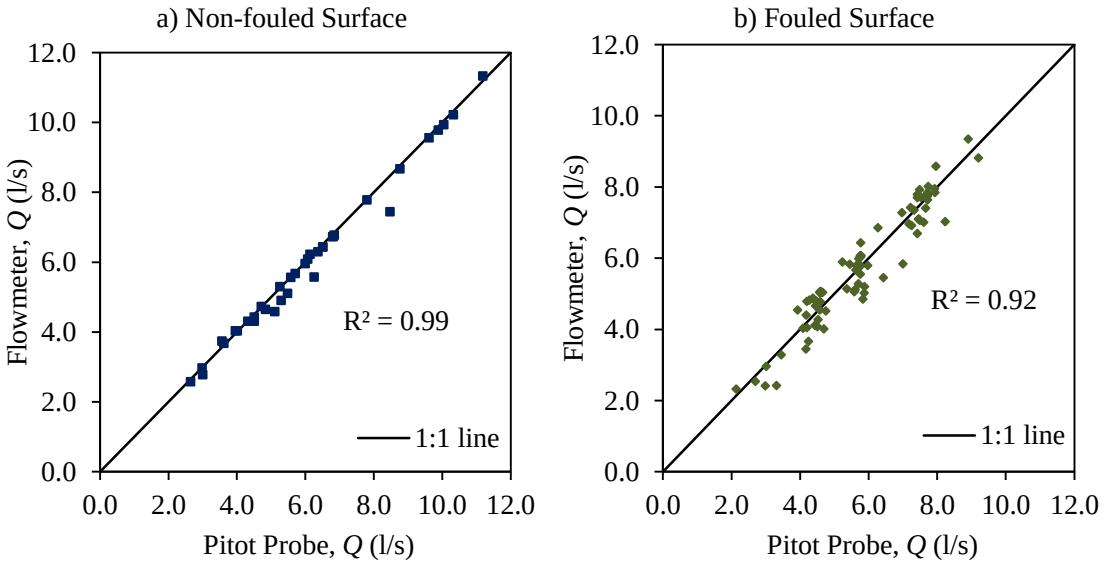

Figure 3.21 Average volumetric flow rate check for a) non-fouled and b) fouled surfaces.

Figure 3.21 illustrates that the values of Q determined from the flowmeter and Pitot probe method had a strong correlation with a coefficient of determination, R^2 of at least 0.92 being attained.

3.3.5 Temperature

Water temperature was recorded concurrently with all other recorded measurements (i.e. P and Q). This enabled the ρ and v, and Re_D to be accurately established and monitored for each discrete measurement. The fluid temperature was measured using two universal temperature probes (model: *LabJack* EI-1034), which had a typical accuracy at room temperature of ±0.22 ºC and an operational range of -17 ºC < T < +110 ºC. The two probes, designated T_{Pipe} and T_{Tank} were located within the test pipe (at x = 8.65m) and the storage tank, respectively. The average temperature between these respective locations was used within the definition of ρ, v and Re_D. The maximum standard deviation recorded between the respective probes was 0.20ºC, which was within the instrumentation uncertainty and therefore, deemed acceptable. The probes were calibrated under non-flow and flow conditions using a mercury thermometer, which had an accuracy of ±0.10ºC. Typical calibration curves for the each of probes are provided in Appendix A.4 in Figure A.9. The established calibrations conformed well to that provided within the manufacturer's specification.

Fluid density (in kg/m^2) μ (in Ns/m^2) and v (in m^2/s) parameters were determined from water temperature, (in ºC) using Equation 3.15, Equation 3.16 and Equation 3.17, respectively. These equations are based on polynomial best fits of tabulated data for water at atmospheric pressure.

$$\rho = 1.58 \times 10^{-5}T^3 - 5.94 \times 10^{-3}T^2 + 2.09 \times 10^{-2}T + 999.97 \qquad \textit{Equation 3.15}$$

$$\mu = (3.11 \times 10^{-8}T^4 - 8.65 \times 10^{-6}T^3 + 9.43 \times 10^{-4}T^2 - 5.35 \times 10^{-2}T + 1.760) \times 10^{-6} \qquad \textit{Equation 3.16}$$

$$\nu = \mu/\rho \qquad \textit{Equation 3.17}$$

3.4 Data acquisition

A *LabJack* multifunction 24-bit datalogger (Model: U6-Pro) streamed all measurement readings from their respective devices to a desktop PC, as shown by Figure 3.22. The appropriate sampling time for all measurements was determined using a cumulative time-averaged approach. The time required for cumulative time-averaged reading to remain

constant (i.e. the standard deviation of the mean value was approximately zero), was taken as the sampling time**.** Figure 3.23 illustrates the cumulative time-averaged pressure readings for the three transducers.

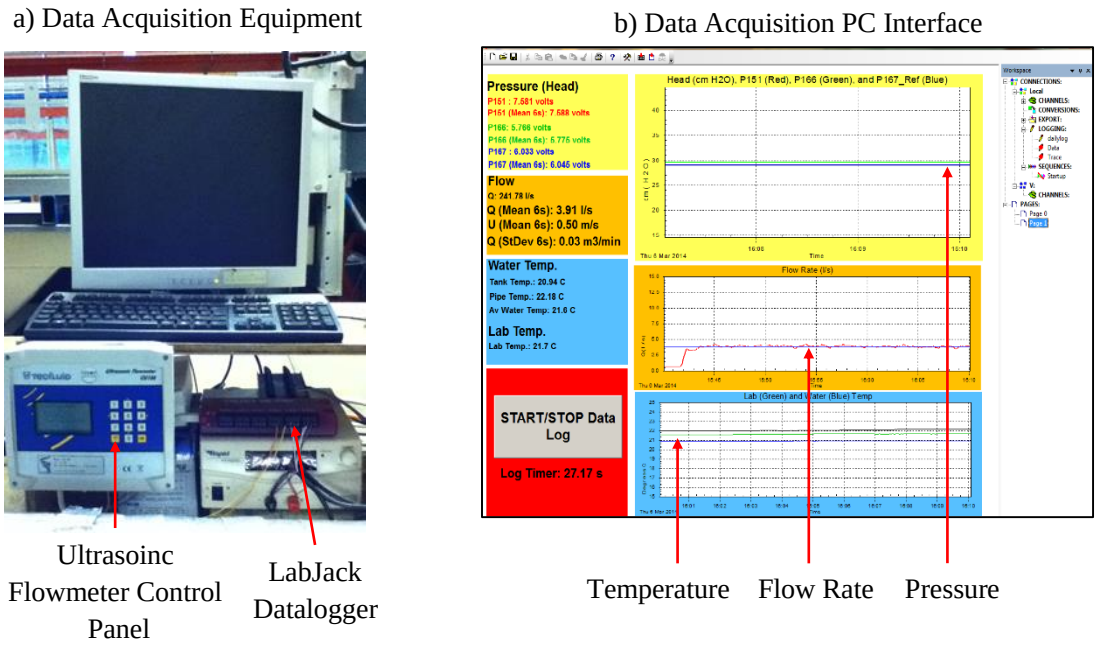

Figure 3.22 Data acquisition a) equipment and b) PC interface for the pilot-scale pipeline.

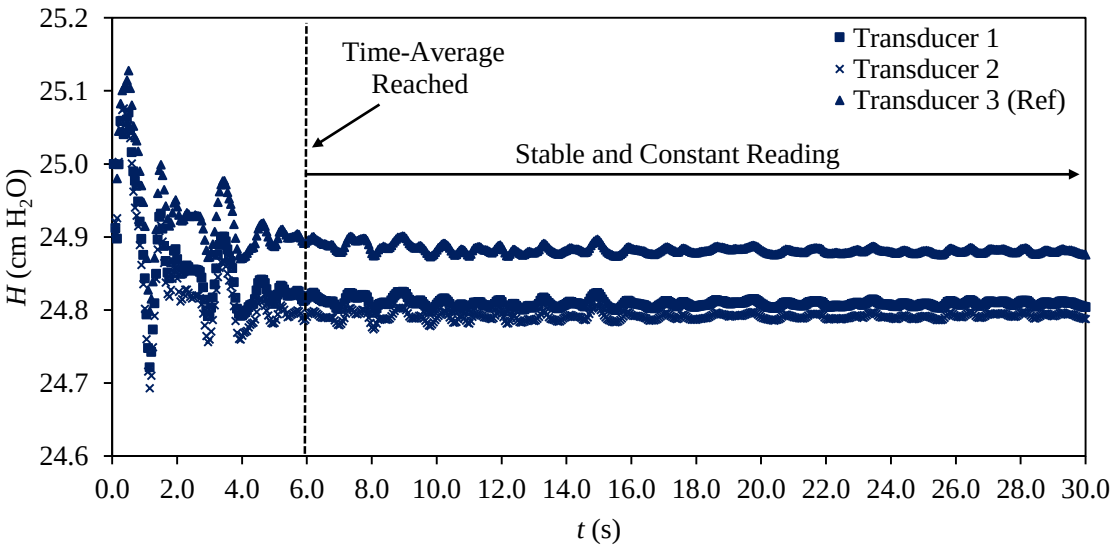

Figure 3.23 Cumulative time-average pressures for the three respective transducers used within the pilot-scale pipeline.

It can be seen from Figure 3.23 that 6 s (at 100Hz) provided sufficient time for the time averaged pressures to reach a constant state. Consequently, a 6 s sampling time was used for all pressure measurements within the current study. Four time-average pressure measurements were recorded for each measurement interval (i.e. 4 x 6 s). As a result, each average headloss and local velocity measurement within the current study was derived from 2400 pressure readings.

The sampling time for all *Q* and *T* measurements was 24 s. Therefore, for every time-averaged *Q* and *T* measurements, four time-averaged pressure measurements were recorded. A settling time of at least 30 s was taken between every measurement interval within the current study, to allow for sufficient measurement stabilisation.

3.4.1 Measurement procedure

The following procedures were used within the current study to establish all headloss and velocity profile assessment. A complete pipe survey included both assessments.

3.4.1.1 PG assessment

To accurately establish the test pipe's PG, the pressure transducers were first individually calibrated and zeroed (with respect to the measurement location P_1) using the manometer board. The pressure at P_1 was recorded by all three transducers as an initial reference point. The static pressure at two respective measurement locations, starting with P_1 and P_5 was then simultaneously recorded, using the "front-side" and "back-side" procedure (outlined in Section 3.4.3). A settling time of at least 30 s was taken between measurements (as outlined in Section 3.4.4). Each measurement interval or static headloss combination was designated with respect to the measurement locations assessed (i.e. P_1-P_2, see Figure 3.5). The process of recording a "front-side" and "back-side" measurements was repeated for all possible headloss combinations of which there were 10 in total (i.e. P_1-P_2, P_1-P_3, P_1-P_3, etc.). A complete list of all 10 headloss combinations is presented in Appendix A.5 in Table A.2. Once all 10 headloss combinations were recorded the initial conditions were checked and recorded. The length of time to measure all 10 headless combinations was typically between 15-20 minutes.

3.4.1.2 Velocity profile assessment

The pressure at P_1 was recorded by all three transducers as a reference point. The Pitot probe was then positioned parallel to pipe's invert-side wall using the digital height gauge as a reference. If required and not already done so, the height gauge was manually zeroed with respect to the invert-side wall. At this position the centre of the Pitot probe was assumed to be one-half the probe diameter (i.e. $d_h/2$ = 0.5 mm). The dynamic and static pressures were

then recorded using the "front-side" and "back-side" procedure (outlined in Section 3.4.3) at the first y-axis position ($y \approx 0$). The Pitot probe was then moved normal to the wall to a predefined position, and after a 30 second delay the pressures were recorded again. This process was repeated for all predefined wall-normal positions. A typical velocity distribution consisted of at least 45 wall-normal positions (as shown in Appendix A.5 in Table A.3). These positions were chosen to give uniform spacing between points when plotted on a logarithmic scale and to give adequate spatial resolution for determination of $\overline{U}$. The smallest positional step was 0.05 mm and the largest step was 5.00 mm. After the completion of the velocity profile assessment the initial conditions were again re-checked and recorded and this marked the end of the pipe survey. The length of time to measure a complete velocity profile was typically 60 minutes.

3.5 Sensitivity analysis – Uncertainty in k_s

A sensitivity analysis was undertaken prior to the experimental study; for the purpose of demonstrating the impact of instrumentation error on the outputs of the key equations employed within the current study, namely the C-W equation. This would allow the intended instrumentation to be vetted and the operational range to be refined in accordance with the established instrumentation limitations. The principal variable and equation under review were k_s and the C-W equation, respectively. Based on the traditional C-W equation k_s is a function of pipe diameter, average freestream velocity, headloss, pipe length, kinematic viscosity, and the gravity acceleration constant:

$$k_s = f\left(D, \overline{U}, H_f, \upsilon, g\right); \quad \upsilon = f(T) \qquad \textit{Equation 3.18}$$

The impacts of each of the parameters in Equation 3.18, with the exception of g on k_s were reviewed discretely and a total uncertainty was established. The total uncertainty was determined using the root-square-sum (RRS) method (Abernethy et al. 1985). Total k_s uncertainties were established for three different scenarios, including; i) a varying flow scenario (i.e. Re_D); ii) a varying surface roughness scenario (i.e. k_s) and iii) a varying temperature scenario. It should be noted that a total k_s uncertainty was estimated for each variable increment for each of the aforementioned scenarios. Table 3.2 provides a summary of the predefined and fixed uncertainties by which each parameter was varied within each of the three scenarios.

Table 3.2 Parameter Uncertainties and Values

Parameter	***Symbol***	***Uncertainty***
Average Freestream Velocity	$\overline{U}$	±1.5%
Hydraulic Headloss	H_f	±0.57mmH_2O
Diameter (=102.08mm)	D	±0.67mm
Pipe Length (= 5.00m)	L	±0.5mm
Fluid Temperature	T	±0.22ºC

These uncertainties were derived from the manufacturer's specifications and worst case measurements. The upper and lower boundaries for each scenario were selected based upon estimated conditions during testing. For instance, the upper and lower limits for the the varying flow scenario were $Re_D = 3.00\text{x}10^4$ ($\overline{U} \approx 0.3$ m/s) and $Re_D = 1.50\text{x}10^5$ ($\overline{U} \approx 1.5$ m/s), respectively (see Section 3.2.2). In the case of the varying roughness scenario the upper and lower limits were selected based upon the expected k_s values for a non-fouled and fouled pipe, respectively. Principally, for the upper limit k_s value was taken as 0.600 mm (Wallingford and Barr 1994), and for the lower limit a k_s value of 0.012 mm (Grann-Meyer 2010). The upper and lower limits of the varying temperature scenario were 17 and 22ºC, respectively and were based upon estimated temperature range within the pipeline during testing.

Figure 3.24 to Figure 3.26 summarise the results of the sensitivity analysis for each of the three scenarios. In particular, Figure 3.24 illustrate the results of the varying flow conditions scenario, for fixed values of k_s equal to 0.012 and 0.600 mm. Figure 3.25 present the results of the varying surface roughness scenario, for $Re_D = 3.00\text{x}10^4$ and $Re_D = 1.50\text{x}10^5$. Fluid temperature within the varying flow and surface roughness scenarios was fixed at 20ºC. Figure 3.26 show the results varying temperature scenario, for $Re_D = 3.00\text{x}10^4$ and $Re_D = 1.50\text{x}10^5$, respectively. The value of k_s within the varying temperature scenario was equal to 0.012 mm. In addition to showing the total k_s uncertainties, Figure 3.24 to Figure 3.26 present the proportional impacts of each of the discrete parameters on the total uncertainty, as a percentage. It is evident that the contribution from the uncertainty in L was insignificant as a proportion of total uncertainty. This was a direct result of the uncertainty in L being several orders of magnitude less than its absolute value (i.e. 5 m). Similarly, the impacts of v and D on the total uncertainty were typically insignificant, though to a lesser extent than L. Generally, it was found that uncertainties in $\overline{U}$ and H_f had the greatest contribution to the overall uncertainty in k_s.

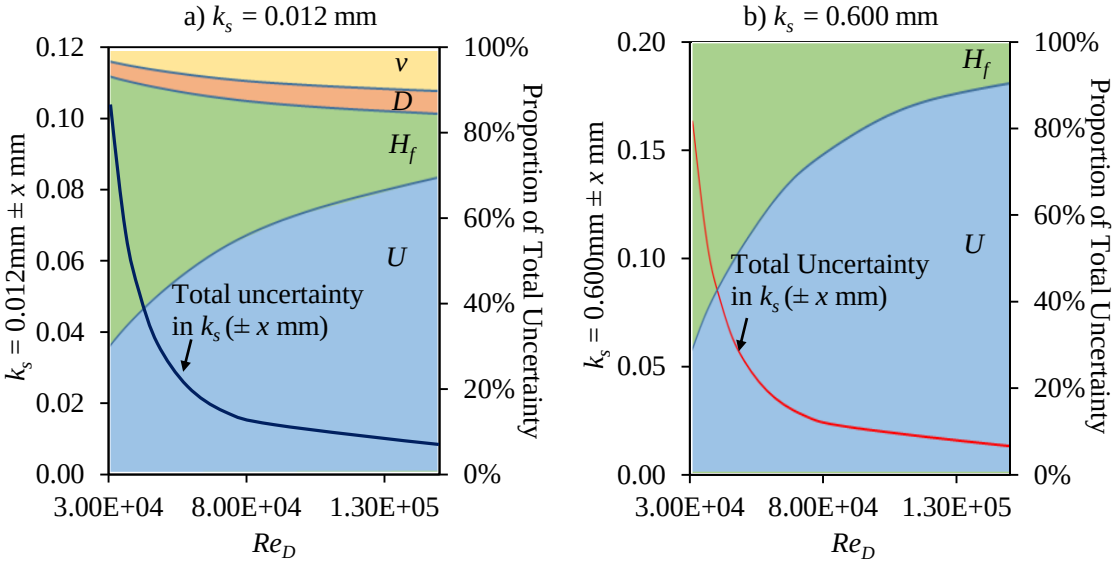

Figure 3.24 Sensitivity analysis on k_s: varying flow scenario, for fixed values of a) k_s = 0.012 mm and b) k_s = 0.600 mm (T = 20ºC). Highlighting the proportional impacts of U, Hf, D and v on the total ks uncertainty.

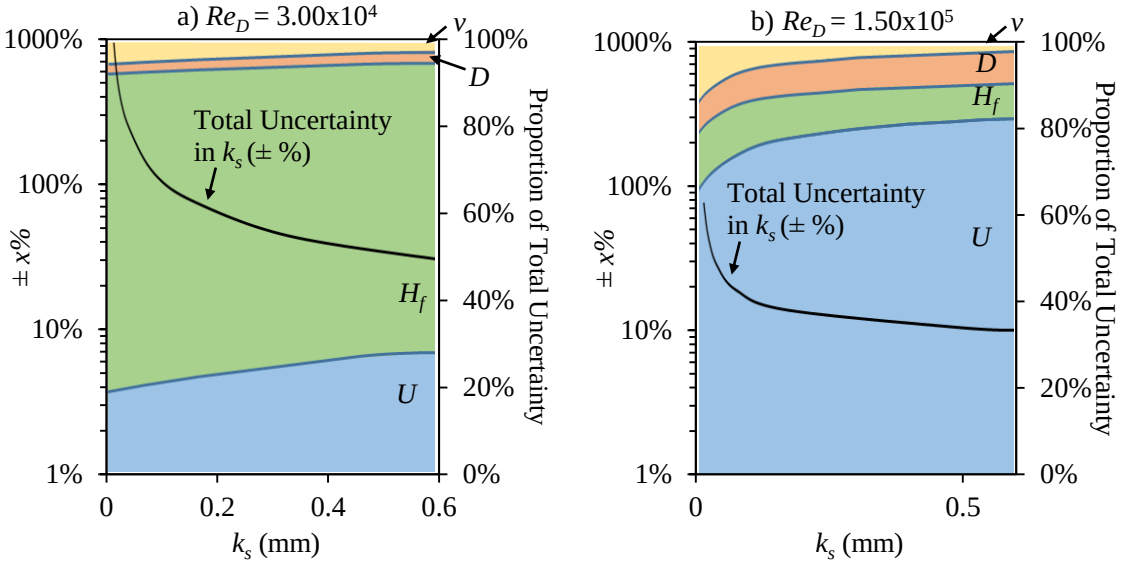

Figure 3.25 Sensitivity analysis on k_s: varying surface roughness scenario for fixed values of a) Re_D = 3.00x10^4 and b) Re_D = 1.50x10^5(T = 20ºC). Highlighting the proportional impacts of U, Hf, D and v on the total ks uncertainty.

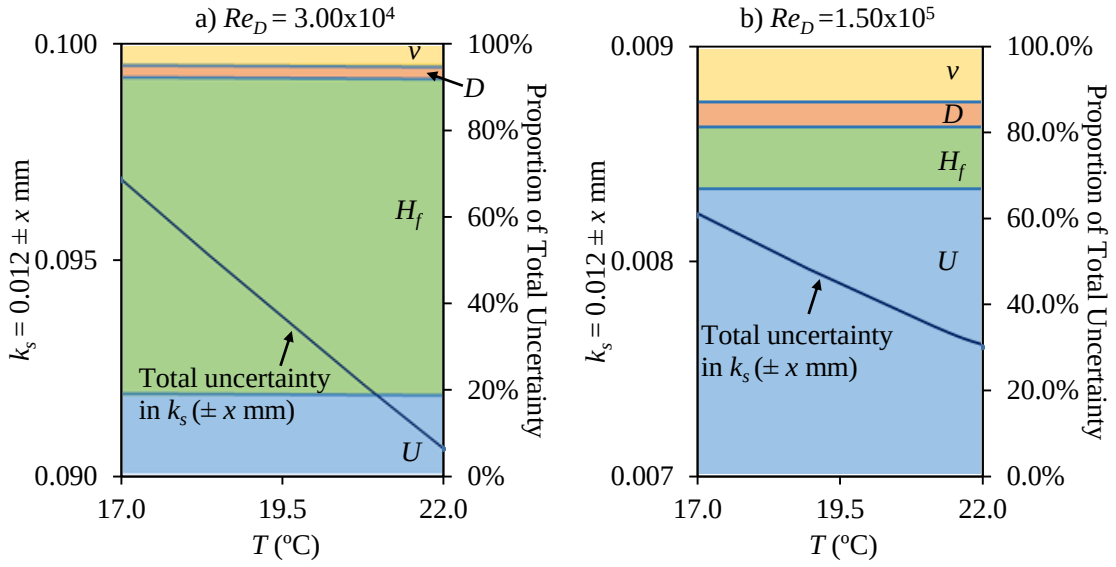

Figure 3.26 Sensitivity analysis on k_s: varying temperature scenario for fixed values of a) Re_D = 3.00x10⁴ and b) Re_D = 1.50x10⁵(k_s = 0.012mm). Highlighting the proportional impacts of U, Hf, D and v on the total ks uncertainty.

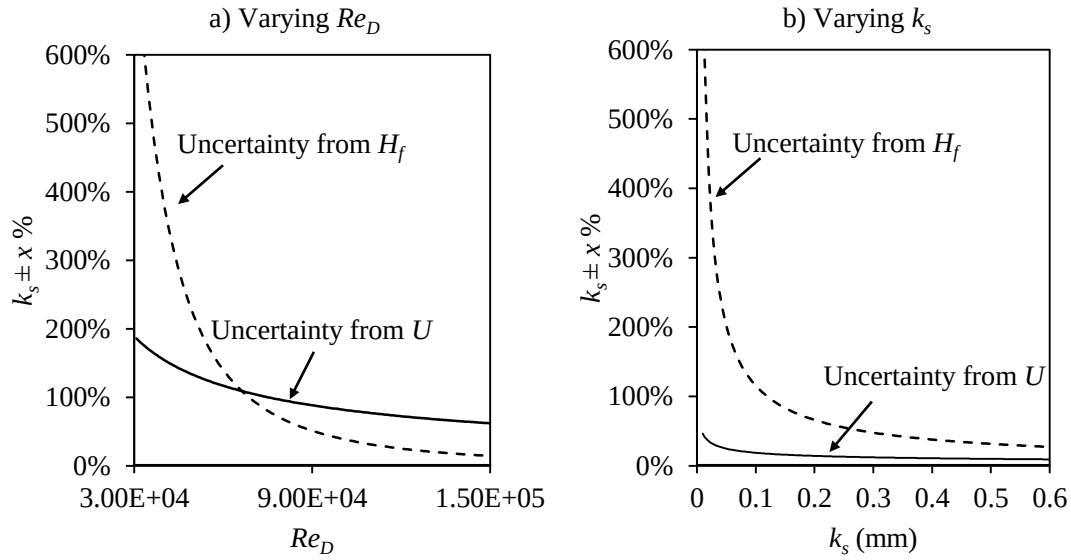

Figure 3.27 Impact of the error in H_f and $\bar{U}$ on total uncertainty in k_s for a) varying Re_D and k_s = 0.0125mm, and b) varying k_s values and Re_D =3.0x10⁴.

The analysis has indicated that the nature of the uncertainties played a significant role in their overall uncertainty in k_s. For instance, the uncertainty in $\overline{U}$ was specified by the manufacturer as a fixed percentage of the absolute reading (±1.5%). Whereas, the uncertainty in H_f was specified as a fixed value and for pressure transducers used within the current study, which equalled ±0.57 mmH_2O. This meant that the uncertainty associated with the pressure transducer would dominate at low values of k_s and/or Re_D, where absolute headloss is inherently small, as shown by Figure 3.27.

It is evident that the total uncertainty in k_s was proportionately large at the lower ends of the spectrum either in terms of k_s or Re_D. For instance, Figure 3.24 illustrates that total k_s uncertainty at $Re_D = 3.0x10^4$ can be an order of magnitude greater than the absolute k_s value (i.e. 0.012 mm). This highlights the difficulty determining accurate values of k_s for very smooth pipes, particularly when operating at Re_D. Consequently, all low Re_D investigations (i.e. $Re_D < 5.0x10^4$) in the current study were repeated several times and were mostly viewed with caution. This was particularly relevant of the non-fouled phase of the current study.

The sensitivity analysis has indicated that surface roughness and Re_D have the greatest impact on total k_s uncertainty. In particular, it was found that as surface roughness or Re_D increases the total uncertainty in k_s decreases, as shown 3.7, which present the contributed impact of surface roughness and Re_D on total k_s uncertainty. The impact of temperature was found to be minor in comparison, particularly for the expected range (i.e. 17ºC < T < 22ºC). The sensitivity analysis has indicated that the intended equipment was suitable for measuring k_s although, caution should be taken when investigating low Re_D and smooth surfaces.

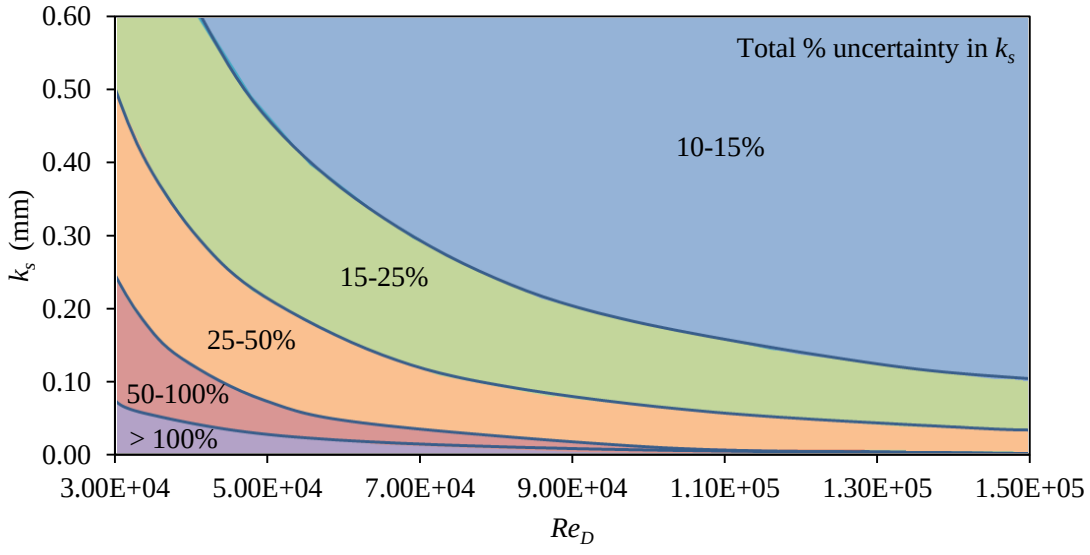

Figure 3.28 Sensitivity analysis on k_s: impact of k_s and Re_D on total k_s uncertainty.

3.6 Synthetic wastewater

A synthetic wastewater was used within the current study as an alternative to actual wastewater. Actual wastewater was considered and trialled, although for health and safety reasons it was precluded from use within the current study. Consequently, the synthetic wastewater was the primary nutrient source for the microorganisms incubated within the study. The synthetic wastewater was prepared according to the specification outlined by the Organisation for Economic Cooperation and Development (OECD) (OCED 1984), whereby untreated tap water was enriched with a balanced mixture of macro- and micro- nutrients. Peptone and meat extract, as the main organic constituents of the wastewater. The concentration ratios of Peptone, meat extract, Urea (CH_4N_2O), and di-potassium hydrogen phosphate (KH_2PO_4) were used to respectively control the synthetic wastewater's Chemical Oxygen Demand (COD), Total Nitrogen (TN), and Total Phosphorus (TP).

The synthetic wastewater specification outlined by the OECD was evaluated with regards to COD, TN and TP, prior to biofilm incubations. The concentration of Total Organic Carbon (TOC), Dissolved Organic Carbon (DOC), Nitrate (NO_3^-), Ammonium (NH_4^+), Iron (Fe), Manganese (Mn) and free Chlorine (Cl) were also established for the wastewater. The purpose of this evaluation was to estimate the concentration ratios required to satisfy specific predefined COD, TN and TP target concentrations. The target concentrations for COD, TN and TP used within the current study were based upon the European average values for medium strength wastewater, as outlined by Pons et al. (2004) (see Table 3.3). In particular, the target concentrations for COD, TN and TP used within the current study were 550 mg/l, 50 mg/l and 10 mg/l, respectively. These target values equate to an approximate supply ratio of Carbon (C), Nitrogen (N) and Phosphorous (P) of 25: 5: 1 (C: N: P). The required C: N: P ratio necessary to sustain aerobic bacterial growth is typically taken as 100: 5: 1.

Table 3.3 European value of COD, TN, TP, BOD and suspended solids in wastewater, as presented by Pons et al. (2004).

Wastewater Strength	***COD (mg/l)***	***TN (mg/l)***	***TP (mg/l)***	***Suspended Solids (mg/l)***	***BOD (mg/l)***
High	810	66	13	464	392
Medium	541	48	8	283	272
Low	273	30	3	103	152

The concentrations of COD, TN and TP were primarily determined using a Benchtop Spectrophotometer (DR3900, *Hach-Lange*) and the relevant standard reagent assays (*Hach Lange*). In particular, COD, TN and TP were measured using the LCI400 (detection range of 0mg/l < COD < 1000mg/l), LCK338 (detection range of 20 mg/l < TN < 100 mg/l), and LCK349 (detection range of 0 mg/l < TP < 1.5 mg/l) cuvette assays, respectively. It should be noted that all water samples were diluted by a factor of 10 when evaluating TP. In order to determine COD, TN and TP using the Benchtop Spectrophotometer the samples required digesting at test specific temperatures and time periods, using a Thermostat (LT 200, *Hach Lange*).The uncertainty (to a 95% confidence interval) associated with the LCI400 assay was ±4.2 mg/l, with the LCK338 assay was ±2.1 mg/l and with the LCK349 assay ±0.01 mg/l. The measured uncertainties in COD, TN and TP were found to be ±2%, ±3% and ±10%, respectively. The respective uncertainties were estimated from repeatability tests (typically from 10 repeats), and represent a 95% confidence interval. The measured uncertainties are slightly higher than those specified by the manufacturer for the respective assays, although, are deemed acceptable for the current study, where orders of magnitude changes in concentration are the primary concern as opposed to finte changes.

A TOC analyser (TOC-V_{CPH} *Shimadzu*) was used to determined TOC and DOC within the current study. The TOC analyser measured the concentrations of Total Carbon (TC) and Inorganic Carbon (IC) for a particular sample (> 20 mm), from which TOC could be estimated (i.e. TOC = TC-IC). The DOC fraction of TOC was determined in the same manner, although, the sample was filtered through a 0.45 μm filter prior to analysis. The TOC analyser was also used to measure TN using the analyser's TNM-1 accompanying unit. Typical TC, IC and TN calibration curves for the TOC analyser are presented in Appendix A.6 in Figure A.10.

The concentrations of NO_3^-, NH_4^+, Fe, Mn and Cl were measured using the Benchtop Spectrophotometer and relevant standard reagent assays (produced by *Hach Lange*). In particular, NO_3^- and NH_4^+ concentrations were determined using the LCK 339 and LCK 304 standard cuvette assays, respectively. Whereas, concentrations in Fe, Mn and Cl were determined using the standard reagent kits. In particular, the FerroMo kit was used for Fe, the 1-(2-Pyrifylazo)-2Naphthol (PAN) kit was used for Mn and the N,N'-diethyl-p-phenylenediamine (DPD) kit was used for Cl (*Hach Lange*).

The results of the OECD wastewater evaluation are presented in Appendix A.7 in Figure A.11. The specification used within the current study to obtain the required target concentrations of COD, TN and TP is presented in Appendix A.7 in Table A.4.

A strong linear correlation (R^2 = 0.99) between TOC and COD (see Appendix A.7, Figure A.12) was determined from the evaluation of the synthetic wastewater, and is given by:

$$\text{TOC (mg/l)} = 0.45\ \text{COD(mg/l)} + 5.67 \qquad \textit{Equation 3.19}$$

Equation 3.18, is a useful means of establishing the TOC or COD of synthetic wastewater, and is consistent to the equivalent equation outlined by Haze et al. (1995) for actual wastewater.

3.7 Molecular analysis

The following sections detail the molecular analysis aspect of the current study, which were undertaken at the Cardiff School of Bioscience, Cardiff University. The biofilms incubated within the current study were evaluated and compared by 16S ribosomal ribonucleic acid (rRNA) gene polymerase chain Reaction-denaturing gradient gel electrophoresis (PCR-DGGE), DNA and EPS quantification.

3.7.1 EPS and DNA extraction protocol

The protocol used within the current study for EPS and DNA extraction was modified from Brown and Lester (1980) as described by Zhang et al. (1999). Zhang et al. (1999) found that the protein and carbohydrate fractions extracted using the method outlined by Brown and Lester (1980) compared well to other commonly used extraction protocols. The modified method is outlined herein.

To the cotton bud (with collected biofilm) contained within a 1.5 ml non-stick tube 1.0 ml of sterile phosphate buffer saline (PBS) was added and mechanically shaken (*Lab Line*, Multi-Wrist Shaker) for 10 minutes. The cotton bud and PBS was then sonicated in a ultrasonic water bath (*Grant* XB2) for 30 s at approximately 60 Hz; and then centrifuged (*Eppendorf* 5424) for 10 minutes at 6000 g. The supernatant was then removed and placed in a sterile 2.0 ml (non-stick) centrifuge tube. This stage was referred to as the wash step.

The bud was then re-extracted, by adding 1.0 ml of 2% ethylenediaminetetraacetic acid (EDTA) in PBS. The solution was then sonicated for 30 s and incubated for 3 h at 4 ^{0}C. After the incubation period the supernatant was then removed and added to the wash step supernatant. The combined supernatant was then used for EPS evaluation.

The remaining cellular material and cotton bud were then further centrifuged for 5 minutes at 14000 g. The cell pellet which formed was then used for DNA extraction and subsequent bacterial community analysis.

The supernatant and pellet obtained from this process were defined as the primary EPS and DNA extract. The whole EPS extraction process was then repeated on the extracted cotton bud and the resultant supernatant and pellet were defined as the secondary extract.

The efficiency of the employed biofilm removal technique was an important consideration within the current study. Cotton swabs have been found to be more effective than polyester and Rayon swabs at removing substrate from surfaces (Rose et al. 2004). Moreover, it is widely suggested that when using cotton swabs multiple passes of the same area are undertaken (Rose et al. 2004; Assere et al. 2008). Both of these criteria were met within the current study. ESEM images taken before and after swabbing indicated the effectiveness of this studies removal technique on a microscopic level (see Figure 3.29). The ESEM images presented in Figure 3.29 were captured as part of a different aspect of the current study although, the removal procedure was the same as outlined within the current section.

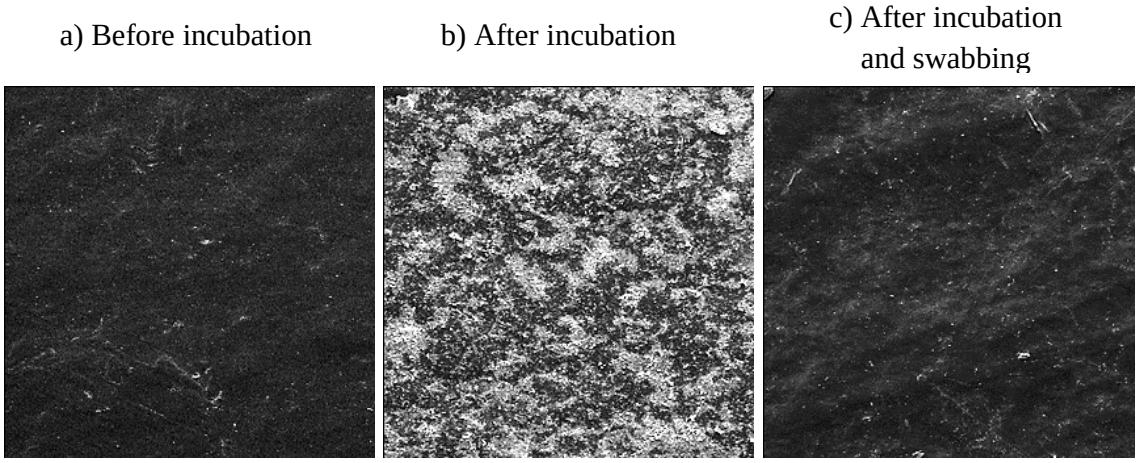

Figure 3.29 ESEM images showing a surface at 200x magnification: a) before incubation, b) after incubation and c) after incubation and swabbing (sample size: 0.5x0.5mm^2).

3.7.2 Total carbohydrate and protein assays

A typical EPS matrix will contain a wide variety of extracellular constituents, including polysaccharides (i.e. carbohydrates), proteins, nucleic acids and lipids. Carbohydrates and proteins are generally the largest constituent of the matrix, representing over 50% of the overall EPS fraction (Horan and Eccles 1986; Jahn and Nielsen 1998; Wingender et al. 2001;

Tsuneda et al. 2003; Flemming and Wingender 2010; Andersson et al. 2011). In particular, Tsuneda et al. (2003) found that proteins and polysaccharides can potentially account for 75-90% of a biofilm's overall EPS. Furthermore, carbohydrates and proteins have been found to contribute to several essential biofilm properties, namely mechanical stability and cohesion (Pratt and Kolter 1999; Wloka et al. 2004; Simoes et al. 2007; Celmer et al. 2008, Flemming and Wingender 2010, Ahimou et al. 2010). Consequently, only the carbohydrate and protein fractions were analysed within the current study.

3.7.2.1 Total extracellular carbohydrate concentration

The total carbohydrate concentration in the EPS for the respective biofilms was determined using a standard phenol-sulphuric acid based assay kit (*Sigma* MAK104). Glucose (2.0 mg/ml solution) was used as the calibration standard in the range 0-20 µg/50µl (i.e. 0-400 µg/ml). The procedure used to determine the total carbohydrate concentration was modified from the manufacturer's specification and is documented herein.

Firstly the required glucose standards were prepared. Glucose (2mg/ml solution) of concentrations 0, 2, 4, 6, 8 and 10µl was added to a 1.5ml (non-stick) centrifuge tube. The total volume of the solution was brought up to 50 µl using sterile nuclease-free molecular-grade water. The EPS sample of volume of 50 µl was then added to a 1.5 ml centrifuge tube. Concentrated sulphuric acid of volume of 150 µl was added to each of the centrifuge tubes. The solutions were then incubated for 15 minutes at 90 ^{0}C in a heating block (*Techne* Dri-Block-3). The samples were protected from natural light during the incubation period. After the incubation period 30 µl of phenol-based developer was added to each of the centrifuge tubes. The solutions were then left for 5 minutes before being transferred to 1.5 ml cuvettes (*Bio-one* 613101). The volume of the solutions was made up to 1.0 ml, by using sterile nuclease-free molecular-grade water. The absorbance was then measured using a Spectrophotometer (*Jenway* 6300), using a wavelength was set to 490 nm.

A preliminary analysis of the unused cotton buds indicated that they contained a considerable amount of carbohydrate (see Appendix A.8, Table A.5). In particular, repeatability tests indicated that the cotton buds had carbohydrate concentration of 279.45 ± 40.98 µg/ml (Based on 7 repeats). Carbohydrate within the bud was thought to have derived from the cellulose within the cotton. The significant carbohydrate concentration within the cotton bud would have had a considerable impact on the established extracellular carbohydrate concentrations. Consequently, 279.45 µg/ml was subtracted from all carbohydrate measurements. Nevertheless, the documented measurements should be used with caution.

The levels of protein from the unused cotton swabs was below the detection limit in all assessed cases and thus, negligible.

3.7.2.2 Total extracellular protein concentration

The total concentration of protein in the EPS was measured using the standard Bradford assay (*Sigma* B6916), with bovine serum albumin (BSA) as the calibration standard in the range 0-20 µg/ml. The procedure used to determine the total protein concentration was outlined by Bradford (1976). The absorbance was measured at 595nm using a Spectrophotometer (*Jenway* 6300).

Typical standard curves for protein and carbohydrate are presented in Appendix A.8 in Figure A.13. It should be noted that all standard curves used within the current study had R^2 values of at least 0.95.

3.7.3 DNA and community analysis

3.7.3.1 DNA extraction and purification

The total community genomic DNA was extracted from the biofilm samples using a standard DNA isolation kit (*Next-Tec* X150). The procedure was per the manufacturer's specification with the exception that after adding 90.0 µl of Buffer, 10.0 µl of Lysozyme and 20.0 µl of RNase A the sample was mechanically shaken (*Lab Line*, Multi-Wrist Shaker) for 5 minutes. In addition, in the final stage all of the extracted DNA was passed through the filter column resulting in a total volume of 200 µl. The DNA extracts were then stored at -80ºC until required for Polymerase Chain Reaction (PCR) amplification. DNA extractions from unused cotton buds were also carried out and analysed, as a negative control.

3.7.3.2 PCR conditions

To minimise potential contamination issues, the PCR was carried out under aseptic conditions using autoclaved and/or UV-treated instruments and sterile nuclease-free molecular-grade water. The amplification of Bacterial 16S rRNA gene sequences were amplified by nested PCR using primer combination 357F-GC-518R (Webster et al. 2003). All PCR reactions were performed within a DNA Engine *Dyad* Thermal Cycler (MJ Research). PCR conditions were as described by Muyzser et al. (1993) and Webster et al. (2003).

Sterile nuclease-free molecular-grade water and *Acetobacterium sp.* Ac1 DNA was used as a negative and positive control, respectively in all sets of PCR reactions.

The reaction mixtures were held at 95°C for 5 minutes followed by 10 cycles of 94°C for 30 seconds, 55 °C for 30 s and 72°C for 60 s plus 20 cycles of 94°C for 30 s, 52°C for 30 s and 72°C for 60 s, with an extension step of 5 minutes at 72 °C. A typical set of PCR products

are present in Figure 3.30 demonstrating that that 16S rRNA gene PCR products were approximately 200 bp.

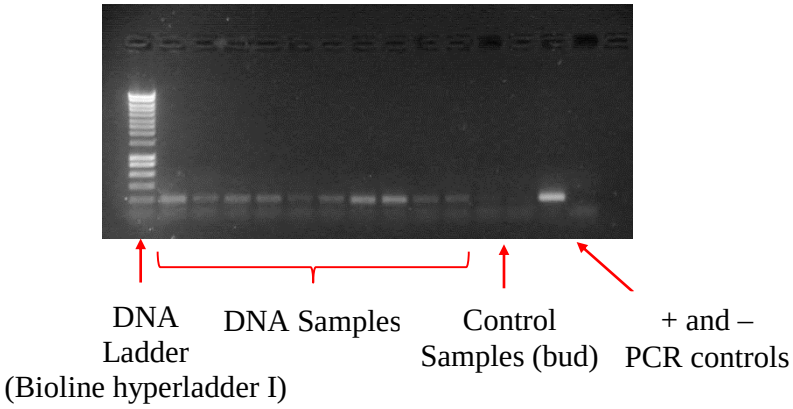

Figure 3.30 A typical Polymerase Chain Reaction (PCR) product.

The bacterial diversity within the biofilm and water samples was determined carrying out Denaturing Gradient Gel Electrophoresis (DGGE) on the nested PCR products (Schäfer and Muyzer 2001; Webster et al. 2002; 2006).

3.7.3.3 DGGE analysis

The PCR products were separated using a *DCode* Universal Mutation Detection System (*Bio-Rad Laboratories*) and 1.0 mm thick (16.0 x 16.0 cm^2 glass plate) 8.0% (w/v) polyacrylamide gels (Acrykogek 2.6 solution, acrylamide: *N,N'*-methylenebisacrylamide; 37:1; *BDH Laboratory Supplies*) with denaturant gradient between 30.0% and 60.0% (Webster et al. 2003). The polyacrylame gels were prepared with a 1 x Tris-Acetate EDTA (TAE) buffer (pH 8; 40mM Tris base, 20.0mM acetic acis, 1.0mM EDTA), using a 50.0 ml volume Gradient Mixer (*Fisher Scientific*). The electrophoresis was performed at 60 ºC and 200 Volts for 5 h (with an initial 10 minutes at 80 Volts). The polyacrylame gels were stained with *SYBRgold* nucleic acid gel stain (*Molecular Probes*) for 30.0 minutes and viewed under UV. A *Gene Genius* Bio Imaging System (*Syngene*) was used to capture images of the Gel.

Distinguishable DGGE bands were excised from the gel and washed in sterile nuclease-free molecular-grade water for 10 minutes. The bands were then air-dried, crushed and re-amplified by PCR for Sanger sequencing as described by O'Sullivan et al. (2008). The sequencing within the current study was undertaken by *Eurofins Genomics GmBH*.

3.7.3.4 Total DNA quantification

The total DNA concentration was measured within the biofilm and bulk water samples using a fluorescent dye assay kit (*Quant-iT PicoGreen* dsDNA) and a multimode microplate reader (*Tecan* Infinite M200 Pro). Samples and standards were prepared on a 96 microplate (*OptiPlate*-96F, black) as per the manufacturer's specification. The pre-defined *PicoGreen* programme (Magellon 7.1) was used to calibrate the microplate reader. Critically, the absorbance was measured at 485 nm. A typical standard curve for the DNA concentration is presented in Appendix A.8 in Figure A.14 (R^2 = 0.99).

A strong linear relationship has been reported within the literature between DNA concentration and the total acridine orange direct cell concentration (McCoy and Olson 1985). The recommendations outlined by McCoy and Olson (1985) were used within the current study to estimate the total cell concentration within biofilm and bulk water samples.

3.8 Experimental program

This section outlines the experimental work undertaken within the pilot-scale pipeline as part of the current study, which comprised of three discrete phases, namely:

1. Non-fouled phase – Assessing the pipeline under non-fouled conditions (Chapter 4)
2. Incubation phase – Biofilm frictional resistance over time (Chapter 5)
3. Mature phase – Impact of increased shear (Chapter 6)

3.8.1 Non-fouled phase

Prior to the fouling investigations the pilot-scale pipeline was extensively evaluated under non-foul conditions. The purpose of this evaluation was to: i) validate the facility for a boundary layer and biofouling investigation and ii) provide an accurate comparison (i.e. control) for the subsequent biofouling investigations. Both of these criteria were essential in establishing the validity and significance of the results obtained under fouled conditions.

The non-fouled pipe was surveyed using the protocols outlined in Section 3.4.1, over the range of $3.15\text{x}10^4 < Re_D < 1.23\text{x}10^5$ (0.31 m/s < $\overline{U}$ < 1.22 m/s), at increments of $Re_D \approx 1.00\text{x}10^4$ ($\overline{U} \approx 0.1$ m/s). Each pipe survey was repeated on average three times.

3.8.2 Incubation phase

Biofilms were incubated within the pilot-scale pipeline under representative, albeit artificial conditions. This provided greater variable control of the biofilms conditioning, which was beneficial from a scientific and safety standpoint. Variable control was essential within the current study for the purpose of establishing the impact of discrete ecological factors on

biofilm frictional development. Furthermore, continuous biofilm monitoring without disruption could also be achieve by incubating the biofilms within a laboratory environment. Most biofouling investigations documented within the literature have incubated biofilms under field conditions and then evaluated them in the laboratory (Schultz 1998; Schultz and Swain 1999; Schultz 2000; Barton 2006; Lambert et al. 2008; 2009; Andrewartha et al. 2008, Andrewartha 2010; Perkins et al. 2013; 2014; Walker et al. 2013). Sufficient variable control and continuous monitoring are limited or precluded by such an approach, although, the resultant biofilm will be extremely representative of the natural ecology. Moreover, the transportation of a biofilm could lead to irreversible damage.

The principal ecological factor under review within the current study was flow hydrodynamics. Several assays were carried out within the pipeline facility in order to evaluate the impact of flow hydrodynamics on biofilm frictional behaviour over time. In particular, biofilms were incubated with synthetic wastewater at three different steady state flow regimes, namely $\overline{U}$ = 0.60 m/s, $\overline{U}$ = 0.75 m/s, and $\overline{U}$ =1.00 m/s. For the purpose of repeatability, all other significant ecological factors, such as temperature and nutrient content were controlled and remained reasonably constant within each of the discrete flow assays. A summary of the key ecological factors within the facility during the three flow assays is presented in Table 3.4.

Table 3.4 Average environmental and operational parameters within the $Re_D = 5.98x10^4$, $Re_D = 7.82x10^4$, and $Re_D = 1.00x10^4$ assays.

Re_D	$\overline{U}$ (m/s)	Water Temperature (°C)	ν (m^2/s)	ρ (kg/m^3)	COD (mg/l)	TN (mg/l)	TP (mg/l)	pH
5.98×10^4	0.58	21.30	9.70×10^{-7}	997.91	536.35	49.77	10.55	8.09
7.82×10^4	0.76	21.27	9.71×10^{-7}	997.99	545.60	51.33	9.91	7.96
1.00×10^5	0.96	21.79	9.78×10^{-7}	997.91	548.10	49.71	10.69	7.80

The biofilms were incubated within the facility for 20 d (480 h), which based upon the sufficient nutrient supply (see Table 3.4) was deemed adequate for the biofilms to reach a state of equilibrium in terms of their frictional resistance (Picologlou et al. 1980; Lambert et al. 2008; 2009; Andrewartha 2010).

The average freestream velocities investigated within the current study were of particular industrial relevance. Generally, as a rule of thumb, the minimum $\overline{U}$ required for a pipe to be self-cleansing is 0.60 m/s (Fair and Geyer 1954). Typically, within the UK and US

wastewater pipelines are designed to achieve an average freestream velocity of 0.60 and 0.75 m/s, respectively. Field measurements documented by Lauchlan et al. (2005), who investigated wastewater pumping mains within the UK, illustrated the prevalence of such design criteria within actual systems. In particular, Lauchlan et al. (2005) found that the majority of the assessed UK systems operated at average freestream velocities between 0.6-1.0 m/s, with most of them operating at the upper limit of this range.

The flow assays will be referred to herein in terms of Re_D, i.e. the 0.60 m/s, 0.75 m/s and 1.00 m/s assays will be referred to as the $Re_D = 5.98 \times 10^4$, $Re_D = 7.82 \times 10^4$, and $Re_D = 1.00 \times 10^4$ assays, respectively.

During the incubation phase a complete set of PG and mean-velocity traverses were taken at least three times a day, with the exception of the $Re_D = 7.82 \times 10^4$ assay were only PG data was collected. A total of 60 PG and velocity (if applicable) profiles were taken during each incubation phase.

The specific details of the pipe's ecology during each of the respective incubations are outlined herein.

3.8.2.1 Incubation temperature

The fluid temperature within the pipeline for all three assays was controlled using the external cooling system outlined in Section 3.2.2. The average fluid temperature recorded during the incubation phase of the three flow assays was 21.5 ± 0.9 °C, as shown by Figure 3.31a. The fluid temperatures recorded during the incubation phase of each of the flow assays are shown within Figure 3.31a, which presents the average daily values, recorded using the universal temperature probes (outlined in Section 3.3.5).

Naturally, the temperature within typical wastewater systems is highly variable and seasonal dependant. As a result, it can range from 5°C < T < 22°C (Hoes et al. 2009; Cipolla and Maglionico 2014). Cipolla and Maglionico (2014) reported that the temperature within a sewer system in Bologna, Italy was approximately: 10°C < T < 14°C in the winter; 14°C < T < 18°C in the spring/autumn and 18°C < T < 22°C in the summer. Consequently, in terms of temperature, all three flow assays were accurate for real sewer systems and provided the maximum representative levels of microbial activity (i.e. summer conditions).

The comprehensive temperature control ensured that μ and ρ remained reasonably constant within the respective flow assays. The maximum variation in μ and ρ recorded within the each of the assays was ±2.5% and ±0.02%, respectively.

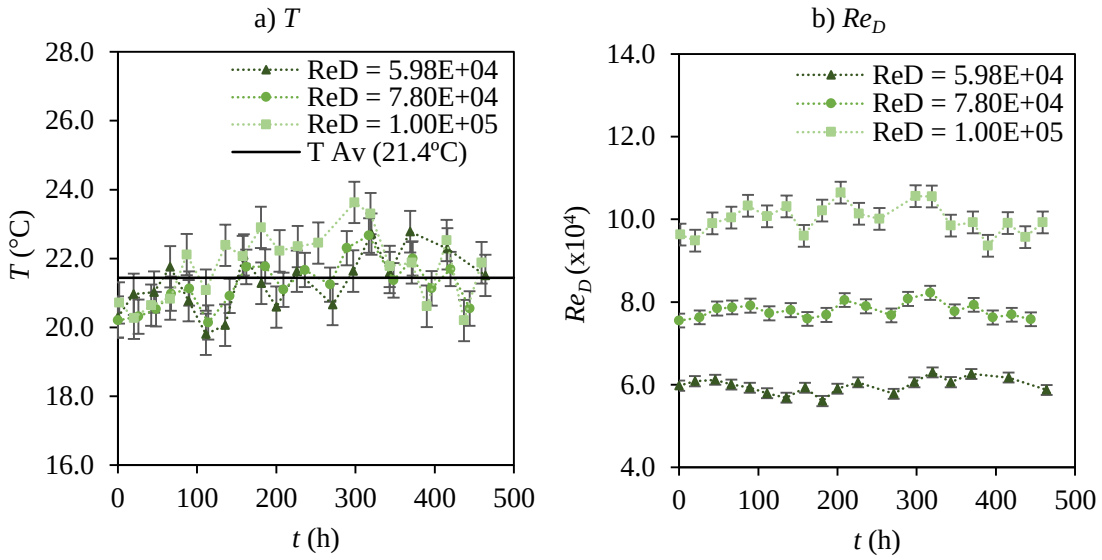

Figure 3.31 a) Water temperature and b) Reynolds Numbers recorded during the biofilm incubation phase of the Re_D = 5.98x10^4, Re_D = 7.82x10^4 and Re_D = 1.00x10^5 assays.

3.8.2.2 Incubation Reynolds Numbers

The hydrodynamic conditions within each of the flow assays was regulated, through a combination of pump and temperature control. In order to satisfy the required steady state conditions within the respective assays, the flow rate was periodically adjusted using the system's gate valve. As a result of the flow rate regulation, the increase in frictional resistance caused by the biofilm manifested itself in terms of an increase in headloss and pump power requirements. Figure 3.31b illustrates the daily average Re_D recorded within each of the flow assays during the incubation phase. The maximum variation in Re_D recorded was ±3%, which indicated that the flow conditions within the respective assays was reasonably constant and homogenous.

3.8.2.3 Hydraulic retention time (HRT)

To ensure a system is well mixed with negligible stagnation periods, the general rule of thumb is to maintain an internal system HRT (= V/Q) of less than a few minutes (Stoodley and Warwood 2003; Teodósio et al. 2010). This criteria was desirable as it would have fostered greater microbial development upon the surface as opposed to within the water column (Eisnor and Gagnon 2003; Stoodley and Warwood 2003; Teodósio et al. 2010). The internal system HRT used within each of the three flow assays was in the range of 73.1s < HRT < 74.3s (as shown in Appendix A.9 in Table A.6, which shows the internal HRT for each of the components of the pipeline facility) and was controlled by adjusting and regulating the

recirculation tank's volume. The volume regulation also maintained steady state conditions within the three flow assays. Consequently, the wastewater within the three flow assays was well-mixed and of a constant volume.

3.8.2.4 Nutrient content – Average daily water concentrations

During the incubation phase, the wastewater's COD, TN and TP concentrations were monitored and regulated daily, in order to ensure the respective parameters remained reasonably constant and satisfied the target concentration criteria. Water samples (20-50 mm) were taken and evaluated from the recirculating tank every 24 h. The results of this evaluation were then used to determine whether the system required diluting or further concentrating, and to what degree. If adjustments were required, a secondary water sample was taken and evaluated; for the purpose of establishing whether the re-adjusted wastewater met the required target criteria. If this was not the case, then the whole process was repeated. The concentrations of NH_4^+, NO_3^-, Fe, Mn and Cl were also measured during each of the incubation phases.

Table 3.5 presents the average chemical parameters recorded during the incubation phase of each of the flow assays at both pre- and post- adjustment time intervals. Figure 3.32 presents the daily average concentrations of COD, TN and TP recorded during the incubation phase of the three flow assays.

The Cl concentration of the local water source was found to be extremely high (< 0.2 mg/l) and as a consequence, it was extensively monitored. It should be noted, that the source water for the pipeline facility was local to the School of Engineering and it differed from the local drinking water. The Cl concentration within the source water was neutralised using sodium thiosulfate. As a result, the concentration of Cl within the synthetic wastewater remained below the detection limit (i.e. < 0.02 mg/l) during each of the flow assays (see Table 3.5).

The COD concentration during each of the incubation phases required daily adjustment, typically through further concentrating. On average the COD concentrations within the respective assays reduced by 34% per day. Daily re-concentrating with case-specific amounts of macro-nutrients, namely Peptone and meat extract compensated for this reduction. The concentrations of TP and TN within the three flow assays required less extensive adjustment. Typically, the respective parameters only required minor adjustments 2-3 times throughout each of the incubation phases. It can be seen from Table 3.5 and Figure 3.32 that as a result of the extensive daily monitoring, the concentrations of COD, TN and TP during the incubation phases of the flows assays remained reasonably constant.

Table 3.5 Average chemical parameters recorded during the incubation phases of the Re_D = 5.98x10^4, Re_D = 7.82x10^4 and Re_D = 1.00x10^5 assays (for both pre- and post- concentration adjustment time intervals).

Parameter		Re_D = 5.98 x 10^4 (mg/l)		n	Re_D = 7.82 x 10^4 (mg/l)		n	Re_D = 1.00 x 10^5 (mg/l)		n
		Av.	σ		Av.	σ		Av.	σ	
Pre Adjustment	COD	371.8	111.0	20	347.7	101.1	20	357.9	108.7	20
	TN	49.8	0.7	10	51.3	3.1	8	50.6	4.8	11
	TP	10.6	0.97	20	9.9	0.6	20	10.7	1.1	20
	pH	8.09	0.13	20	7.96	0.18	20	7.80	0.26	20
Post Adjustment	COD	536.4	40.5	20	545.6	21.2	20	548.1	23.4	20
	TOC	238.2	16.1	10	251.2	9.5	20	241.6	12.2	9
	DOC	211.5	14.3	10	-	-	-	190.6	9.6	9
	TN	49.5	0.6	2	50.3	0.4	2	51.2	0.9	11
	TP	12.1	1.20	2	10.8	0.8	4	11.0	0.8	3
	pH	8.09	0.13	20	7.96	0.18	20	7.80	0.26	20
	NH_4^+	0.41	0.23	6	0.25	0.23	4	0.75	0.02	4
	NO_3^-	0.50	0.28	6	0.33	0.28	4	1.09	0.11	4
	Fe	0.11	0.05	6	0.10	0.07	4	0.15	0.09	5
	Mn	0.13	0.06	6	0.30	0.20	4	0.39	0.10	5
	Cl	0.01	0.01	6	0.00	0.01	4	0.00	0.01	5

***** *Derived from COD using Equation 3.25*

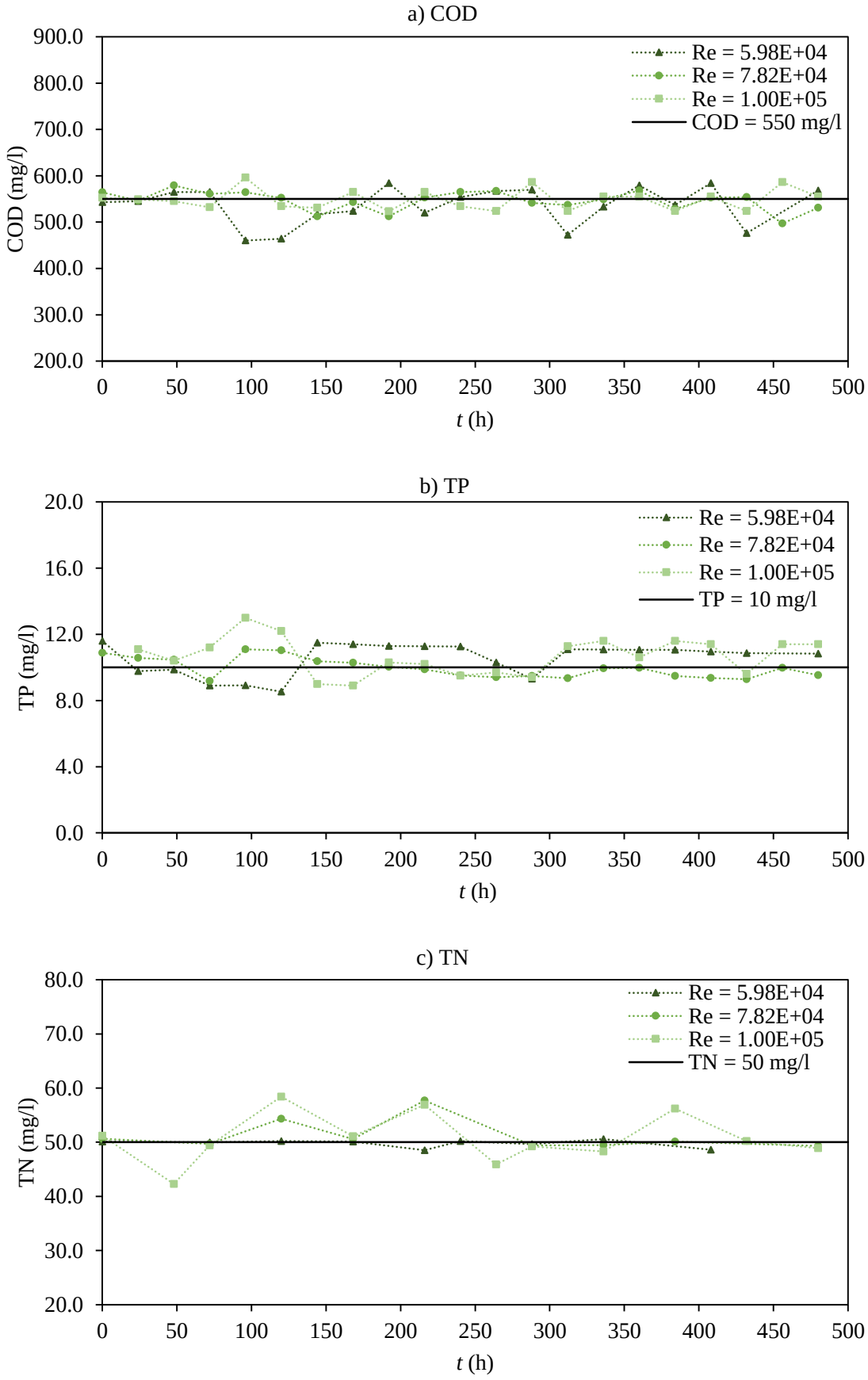

Figure 3.32 Concentrations of a) COD b) TP and c)TN recorded during the incubation phase of the Re_D = 5.98x10^4, Re_D = 7.82x10^4 and Re_D = 1.00x10^5 assays, post concentrations adjustments, with the exception of TN, which represent the pre concentration adjustment values.

3.8.3 Mature phase

Once the biofilms incubated within the Re_D = 5.98x10^4 and Re_D = 1.00x10^5 assays had reached a state of equilibrium, in terms of their frictional resistance they were then subjected to varying flow regimes (over the range of 3.05x10^4 < Re_D < 1.23x10^5). A total of 10 Re_D increments were assessed within each of the varying flow investigations. Typically, this phase of testing commenced after approximately 480-500 h of incubation and took approximately 12-15 h to complete. An unforeseen complication, which led to the death of the biofilm incubated within the Re_D = 7.82x10^4 assay prior to the 500 h mark precluded it from this phase of testing.

The mature phase consisted of four discrete aspects, including: i) frictional evaluations; ii) bulk water chemistry evaluations; iii) visual evaluations and iv) molecular evaluations.

A brief sediment transport investigation was also undertaken as part of the mature phase. Only the biofilm incubated within the Re_D = 1.00x10^5 assay was evaluated with sediment, owing to the respective biofilm's perceived strength, which was based upon it's conditioning. This allowed a greater range of flow conditions to be assessed without causing significant detachment.

The specific details of each aspect of the mature phase, including the sediment investigation are outlined herein.

3.8.3.1 Frictional evaluation

Each of the fouled pipes, at each Re_D increment were surveyed using the protocols outlined in Section 3.4.1.

3.8.3.2 Bulk water chemistry evaluation

Water samples were taken at each Re_D increment; for the purpose of indirectly establishing whether the increase in flow shear could actively remove the biofilm from the surface. Due to the relatively short time it took to complete each of the varying flow investigations (i.e. < 15 h) any changes in water chemistry, especially in terms of organic content (i.e. COD and TOC) during the mature phase would have been likely caused by biofilm detachment. Biofilm detachment has also been reported to cause an increase in the Fe and Mn concentration in bulk water samples (Husband et al. 2008; Douterelo et al. 2013).

At the start of each of the varying flow investigations the flow within the facility was stopped and the bulk water sealed within the network. The storage tank was then emptied and refilled. A water sample (100 ml) was taken prior to the tank being emptied. This sample is herein referred to as the "initial" water sample. This marked the end of the incubation phase. The

water within the tank was then combined with the water sealed within the pipeline and circulated at a very low flow rate for a period of 15 minutes (to ensure thorough mixing). At the end of this mixing period a water sample (100 ml) was taken. This sample is referred to herein as $Re_D = 0$. The water in the system was diluted to improve the resolution of the subsequent chemical measurements, which are outlined herein.

Water samples (100 ml) were taken at the start and end of each of the Re_D increments. A settling time of 5 minutes was used before the first sample was taken. Each of the water samples were evaluated for Fe, Mn, COD and TOC using the protocols and standard reagent assays outlined in Section 3.6, with the exception of TOC which was derived indirectly from COD using Equation 3.35.

The concentration of DNA within the each water sample was also established, using a fluorescent dye technique (full details of which are provided in Section 3.7.3.4). Before being evaluated using the fluorescent dye technique, 10 ml of the total water sample was incrementally centrifuged (*Eppendorf* 5424) 1 ml at a time for 10 minutes at 6000 g to attain a cell pellet. A strong correlation between DNA concentration and total bacterial cell counts has been reported within the literature (McCoy and Olson 1985) and as a consequence, an increase in DNA within the bulk water would suggest an increase in bacteria and thus, indicate biofilm detachment.

3.8.3.3 Visual evaluation

Video recordings, which captured the visualisation pipe were taken during each of the varying flow investigations, using a high definition web camera (*HP* HD 2300). The camera captured a 0.3 m length of the pipe, and was positioned on the invert side of the pipe. The purpose of the video recordings were to establish visually whether biofilm detachment occurred within the respective varying flow investigations. All video recording captured during each of the varying flow investigations can be found on the accompanying CD.

3.8.3.4 Molecular evaluation

Biofilm samples were taken of the mature biofilm before and after each of the respective varying flow investigations. Samples were collected from the fouled pipe using sterile cotton swabs (*Fisher Scientific*). The cotton buds from the swab were aseptically placed in sterile 1.5ml (non-stick) centrifuge tubes (*Alpha Laboratories*). All samples were stored at -80^{0}C until extraction and evaluation (i.e. using the protocols outlined in Section 3.7). It is best practice to evaluate or store a biofilm sample within 3 h of being removed from its natural environment to avoid biological and physico-chemical evolution (El Samani et al. 2004). Biofilm samples were taken from four separate locations around the circumference of the

pipe, within the downstream region of the system, at approximately 8.5m from the test pipe inlet. This meant that no disruption would have been caused to any post sampling frictional measurements. A 1.5 cm diameter circular sample, with an equivalent area of 1.77 cm^2 was taken at each of the four circumferential locations. The sampling locations were located at approximately 0°, 180°, 90° and 270° from the pipe's vertical centreline, and will be referred to herein as (1), (3), (2), and (4), respectively (as shown by Figure 3.33).

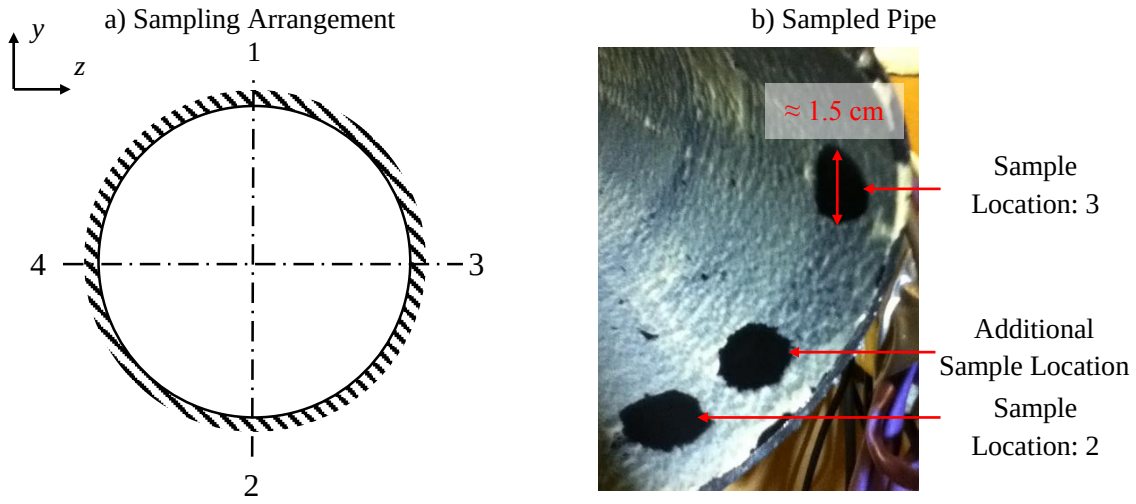

Figure 3.33 a) Biofilm sampling arrangement and b) image of a sampled pipe (for the Re_D = 1.00x10^5 assay).

3.8.3.5 Sediment investigation

The purpose of the sediment investigation was to establish whether the change in surface characteristics caused by biofouling affected the pipe's ability to convey non-cohesive sediment and be self-cleansing. The sediment transport investigation was undertaken 72 h after the varying flow investigation within the Re_D = 1.00x10^5 assay and was repeated under non-fouled conditions (i.e. after total biofilm removal).

To determine the self-cleansing velocity and critical shear stress with and without fouling, sand was injected into the pipeline at different flow regimes. The Re_D range assessed was 2.67x10^4 < Re_D < 1.23x10^5. A total of 74 sediment transport surveys were conducted within the pipeline with and without fouling.

Beach sand was used within the current study to represent municipal sediment. Despite, its non-cohesive nature beach sand is commonly used to represent sewer sediment (Betancourt

2001; Guzmán et al. 2007). The key grain size characteristics of the sand were established from the results of a particle-size distribution analysis, undertaken in accordance with BS 1377-2: 1990 (as shown in Appendix A.10 by Figure A.15 and Figure A.15). In particular, 184.1 g of sediment was passed through 8 sieves, which were sized from 2.0 mm to 63.0 μm. The beach sand was found to be of medium grain (based on the Wentworth grain size scale (Soulsby 1997)) with size characteristics of d_{50} = 0.30 mm, d_{16} = 0.21 mm, d_{84} = 0.38 mm, d_{90} = 0.40 mm, d_g = 0.04 mm and σ_g = 1.34 mm (where d_n is the grain diameter for which n% of the grains by mass is finer, $d_g = (d_{84}\, d_{16})^{0.5}$ is the geometric mean grain size and $\sigma_g = (d_{84}/d_{16})^{0.5}$ is the geometric standard deviation of sediment sizes). The relatively low value of σ_g (i.e. σ_g < 2) indicated that the sand was well sorted and uniform (Soulsby 1997). The density, ρ_s and specific gravity, *SG* of the sand was estimated to be 2658 kg/m^3 and 2.66, respectively. Particles deposited in DNs, which are larger than those transported in suspension typically have a d_{50} of between 0.20-1.00 mm; *SG* of between 1.80-2.60 and are transported along the pipe's invert by rolling and sliding (Cradtree 1989; Bertrand-Krajewski et al. 1993; Ashley et al. 1996; Betancourt 2001). This mode of movement is known as bed load transport. Consequently, the characteristics of the medium beach sand used in the current study was within the range expected for bed load particles within typical DNs.

A 2.0 cm diameter hole was cut into the soffit of the test pipe at 0.5 m from pipe's inlet to allow the sand to be injected. In each of the sediment transport surveys a sample of approximately 100 g of sand was introduced to the pipeline using a funnel. The hole was then sealed, and the time of the injection recorded. The flow rate was then adjusted to the desired level using the gate valve. The sand was collected at the downstream end of the pipe in a purpose built collection device (see Figure 3.34). The collection device was located 8.80 m from the injection hole. The unique design of the collection device allowed sand to be extracted from the pipeline at any time interval, without disrupting the overall flow conditions within the system. Samples were typically extracted after 30 and 60 minutes. However, depending on the rate of sediment transport, additional samples were also taken after 15 and 45 minutes. After 60 minutes any residual sand was flushed out by increasing the flow rate. Care was taken to ensure the increase in flow did not cause significant biofilm detachment. The extracted sand was then desiccated at 105°C for at least 2 h in a furnace before being weighed. The total mass of the transported sand (including the residual) was then calculated. The maximum discrepancy between the initial and total transported dry mass was ±1.66%, which indicated that the vast majority of the sand was transported and successfully collected.

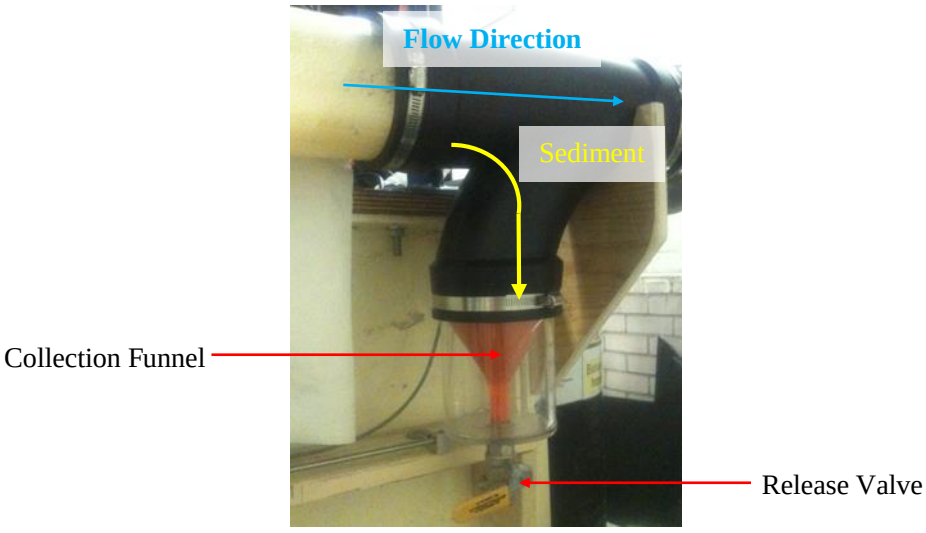

Figure 3.34 Sediment collection device within the pilot-scale pipeline.

For sediment transport to occur the operating conditions must be equal to or greater than the critical conditions required to carry particles of a given size, i.e. $\theta \geq \theta_{cr}$, where θ is the actual Shields parameter and θ_{cr} is critical Shields parameter as given by (Soulsby 1997):

$$\theta = \frac{\tau_w}{(\rho_s - \rho)gd} = \frac{u^*}{gd\Delta} \qquad \textit{Equation 3.20}$$

$$\theta_{cr} = \frac{0.30}{(1 + 1.2D^*)} + 0.055\left[1 - e^{(-0.02D^*)}\right] \qquad \textit{Equation 3.21}$$

where D^* (= $d_{50}(g\Delta/\nu^2)^{1/3}$) is the dimensionless grain size and $\Delta = (\rho_s\text{-}\rho)/\rho$.

Based on the specific grain size characteristics, the key sediment transport parameters for the beach sand were w_s = 4.52 cm/s D^* = 7.66, θ_{cr} = 0.037, u^*_{cr} = 1.35 cm/s and τ_{cr} = 0.18 N/m^2 (where w_s is the settling velocity, u^*_{cr} is the critical friction velocity and τ_{cr} is the critical wall shear stress). Full details on the key sediment transport parameters can be found in Appendix A.11 in Table A.8 and Table A.9. The settling velocity is defined as (Soulsby 1997):

$$w_s = \frac{\nu}{d}\left[\left(10.36^2 + 1.049D^{*3}\right)^{1/3} - 10.36\right] \qquad \textit{Equation 3.22}$$

3.9 Facility maintenance pre- and post- fouling

Before incubating with wastewater, the whole facility was disinfected using a concentrated chlorine solution. The system was flushed for 48 h at the maximum flow rate (Q = 10 l/s).

After the flushing the bulk water within the facility was left to stand for a further 24 h, before flushing with fresh water. The water within the facility was constantly replaced until the chlorine levels were negligible. Sodium thiosulfate was also used to neutralise any residual chlorine within the facility. The aforementioned process was repeated post fouling. However, in the case of heavy fouling, the biofilms were physically scraped from the surface using an extendable brush. A drying phase was also incorporated to aid with the biofilm removal. The maintenance regime used within the current study was based upon that outlined by Douterelo et al. (2013) for a pilot DWDSs.

3.10 Summary

This chapter has outlined all aspects of the pilot-scale pipeline facility developed within the current study. The arrangement and key components of the facility were explained in Section 3.2.1 and Section 3.2.2, respectively. Comprehensive details on the test pipe, including entrance conditions, measurement locations and surface finish were outlined in 3.2.3. In particular, it was found that an entrance length of 3.35 m was sufficient to attain fully developed flow within the pipeline (at least in terms of mean flow criteria). The physical roughness of the test pipe was estimated from ESEM imaging and specialised software. The S-HDPE test pipe had an average k_{rms} of 2.35 μm and k_{av} of 1.56 μm. The key instrumentation used within the facility was outlined in detail in Section 3.3. Included within these descriptions was the relevant calibration information.

The sensitivity analysis outlined in Section 3.5 indicated that the uncertainty in k_s could potentially be extreme, particularly for low operating conditions (i.e. for $Re_D < 5.0\text{x}10^5$). On this basis all experimental investigations undertaken at low Re_D were repeated several times and were viewed with caution. The sensitivity analysis also indicated that in theory the increase in roughness induced by biofouling would result in a reduction in overall k_s uncertainty.

The details of the synthetic wastewater used within the current study were comprehensively outlined in Section 3.6.

The experimental programs undertaken within the pilot-scale pipeline were outlined in detail in Section 3.8. In particular, all operating conditions, sampling protocols and analysis techniques for each of the three investigation phases, including the non-fouled; incubation; and mature phases were outlined in detail.

Chapter 4 Non-foul phase

4.1 Introduction

The purpose of this chapter is to outline the results of the non-fouled phase of the current study. On the basis that the conditions within the pipeline when fouled are inherently unknown, it was essential to validate the pipeline under non-fouled conditions where the governing equations are reasonably well understood. This was particularly important given the small nature and high potential for uncertainties of the associated frictional parameters, namely k_s. The non-fouled pipe was surveyed over the range of $3.15\text{x}10^4 < Re_D < 1.23\text{x}10^5$. It's frictional capacity was established via direct and indirect means from pressure gradient and mean-velocity data. The methods and equations required to establish the frictional capacity of the test pipe are outlined and discussed in detail within this chapter. The measured uncertaintities associated with each parameter are presented within this chapter. The Log-Law constants of κ and C were also established under non-fouled conditions within this chapter. A brief summary is presented at the end of the chapter.

4.2 Uncertainty analysis

The uncertainties associated with the parameters measured and calculated within the current study are given in Table 4.1. The uncertainties listed in Table 4.1 represent a 95% confidence interval, determined from i) repeated measurements within a discrete pipe survey and ii) repeated pipe surveys for equivalent Re_D. Each of the pipe surveys, which included a PG and velocity profile survey were repeated at least three times. In order to estimate the 95% confidence in a statistical average (i.e. $\bar{x}$), the standard deviation in x, σ_x was multiplied by an appropriate two-tailed t-value for the relevant degree of freedom, which is dependent on the sample size, n_x (where $\alpha = 0.05$). The uncertainty in x is therefore given by:

$$\pm x = t\left(\frac{\sigma_x}{\sqrt{n_x}}\right) \qquad \textit{Equation 4.1}$$

Table 4.1 Uncertainty estimates derived from the evaluation of the non-fouled pipe.

Parameter	Symbol	Uncertainty (% unless noted)			
		Repeated Measurements		Repeated Pipe Surveys (i.e. Re_D)	
		Av.	Max.	Av.	Max.
Hydraulic head	h	0.10	0.33	4.90	9.64
Pipe fluid temperature	T_{pipe}	0.15	0.35	5.00	8.00
Tank fluid temperature	T_{Tank}	0.14	0.31	5.00	8.00
Fluid density	ρ	0.00	0.00	0.02	0.03
Fluid kinematic viscosity	ν	0.06	0.18	2.39	4.14
Volumetric flow rate (Flowmeter)	Q	0.94	2.09	10.01	15.99
Volumetric flow rate (Pitot Probe)		-	-	6.43	11.61
Average freestream velocity (Flowmeter)	$\overline{U}$	0.94	2.09	10.01	15.99
Average freestream velocity (Pitot Probe)		-	-	6.43	11.61
Reynolds Number (Flowmeter)	Re_D	0.94	2.09	8.59	15.80
Reynolds Number (Pitot Probe)		-	-	6.85	11.24
Local velocity, near wall region ($y^+ < 50$)	u	-	-	3.85	4.40
Local velocity, Log-Law region ($50 < y^+ < 300$)		-	-	1.21	1.79
Local velocity, wake region ($300 < y^+ < R^+$)		-	-	0.70	1.08
Von Kármán*	κ	-	-	2.38	-
Smooth wall Log-Law constant *	C	-	-	9.48	-
Wall-normal position	y	0.01mm	-	-	-
Friction factor	λ	2.91	4.17	5.15	7.30
Shear velocity	u^*	1.76	3.96	6.49	14.27
Wall shear stress	τ_w	3.44	7.21	13.44	28.53
Skin friction coefficient	c_f	1.51	3.95	4.53	15.36
Equivalent sandgrain roughness	k_s	66.83	125.56	58.00	-
Manning coefficient	n	3.00	7.00	12.00	
Pipe diameter	D	0.43	0.67	-	-
Pipe length	L	0.5mm	-	-	-

**Derived from the linear regression approach (see Section 4.6)*

Generally, it is evident from Table 4.1 that the uncertainties determined from the repeated pipe surveys were considerably higher than those derived from the repeated measurements within a discrete survey. This was attributed to the difficulty in attaining equivalent flow conditions for each of the repeated pipe surveys, using the gate valve. The uncertainty in Re_D associated with the repeated pipe surveys of ±4.90% confirms this conclusion. Schultz and Swain (1999) reported a similar flow control problem which led to high experimental uncertainties.

The uncertainties in local velocity measurements are illustrated by Figure 4.1, which presents a typical mean-velocity profile in semi-log form. As expected, it is evident from Figure 4.1 that the uncertainty in u is a function of its normal-wall position, with maximum uncertainties associated with the near wall region.

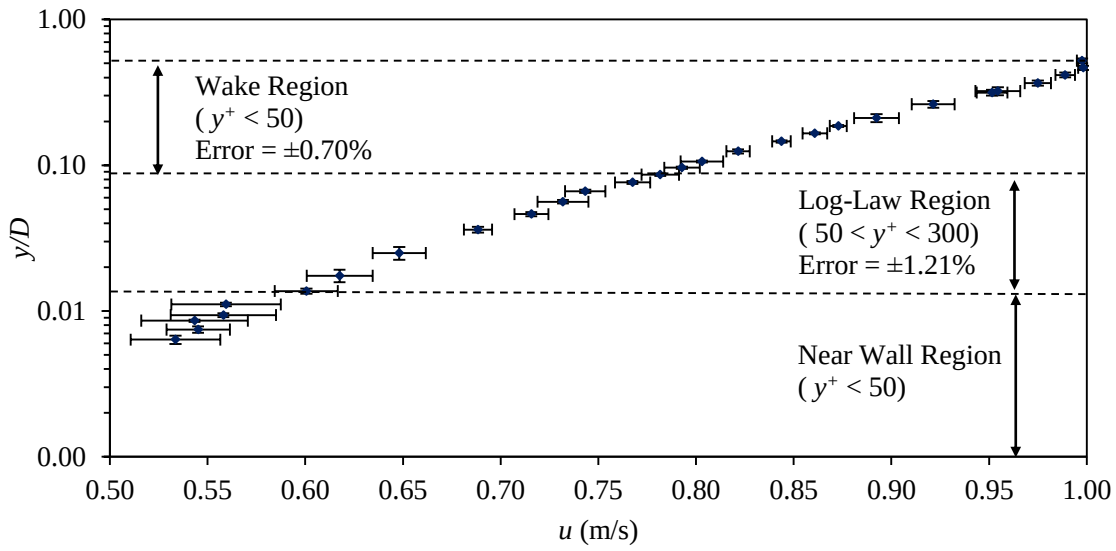

Figure 4.1 Uncertainties associated with mean-velocity profiles (for y/D < 0.5).

The uncertainties listed in Table 4.1 for the non-fouled pipe represent the worst case conditions for the facility, and are referred to as such herein. This is as a result of the smoothness of the non-fouled pipe and the Re_D assessed (as shown by the sensitivity analysis presented in Section 3.5). Higher Reynolds Numbers, in excess of $Re_D = 1.30 \times 10^5$, which would have improved the experimental uncertainties listed in Table 4.1, especially in k_s could not be achieved using the facility in its current arrangement (as discussed in Section 3.2.2). A Test Section of greater overall length, would also have improved the experimental uncertainties, although, this could not be achieved due to laboratory restrictions, which had a limiting factor on the facility's total length.

4.3 Global frictional resistance

The frictional data presented within this section was established from the system's PG and therefore, it represents the space-averaged (i.e. global) conditions within the system.

Figure 4.2 and Figure 4.3 illustrate the actual and normalised (with respect to P_1, i.e. P_n/P_1) static pressure profiles for the non-fouled pipe. It is evident from these Figures that h decreases linearly with L at a constant rate. This indicates that the flow within the Test Section was fully developed and no longer influenced by the system's entrance conditions, at least as far as the pressure head distribution in the flow direction was concerned. Consequently, the fitted linear regression lines of best fit represent the system's PG to a high degree of conformity ($R^2 > 0.99$). The slight discrepancies in the linearity in the profiles observed at 0.0 m < x < 0.3 m and 3.0 m < x < 3.3 m (i.e. across P_1-P_2 and P_3-P_4, see Figure 3.5) evident within Figure 4.2 and Figure 4.3, are attributed to the increased local flow resistance caused by the pipe joints. The frictional data associated with these locations will relate directly to the pipe joints herein.

Two averaging approaches were used within the current study to evaluate the system's PG, both for the fouled and non-fouled phases.

In the first approach, herein referred to as the "Slope Fit Method" (SFM) PG was derived from a linear fit on profiles of static pressure. The PG was then used to determine all the required frictional resistance parameters and effective roughness coefficients.

In the second approach, referred to as "Combined Average Method" (CAM) PG was evaluated from the discrete static headloss combinations (i.e. P_1-P_5, P_1-P_4, P_1-P_3 etc.) by averaging them. Again the established PG was used to determine all the essential frictional data. Excluded from the average were the data associated with pipe joint locations (i.e. P_1-P_2 and P_3-P_4). The CAM should provide a greater indication of the frictional variance at discrete locations, which would be of particular interest within the fouled phases of the current study.

The results attained from the two averaging approaches are given in Appendix B.1 in Table B.1 and Table B.2. A summary of which are presented in Figure 4.4 to Figure 4.7. The non-fouled pipe's k_s and n values detailed within Appendix B.1 in Table B.1 and Table B.2 were estimated using the traditional forms of the C-W equation (i.e. Equation 2.42) and Manning equation (i.e. Equation 2.45), respectively.

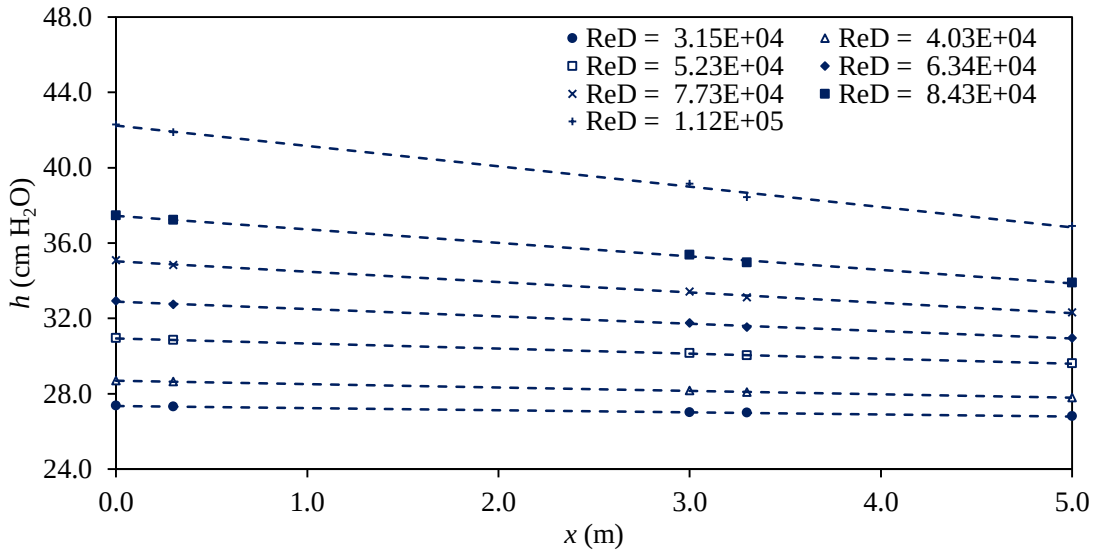

Figure 4.2 Static head profiles for the non-fouled test pipe (for the range of $2.98x10^4<Re_D<1.12x10^5$).

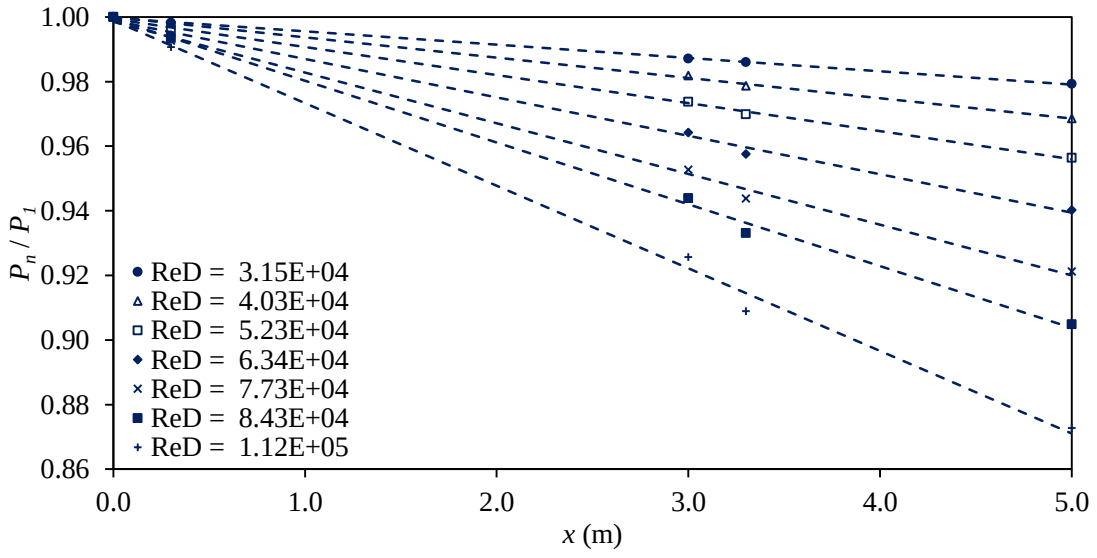

Figure 4.3 Normalised (with respect to P_1) static head profiles for the non-fouled test pipe (for the range of $2.98x10^4<Re_D<1.12x10^5$).

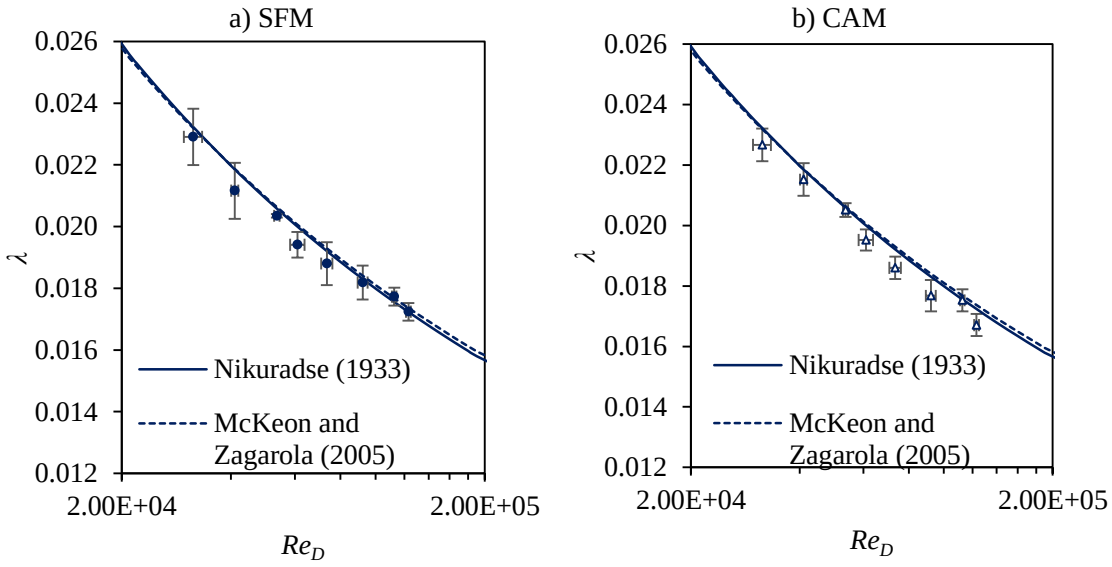

Figure 4.4 Moody Diagram, illustrating the experimentally determined values of λ for the non-fouled pipe, estimated using a) the SFM and b) the CAM (for the range of $2.98x10^4<Re_D<1.12x10^5$).

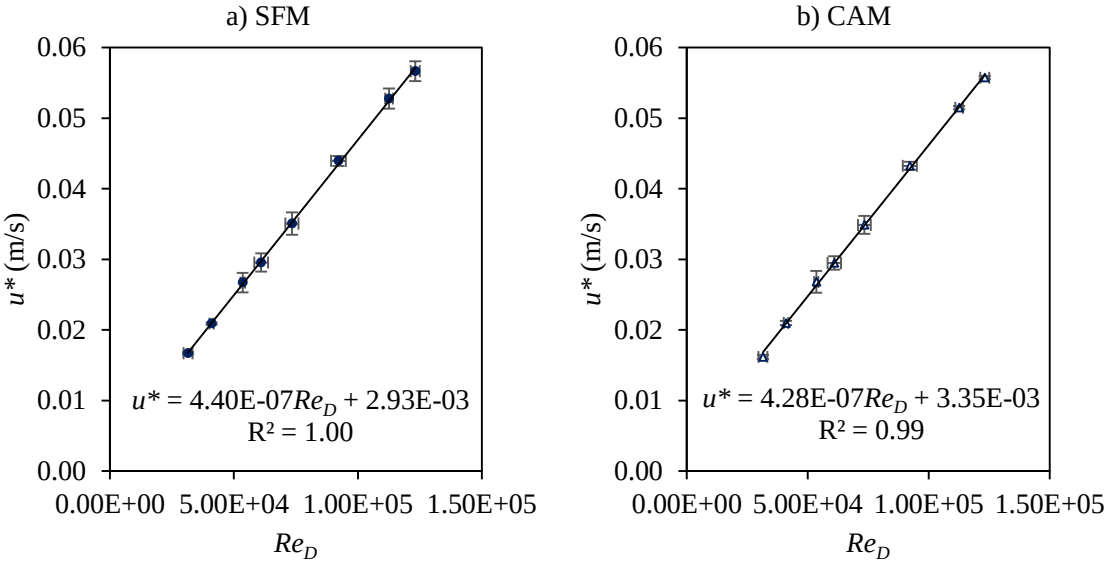

Figure 4.5 Non-fouled pipe values of u determined using a) the SFM and b) the CAM (for the range of $2.98x10^4<Re_D<1.12x10^5$).*

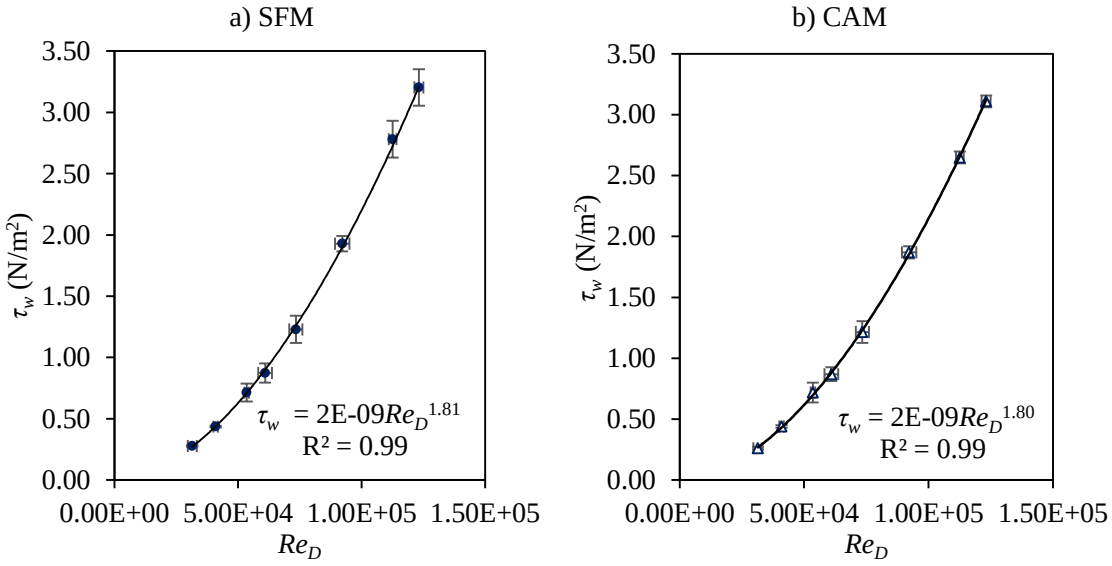

Figure 4.6 Non-fouled pipe values of τ_w determined using a) the SFM and b) the CAM (for the range of $2.98x10^4<Re_D<1.12x10^5$).

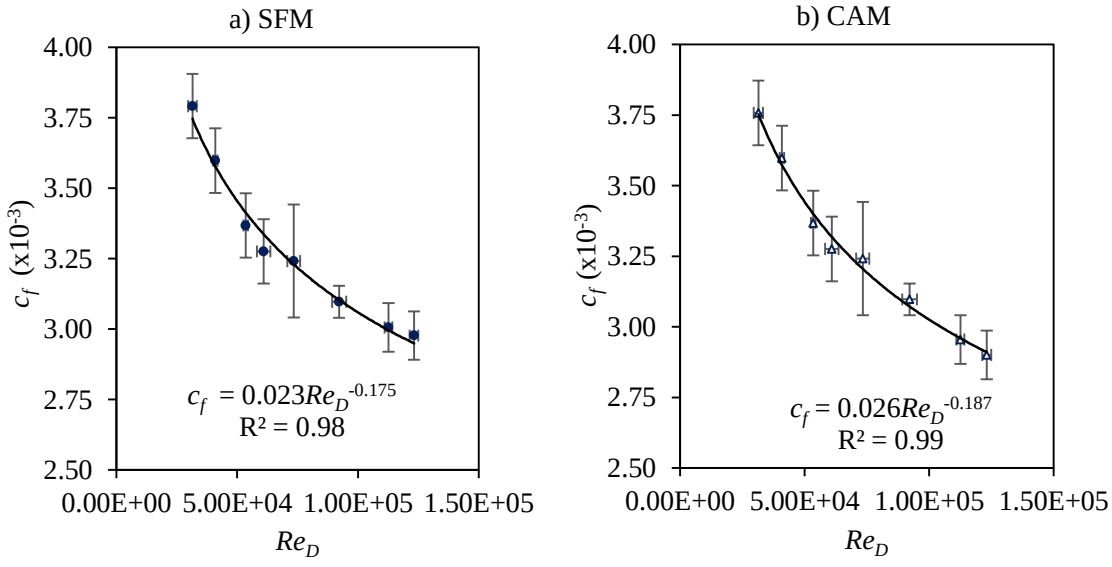

Figure 4.7 Non-fouled pipe values ofc_f determined using a) the SFM and b) the CAM (for the range of $2.98x10^4<Re_D<1.12x10^5$).

It is evident from Figure 4.4 to Figure 4.6 that the frictional data derived from the two averaging approaches were equvilent. This was attributed to the homogeneity of the pipe's roughness distribution under non-fouled conditions.

The experimentally determined values of λ had a reasonably strong agreement with the smooth pipe relationships proposed by both Nikuradse (1933) (i.e. Equation 2.11) and McKeon and Zagarola (2005) (i.e. Equation 2.12). The percentage deviations between the measured and theoretically established friction factors are presented within Figure 4.8. The maximum discrepancy between the measured and theoretical values of λ was ±3.97%, which was within the experimental uncertainties (i.e. ±5.15%, see Table 4.1).

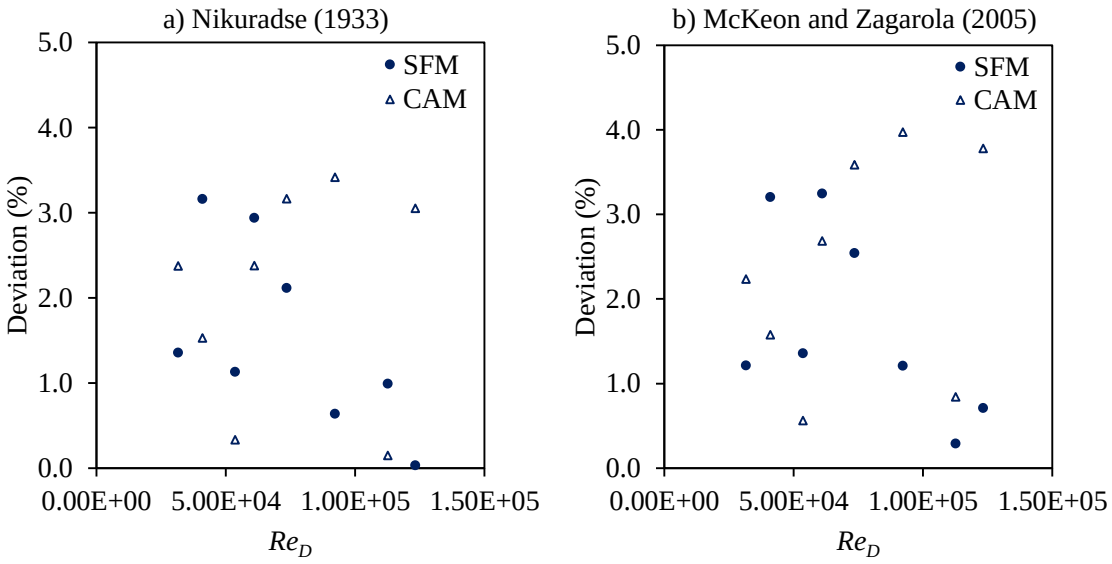

Figure 4.8 Deviation of the measured friction factor from a) Nikuradse (1933) and b) McKeon and Zagarola (2005) relationships.

The average values of k_s and n determined using the SFM were found to be 0.010 mm ± 43% and 0.009 ± 4%, respectively. Similarly, the average values of k_s and n using the CAM were 0.008 mm ± 58% and 0.008 ± 12%, respectively. The overall average values of k_s and n determined from the combined SFM and CAM datasets were 0.009 mm ± 32% and 0.008 ± 6%. The maximum value of k_s^+ was found to be 0.51 (i.e. for $Re_D = 1.23 \times 10^5$). Consequently, the surface was considered to be hydraulically smooth for the full Re_D range assessed.

The high established uncertainties in k_s (i.e. > ±32%) were to be expected for the test pipe, when evaluated over the range of $2.98 \times 10^4 < Re_D < 1.12 \times 10^5$, due to the extremely smooth nature of the pipe. This was illustrated by the sensitivity analysis outlined in Section 3.5, and in particular, Figure 3.28.

The friction factors associated with the pipe joints were found to correlate reasonably well with the theoretical values derived from the C-W equation (as shown, by Figure B.1 in Appendix B.1). The average k_s and n values associated with the pipe joints were found to be 0.54mm ± 28% and 0.011 ± 4%, respectively. The minor headloss coefficient was found to be 0.094 ± 8%.

4.4 Mean-velocity profiles

Mean-velocity profiles, which were recorded using the Pitot probe for the range of $3.83 \times 10^4 < Re_D < 1.13 \times 10^5$ are presented in Figure 4.9 to Figure 4.11 in non-dimensional form. Velocity defect profiles are presented within Figure 4.12. For improved clarity Figure 4.10 and Figure 4.12 present the mean-velocity data, for the range of $0 < y < R$ in both traditional and semi-log form

The dimensionless mean-velocity profiles presented in Figure 4.9 and Figure 4.10 were normalised with respect to U, whereas the profiles within Figure 4.11 were normalised with respect to u^*. The values of u^* used to scale the velocity profiles were attained from the SFM. As the effective roughness distribution of the non-fouled pipe was considered to be homogeneous in nature, it was deemed acceptable to apply the globally attained frictional data locally. This would not be possible for a fouled pipe, due to the likely irregularity of its surface roughness distribution (Schultz and Swain 1999; Schultz 2000; Andrewartha 2010; Barton 2006; Walker et al. 2014).

It is evident from Figure 4.9 that the normalised mean-velocity profiles were symmetrical in the vertical direction and in reasonable agreement with the Log-Wake Law. The correlation between the experimentally determined mean-velocity profiles and the Log-Wake Law is particularly well highlighted by Figure 4.10.

As expected, Figure 4.11 illustrates that the data for each Re_D collapses well onto the same curve within the Log-Law region of the boundary layer. The viscous sublayer, buffer, and Log-Law, and wake regions were fitted to the mean-velocity profile shown in Figure 4.11 using Equation 2.18, Equation 2.21 and Equation 2.25, respectively.

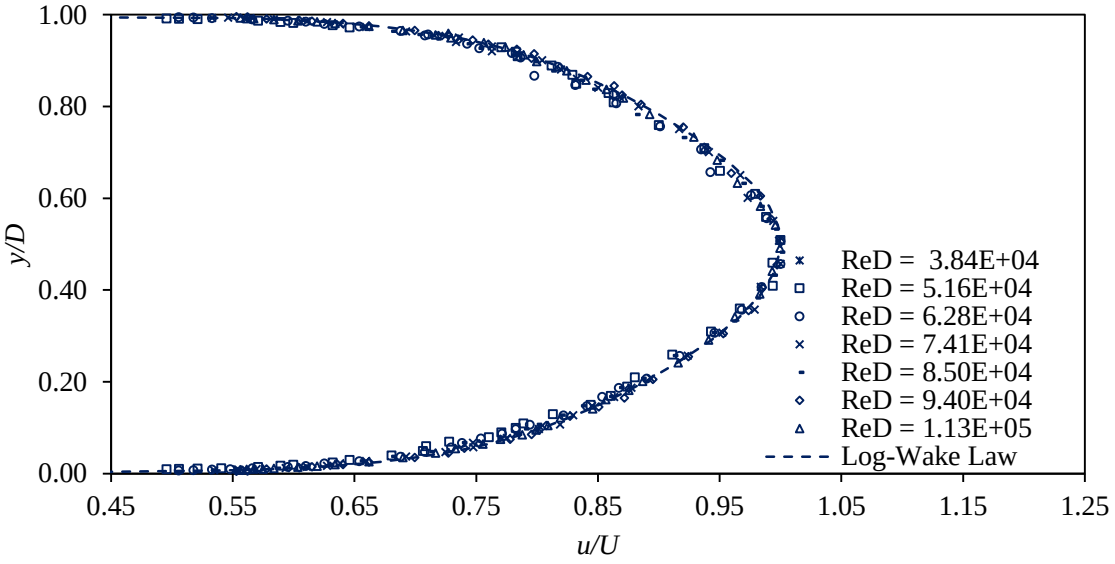

Figure 4.9 Normalised mean-velocity profiles for the non-fouled pipe (for the range of 5.23 x 10^4 < Re_D < 1.13 x 10^5).

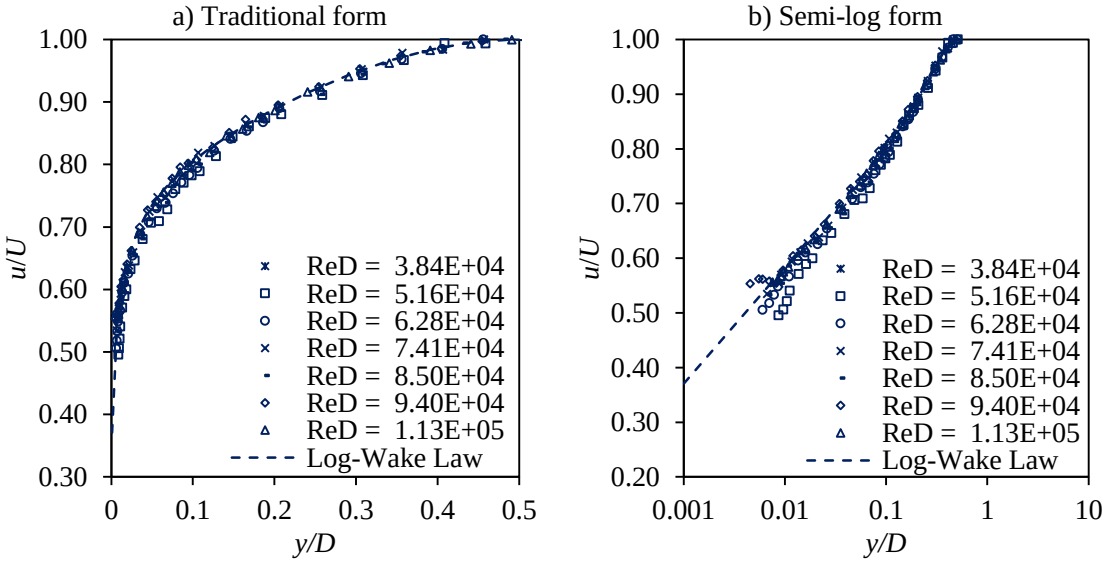

Figure 4.10 Normalised mean-velocity profiles (y/D < 0.5), in a) traditional and b) semi-log forms for the non-fouled pipe (for the range of 5.23 x 10^4 < Re_D < 1.13 x 10^5).

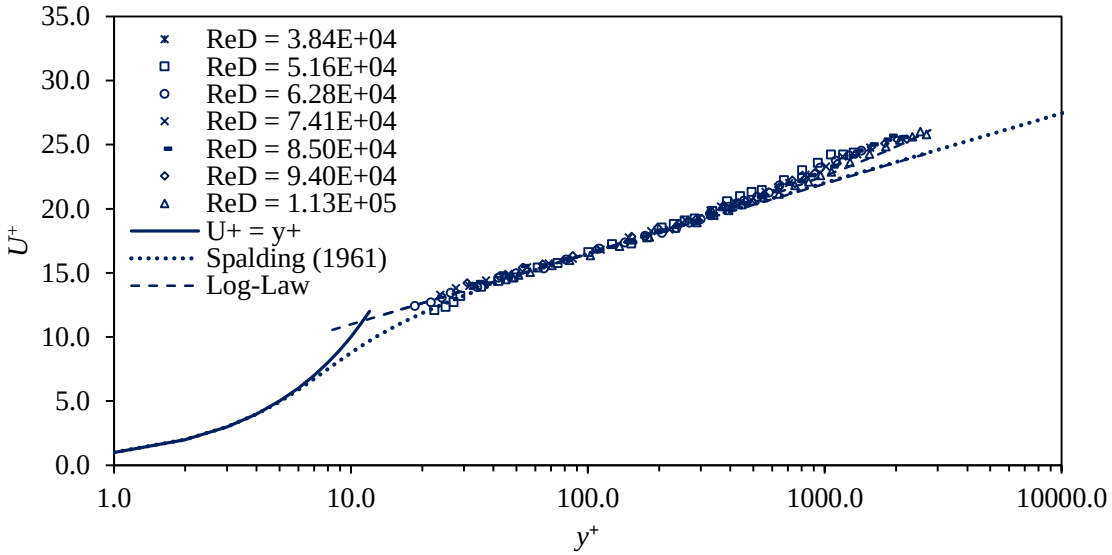

Figure 4.11 Dimensionless mean-velocity profiles for the non-fouled pipe (for the range of 5.23 x 10^4 < Re_D < 1.13 x 10^5).

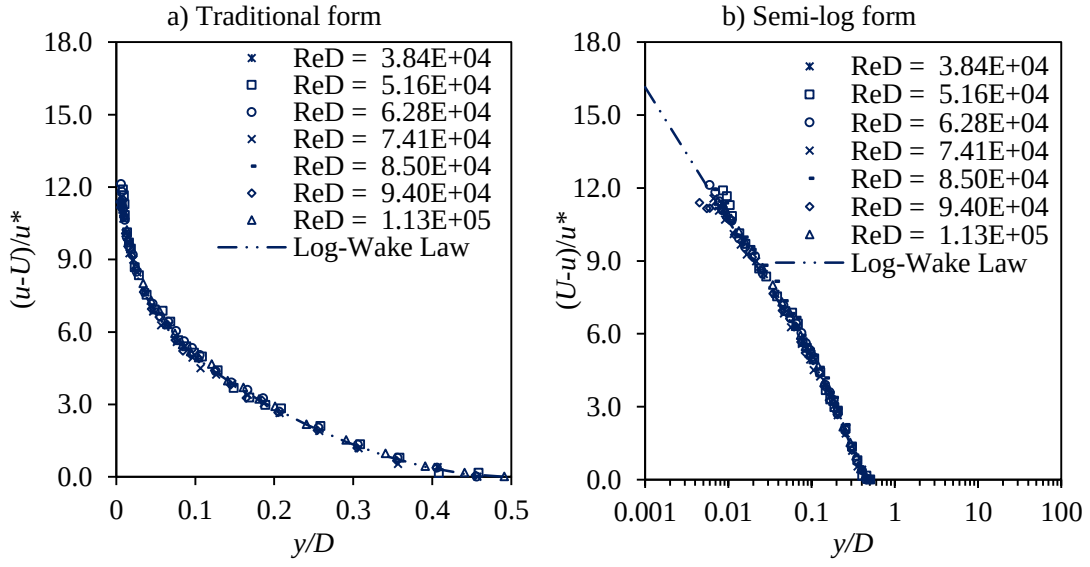

Figure 4.12 Dimensionless mean-velocity defect profiles both in a) traditional and b) semi-log forms for the non-fouled test pipe (for the range of 5.23 x 10^4 < Re_D < 1.13 x 10^5).

The velocity defect (i.e. *U*-*u*) at any wall-normal position is a function of τ_w. For fully developed pipe flow, with an evenly distributed sandgrain roughness the velocity defect law is valid for both smooth and rough surfaces (Zagarola and Smits 1998; Krogstad and Antonia 1999; Flack et al. 2005; Bakken et al. 2005; Shockling et al. 2006; Wu and Christensen 2007). This implies that the outer region of a smooth or rough boundary layer is insensitive to the way in which τ_w is generated and therefore, Townsend's Wall Similarity Hypothesis applies (Barton 2006). The velocity defect profiles presented in Figure 4.12 show good collapse and are in strong agreement with the Log-Wake Law (Equation 2.25). Consequently, the velocity defect law and Townsend's Wall Similarity Hypothesis are valid for the non-fouled pipe.

The wake strength parameters, which were established by fitting the mean-velocity data to the Log-Wake Law (i.e. Equation 2.26) are presented in Table 4.2. The values of Π listed within Table 4.2 are typically higher than that suggested by Guo and Julien (2003) for smooth pipe flow (i.e. $\Pi = \kappa = 0.42$), although, they are in reasonable agreement with those documented by Walker et al. (2013). The average value of Π determined for the non-fouled pipe was 0.46 ± 0.05.

The essential boundary layer parameters established from the velocity data are given in Table 4.2. The values of u^* attained from the SFM were used to derive the boundary layer parameters listed. The boundary layer thickness is not an easy parameter to measure accurately, as it is heavily dependent upon a single velocity measurement in a region where velocity is asymptotic to *U*. Consequently, the boundary layer displacement thickness, δ^* and the momentum thickness, θ are commonly used to indirectly estimate δ. This is beacuase δ^* and θ are less dependent upon discrete measurements as they are derived by integrating over the whole boundary layer. Furthermore, the δ^* is also less reliant on an accurate wall origin, which is particularly beneficial for rough boundary investigations, such as those outlined within the fouled phases of the current study.

The displacement thickness refers to the distance normal to the wall where the streamlines are first displaced by the boundary layer, and is given by:

$$\delta^* = \int_0^R \left(1 - \frac{u}{U}\right) dy \qquad \textit{Equation 4.2}$$

The momentum thickness is analogous to the displacement thickness and is given by:

$$\theta = \int_0^R \frac{u}{U}\left(1 - \frac{u}{U}\right) dy \qquad \textit{Equation 4.3}$$

The boundary layer thickness can be calculated from the θ using the 1/7th power law, as given by:

$$\delta = \frac{72\theta}{7} \qquad \textit{Equation 4.4}$$

For completeness the kinetic energy thickness, δ** is given by:

$$\delta^{**} = \int_0^R \frac{u}{U}\left(1 - \left(\frac{u}{U}\right)^2\right) dy \qquad \textit{Equation 4.5}$$

The velocity profile shape factor is given by:

$$H = \frac{\delta^*}{\theta} \qquad \textit{Equation 4.6}$$

Table 4.2 Boundary layer parameters for the non-fouled test pipe.

Re_D	Wall Origin Error, ε (mm)	δ (mm)	δ* (mm)	δ** (mm)	θ (mm)	H	Π
5.20 x 10^4	0.87	46.39	5.80	1.34	4.53	1.28	0.53
6.10 x 10^4	0.68	43.91	5.48	1.27	4.28	1.28	0.48
7.41 x 10^4	0.67	42.54	5.32	1.21	4.22	1.26	0.41
9.40 x 10^4	0.45	42.50	5.31	1.20	4.22	1.27	0.41
1.13 x 10^5	0.75	42.65	5.33	1.21	4.25	1.26	0.48

The boundary layer parameters listed within Table 4.2 were largely used as a point of reference for biofouled investigation.

4.4.1 Wall origin error, ε determination

The Pitot probe's location within the test pipe, which was 0.15 m downstream from the nearest aperture made it difficult to accurately determine the probe's wall-normal position. Consequently, a wall origin error, ε was applied. The wall origin error is relative to a known arbitrary datum, which in the current study was taken has the internal invert of the pipe (i.e. at $y \approx 0$).

The method used in the current study to determine ε was first proposed by Perry and Joubert (1963). This method has been successfully used to estimate ε for both engineered and

biofouled surfaces (Schultz and Swain 1999; Andrewartha 2010; Walker 2014). The Perry and Joubert (1963) method, which will be referred to herein as the PJ Correction Method uses plots of u/U against log(y) to determine ε. The Log-Law region of these plots will most likely be curved, as opposed to linear. The distance above the known datum is then incrementally adjusted by ε (i.e. $y + \varepsilon$) until the Log-Law region becomes linear. The adjustment criteria, i.e. whether ε is positive or negative is based upon whether the Log-Law region's curve has a positive or negative second derivative. For instance, if the curve as a positive second derivative then y is incremented by a positive value of ε whereas, if the curve as a negative second derivative y is incremented by a negative value of ε.

A wall origin error will be essential in the evaluation of the fouled surfaces within the current study, due to such surfaces typically rough nature. The nature of a rough surface poses several question as to where the boundary layer profile should begin i.e. in the gaps between roughness elements; at the peak or trough of the roughness element; or at some point in between (Perry and Joubert 1963; Perry and Li 1990; Andrewartha 2010).

Wall similarity techniques, which a commonly used to indirectly determined the local frictional conditions for smooth and rough boundaries from mean-velocity data require the exact location of the wall to be known. The use of ε within wall similarity techniques therefore introduces an additional degree of freedom and induces greater uncertainties within the derived frictional parameters. Furthermore, doubts have been raised over the validity of wall origins established from the PJ Correction Method, particularly when a linear regression line is applied (Musker 1990; Candires 2001). Consequently, any wall similarity method applied to experimental data is devoted specifically to the problem of identifying ε. (Perry and Joubert 1963; Musker 1990; Candries 2001). Perry and Joubert (1963) found that many combinations of ε gave equally good fits to experimental data. Furthermore, Candires (2001) suggested that a linear regression puts too much emphasis on certain points and as a result, in some instances the obtained values of ε were deemed to be physically unacceptable. Candires (2001) suggested that to attain acceptable results using the PJ correction method a non-linear regression line should be applied to the plots of u/U against log(y). Consequently, a 2nd order polynomial relationship was fitted to all plots of u/U against log(y) within the current study. Nevertheless, it was still believed that in some situations the wall origins established from the PJ Correction Method were physically unrealistic. As no better method was available at the time of the study the effective wall locations estimated using the PJ correction were compared to the relative wall location determined from the McKeon Method. It should be stated, that the McKeon Method is reliant on the probe being positioned perfectly parallel to the wall, which based upon the probe's location within the pipe was difficult to achieve. Despite this,

the McKeon Method should provide a reasonably acceptable wall location. Using the McKeon Method the effective location of the probe's centreline was found to be 0.56 mm above the wall. The location of a Pitot probe above the wall has also been taken as $0.65d_p$ within the literature (Barton 2006). For the current study this would equate to $\varepsilon = 0.65$ mm.

Figure 4.13 illustrates the effective wall origins derived from the PJ correction method. The values of ε shown in Figure 4.13 were determined using the values of u^* estimated from the PG (SFM), Bradshaw, Log-Law Slope, Perry and Li, and the Preston Probe Methods. The full details of the wall similarity methods (i.e. the Bradshaw, Log-Law Slope, Perry and Li, and the Preston Probe Methods) are provided in Section 4.5.3. The values of ε presented in Figure 4.13 are tabulated in Appendix B.2 in Table B.3. The effective wall locations determined from the PJ correction method were independent of Re_D and were between 0.43-0.94 mm. Furthermore, these values of ε were in close proximity to the values determined by the McKeon Method and $\varepsilon = 0.65d_p$. This indicates the Pitot probe was positioned reasonably close to the wall. However, the effective wall locations determined from the PJ correction were generally higher than the equivalent values determined from the McKeon Method and $\varepsilon = 0.65d_p$. This was likely to have been caused by procedural errors induced by the manual positioning of the probe within the pipe, as opposed to the PJ Method itself. The large scatter in values of ε presented in Figure 4.13 was attributed to typical errors associated with near wall measurements. Therefore, the PJ Method was considered to be an adequate measure of the effective wall location.

The wall origin errors determined in the current study were found by using a purpose built *Microsoft Excel* spreadsheet. The spreadsheet fitted a 2nd order polynomial relationship to experimentally determined plots of u/U against $\log(y)$, within the Log-Law region. The relationship's second derivative was then established. The wall origin error was incrementally adjusted until the relationship's second derivative equalled 0. This process was completed manually and automatically using *Microsoft Excel's* "goal seek" function. Figure 4.14 illustrates a typical corrected and uncorrected velocity profile.

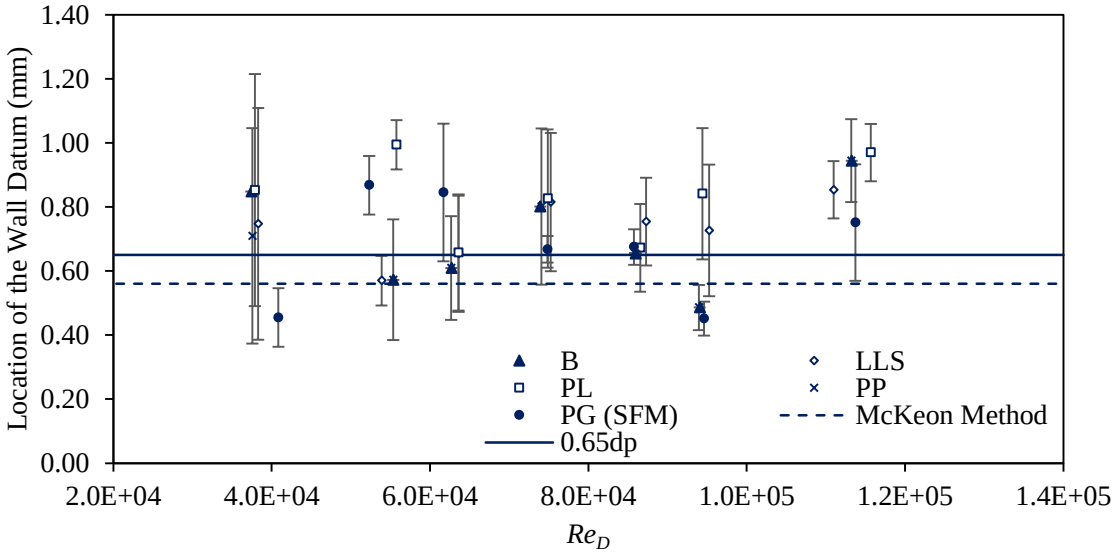

Figure 4.13 Comparison between wall locations determined using the PJ correction and McKeon methods, where u was determined using the SFM, the B Method, the LLS Method, the PL Method, and the PP Method. The average uncertainty in Re_D was ±7%.*

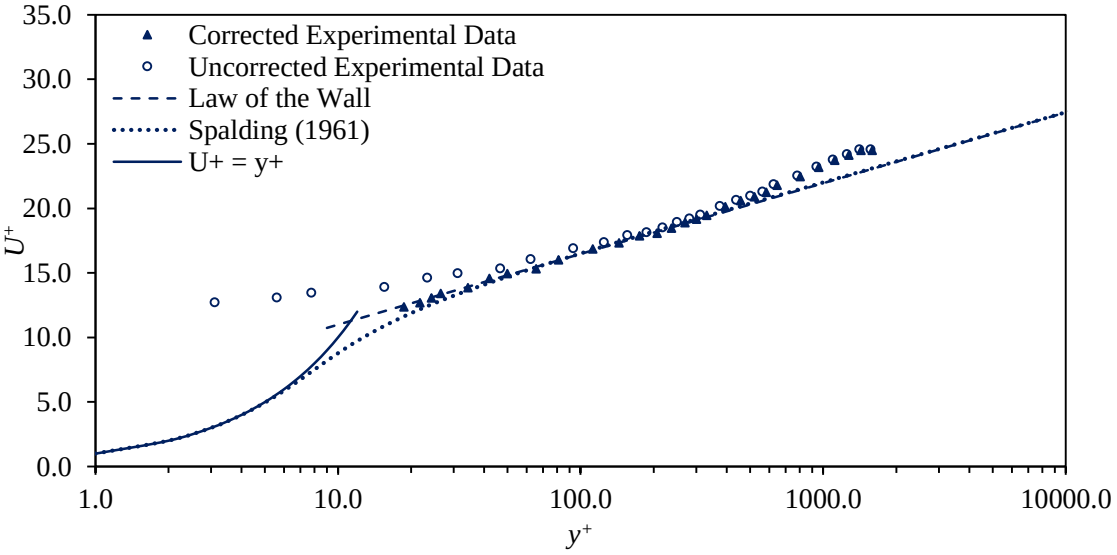

Figure 4.14 Typical corrected and uncorrected velocity profiles (for Re_D = 8.48 x 10^4).

4.5 Local frictional resistance

The local frictional resistance of a surface can be determined using wall similarity techniques, which include velocity profiles and similarity of flow around obstacles, such as Preston Probes. These methods, which rely on mean-velocity data recorded using a Pitot probe are outlined and discussed within this section. Due to the homogeneity of the non-fouled pipe's roughness distribution, it is expected, that the local frictional data should be equivalent to the global frictional data derived from the system's PG.

4.5.1 Preston probe method

The Preston Probe (PP) method (Preston 1954) is based upon flow similarity principles about an obstacle. The obstacle in this case was a Pitot probe positioned at the wall. Providing the probe is small enough not to have a notable effect on the growth of the boundary layer, then the ΔP between the dynamic pressure (recorded by the Pitot probe) and the undisturbed static wall pressure (i.e. $\Delta P = P_p - P_s$) can be used to derive τ_w using the following non-dimensional relationship (Preston 1954):

$$\frac{\Delta P d^2}{\rho v^2} = f\left[\frac{{d_p}^2 \tau_w}{\rho v^2}\right] \qquad \textit{Equation 4.7}$$

where, d is the outer diameter of the Pitot probe (i.e. d_p = 1.0 mm in the current study), and the function f can be determined using the apparent Preston tube correlation.

An extensive series of calibrations of Preston Probes in both favourable and adverse pressure gradients were carried out by Patel (1965). The established calibrations are typically expressed in terms of the parameters X^* and Y^*, which are given by:

$$X^* = \log_{10}\left(\frac{\Delta P d^2}{4\rho v^2}\right) \qquad \textit{Equation 4.8}$$

$$Y^* = \log_{10}\left(\frac{\tau_w d^2}{4\rho v^2}\right) \qquad \textit{Equation 4.9}$$

where X^* and Y^* for a zero pressure gradient are expressed as three parts: the viscous sublayer, the transition region, and the fully rough region (Chue 1975, Winter 1977):

$$\begin{aligned} &\text{for } 0 < Y^* < 1.5 && Y^* = 0.5X^* + 0.037\ ; \\ &\text{for } 1.5 < Y^* < 3.5 && Y^* = 0.8287 - 0.1381(X^*) + 0.1437(X^*)^2 \\ & && \quad - 0.0006(X^*)^3\ ; \\ &\text{for } 3.5 < Y^* < 5.3 && X^* = Y^* + 2\log(1.95Y^* + 4.10) \end{aligned} \qquad \textit{Equation 4.10}$$

The PP method was only applied to the non-fouled pipe, as the calibration data currently available is only valid when the Pitot probe is positioned perfectly parallel to the wall. Under fouled conditions the wall origin will be unknown and therefore, the current calibration data will be invalid.

It should be noted that all measurements determined using the PP Method were corrected for the effects of deflecting streamlines using the McKeon Method (as outlined in Section 3.3.2)

A summary of the results attained from the PP Method are given in Appendix B.2 in Table B.3 and are discussed in detail in Section 4.5.3.

4.5.2 Wall similarity methods

The length scale of the inner region of a turbulent boundary layer is typically taken as the viscous length (i.e. ν/u^*). Consequently, the velocity gradient in the viscous sublayer can be used to determined u^*. However, taking accurate measurements with a Pitot probe in what is a very thin layer is not an easy task, due mostly to the probe's size (Schultz and Flack 2005). To overcome this problem wall similarity methods are commonly used. Wall similarity methods are grouped into two categories, namely inner and outer similarity layer methods. The former refers to the techniques which only utilise data recorded within the inner region of the boundary layer, whereas, the latter refers to the techniques which utilise the data recorded for the whole boundary layer. Common inner layer similarity methods include the Clauser chart Method (Clauser 1954), the Bradshaw Method (Bradshaw 1959), the Log-Law Slope Method (Perry and Joubert 1964; Lewthwaire et al. 1985) and the Perry and Li's method (Perry and Li 1990). The most widely used outer layer similarity methods are based upon the work outlined by Hama (1954) and Cole (1956). These techniques have been comprehensively reviewed over the years with regards to the accuracy of their products. Most recently by Walker (2014), who compared the values of u^* determined from several wall similarity methods with those determined from independent approaches, including from direct numerical simulations (DNS), total stress, direct force and Preston probe measurements. The Bradshaw and Perry and Li inner similarity methods were found to have the lowest experimental uncertainties and produced values of u^* to within 0.001 m/s of the known DNS values. Moreover, the determined u^* values compared well with those determined from the Total Stress, Direct Force and PP Methods. However, the Bradshaw Method is only applicable to smooth boundaries and therefore, can be applied to most biofouled surfaces. Walker (2014) found that the outer similarity method proposed by Hama (1954) did not provide a good fit with the expected values, and as a result recommended that

it should not be used in evaluation of smooth and rough boundaries. For this reason, outer similarity methods have been disregarded within the current study.

As doubts have been raised over the validity of the frictional data derived from wall similarity techniques, several techniques were evaluated and critically assessed within the current study. Each of the techniques were assessed with regards to their accuracy, reliability and ability to produce realistic results. This was achieved by comparing the products of each wall similarity technique with those established from the system's PG and from PP measurements. The comparison with the PG frictional data will be of particular interest given that a pipe's frictional capacity can be accurately determined from the system's PG (Wei et al. 2005). The inner similarity methods evaluated within the current study included the Bradshaw (B), Log-Law Slope (LLS) and Perry and Li (PL) Methods. These methods were selected based on the recommendations outlined by Walker (2014), with the exception of the LLS Method, which was included due to its frequent use within biofouled investigations and despite, the high uncertainties associated with the method (Schultz 1998; Schultz and Swain 1999; Barton 2007).

The results attained from the aforementioned wall similarity methods are given in Appendix B.2 in Table B.4 and are discussed in detail in Section 4.5.3. The relevant theory for each of the wall similarity methods used within the current study is outlined herein.

4.5.2.1 Bradshaw Method

Clauser (1954) was the first to observe a similarity in the inner region of the boundary layer when scaled with u^*. Based upon these observations a graphical method of determining c_f was proposed, which was known as the Clauser Chart. Bradshaw (1959) later developed a more convenient form of the Cluaser Chart Method, which employed a predefined Log-Law reference curve. The Log-Law reference values of $y^+ = 100$ and $U^+ = 16.24$ ($\kappa = 0.41$ and $B = 5.0$) were used in the current study. When a Bradshaw reference curve is plotted with experimentally determined values of u/U against yU/ν, then the value of u/U at the intersection of the curves can be used to determine c_f, as given by:

$$c_f = 2\left(\frac{u^*}{U}\right)^2 = 2\left(\frac{u}{U}\right)^2 \Big/ \left(\frac{u}{u^*}\right)^2_{ref} \qquad \textit{Equation 4.11}$$

As doubts have been raised with regards to the effective wall location, a wall origin error was determined for all cases. A *Microsoft* spreadsheet was developed to automatically determine the intersection point and subsequent frictional parameters. The programme incrementally

changed the value ε (as outlined in Section 4.4.1), calculated the intersection point and determined u^*. The new value of u^* was then used to determine a new value of ε. In doing so, for each iteration the y^+ values were re-calculated and the appropriate Log-Law data re-determined and utilised. A typical example of a Bradshaw plot is presented in Appendix B.2 in Figure B.2.

4.5.2.2 Log-Law Slope Method

The Bradshaw Method can only be applied to smooth walls since the wall origin is generally unknown for rough walls, as discussed in Section 4.4.1. Consequently, the LLS Method was proposed by Lewthwaite et al. (1985), which like the Bradshaw Method is an adaptation of the Clauser Chart Method. In this method a linear regression line is fitted to experimentally determined values of u/U against $\ln(yU/\nu)$. The slope of the regression line can be used to establish c_f and u^* using Equation 4.12 and Equation 4.13, respectively. As the slope of the regression line is not affected by surface roughness, the LLS Method is valid for both smooth and rough surfaces provided ε is taken into account, within the latter.

$$c_f = 2\kappa\left(\frac{d(u/U)}{d(\ln(yU/\upsilon))}\right)^2 \qquad \textit{Equation 4.12}$$

$$u^* = \frac{U}{\sqrt{2/c_f}} \qquad \textit{Equation 4.13}$$

Naturally, only data within the Log-Law region is used to determine c_f from Equation 4.12. Consequently, the Log-Law region needs to be defined first. However, this is no easy task when u^* is not initially known. To overcome this problem several inner and outer cut-off limits have been presented within the literature (Barton 2006, Lewthwaite et al. 1985, Schultz 1998). Typically, the inner cut-off is taken as $y = \alpha\nu/U$ (where α, is an inner cut off constant, taken as 1.5 (Lewthwaite et al. 1985)). The outer cut-off limit is generally taken as y = 0.1-0.2 δ (Lewthwaite et al. 1985; Schultz 1998; Barton 2007). Barton (2006) adjusted the outer cut-off limit iteratively, depending on the fit of the experimental data. This approach was also used within the current study.

A *Microsoft Excel* Spreadsheet was developed to establish ε, c_f and u^* simultaneously. The Log-Law slope Method is basically an iterative technique that determines ε and c_f by forcing a Log-Law slope over a selected region of experimental data. Consequently, the spreadsheet worked by incrementally adjusting ε, (as outlined in Section 5.3.1) and then re-calculating

the boundary layer parameters of δ and y^+ required to establish new inner and outer cut-off limits. The value of c_f was then determined using Equation 4.12. For each new iteration of ε the inner and outer cut off constants were manually reviewed with respect to the new values of y^+. This ensured only the appropriate Log-Law data was used in the determination of c_f and u^*. Based on this approach the inner cut-off constants and outer cut-off limits used within the current study are presented in Figure 4.15, which illustrates the respective variables were a function of Re_D. The derived limits can be considered more applicable for pipe flow than the previously documented within the literature, which typically relate to channel flow conditions.

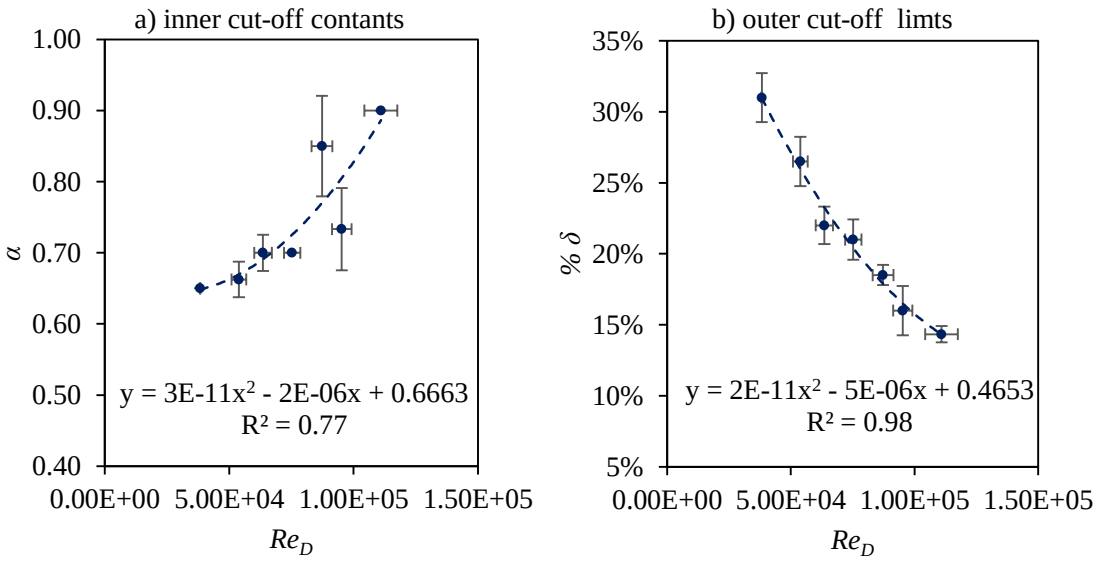

Figure 4.15 a) inner cut constants and b) outer cut off limits used within the LLS Method.

4.5.2.3 Perry and Li Method

Perry and Li (1990) proposed a method to estimate ε and u^* simultaneously using experimental data rerorded in the inner region of the boundary layer. The relationship suggested by Perry and Li of the mean-velocity in the Log-Law region is given by:

$$\frac{u}{U} = 1 + \frac{1}{\kappa}\frac{u^*}{U}\ln\left(\frac{y}{\delta^*}\right) + \frac{1}{\kappa}\frac{u^*}{U}\ln\left(\frac{y}{U}\right) + 0.493\frac{u^*}{U} \qquad \textit{Equation 4.14}$$

Equation 4.14 is valid when $\kappa = 0.42$ and $\Pi = 0.55$. Using the velocity defect law and Coles (1956) solutions for δ, $w(1)$ and $w(y/\delta)$, Perry and Li's (1990) derived Equation 4.15 and Equation 4.16, which are valid for both rough and smooth walls.

$$\frac{U-u}{u^*} = -\frac{1}{\kappa}\ln\left(\frac{y+\epsilon}{\delta}\right) + \frac{\Pi}{\kappa}\left[w(1) - w\left(\frac{y+\epsilon}{\delta}\right)\right] \qquad \textit{Equation 4.15}$$

$$\frac{u}{U} = 1 + \frac{1}{\kappa}\frac{u^*}{U}\ln\left(\frac{y+\epsilon}{\delta^*}\right) + \frac{1}{\kappa}\frac{u^*}{U}\ln\left(\frac{u^*}{U}\right) + \frac{1}{\kappa}\frac{u^*}{U}\ln\left(\frac{1+\Pi}{\kappa}\right) - \frac{u^*}{U}\frac{2\Pi}{\kappa} \qquad \textit{Equation 4.16}$$

A *Microsoft Excel* spreadsheet was developed to solve for ε and u^*. This was achieved by iteratively adjusting ε, as outlined in Section 4.4.1, in order to determine u^*. For each new value of ε, experimentally determined values of u/U were plotted against theoretical values of u/U determined using Equation 4.16. A linear regression line of best fit was attached to the data and the y intercept determined. Only the data within the Log-Law region was used, which was defined as $y/\delta^* < 0.9$ (Andrewartha 2010). The value of u^* was iteratively adjusted until the y intercept was equal to 0. The new value of u^* was then used to re-calculate ε. This iterative process of adjusting one parameter with the other was continued until the respective convergence criteria for u^* and ε were reached, which typically took 3-4 increments. The initial u^* used for the first increment of ε, was determined from the ssytem's PG using the SFM. Figure 4.16 illustrates a typical u/U against y/δ^* plot for the final iteration of the Perry and Li Method (for $Re_D = 1.13\text{x}10^5$).

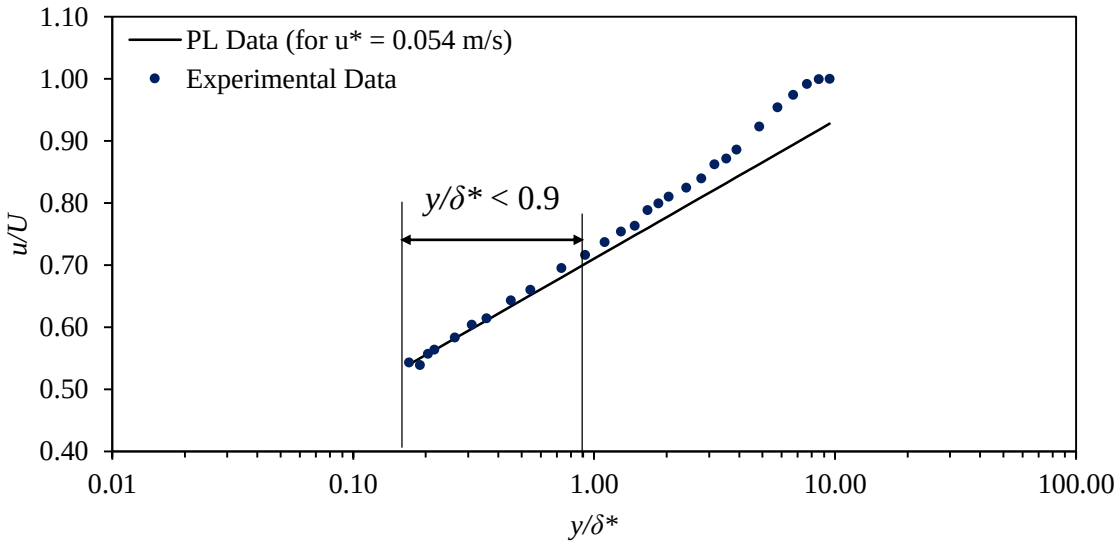

Figure 4.16 A typical u/U against y/δ plot for the final iteration of the PL method (for Re_D = 1.13x10^5).*

4.5.3 Evaluations of wall similarity methods

The wall similarity methods of PP, B, LLS and PL as outlined within Section 4.5 are evaluated and compared within this section. The wall similarity techniques were applied to the velocity profiles recorded over the range of $3.83x10^4 < Re_D < 1.13x10^5$. Table 4.2 presents the uncertainty estimates to a 95% confidence interval for each of the frictional parameters estimated from each of the techniques. In particular, the average and worst case uncertainties for each of the methods are presented within Table 4.2. The uncertainties established for the B and PL Methods compared well with the literature (Schultz and Swain 1999, Schultz 1999). For instance, Schultz (1999) reported an uncertainty in values of c_f derived from the PL Method of ±10%. The equivalent uncertainty reported within the current study was ±11%. The uncertainties listed within Table 4.2 for the LLS Method were slightly higher than those quoted by Schultz and Swain (1999), who documented an average uncertainty in c_f of ±7%. The equivalent uncertainty quoted within the current study was ±15%. The uncertainties quoted by Schultz (1999) and Schultz and Swain (1999) were determined to a 95% confidence interval from 10 repeatability tests. Whereas, within the current study on average only three repeats were conducted for each Re_D survey. Nevertheless, the established uncertainties quoted within Table 4.2 are in reasonable agreement with those quoted within the literature, especially for the B and PL Methods, despite, the reduced number of repeats.

Table 4.3 Uncertainty Estimates of the PP, B, LLS and PL Methods.

Method	u^*		c_f		τ_w	
	Av	**Max**	**Av**	**Max**	**Av**	**Max**
PP	±7%	±11%	±6%	±7%	±14%	±21%
B	±8%	±14%	±7%	±12%	±16%	±26%
LLS	±8%	±14%	±15%	±20%	±16%	±29%
PL	±4%	±7%	±11%	±15%	±8%	±15%

Dimensionless mean-velocity profiles are presented in Figure 4.17 to Figure 4.20. The mean-velocity profiles presented in Figure 4.17 to Figure 4.20 were normalised by the independent u^* values determined by the respective wall similarity methods. The skin friction coefficients determined from the respective methods are compared to the equivalent values the established from the system's PG in Figure 4.21 and Figure 4.22. It is evident from Figure 4.17 to Figure 4.20 that the B and PL Methods were the best performing of the respective wall similarity methods, as they consistently collapsed the mean-velocity profiles onto expected smooth pipe

Log-Law (i.e. Equation 2.21). Furthermore, it is evident from Figure 4.21 and Figure 4.22 that the values of c_f determined from the B, PL and PG Methods are in agreement, within the experimental uncertainties. The maximum discrepancy between the values of c_f determined from the PL and PG Methods was found to be ±6%. The PL and B Methods were also found to have the lowest experimental uncertainties of the respective methods, with the former having the lower of the two. Consequently, the current study supports the findings of Walker (2014) with regards to the strong performance of the B and PL Methods for establishing the frictional resistance of a surface. However, unlike Walker (2014) this was illustrated within the current study by comparisons with frictional data attained from the system's PG, which for pipe flow is highly accurate.

The PP Method significantly overestimated the frictional data, when compared against the equivalent PG data. For instance, values of c_f determined using the PP Method were found to be on average 21% higher than the equivalent values determined from the PG Methods, as shown by Figure 4.22. The evident downward shift in the respective mean-velocity profiles relative to the Log-Law, shown in Figure 4.17 further illustrates the overestimated nature of the PP data. It is suggested that the overestimated frictional data was caused by the PP Method itself, as opposed to physical differences in the local and global conditions. This is because the surface of the pipe was considered to have a homogeneous roughness distribution, which is illustrated by the agreement of the local frictional data, estimated from the other wall similarity methods with the global PG data. The frictional data derived from the PP Method is reliant on a single velocity measurement taken at the wall. If the probe is not positioned perfectly parallel to the wall then the frictional data determined from the available calibration data would not be representative of the actual conditions. It was suggested that the the probe was typically located slightly above the wall, as illustrated by the effective wall locations presented within Figure 4.13. The overestimated nature of the PP data could have been attributed to the probe's location above the wall, given that, in the near wall region freestream velocity increase significantly in the wall-normal direction due to reduced viscous effects. The relatively low uncertainties associated with PP Method would also suggest the overestimation was due to the probe location and not procedural error.

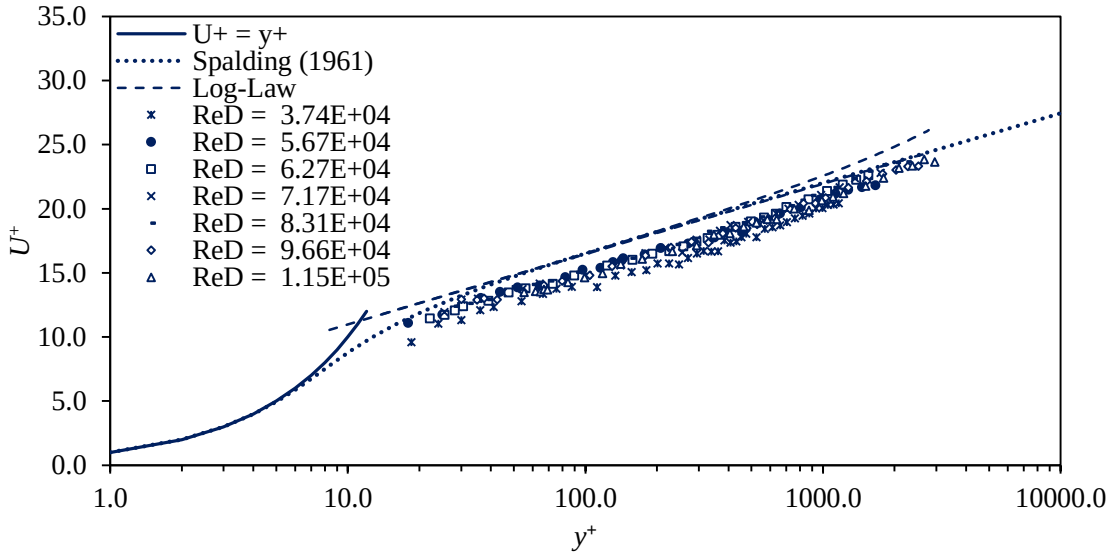

Figure 4.17 Normalised mean-velocity profiles derived using the PP Method (for the range of 3.74 x 10^4 < Re_D < 1.15 x 10^5).

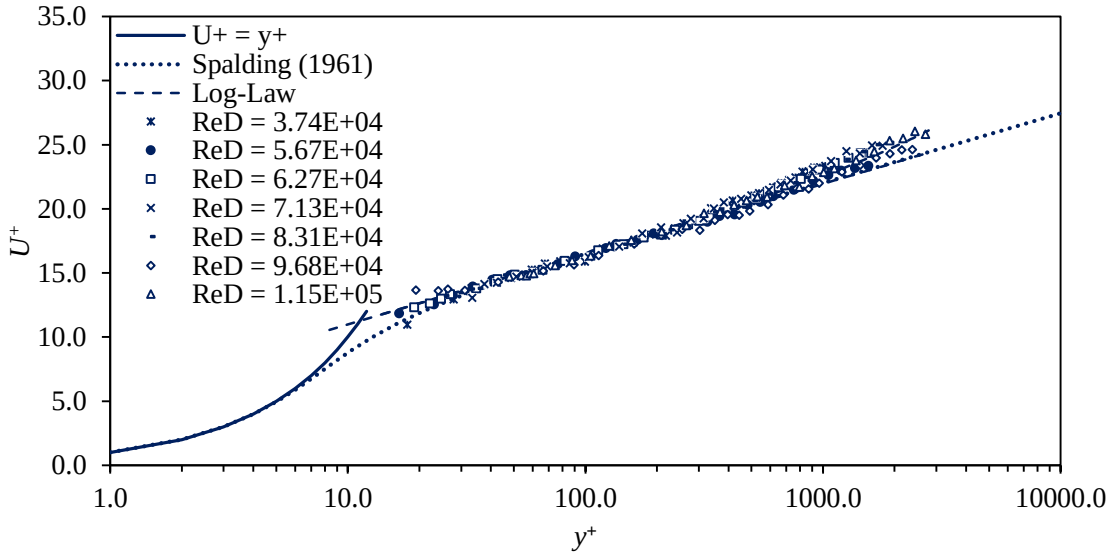

Figure 4.18 Normalised mean-velocity profiles derived using the B Method (for the range of 3.74 x 10^4 < Re_D < 1.15 x 10^5).

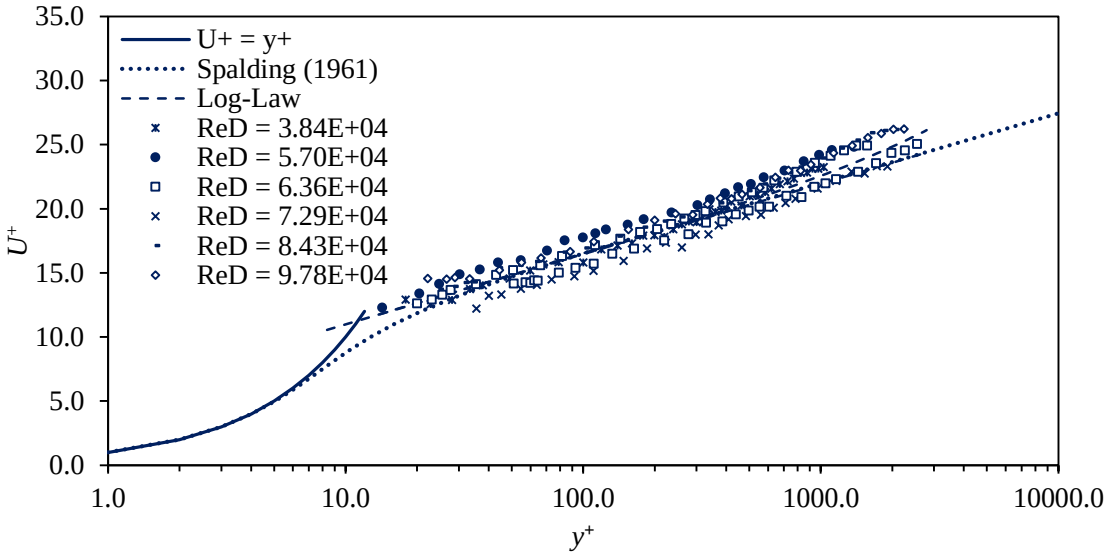

Figure 4.19 Normalised mean-velocity profiles derived using the LLS Method (for the range of 3.84 x 10^4 < Re_D < 1.04 x 10^5).

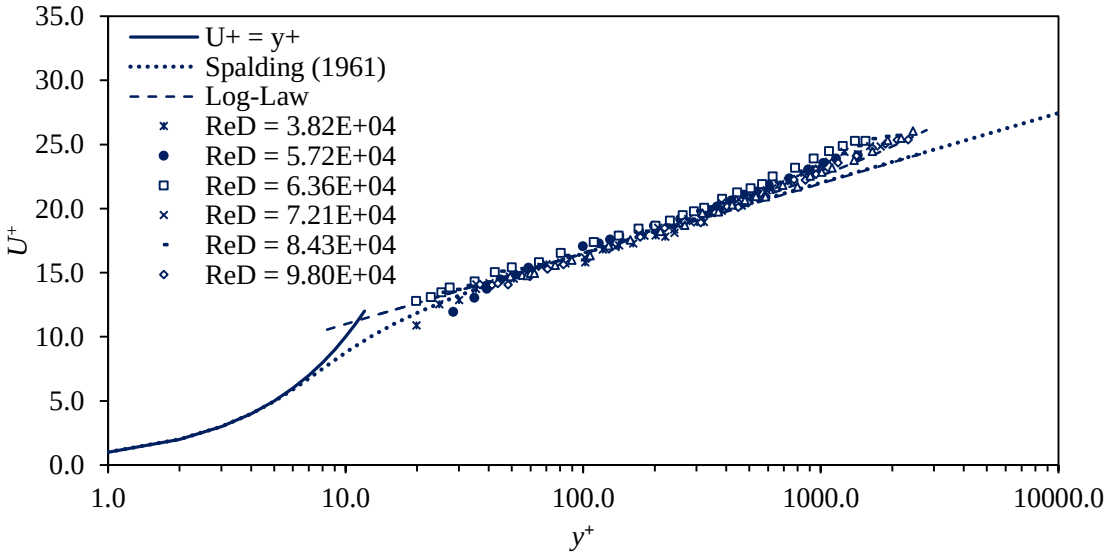

Figure 4.20 Normalised mean-velocity profiles derived using the PL Method (for the range of 3.82 x 10^4 < Re_D < 1.17 x 10^5).

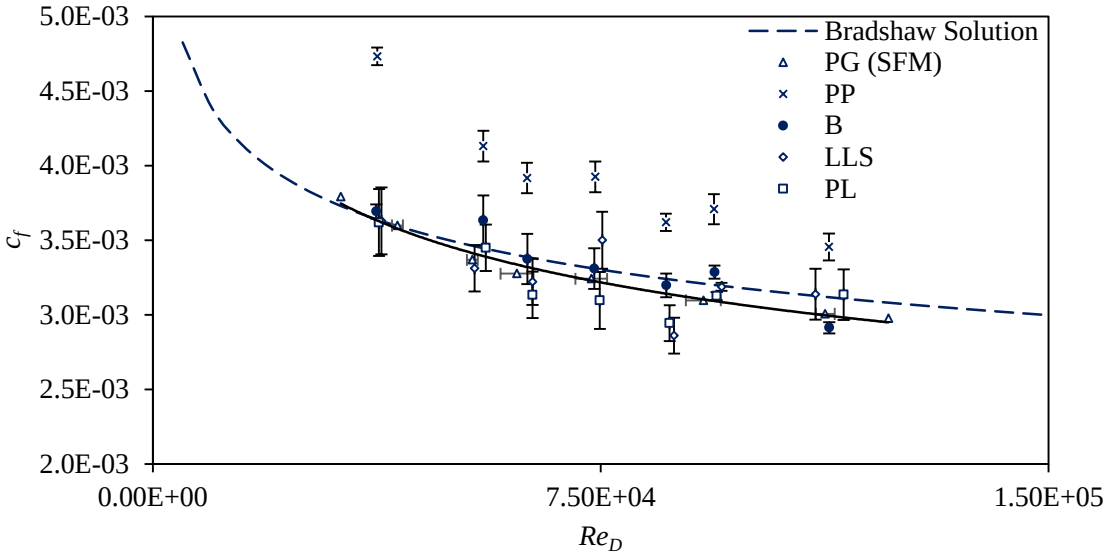

Figure 4.21 Local c_f determined using the PP, B, PL, LLS) and PG Methods.

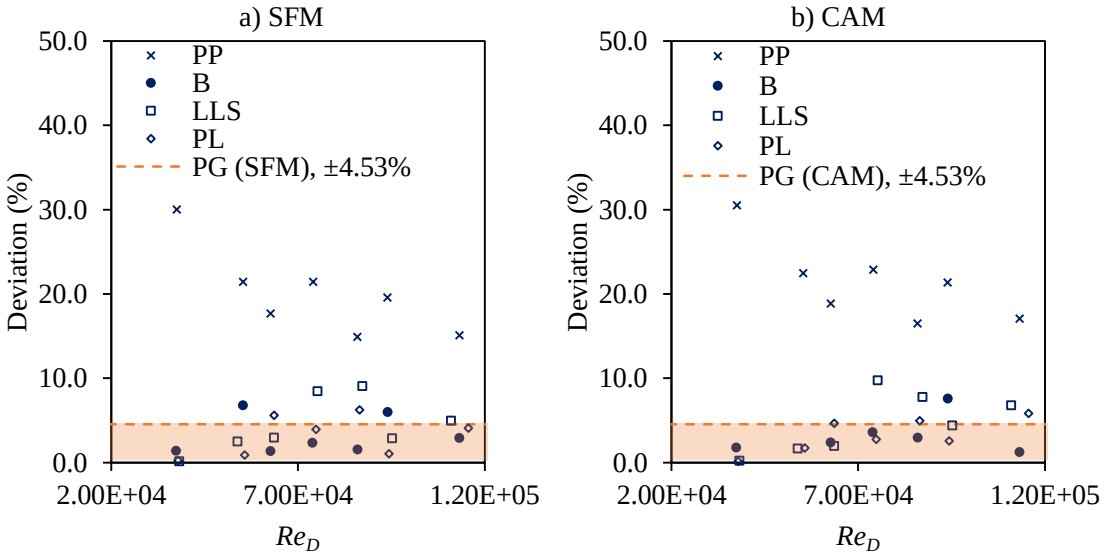

Figure 4.22 Percentage deviation in c_f determined form the PP, B, PL, and LLS Methods relative to the c_f determined using the PG Methods of a) SFM and b) CAM. The average experimental uncertainty in c_f values determined from the SFM and CAM was ±4.53%.

The LLS Method performed better than the PP Method in terms of its capacity to collapse the mean-velocity data onto the Log-Law (see Figure 4.19). However, the frictional data determined from the LLS Method had the highest uncertainty of the respective wall similarity methods. Similar findings, with regards to the LLS Method have been reported in the literature (Perry and Joubert 1964; Schultz and Swain 1999; Andrewartha 2010; Walker 2014). The LLS Method is widely considered to be insensitive and unreliable, since many combinations of ε, u^* and c_f can give equally good fits to experimental data (Perry and Joubert 1964). Due to its high associated uncertainties, the LLS Method was not applied within the biofouled phases of the current study. Furthermore, as the B Method is not applicable to rough surfaces only the PL Method can apply to biofouled surface, in order to estimated their local frictional conditions to a reasonable degree of certainty.

4.6 Determining κ for a smooth pipe

The validity of a universal von Kármán constant within the classical theory has been questioned in recent years (Zanoun et al. 2003; Wei et al. 2005; Nagib and Chauhan 2008). It has been suggested that κ along with the other Log-Law constants of C, C', B and B' could in fact be dependent on the flow conditions under consideration (Nagib and Chauhan 2008). For instance, in turbulent boundary layers Österlund et al. (2000) reported that $\kappa = 0.384$, $C = 4.17$ and $C' = 3.6$, while measurements in open channels indicated that $\kappa = 0.37$ and $C = 3.7$ (Zanoun et al. 2003). McKeon et al. (2004b) found that for pipe flow and at high Re_D $\kappa = 0.421$ whereas, at low Re_D Monty (2005) found that $\kappa = 0.386$. However, the vast majority of the aforementioned values were derived from regression fits to the Log-Law or its derivatives, which could have led to bias errors, particularly as the upper and lower limits of the Log-Law region are still under debate (Smits et al 2011; Bailey et al. 2014). Consequently, the exact location of the Log-Law needs to be defined before the determination of any constants. However, this is no easy task, particularly if u^* is unknown.

If for argument's sake κ was not non-universal and equal to 0.42 then the implications could be significant. The traditional C-W equation has a natural reliance on κ (Matthews 1990) and as a result, changes in κ will ultimately affect values of k_s derived from it. Furthermore, changes in κ will ultimately impact on the effectiveness of traditional wall similarity techniques, due to their inherent reliance on the classical theory and in particular, the Log-Law (in which $\kappa \approx 0.42$). For instance, if κ was not equal to 0.42 then the frictional data determined from a wall similarity, such as PL Method not be an accurate representation of the actual conditions. As the data will have been artificially collapsed onto a Log-Law relationship derived by inappropriate constants, which illustrated by Wei et al. (2005).

A partial sensitivity analysis was undertaken within the current study to illustrate the influence of κ on values of u^* and ε determined using the PL Method. Three different Re_D were assessed, including $Re_D = 6.36x10^4$, $Re_D = 8.88x10^4$ and $Re_D = 1.18x10^5$. The von Kármán constant was taken as 0.35, 0.40 and 0.45 and C constant was taken as 5.5. Table 4.4 and Figure 4.23 and present the results of the analysis.

Table 4.4 Impact of κ on determined values of u^* and ε using the PL Method

κ	Re_D	u^*(m/s)	ε (mm)
0.35	$6.36x10^4$	0.026	0.75
0.40		0.030	0.66
0.45		0.032	0.57
0.35	$8.88x10^4$	0.035	0.85
0.40		0.039	0.68
0.45		0.045	0.82
0.35	$1.17x10^5$	0.048	1.23
0.40		0.052	0.91
0.45		0.057	0.87

The values of u^* determined for the lowest values of κ assessed, i.e. $\kappa = 0.35$ were typically 12% lower than the equivalent values determined for $\kappa = 0.40$. The values of u^* determined for $\kappa = 0.45$ were typically 9% higher than the equivalent values determined for $\kappa = 0.40$. The established wall origin errors determined for $\kappa = 0.35$ and 0.45 were also typically over- and under-estimated, respectively when compared to the equivalent values determined for $\kappa = 0.40$.

Within the aforementioned situations, where the universality of the Log-Law constants has been questioned all relate to conventional engineered surfaces and systems. Non-conventional boundaries, such as biofouled surfaces add an additional layer of complexity into the debate. It has been suggested that the von Kármán constant for biofouled surfaces is non-universal and fact dependent on Re_D (Lambert 2009; Perkins 2013; 2014). Therefore, it was important to verify κ under non-fouled conditions in order to ensure the validity of the values determined under fouled conditions. This evaluation would also contribute to the ongoing dabate on the universality of κ within the classical theory.

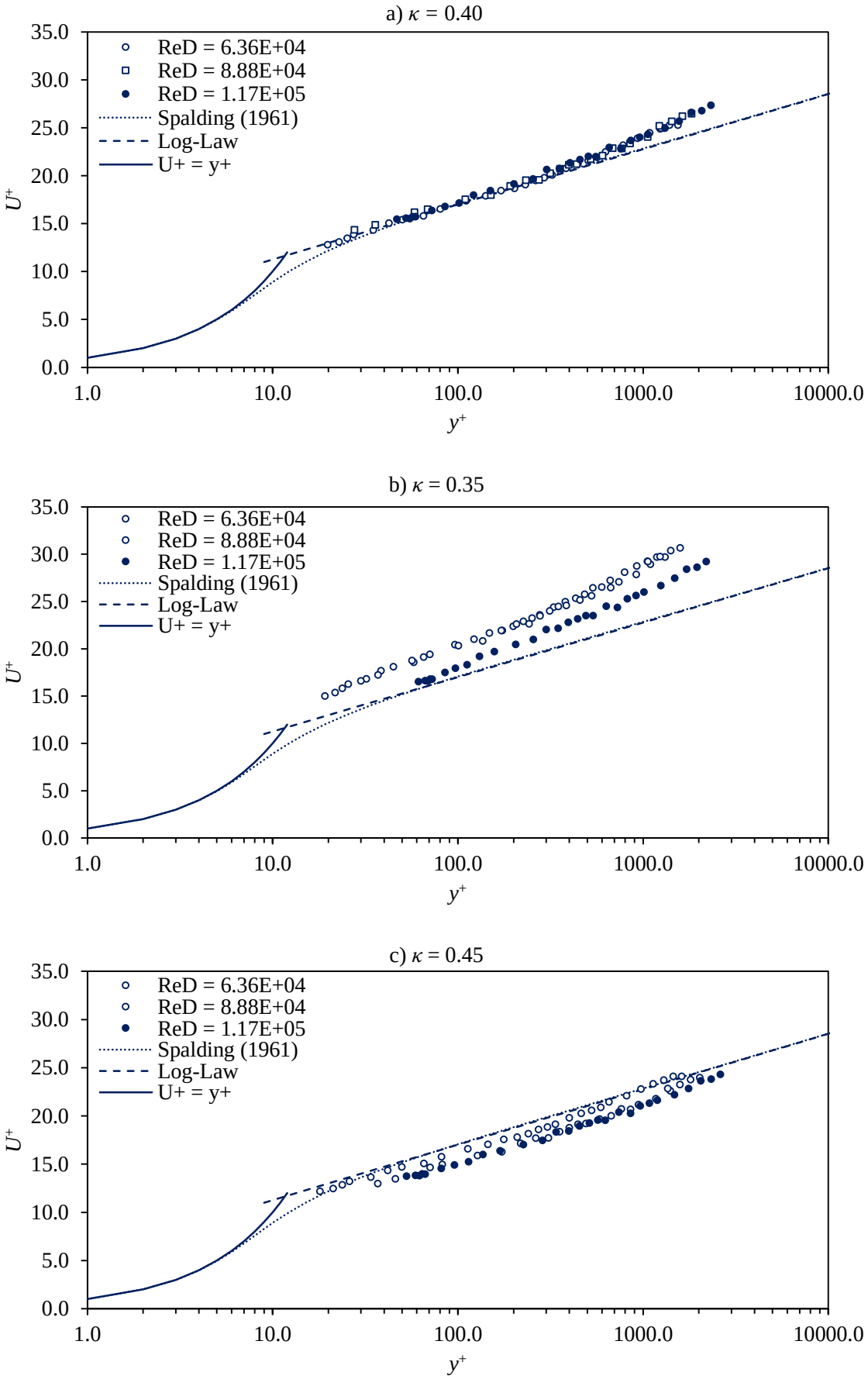

Figure 4.23 Impact of a) κ = 0.40, b) κ = 0.35 and c) κ = 0.45 on determined values of u and ε using the PL Method (for the range of 6.36 x 10^4 < Re_D < 1.17 x 10^5).*

Several methods were used to establish appropriate values of κ and C for the non-fouled within the current study, as discussed herein.

The von Kármán and C constants can be determined from c_f and the boundary layer momentum thickness Reynolds number, Re_θ by fitting experimental data to a variant of the logarithmic skin friction law, as given by (Österlund et al. 2000):

$$c_f = 2\left[\frac{1}{\kappa}\ln(Re_\theta) + C\right]^{-2} \qquad \textit{Equation 4.17}$$

The values of c_f used in this determination method were established from the system's PG and were therefore, independent from the mean-velocity profile data. As a result, this approach was unaffected by potential errors associated with ill-defined Log-Law region limits. The value of κ and C determined from this approach were 0.41 and 4.97, respectively, as shown by Figure 4.24 and Figure 4.25. Figure 4.24 presents how the respective constants were derived from the regression line of best fit. Figure 4.25 illustrates the experimentally determined values of c_f along with equivalent values calculated from Equation 4.17 (where κ = 0.41 and C = 4.97). As expected, the values of c_f derived from Equation 4.17 correlate well with those determined from the PG Methods. This method is only valid for hydraulically smooth flow conditions and as a result, it cannot be applied to transitionally rough and fully rough boundaries, such as those associated with biofouled surfaces.

A more universally applicable approach is to establish κ from the slope of a normalised mean-velocity profile, as given by;

$$\Xi = y^+\frac{d(U^+)}{d(y^+)} \qquad \textit{Equation 4.18}$$

where Ξ is typically referred to as the von Kármán diagnostic function.

In the Log-Law region of the boundary layer Ξ is constant and equal to $1/\kappa$. Therefore, the existence and location for the Log-Law region can also be determined from this approach. The values of Ξ were calculated from the mean-velocity profiles recorded for the range of $5.23\text{x}10^4 < Re_D < 1.13\text{ x}10^5$. These profiles were normalised using the values of u^* determined from the PG, B, and PP Methods. Appropriate values of ε were established using the respective values of u^* and the PJ Correction Method. Figure 4.26 and Figure 4.27 present the values of Ξ determined using the respective u^* data.

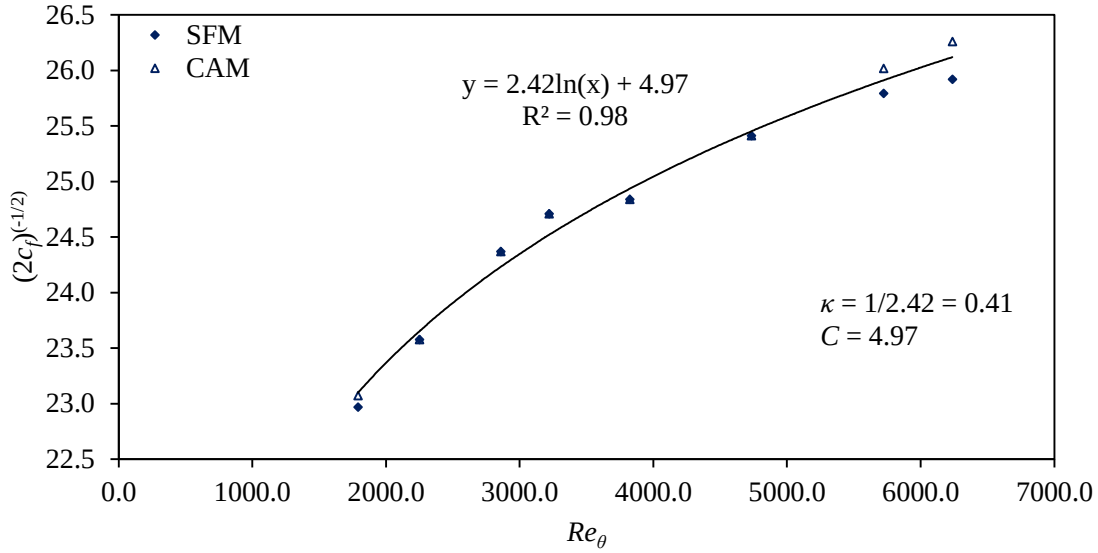

Figure 4.24 Deriving κ and C from c_f.

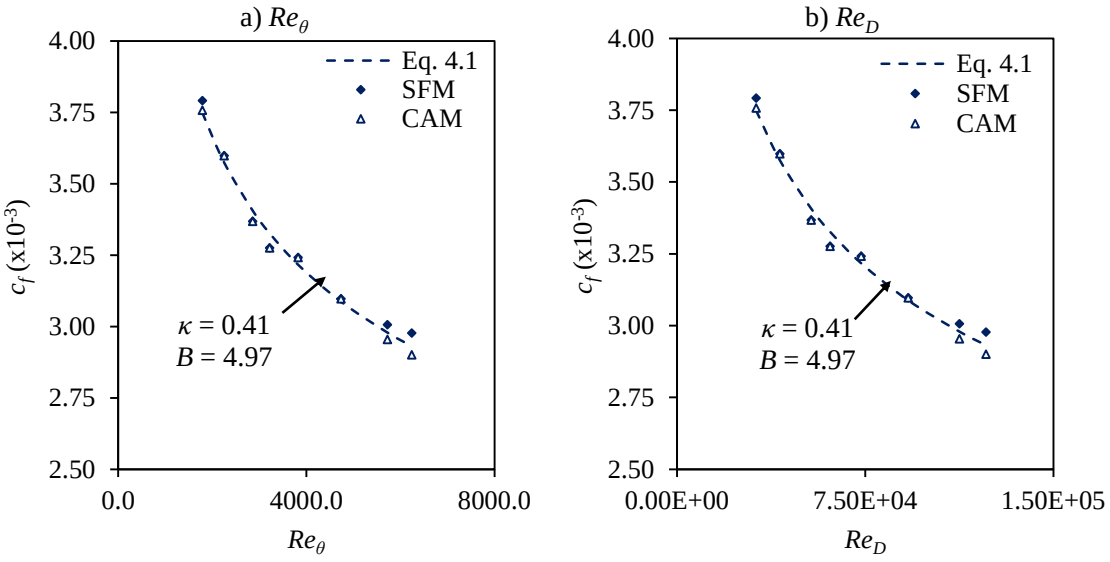

Figure 4.25 Values of c_f against a) Re_θ and b) Re_D.

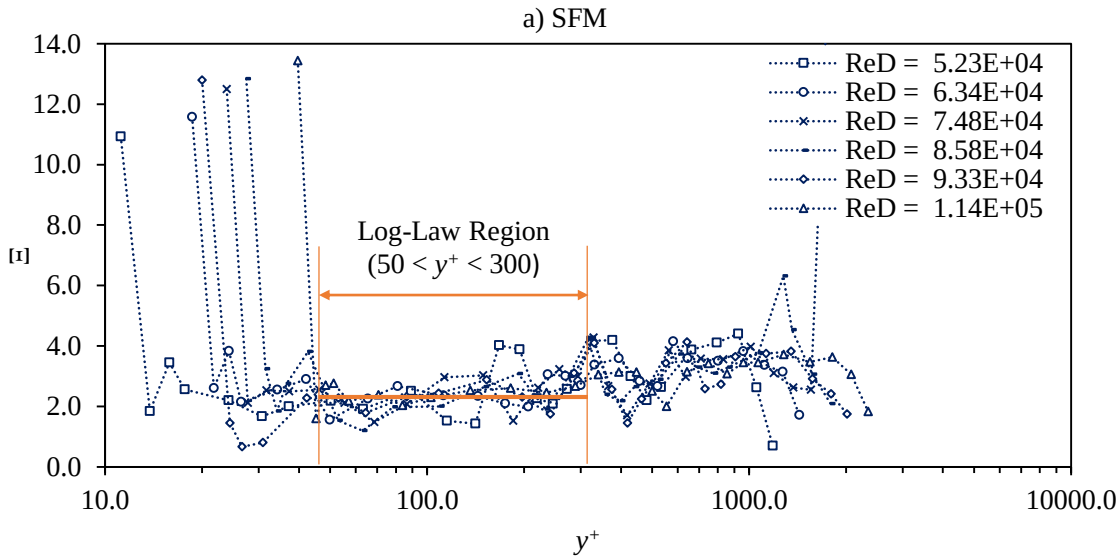

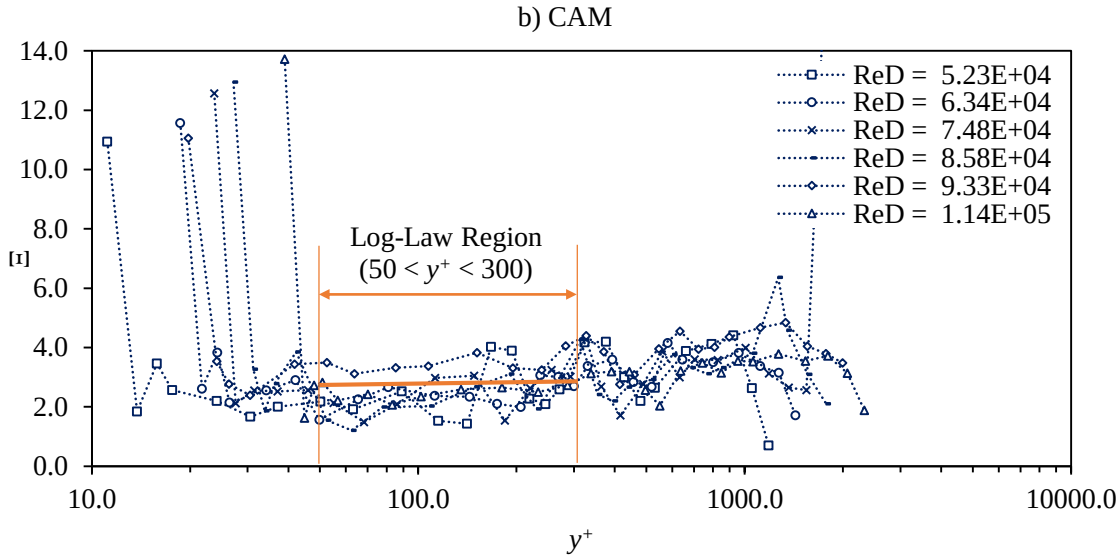

Figure 4.26 Ξ against y^+ for the a) SFM and b) CAM (i.e. PG) data (for the range of 5.23 x 10^4 < Re_D < 1.14 x 10^5).

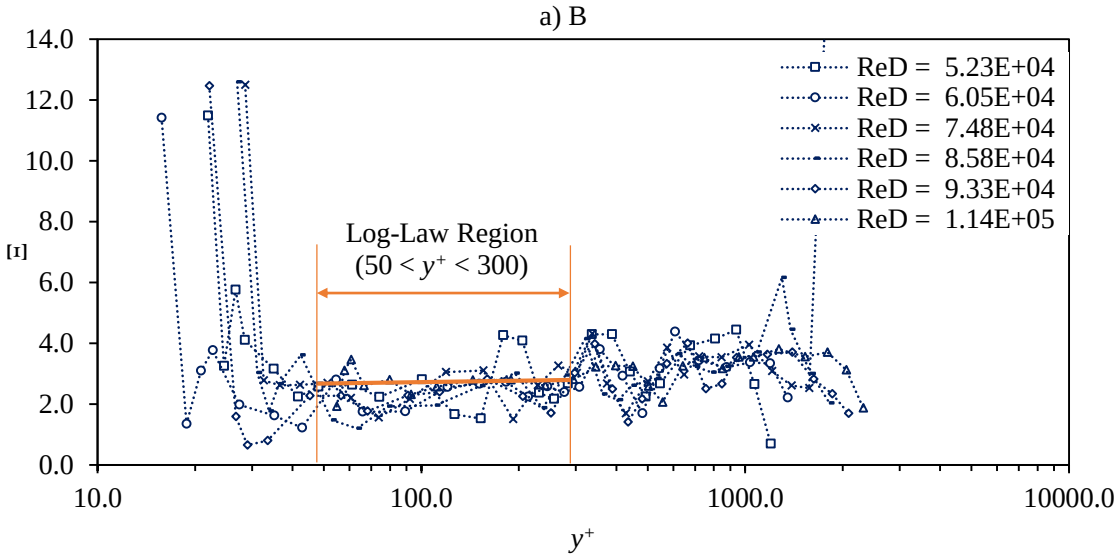

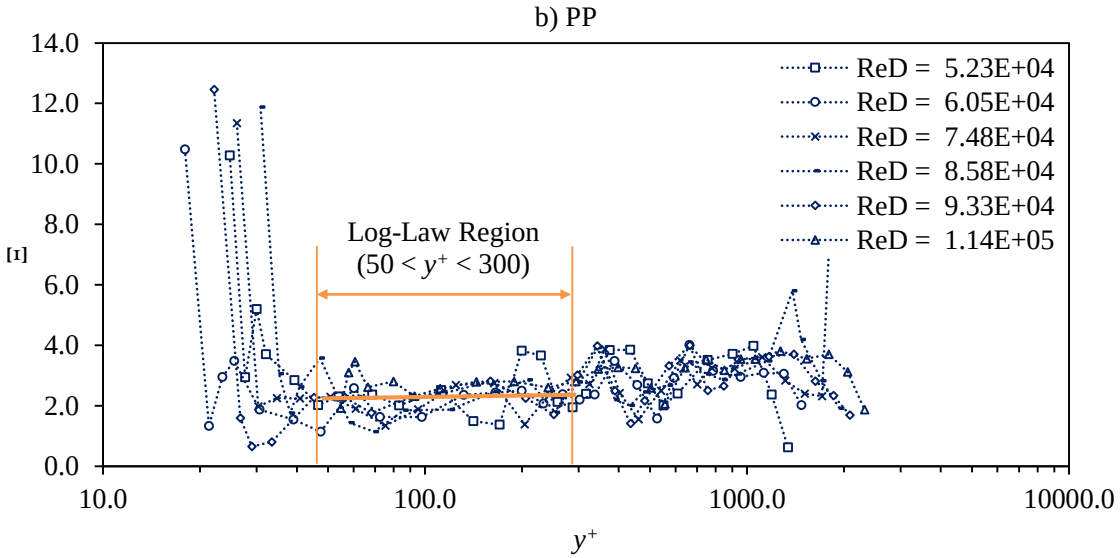

Figure 4.27 Ξ against y^+ for the a) B and b) PP data (for the range of 5.23 x 10^4 < Re_D < 1.14 x 10^5).

A region were Ξ remains reasonably constant is evident in both Figure 4.26 and Figure 4.27, which supports the existence of a Log-Law region. A summary of the average values of κ determined from respective mean-velocity and frictional data using the Ξ approach is presented in Table 4.5. The combined average value of κ (i.e. the average of the averages) determined from the Ξ approach was 0.43 ± 0.02.

The empirical *C* constant can be established using the diagnostic function of ψ, as given by:

$$\psi = U^+ - \frac{1}{\kappa}\ln(y^+) \qquad \textit{Equation 4.19}$$

The ψ parameter remains constant in the region governed by the Log-Law. Values of ψ were calculated using the same mean-velocity and u^* data applied within the Ξ approach. Figure 4.28 and Figure 4.29 present the values of ψ determined using the respective mean-velocity and u^* data. Figure 4.28 and Figure 4.29 further support the existence of a Log-Law region, as a region were ψ remains constant is evident in both figures. A summary of values of *C* determine from respective mean-velocity and frictional data using the ψ approach is presented in Table 4.5. The combined average value of *C* determined from the ψ approach was 5.00 ± 0.22.

Based on the Ξ and ψ dataset, the location of the Log-Law region within the boundary layer was found to be $50 < y^+ < 300$ or $50 < y^+ < 0.2R^+$. This location was approximately where standard convention states it should be for turbulent flow in pipes, i.e. $30\text{-}50 < y^+ < 0.1\text{-}0.2R^+$ (George 2007). It can be concluded that the Log-Law region does exist, and that the Log-Law, along with its derivatives provides a good representation of the mean-velocity profile within a pipe, especially for the range of $5.23\text{x}10^4 < Re_D < 1.13\text{x}10^5$. Consequently, the current study is in agreement with Österlund et al. (2000), Saleh (2005) and Zanoun et al. (2003; 2007). However, it should be stated that the mean-velocity profiles recorded within the current study have not been evaluated with respect to the power law relationship criteria.

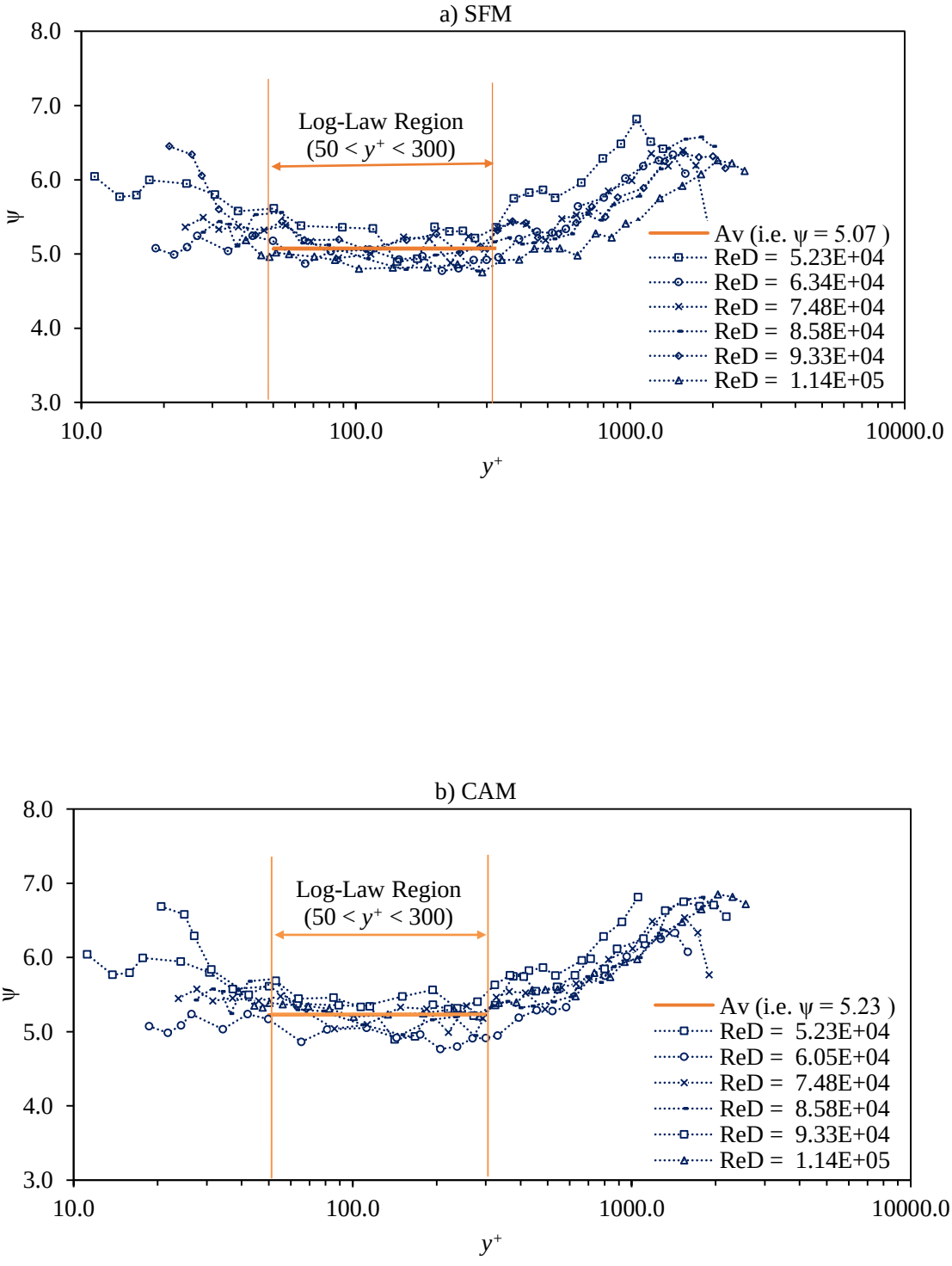

Figure 4.28 ψ against y^+ for the a) SFM and b) CAM (i.e. PG) data (for the range of 5.23 x 10^4 < Re_D < 1.14 x 10^5).

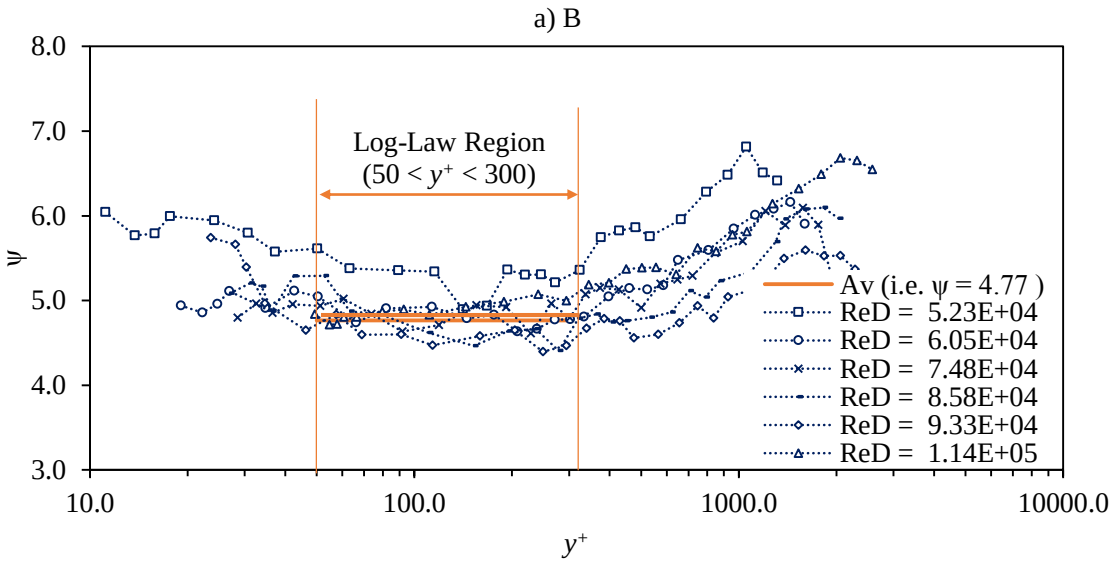

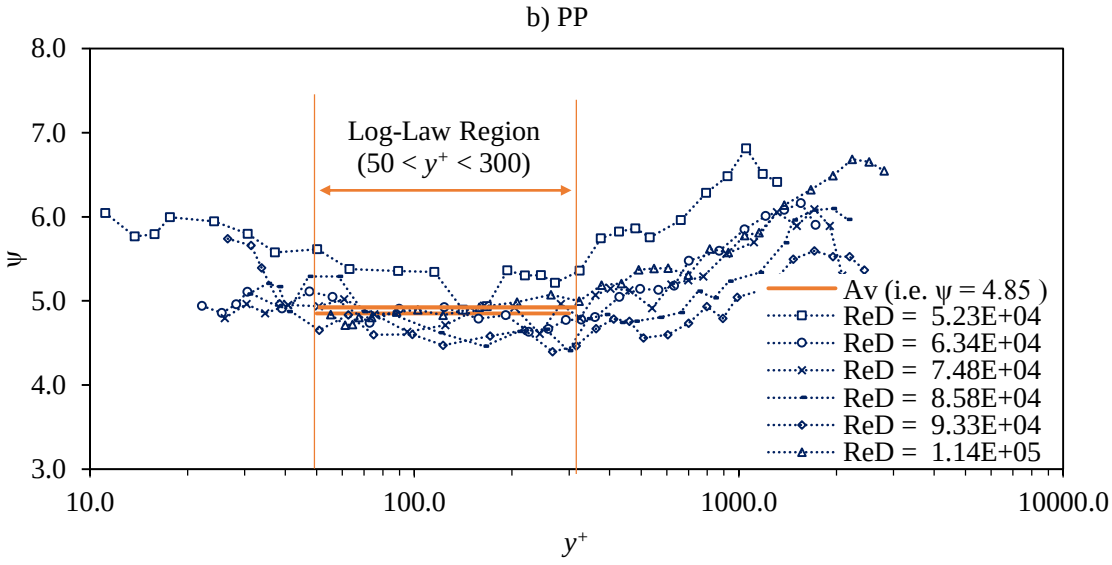

Figure 4.29 ψ against y^+ for the a) B and b) PP data (for the range of 5.23 x 10^4 < Re_D < 1.14 x 10^5).

The average value of the Log-Law constants determined from the Ξ and ψ approaches of κ = 0.43 ± 0.05 and C = 5.00 ± 0.22 are in good agreement with that outlined within the literature for turbulent flow in pipes (McKeon et al. 2004b; George 2007). However, the uncertainties associated with the respective constants were found to be significantly higher than those presented within the literature, especially by McKeon et al. (2004b). For instance, the average uncertainties in κ and C found within the current study were ±12% and ±4%, respectively. Whereas, McKeon et al. (2004b) reported uncertainties in κ and C of ±0.48% and ±1.5%, respectively. The high uncertainties documented within the current study were attributed to the significant emphasis that the Ξ and ψ approaches placed on discrete mean-velocity values. To improve the averages and uncertainties in the respective constants a linear regression approach was utilised; whereby, a linear regression line of best fit was fitted to the normalised mean-velocity profiles within the Log-Law region (i.e. $50 < y^+ < 0.2R^+$). The inverse of the slope of the regression line was equal to κ (i.e. $\kappa = 1/[d(U^+)/d(\ln y^+)]$. Moreover, the y axis intercept of the regression line was equal to C. The values of u^* and ε determined from the PG, B and PP Methods were used to normalise and offset the respective mean-velocity profiles, within this approach. Table 4.5 and Figure 4.30, Figure 4.31 summarise values of κ and C determine from the linear regression approach.

Table 4.5 Values of κ and C determined from non-fouled pipe determined using the linear regression, Ξ and ψ approaches.

Method	Ξ and ψ approaches		linear regression approach	
	κ	C	κ	C
PG (SFM)	0.44 ± 0.03	5.06 ± 0.13	0.42 ± 0.01	5.77 ± 0.32
PG (CAM)	0.43 ± 0.08	5.22 ± 0.20	0.42 ± 0.01	5.86 ± 0.39
B	0.42 ± 0.04	4.85 ± 0.12	0.41 ± 0.02	5.12 ± 0.55
PP	0.44 ± 0.05	4.85 ± 0.20	0.44 ± 0.02	4.49 ± 0.55

It is evident from Figure 4.30, Figure 4.31 and Table 4.5 that the established values of κ and C are within the bounds suggested by Reynolds (1974) and independent of Re_D. Moreover, the values of the respective Log-Law constants established from each of the different frictional datasets, with the exception of those determine from the PP dataset are reasonably consistent. The disparity in the values determined from the PP data was attributed to the overestimated nature of the respective data, as outlined in Section 4.5.3.

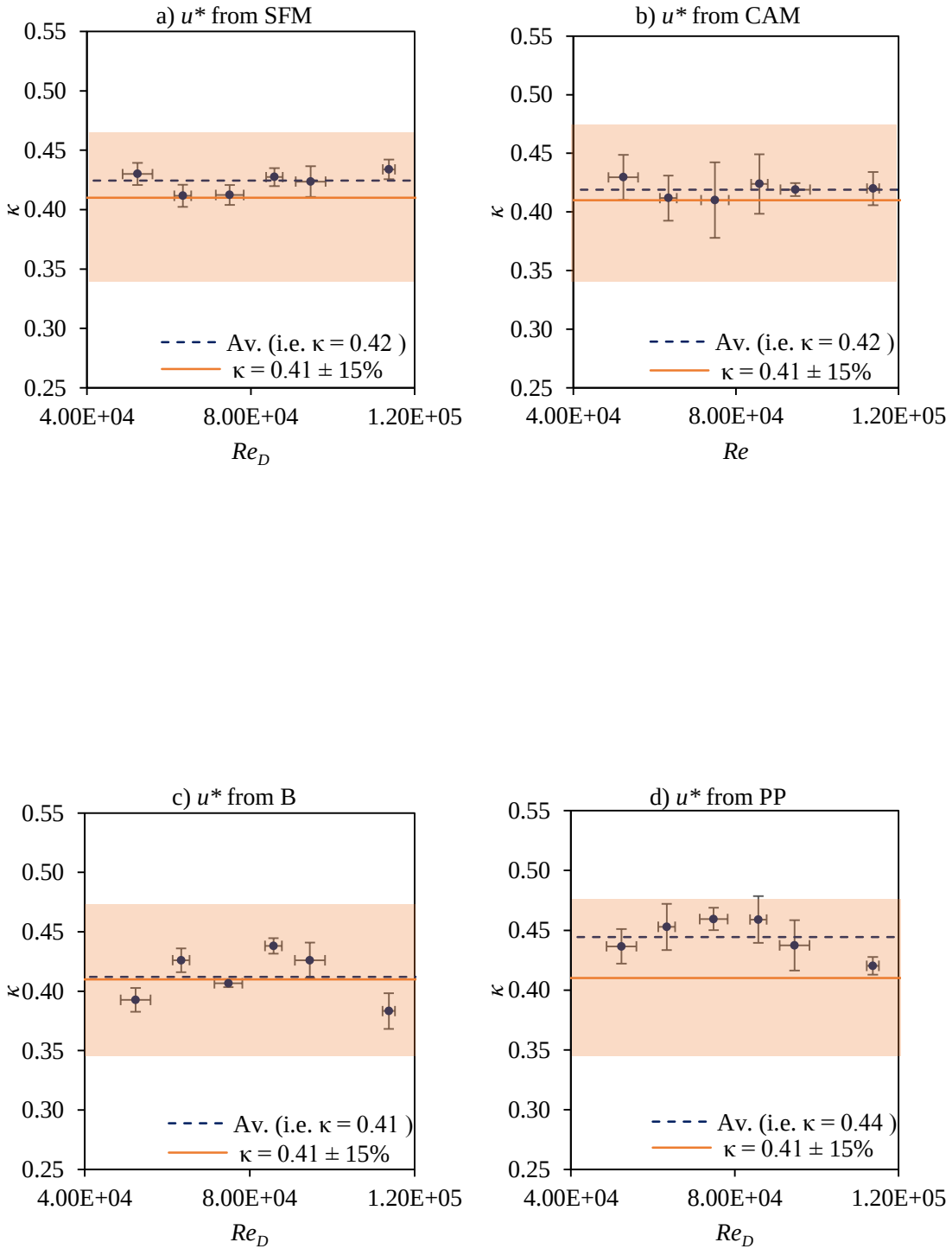

Figure 4.30 Values of κ determined using u and ε values established from a) SFM, b) CAM, c) B Method and d) the PP Method.*

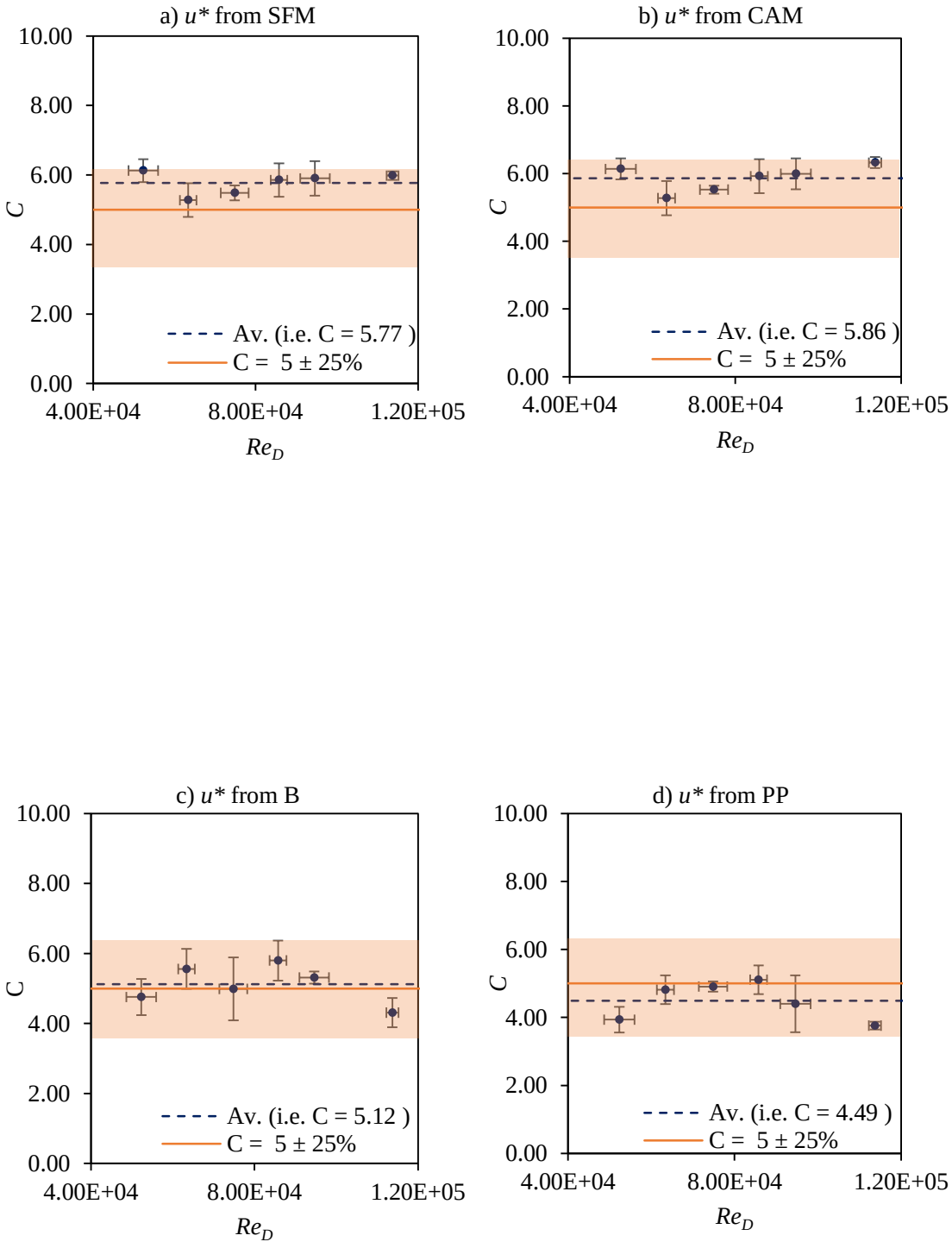

Figure 4.31 Values of C determined using u and ε values established from a) SFM, b) CAM, c) B Method and d) the PP Method.*

The combined average values of κ and C determined from linear regression approach, excluding the PP data were 0.42 ± 0.01 and 5.59 ± 0.53, respectively. These values are confirmed by Figure 4.32, which illustrates the combined curve fits of the full range of Re_D assessed. The respective profiles presented in Figure 4.32 were normalised and offset by the frictional data determined from system's PG using the SFM and CAM. This approach yielded a value of κ of 0.42 and values of C of between 5.56-5.72. The values of κ and C determined from the linear regression approach were consistent with the respective values established from the Ξ and ψ approaches.

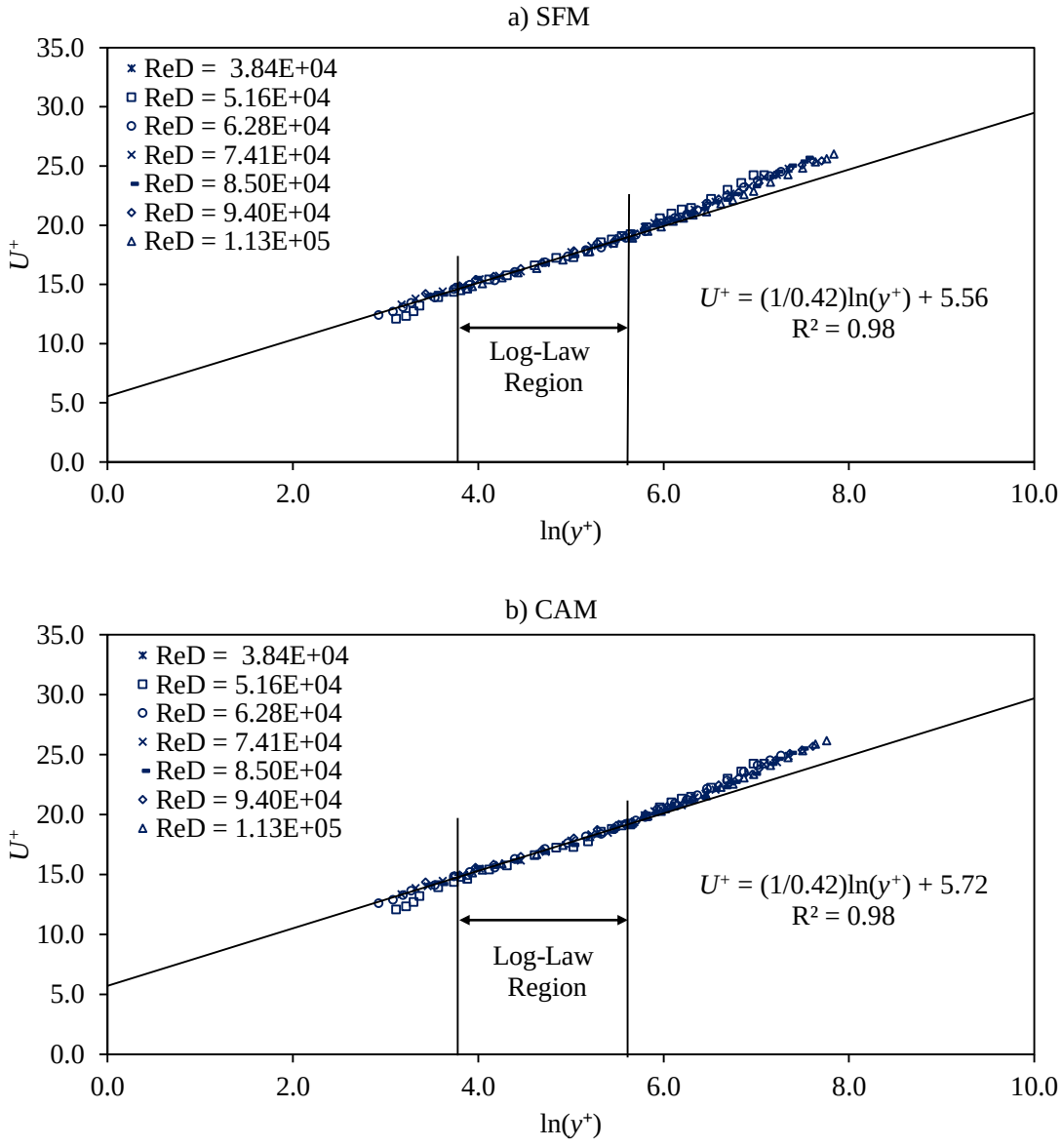

Figure 4.32 Mean-velocity profiles normalised by values of u determined from the system's Pressure Gradient using a) SFM and b) CAM. For the range of 3.84 x 10^4 < Re_D < 1.13 x 10^5.*

The established Log-Law constants were in agreement with the accepted literature values for turbulent flow in a pipe (McKeon et al. 2004b; George 2007). However, the values determined directly from the mean-velocity data (i.e. using the Ξ, ψ and linear regression approaches) were generally higher than the equivalent values determined independently from the velocity data (i.e. κ = 0.41 and C = 4.97). These differences could have been caused by potential errors in ε. Each of the Log-Law constant determination approaches outlined within this section, which directly utilised the mean-velocity data had an inherent reliance on ε. Potential errors in ε would have had implications on the both the values of the constants and the relative location of the Log-Law region. The validity of the values of ε has already been questioned within the current study (see Section 4.4.1).

A partial sensitivity analysis was undertaken to establish the influence ε on κ and C. The results of this analysis are presented within Table 4.6. The sensitivity analysis identified that a change in ε of ±0.05mm would have caused an average deviation in κ of ±1.20% and C of ±3.38%. Similarly, a change in ε of ±0.10mm would have caused on average a deviation in κ of ±2.97% and C of ±8.18%. Consequently, the values of κ and C derived directly from the mean-velocity data should be viewed with caution.

Table 4.6 Impact of ε on values of κ and C derived for the linear regression approach.

Change in ε	***Re_D***	***Deviation from Original***	
		κ	C
-0.10mm	$6.28x10^4$	+3%	+8%
	$7.17x10^4$	+2%	+7%
	$8.35x10^4$	+3%	+8%
-0.05mm	$6.28x10^4$	+2%	+4%
	$7.17x10^4$	+1%	+2%
	$8.35x10^4$	+1%	+4%
+0.05mm	$6.28x10^4$	-1%	-3%
	$7.17x10^4$	-2%	-5%
	$8.35x10^4$	-2%	-6%
+0.10mm	$6.28x10^4$	-3%	-7%
	$7.17x10^4$	-3%	-10%
	$8.35x10^4$	-4%	-12%

Theoretical mean-velocity profiles were calculated using the Log-Wake Law (where κ = 0.42 and C = 5.59) and are are presented in Figure 4.33. The experimentally determined mean-

velocity data for the range of $5.23x10^4 < Re_D < 1.13x10^5$ is also presented in Figure 4.33. It is evident from Figure 4.33 that theoretically derived profiles are in good agreement with the experimentally determined profiles.

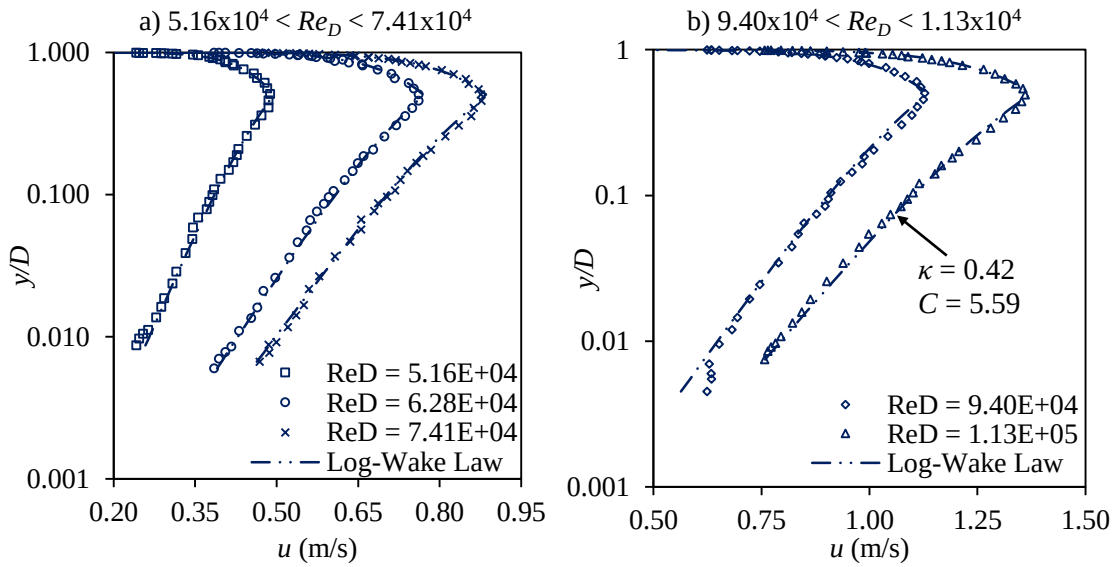

Figure 4.33 Theoretically and experimentally mean-velocity profiles for the Re_D ranges: a) $5.16x10^4 < Re_D < 7.41x10^4$ and b) $9.40x10^4 < Re_D < 1.13x10^4$.

4.7 Summary

The purpose of this chapter was to present the results of the non-fouled phase of the current study; for the primary purpose of validating the pipeline facility for the fouled phases. The results have shown that the pipeline facility was capable of consistently establishing the frictional capacity of the test pipe over the range of $3.15x10^4 < Re_D < 1.23x10^5$.

It was established experimentally that the 3.35 m (33 *D*) Run-Section was sufficient for fully development flow to be attained within the Test Section, at least as far as the pressure head distribution in the flow direction was concerned. Therefore, the frictional data derived from the system's PG can be considered highly accurate to within the experimental uncertainties.

The values of k_s and n established for the non-fouled S-HDPE pipe of k_s = 0.009 mm ± 32% and n = 0.008 ±6% are within the range expected for the material (Grann-Meyer 2010). The established value of k_s of 0.009 mm equated to a maximum value of k_s^+ of 0.51 (i.e. for $Re_D = 1.23x10^5$) and as a consequence, the non-fouled pipe was considered hydraulically smooth for all Re_D assessed (i.e. $k_s^+ < 5$). The experimentally determined values of λ were found to be in reasonable agreement with the smooth pipe relationships proposed by Nikuradse (1933)

(i.e. Equation 2.11) and McKeon and Zagarola (2005) (i.e. Equation 2.12). The maximum discrepancy between the measured and theoretical values of λ was ±3.97% and was within the experimental uncertainty (i.e. ±5.15%, see Table 4.1). This illustrates the capacity of the pipeline facility to measure very smooth surfaces. As the non-fouled pipe in theory represents the worst case situation (in terms of the pipe's smoothness) it was considered that the facility more than capable of measuring the finite changes in roughness caused by a biofilm.

Contributions to knowledge on the topic of turbulent smooth pipe flow were also presented within this chapter. In particular, it was found that Townsend's Wall Similarity Hypothesis was valid and the frictional data derived from the Perry and Li (1990) and Bradshaw (1959) wall similarity methods were reasonably accurate. For instance, the maximum discrepancy in the values of c_f established from the PL and PG Methods was ±6%. The PL and B Methods are therefore, recommended for use in pipes. This supports the conclusion drawn by Walker (2014), who critically appraised commonly used wall similarity techniques within a purpose built water tunnel, which had a rectangular cross-section. As the B Method is not applicable to rough walls, only the PL Method was applied to the biofouled surfaces within the current study.

The results of this chapter were in support of a universal Log-Law, the validity of which has been questioned in recent years (Zanoun et al. 2003; Wei et al. 2005; Nagib and Chauhan 2008,). Furthermore, the established location of the Log-Law within the boundary layer of $50 < y^{=} < 0.2R^{+}$ was where standard convention states it should be (George 2007). Furthermore, the experimentally determined Log-Law constants of κ and C for the non-fouled pipe were found to be in the range expected for turbulent pipe flow and were independent of the flow conditions (McKeon et al. 2004b; George 2007). The values of κ and C found within the current study were 0.42 ± 0.01 and 5.59 ± 0.53, respectively. The linear regression method for determining κ and C produced the best results in terms of consistency. However, it was found that the value of κ has a strong dependency on ε. It was also found that κ had a significant influence on the frictional data derived from wall similarity techniques and, in particular, the PL Method. These associated issues in the liner regression method could have significant implications on the fouled phases of the current study given the expected non-universality of κ biofouled surfaces (Lambert et al. 2009; Perkin et al. 2013; 2014).

This chapter has illustrated that the purpose built pipeline facility is an effective instrument for establishing the PG and boundary layer characteristics of the test pipe and therefore, capable of satisfying the primary research aims outlined in Chapter 1.

Chapter 5 Incubation phase

5.1 Introduction

The purpose of this chapter is to present the results of the incubation phase of the current study. In particular, this chapter outlines the frictional data established from the PG and mean-velocity data recorded during the incubation phases of the $Re_D = 5.98x10^4$, $Re_D = 7.82x10^4$ and $Re_D = 1.00x10^5$ assays. A description of each of the fouled pipes is first presented. The frictional data derived from the system's PG is then presented, which is followed by the evaluation of the mean-velocity data using the traditional PL Method. The validity of a universal Log-Law for biofouled pipes is questioned in detail within this chapter. The potential implications of a non-universal Log-Law on local and global measurements are also discussed. The process of biofilm frictional evolution within pipelines is outlined at the end of this chapter, which culminates in the formulation of a novel dynamic k_s parameter. A detailed summary and discussion completes the chapter.

5.2 Description of the fouled pipes

The biofilms incubated with wastewater within the current study had a predominantly low-form gelatinous structure, as shown for example by Figure 5.1 and Figure 5.2. Filamentous type development was observed but very rarely, with filaments seldom exceeding 10 mm.

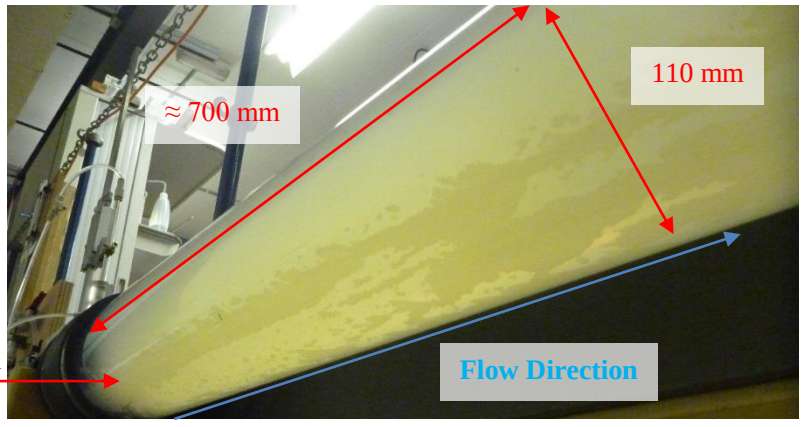

Figure 5.1 Biofilm development in the pilot-scale pipeline for $Re_D = 5.98x10^4$ assay.

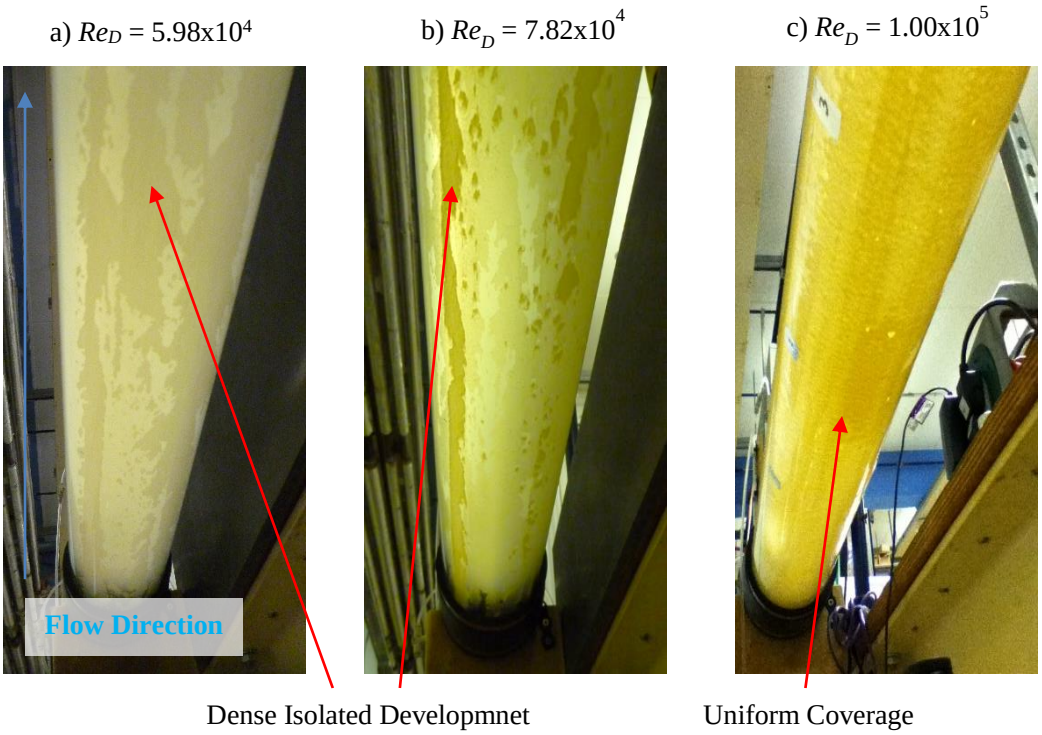

Figure 5.2 Biofilm development in the pilot-scale pipeline for a) Re_D = 5.98x10^4, b) Re_D = 7.82x10^4 and Re_D = 1.00x10^5 assays.

When fouled the pipes showed various amounts of microbial material with very different morphologies, depending on the conditioning, as shown by Figure 5.2. Typically, the biofilm incubated at high shear (i.e. in the Re_D = 1.00x10^5 assay) had a seemingly more uniform coverage than the biofilm incubated at low shear (i.e. in the Re_D = 5.98x10^4 assay), which had a more isolated structure.

5.3 Global frictional resistance

The frictional data presented in this section was established from the system's PG using SFM and CAM, and therefore, represents the global conditions within the pipeline.

Normalised static head profiles established at several different time intervals within the Re_D = 5.98x10^4 and Re_D = 1.00x10^5 assays are presented in Appendix C.1 in Figure C.1 and Figure C.2, respectively.

The incubation phase frictional data as established from the SFM and CAM for the three flow assays are listed in Appendix C.1 in Table C.1 to Table C.6, which present the average daily

values for each frictional parameter. Noting that at least three pipe surveys were conducted daily. A summary of the frictional data established during the equilibrium stages of each of the flow assays is presented within Table 5.1. The biofilms were assumed to have reached a state of equilibrium when their frictional resistance remained unchanged with time. Within the current study equilibrium conditions were observed after approximately 180 h (or 8 d) of incubation with the wastewater, as indicated by k_s (see Figure 5.8). This time was independent of the conditioning shear.

Table 5.1 Frictional data determined from the system's PG using SFM and CAM during the equilibrium stage of the $Re_D = 5.98x10^4$, $Re_D = 7.82x10^4$ and $Re_D = 1.00x10^5$ assays.

Parameter	$Re_D = 5.98x10^4$				$Re_D = 7.82x10^4$				$Re_D = 1.00x10^5$			
	SFM		CAM		SFM		SFM		SFM		SFM	
	Av.	σ	Av.	σ	Av.	σ	Av.	σ	Av.	σ	Av.	σ
***Re* (x10^{-4})**	6.01	0.22	6.01	0.22	7.86	0.21	7.86	0.21	10.14	0.35	10.14	0.35
λ	0.034	0.00	0.035	0.00	0.030	0.00	0.030	0.00	0.026	0.00	0.025	0.00
u^* (m/s)	0.038	0.00	0.038	0.00	0.045	0.00	0.045	0.00	0.054	0.00	0.054	0.00
c_f (x10^{-3})	5.22	0.08	5.19	0.11	4.62	0.06	4.56	0.07	4.16	0.14	4.08	0.14
τ_w (N/m^2)	1.42	0.07	1.46	0.07	2.15	0.05	2.14	0.04	2.95	0.07	2.89	0.07
n	0.011	0.00	0.011	0.00	0.010	0.00	0.010	0.00	0.010	0.00	0.010	0.00
k_s (mm)	0.637	0.02	0.723	0.03	0.445	0.03	0.460	0.04	0.223	0.03	0.209	0.03
k_s^+	25.05	1.76	28.73	1.95	20.94	1.34	21.65	1.80	12.79	1.41	11.86	1.44

It should be noted that the values of k_s and n listed in Table 5.1 for were determined using the traditional C-W equation (i.e. Equation 2.42) and the traditional Manning equation (i.e. Equation 2.45). It has been widely suggested that the complex surface dynamics of a biofilm cannot be adequately defined by a single one-dimensional parameter, such as the Nikuradse equivalent sandgrain height (Picloglou 1980; Schultz and Swain 1999; Barton 2005; Lambert et al. 2008; 2009; Andrewartha 2010). However, as such a parameter (or potential series of parameters) has yet to be successfully formulated, the Nikuradse equivalent sandgrain height was used herein to define k_s.

The biofilms frictional evolution over time within the three flow assays is illustrated by Figure 5.3 to Figure 5.6, in terms of S_f, λ, u^* and τ_w. It is evident from Figure 5.3 to Figure 5.6 that the frictional resistance imparted by biofilms was significant, particularly with respect to the initial non-fouled conditions (see Section 4.3).

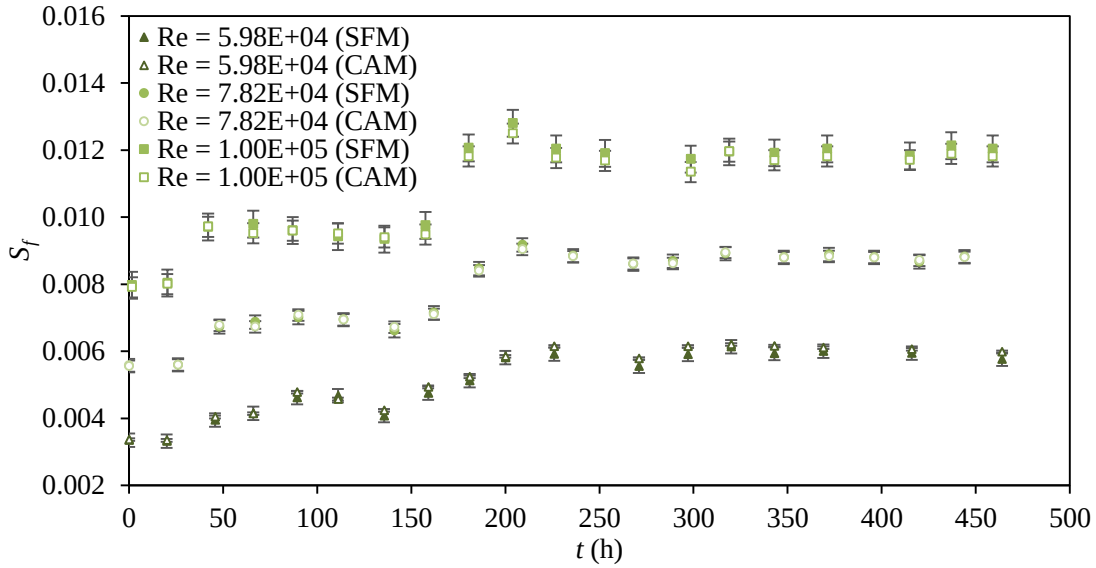

Figure 5.3 Influence of biofilm development over time on global S_f within the Re_D = 5.98x10^4, Re_D = 7.82x10^4 and Re_D = 1.00x10^5 assays.

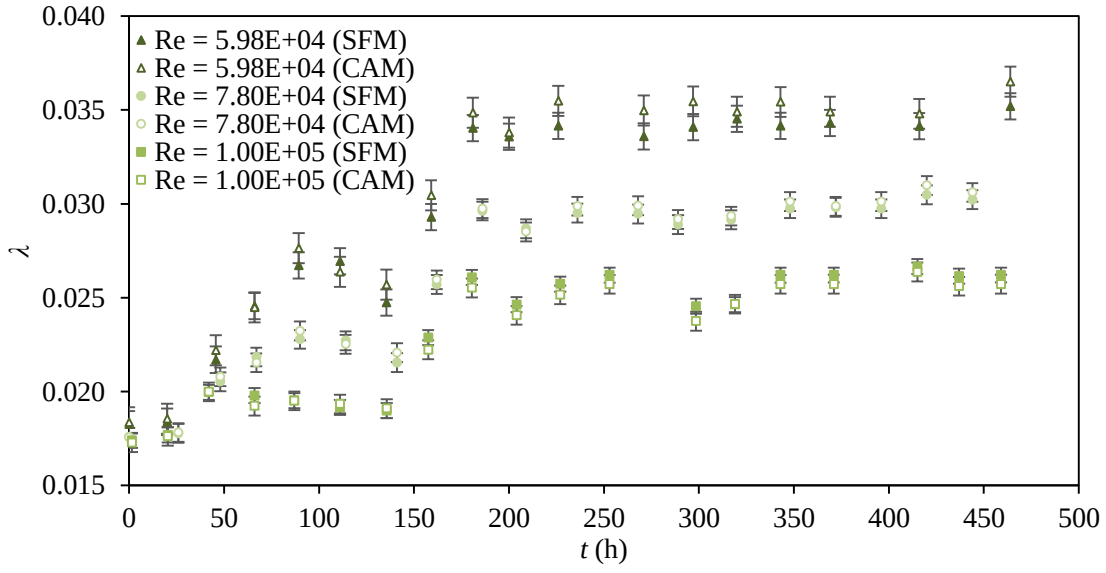

Figure 5.4 Influence of biofilm development over time on global λ within the Re_D = 5.98x10^4, Re_D = 7.82x10^4 and Re_D = 1.00x10^5 assays.

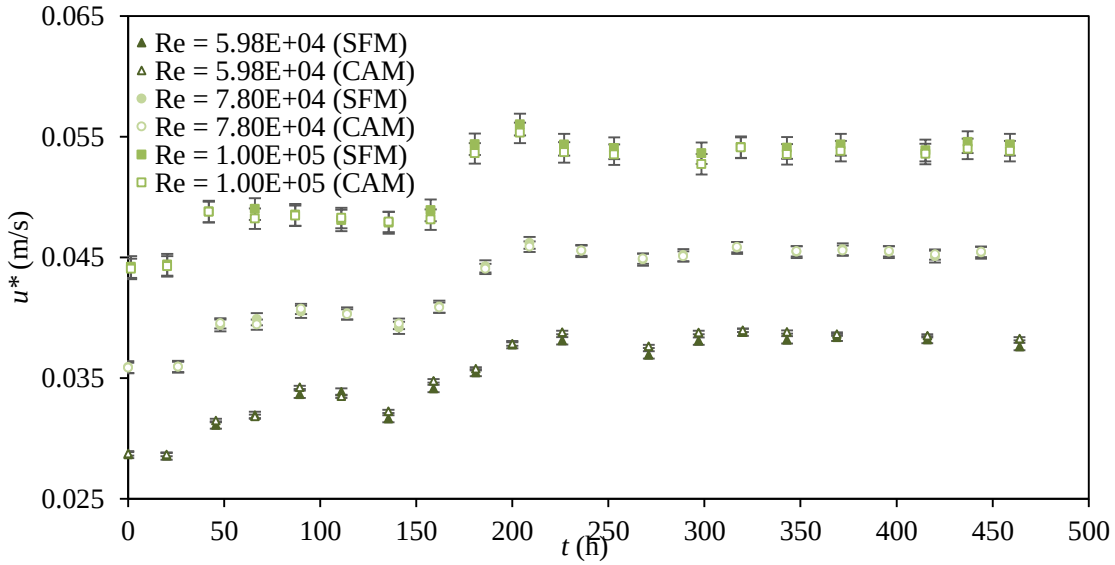

Figure 5.5 Influence of biofilm development over time on global u within the Re_D = 5.98x10^4, Re_D = 7.82x10^4 and Re_D = 1.00x10^5 assays.*

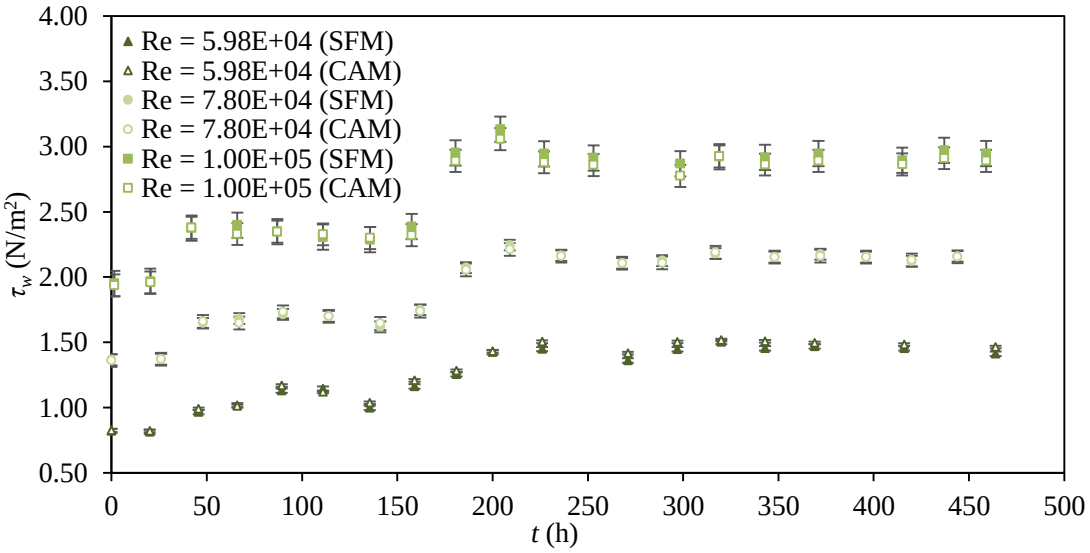

Figure 5.6 Influence of biofilm development over time on global τ_w within the Re_D = 5.98x10^4, Re_D = 7.82x10^4 and Re_D = 1.00x10^5 assays.

The deviation between the frictional data determined with and without fouling are illustrated by Figure 5.7. In particular, Figure 5.7 presents the average increase in S_f, λ, u^* and τ_w (determined using the SFM) after the biofilms had reached a state of equilibrium. It can be seen from Figure 5.7 that the increase in S_f with fouling was 76% for the $Re_D = 5.98\text{x}10^4$ assay, 58% for the $Re_D = 7.82\text{x}10^4$ assay and 51% for the $Re_D = 1.00\text{x}10^5$ assay. Similarly, it is evident from Figure 5.7 that the increase in λ with fouling was 85% for the $Re_D = 5.98\text{x}10^4$ assay, 68% for the $Re_D = 7.82\text{x}10^4$ assay and 48% for the $Re_D = 1.00\text{x}10^5$ assay.

The impact of the biofilm development on global k_s is illustrated by Figure 5.8 and Figure 5.9. Figure 5.8 and Figure 5.9, respectively illustrate k_s in traditional and non-dimensional (i.e. k_s^+) forms. It is evident from Figure 5.8 that k_s begins to depart from the non-fouled value after approximately 25 h of incubation. After approximately 180 h the values of k_s for the $Re_D = 5.98\text{x}10^4$, $Re_D = 7.82\text{x}10^4$ and $Re_D = 1.00\text{x}10^5$ assays reach their respective maximums of 0.723, 0.445 and 0.223 mm (based on the SFM).

The influence of biofilm development on Manning roughness coefficient within respective flow assays is presented within Figure 5.10

The sensitivity analysis presented in Section 3.5 indicated that large errors are common for k_s measurements. Based on the sensitivity analysis, and in particular Figure 3.28 the estimated error in the k_s values for the respective flow assays was approximately ±10-25%. To establish whether the differences between the discrete assays were statistically significant within the experimental uncertainties a single factor analysis of variance (ANOVA) was performed. The significance level of all ANOVAs within the current study was set at $\alpha = 0.05$. The ANOVAs on k_s indicated that the differences between the respective assays were statistically significant. The k_s values recorded during the equilibrium stage were used for the ANOVA.

The k_s induced by a biofilm is generally considerably larger than its absolute roughness or thickness. This is typically due to their vibrating and oscillating behaviour, which is fostered by their viscoelastic nature (Picologlou 1980; Barton 2006; Andrewartha 2010). Barton (2006) reported the average ratio of k_s/k_{av} for biofilms incubated on smooth plates was 3.0. It has been suggested that the roughness parameter of k_t has the strongest agreement with biofilm induced k_s (Barton 2006; Andrewartha 2010). Typically, ratios of k_s/k_t for biofilms incubated on smooth plates range from 0.3-4.8 (average: 1.5) (Barton 2006; Andrewartha 2010). Based on the ratios reported within the literature the approximate value of k_t for the equilibrium stage biofilms was 0.482 mm for the $Re_D = 5.98\text{x}10^4$ assay, 0.297 mm for the $Re_D = 7.82\text{x}10^4$ assay and 0.149 mm for the $Re_D = 1.00\text{x}10^5$ assay.

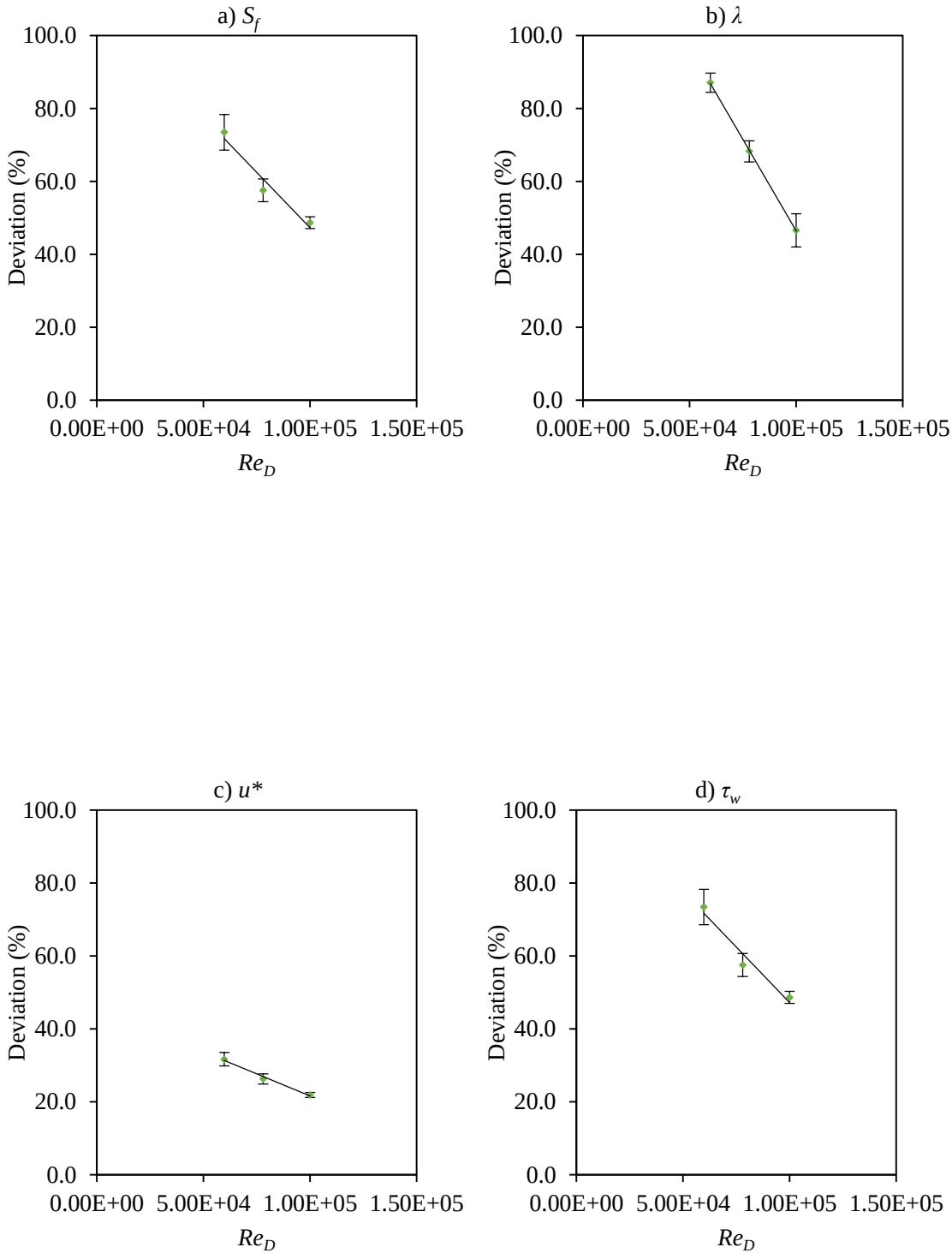

Figure 5.7 Deviation between in the equilibrium stage values of a) S_f, b) λ, c) u^* and d) τ_w with non-fouled data (frictional data determined using the SFM).

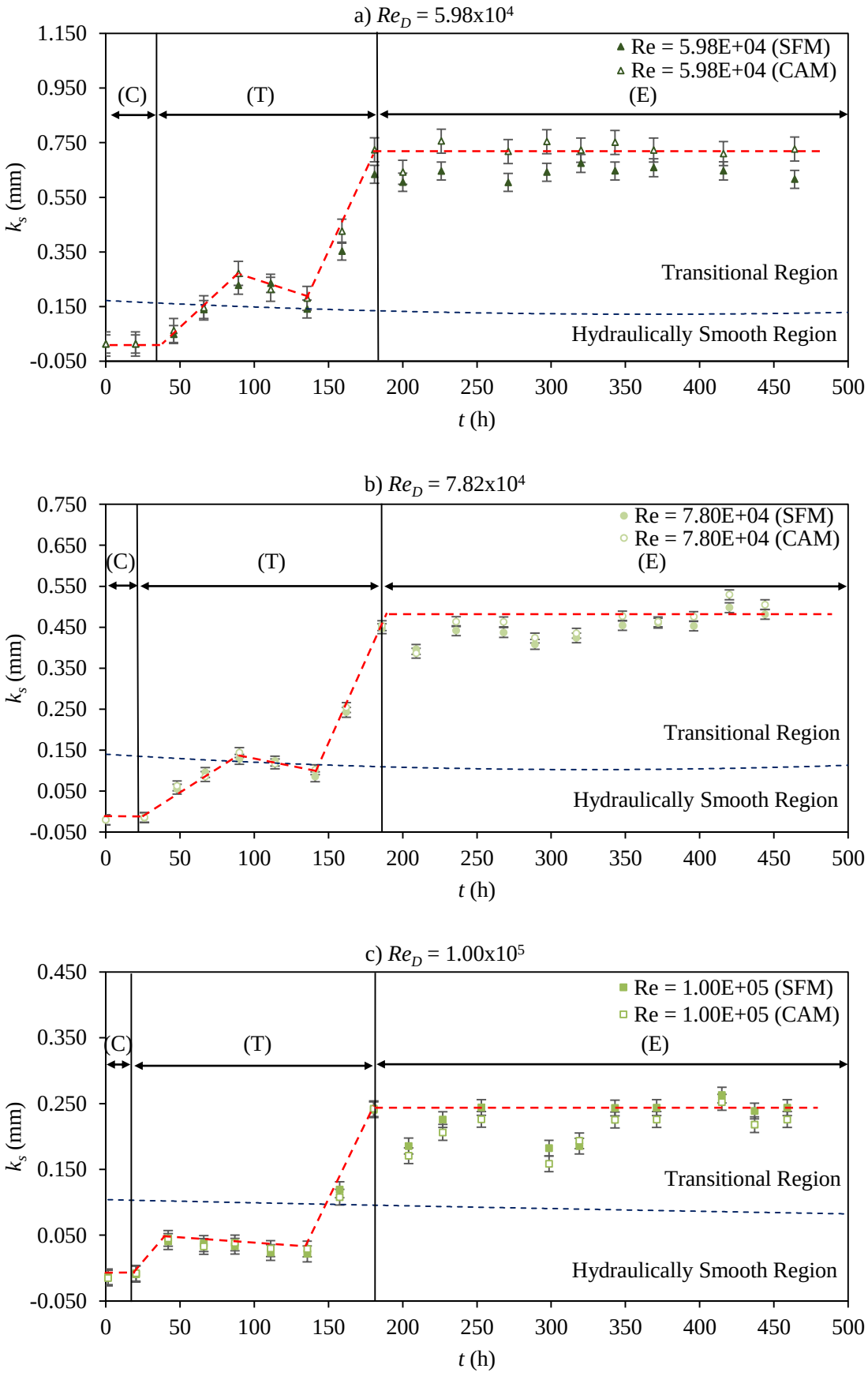

Figure 5.8 k_s against time for the a) Re_D = 5.98x10⁴, b) Re_D =7.82 x10⁴ and c) Re_D =1.00x10⁵ assays (highlighting the Conditioning (C), Transitional (T), and Equilibrium (E) development stages, along with the limits of hydraulically smooth and transitional flow).

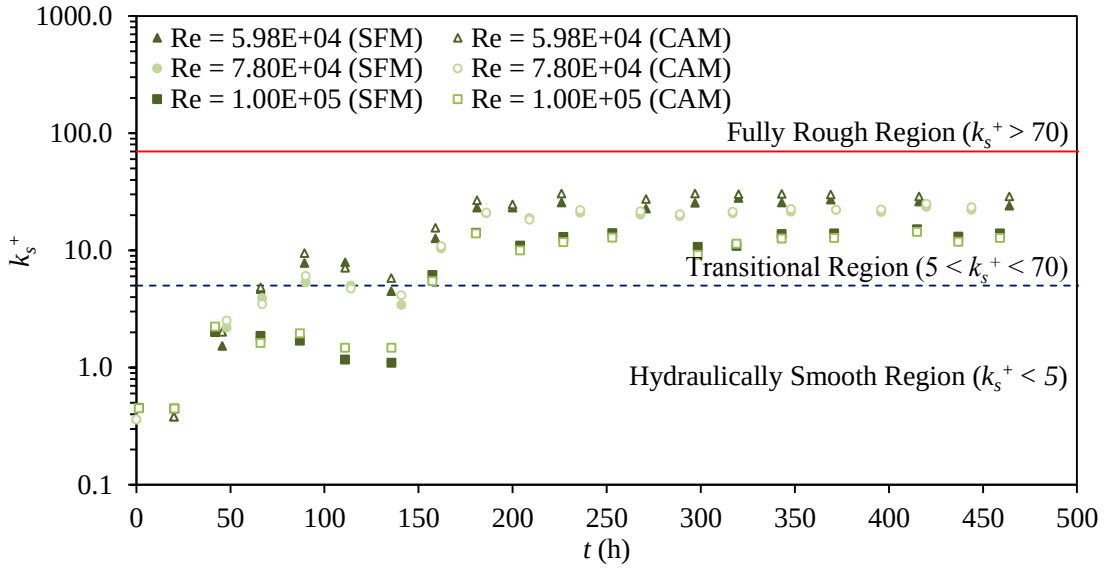

Figure 5.9 k_s^+ against time for the $Re_D = 5.98x10^4$, $Re_D = 7.82 x10^4$ and $Re_D = 1.00x10^5$ assays (highlighting the hydraulically smooth, transitional and fully rough flow).

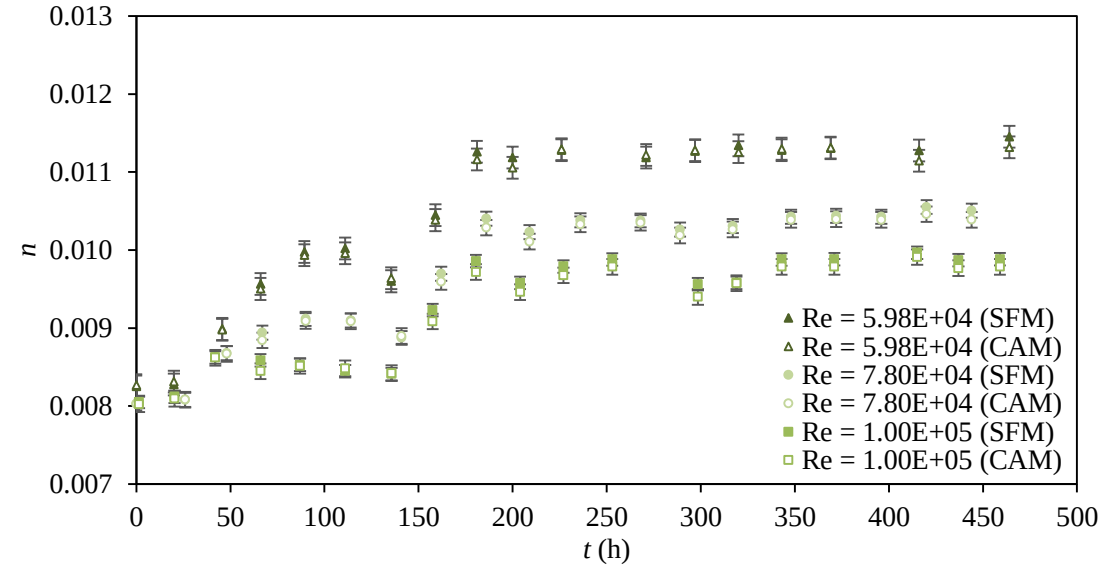

Figure 5.10 n against time for the $Re_D = 5.98x10^4$, $Re_D = 7.82x10^4$ and $Re_D = 1.00x10^5$ assays.

The frictional resistance imparted by the biofilms over time, followed a universal pattern. Equivalent biofilm frictional development patterns have also been reported within the literature for pipes, although, for pipelines of small diameters (i.e. 25 mm < D < 50 mm) (Picologlou et al. 1980; Lambert et al. 2008; 2009). Furthermore, the observed development pattern for the biofilms frictional resistance was consistent with the development patterns associated with physical biofilm attributes, such as absolute thickness, cell density and population counts etc. (as shown conceptually by Figure 2.1) (Bryer and Characklis 1981; Peyton 1996). The biofilm frictional resistance over time comprised of three discrete stages, namely the conditioning stage, transitional development stage, and equilibrium stage (see Section 5.8 for detailed discussion of the process of biofilm frictional development over time). Figure 5.8 highlights the three stages of biofilm frictional development in terms of k_s.

It was found that the presence of the mature (i.e. equilibrium stage) biofilms caused an increase in pipe k_s of 7700% for the Re_D = 5.98x10^4 assay, 5100% for the Re_D = 7.82x10^4 assay and 2200% for the Re_D = 1.00x10^5 assay. The equivalent values of n were found to have increased from 0.008 by 37% for the Re_D = 5.98x10^4 assay, 29% for the Re_D = 7.82x10^4 assay and 37% for the Re_D = 1.00x10^5 assay. The values of n recorded for the respective biofilms are approximately equivalent to the typically accepted value of a concrete/mortar lined channel (i.e. n = 0.011) (Chadwick et al. 2004).

The biofilm which induced the greatest increase in equivalent roughness was also the biofilm conditioned at the lowest shear (i.e. in the Re_D = 5.98x10^4 assay). This was to be expected, as the shear forces within the Re_D = 5.98x10^4 assay were inherently lower those within other flow assays (see Figure 5.6). It has been reported that the overall thickness of a biofilm is heavily dependent upon the shear conditions in which it is incubated and that typically, the higher the conditioning shear the thinner the biofilm (Vieira et al. 1993; Stoodley et al. 1998a; Barton 2006; Celmer et al. 2008; Lambert et al. 2008; 2009; Perkins et al. 2014). As biofilm thickness defines to some extent the physical and equivalent roughness of a biofouled surface, the thinner the biofilm the lower the k_s (Barton 2006; Lambert et al. 2008; 2009; Andrewartha 2010). Naturally, the opposite is true of thicker biofilms. Furthermore, the mass transfer and drag limitations associated with lower Re_D would have given rise to an isolated and irregularly distributed biofilm, as illustrated by Figure 5.1 (Lewandowski and Stoodley 1995; Stoodley et al. 1998a). The resultant roughness distribution will induce a higher overall frictional resistance than that imposed by a uniformly distributed biofilm (Stoodley et al. 2002; Andrewartha 2010). For instance, Andrewartha (2010) observed that where biofilm coverage was heterogonous in nature, the overall drag measurements showed a greater increase in skin friction. Consequently, the fostered irregularity of the biofilms coverage could further explain

the high global values of k_s recorded within the Re_D = 5.98x10^4 assay. Alternatively, the increased mass transfer and diffusion potentials associated with the higher Re_D would have induced a more uniformly distributed biofilm, as shown by Figure 5.2 (Liu and Tay 2001; Stoodley et al. 2002; Celmer et al. 2008). For instance, Liu and Tay (2001) found that biofilms grown at higher flow conditions were smoother and more dense than those grown at low flow conditions. The increased biofilm uniformity coupled with the limits imposed on maximum thickness by the inherently high drag could explain the low global values of k_s recorded within the Re_D = 1.00x10^5 assay.

It is evident that the frictional resistance induced by a biofilm is a function of the biofilm's incubation conditions, and in particular, the lower the incubation Re_D the greater the frictional resistance imposed by the resultant biofilm. This is consistent with the findings of Lambert et al. (2008) who reported that biofilms conditioned at higher velocities were less rough and had a lower k_s than those conditioned at lower velocities.

The limits of hydraulically smooth, transitional and fully rough flow are shown in Figure 5.8 and Figure 5.9. It is evident from Figure 5.8 and Figure 5.9 that the increase in k_s due to the biofilm development caused the overall flow to progress from hydraulically smooth flow to transitional rough flow within all three flow assays. This progress was induced by the respective biofilms after approximately 150 h of incubation. Fully rough flow was not experienced within any of the flow assays.

5.3.1 Variations in space-averaged conditions

Figure 5.11 illustrates the standard deviation in the space-averaged roughness (in terms of k_s), as established from the evaluation of the discrete static headloss combinations (i.e. P_1-P_5, P_1-P_4, P_1-P_3 etc., see Figure 3.5). In other words the variation in k_s along the pipeline is illustrated by Figure 5.11. To highlight the contrast between the high and low shear conditions, only the data for the Re_D = 5.98x10^4 and Re_D = 1.00x10^5 assays are presented in Figure 5.11. The average standard deviation in k_s determined for the non-fouled pipe is also presented within Figure 5.11 as a reference. Figure 5.12 presents the values of k_s determined from each of the discrete headloss combinations recorded within the Re_D = 5.98x10^4 and Re_D = 1.00x10^5 assays.

It is highly unlikely that the respective biofilms would have grown uniformly and induced a homogenous roughness distribution across the pipe's length. The potential irregularity of a biofilm's roughness distribution is illustrated by Figure 5.2. The variation in space-averaged roughness along the pipeline after the biofilms had reached a state of equilibrium was far greater within the Re_D = 5.98x10^4 assay than within the Re_D = 1.00x10^5 assay. This was

supported by the results of single factor ANOVAs performed on the respective assays (α = 0.05), which indicated that the differences recorded between the discrete headloss combinations for the Re_D = 5.98x10^4 assay were statistically significant whereas, the ANVOAs for the Re_D = 1.00x10^5 assay showed that the differences were insignificant.

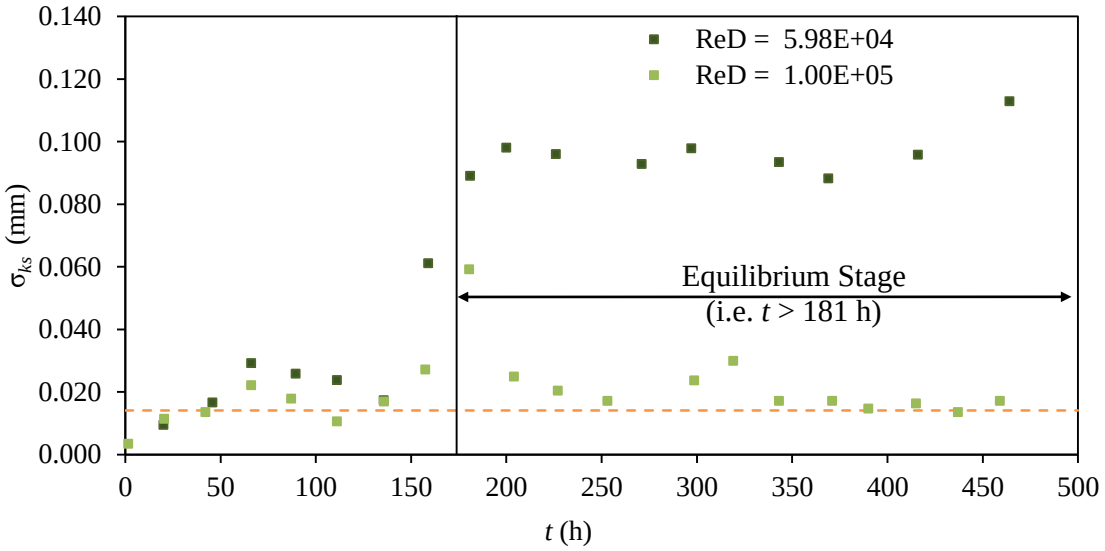

Figure 5.11 Standard deviation in space-averaged k_s along the pipeline against time for the Re_D = 5.98x10^4 and Re_D = 1.00x10^5 assays.

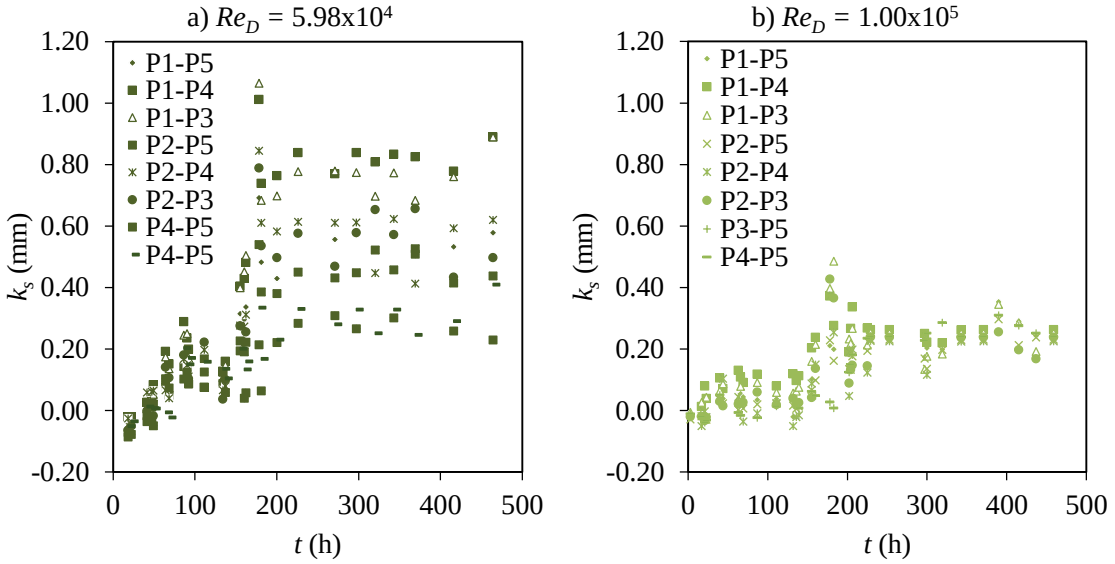

Figure 5.12 k_s values determined from each of the discrete static headloss combinations within a) the Re_D = 5.98x10^4 and b) Re_D = 1.00x10^5 assays.

The results show indirectly that the biofilm coverage within the $Re_D = 5.98x10^4$ assay can be considered more irregular, and thus, less uniform (over the length of the system) than the respective coverage within the $Re_D = 1.00x10^5$ assay. The uniformity of the biofilm coverage within the $Re_D = 1.00x10^5$ assay is highlighted by the strong agreement between the fouled and non-fouled frictional data for the assay, as shown in Figure 5.11. This agreement is most notable at $343 < t$ (h) < 459 in Figure 5.11. The observed differences in coverage were to be expected based upon the inherent mass transfer and shear conditions within the respective flow assays. That is to say, it was expected that the biofilm conditioned at the higher Re_D, due to increased mass transfer and diffusion potentials would have been more uniform in its coverage than the biofilm conditioned at the lower Re_D. The observations made within this section therefore, confirm and provide strong evidence for what was until now just conjecture.

5.3.2 Pipe joint roughness

The frictional resistance associated with the pipe joints (i.e. across P_1-P_2 and P_3-P_4, see Figure 3.5) increased significantly as a direct result of biofilm development. Furthermore, the observed increase in frictional resistance in the vicinity of the joints was far greater than that observed for the rest of the pipe. For instance, within the $Re_D = 5.98x10^4$ assay the equilibrium stage value of k_s for the joints was 4.051mm ± 40%. This represented a 750% increase in k_s from the initial conditions (i.e. 0.54mm ± 40%). Moreover, the k_s value associated with the pipe joints with fouling was 596% greater than the k_s value associated with the rest of the fouled pipe. The significant increase in biofilm induced roughness in the vicinity of the joints was to be expected, as areas which are initially high in roughness will foster greater microbial attachment and accumulation by providing additional protection (Gjaltema et al. 2004; Barton 2006; Yu et al. 2010; Walker et al. 2013). By fostering, initial attachment when internal cohesive forces are at their weakest, rough surfaces are likely to accommodate more mature microbial development. Walker et al. (2013) reported that the type of substratum is an important aspect in biofilm development, particularly, in its developing stages. In particular, Walker et al. (2013) found that when a rough and smooth plate were incubated under the same conditions for 2 weeks the smooth plate had a much lower frictional resistance than the rough plate. This also observed by Barton (2006).

5.4 Time-lapse images – Biofilm development over time

During the incubation phase of the $Re_D = 1.00x10^5$ assay a high resolution camera captured images of the biofilms development in the visualisation pipe, as shown by Figure 5.14 and Figure 5.15. The high resolution images were captured in conjunction with the pipe frictional surveys. A total of three images were recorded at each time interval, by traversing the camera in a streamwise direction along the visualisation pipe.

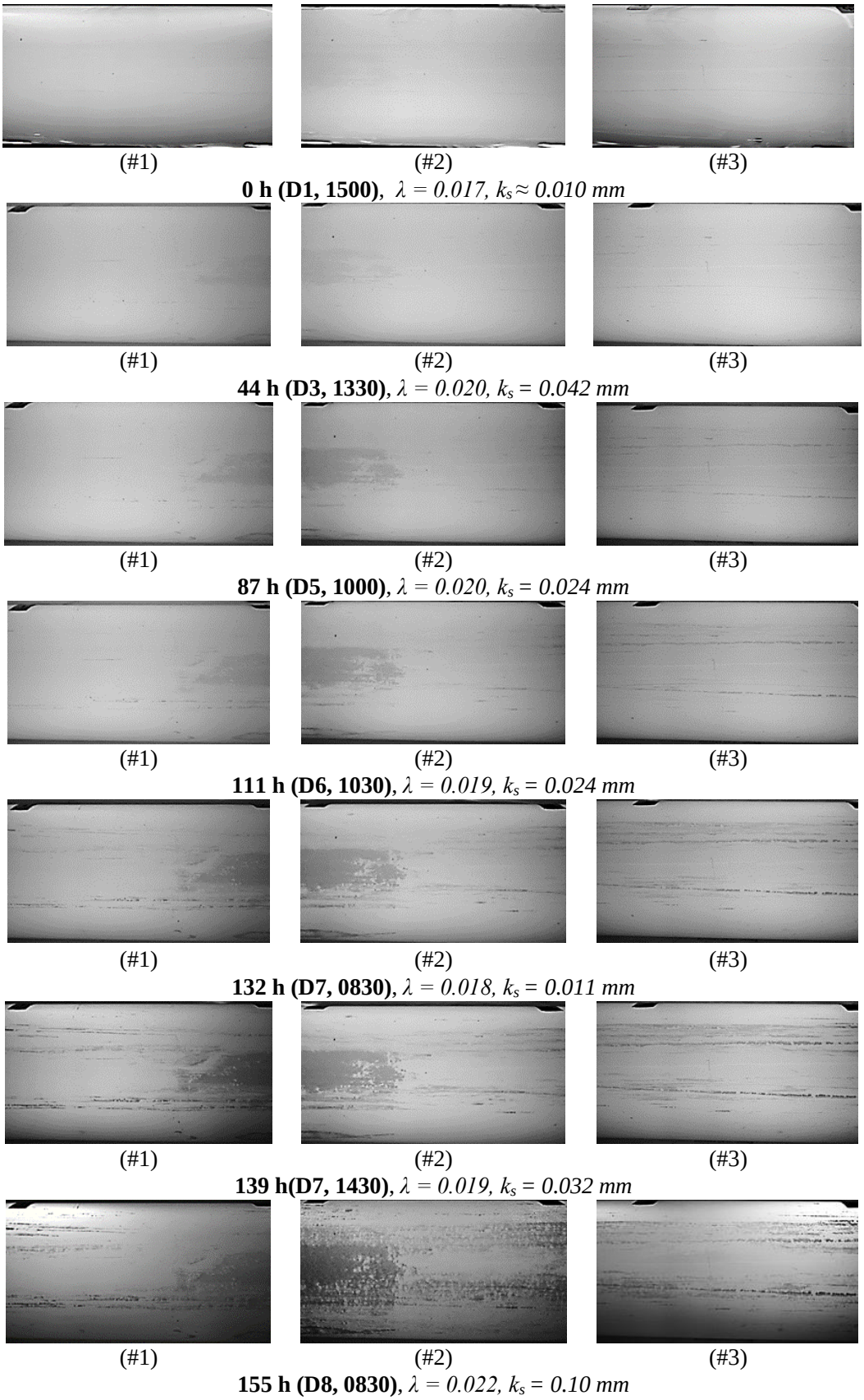

Figure 5.13 High resolution images captured during the incubation phase of the $Re_D = 1.00x10^5$ (for 0 h < t < 155 h).

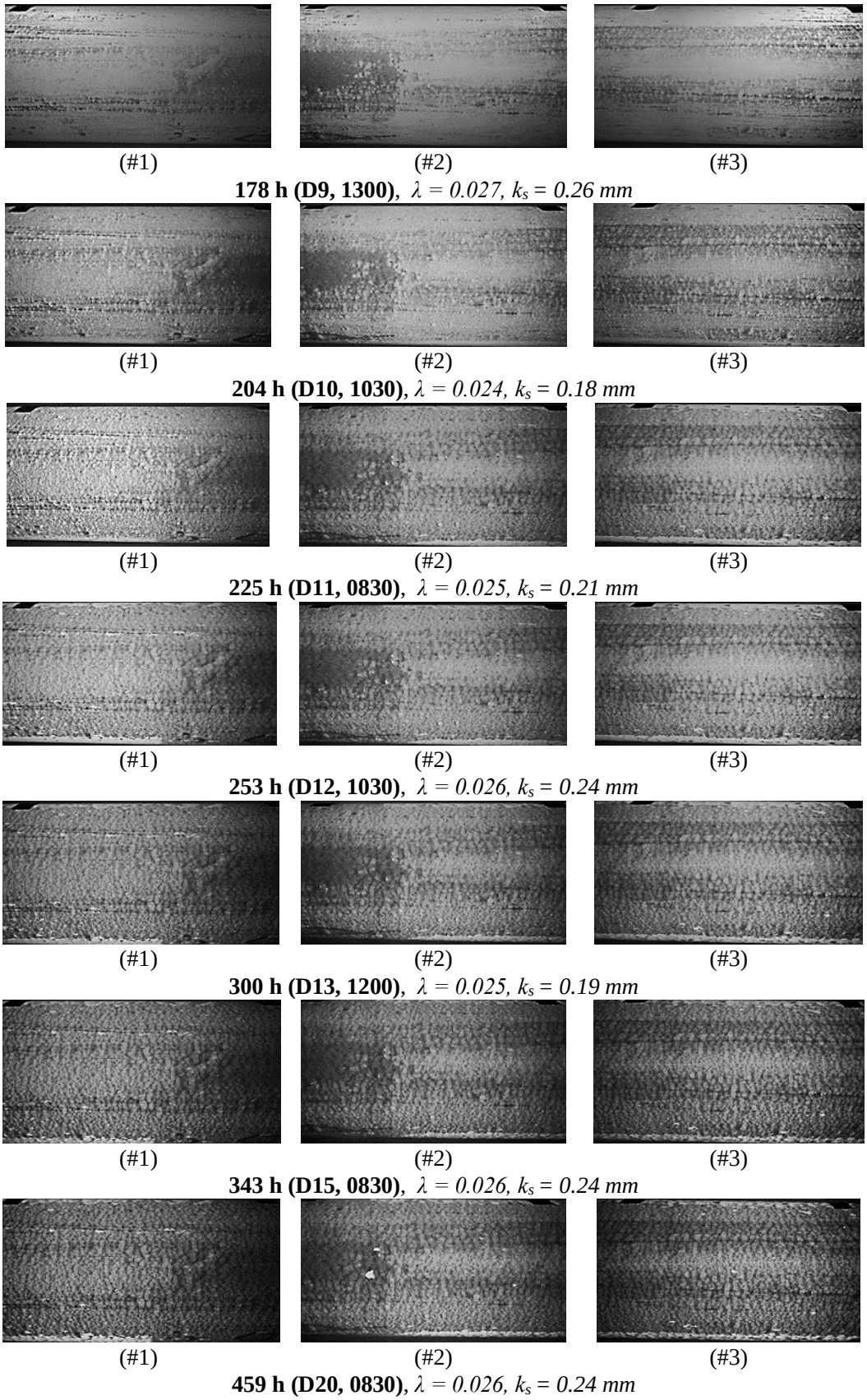

Figure 5.14 High resolution images captured during the incubation phase of the $Re_D = 1.00x10^5$ (for 178 h < t < 155 h).

An increase in microbial material on the pipe over time can be seen from Figure 5.14 and Figure 5.15.This indicate that the observed increase in frictional resistance was likely caused by the biofilm.

5.5 Mean-velocity profiles

The impact of biofilm development on mean-velocity distribution was evaluated within Re_D = 5.98x10^4 and Re_D = 1.00x10^5 assays using a Pitot probe (as outlined in Section 3.3.4). The Pitot probe was located at permanently located P_5 and as a consequence, the frictional data indirectly determined from the mean-velocity data is local to this region.

During the Re_D = 5.98x10^4 assay, the Pitot probe was periodically removed (typically, every two days) to determine visually whether the probe's aperture had been compromised by biofouling. If the aperture had become compromised then considerable bias could have been introduced into the recorded measurements. From these comprehensive visual inspections, it was found that no significant biofilm development was observed within the near vicinity of the probes aperture. Repeatability surveys conducted pre- and post- maintenance further supported the findings of the visual inspections, as the recorded differences between the pre- and post- maintenance measurements were within experimental uncertainties. When measurements were not being taken, the Pitot probe was positioned at the centre of the pipe (i.e. $y = R$) where the freestream velocities are at their maximum. The high respective shear forces within this region would have significantly impaired any potential biofilm development upon the probe, particularly in the vicinity of its aperture. Furthermore, the probe itself was fabricated from very smooth stainless steel, which would have also limited potential microbial attachment and development (Percival et al. 1999).

Figure 5.15 illustrates typical mean-velocity profiles for the Re_D = 5.98x10^4 and Re_D = 1.00x10^5 assays.

The mean-velocity profiles presented within Figure 5.15 have been normalised with respect to U and D. The respective profiles relating to the fouled cases were recorded after the biofilms had reached a equilibrium state. As expected, the dimensionless mean-velocity profiles presented for the fouled cases do not collapse onto the equivalent non-fouled profiles, which indicates an increase in surface roughness (Andrewartha 2010). The magnitude of the respective increases is a function of the retardation in the near wall velocities.

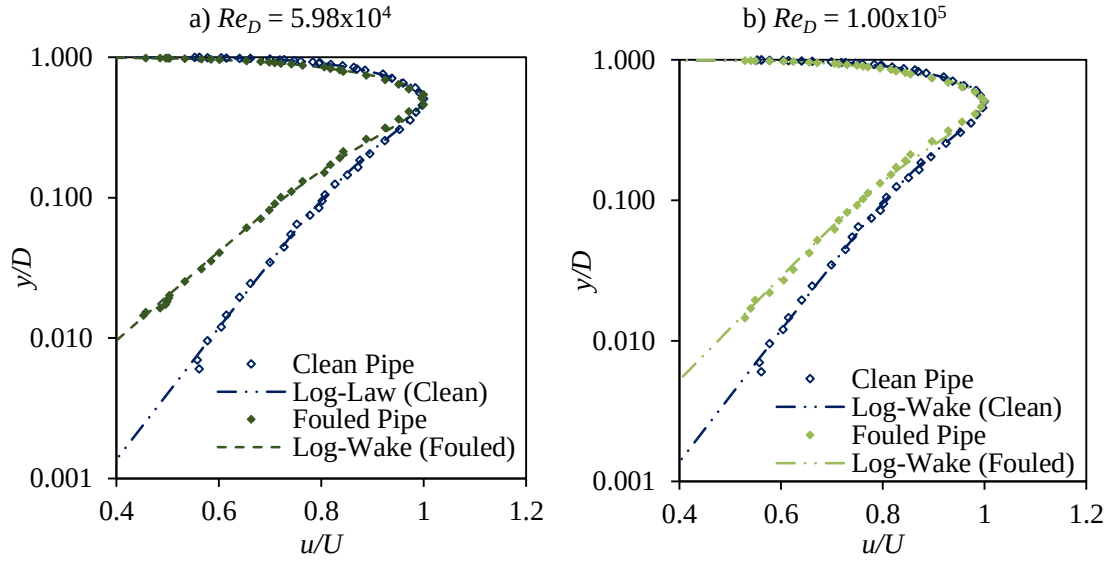

Figure 5.15 Typical mean-velocity profiles in semi-logarithmic for the a) Re_D = 5.98x10^4 and b) Re_D = 1.00x10^5 assay.

5.6 Local frictional resistance – Conventional approach

The mean-velocity data recorded within the Re_D = 5.98x10^4 and Re_D = 1.00x10^5 assays was analysed using the conventional PL Method (as outlined in Section 4.5). The values of κ was taken as 0.42. The Nikuradse's roughness function, B, which assumes different values determining on the flow regime was determined using Equation 2.33 (for fully rough flow B = 8.48). The incubation phase frictional data established from the PL Method for the Re_D = 5.98x10^4 and Re_D = 1.00x10^5 assays are presented in Appendix C.2 in Table D.7 and Table D.8. The data listed in Table D.7 and Table D.8 represent the average daily values recorded within the respective flow assays. A summary of the frictional data recorded during the equilibrium stages are presented in Table 5.2.

Table 5.2 Frictional data determined using the PL Method during the equilibrium stages of the Re_D = 5.98x10^4 and Re_D = 1.00x10^5 assays.

Assay		***Re*** **(x10^{-4})**	***u**** **(m/s)**	c_f **(x10^{-3})**	k_s **(mm)**	ε **(mm)**	ε^+	k_s^+	ΔU^+
Re_D **= 5.98x10^4**	Av.	6.09	0.042	6.60	2.30	2.29	102.26	101.24	7.91
	σ	0.33	0.002	0.42	0.55	0.40	25.81	16.98	0.67
Re_D **= 1.00x10^5**	Av.	10.14	0.050	3.55	0.21	1.06	11.07	56.34	2.33
	σ	0.35	0.003	0.39	0.10	0.18	5.50	10.82	1.56

The local k_s values were estimated from the mean-velocity profiles by fitting the velocity data to the Rough Wall Log-Law (i.e. Equation 2.37). Barton (2006) reported that values of k_s determined in this manner were highly sensitive to ε. In particular, Barton (2006) found that an error in ε of ±0.10 mm yields an error in k_s of ±0.41 mm. Consequently, the values of k_s estimated from Equation 2.37 should be viewed with caution.

The roughness functions were determined by fitting the mean-velocity data to Equation 2.36.

The local skin friction coefficients and wall shear velocities recorded within the two flow assays are presented within Figure 5.16. The c_f provides a more meaningful indication of the frictional resistance imposed locally by the biofilm than u^* (Barton 2006). However, u^* is critical in the assessment of turbulent boundary layer profiles as a scaling factor (Wei et al. 2005). Consequently, both parameters have significance within the current study.

Based on the local frictional data it is evident that the biofilm incubated within the Re_D = 5.98x10^4 assay imparted the greatest frictional resistance. This was to be expected, due on the relative shear and mass transfer conditions within the respective assay, as discussed in Section 5.3. Consequently, the local frictional data is in agreement with the global data in terms of the relative impact of conditioning shear on biofilm development.

Dimensionless mean-velocity profiles are presented within Figure 5.18 and Figure 5.19 for the range of $0 < (y+\varepsilon) < R$. The profiles have been normalised with respect to U and D. For improved figure clarity the respective profiles have been grouped by time. In particular, the profiles are grouped with respect to the three stages of biofilm development, namely the conditioning stage, transitional development stage, and equilibrium stage. The influence of biofilm development over time on surface roughness is illustrated within Figure 5.18 and Figure 5.19 by a gradual progression away from the non-fouled data. In other words, the velocity defect increased with biofilm development. Walker et al. (2013), who incubated biofilms on stainless steel plates within a hydropower channel for between 2-52 weeks (at $\overline{U}$ ≈ 1.0 m/s) reported a similar observation. Figure 5.18 and Figure 5.19 show varying degrees of biofilm induced roughness within the respective assays. Typically, the biofilm cultivated within the Re_D = 5.98x10^4 assay had the greatest influence on surface roughness, as illustrated by the greatest shift away from the non-fouled data. This was to be expected, as the biofilm incubated within the Re_D = 5.98x10^4 assay imparted the greatest local and global roughness for the respective biofilms. Once the biofilms had reached a state of equilibrium the respective profiles appeared to collapse well on a single curve (as shown by Figure 5.18c and Figure 5.19c). However, there was slightly more separation between the mean-velocity profiles recorded within the Re_D = 1.00x10^5 assay.

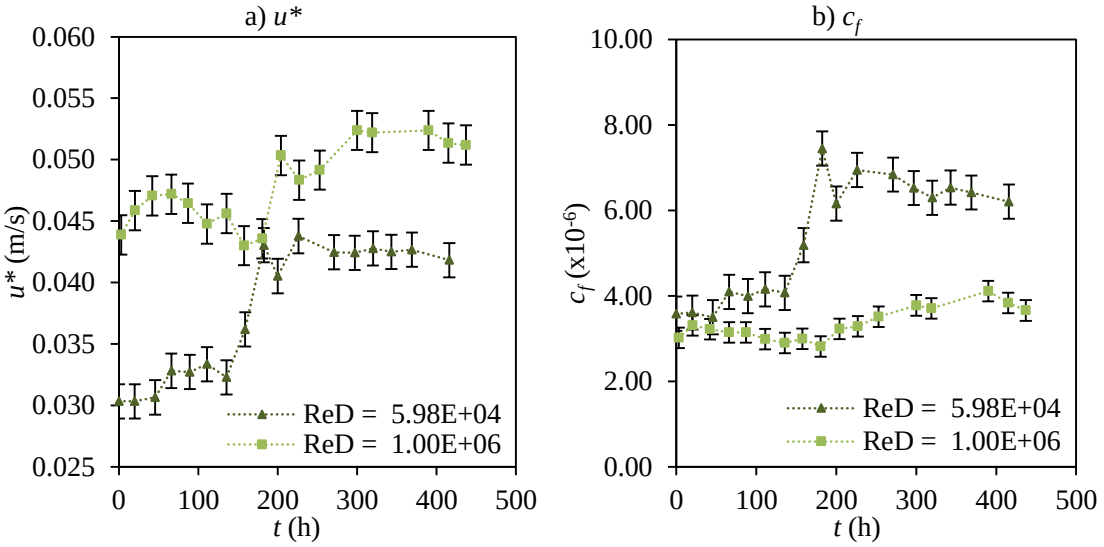

Figure 5.16 Influence of biofilm development over time on local values of a) u and b) c_f during the Re_D = 5.98x10^4 and Re_D = 1.00x10^5 assays.*

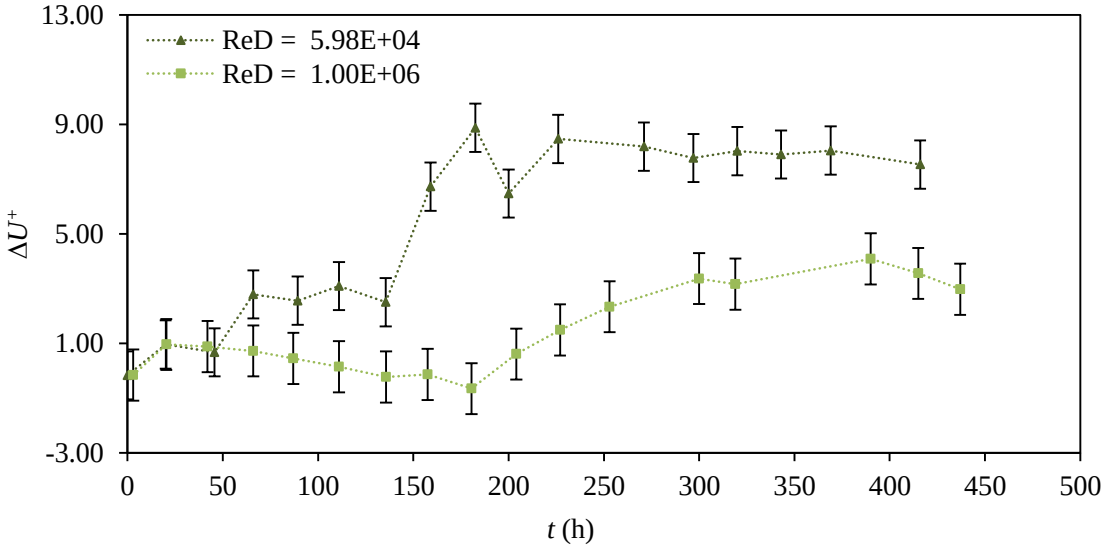

Figure 5.17 Influence of biofilm development over time on ΔU^+ during the Re_D = 5.98x10^4 and Re_D = 1.00x10^5 assays.

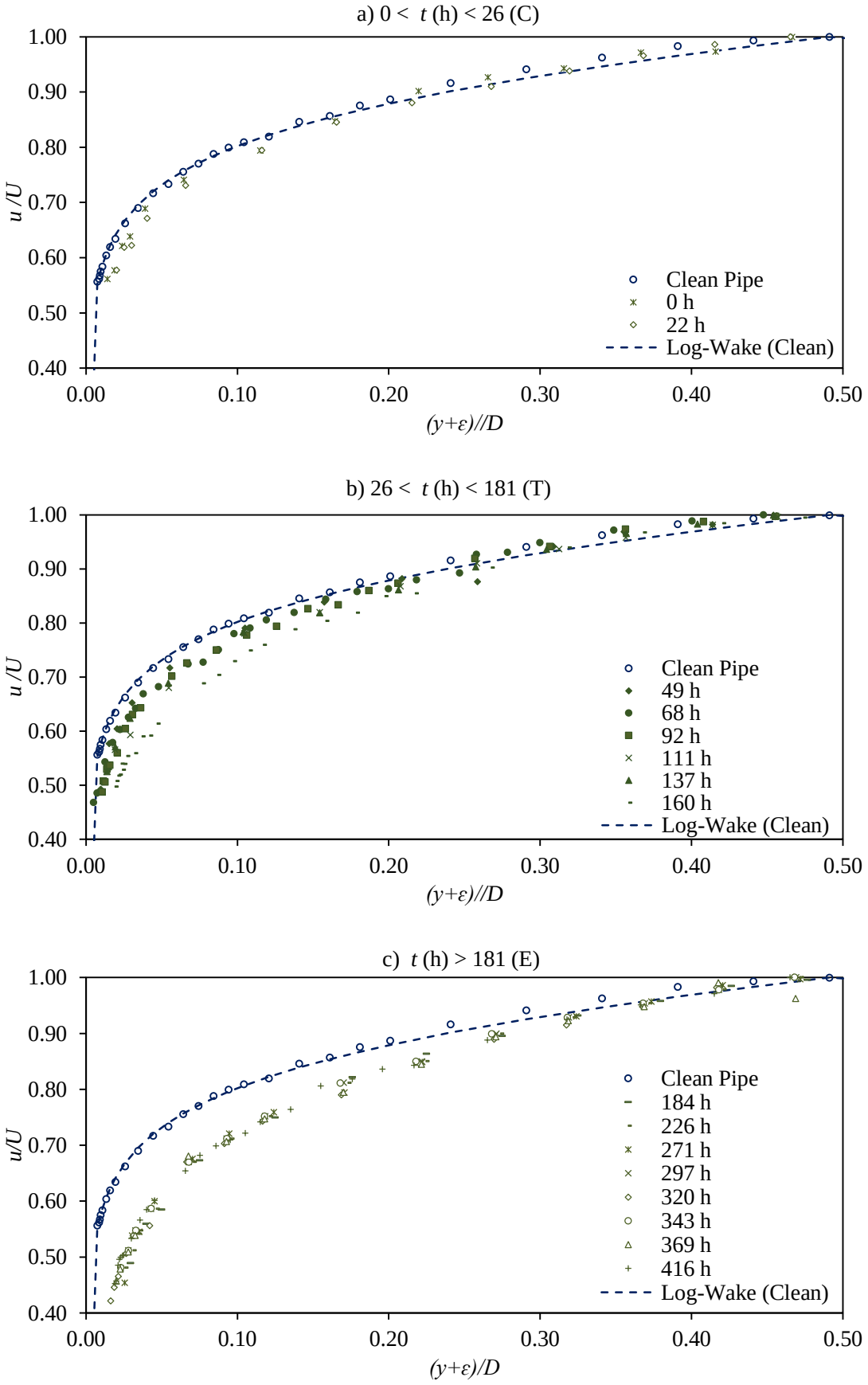

Figure 5.18 Normalised mean-velocity profiles for the Re_D = 5.98x10^4 assay at a) 0 < t (h) < 26 (Conditioning stage, C), b) 26 < t (h) < 181 (Transitional Stage, T), and c) t (h) > 181 (Equilibrium Stage, E).

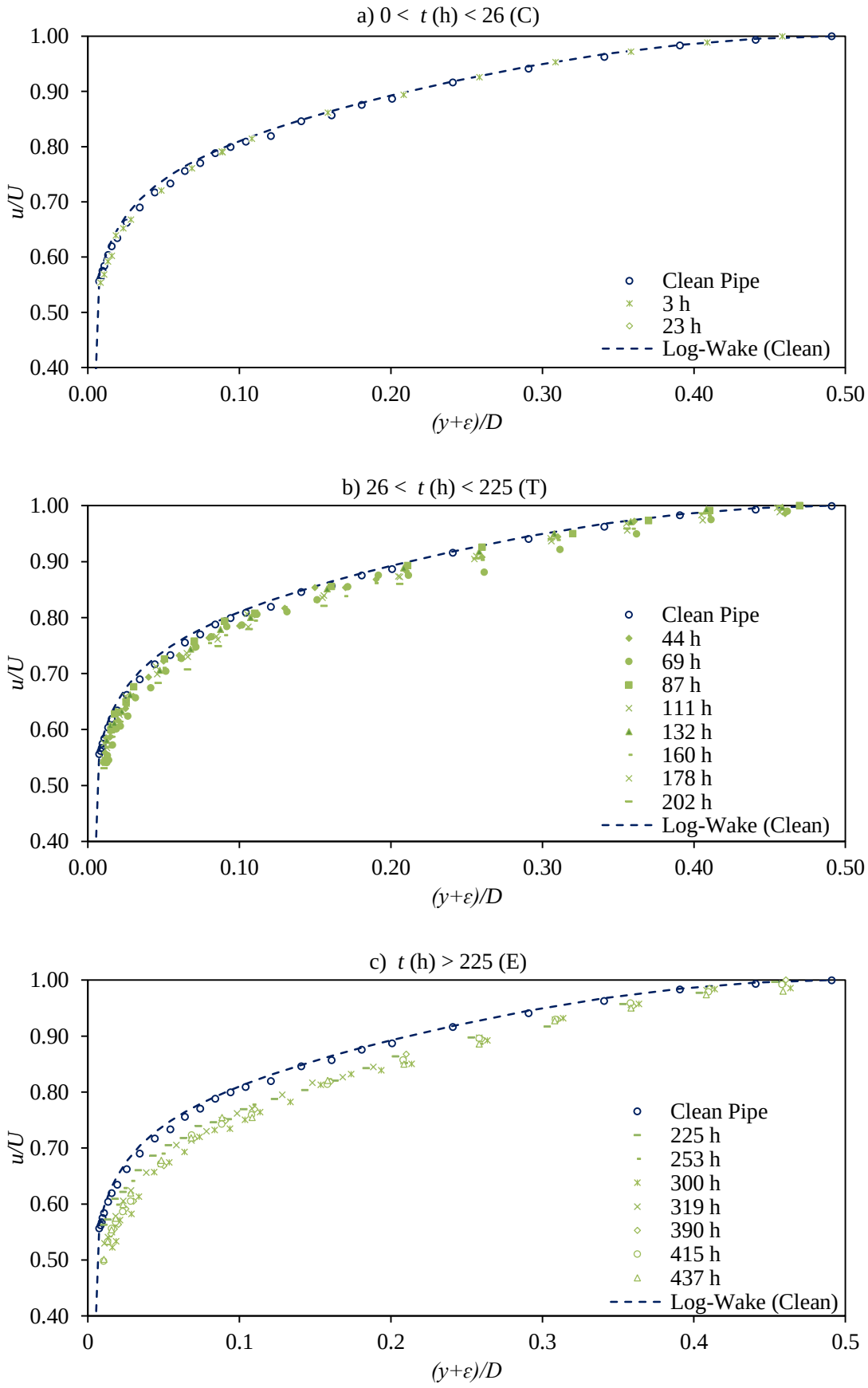

Figure 5.19 Normalised mean-velocity profiles for the Re_D = 1.00x10^5 assay at a) 0 < t (h) < 26 (Conditioning stage, C), b) 26 < t (h) < 181 (Transitional Stage, T), and c) t (h) > 181 (Equilibrium Stage, E).

5.6.1 Boundary layer parameters

The basic boundary layer parameters determined for each of the flow assays are presented within Table 5.3. The recorded wake strengths, which were determined by fitting the mean-velocity data to the Log-Wake Law (i.e. Equation 2.26) are also listed in Table 5.3. The parameters listed in Table 5.3 for the two flow assays represent the average values established after the respective biofilms had reached a state of equilibrium. The equivalent boundary layer parameters recorded for the non-fouled pipe are also presented within Table 5.3 as a reference.

Table 5.3 Boundary layer parameters for the fouled and non-fouled test pipe (the respective fouled pipe parameters refer to the average value recorded once the biofilms had reached a pseudo equilibrium state).

Surface	***Re_D***	***ε*** **(mm)**	***k_s*** **(mm)**	***ε^+***	***k_s^+***	***δ*** **(mm)**	***δ^**** **(mm)**	***θ*** **(mm)**	***H***	**Π**
Fouled	$6.07x10^4$	2.29	2.301	101.24	102.26	45.45	6.80	4.42	1.54	0.52
	$1.00x10^5$	1.06	0.206	11.06	56.37	44.98	6.36	4.37	1.46	0.71
Non-fouled	$6.10x10^4$	-	-	-	-	43.91	5.48	4.28	1.28	0.48
	$9.40x10^4$	-	-	-	-	42.50	5.33	4.25	1.26	0.41

It is evident from Table 5.3 that the values of Π for the fouled cases are considerably higher than the equivalent values for the non-fouled cases. In particular, the presence of the biofilm incubated within the Re_D = $1.00x10^5$ assay increased Π by approximately 73%. It was expected that Π would vary with roughness however, the values of Π for the fouled cases reported in the current study are typically far higher than the equivalent values reported by Walker et al. (2013) albeit, for biofilms incubated on plates within a hydropower channel. The increase in wake strength with fouling could therefore, be contributed to the nature of wastewater and as well as the biofilm.

Previous investigations have suggested that the presence of a biofilm can significantly alter boundary layer structure (Lewkowicz and Das 1986; Schultz and Swain 1999; Schultz 2000; Barton 2006; Andrewartha and Sargison 2011). Typically, a biofilm thickens the boundary layer above that of the background roughness. For instance, Lewkowicz and Das (1986) found that an artificial biofilm increased the δ by between 25-30%. A similar phenomenon was also reported by Schultz and Swain (1999) for actual biofilms. In particular, Schultz and Swain (1999) reported a statistically significant increase in H with fouling of between 7-13%. However, Schultz and Swain (1999) found δ was statistically unaffected a biofilm, although,

this was attributed to experimental uncertainties as opposed to the biofilm. The biofouled surfaces evaluated by Schultz and Swain (1999) consisted of a combination of filamentous and low-form gelatinous structures. The overall impact of long filamentous biofilms on boundary layer structure is known to be extreme. For instance, Schultz (2000) reported an increase in δ^* for up to 83% above the non-fouled values, as a direct result of long filament growth. However, the filaments observed by Schultz (2000) of between 58-71 mm were far longer than those observed within the current study, which rarely exceed 10 mm. Consequently, any change in boundary layer structure, with fouling reported within the current study would have been attributed to low-form gelatinous growth.

It is evident from Table 5.3 that biofilm growth did have an impact on the boundary layer structure. Furthermore, in all cases the presence of the biofilm actively thickened the boundary layer above the expected values. For instance, the average increase in H with fouling was 20% for the Re_D = 5.98x10^4 assay and 15% for the Re_D = 1.00x10^5 assay. Similarly, the average increase in δ^* with fouling was 24% for the Re_D = 5.98x10^4 assay and 19% for the Re_D = 1.00x10^5 assay. Large experimental uncertainties are common within boundary layer investigations. Consequently, to establish whether the reported differences were statistically significant within the experimental uncertainties, a single factor ANOVA was performed (α = 0.05). The ANOVAs on δ indicated that the differences between non-fouled and fouled conditions were statistically insignificant. Whereas, the ANOVAs on δ* and H indicated that the differences in boundary layer structure with and without fouling were statistically significant.

The observed increases in δ^* and H within the current study were typically higher than that reported by Schultz and Swain (1999). However, Schultz and Swain (1999) investigated freshwater biofilms incubated within a lagoon, the ecology of which is naturally very different to a pipe, and these differences would be reflected in the resultant biofilms. Furthermore, the physico-chemical characteristics of wastewater also differ significantly from freshwater, which could have also contributed to the observed disparities between the studies.

5.6.2 Inner region (y^+< 300)

Figure 5.20 and Figure 5.21 present the normalised mean-velocity profiles measured within the Re_D = 5.98x10^4 and Re_D = 1.00x10^5 assays, respectively. These profiles were normalised with respect to u*, and therefore, are in the form of Law of the Wall plots. The effect of roughness is typically represented on a Law of the Wall plot by ΔU^+ and a downward shift in the mean-velocity profile relative to the Log-Law (Flack and Schultz 2010).

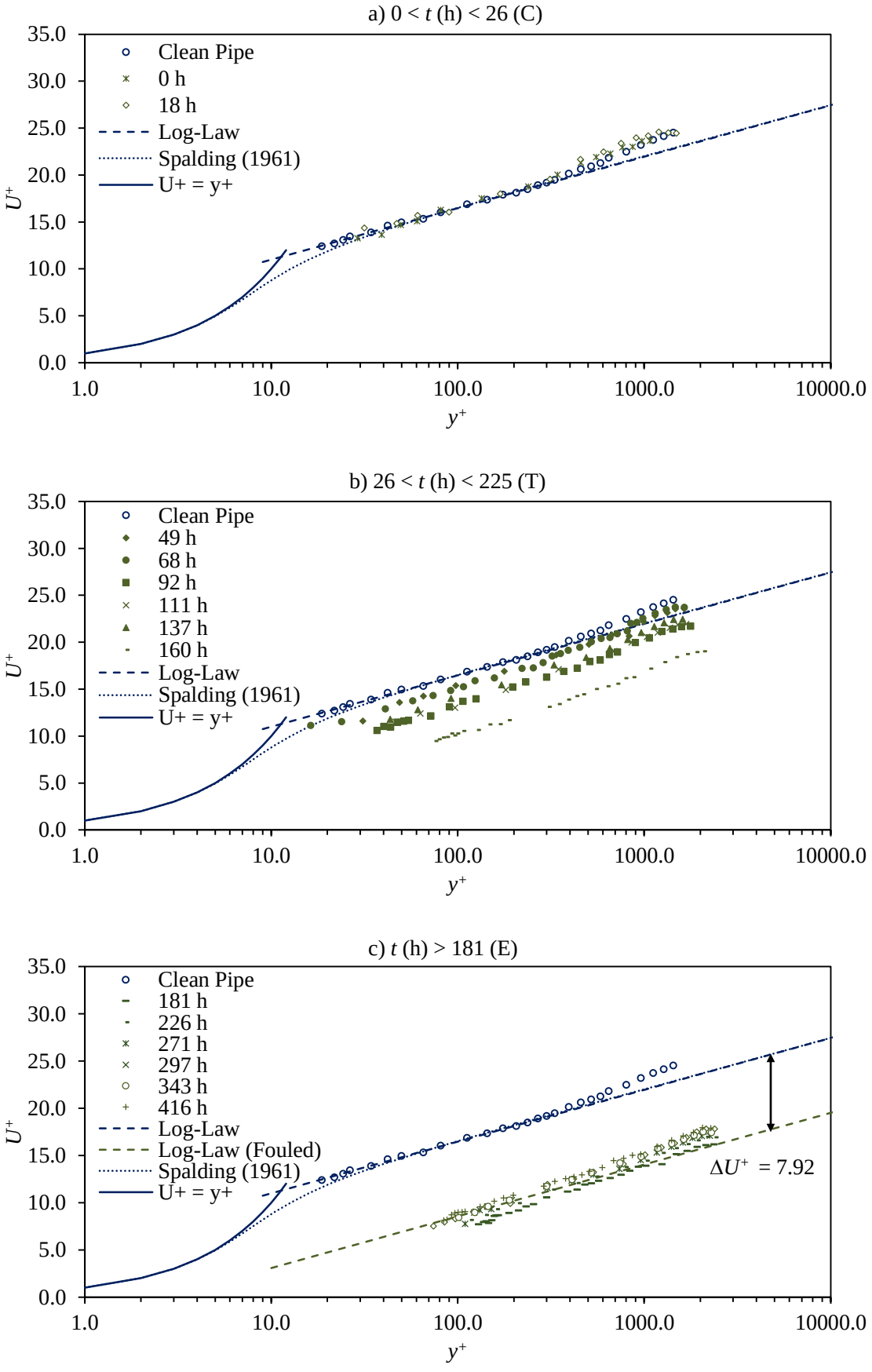

Figure 5.20 Normalised mean-velocity profiles for the Re_D = 5.98x10^4 assay at a) 0 < t (h) < 26 (Conditioning stage, C), b) 26 < t (h) < 181 (Transitional Stage, T), and c) t (h) > 181 (Equilibrium Stage, E) time intervals.

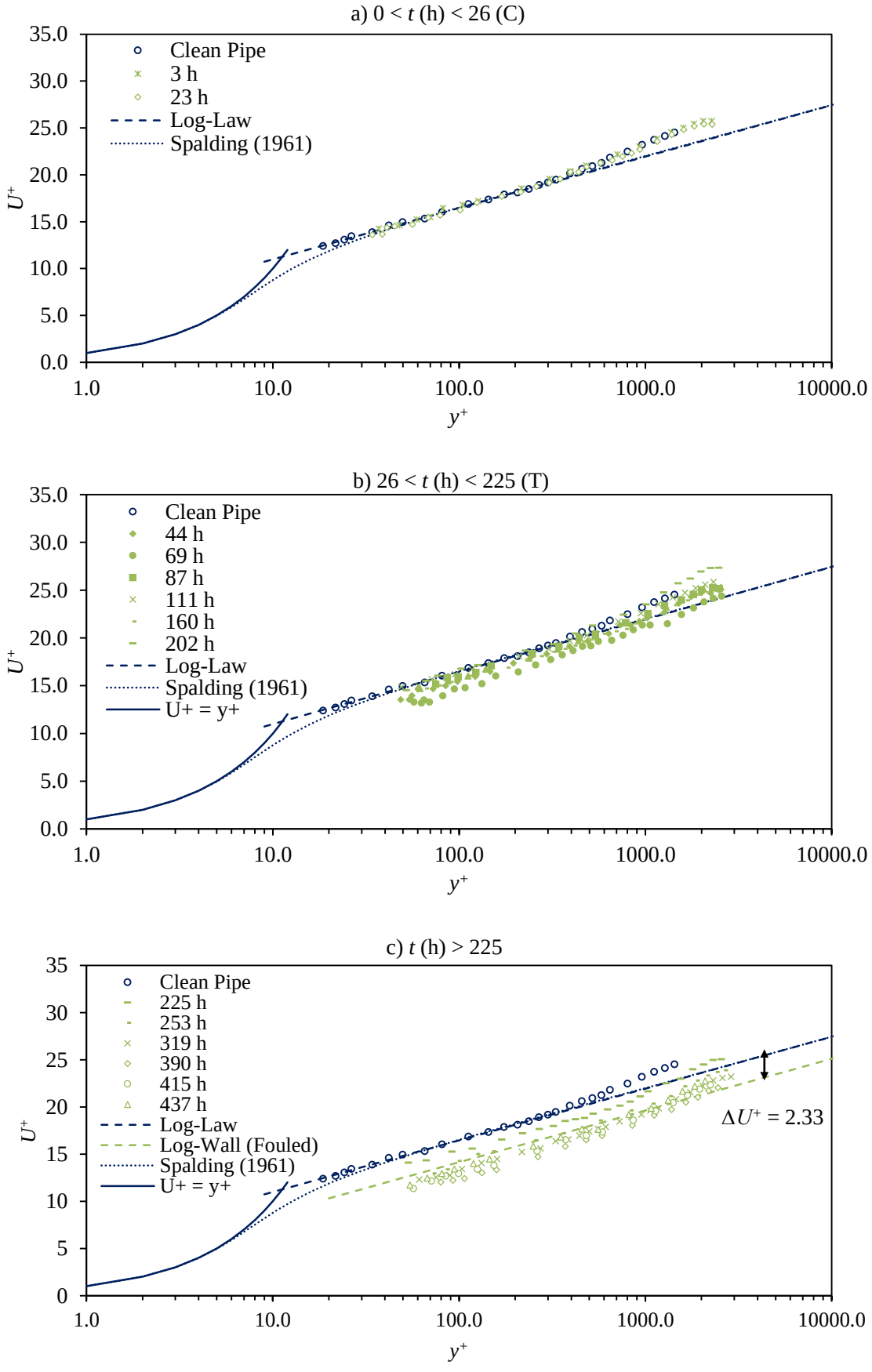

Figure 5.21 Normalised mean-velocity profiles for the Re_D = 1.00x10^5 assay at a) 0 < t (h) < 26 (Conditioning stage, C), b) 26 < t (h) < 181 (Transitional Stage, T), and c) t (h) > 181 (Equilibrium Stage, E) time intervals.

A downward shift in the respective mean-velocity profiles is evident within Figure 5.20 and Figure 5.21. The observed shift of the profiles increased with time and is therefore, a function of the biofilms development. The impact that biofilm development had on the measured velocity profiles is quantitatively illustrated by Figure 5.17, which presents the established roughness functions over time. The roughness functions recorded within the $Re_D = 5.98 \times 10^4$ and $Re_D = 1.00 \times 10^5$ assays plateaued at 7.92 ± 0.67 and 2.33 ± 1.56, respectively. Similar observations have been reported within the literature for both freshwater and marine biofilms (Schultz and Swain 1999; Schultz 2000; Barton 2006; Andrewartha 2010; Walker et al. 2013). For instance, Walker et al. (2013) observed that the presence of a freshwater biofilm on a stainless steel plate caused a shift in the velocity profile equal to that expected for an increase in roughness.

The influence of biofilm development on the local roughness (i.e. k_s) is shown in Figure 5.22, which presents the local k_s values in both traditional and non-dimensional forms. As expected, the biofilms induced an increase in local roughness. The local values of k_s imposed by the biofilms incubated within the $Re_D = 5.98 \times 10^4$ and $Re_D = 1.00 \times 10^5$ assays plateaued at 2.301 ± 0.550 mm and 0.206 ± 0.099 mm, respectively. It is also evident from Figure 5.22 that the increase in local k_s within the $Re_D = 1.00 \times 10^5$ assay caused the local flow conditions to progress from being hydraulically smooth to transitionally rough. Alternatively, the local increases in k_s over time within the $Re_D = 5.98 \times 10^4$ assay caused the local flow conditions to become fully rough. Therefore, the localised conditions within the $Re_D = 5.98 \times 10^4$ assay differed considerably from the global conditions observed within the assay (see Section 5.3.1). Differences in local and global conditions were to be expected, and based upon the observations outlined in Section 5.3.1 were especially expected within the $Re_D = 5.98 \times 10^4$ assay, due to biofilms highly irregular roughness distribution. Schultz and Swain (2000) suggested that natural variations in biofilm coverage would explain any potential differences in local frictional data recorded at different locations.

The negligible variation in space-averaged conditions observed within the $Re_D = 1.00 \times 10^5$ assay (see Section 5.3.1) suggested a uniform roughness distribution within the respective assay, and therefore, the local and global conditions would be of equivalent magnitude. The average values of the equilibrium stage k_s measured globally (using the SFM) and locally were 0.223 ± 0.027 mm and 0.206 ± 0.099 mm, respectively.

The variations between local and global roughness for the $Re_D = 5.98 \times 10^4$ and $Re_D = 1.00 \times 10^5$ assays are presented within Figure 5.23.

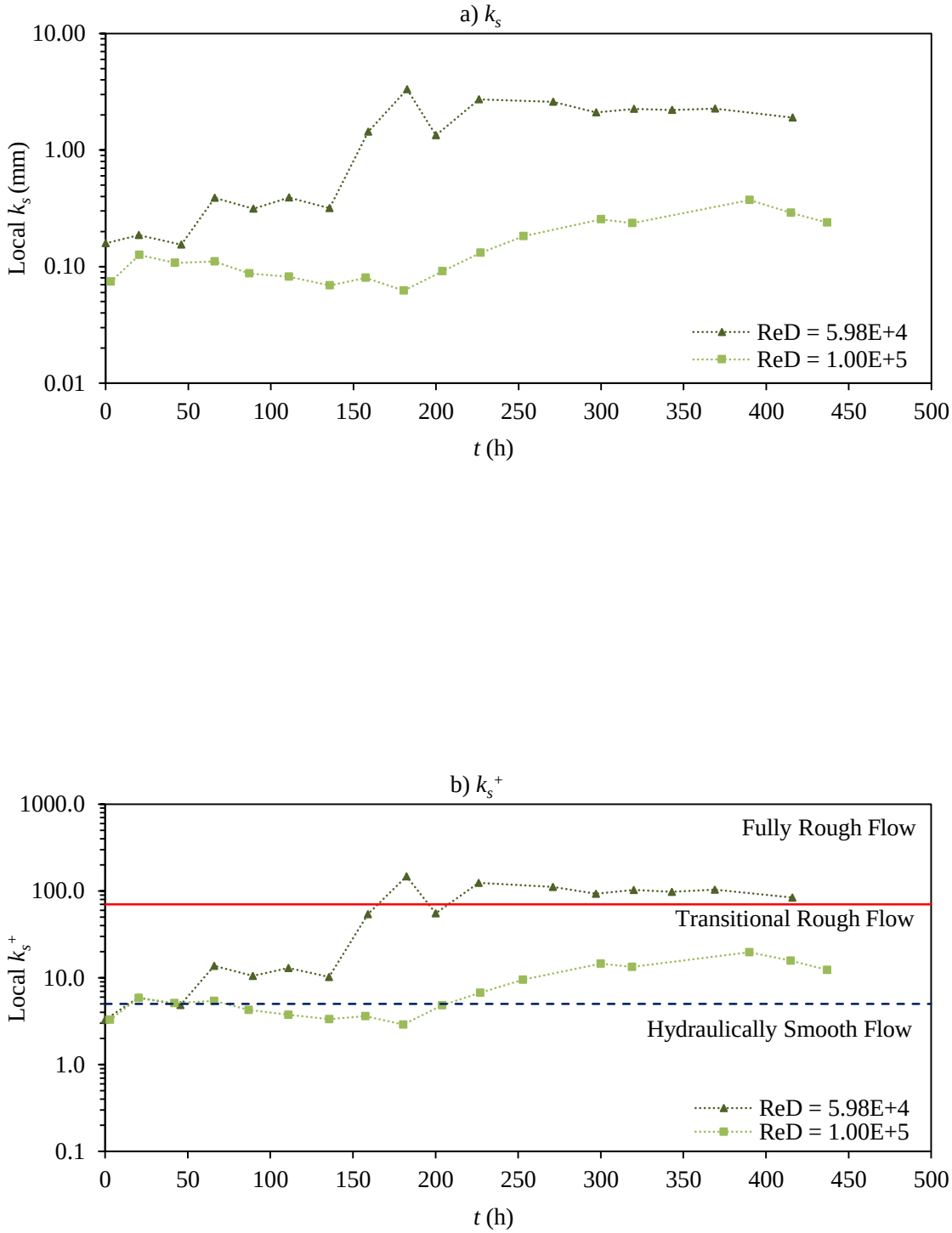

Figure 5.22 Influence of biofilm development over time on a) k_s and b) k_s^+ for Re_D = 5.98x10^4 and Re_D = 1.00x10^5 assays (highlighting the hydraulically smooth, transitional and fully rough flow).

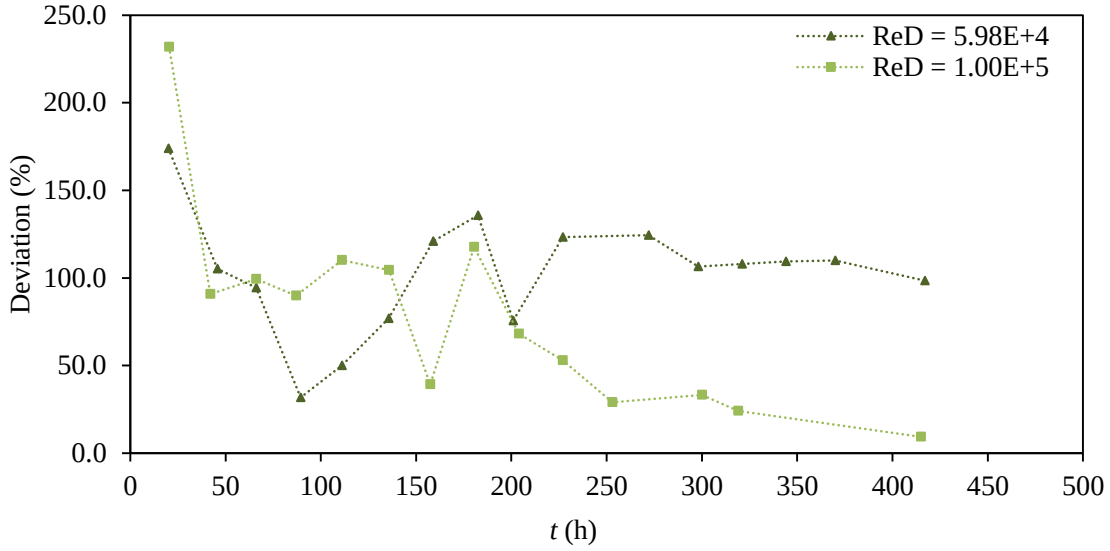

Figure 5.23 Deviation between local and global roughness (k_s) against time for the Re_D = 5.98x10^4 and Re_D =1.00x10^5 assays.

5.6.3 Outer region ($50 < y^+ < R^+$)

The mean-velocity profiles recorded within the Re_D = 5.98x10^4 and Re_D = 1.00x10^5 assays are presented in the form of velocity defect plots by Figure 5.24 and Figure 5.25, respectively. To highlight any potential differences more clearly the respective profiles, which are grouped by time are presented in both traditional and semi-logarithmic forms.It is evident from Figure 5.24 and Figure 5.25 that the respective non-fouled and fouled data seemingly collapse well onto one curve in the outer region of the boundary layer. This indicates that the presence of the biofilm had no affect on the mean-velocity structure in the outer flow region, and as a consequence, the data supports Townsend's Wall Similarity Hypothesis for biofouled surfaces. In other words the increase in roughness induced by the biofilm only manifested itself in the outer region of the boundary layer in terms of changing τ_w. Andrewartha (2010) and Walker et al. (2013) also observed good collapse within the outer region of velocity defect plots recorded over freshwater low-form gelatinous biofilms.

The data also shows reasonable collapse in the near wall region of the boundary layer, which was also observed by Andrewartha (2010) for freshwater biofilms.

Figure 5.26 illustrates that the fouled data had a strong agreement with the Log-Wake Law (i.e. Equation 2.26), which was used to determine the wake strengths listed in Table 5.3.

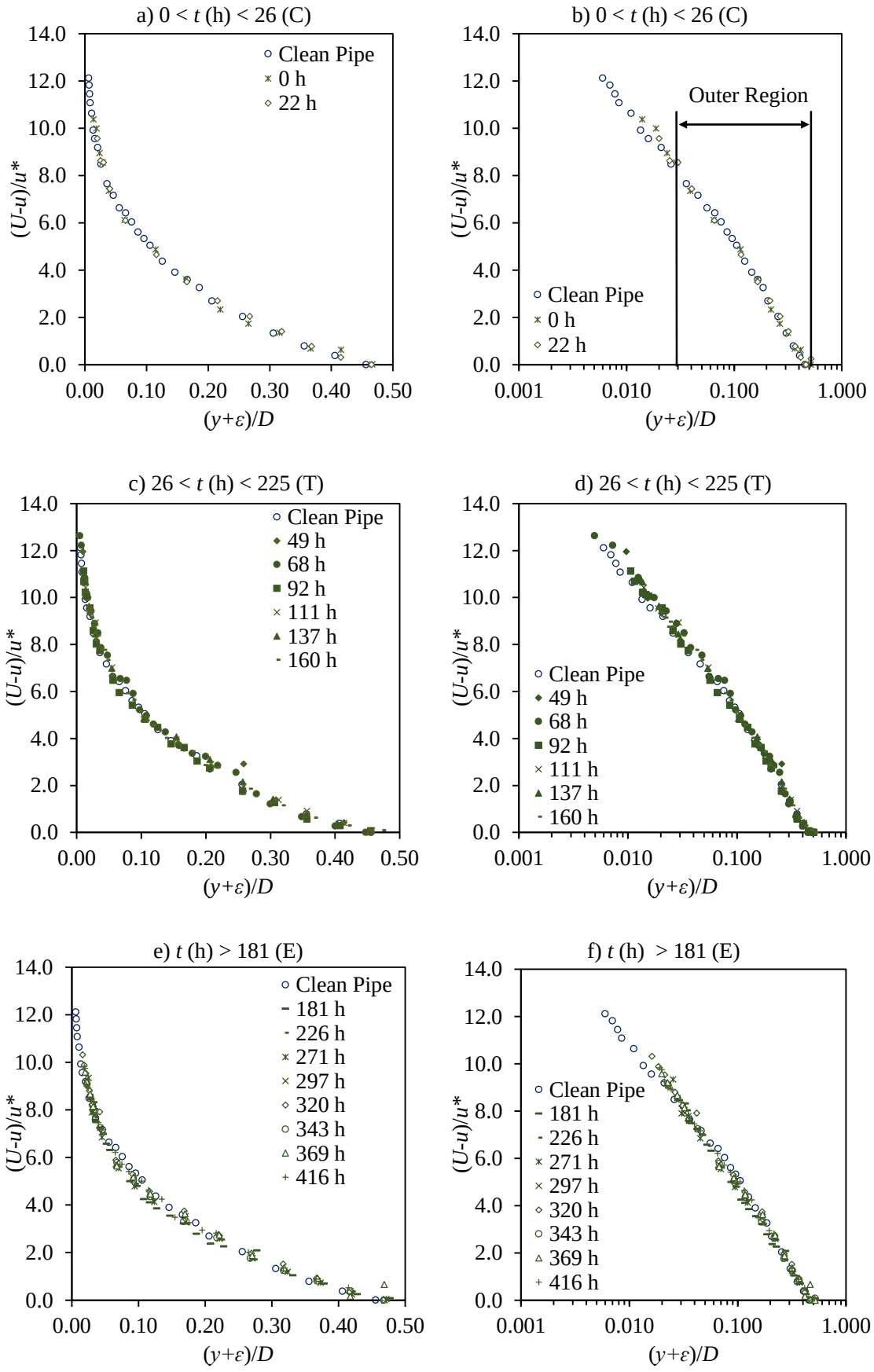

Figure 5.24 Velocity defect profiles in both traditional and semi-log forms for the Re_D = 5.98x10^4 assay at a)-b) 0 < t (h) < 26 (Conditioning stage, C), c)-d) 26 < t (h) < 181 (Transitional Stage, T), and e)-f) t (h) > 181 (Equilibrium Stage, E).

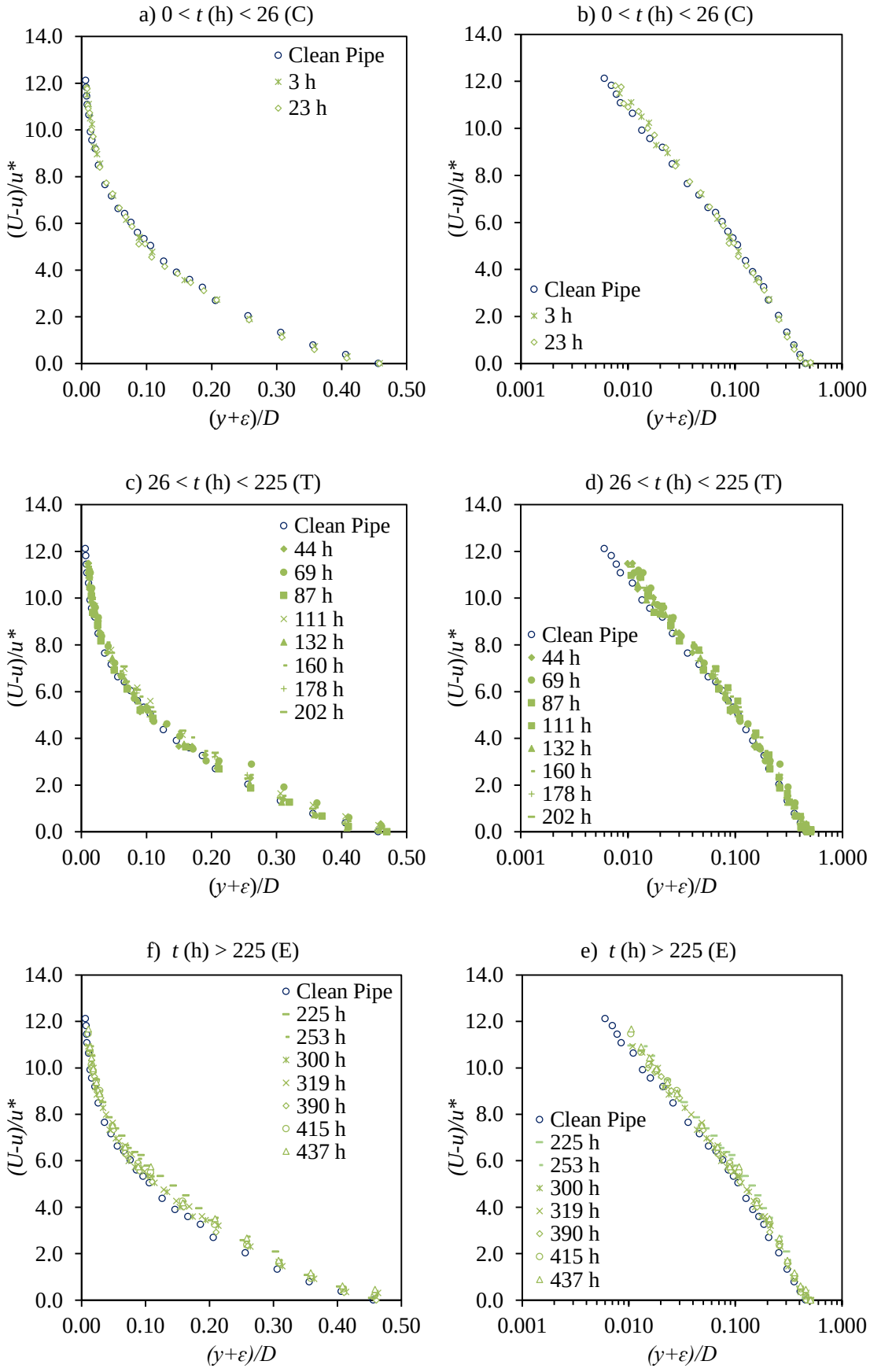

Figure 5.25 Velocity defect profiles in both traditional and semi-log forms for the Re_D = 1.00x10^5 assay at a)-b) 0 < t (h) < 26 (Conditioning stage, C), c)-d) 26 < t (h) < 181 (Transitional Stage, T), and e)-f) t (h) > 181 (Equilibrium Stage, E).

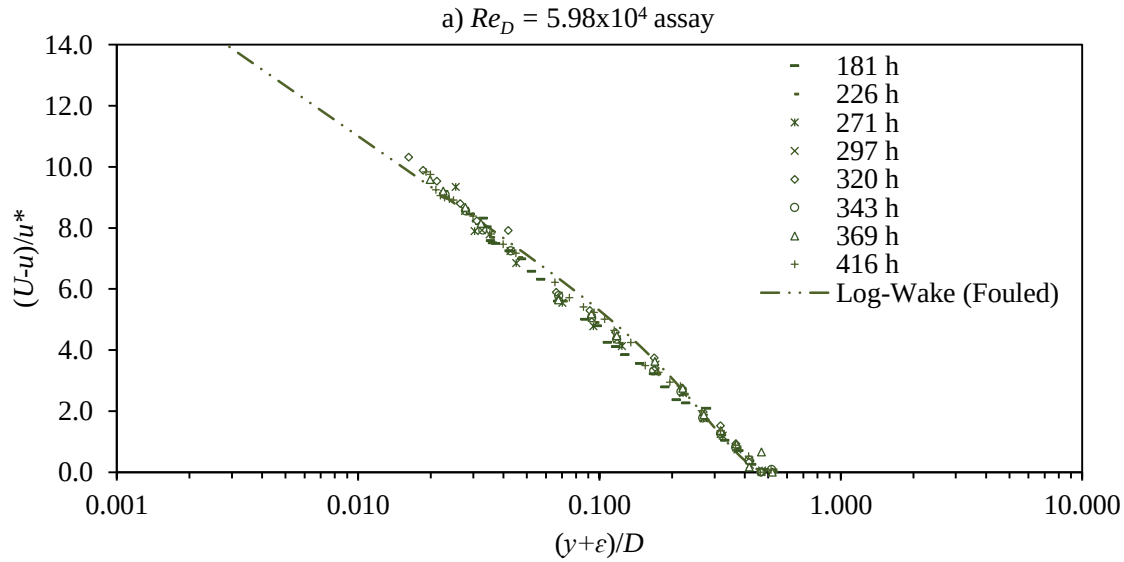

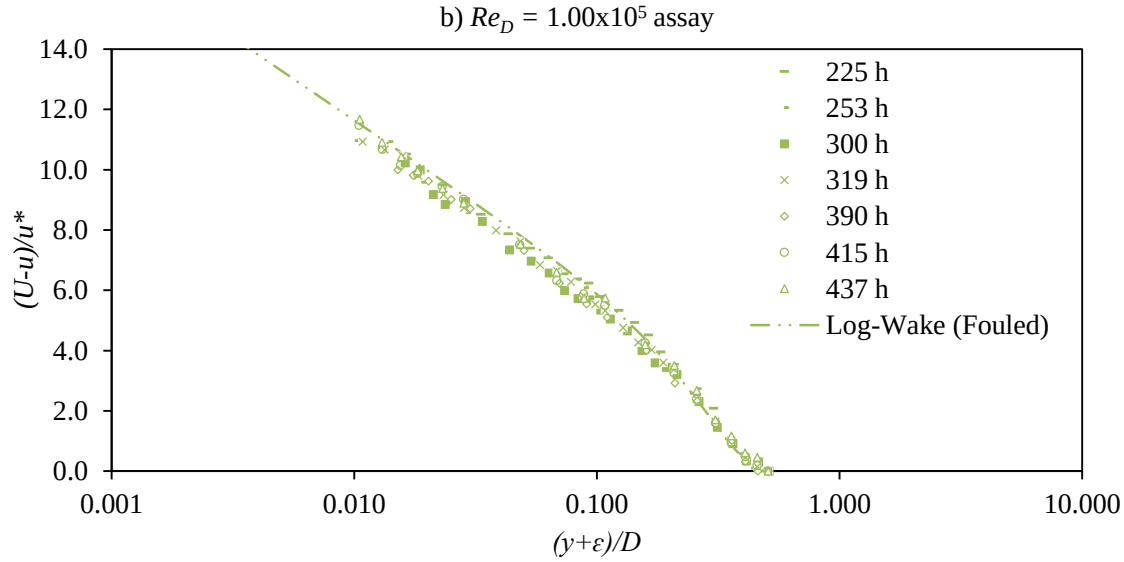

Figure 5.26 Mean-velocity defect profiles recorded during the equilibrium stage of a) the Re_D = 5.98x10^4 and Re_D = 1.00x10^5 assays. Highlighting the agreement between the respective profiles and the Log-Wake Law.

5.6.4 Roughness plots

Figure 5.27a presents a plot of ΔU^+ against k_s^+ for the combined data recorded within the two flow assays. The experimentally determined frictional data was in agreement with the Rough Wall Log-Law asymptote. This was to be expected, as the frictional data was derived from Log-Law principles. The frictional data was scaled by ε in Figure 5.27b and despite, the large scatter, a trend of increasing ΔU^+ with increasing ε^+ is evident. The roughness function can be related to ε^+ using (R^2 = 0.7):

$$\Delta U^+ = \frac{2.57}{\kappa}\ln\left(\frac{\varepsilon u^*}{\nu}\right) - 21.28 \qquad \textit{Equation 5.1}$$

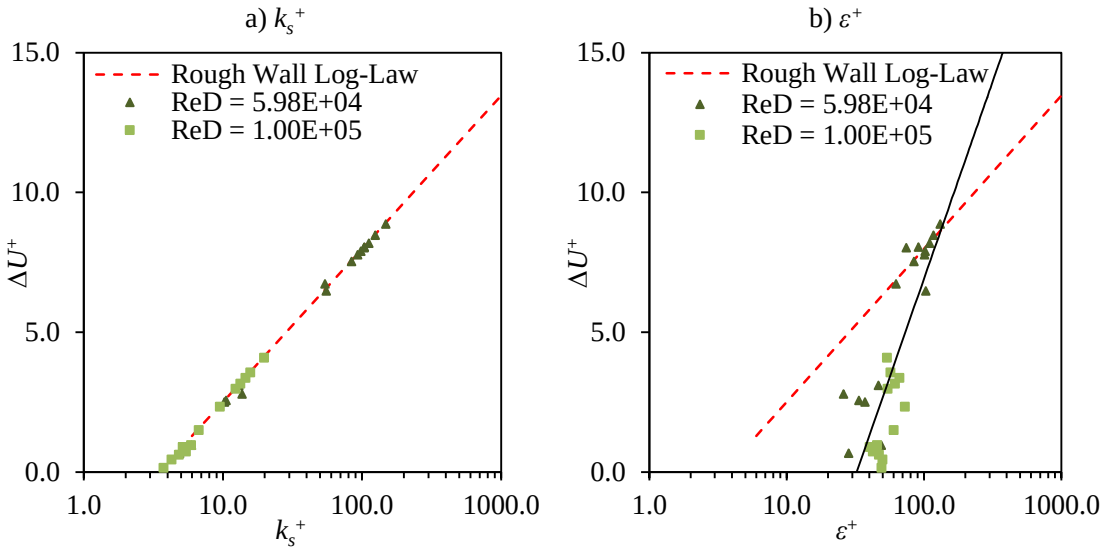

Figure 5.27 ΔU^+ against a) k_s^+ and b) ε^+ (for the Re_D = 5.98x10^4 and Re_D = 1.00x10^5 assays).

Detailed topographic measurements of the fouled pipes were not recorded within the current study, and therefore, other roughness parameters, such as k and k_{rms} could not be evaluated as possible scaling lengths. Nevertheless, it is expected that a single scaling parameter would not be able to adequately define the complex surface dynamics of a biofilm.

Mean-velocity profiles, which have been scaled by local k_s are presented in Figure 5.28 and Figure 5.29 in the form of roughness plots. The increase in frictional resistance imposed by the biofilms is illustrated by a progression down the Rough Wall Log-Law (i.e. Equation 2.32) in the respective plots. As expected, the biofilm incubated within the Re_D = 5.98x10^4 assay showed the greatest downward progression down.

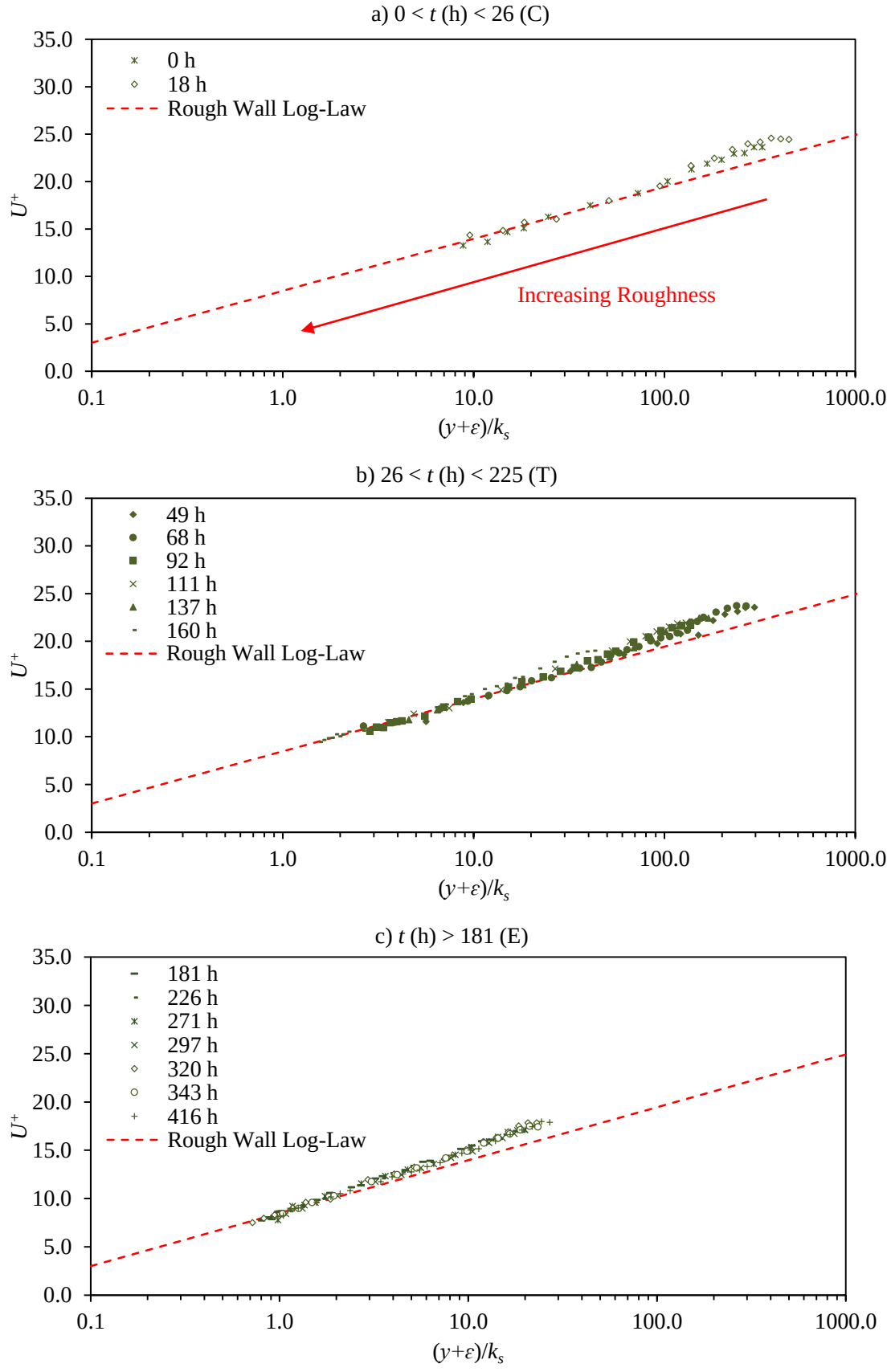

Figure 5.28 Mean-velocity profiles normalised by k_s for the Re_D = 5.98x10^5 assay at a) 0 < t (h) < 26 (Conditioning stage, C), b) 26 < t (h) < 181 (Transitional Stage, T), and c) t (h) > 181 (Equilibrium Stage, E).

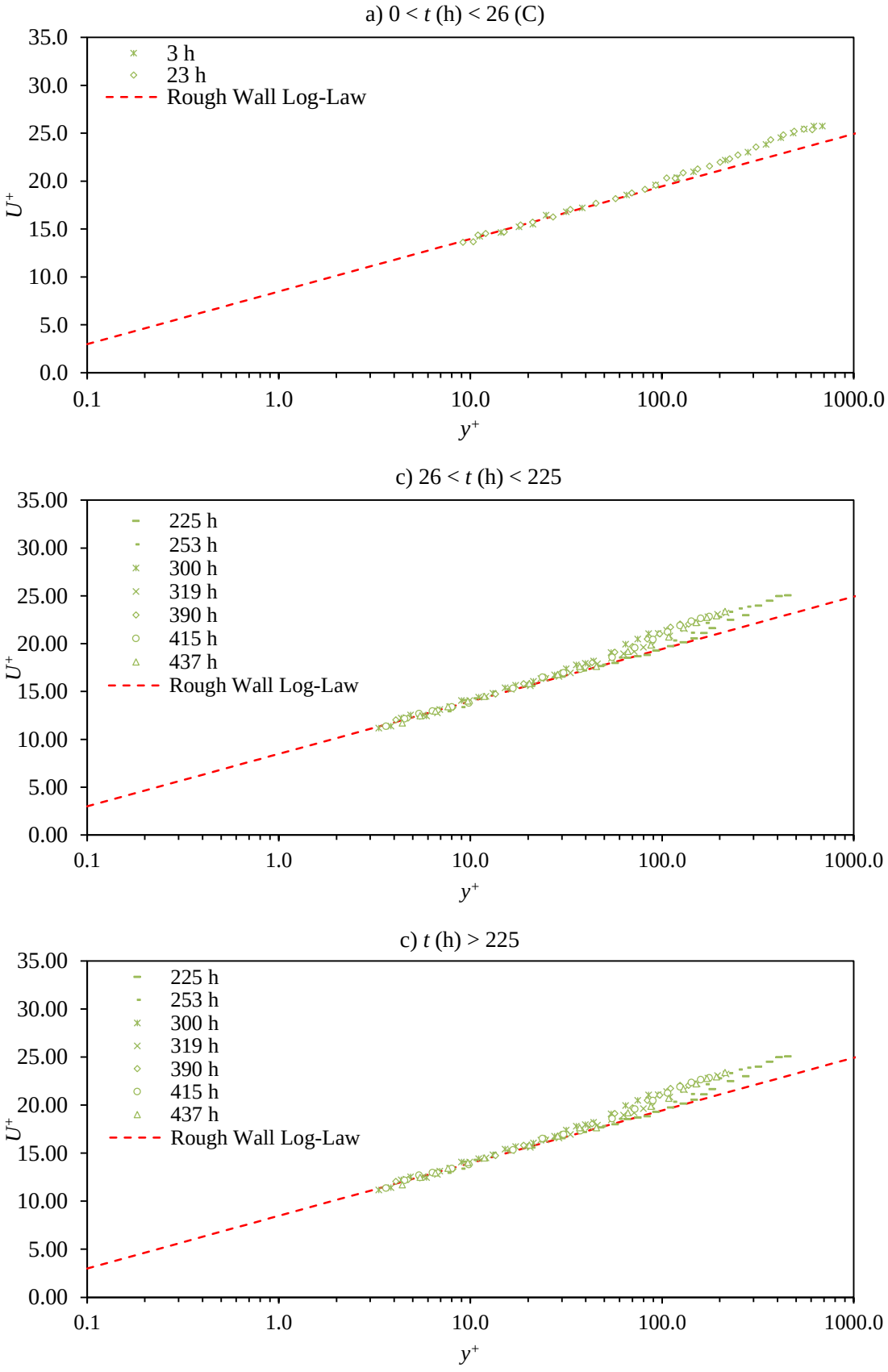

Figure 5.29 Mean-velocity profiles normalised by k_s for the Re_D = 1.00x10^5 assay at a) 0 < t (h) < 26 (Conditioning stage, C), b) 26 < t (h) < 181 (Transitional Stage, T), and c) t (h) > 181 (Equilibrium Stage, E).

5.7 Non-universal Log-Law for biofouled surfaces

5.7.1 Implications on local measurements

The highly dynamic nature of a biofilm brings the underlying assumptions of boundary layer equilibrium, which is a vital aspect of most wall similarity techniques into question (Schultz and Swain 1999).

Townsend's Wall Similarity Hypothesis was first introduced in Chapter 2. The hypothesis states that providing that the surface roughness is small compared to D he boundary layer outside the roughness sublayer (which typically, taken as 3-5k), for sufficiently high Re is not affected by the characteristics of the surface or viscosity, except for their role in defining u^*. Consequently, this implies that all roughness effects are restricted to the near vicinity of the wall (i.e. within the roughness sublayer) and that the boundary layer profile outside this region should collapse for all surface types when suitably scaled. Jimenez, (2004) proposed that wall similarity exists providing that there is no sufficient scale separation between the roughness height and the outer length scale (taken as D within the current study). Typical thresholds for wall similarity are taken as $D/k \geq 40$ (Jimenez 2004) or $D/k_s \geq 40$ (Flack et al. 2005). As expected, the scale separation for the non-fouled pipe was well within the limits for wall similarity. Consequently, wall similarity applied to the non-fouled pipe within the current study. The velocity defect plots presented in Figure 4.12 (in Section 4.4) for the non-fouled pipe, further support the existence of wall similarity. With fouling the scale separation found within the current study was at worst $D/k_s < 43.5$ (i.e. for $k_s = 2.30$ mm, see Table 5.2). This figure is similar to the maximum scale separation reported by Andrewartha (2010) for low-form gelatinous biofilms of $\delta/k_s < 42.3$. The maximum scale separation recorded within the current study suggest that wall similarity may not have been valid for all the biofouled surfaces. However, the observed collapses of the velocity defect plots presented in Figure 5.24 and Figure 5.25 (in Section 5.6.3) refute this claim. The velocity defect plots presented in Figure 5.24 and Figure 5.25 were scaled by values of u^* derived from mean-velocity data using the PL Method. Wall similarity techniques, such as the PL Method have their limitations particularly, when applied to biofouled surfaces. These limitations are discussed herein.

The problem of using wall similarity techniques to determine u^* for rough walls is that ε is not known, and as a consequence, it must be found by fitting the mean-velcoity data to the universal Log-Law based upon a predefined value of κ. Therefore, wall similarity techniques, such as the PL Method assume the existence of a universal Log-Law, which in recent years has been questioned, as discussed in Section 4.4.4. In particular, there is debate as to whether the Log-Law constants of κ and B are truly independent of Re in the classical theory. Within

the current study the existence of a universal Log-Law was confirmed for the non-fouled pipe. Furthermore, under non-fouled conditions κ was found to be independent of *Re* and equal to 0.42. Nevertheless, there is compelling evidence to suggest that this is not the case for biofouled surfaces (Lambert et al. 2009; Perkins et al. 2013; 2014). In particular, it has been reported that κ and *B* for biofouled surfaces are dependent on *Re* and are typically lower than the conventionally accepted values. However, any natural dependences that the Log-Law or its constants may have with *Re*, will be masked through the use of conventional wall similarity techniques. As the use of such techniques to compute ε and u^* results in an artificial collapse of the data onto a predefined Log-Law relationship. Given that values of u^* derived from wall similarity techniques are known to be highly sensitive to κ (Wei et al. 2005) the implications of non-universal constants could be considerable. The influence of κ on u^* was highlighted by the partial sensitivity analysis undertaken in Section 4.6, which found that an error in κ of +0.05 yielded an error u^* of +9%. The values of k_s determined from mean-velocity data are also heavily influenced by κ and *B*, as shown by Equation 4.17.

Consequently, as κ and *B* were likely to have been lower than the applied values it is suggested, that the values of u^* and k_S determined from the mean-velocity data overestimated the actual conditions. Furthermore, the frictional parameters determined from u^*, such as c_f will also be overestimated. The observed differences between the local and global conditions outlined in Section 5.6 for the $Re_D = 5.98\text{x}10^4$ assay would at first glance support this claim. As the frictional data determined within the $Re_D = 5.98\text{x}10^4$ assay using the PL Method (i.e. local data) was typically far higher than the equivalent data determined using the PG Method (i.e. global data). In particular, the average equilibrium state k_s determined using the PL Method was at least 3.6 times greater than the average equilibrium state k_s determined using the PG Methods. Similarly, the average equilibrium state value of u^* determined using the PL Method was typically 12% higher than the equivalent value established using the PG Methods.

Potential errors in ε could also have influenced the agreement between the values of k_s and u^*determined both locally and globally using the respective methods. Values of k_s determined from mean-velocity data have also been documented to be highly sensitive to ε (Barton 2006). In addition, some of the reported variations may have resulted from the PL Method itself (Musker 1990; Schultz and Swain 1999; Candires 2001). The PL Method, like most wall similarity techniques introduces two additional unknowns (i.e. ΔU^+ and ε) into the analysis of a rough boundary. While the additional parameters produce an improved Log-Law fit in a statistical sense, they also lead to increased errors (Schultz and Swain 1999). Even the evaluation of traditional surfaces, which have regular and fixed roughness distributions can

be difficult using wall similarity techniques (Candires 2001; Walker 2014). This was highlighted within the current study in Section 5.3.3, which evaluated the frictional data determined from several commonly used wall similarity techniques (including, the PL Method) against the equivalent data established globally from the PG Methods. It should be noted that, this evaluation was undertaken under non-fouled conditions and as a result, the global and local frictional data should be equivalent. Despite, the PL Method producing the most consistent results of the assessed techniques, deviations between the frictional data determined locally and globally were evident. The maximum disparity in $u^*$of ±3.96% was determined between the PL and PG Methods. However, it should be stated that a disparity of ±3.96% is within the experimental uncertainties (see Table 3.5).

Biofilms will typically have highly heterogeneous roughness distributions, and therefore, the observed disparities between the respective datasets could be explained by natural variations in roughness along the pipeline. The significant variations observed in space-averaged roughness within the Re_D = 5.98x10^4 assay highlighted the potential irregularity of the roughness distribution within the respective assay. However, biofilms with homogeneous roughness distributions were also reported within the current study. In particular, it was found that the shear conditioning within the Re_D = 1.00x10^5 assay fostered a seemingly uniformly rough biofilm. As a consequence, the frictional data recorded locally and globally within the respective assay were in reasonable agreement, at least as far as experimental uncertainties were concerned. The variations in space-averaged roughness were also found to be negligible within the Re_D = 1.00x10^5 assay as a result of the biofilm's uniformity. In such situations, the underlying assumptions of boundary layer equilibrium are less in doubt. Furthermore, the agreement between the frictional data determined from the PL and PG Methods refutes the argument for revised Log-Law constants for biofouled surfaces.

It is generally suggested that a method independent from mean-velocity should be used in conjunction with wall similarity techniques to determine the frictional resistance of a surface (Schultz and Swain 1999; Candires 2001; Walker et al. 2013). However, typical independent methods, such as a floating element force balance (Barton 2006, Barton et al. 2005; 2007; Andrewartha 2010; Walker et al. 2013) and pressure taps (Lambert et al. 2008; 2009; Perkins et al. 2013; 2014) would generally only give an accurate indication of the biofilm's global frictional resistance, which has its limitations when applied locally, particularly for biofilms heterogenetic roughness distributions.

5.7.2 Implications on global measurements

The von Kármán constant is an integral part of the traditional C-W equation (Matthew 1990) and therefore, the potential non-universality of it will naturally have an impact on the values of k_s established using the traditional C-W equation (where κ is taken as ≈0.40). It is expected, that if κ is non-universal and lower than the traditionally accepted value then the traditional C-W equation will overestimate k_s values.The implications of these potential disparities on Q predictions was illustrated by Figure 2.12 (in Section 2.6.3). Typically, if k_s is overestimated then Q is overestimated. This could have an influence on pipe size selection and generally leads to oversizing, which could add unnecessarily to the cost for an intended project, as discussed in Chapter 2.

5.7.3 Determining κ and B for biofouled surfaces

In order to establish whether or not revised constants are required for biofouled surfaces, the mean-velocity data was evaluated using the linear regression approach outlined in Section 4.6. Modified B constants were determined using a similar regression method to that outlined for the C constant in Section 4.6; whereby, a linear regression line of best fit was fitted to the Log-Law region of a U^+ against $\ln((y+\varepsilon)/k_s)$ plot. The y-axis intercept of the regression line is equal to B.

The local frictional data determined from the PL Method could not be used to establish the revised constants. Consequently, with no other means of establishing the local $u^*$and k_s, the global values determined from the PG Methods were used. In particular, the frictional data determined between P_3 and P_5 were used in conjunction with those determined for the whole system (derived from the system's PG using the SFM). It should be noted, that the global k_s values used initially to derive B were calculated using the traditional C-W equation and therefore, a universal value of κ = 0.42.

The products of this evaluation had a natural bias towards the global conditions, and should be viewed with caution. This is particularly relevant for the Re_D = 5.98x10^4 assay given the irregular nature of the respective assay's biofilm.

The uniquely derived values of κ and B determined from the respective mean-velocity data recorded within the two flow assays, are presented in Appendix C.3 in Table C.9. New values of ε and ΔU^+ were also established from the global u^* datasets (see Appendix C.3, Table C.10 and Table C.11). The location of the Log-Law region within the boundary layer was unaffected by presence of the biofilm, and was taken as $50 < y^+ < 0.18R^+$, as shown for example by Figure 5.30, which presents the values of Ξ determined from the mean-velocity data recorded within the Re_D = 5.98x10^4 assay.

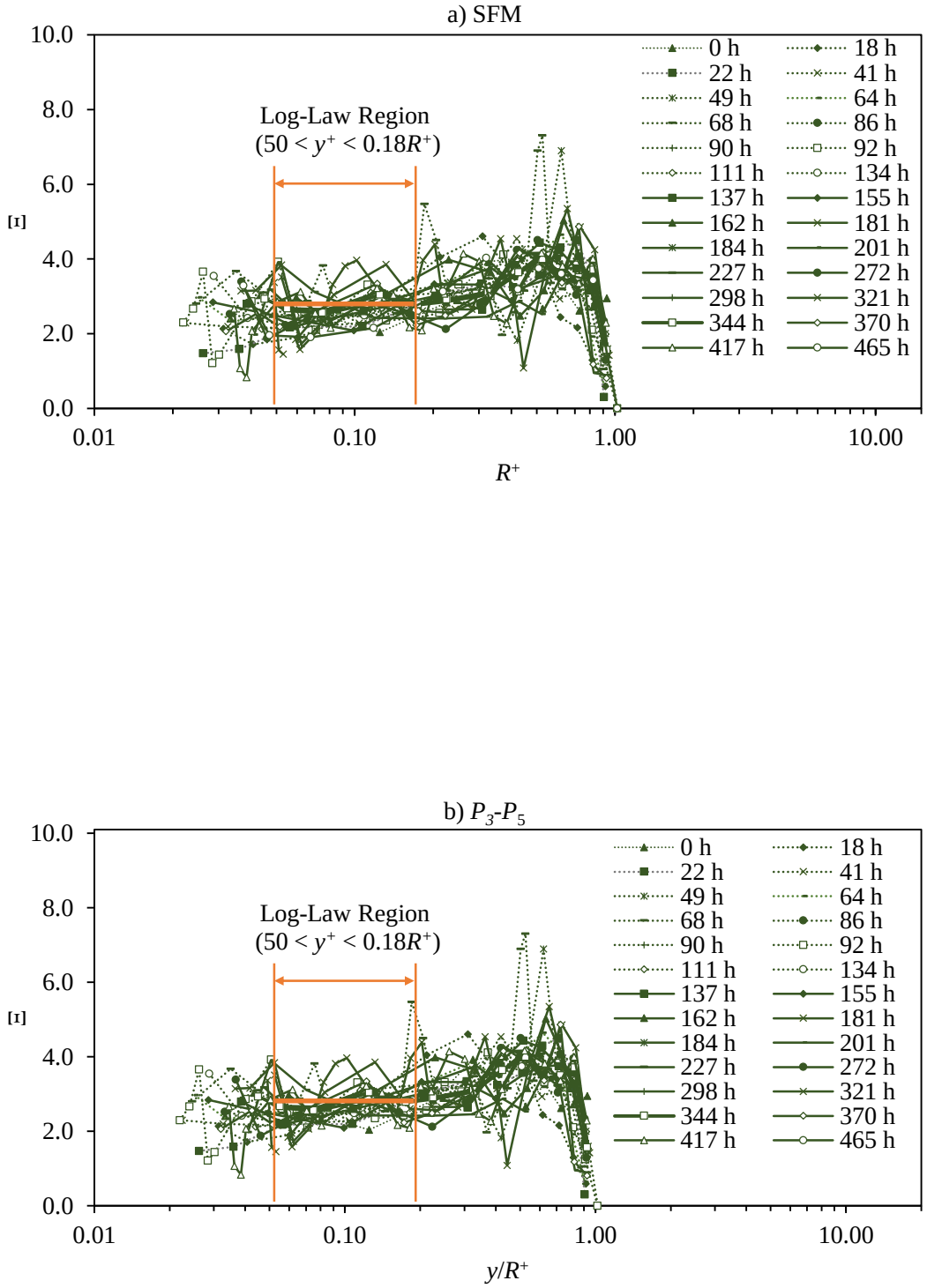

Figure 5.30 Ξ against y/R^+ established using a) SFM and b) P_3-P_5 datasets during the Re_D = 5.98x10^4 assay.

The average discrepancy between the values of κ determined from the two u^* datasets was found to be ±4.96% for the Re_D = 5.98x10^{4}assay and ±3.24% for the Re_D = 1.00x10^5 assay. These discrepancies are slightly higher than the experimental uncertainty in κ of ±2.08% (see Table 4.1). The average discrepancy in B determined from the two u^* datasets was found to be ±17.92% for the Re_D = 5.98x10^4 assay and ±16.02% for the Re_D = 1.00x10^5 assay. The discrepancies illustrate the influence of u^* on κ. It therefore, highlights the potential limitations of applying the global frictional data locally, particularly for irregularly rough biofilms. However, this limitation had to be accepted as it was not possible, using current techniques to establish the local values of u^* from the mean-velocity data without initially knowing κ.

The uniquely derived von Kármán constants for the biofouled pipes are plotted against ΔU^+ in Figure 5.31. The Figure shows considerable scatter, however, it is evident that κ is not universal with roughness. In particular, a trend of decreasing κ with increasing roughness can be observed. Consequently, κ is seemingly a function of the biofilm's development, and in particular it's effective roughness. It is evident from Figure 5.31 that κ begins to depart from the universal value at $\Delta U^+ \approx 1.7$. The reduction in κ was therefore, halted when the frictional development of the respective biofilms reached a state of equilibrium. The value of κ during the equilibrium stage of the Re_D = 5.98x10^4 and Re_D = 1.00x10^5 assays was κ = 0.35 ± 0.02 and κ = 0.39 ± 0.01, respectively, based on the SFM datasets. The respective values determined using the P_3-P_5 datasets were κ = 0.34 ± 0.03 for the Re_D = 5.98x10^4 assay and κ = 0.39 ± 0.01 for the Re_D = 1.00x10^5 assay.

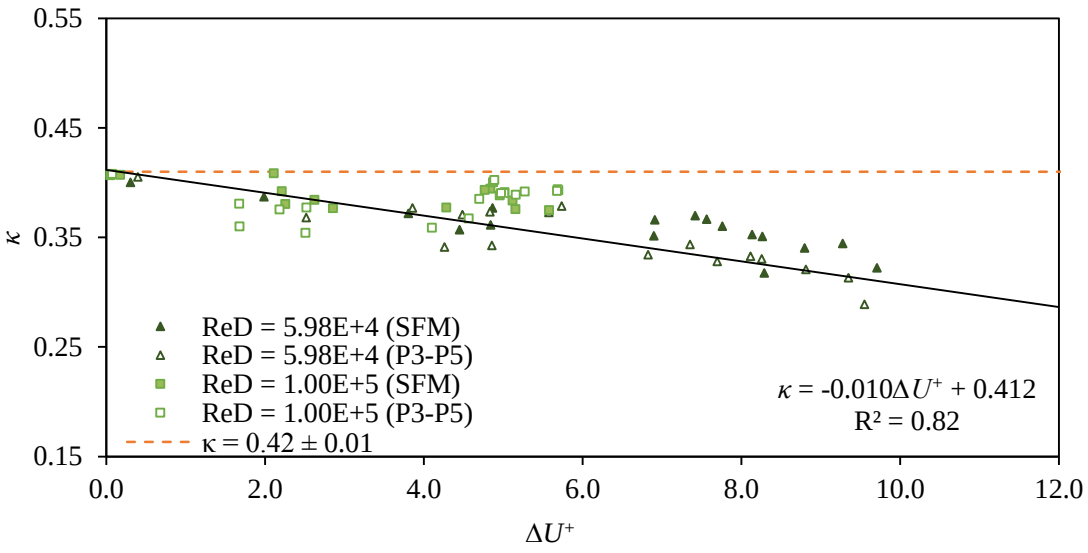

Figure 5.31 Influence of ΔU^+ on κ for the Re_D = 5.98x10^4 and Re_D =1.00x10^5 assays.

As it is suggested that κ and B for biofouled surfaces are dependent on Re_D, the respective biofilms were subject to varying flow conditions. It should be noted that this evaluation took place typically after 500 h of incubation. During this evaluation a total of 62 mean-velocity profiles were recorded within range of $2.50 \times 10^5 < Re_D < 1.22 \times 10^5$.

The relationships between κ and Re_D established for the two flow assays using both u^* datasets are presented in Appendix C.3 in Figure C.3. It was not possible to distinguish between the flow assays and therefore, the two datasets were combined as shown in Figure 5.32. This suggests that the biofilm morphology and roughness had less of an impact on κ than first thought. A dependency on Re_D is evident within Figure 5.32, and in particular a trend of increasing κ with increasing Re_D can be observed. It is believed that the elastic nature of a biofilm may have attributed to the observed variations in κ with Re_D. At lower Re_D the reduction in κ from the conventional value was at its greatest. For instance, at $Re_D = 2.50 \times 10^5$ the value of κ was found to be 0.32. Conversely at higher Re_D the reduction in κ from conventional value is lessened. This could have been caused by either the biofilm becoming compressed or removed as a result of increased flow shear.

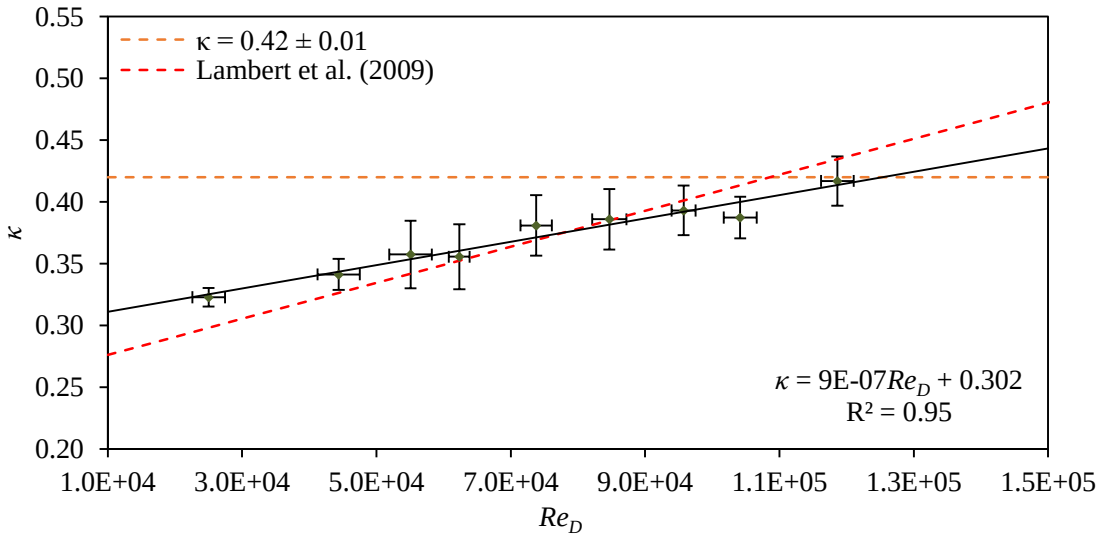

Figure 5.32 Influence of Re_D on κ for the combined data from the $Re_D = 5.98 \times 10^4$ and $Re_D = 1.00 \times 10^5$ assays.

A linear relationship was attached to the plot of κ against Re_D (see Figure 5.32). The fitted relationship for the combined datasets had a R^2 of 0.95 and was given by:

$$\kappa = 9.443 \times 10^{-7} Re_D + 0.302 \qquad \textit{Equation 5.2}$$

The trend observed within Figure 5.32 is consistent with that documented by Perkins (2014). However, the values of the respective constants found within the current study are generally higher than the equivalent reported by Perkins (2014). Perkins (2014) assessed the impact of biofouling on κ within a pipe of similar diameter to that used within the current study (i.e. D = 101.6mm). However, the biofilms observed by Perkins (2014) had a significant filamentous component. Visually, the filaments pictured by Perkins (2014) were considerably more abundant than those observed within the current study. Filamentous type development is known to induce a considerable amount of drag on a system, and in some extreme cases it can alter the mean flow structure in the outer region of the boundary layer (Barton et al. 2006; Andrewartha and Sargison 2008; Andrewartha 2010). However, based on the ecology of a pipe it was unlikely that the filaments observed by Perkins et al. (2014) would have been as long as those reported in the extreme cases, which typically relate to biofilms incubated within open channels. Nevertheless, the interactions between the filaments and the fluid may have attributed to the lower values of κ observed by Perkins et al. (2014). Consequently, the degree and type of biofouling may have had a greater influence on κ than was first thought, based on the observations outlined previously within this study.

Lambert et al. (2009) fitted a linear relationship to express κ as a function of Re_D, which was given by Equation 2.47 and is presented within Figure 5.32. It is evident that Equation 2.47 produces values which are consistent with those obtained within the current study. The biofilms reported by Lambert et al. (2009) were also predominantly low-form gelatinous in nature. However, Equation 2.47 was derived from a very limited dataset at low Re_D and as a consequence, Equation 5.3 was considered more representative of low-form gelatinous biofilms (particularly, for the range of $2.50\text{x}10^4 < Re_D < 1.22\text{x}10^5$).

The observed non-universality of κ confirms that the values of k_s derived from the traditional C-W equation were unrepresentative of the actual fouled surface. Consequently, updated values of k_s were determined using the modified C-W equation proposed by Lambert et al. (2009) (i.e. Equation 2.47) in conjunction with the uniquely derived values of κ. The revised k_s values for the $Re_D = 5.98\text{x}10^4$ and $Re_D = 1.00\text{x}10^5$ assays are presented in Figure 5.33. As a reference, the values of k_s derived from the traditional C-W equation are also presented. It is evident from Figure 5.33 that the k_s values derived using the traditional C-W equation significantly overestimate the actual conditions. On average, the traditionally derived k_s values overestimated the actual condtions by 49% for the $Re_D = 5.98\text{x}10^4$ assay and 85% for the $Re_D = 1.00\text{x}10^5$ assay.

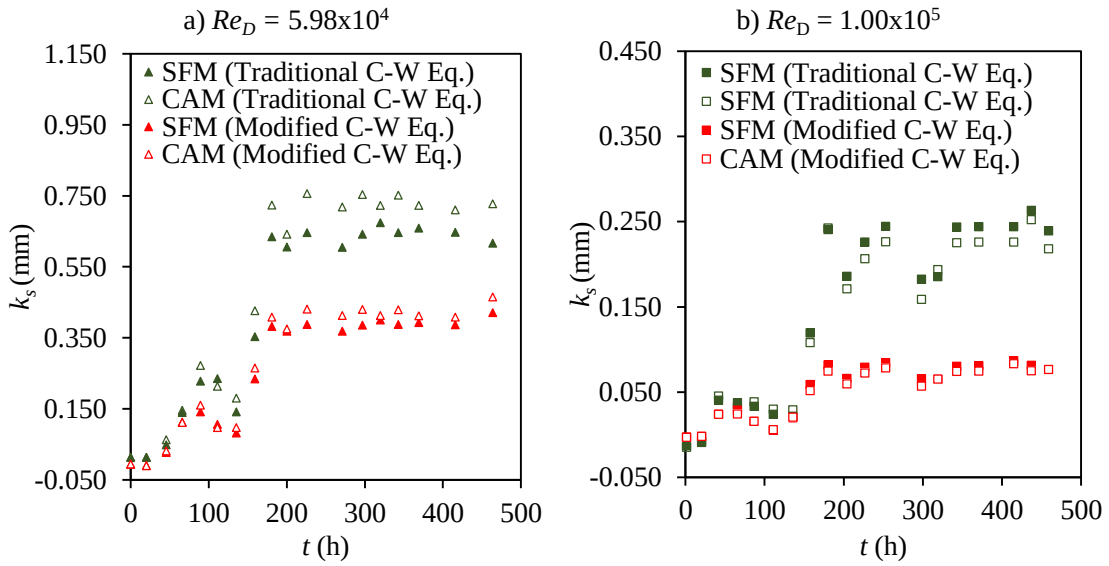

Figure 5.33 ks against time for the a) Re_D = 5.98x10^4 and b) Re_D =1.00x10^5 assays (the presented values where derived using transitional and modified C-W equation.

The unrepresentative nature of the traditionally derived values of k_s means that the values of B established from them (i.e. those given in Appendix C.3 in Table C.9) will also be unrepresentative of the actual surfaces. Therefore, the revised k_s values were used to determine revised values of B. It should be noted, that k_s only influenced the intercept of the regression line and not its slope, and as a result, the values of κ were unaffected by the subsequent changes in k_s. The relationships between the new values of B and Re_D are presented in Appendix C.3 in Figure C.4 for the two flow assays. Figure 5.34 presents the combined data for the two flow assays and shows a trend of decreasing B with increasing Re_D. A linear relationship was attached to the plot of B against Re_D (see Figure 5.34). The fitted relationship had a R^2 of 0.98 and was given by:

$$B = -1.964 \times 10^{-5} Re_D + 6.001 \qquad \textit{Equation 5.3}$$

Figure 5.35 and Figure 5.36 presents plots of κ and B against k_s^+ (where k_s^+ was established from the modified C-W equation). As a reference, values of B derived from Equation 2.36 are also presented within Figure 5.36. Despite, the considerable scatter it is evident that for $k_s^+ > 0.40$ the uniquely derived values of κ and B are typically lower than the values traditionally accepted. Furthermore, it is evident that as k_s^+ increases, so also does B, whereas κ decreases.

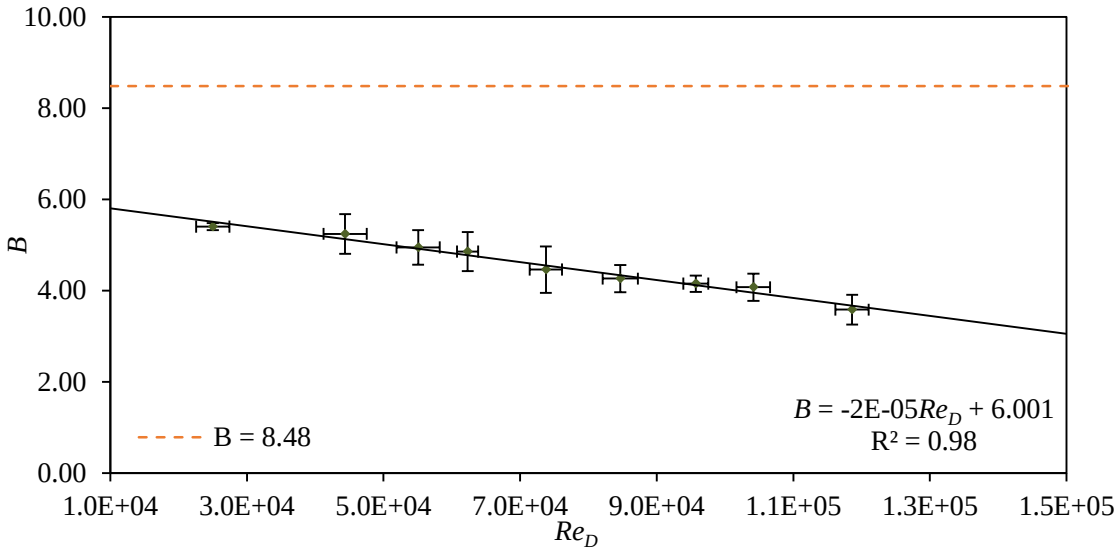

Figure 5.34 Influence of Re_D on B for the combined data from the Re_D = 5.98x10^4 and Re_D = 1.00x10^5 assays

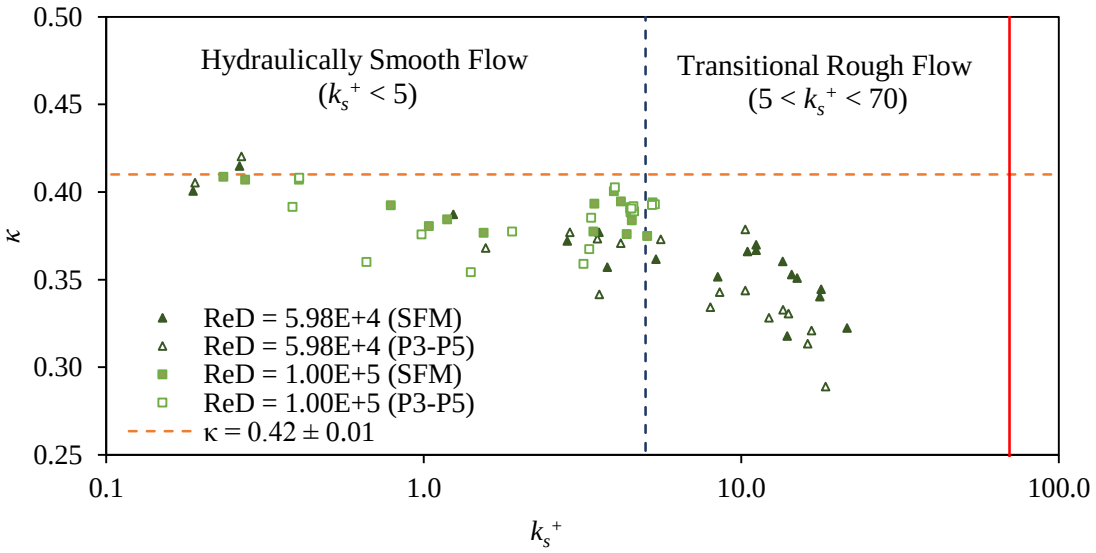

Figure 5.35 Influence of k_s^+ on κ for the combined data from the Re_D = 5.98x10^4 and Re_D =1.00x10^5 assays. Whereby k_s was calculated using the modified C-W equation.

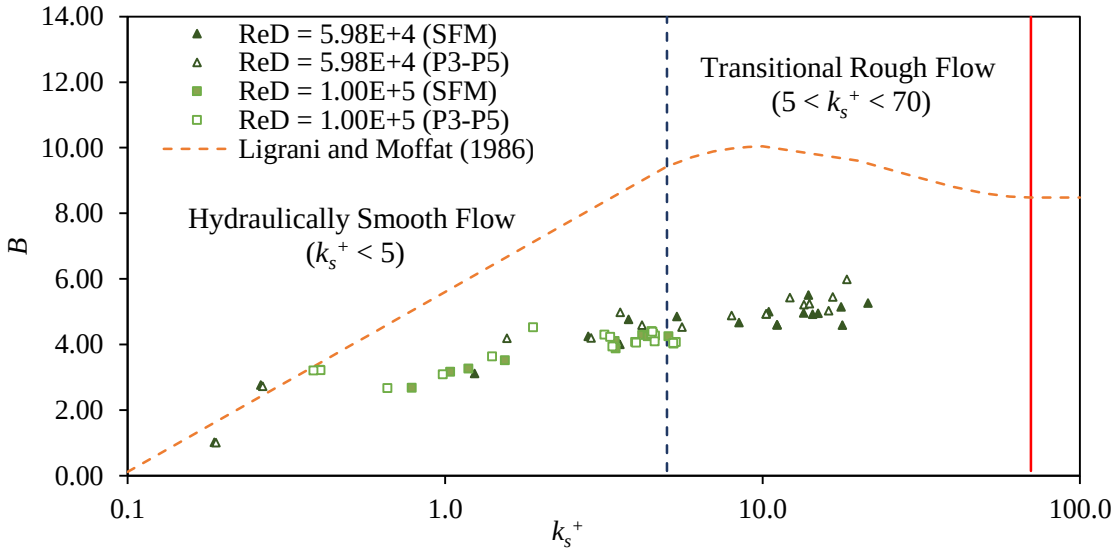

Figure 5.36 Influence of k_s^+ on B for the combined data from the Re_D = 5.98x10^4 and Re_D =1.00x10^5 assays. Whereby k_s was calculated using the modified C-W equation.

5.7.4 Log-Wake Law for biofouled surfaces

A typical series of mean-velocity profiles are presented in Figure 5.37 for the range of 6.36x10^4 < Re_D < 9.57x10^4. The presented profiles were recorded within the Re_D = 1.00x10^5 assay. Theoretically derived profiles determined using the Log-Wake Law are also presented within Figure 5.37. The theoretical profiles were derived using the conventional and uniquely derived Log-Law constants. The profiles established from the uniquely derived constants are designated the "Revised Log-Wake Law" in Figure 5.37. Wake strengths were also determined for each of the measured velocity profiles using the conventional and uniquely derived constants. No distinguishable trend was observed between Π and Re_D or surface roughness. The average Π determined using the uniquely derived constants was 0.43 ± 0.11.

The inadequacy in applying the Log-Law constants in their conventional form for biofouled surfaces is evident within Figure 5.37. The disagreement between the conventionally derived and measured profiles is particularly significant in the near wall region. This is highlighted by Figure 5.38, which presents the deviations between the measured and theoretical velocity profiles.

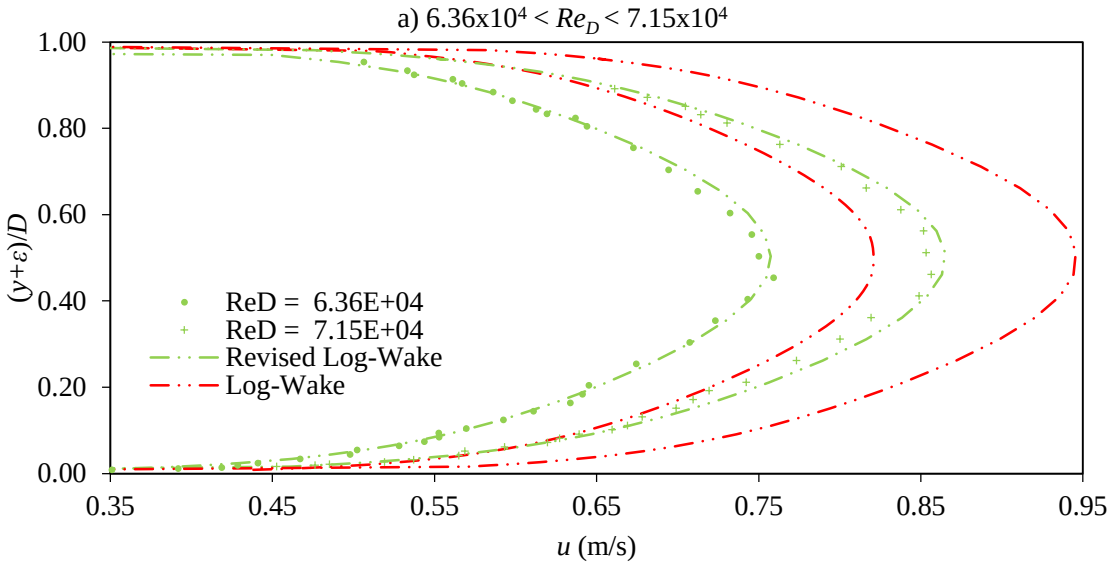

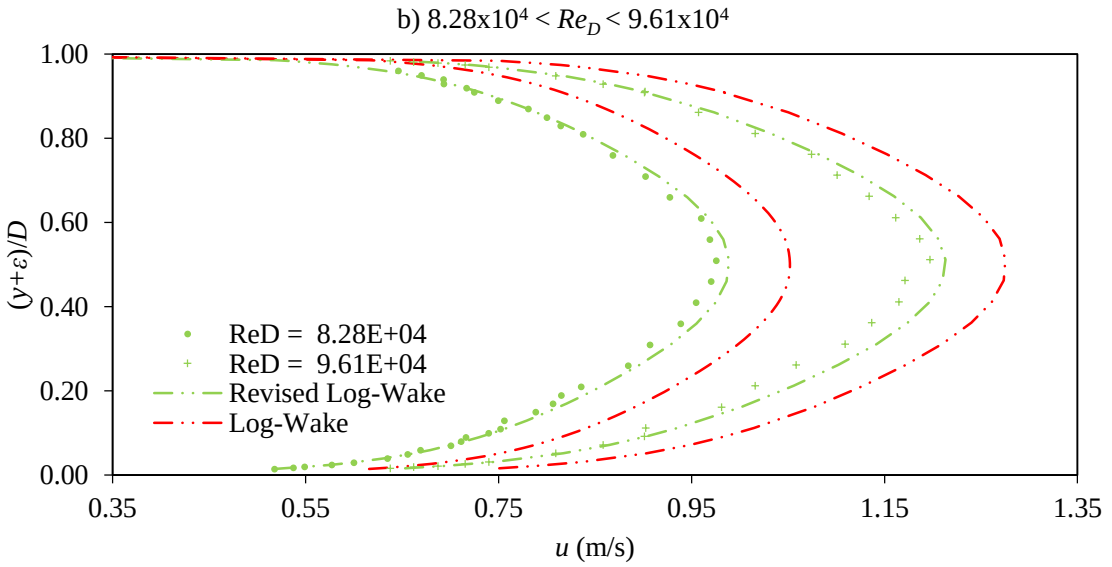

Figure 5.37 Mean-velocity profiles for the ranges of a) $4.02x10^4 < Re_D < 6.36x10^4$ and b) $7.15x10^4 < Re_D < 9.57x10^4$ (highlighting the comparison between theoretical Log-Wake Law profiles derived from revised and conversional constants).

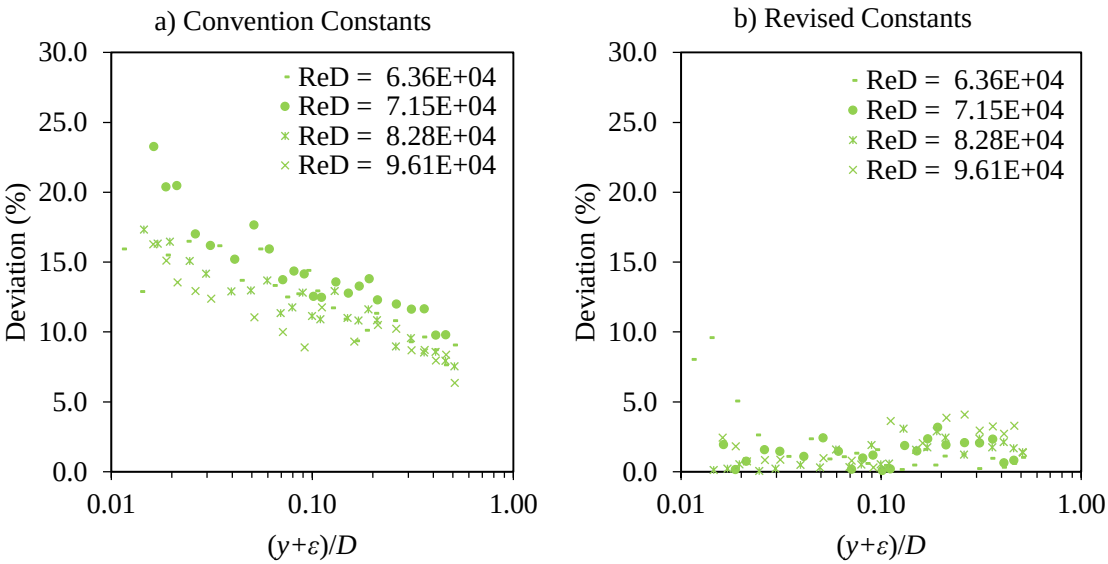

Figure 5.38 Deviation between the measured and theoretical (Log-Wake Law) velocity profiles, estimated from the a) conventional and b) revised constants.

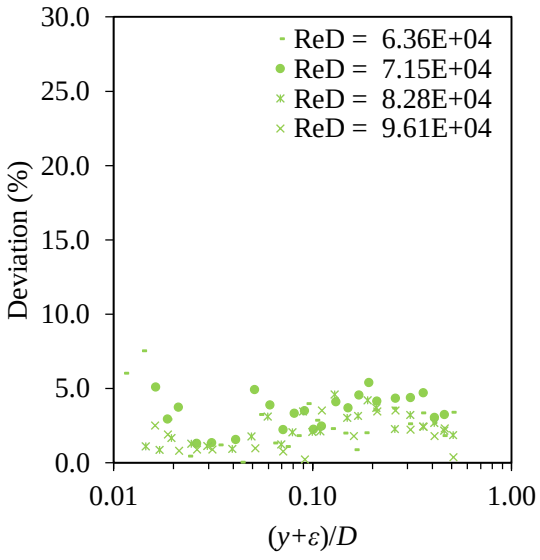

Figure 5.39 Deviation between the measured and theoretical (Log-Wake Law) velocity profiles, estimated from the revised constants derived from Equation 5.2 and Equation 5.3.

The average discrepancy between the measured and conventionally derived profiles was found to be ±17.98% in the inner region of the boundary layer. Alternatively, the average discrepancy between the measured and revised profiles in the inner region of the boundary layer was found to be ±1.22%. Furthermore, in the outer region of the boundary layer the average discrepancy between the measured and conventionally derived profiles was found to be ±13.13%. Whereas, the average discrepancy between the measured and Revised Log-Wake Law profiles in the outer region of the boundary layer was found to be ±1.95%.

Equivalent theoretical velocity profiles were also established using values of κ and B respectively derived from Equation 5.2 and Equation 5.3. The average discrepancy between the theoretical and measured profiles in the inner was ±2.30% and in the outer regions was ±2.95% (see Figure 5.39).

5.7.5 Mean-velocity data scaled by the global frictional data

5.7.5.1 Inner and outer regions

Revised Law of the Wall and velocity defect plots were produced using the global frictional data (i.e. the SFM and P_3-P_5 datasets) as the scaling factors. The values of ε determined from the global frictional data (see Appendix C.3, Table C.10 and Table C.11) were also applied. The purpose of this evaluation was to establish whether the trends outlined in Section 5.6 using the PL Method were valid, and were not artificially influenced by the use of an inappropriate value of κ. If the established trends were artificially fabricated the potential implications could be considerable, particularly as the current prevailing understanding of biofilm frictional dynamics is predominantly based on observations established from conventional wall similarity techniques and a universal Log-Law (Barton 2006; Barton et al. 2007; 2010; Andrewartha et al. 2007; 2008; 2011; Andrewartha 2010, Walker et al. 2013). The revised Law of the Wall plots are presented within Figure 5.40 to Figure 5.43 and the revised velocity defect plots are presented within Figure 5.44 to Figure 5.47.

A downward shift in the respective velocity profiles following biofilm development is evident within Figure 5.40 to Figure 5.43. The slope of the velocity profiles in the Log-Law region with fouling differed from the equivalent slope for the non-fouled profiles. This was to be expected, as it indicates a change in the κ with fouling from 0.42.

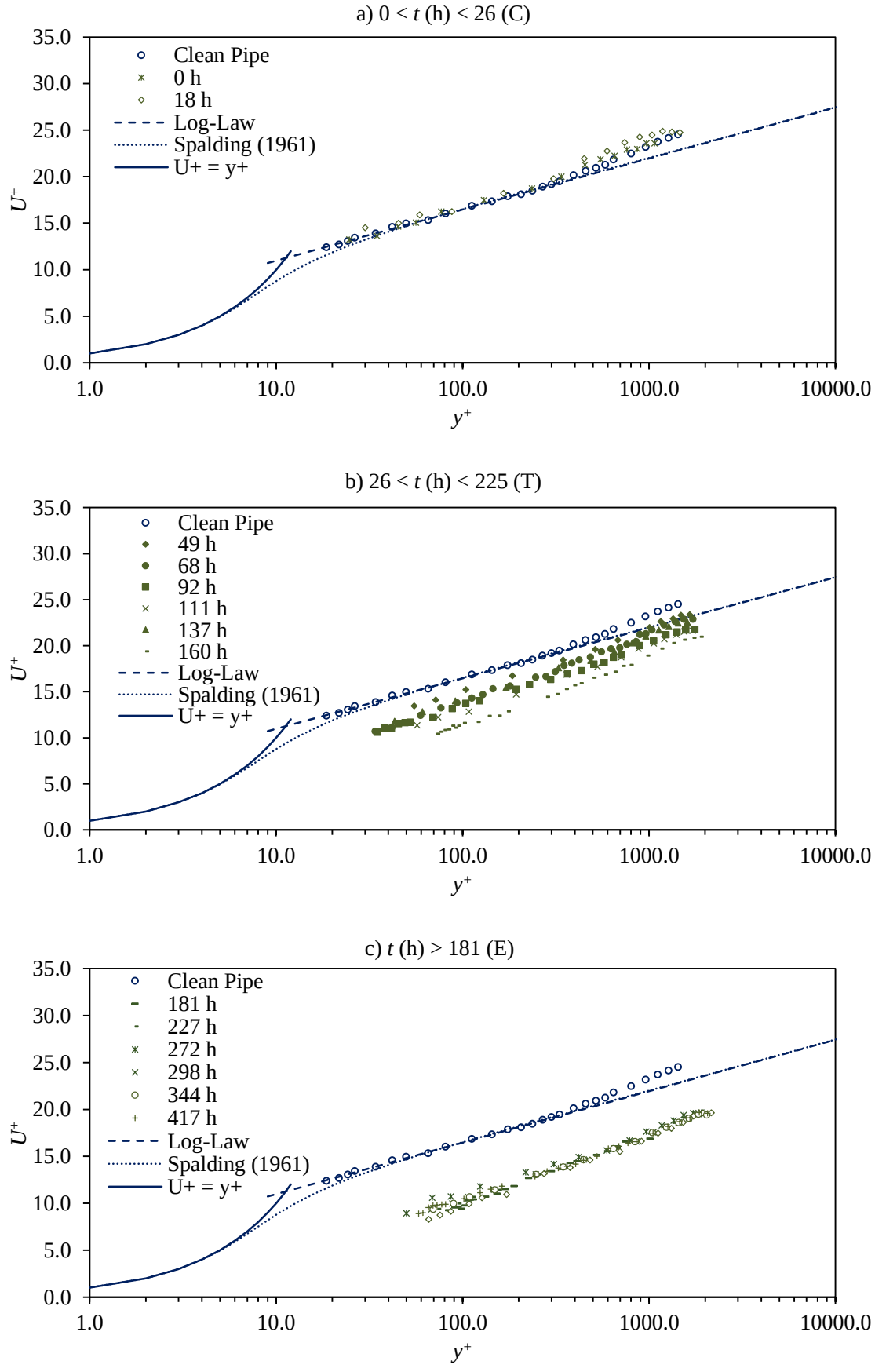

Figure 5.40 Normalised mean-velocity profiles for the Re_D = 5.98x10^4 assay at a) 0 < t (h) < 26 (Conditioning stage, C), b) 26 < t (h) < 181 (Transitional Stage, T), and c) t (h) > 181 (Equilibrium Stage, E) time intervals. The profiles were established using the SFM dataset.

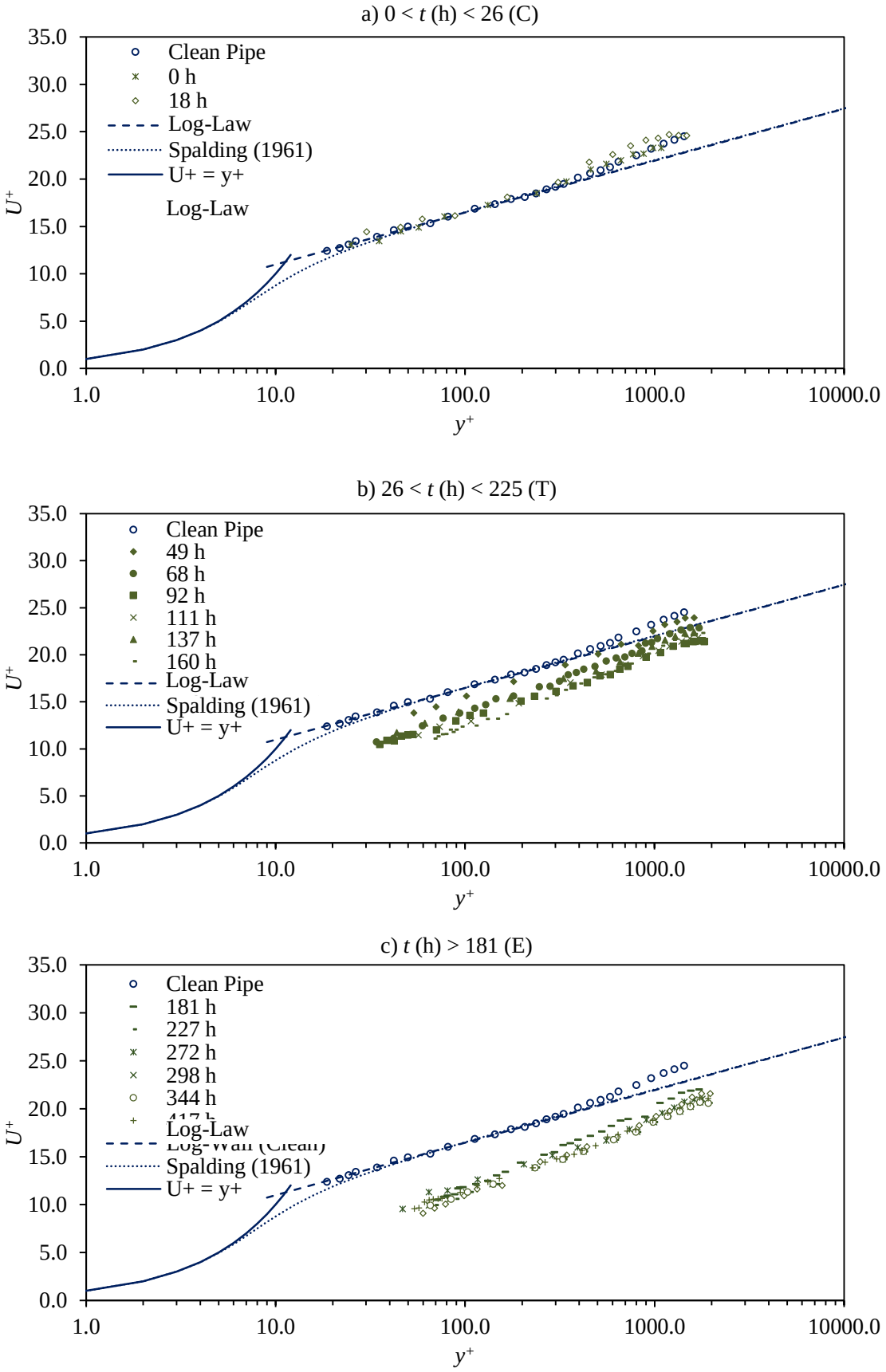

Figure 5.41 Normalised mean-velocity profiles for the $Re_D = 5.98x10^4$ assay at a) 0 < t (h) < 26 (Conditioning stage, C), b) 26 < t (h) < 181 (Transitional Stage, T), and c) t (h) > 181 (Equilibrium Stage, E) time intervals. The Profiles were normalised using P_3-P_5 u values.*

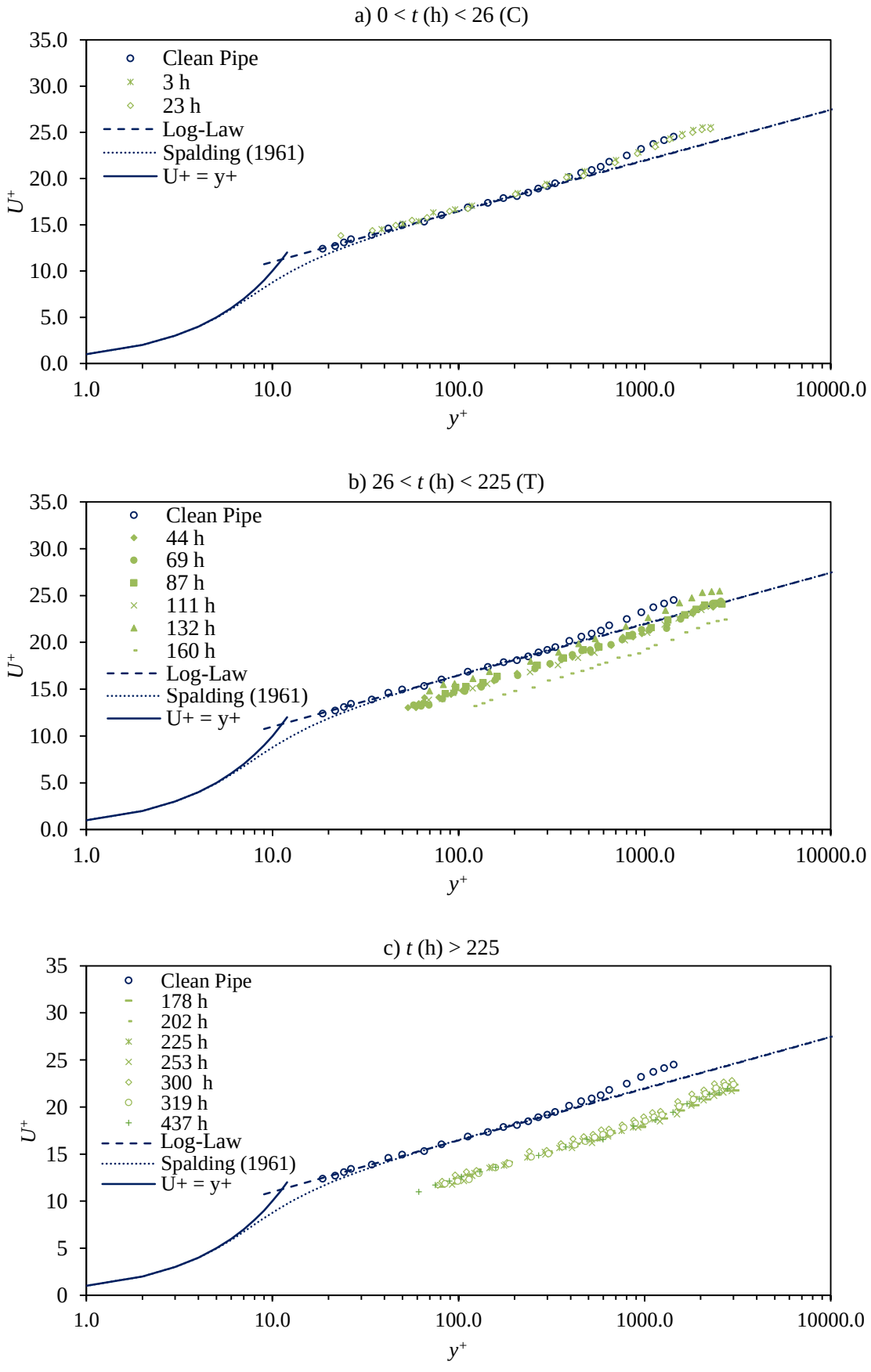

Figure 5.42 Normalised mean-velocity profiles for the Re_D = 1.00x10^5 assay at a) 0 < t (h) < 26 (Conditioning stage, C), b) 26 < t (h) < 181 (Transitional Stage, T), and c) t (h) > 181 (Equilibrium Stage, E) time intervals. The profiles were established using the SFM dataset.

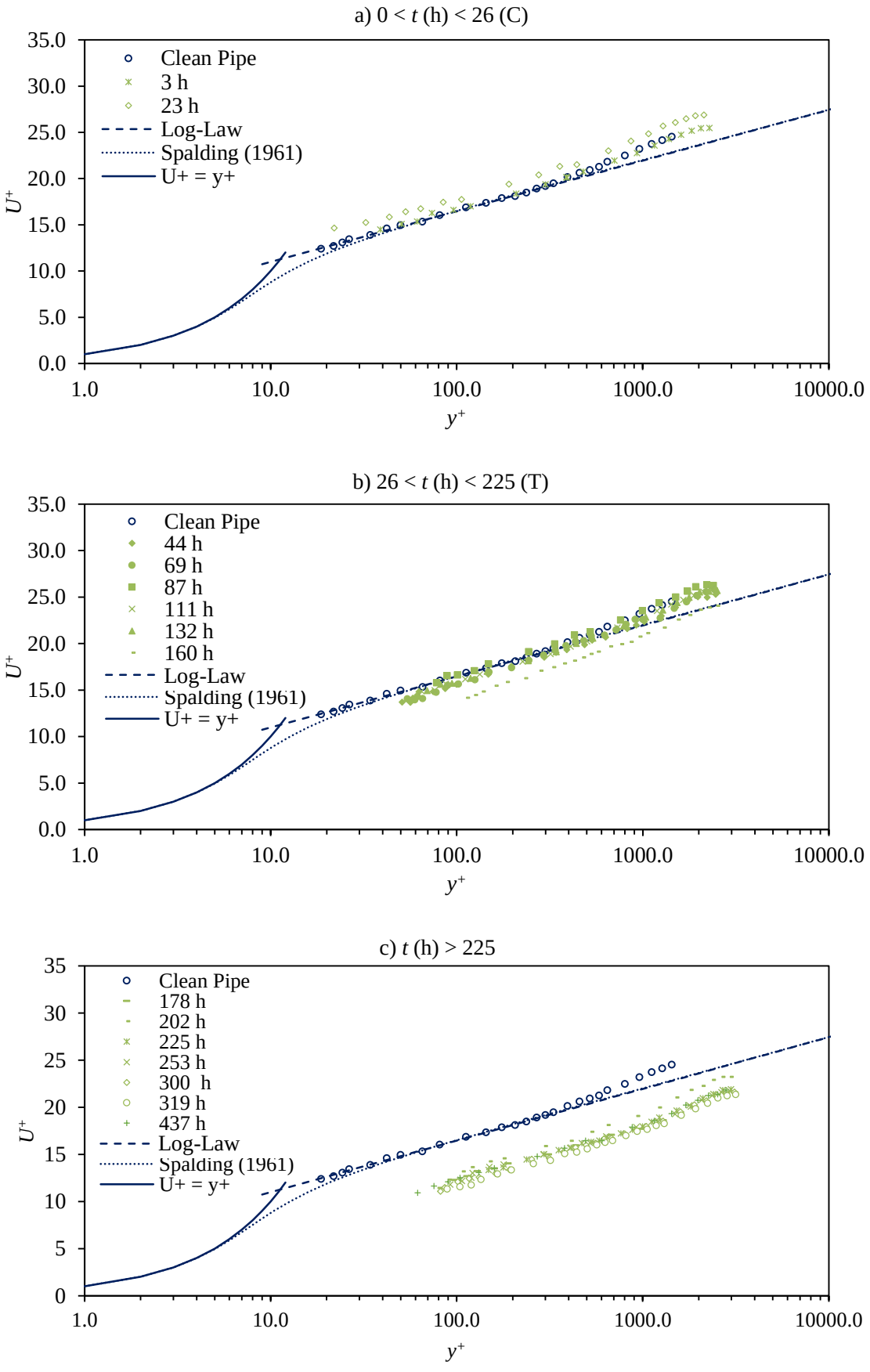

Figure 5.43 Normalised mean-velocity profiles for the Re_D = 1.00x10^5 assay at a) 0 < t (h) < 26 (Conditioning stage, C), b) 26 < t (h) < 181 (Transitional Stage, T), and c) t (h) > 181 (Equilibrium Stage, E) time intervals. The profiles were established using the P_3-P_5 dataset.

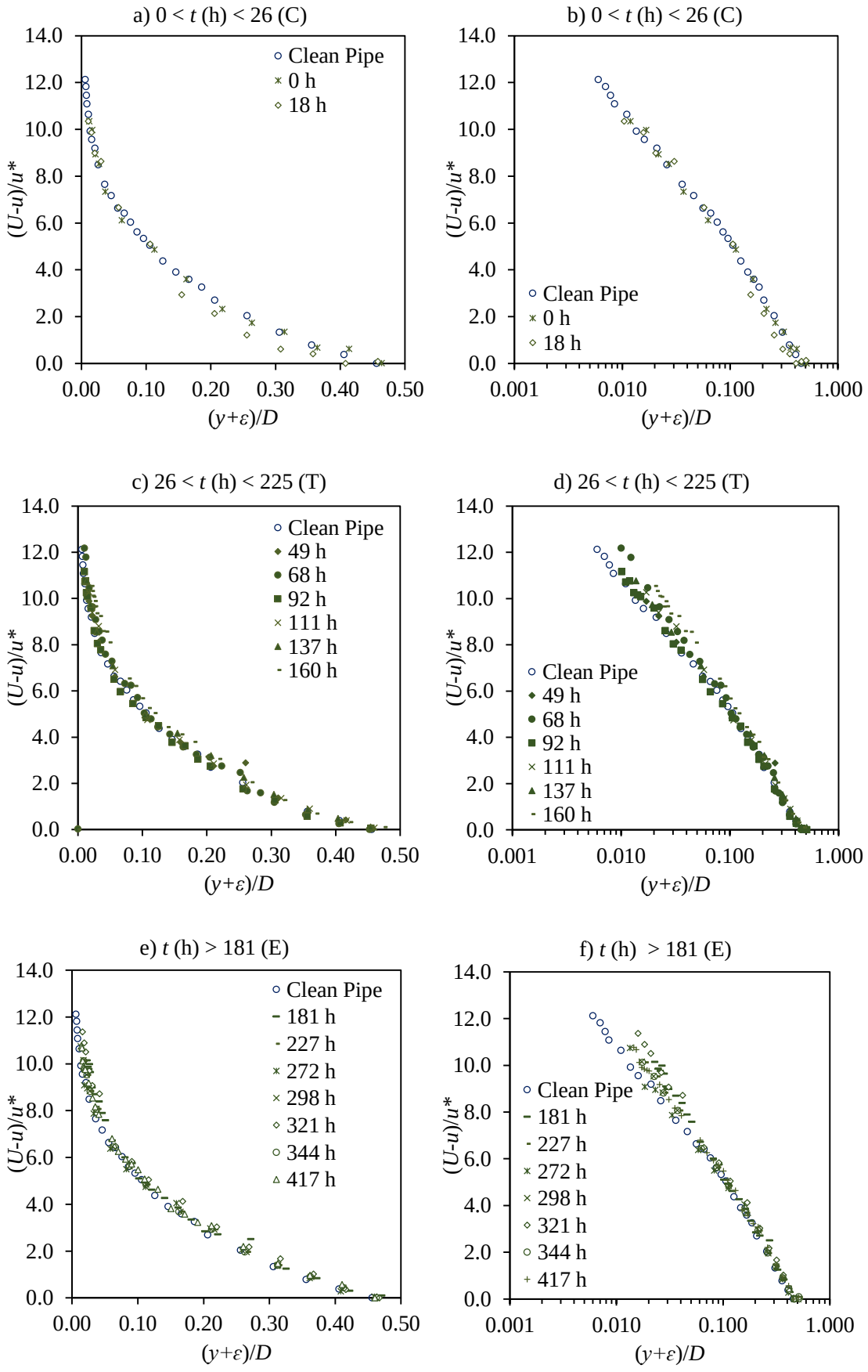

Figure 5.44 Velocity defect profiles for the Re_D = 5.98x10^4 assay at a) 0 < t (h) < 26 (Conditioning stage, C), b) 26 < t (h) < 181 (Transitional Stage, T), and c) t (h) > 181 (Equilibrium Stage, E) time intervals. The profiles were established using the SFM dataset.

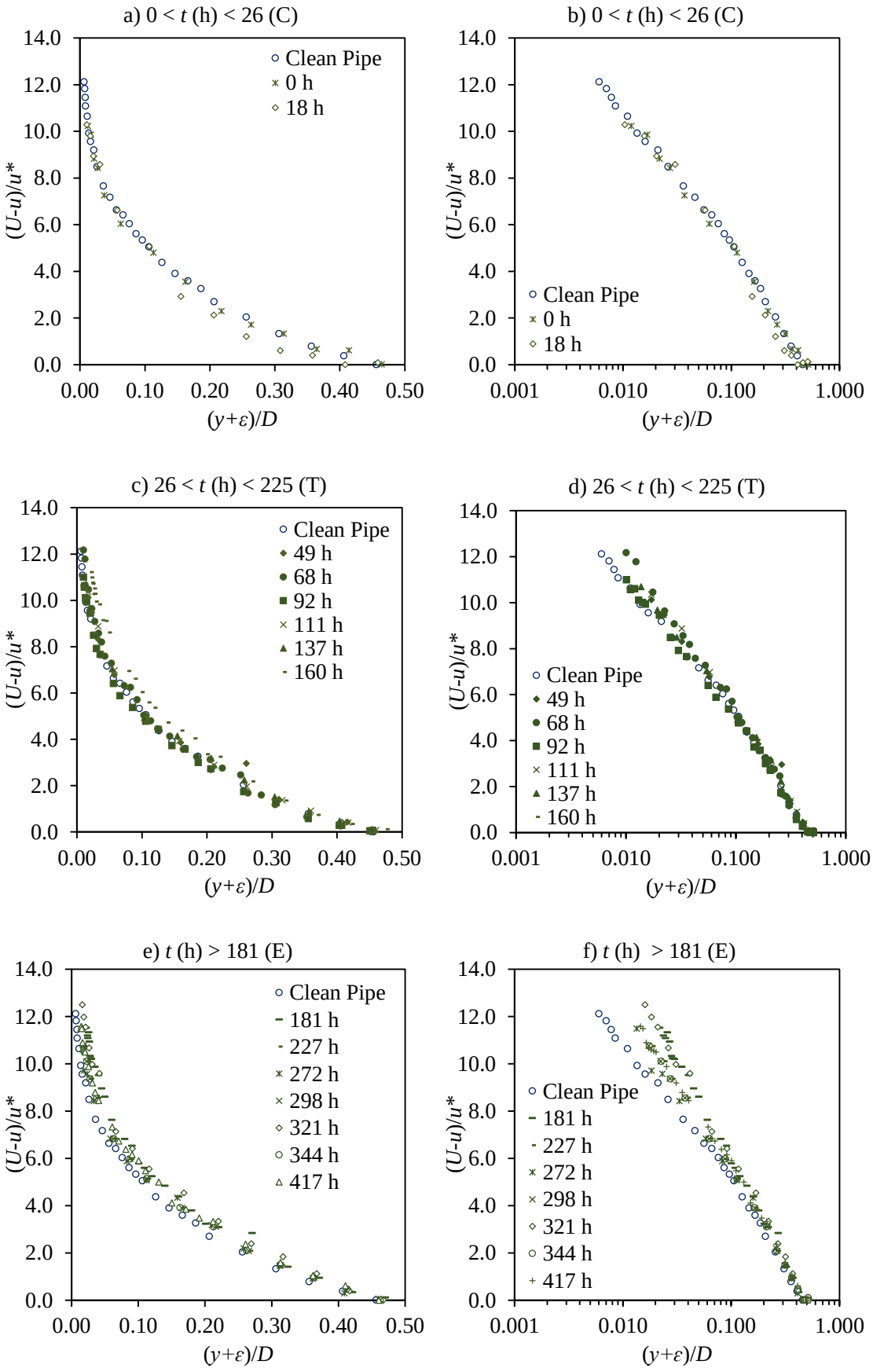

Figure 5.45 Velocity defect profiles for the Re_D = 5.98x10^4 assay at a) 0 < t (h) < 26 (Conditioning stage, C), b) 26 < t (h) < 181 (Transitional Stage, T), and c) t (h) > 181 (Equilibrium Stage, E) time intervals. The profiles were established using the P_3-P_5 dataset.

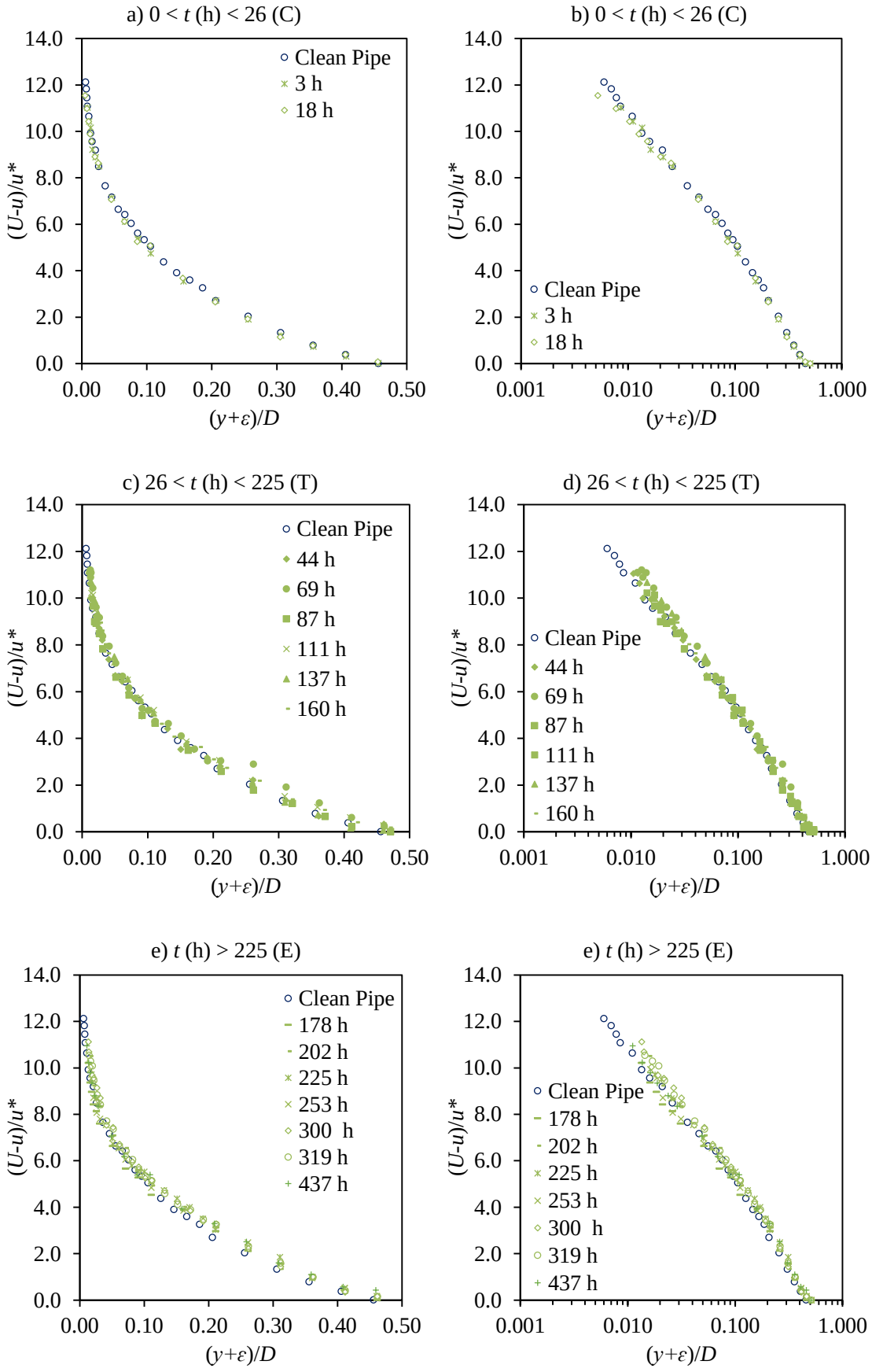

Figure 5.46 Velocity defect profiles for the Re_D = 1.00x10^5 assay at a) 0 < t (h) < 26 (Conditioning stage, C), b) 26 < t (h) < 181 (Transitional Stage, T), and c) t (h) > 181 (Equilibrium Stage, E) time intervals. The profiles were established using the SFM dataset.

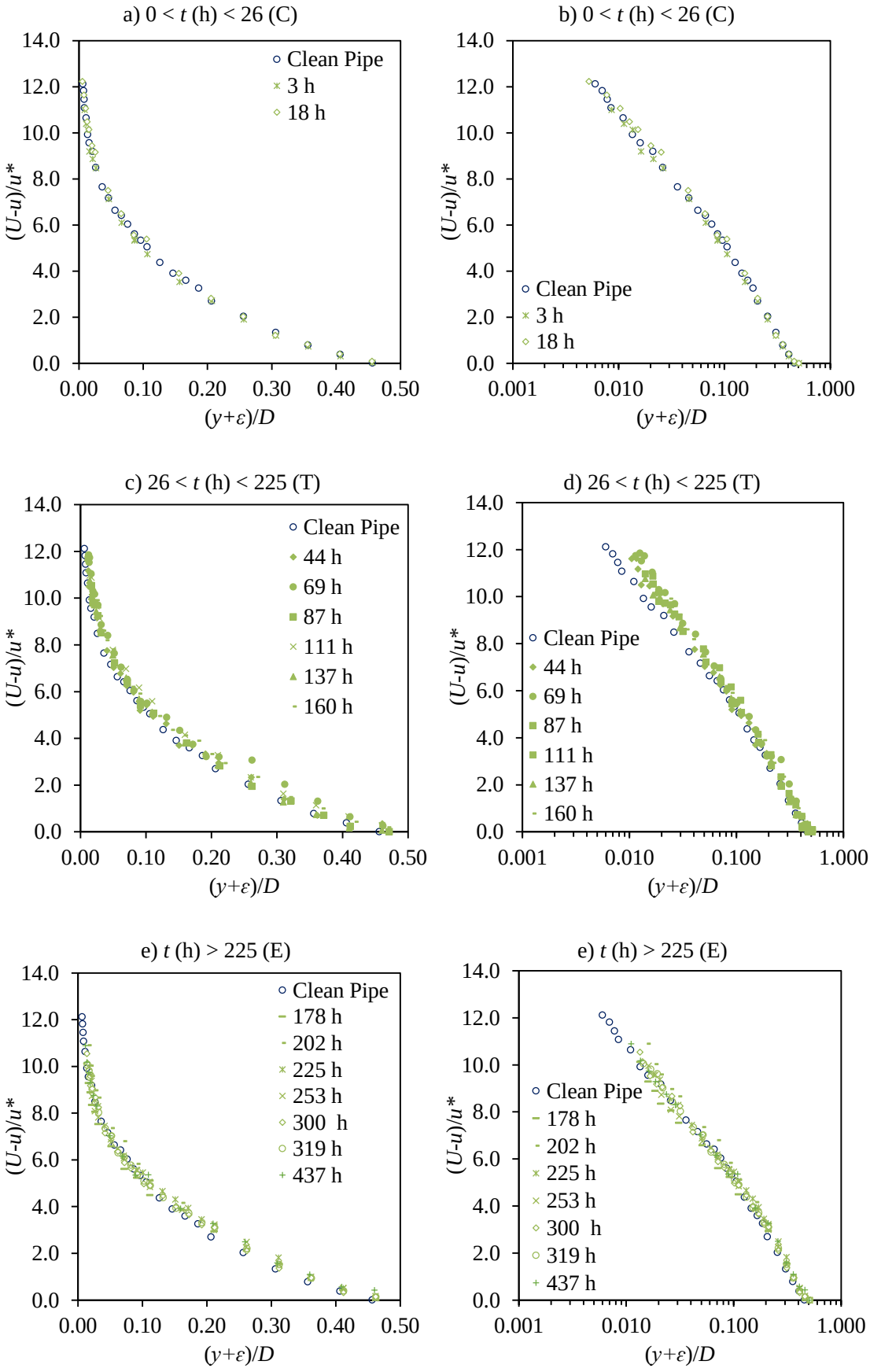

Figure 5.47 Velocity defect profiles for the Re_D = 1.00x10^5 assay at a) 0 < t (h) < 26 (Conditioning stage, C), b) 26 < t (h) < 181 (Transitional Stage, T), and c) t (h) > 181 (Equilibrium Stage, E) time intervals. The profiles were established using the P_3-P_5 dataset.

It is evident from the velocity defect plots presented within Figure 5.44 and Figure 5.47, that the mean-velocity structure in the outer flow region was unaffected by the biofilm development. This supports the conclusion drawn from the PL Method that Townsend's Wall Similarity Hypothesis is valid for biofouled surfaces. However, unlike the velocity defect profiles derived from the PL Method, the profiles presented within Figure 5.44 and Figure 5.47 do not show good collapse in the near wall region. This was particularly evident, for the respective profiles relating to the more established biofilms.

5.7.5.2 Boundary layer parameters

Revised boundary layer parameters were determined using the values of ε derived from the SFM and P_3-P_5 datasets (as outlined in Appendix C.3, Table C.10 and Table C.11) and are presented within Table 5.4. The parameters listed within these tables represent the average values recorded once the biofilms had reached a state of equilibrium.

Table 5.4 Boundary layer parameters for the fouled test pipe and non-fouled test pipe, determined using the SFM and P_3-P_5 dataset. The fouled pipe parameters refer to the average value recorded once the biofilms had reached a pseudo equilibrium state.

Dataset	***Surface***	***Re_D***	***ε* (mm)**	***ε^+***	***k_s^+***	***δ* (mm)**	***δ^** (mm)**	***θ* (mm)**	***H***	**Π**
SFM	**Fouled**	$6.06x10^4$	1.62	63.79	25.10	45.84	5.78	4.46	1.34	0.39
		$1.00x10^5$	1.46	83.63	12.98	45.17	5.88	4.39	1.27	0.46
	Non-Fouled	$6.10x10^4$	-	-	-	43.91	5.48	4.28	1.28	0.48
		$9.40x10^4$	-	-	-	42.50	5.33	4.25	1.26	0.41
P_3-P_5	**Fouled**	$6.06x10^4$	1.52	55.66	13.22	45.84	5.78	4.46	1.34	0.42
		$1.00x10^5$	1.46	83.78	13.44	45.17	5.88	4.39	1.27	0.46
	Non-Fouled	$6.10x10^4$	-	-	-	43.91	5.48	4.28	1.28	0.48
		$9.40x10^4$	-	-	-	42.50	5.33	4.25	1.26	0.41

Based on single factor ANOVAs the differences between the fouled and non-fouled boundary layer parameters were statistically insignificant and within experimental uncertainties. This conclusion differs from that observed from the PL Method (outlined in Section 5.6.1) and within the literature (Lewkowicz and Das 1986; Schultz and Swain 1999; Schultz 2000; Andrewartha and Sargison 2011; Barton 2006). However, the aforementioned studies also employed standard wall similarity techniques based on a universal value of κ (= 0.42). Therefore, it is suggested that the reported differences between fouled and non-fouled

boundary layer parameters established using conventional wall similarity techniques, may have been artificially created.

The wake strengths listed within Table 5.4 with fouling are in reasonable agreement with the equivalent non-fouled values. Moreover, single factor ANOVAs indicated that any difference between the non-fouled and fouled conditions were statistically insignificant and within the experimental uncertainties. This again suggests that the reported differences in the non-fouled and fouled Π values determined from the PL Method, which in some cases were extreme, may have been artificially influenced by the application of a universal value of κ.

5.8 Dynamic k_s formulation

The highly diverse and complex nature of a biofouled surface means that standard generic solutions to quantify its effective roughness are generally inadequate. Consequently, a dynamic k_s approach, which is capable of qualifying both space- and time- averaged conditions for different environmental and operational scenarios appeared more applicable. The formulation of such an approach is outlined herein.

5.8.1 The process of biofouling within pipelines

On the basis that the biofilms incubated within the current study were cultivated using equivalent nutrient and temperature conditions (see Section 3.8.2) all observations and relationships documented on their development can be generally explained by the variations in mass transfer and shear characteristics imposed by the different flow regimes.

It was evident that under steady state conditions a biofilms frictional development over time follows a consistent sigmoidal growth pattern, as shown by Figure 5.48. Figure 5.48 presents the evolution of biofilm induced k_s over time based on the modified C-W equation (i.e. Equation 2.50) and case-specific values of κ. Figure 5.49 conceptually depicts the evolution of biofilm induced roughness (in terms of k_s) over time. The key stages of a biofilm's frictional development, namely: i) the conditioning, ii) transitional and iii) equilibrium stages are discussed herein. This discussion incorporates all experimental observations outlined previously within this chapter.

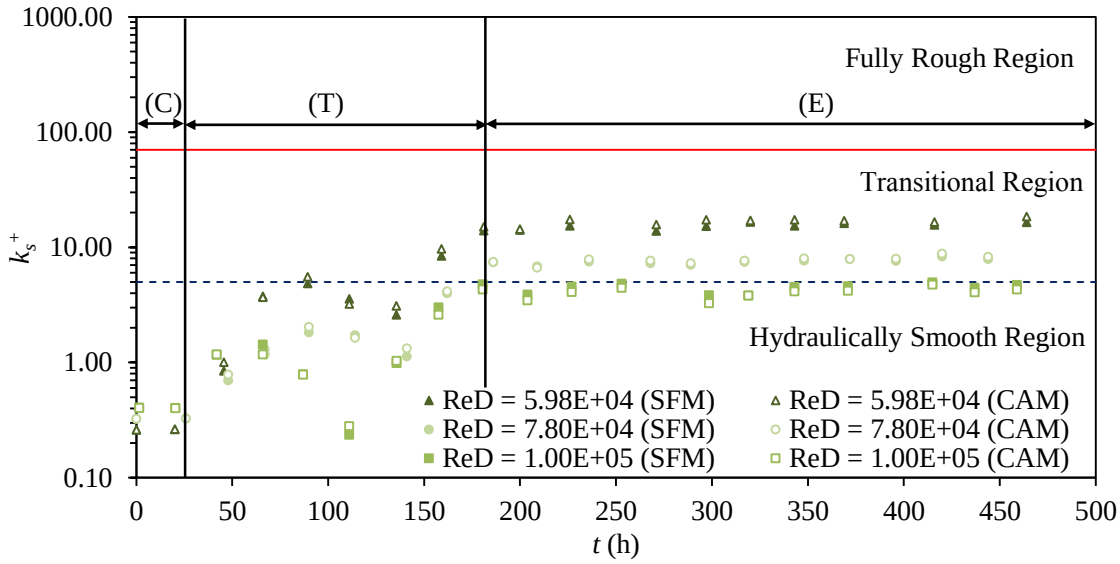

Figure 5.48 k_s^+ against time of the Re_D = 5.98x10^4, Re_D =7.82 x10^4 and Re_D =1.00x10^5 assays (highlighting the Conditioning (C), Transitional (T), and Equilibrium (E) development stages).

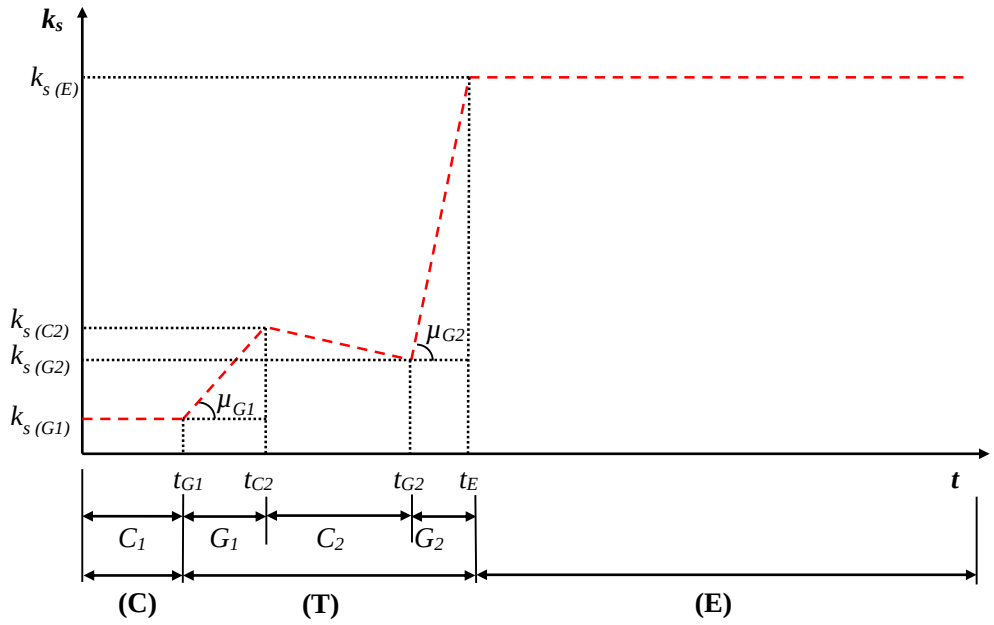

Guide

C	= Conditioning Stage	t_{C2}	= Time for start C_2
T	= Transitional-Development Stage	t_E	= Time for start E
E	= Equilibrium Stage	$k_{s\,(G1)}$	= k_s at t_{G1}
C_1	= Primary Conditioning Stage	$k_{s\,(G2)}$	= k_s at t_{G2}
G_1	= Primary Growth Stage	$k_{s\,(C2)}$	= k_s at t_{C2}
C_2	= Secondary Conditioning Stage	$k_{s\,(E)}$	= k_s at t_E
G_2	= Secondary Growth Stage	μ_{G1}	= G_1 Development Rate (i.e. k_s/t)
t_{G1}	= Time for start G_1	μ_{G2}	= G_2 Development Rate
t_{G2}	= Time for start G_2		

Figure 5.49 Conceptual diagram of the time evolution of k_s as a result of biofilm development.

5.8.1.1 Conditioning Stage

The primary conditioning stage, C_1 of a biofilm's frictional development is equivalent to the conventional conditioning stage associated with bacterial growth (i.e. λ_A, see Section 2.3.1). In this instance λ_A is defined as t_{G1} and is a function of the system's mass transfer and diffusion characteristics. Typically, an increase in mass transfer and diffusion fostered by an increase in Re_D will ultimately result in a reduction in t_{G1} (see Figure 5.50a), providing the overall shear forces remain below the critical levels for detachment (Vieira et al. 1993; Tsvetanova 2006; Simoes et al. 2010). The t_{G1} can be related to Re_D by (R^2 =0.99):

$$t_{G1} = -4.44 \times 10^4 Re_D + 61.89 \qquad \textit{Equation 5.4}$$

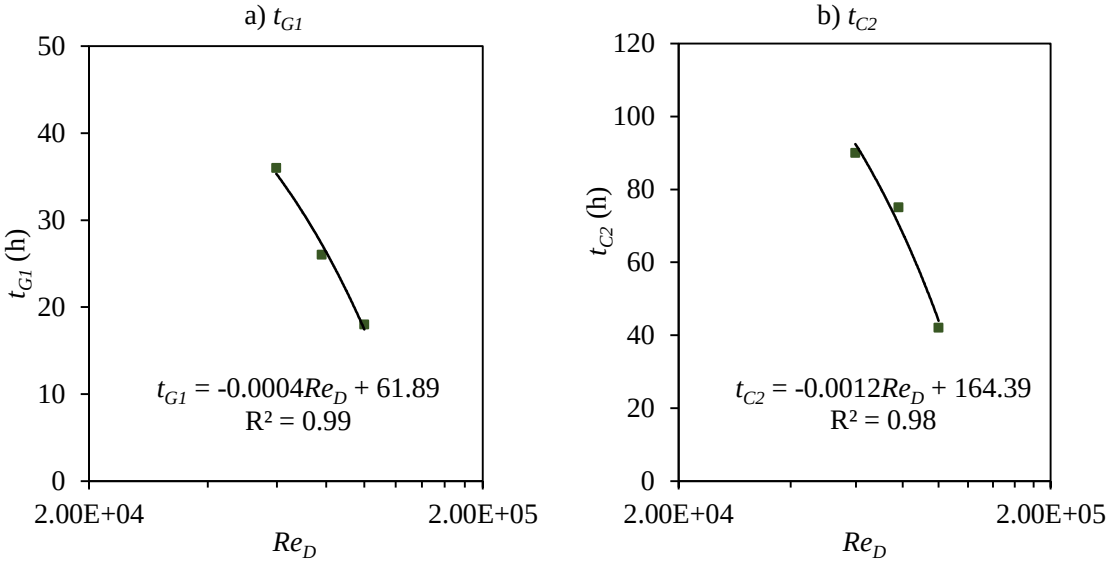

Figure 5.50 a) t_{G1} and b) t_{C2} against Re_D.

5.8.1.2 Transitional-development stage, T

The primary conditioning stage was followed by the transitional development stage. Based upon consistent experimental observations, this stage can be further divided into three sub-stages (as illustrated in Figure 5.49); namely (i) primary growth stage (i.e. initial cell attachment); (ii) secondary conditioning stage; (iii) secondary growth stage (i.e. main development stage).

The initial increase in k_s observed following the conditioning stage (i.e. at t_{G1}) would have been triggered by the initial colonising cells growing normal to the wall (on the top or within the roughness element) in a seemingly sporadic manner (Bryers and Characklis 1981; Stoodley et al 1999; Nikora et al. 2002; Barton 2006; Andrewartha 2010).

The k_s triggered by the initial colonising cells reached a local maximum at the start of the secondary conditioning stage, t_{C2}, which can be related to Re_D by (R^2 =0.99):

$$k_{s(C2)} = 2.56 \times 10^{15} Re_D^{-3.41} \qquad \textit{Equation 5.5}$$

During the initial stages of its development the biofilm is likely to be well within the limits of the viscous sublayer, where relatively speaking conditions are very suitable for microbial growth, as discussed in Chapter 2. The internal and external binding forces of a biofilm are relatively weak during the early stages of its development (Vigeant et al. 2002). Consequently, a young biofilm is more susceptible to flow shear than a mature biofilm. As a result, a young biofilm will seek to exploit the added protection supplied by the surface roughness. Interstitial voids and channels formed by the biofilm itself may also provide additional protection for weaker species. The increasingly adverse conditions normal to the wall coupled with the relative weak nature of a biofilm suggests that it is more likely to grow parallel as opposed to normal to the wall during the early stages of its development. Ultimately, this will increase the overall surface coverage of the biofilm and induce a more uniformly distributed structure, as it fills the voids and channels formed during the initial stages of its development. This concept is supported by the work of Stoodley et al. (1999), who observed a more significant increase in biofilm surface coverage relative to thickness with time. The encouraged roughness uniformity will likely reduce the biofilm's overall frictional resistance and k_s (Barton 2006; Andrewartha 2010). It was suggested by Barton (2006) and Andrewartha (2010) that low level fouling could potentially smoothen a surface. This growth phenomenon could explain the observed decrease in k_s with time during the secondary conditioning stage, as shown in Figure 5.48 (i.e. for 50 h < t < 150 h).

The time in which the secondary conditioning stage commenced, t_{C2} was found to be a function of Re_D, as illustrated by Figure 5.50b. This was in part attributed to the reduction in δ' caused by the increase in Re_D, as the area normal to the wall deemed suitable for a young biofilm's development reduces proportionally with increasing Re_D. This reduced area would likely limit the biofilms initial thickness and subsequently encourage parallel as oppose to normal directional growth more rapidly and thus, reduce t_{C2}. Moreover, the increased uniformity fostered by the increase in Re_D and subsequent mass transfer (Pecival 1999; Liu and Tay 2001; Stoodley et al. 2002; Celmer et al. 2008) will ultimately reduce the biofilm's overall k_s value. The reduction in k_s with Re_D would have likely manifested itself in terms of a seemingly reduced t_{C2} with Re_D, as the initiation criteria wouldhave been lowered.

The t_{C2} can be related to Re_D by (R^2 =0.98):

$$t_{C2} = -2.48 \times 10^4 Re_D + 144.64 \qquad \textit{Equation 5.6}$$

The secondary conditioning stage was followed by a secondary growth stage, in which k_s increased significantly within a 48 h period, as shown in Figure 5.48 and Figure 5.51 (i.e. for 136 h < t < 181 h). In particular, Figure 5.51 presents high resolution images recorded during the Re_D = 1.00x10^5 assay, at the 87, 136 and 181 h time intervals. It is evident from Figure 5.51 that the biofilm grew considerably between 136 and 181 h time intervals. The observed increase in growth between the respective time intervals resulted in an increase in k_s of 392%.

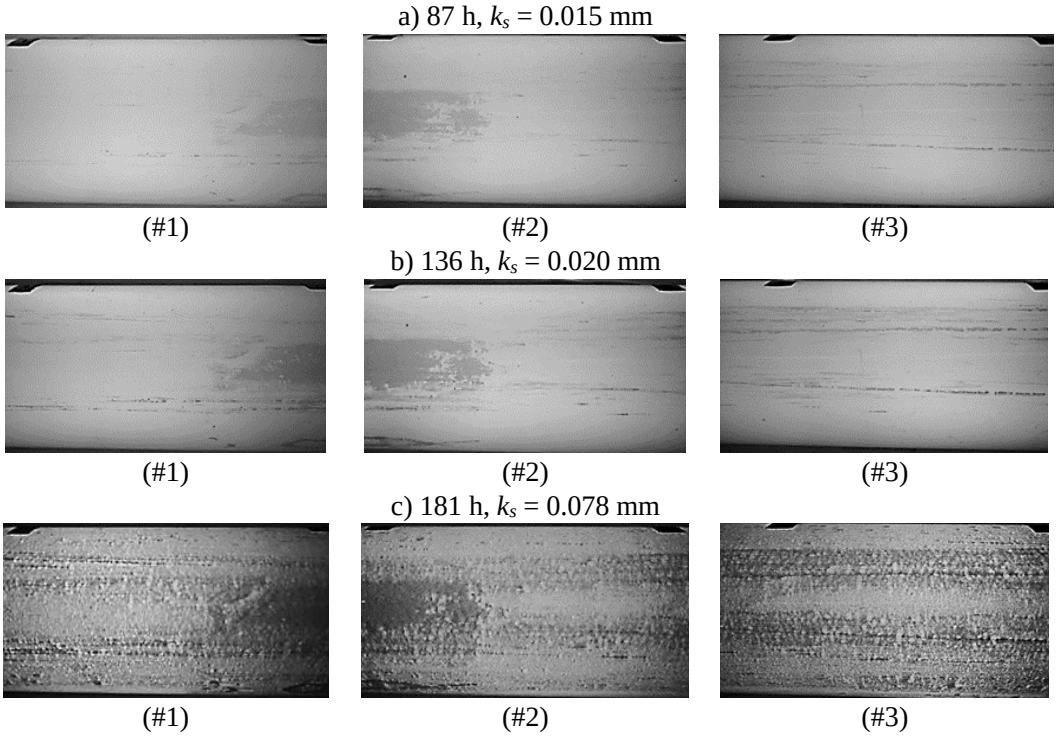

Figure 5.51 High resoultion images taken during the Re_D = 1.00x10^5 assay at a) 87 h, b) 136 h and 181 h time intervals

This observed increase in k_s would have been triggered by the formation of strong and irreversible bonds remediated by the presence and growth of main development species and extracellular polymers, namely carbohydrates (Peyton 1999; Stoodley et al. 2002; Ahimou et al. 2007). Ahimou et al. (2007) found that over time a biofilm's cohesive strength and thickness increased proportionally with extracellular carbohydrate content. The stronger

internal and external binding forces would therefore have allowed the biofilm to progress through the viscous sublayer. This in turn would increase the biofilm's overall nutrient intake capabilities, by virtue of its proximity to the diffusion sublayer (Nikora et al. 2002). An increase in growth rate (both physical and in terms of k_s) would therefore be expected. This is illustrated by Figure 5.51, which shows a significant increase in growth during the secondary growth stage.

Figure 5.52 presents the rates at which k_s changed with time during the primary and secondary growth stages for each of the respective flow assays. It is evident from Figure 5.52 that as Re_D increased the rate of change in k_s decreased.

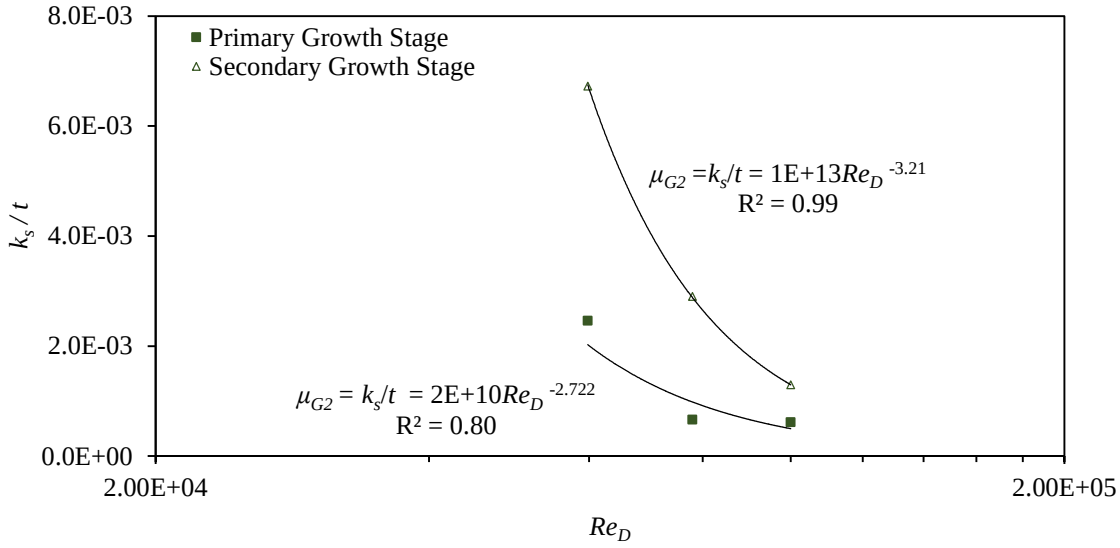

Figure 5.52 Rates of change k_s with time during the primary and secondary growth stages.

The rate of change in k_s during the primary growth stage, μ_{G1} is given by (R^2 =0.80):

$$\mu_{G1} = k_s/t = 2.04 \times 10^{10} Re_D{}^{-2.722} \qquad \textit{Equation 5.7}$$

Similarly, the rate of change in k_s during the primary growth stage, μ_{G1} is given by (R^2 =0.99):

$$\mu_{G2} = k_s/t = 1.37 \times 10^{13} Re_D{}^{-3.205} \qquad \textit{Equation 5.8}$$

No distinguishable trend was observed between the time in which the secondary growth stage commenced, t_{G2} and Re_D. The average t_{G2} for the three flow assays was 129 h.

5.8.1.3 Equilibrium Stage, E

The time, in which the biofilm reached a state of equilibrium, t_E was found to be independent of Re_D and was on average 183 h. Lambert et al. (2008) observed a similar phenomenon, whereby biofilms cultivated using the same nutrient medium, at different flow regimes reached a state of equilibrium at reasonably equivalent times.

Biofilm soughing was not indicated from the recorded frictional data for the current study.

The equilibrium stage equivalent sandgrain roughness, $k_{s(E)}$ was found to be dependent on Re_D, as shown by Figure 5.53. For completeness, Figure 5.53 also illustrates the equilibrium stage n, $n_{(E)}$ against Re_D.

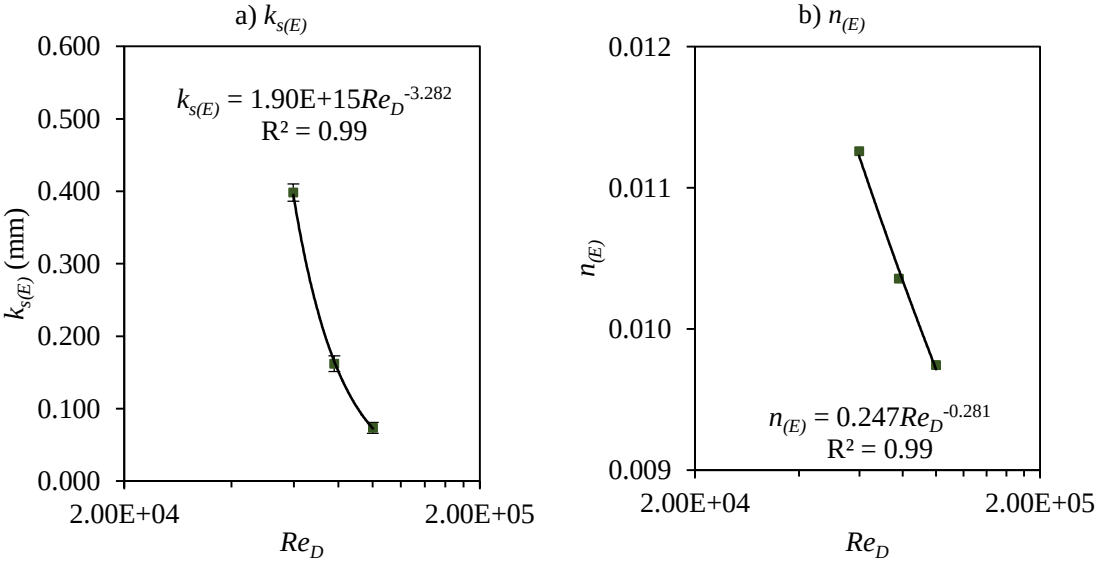

Figure 5.53 $k_{s(E)}$ against Re_D

The observed relationship of decreasing $k_{s(E)}$ with increasing Re_D illustrated within Figure 5.53 was to be expected based on the mass transfer and drag principles, whereby the thickness and uniformity of a biofilm, which controls its impact on k_s are proportional to its conditioning. In particular, at low Re_D the conditions are less restrictive and as a result, more conducive to both thick and isolated development (as shown by Figure 5.1 and Figure 5.2), resulting in a high associated k_s value (Stoodley et al. 1998a; Barton 2006; Celmer et al. 2008; Lambert et al. 2008; 2009; Perkins et al. 2014,). Conversely, the inherently high shear and mass transfer conditions associate with high Re_D would induce a thin and uniformly distributed structure (as shown by Figure 5.2), which would impart a low k_s as a result (Barton 2006; Celmer et al. 2008; Andrewartha 2010).

Power law relationships were attached to the plots of $k_{s(E)}$ and $n_{(E)}$ against Re_D. The fitted relationships had an R^2 of at least 0.99. The experimentally determined relationships for $k_{s(E)}$ and $n_{(E)}$ for the range of $5.98 \times 10^4 < Re < 1.00 \times 10^5$ are given by:

$$k_{s(E)} = 1.90 \times 10^{15} Re_D^{-3.282} \qquad \textit{Equation 5.9}$$

$$n_{(E)} = 0.247 Re_D^{-0.281} \qquad \textit{Equation 5.10}$$

Similar power law relationships have been previously presented within the literature for describing the impact of flow shear upon the hydraulic roughness (including n and k_s) for fouled pipes (Barr and Wallingford 1998; Lauchlan et al. 2005; Guzmán et al. 2007,). However, the relationships outlined within the current study can be considered more representative of a biofouled S-HDPE pipe (for the range of $5.98 \times 10^4 < Re < 1.00 \times 10^5$).

5.8.2 Dynamic k_s formation

Since bacterial growth is exponential, it is typically modelled with respect to time by a logarithm of the relative population size (i.e. $y = \ln(N/N_0$, where N is the number of organisms) (Zwiethering et al. 1990). When the growth curve is defined as the logarithm of the number of organisms plotted against time the result is a sigmoidal curve, as shown by Figure 5.54. Whereby, the maximum specific growth rate, μ_m is defined as the tangent to the inflection point; λ_A (lag-time), is defined as the x-axis intercept of this tangent and the asymptote, B ($=\ln(N_\infty/N_0)$ is the maximum value reached. Numerous models have been outlined within the literature to describe such a sigmoidal curve (Zwiethering et al. 1990). The model adopted for use within the current study to describe a biofilm frictional development over time is known as the "simple logistic model" and is given by:

$$N = \frac{B}{\left\{1 + exp\left[\frac{4\mu_m}{B}(A - t) + 2\right]\right\}} \qquad \textit{Equation 5.11}$$

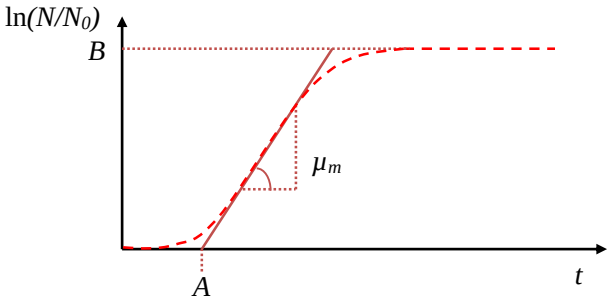

Figure 5.54 Conceptual diagram illustrating key components of a bacterial sigmoidal growth curve.

Based on the observations outlined in Section 5.8.1 it is evident that the biofilm's frictional development (in terms of k_s) comprised of two sigmoidal development curves and thus, two expressions in series.

The first curve, which will be referred to as the initial development curve encompasses the conditioning, primary growth and secondary conditioning stages. The initial development curve is therefore, valid for the range of 0 h < t < 145 h.

The second curve, which will be referred to as the main development curve commenced from the asymptote of the secondary conditioning stage and incorporates the main growth and equilibrium stages. This main development curve is valid for t > 145 h.

Based on Equation 5.11 and observations outlined in Section 5.8.1, the initial development curve can be expressed by the following dynamic k_s parameter (for 0 h < t <145 h, 5.98×10^4 < Re_D < 1.00×10^5);

$$k_{s(t)} = \frac{k_{s(C2)}}{1 + e^{\left[\frac{4\mu_{G1}}{k_{s(C2)}}(t_{G1} - t) + 2\right]}} \qquad \textit{Equation 5.12}$$

Similarly, the main development curve can be expressed by the following dynamic k_s parameter (for t >145 h, 5.98×10^4 < Re_D < 1.00×10^5);

$$k_{s(t)} = k_{sC2} + \left(\frac{\Delta k_{s(E)}}{1 + e^{\left[\frac{4\mu_{G2}}{\Delta k_{s(E)}}(125 - t) + 2\right]}} \right) \qquad \textit{Equation 5.13}$$

where, $\Delta k_{s(E)} = k_{s(E)} - k_{s(C2)}$

The novel dynamic k_s expressions presented by Equation 5.12 and Equation 5.13 provide a realistic representation of the frictional resistance imparted by a biofouled surface during its development stages, as illustrated by Figure 5.55, which presents the experimentally determined k_s (derived from the modified C-W equation) with the predicted k_s values derived from Equation 5.12 and Equation 5.13.

It is evident from Figure 5.55 that the predicted values derived from the novel dynamic k_s parameters are typically in strong agreement (R^2 > 0.81) with the experimental data. However, it is evident that the parameters fail to incorporate the slight reduction in k_s with time observed during the secondary conditioning stage. The strong agreement between the experimentally determined and predicted values of the k_s is further illustrated by Figure 5.56, which presents the experimentally determined values against the predicted values. This shows that the dynamic k_s expressions outlined within this chapter are a useful tool in the prediction biofilm frictional development over time.

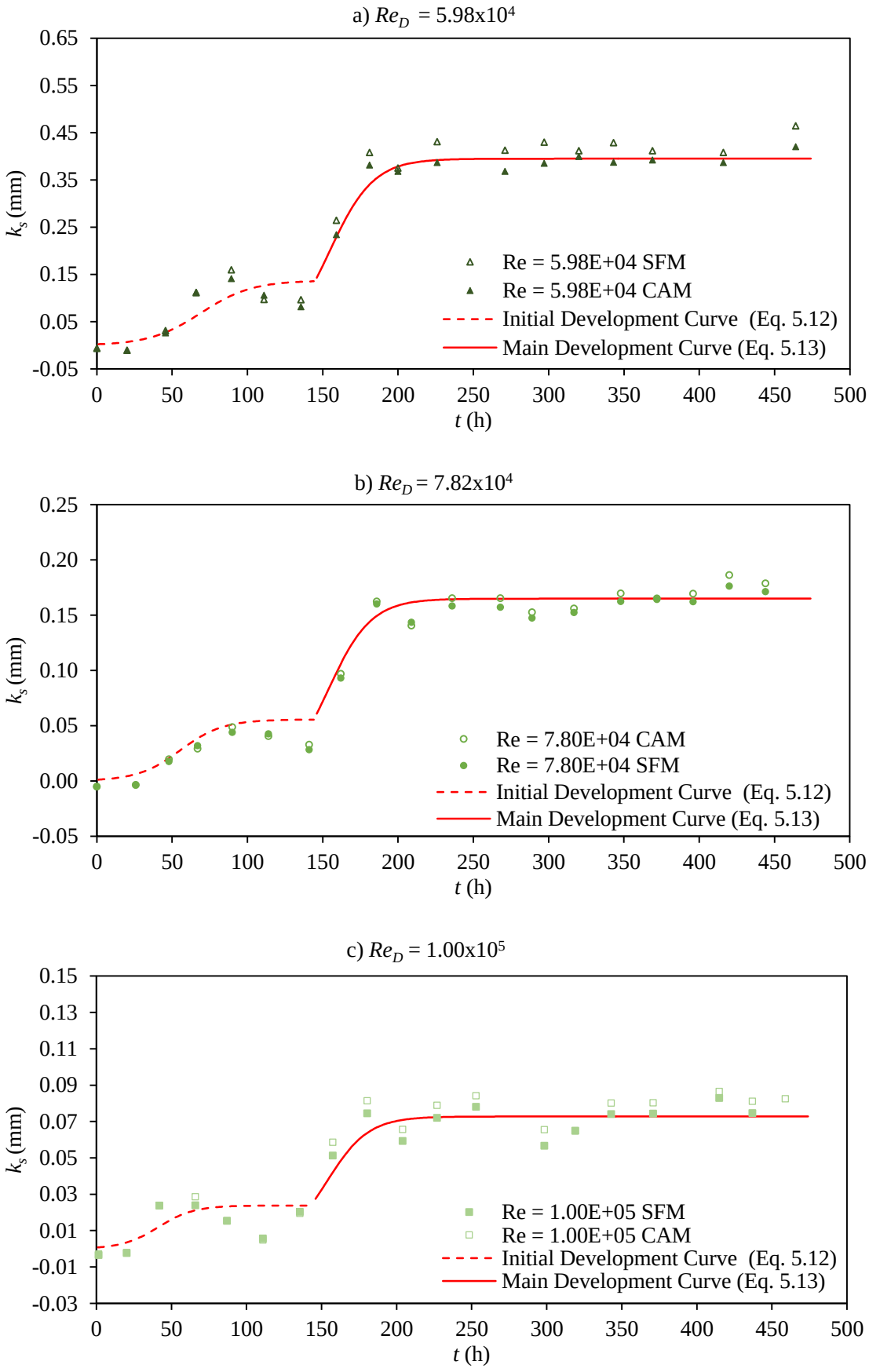

Figure 5.55 Predicted and measured k_s values against time for the a) Re_D = 5.82x10⁴, b) Re_D = 7.82x10⁴and c) Re_D = 1.00x10⁵ assays (predicted values derived from the initial and main development novel k_s expressions).

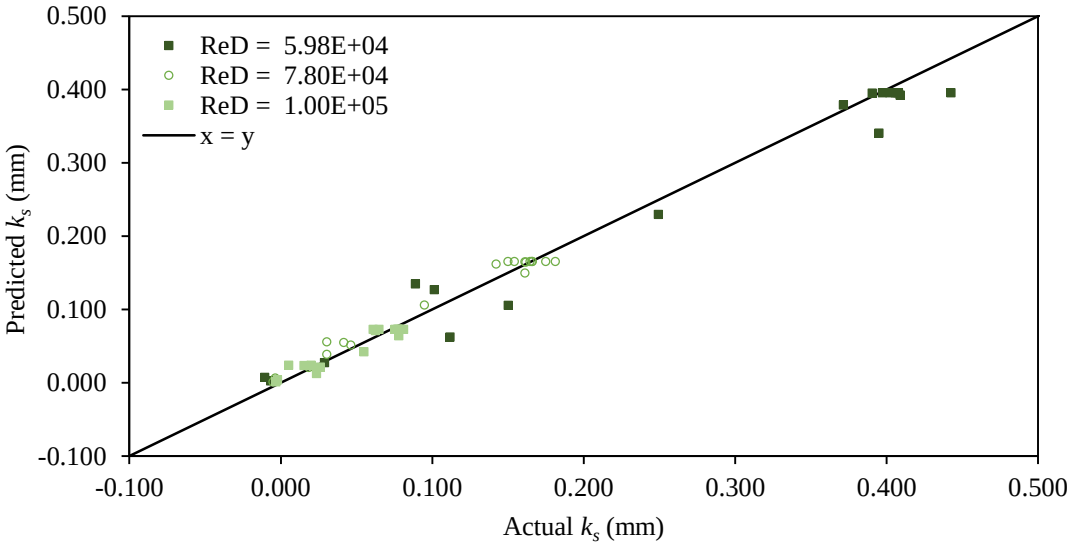

Figure 5.56 Predicted against actual k_s (predicted values derived from the initial and main development novel k_s expressions).

5.9 Summary

This chapter has presented the frictional data recorded locally and globally during the incubation phase of the $Re_D = 5.98\text{x}10^4$, $Re_D = 7.82\text{x}10^4$ and $Re_D = 1.00\text{x}10^5$ assays.

A comprehensive approach has been used to improve the understanding of biofilm development over time. The results presented within this chapter, with regards to the influence of flow hydrodynamics on biofilm frictional development over time have gone beyond that previously documented within the literature (Picologlou et al. 1980; Lambert et al. 2008; 2009). Moreover, for the first time the influence of biofilm development on a S-HDPE pipe within a representative wastewater environment has been documented.

The results have indicated that biofilms incubated with wastewater can have a substantial impact on the frictional resistance of a S-HDPE pipe. In particular, it was found that biofilm development can result in an increase in λ of between 48-85% and cause global k_s to increase from 0.009 mm to as high as 0.460 mm.

The observed increases in frictional resistance would have potentially resulted in a reduction in Q of between 15-22%, had ΔP been held constant within each of the flow assays.

The profound detrimental impact of biofouling on frictional resistance and equivalent surface roughness documented within the current study for wastewater systems, is consistent with the findings outlined previously within the literature, albeit for different applications, namely

hydropower (Picologlou 1980; Lambert et al. 2008; 2009; Barton 2006; Barton et al. 2008). For instance, Lambert et al. (2008) reported that biofilms incubated with river water on a 25 mm internal diameter pipe caused λ to increase by 600% in just 418 h.

An initial increase in frictional resistance was observed after just 25 h of incubation and the biofilms reached a state of equilibrium, in terms of their frictional development after approximately 180 h (or 8 d). This in an industrial sense is a relatively short period of time and it highlights the inevitability of the problem. The time at which the biofilms reached a state of equilibrium was found to be independent of the conditioning shear, which is consistent with the findings of Lambert et al. (2008). It is therefore suggested, that other factors, such as nutrient content and/or temperature may have a greater influence on t_E than flow hydrodynamics. However, it should be noted that only a small, albeit representative range of Re_D were evaluated within the current study.

The magnitude of the biofilm's impact on frictional resistance and equivalent surface roughness was evidently a function of the shear conditions in which it was incubated. Most notably, it was found that the lower the conditioning shear the higher the frictional resistance imparted by the biofilm. This was explained by the influence of mass transfer and drag limitations on biofilm morphology and thickness and is consistent with known literature (De Beer et al. 1994; Lewandowski and Stoodley; 1998a). In particular, it was evident that the equivalent roughness of the biofilm incubated at the lowest shear (i.e. in the $Re_D = 5.98\text{x}10^4$ assay) was highly irregular along the pipe's length (as shown by Figure 5.1), which in part could have explained the higher overall frictional resistance of the system. The irregularity of the biofilm's roughness was illustrated by deviations in global roughness along the pipeline. Conversely, the biofilm incubated at high shear (i.e. in the $Re_D = 1.00\text{x}10^5$ assay) was shown to have a uniform distribution and a lower overall k_s. It was also likely that restrictions imposed on overall thickness by the respective assay's conditioning shear could have explained the observed difference in k_s (Barton 2006; Lambert et al. 2008; 2009; Andrewartha 2010) although, physical measurements could not be undertaken.

The high initial roughness associated with the pipe joints was found to promote considerable biofilm development, as indicated by a significant increase in k_s with fouling. For instance, within the $Re_D = 5.98\text{x}10^4$ assay the k_s value associated with the pipe joints with fouling was 596% greater than the equivalent value associated with the rest of the fouled system. This illustrates that surface roughness can be an important factor in the development of a biofilm, which was also found to be the case within previous biofouling and biofilm investigations

(Percival et al. 1999; Gjaltema et al. 2004; Barton 2006; Kurth 2008; Yu et al. 2010 Walker 2014).

It was conclusively found that the Log-Law constants of κ and B for biofouled surfaces were non-universal and dependent on Re_D. Linear relationships (namely, Equation 5.2 and Equation 5.3) were found to express κ and B as a function of Re_D to a high degree of conformity ($R^2 > 0.95$). The results outlined within this chapter have significantly extended the knowledge on this topic, expanding on the concepts previously documented by Lambert et al. (2009) and Perkins et al. (2013; 2014). In particular, the implications of non-universal constants on global and local frictional measurements have for the first time been discussed in detail. The ramifications of which could extend into the classical theory, where the universality of the Log-Law and its constants has also been questioned (Zanoun et al. 2003; Wei et al. 2005; Nagib and Chauhan 2008), albeit not by the current study, as discussed in Chapter 4.

It was found that the traditionally accepted universal value of κ significantly overestimated the k_s of biofouled surface by between 49-85% using the C-W equation. This could have considerable implications on Q predictions and pipe sizing in the design process.

Furthermore, it was found that although, wall similarity is valid and can be applied to biofouled surfaces it is reliant on either κ or u^* being known, without which the results are likely to be unrepresentative of the actual conditions. Consequently, this study is in agreement with the general opinion that a method independent from mean-velocity should be used in conjunction with wall similarity to determine the frictional data of a biofouled surface (Schultz and Swain 1999; Candires 2001; Walker et al. 2013). Such a method should ideally be able to measure local frictional conditions, given the likely heterogeneous nature of a biofouled surface.

A novel series of dynamic k_s expressions capable of defining biofilm frictional development over time and under different flow regimes were the culmination of all the experimental observations outlined within this chapter. Such expressions could become the basis of a more advanced mathematical modelling framework that can be used to predict critical efficiency losses which includes adequate representations of the dynamic and case-specific nature of biofouling. This could give rise to a real time monitoring platform to assist the adoption of more cost-effective approaches to maintenance and repairs. However, further research is required, which evaluates biofilm development over a greater range of flow regimes and for different nutrient and temperature conditions for such a framework to be all encompassing and truly representative of the dynamic nature of biofouling.

Chapter 6 Mature phase

6.1 Introduction

The purpose of this chapter is to outline the results of the mature phase aspect of the current study. In particular, this chapter presents the frictional, water and image data captured during each of the varying flow investigations undertaken on the biofilms incubated within the Re_D = 5.98x10^4 and Re_D = 1.00x10^5 assays. The results of the molecular analysis for the biofilm and water samples taken during the mature phase are also presented within current chapter. The biofilms molecular structure was evaluated and compared by 16S rRNA gene PCR-DGGE, DNA and EPS quantification. A summary is presented at the end of this chapter.

6.2 Impact of varying flow conditions on biofilm dynamics

Typically, the interaction between a fluid and biofilm is governed by the flow hydrodynamics and surface characteristics of the biofilm. Though, the fluid will impart a drag force on the biofilm, it is generally assumed that the shear force created as the fluid flows over the surface is the principle physical force acting on the biofilm (Stoodley et al. 2002). This means the biofilm incubated within the Re_D = 5.98x10^4 assay had been conditioned at shear forces of 0.82 N/m^2 < τ_w < 1.42 N/m^2. Similarly, the biofilm incubated within the Re_D = 1.00x10^5 assay had been conditioned at shear forces of 1.95 N/m^2 < τ_w < 2.97 N/m^2. The lower and upper limits of the respective ranges represent the initial and equilibrium state values of τ_w measured within each flow assays. Consequently, the conditioning shear at the point at which each of the varying flow investigations commenced was τ_w = 1.42 N/m^2 for the Re_D = 5.98x10^4 assay and τ_w = 2.96 N/m^2 for the Re_D = 1.00x10^5 assay.

6.2.1 Frictional evaluation

The fouled pipes frictional resistance was determined from the system's PG using the SFM. The frictional data established from the SFM for each of the varying flow investigations is presented within Appendix D.1 in Table D.1 and Table D.2. Also presented within Table D.1 and Table D.2 are the case-specific κ values calculated using Equation 5.2. The k_s values

listed within Table D.1 and Table D.2 were calculated using the C-W equation in its traditional (i.e. Equation 2.38) and modified (i.e. Equation 2.50) forms.

The influence of Re_D on λ is illustrated by Figure 6.1 and Figure 6.2 in the form of Moody Diagrams. Figure 6.3 presents the impact of increasing Re_D on k_s determined using the modified C-W equation.

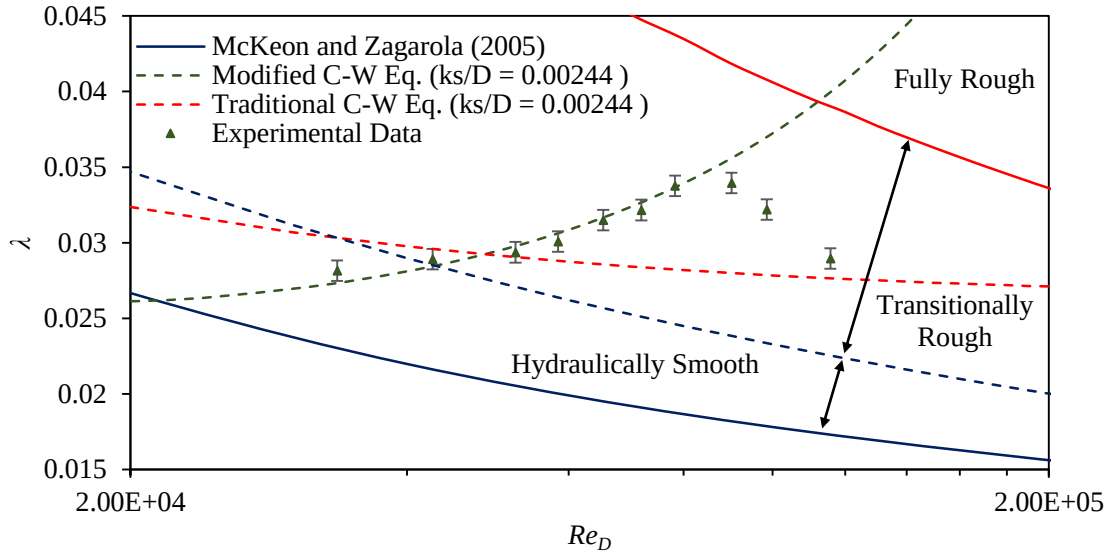

Figure 6.1 λ against Re_D for the biofilm incubated within the $Re_D = 5.98x10^4$ assay (for $3.36x10^4 < Re_D < 1.15x10^5$).

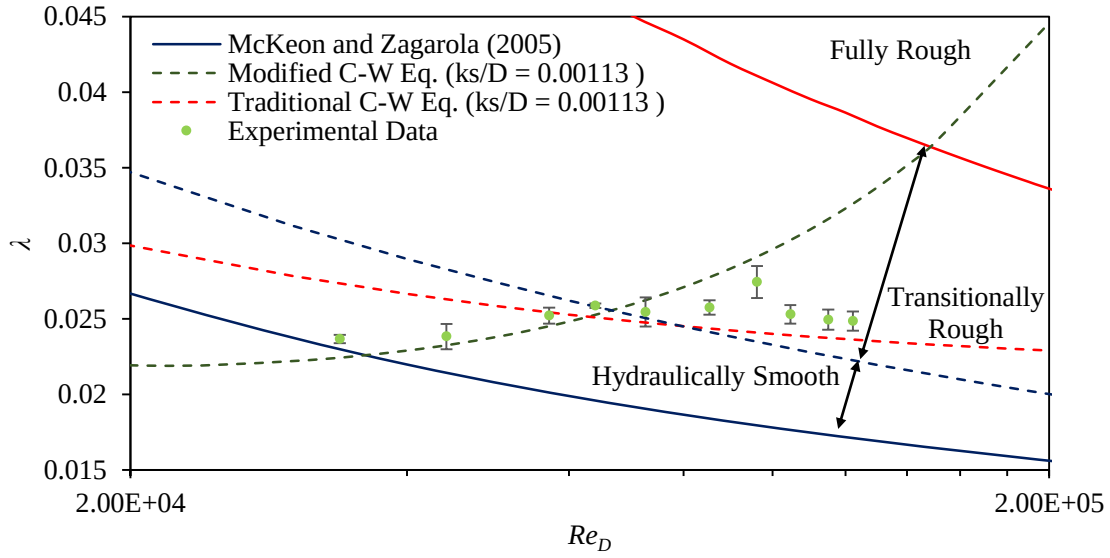

Figure 6.2 λ against Re_D for the biofilm incubated within the $Re_D = 1.00x10^5$ assay (for $3.38x10^4 < Re_D < 1.22x10^5$).

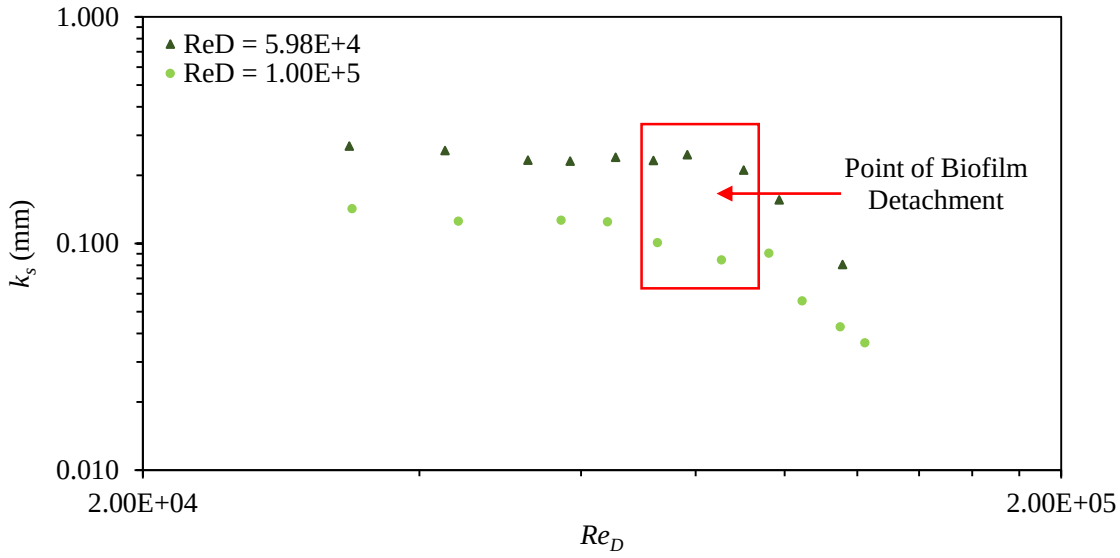

Figure 6.3 k_s against Re_D for the biofilm cultivated within the Re_D = 5.98x10^4 and Re_D = 1.00x10^5 assays. The k_s values were determined using the modified C-W equation and the uniquely derived values of κ.

The relationships between Re_D and λ depicted within Figure 6.1 and Figure 6.2 for biofouled pipes are evidently different to that expected based on the traditional C-W equation. Consequently, the current study is in agreement with the general consensus that the traditional C-W equation is not always applicable to biofouled surfaces (Schultz and Swain 1999; Schultz 2000; Barton 2006; Barton et al. 2008; Lambert et al. 2008; 2009; Perkins et al. 2013; 2014).

It is evident from Figure 6.1 and Figure 6.2 that λ increases with increasing Re_D. For the Re_D = 5.98x10^4 assay, the λ rises to a maximum of 0.034 at Re_D = 7.83x10^4. Whereas, the λ for the Re_D = 1.00x10^5 assay increases to a maximum of 0.027 at Re_D = 9.61x10^4. Prior to these local maximums being reached the modified C-W curves established using the case-specific values of κ are in good agreement with the experimentally determined values of λ. In particular, it was found that the maximum discrepancy between the measured and predicted values was ±7.51%. The average discrepancy between the respective friction factors was ±2.82%. These discrepancies are within the experimental uncertainty in λ outlined in Table 4.1. Consequently, the frictional data determined independent from the mean-velocity data is in support of a non-universal κ, and in particular, the data is with agreement of the values of κ determined from Re_D using Equation 5.2 (see Section 5.7.3). This independently validates Equation 5.2, which is important given the errors associated with mean-velocity measurements (see Section 5.7)

The magnitude at which λ increases was a function of the biofilm's k_s. In particular, the greater the k_s the greater the increase in λ. Lambert et al. (2009) reported a similar phenomenon for biofouling albeit, for smaller diameter pipes (i.e. D = 25-50 mm). Lambert et al. (2008) also found that at low Re_D the λ induced by a biofilm followed the traditional smooth pipe curve. This conclusion could not be adequately confirmed from the available data within the current study. However, it is evident from Figure 6.2 (i.e. for the $Re_D = 1.00\text{x}10^5$ assay) that the value of λ at $Re_D = 3.38\text{x}10^4$ is in closer agreement with the smooth pipe curve than with the modified C-W curve.

The type of behaviour, whereby λ increases from the smooth pipe curve before meeting the fully rough value, is known as an inflectional type roughness (Allen et al. 2007). Traditional C-W curves, as depicted on the Moody Diagram where λ approaches the fully rough values from the smooth pipe curve from above are described as monotonic. Studies have shown that engineered and naturally rough surfaces will typically behave more like an inflectional- rather than monatomic- type roughness (Nikuradse 1933; Hama 1954; Ligrani and Moffat 1986; Shockling et al. 2006; Allen et al. 2007). However, the inflectional behaviour reported within the current study for biofouled surfaces was far more extreme than the previously reported cases of engineered surfaces. The extreme inflectional behaviour reported within the current study was likely fostered by the observed non-universality of κ.

Once the local maximum was reached λ begins to decrease with increasing Re_D. In the case of the $Re_D = 5.98\text{x}10^5$ assay this decrease in λ was significant. The equivalent decrease in the $Re_D = 1.00\text{x}10^5$ assay was far more gradual. Similar trends for λ against Re_D have been reported within the literature (Barton et al. 2008; Lambert et al. 2008; 2009; Perkins et al. 2013; 2014). For instance, Perkin et al. (2014) found that the λ of a biofilm incubated within a hydropower pipeline increased gradually with increasing Re_D between $9.32\text{x}10^4$-$1.57\text{x}10^5$ to a maximum of 0.033, before decreasing significantly with increasing Re_D between $1.57\text{x}10^4$-$2.66\text{x}10^5$. The biofilm assessed by Perkin et al. (2014) was conditioned at $\overline{U}$ = 1.30 m/s.

The apparent reduction in λ with Re_D after the local maximum was reached could be explained by a reduction in biofilm thickness caused by the biofilm compressing itself under loading (Percival 1999; Douterelo et al. 2013; Perkins et al. 2014) or by it being sheared from the surface (Schultz and Swain 1999; Barton 2006; Barton et al. 2008; Lambert et al. 2008; 2009; Andrewartha 2010; Douterelo et al. 2013). The usual reduction in λ with Re_D could also explain the evident trend (Perkin et al. 2014).

The biofilm incubated within the Re_D = 5.98x10^2 assay was subject to a secondary varying flow investigation approximately 48 h after the first. The friction factors established during the secondary varying flow investigation are presented in the form of a Moody Diagram by Figure 6.4, which further illustrates the initial agreement between the measured and predicted values.

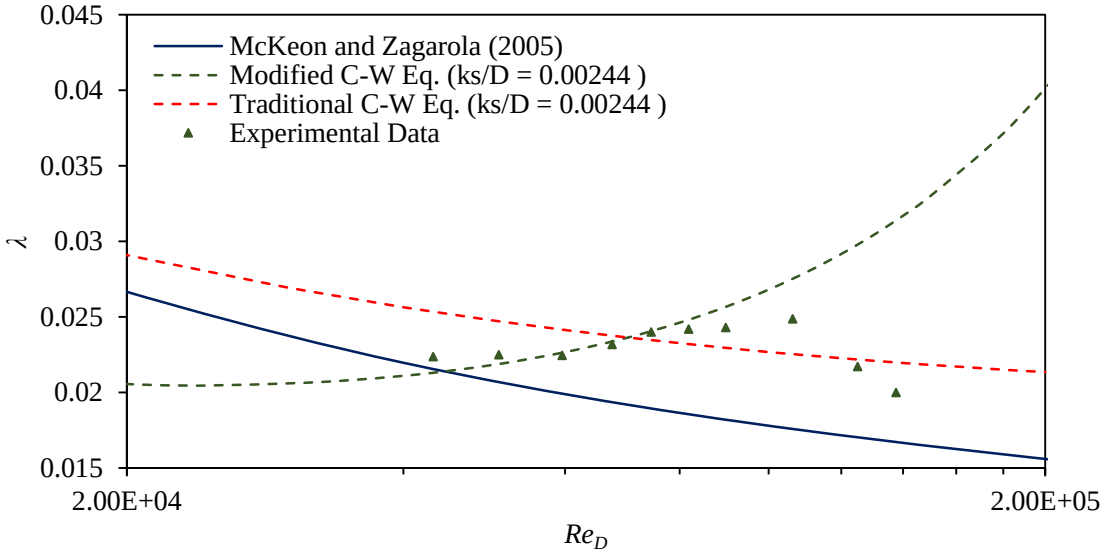

Figure 6.4 λ against Re_D for the secondary varying flow investigation undertaken on the biofilm incubated within the Re_D = 5.98x10^4 assay.

6.2.2 Bulk water chemistry evaluation

The concentrations of Fe, Mn, COD and TOC recorded within the bulk water during each of the varying flow investigations are presented in Figure 6.5 and Figure 6.6. It is evident from Figure 6.5 and Figure 6.6 that the concentrations of each of the measured parameters increased significantly within the Re_D = 5.98x10^4 assay as flow shear increased. In particular, a significant increase in each of the respective parameters were evident when Re_D and τ_w respectively exceeded 6.54x10^4 and 1.79 N/m^2. The increase in each of the parameters was less extreme in the Re_D = 1.00x10^5 assay. Nevertheless, increases were evident when Re_D and τ_w respectively exceeded 9.60x10^4 and 2.92 N/m^2. The shear force which caused the initial increase in organic and inorganic content within the bulk water was equivalent to the respective biofilm's conditioning shear (i.e. τ_w = 1.46 N/m^2 for the Re_D = 5.98x10^4 assay and τ_w = 2.95 N/m^2 for the Re_D = 1.00x10^5 assay).

The observed increase in organic and inorganic content within the bulk water suggests that biofilm detachment was likely to have occurred within both assays, particularly, given the

short duration of each of the investigation. However, based on the magnitudes of the respective increases the degree of detachment will have varied between the assays. For instance, the concentration of TOC within the bulk water of the Re_D = 5.98x10^4 assay following the increase in flow shear was 62.5 mg/l whereas, the equivalent concentration within the bulk water of the Re_D = 1.00x10^5 assay was 10.9 mg/l. Therefore, it can be implied that greater biofilm detachment was likely to of occurred within the Re_D = 5.98x10^4 assay than within the Re_D = 1.00x10^5 assay. This observation supports the assumption that the biofilm within the Re_D = 1.00x10^5 assay was merely thinned by the increase in flow shear, as opposed to being completely detached, as suggested based on the frictional data.

The presumed detachment point for the Re_D = 1.00x10^5 assay's biofilm, as suggested by the increase in bulk water organic and inorganic content is the same point at which a reduction in λ was first recorded (see Figure 6.2). This supports the argument that the increase in organic and inorganic content within the bulk water was a result of biofilm detachment. Furthermore, the nature of the reduction in λ, i.e. gradual would also support the conclusion that the biofilm was merely thinned by the increase in flow shear. Alternatively, the considerable decrease in λ following the post shear (see Figure 6.2) would support the argument that large scale biofilm detachment occurred within the Re_D = 5.98x10^4 assay. However, as λ did not approach the non-fouled curve post shear, it was unlikely that the biofilm was completely removed. The point at which λ began to decrease with Re_D within the Re_D = 5.98x10^4 assay did not coincide with the detachment point implied by the changes in bulk water chemistry (i.e. Re_D > 6.54x10^4 and τ_w > 1.79N/m^2). In fact, λ continued to increase beyond the presumed detachment point, which suggests that biofilm detachment did not occur. However, it is possible that the initial detachment, which gave rise to the increases in bulk water organic and inorganic content had a negligible effect on the biofilm's frictional capacity. Conversely, it is equally possible that the initial biofilm detachment could have given rise to a more heterogeneous roughness distribution, which could have directly contributed to, or been the reason for the observed λ relationship.

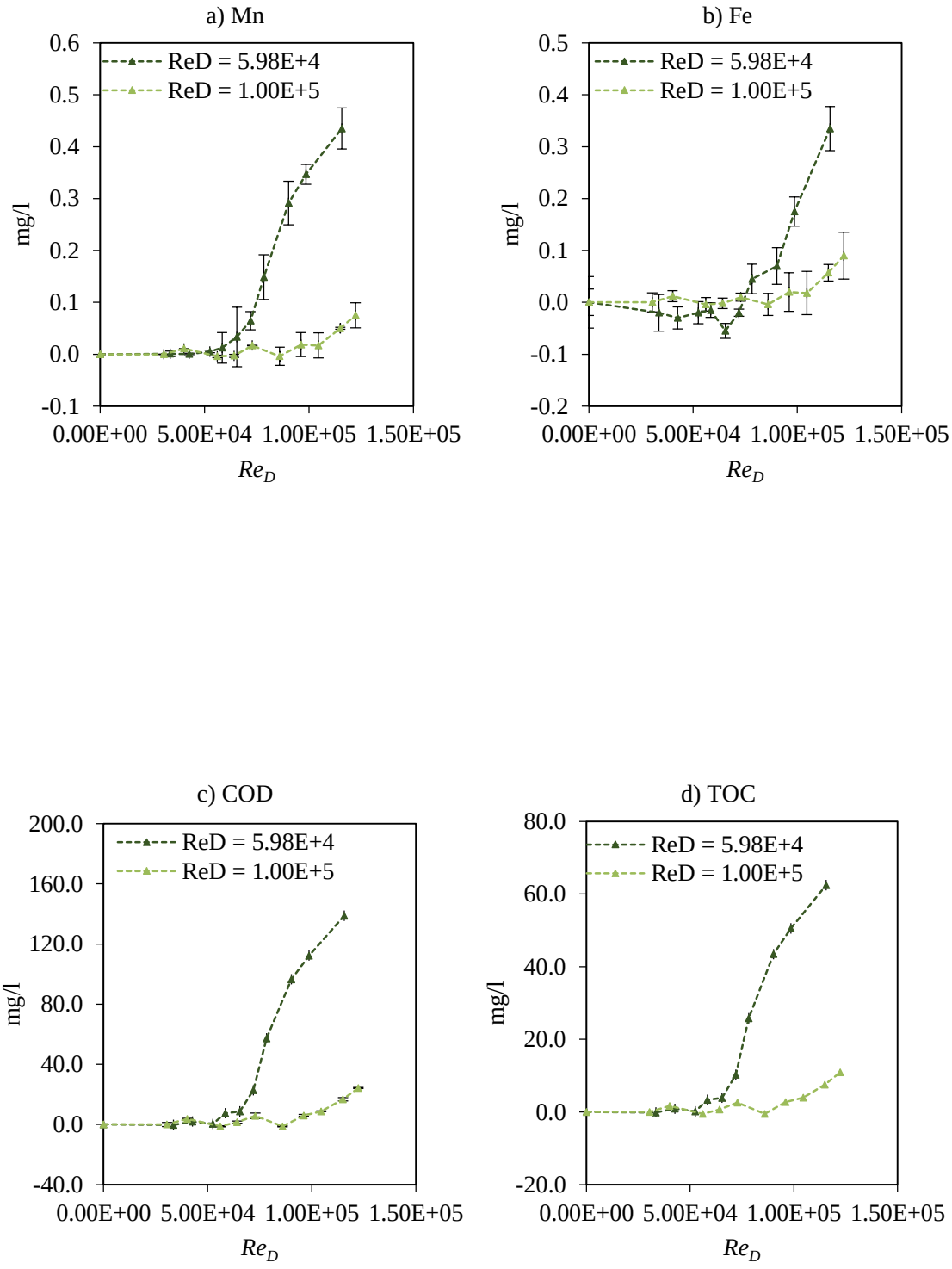

Figure 6.5 Concentration of a) Mn, b)Fe, c) COD and d) TOC within the bulk water as Re_D increase.

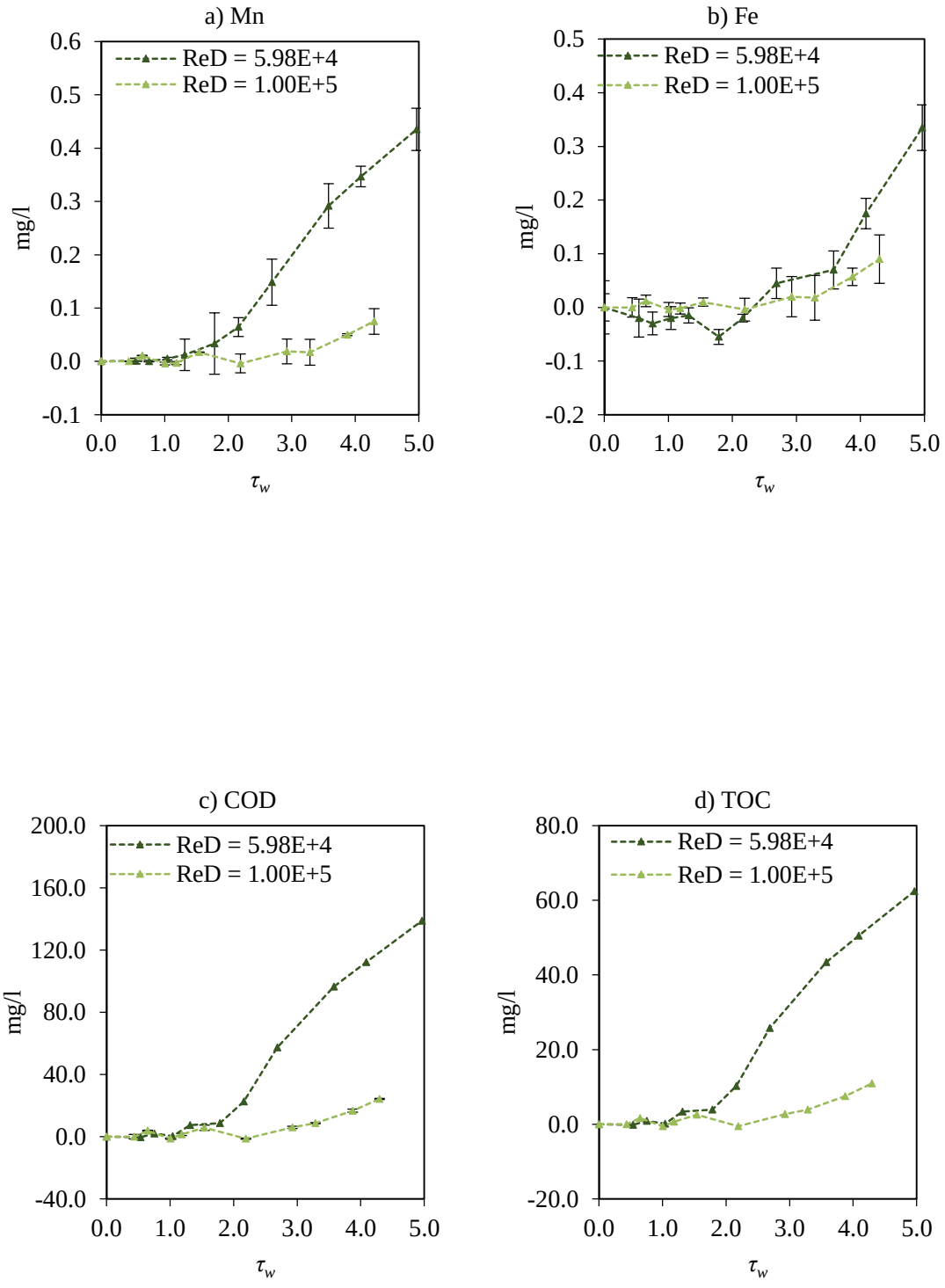

Figure 6.6 Concentration of a) Mn, b)Fe, c) COD and d) TOC within the bulk water as τ_w increase.

Figure 6.7 presents the concentrations of DNA recorded within the bulk water of Re_D = 5.98x10^4 and Re_D = 1.00x10^5 assays as flow shear was increased. A significant increase in DNA was observed within the Re_D = 5.98x10^4 assay following the increase in flow shear. In particular, the concentration of DNA within the bulk water increased by 806% post shear, which would imply that large scale biofilm detachment occurred within the Re_D = 5.98x10^4 assay. The DNA concentration within the bulk water of the Re_D = 1.00x10^5 assay remained reasonably unaffected by the changes in shear conditions, which suggests that biofilm detachment did not occur and is in contrast to the previous findings outlined in this section.

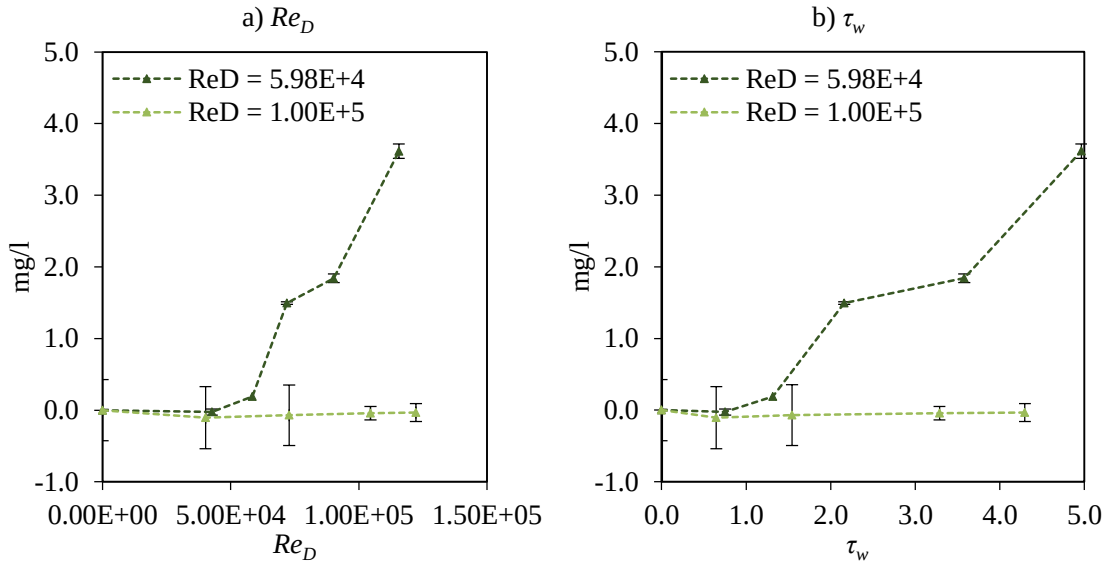

Figure 6.7 DNA concentrations within the bulk water for increasing a) Re_D and b) τ_w

Relationships between each of the measured chemical parameters relative to each other were determined and are presented in Appendix D.2 in Figure D.1. The established relationships had an R^2 of at least 0.84, indicating strong correlations between the respective parameters, which implies that measured chemical parameters were related to each other and likely to the biofilm. Relationships between each of the chemical parameters and with DNA were also established (see Appendix D.2, Figure D.2). Again strong correlations were observed were an R^2 of least 0.77 being attained.

6.2.3 Image analysis – Biofilm detachment

Images recorded at each Re_D increment are presented in Figure 6.8. These images were extracted directly from the video recordings captured using a high definition web camera during each of the varying flow investigations.

The images captured of the biofilm within the Re_D = 1.00x10^4 assay were inconclusive in terms of identifying whether the increase in flow shear actively removed the biofilm from the surface (see Figure 6.8a). Naturally, the presented images are subjective and have inherent bias towards the smaple area. However, irrespective of the sampling location if the biofilm was merely thinned or compressed by the increase in flow shear (as theorised for the Re_D = 1.00x10^4 assay) it is highly unlikely it would have been captured by the recorded images, particularly given the position and sensitivity of the camera.

Large-scale biofilm detachment was evident from images captured of the biofilm within Re_D = 5.98x10^4 assay, as shown by Figure 6.8b. In particular, significant detachment was apparent once Re_D and τ_w respectively exceded Re_D = 7.83x10^4 and τ_w = 2.69 N/m^2, which coincides with the point at λ begins to decrease with increasing Re_D (see Figure 6.1). This indicates that large-scale detachment was the cause of the profound decrease in λ with Re_D. Furthermore, some detachment is evident within Figure 6.8b just prior to the large-scale detachment. The initiation point for this detachment was Re_D = 6.54x10^4, which coincides with the point at which an increase in organic and inorganic content was first evident. This confirms that the increase in organic and inorganic content during the Re_D = 5.98x10^4 assay was a direct result of the biofilms detachment, which until now was just conjecture.

An equivalent confirmation on the relationship between changes in water chemistry and biofilm detachment could not be made for the Re_D = 1.00x10^4 assay due to the negligible detachment observed within the captured images. Nevertheless, based on the recorded frictional data it was likely that some detachment will have occurred within the Re_D = 1.00x10^4 assay. Furthermore, Figure 6.9, which shows the internal surface of the pipeline during the Re_D = 1.00x10^4 assay at pre- and post- shear time intervals, illustrates that some albeit, minimal detachment occured following the increase in shear. This detachment could have trigger the observed increase in water chemistry.

The internal and external binding forces of a biofilm are typically in a state of equilibrium with the shear force in which it is conditioned. Consequently, in order to successfully remove a mature biofilm these integral forces need to be overcome (Korstgens et al. 2001). This could explain why the biofilm incubated at the higher conditioning shear (i.e. within the Re_D = 1.00x10^5 assay) was more resilient to the increase in flow shear than the biofilm conditioned at lower shear (i.e. within the Re_D = 5.98x10^4 assay). Stoodley et al (2002) also found that biofilms conditioned at high shear had greater substrate adhesion and were supported by a stronger EPS matrix than those conditioned at low shear.

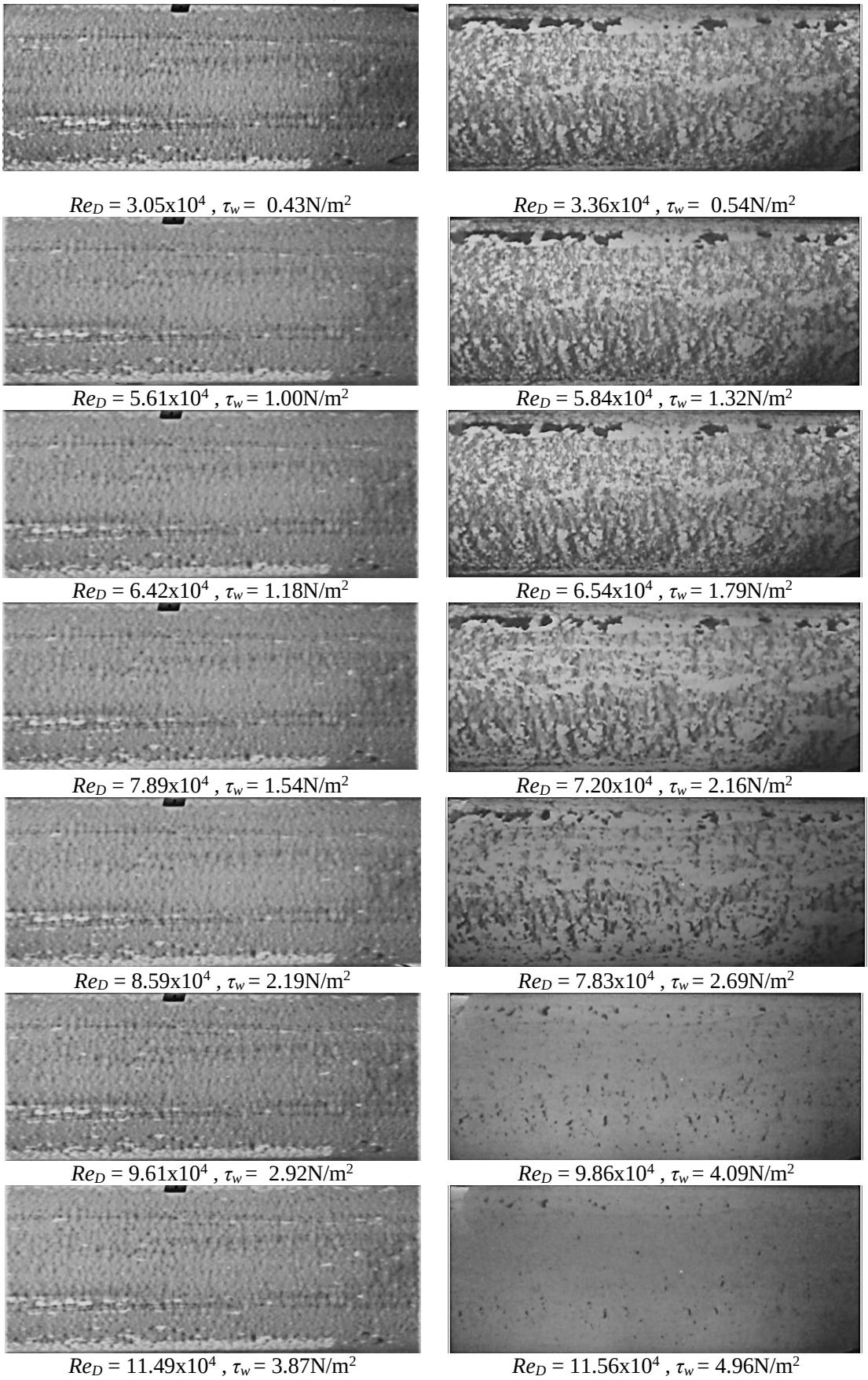

Figure 6.8 Images recorded at each Re_D increment within a) Re_D = 1.00x10^5 and b) Re_D = 5.98x10^4 assays.

Stoodley et al. (2002) suggested the increased stability, induced by the higher conditioning shear was a result of the biofilm's extracellular polymer strands becoming physically stretched, aligned and pulled closer together, which increased the likelihood of stronger and irreversible bond formation. Other studies have also shown that biofilms incubated under higher shear conditions are more resilient than those incubated under low shear conditions (Percival et al. 1999; Manuel et al. 2010; Sharpe et al. 2010; Vrouwenvedlder et al. 2010; Douterelo et al. 2013). In particular, Sharpe et al. (2010) who investigated biofouling within DWDSs, found that high conditioning shear resulted in higher biofilm surface retention and less microbial detachment after an increased flow event. Despite, the biofilm being incubated with drinking water the principle is the same.

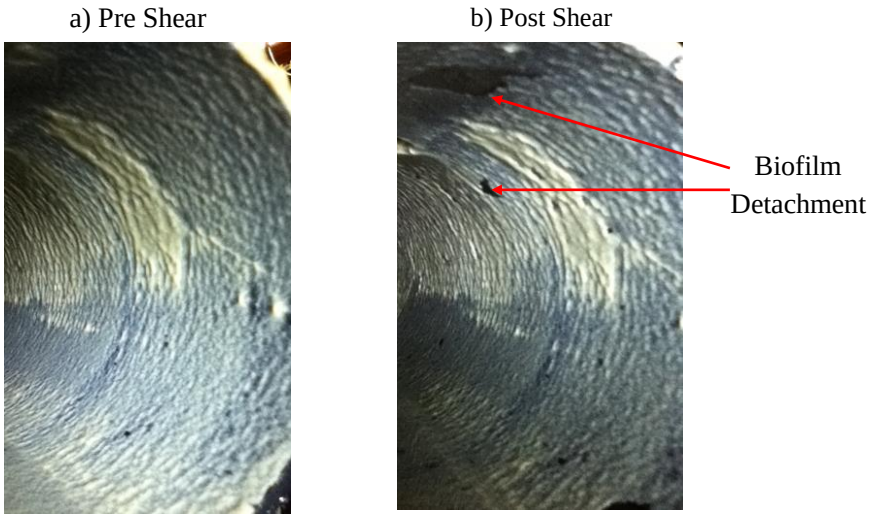

Figure 6.9 Photographs of the internal surface of the pilot-scale pipe during the Re_D = 1.00x10^5 at both a) pre- and b) post- shear time intervals.

A simple MATLAB programme was written to evaluate the images captured within the Re_D = 5.98x10^4 assay. The programme converted the captured images into entirely black and white pixels and then counted the number of each. The overall percentage coverage of the biofilm was assumed to be equivalent to the overall percentage of black pixels within each of the captured images. The results of the MATLAB image evaluation are presented in Figure 6.10. The concentrations of TOC recorded within the bulk water during the Re_D = 5.98x10^4 assay are also presented within Figure 6.10. It is evident from Figure 6.10 that the overall reduction in biofilm coverage is inversely proportional to the increase in bulk water TOC, which supports the argument that biofilm detachment was the cause of the changes in water chemistry.

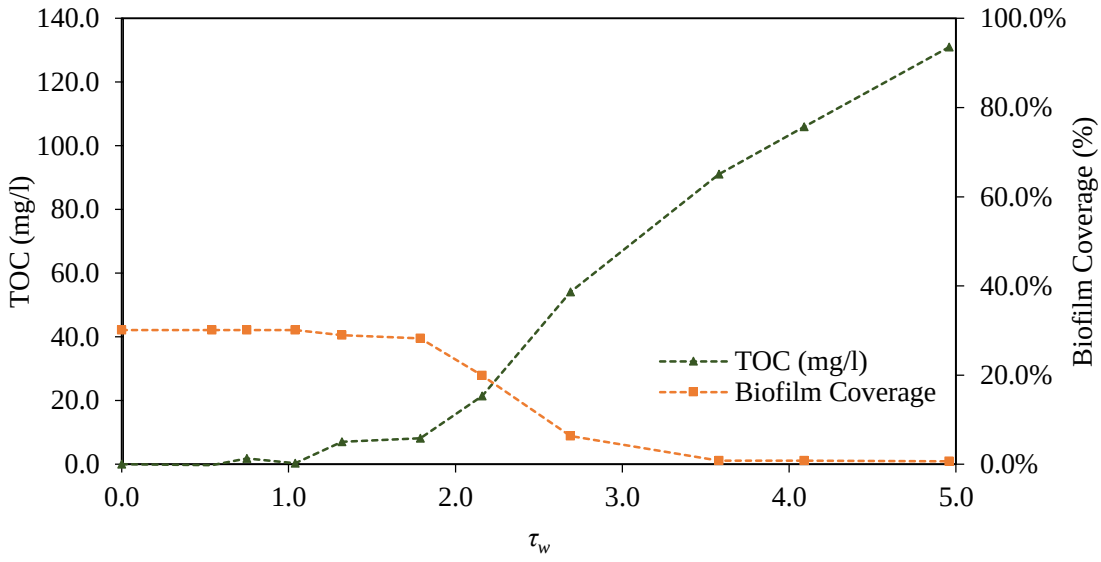

Figure 6.10 Influence of τ_w on biofilm coverage and bulk water TOC within the Re_D = 5.98x10^4 assay.

6.3 Molecular evaluation

The biofilm samples that were taken at the four different circumferential positions, both pre- and post- shear are evaluated within this section.

6.3.1 Bacterial community composition

The dominant bacterial communities residing within the biofilm and bulk water samples taken within the Re_D = 5.98x10^4 and Re_D = 1.00x10^5 assays (both pre- and post- shear) were identified by 16S rRNA gene PCR-DGGE, using the protocols outlined within Section 3.7.3. Sequencing the excised DGGE bands identified the dominant bacterial members.

In total 36 (or 71%) of the distinguishable bands were excised and sequenced from two polyacrylamide gels. The results of the PCR analysis are presented in Appendix D.3 in Figure D.3 and Figure D.4. The PCR-DGGE analysis results for the biofilm and bulk water samples are presented within Figure 6.11 and Figure 6.12 and a summary is provided within Figure 6.13.

The dominant phyla within the assessed biofilm and bulk water samples were found to be *Bacteroidetes*, *Actinobacteria*, *Alphaproteobacteria*, *Betaproteobacteria* and *Firmicutes*.

Based on the PCR-DGGE analysis no distinguishable differences were observed in the microbial community around the circumference of the pipe. Douterelo et al. (2013) reported a similar finding for biofilms incubated within drinking water under full bore conditions,

using a pyrosequencing analysis. In particular, Douterelo et al. (2013) found that the sampling position along and around a 2030 m long S-HDPE pipeline (of D = 79.3 mm) did not significantly affect the microbiological characteristics of the assessed biofilms. Assuming this was the case within the current study, the samples taken at approximately 8.5m from the test pipe inlet can be considered representative of the whole system.

Typically, wastewater systems with the exception of rising/force mains are not operated at full bore conditions. Consequently, the bacterial communities within a typical DN will differ considerably around the pipe, particularly at the invert and soffit sides (Santo Domingo et al. 2011). Therefore, the findings of the current study only relate to the bacterial communities found within typical rising/force mains and at the invert side of non-full bore systems. This is due to the likely submergence of the respective communities within these systems and at these locations.

Santo Domingo et al. (2011), who surveyed 16 concrete sewer surfaces (including: manholes; combined sewer overflows and sections of a corroded sewer pipe) found that the most dominant phylum within biofilms residing at the invert of a concrete sewer was *Bacteroidetes*, which represented 48.5% of the total community. At the genus level some of the *Bacteroidetes* documented by Santo Domingo et al. (2011) were closely related to *Parabacteroides* and *Dysgonomonas sp.*, which are both typically found within the human gut (Xu et al. 2007). *Proteobacteria*, namely *Betaproteobacteria* (16.4%) and *Deltaproteobacteria* (11.7%) were also abundant at the sewer's invert (Santo Domingo et al. 2013). The communities outlined by Santo Domingo et al. (2011) from real sewers, albeit, concrete ones are reasonably consistent with those documented within the current study for synthetically grown biofilms. The slight disparities, particularly in phylum dominance may be attributed to the differences in which the respective biofilms were incubated (Donlan et al. 2002, Prakash et al. 2003; Qi et al. 2008; Santo Domingo et al. 2011; Douterelo et al. 2013). The community structure of a biofilm is significantly influenced by the hydrodynamic conditions to which it is grown (Donlan et al. 2002; Prakash et al. 2003; Qi, et al. 2008; Douterelo et al. 2013). The biofilms assessed by Santo Domingo et al. (2011) will have been incubated under very different hydrodynamic conditions to those evaluated within the current study. Moreover, Santo Domingo et al. (2011) assessed concrete sewers; the alkaline nature of concrete would have given rise to very different communities to those expected on plastic. For instance, certain *Bacteroidetes*, namely *Alkalifexus sp.* are only abundant within alkaline environments (Santo Domingo et al. 2011).

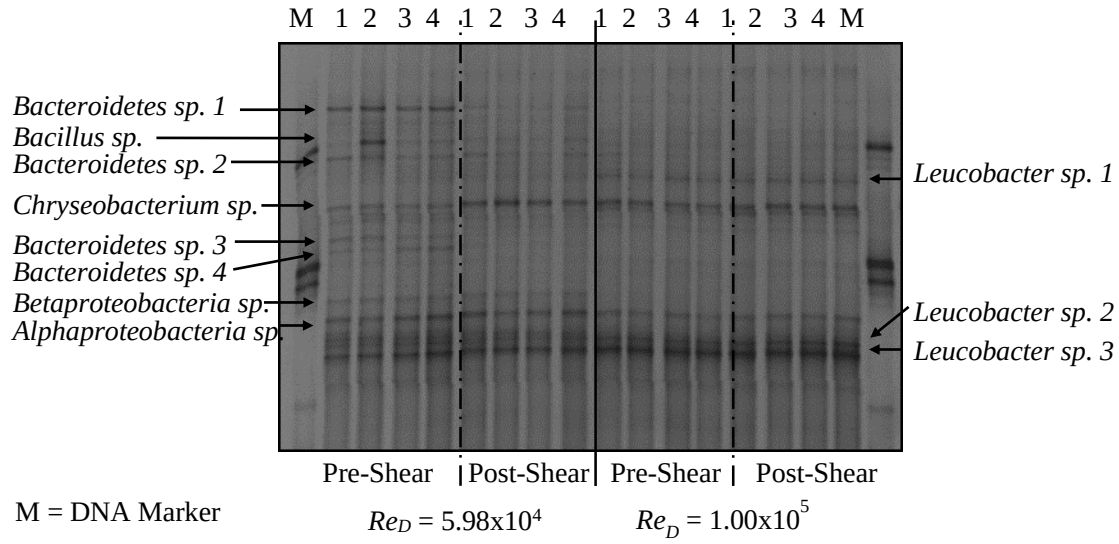

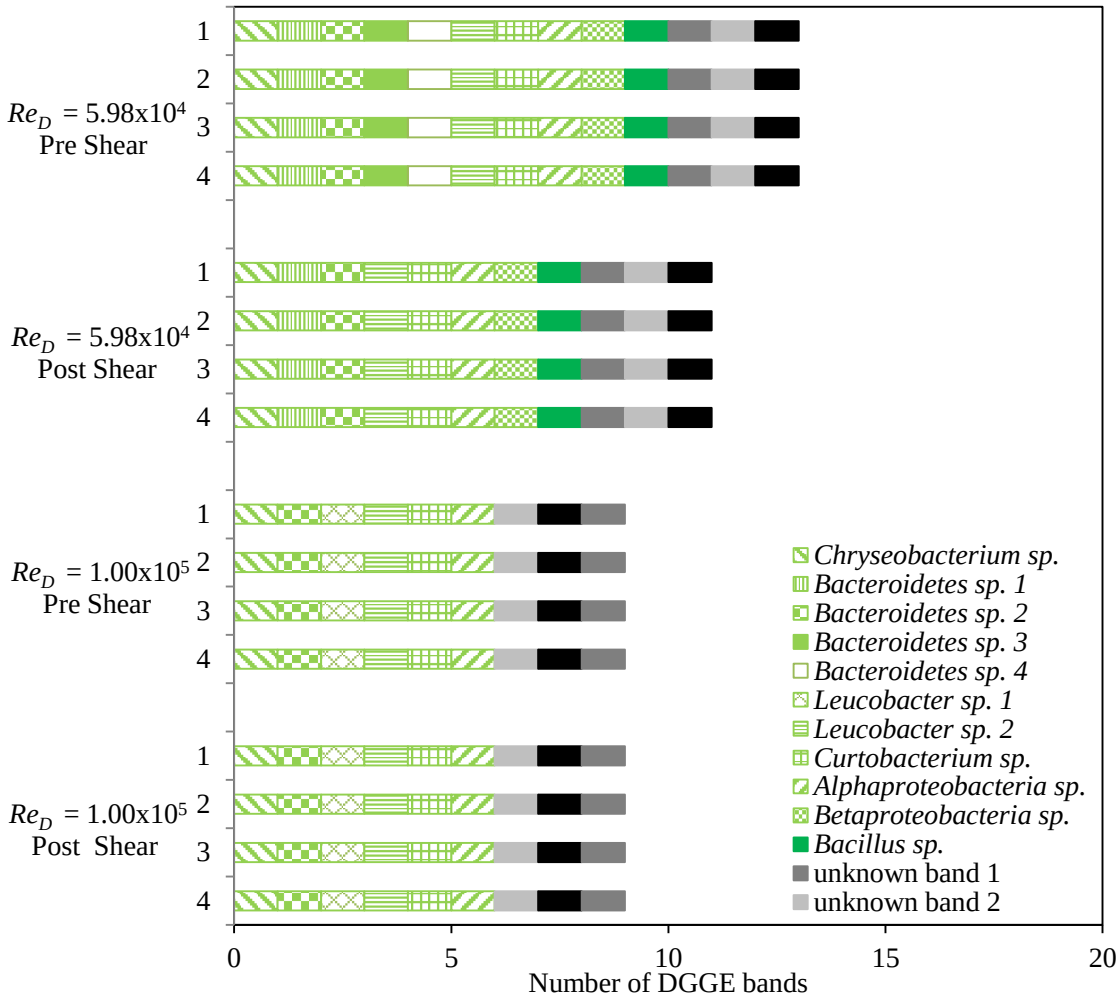

Figure 6.11 PCR-DGGE analysis of bacterial 16S rRNA genes from biofilms cultivated on test pipes at four different circumferential locations (i.e. 1,2,3 and 4) within the $Re_D = 5.98x10^4$ and $Re_D=1.00x10^5$ assays, pre- and post- shear.

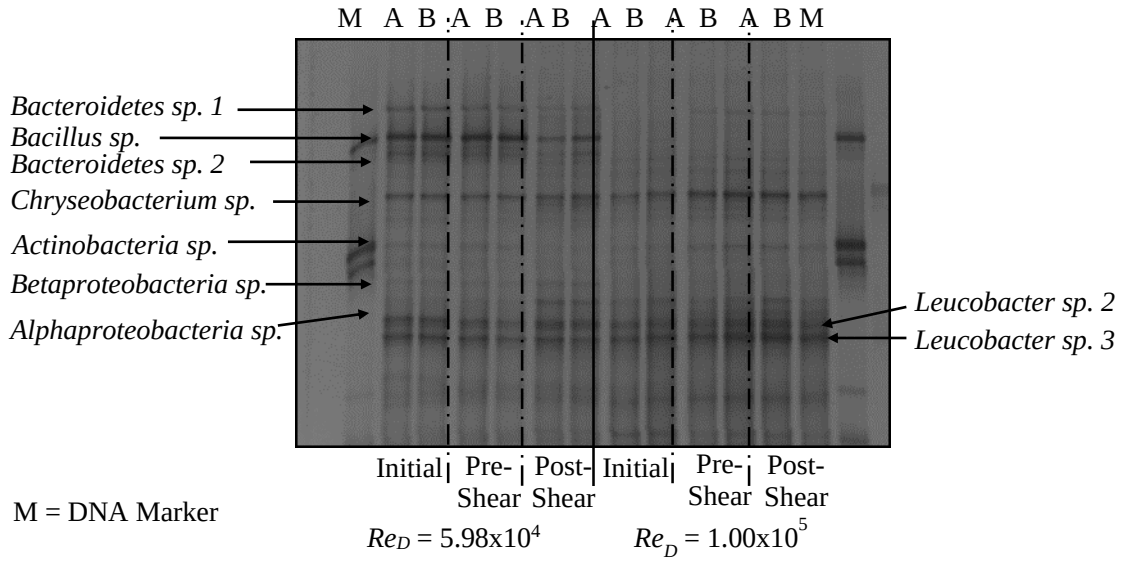

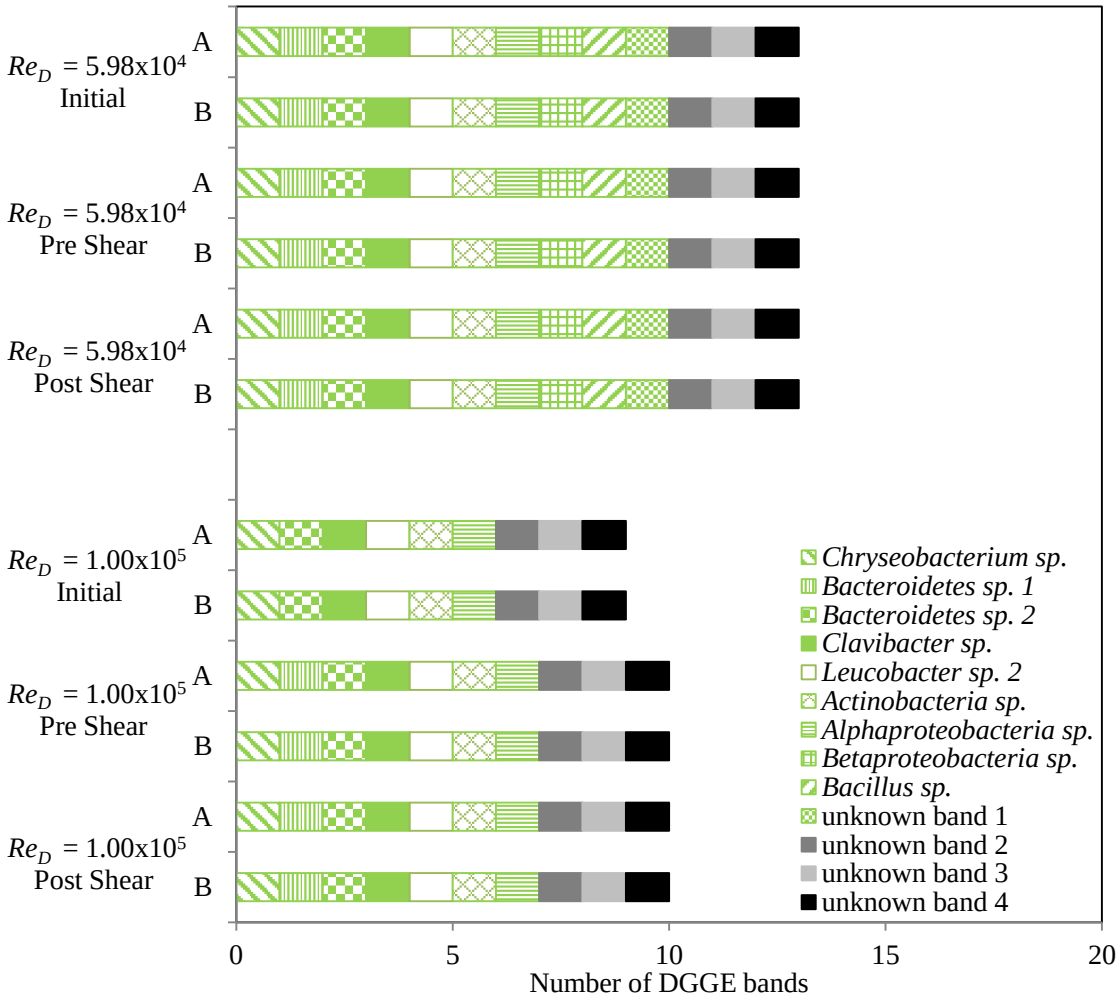

Figure 6.12 PCR-DGGE analysis of bacterial 16S rRNA genes for two replicate water samples (i.e. A and B) taken during the Re_D = 5.98x10^4 and Re_D=1.00x10^5 assays, pre- and post- shear.

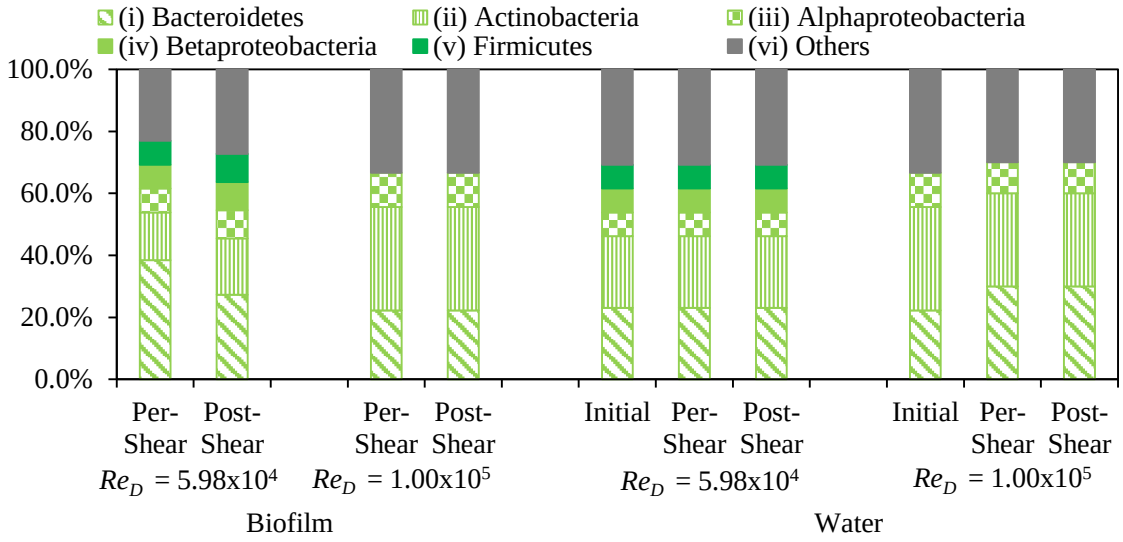

Figure 6.13 PCR-DGGE analysis of bacterial 16S rRNA genes both biofilm and water samples taken during the Re_D = 5.98x10^4 and Re_D=1.00x10^5 assays, pre- and post- shear.

The influence of shear conditioning on biofilm community composition is evident within Figure 6.11 and Figure 6.13. Within the high flow case (i.e. the Re_D = 1.00x10^5 assay) pre shear, *Actinobacteria* dominated the biofilm, representing 33% of the total evaluated bands. Also abundant within the Re_D = 1.00x10^5 assay's biofilm were *Bacteroidetes* (22%) and *Alphaproteobacteria* (11%). The biofilm incubated within the low flow case (i.e. the Re_D = 5.98x10^5 assay) pre shear, was dominated by *Bacteroidetes* (38%). The phyla of *Actinobacteria* (15%), *Alphaproteobacteria* (8%) *Betaproteobacteria* (8%) and *Firmicutes* (8%) were also abundant within the Re_D = 5.98x10^4 assay. Interestingly, the *Firmicutes* and *Betaproteobacteria* were only evident within the biofilm and bulk water samples taken within the Re_D = 5.98x10^4 assay, which suggests these phyla prefer lower flow conditions to propagate.

Post shear, the biofilm community within the Re_D = 1.00x10^5 assay remained unchanged and therefore, was unaffected by the increase in shear conditions. Whereas, the community composition within the Re_D = 5.98x10^4 assay was significantly influenced by the increase in shear conditions. In particular, members of the *Betaproteobacteria* and *Firmicutes* phyla were no longer evident within the biofilm post shear. Furthermore, the *Bacteroidetes* population decreased by 40% as a result of the increase in shear conditions. The complete removal of the *Betaproteobacteria* and *Firmicutes* phyla post shear suggests that they were less resistant than the other bacteria to shear forces in the order of 4.96 N/m^2. The phyla found to have the

highest resistance to increased shear conditions were *Alphaproteobacteria* and *Actinobacteria*.

The microbial compositions within the bulk water were not significantly influenced by the different incubation conditions, with the exception of *Firmicutes* and *Betaproteobacteria*, which were only evident within the bulk water samples taken from the $Re_D = 5.98x10^4$ assay.

6.3.2 Biofilm EPS composition

The biofilm sample's extracellular carbohydrate and protein concentrations were quantified using the protocols outlined in Section 3.7.2. Figure 6.14 presents the individual extracellular carbohydrate and protein concentrations obtained from each of the four sampling locations (see Figure 3.33). The detection limit presented within Figure 6.14a represents the total carbohydrate resonating from the cellulose within the cotton bud (i.e. 316.23 ± 46.38 µg/cm^2, see Appendix A.8, Table A.5).

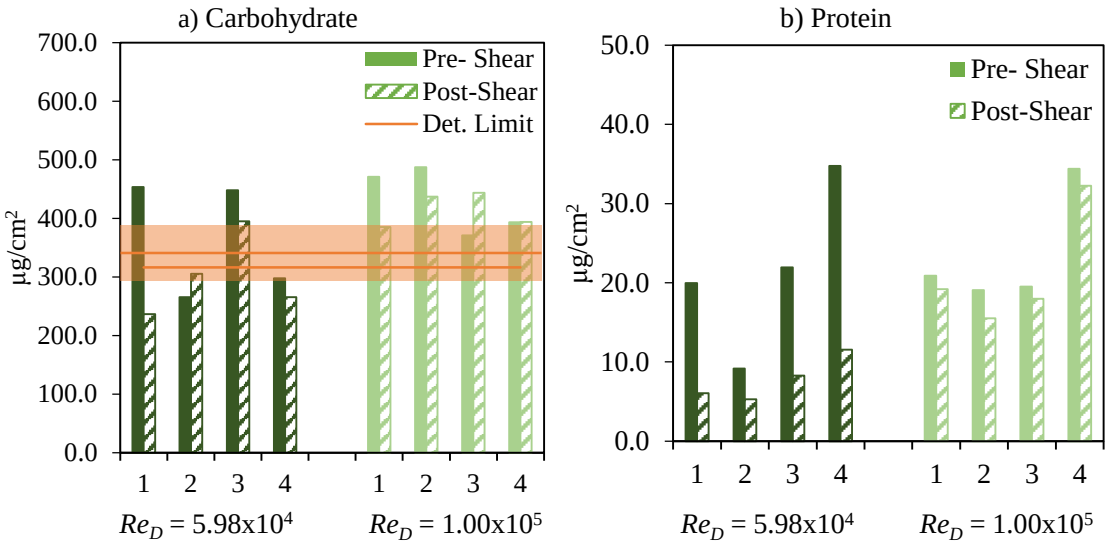

Figure 6.14 Total concentrations of a) carbohydrate and b) protein within the EPS fraction of the biofilms incubated on test pipes at four different circumferential locations (i.e. 1,2,3 and 4) of the $Re_D = 5.98x10^4$ and $Re_D = 1.00x10^5$ assays at both pre- and post- shear time intervals.

Figure 6.15 represents the average concentrations of extracellular carbohydrate and protein within the biofilms incubated in the $Re_D = 5.98x10^4$ and $Re_D = 1.00x10^5$ assays, for both pre- and post- shear time intervals. It should be noted that the carbohydrate concentrations which were below the detection limit were taken as zero. It is evident from Figure 6.15 that the majority of the extracellular carbohydrate and protein was extracted within the primary

extraction phase. In particular, it was found that at least 75% of the overall carbohydrate and at least 86% of the overall protein was obtained following the primary extraction.

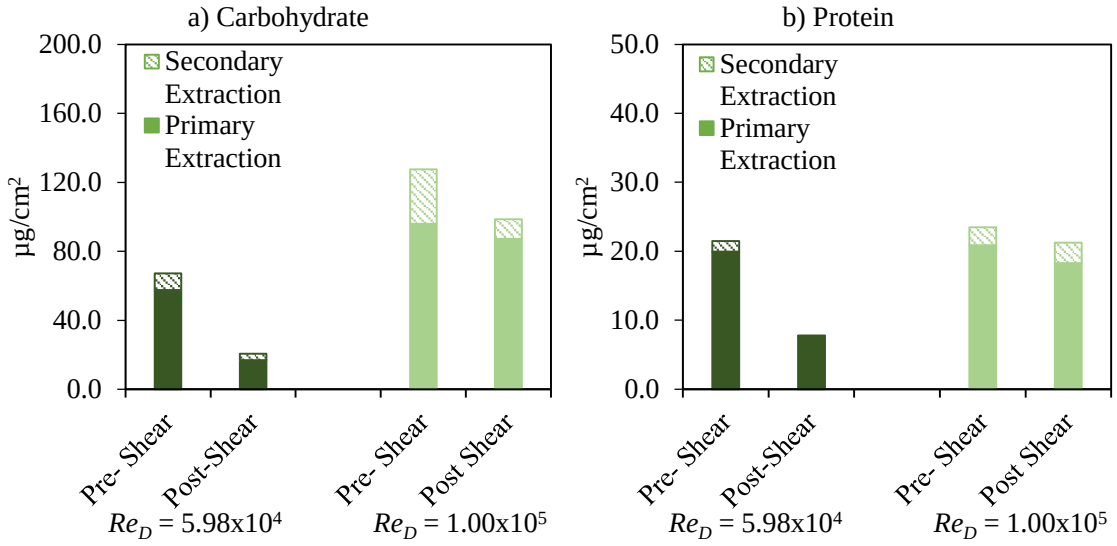

Figure 6.15 Average concentrations of extracellular a) carbohydrate and b) protein obtained from the primary and secondary extractions, for the biofilms cultivated within the $Re_D = 5.98x10^4$ and $Re_D = 1.00x10^5$ assays at both pre- and post-shear time intervals.

The concentration of DNA within each of the EPS samples was quantified using the florescent dye protocol outlined in Section 3.7.3.4; for the purpose of establishing whether any non-EPS material had been inadvertently extracted along with the EPS. It was found that the DNA within the primary and secondary EPS extracts only represented 2.8% of the total biofilm DNA. A small proportion of extracellular DNA is typically expected within the EPS (Flemming and Wingender 2010; Jiao et al. 2010) and as a result, it was concluded that the established extracellular carbohydrate and protein concentrations were not influenced by non-EPS material.

The proportional composition of carbohydrate and protein within a biofilm's EPS is significantly influenced by the environment to which the biofilm is incubated and the bacterial communities present (Simoes et al. 2007; Ahimou et al. 2007). Consequently, the dominance of these discrete constituents, on a mass basis, as reported in the literature is seemingly conflicting. A number of studies have suggested that proteins are more dominant than carbohydrates within a biofilm's EPS (Jahn and Nielsen 1998; Conrad et al. 2003; Ahimou et al. 2007; Adav and Lee 2008; Celmer et al. 2008), while other studies suggest that carbohydrates are the dominant fraction (Tay et al. 2001; Wingender et al. 2001; Simoes et

al. 2007; Vu et al. 2009). For instance, Jahn and Nielsen (1998) found that proteins were more dominant than carbohydrates in sewer biofilms. Jahn and Nielsen (1998) documented a carbohydrate to protein ratio (C/P) of between 0.25-0.6. The C/P ratios documented by Jahn and Nielsen (1998) were consistent with those found by Celmer et al. (2008), who reported C/P ratios of between 0.1-0.8 for biofilms incubated with municipal wastewater. Alternatively, Simoes et al. (2007) found that under turbulent flow conditions, polysaccharides (i.e. carbohydrates) were more dominant than proteins within the EPS, with an approximate C/P ratio of 2.0 being recorded.

The biofilms within the current study were incubated at relatively high shear conditions (i.e. in the range of 1.42 $N/m^2 < \tau_w < 2.97$ N/m^2). Furthermore, the ratios of Total Carbon to Total Nitrogen (TC/TN) in which the biofilms were conditioned was at least 10.8 can, which can be considered relatively high. Significant aeration was induced by the facility's outlet arrangement (i.e. the overflow and drop over the stand pipe). Under such conditions, it was evident that extracellular carbohydrates were the dominant EPS component, at least compared to the extracellular proteins, as illustrated by Figure 6.15. Based solely on the incubation conditions the high levels of extracellular carbohydrates were to be expected, as carbohydrate production is generally encouraged within biofilms which have been incubated at high shear (Ohashi and Harada 1994; Pratt and Kolter 1999), high TC/TN ratios (Miqueleto et al. 2010) and high aeration (Tay et al. 2001; Ahimou et al. 2007).

Figure 6.16 further illustrates the dominance of extracellular carbohydrates over extracellular proteins within the biofilms incubated with wastewater. Figure 6.16a shows the C/P ratios determined for the $Re_D = 5.98x10^4$ and $Re_D = 1.00x10^5$ assays, at both pre- and post- shear time intervals. It is evident from Figure 6.16a that the C/P ratios for the biofilm incubated within the $Re_D = 5.98x10^4$ and $Re_D = 1.00x10^5$ assays pre shear were 3.13 and 5.44, respectively. Post shear the C/P ratios dropped to 2.65 for the $Re_D = 5.98x10^4$ assay and 4.64 for the $Re_D = 1.00x10^5$ assay. Figure 6.16b illustrates the percentage by mass/area of carbohydrate and protein within the EPS of the biofilm incubated within the $Re_D = 5.98x10^4$ and $Re_D = 1.00x10^5$ assays. It can be seen from Figure 6.16b that the carbohydrate represented 75% and 84% of the total carbohydrate and protein fraction of the biofilms incubated within $Re_D = 5.98x10^4$ and $Re = 1.00x10^5$ assays, respectively. It should be noted that the quoted C/P ratios presented by Figure 6.16a are naturally unaffected by any inaccuracies in sample area measurements, which is a common problem when a coupons sampling approach is not used. Consequently, the quoted C/P relationships can be considered more reliable than the discrete protein and carbohydrate concentrations presented by Figure 6.14 and Figure 6.15.

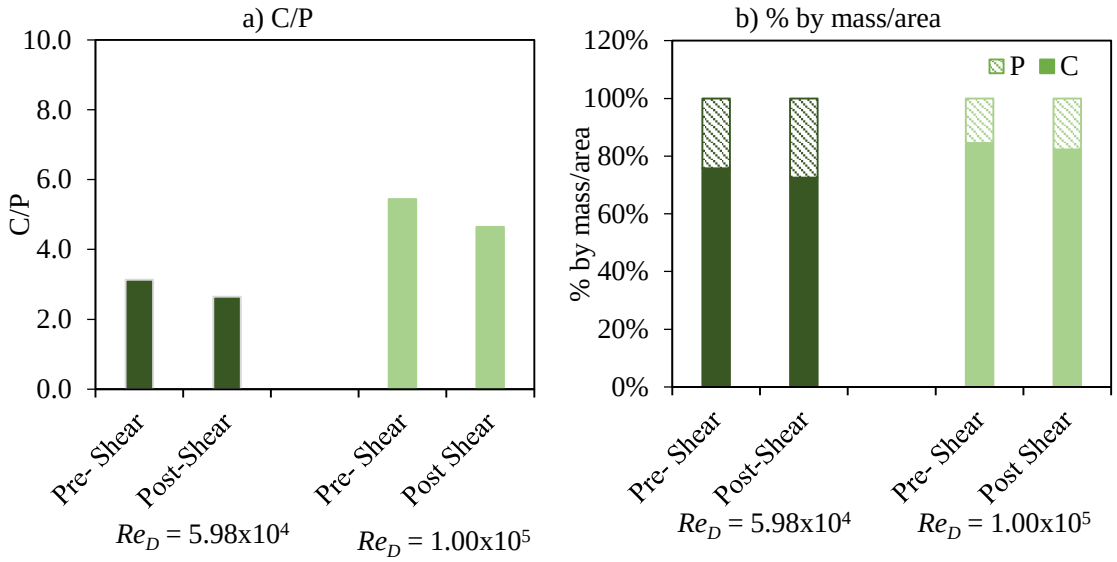

Figure 6.16 a) C/P ratios and b) percentage by mass/area of carbohydrates and proteins within the EPS for the biofilms cultivated within the Re_D = 5.98x10^4 and Re_D = 1.00x10^5 assays at both pre- and post-shear time intervals.

Polysaccharides (i.e. carbohydrates), due to their filamentous nature and ability to form and fill the spaces between cells, have been shown to provide the majority of a biofilms mechanical stability and cohesion (Ohashi and Harada 1994; Pratt and Kolter 1999; Korstgens et al. 2001; Wloka et al. 2004; Flemming and Wingender 2010; Ahimou et al. 2010). Consequently, extracellular carbohydrates have often been regarded as the most important extracellular constituent (Christensen 1989). Ahimou et al. (2007) found that the EPS concentration in terms of protein and polysaccharides correlated well with the biofilms cohesive energy (R^2 = 0.9), and in particular the carbohydrate concentration the greater the cohesion. However, this may not always be the case, as other factors, namely protein content and bacterial community composition have also been found to have an influence on biofilm stability (Houghton and Quarmby 1999; Allison et al. 1998; Simoes et al. 2007; Celmer et al. 2008). For instance, Simoes et al. (2007) found that a *Bacillus cereus* based biofilm had a higher mechanical stability than a *Pseudomonas fluorescens* based biofilm, despite having equivalent C/P ratios of approximately 2. Furthermore, it has been reported that proteins typically provide the majority of the binding sites within a biofilm, and thus a lower C/P ratio (i.e. a higher protein fraction) would induce a more stable and resilient biofilm (Houghton and Quarmby 1999).

Figure 6.17 presents the percentage of carbohydrate and protein removed following the increased shear conditions within each of the flow assays. It is evident that significant

amounts of carbohydrate and protein were removed as a result of the increased shear conditions within the $Re_D = 5.98x10^4$ assay. In particular, the concentration of carbohydrate and protein on the surface reduced by 69% and 64%, respectively within the $Re_D = 5.98x10^4$ assay. The biofilm incubated within the $Re_D = 1.00x10^5$ assay was seemingly more resilient, as the concentrations of carbohydrate and protein on the surface reduced only by 23% and 10%, respectively. The observed resilience of the biofilm conditioned at high shear is consistent with the literature (Korstgens et al. 2001; Stoodley et al. 2002) and with the findings outlined in Section 6.2, where minimal biofilm detachment was observed, indicated by the small change in water chemistry and physical appearance.

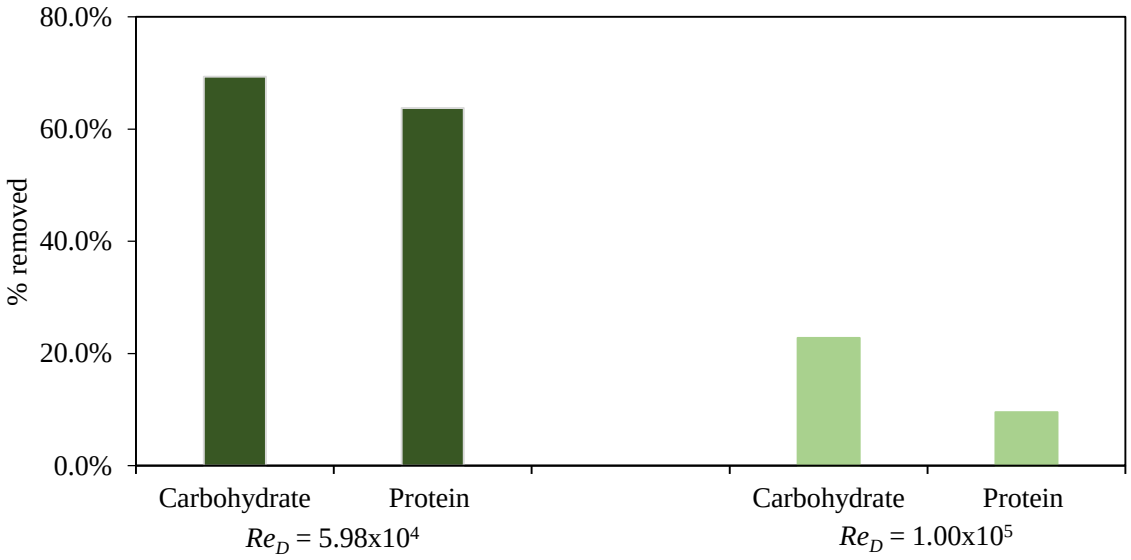

Figure 6.17 Percentage of carbohydrate and protein removed following the increased shear event during the $Re_D = 5.98x10^4$ and $Re_D = 1.00x10^5$ assays.

A biofilms visco-elastic properties are primarily provided by the EPS (Picologlou et al. 1980). Consequently, the suggestion that the biofilm incubated within the $Re_D = 1.00x10^5$ assay was merely thinned and compressed by the increased shear conditions is supported by the high amount of EPS retained post shear.

The biofilm incubated within the $Re_D = 1.00x10^5$ assay was found to have a greater carbohydrate fraction, and thus higher C/P ratio than the biofilm incubated within the $Re_D = 5.98x10^4$ assay. The differences in the respective biofilms protein fractions were seemingly insignificant, particularly when compared to the differences extracellular carbohydrates. For instance, the average difference in protein between the $Re_D = 5.98x10^4$ and $Re_D = 1.00x10^5$

assays was ±2.01 μg/cm^2, whereas the equivalent difference in carbohydrate between the respective assays was ±77.72 μg/cm^2.

Based on the results outlined within this section, the increased resilience and stability observed for the biofilm incubated at high shear (i.e. in Re_D = 1.00x10^5 assay) can be attributed to the high concentrations of extracellular carbohydrate found within the respective biofilm. The current study is therefore, in agreement with previous studies which found that extracellular carbohydrates provide the majority of the biofilms mechanical stability (Ohashi and Harada 1994; Pratt and Kolter 1999; Korstgens et al. 2001; Wloka et al. 2004; Ahimou et al. 2010; Flemming and Wingender 2010).

6.3.3 Biofilm DNA concentration

The biofilm's DNA concentration was quantified using the florescent dye protocol outlined in Section 3.7.3.4. Estimates of the total cell concentration were derived indirectly from the DNA concentration using the recommendations outlined by McCoy and Olson (1985). A single factor ANOVA (α = 0.05) indicated that the difference between the number of cells per unit area, pre shear in the biofilms incubated in the Re_D = 1.00x10^5 and Re_D = 5.98x10^4 assays was statistically insignificant. This confirms that the nutrient loading was reasonably equivalent between the respective assays, by virtue of conservation of mass. This in turn confirms that the variations in mass transfer and shear characteristics imposed by the different flow regimes were the main factors influencing the biofilm within the incubation (i.e Chapter 5) and mature phases of the current study. The estimated cell concentrations at the four sampling locations pre shear ranged from 6.7x10^6-2.3x10^7 Cells/cm^2 for the Re_D = 5.98x10^4 assay and 1.49x10^7-2.2x10^7 Cells/cm^2 for the Re_D = 1.00x10^5 assay. The average estimated cell concentration for the two flow assays pre shear was 1.77x10^7 Cells/cm^2.

Figure 6.18 presents the individual DNA and total estimated cell concentrations obtained from the four sampling locations (see Figure 3.33) of the Re_D = 5.98x10^4 and Re_D = 1.00x10^5 assays, at both pre – and post- shear time intervals. The average DNA and estimated cell concentrations obtained from the four sampling locations around the pipe within the Re_D = 1.00x10^5 and Re_D = 5.98x10^4 assays are presented in Figure 6.19. It is evident from Figure 6.18 that the overall cell distribution around the circumference of the pipe was more uniform within the Re_D = 1.00x10^5 assay than within the Re_D = 5.98x10^4 assay. The standard deviations established from the four sampling locations was 7.45x10^6 Cells/cm^2 (±42%) for the Re_D = 5.98x10^4 assay and ±3.35x10^6 Cells/cm^2 (±19%) for the Re_D = 1.00x10^5 assay. The respective standard deviations further illustrate that the cell distribution around the pipe was more uniform within the Re_D = 1.00x10^5 assay than within the Re_D = 5.98x10^4 assay.

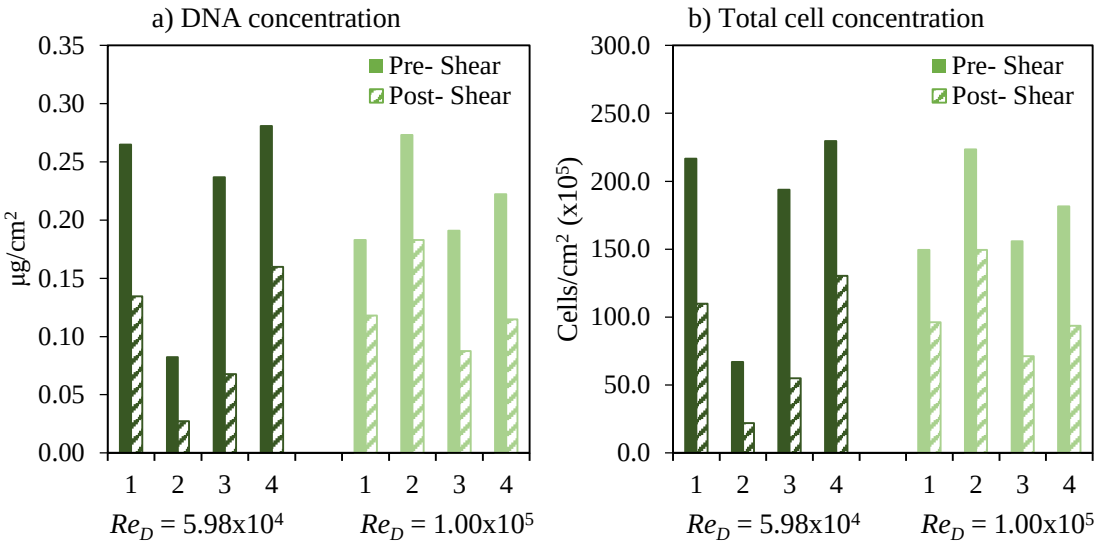

Figure 6.18 Total concentrations of a) DNA and b) Cells within biofilms cultivated on test pipes at four different circumferential locations (i.e. 1,2,3 and 4) of the $Re_D = 5.98x10^4$ and $Re_D = 1.00x10^5$ assays at both pre- and post-shear time intervals.

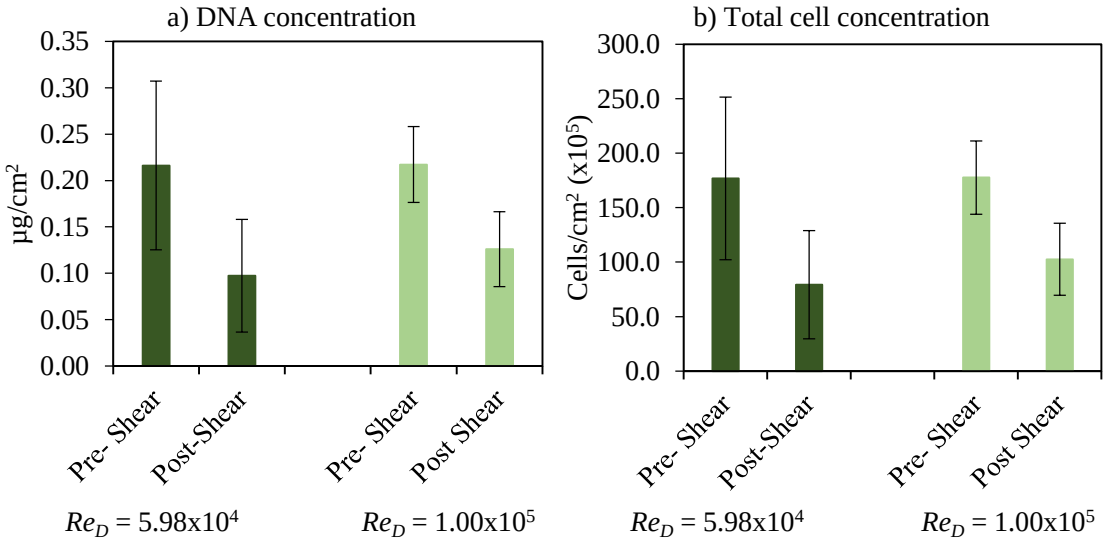

Figure 6.19 Average concentrations of of a) DNA and b) Cells within biofilms cultivated within the $Re_D = 5.98x10^4$ and $Re_D = 1.00x10^5$ assays at both pre- and post-shear time intervals.

The concentration of extracellular material (namely carbohydrates) per unit area was also higher within the $Re_D = 1.00x10^5$ assay compared to the $Re_D = 5.98x10^4$ assay. In particular, the mass per unit area of extracellular material was 1.7 times higher within the $Re_D = 1.00x10^5$ assay than within the $Re_D = 5.98x10^4$ assay. This would suggest that the overall structure of the biofilm incubated within the $Re_D = 1.00x10^5$ assay was more dense than the structure of the biofilm incubated within the $Re_D = 5.98x10^4$ assay.

Following the increase in shear conditions it is evident that the overall DNA and estimated cell concentrations within both of the flow assay's biofilms decreased. However, the magnitude of the decrease was a function of the shear conditioning. In particular, the higher the shear conditioning the lower the decrease. For instance, the average reduction in cells on the surface after the increased shear event was 55.1% for the $Re_D = 5.98x10^4$ assay and was 42.2% for the $Re_D = 1.00x10^5$ assay. This aligned with the equivalent EPS removal rates observed for the respective assays, as shown in Figure 6.17. However, the percentage of cells removed following the increase in shear within the $Re_D = 1.00x10^5$ assay, was higher than expected based on the amount of EPS removed within the respective assay (i.e. 10-23%). The cell distribution of the biofilms was also affected by the increase in shear conditions. The standard deviation as a percentage post shear was ±63% for the $Re_D = 5.98x10^4$ assay and ±32% for the $Re_D = 1.00x10^5$ assay. These values represent an increase on the equivalent pre shear values (i.e. ±42% for the $Re_D = 5.98x10^4$ assay and ±19% for the $Re_D = 1.00x10^5$ assay). Consequently, it is suggested that the cell distribution around the pipe became more irregular post shear. The observed biofilm detachment documented within Section 6.2.2 and Section 6.2.3 would support this conclusion.

6.4 Sediment evaluation

The purpose of this section is to outline the results of the sediment investigation undertaken as part of the $Re_D = 1.00x10^5$ assay. The non-fouled pipe was also evaluated with non-cohesive sediment, and the results of this are also presented within this section.

6.4.1 Frictional characteristics

The global frictional data outlined in Section 4.3 was used define surface of the non-fouled pipe. The frictional characteristics for the fouled pipe were established pre- and post-sediment testing from the system's PG using the SFM. The frictional data determined using the SFM is presented in Appendix D.4 in Table D.3 and Table D.4. Figure 6.20 presents the friction factors for the fouled pipe pre- and post- testing in the form of a Moody Diagram.

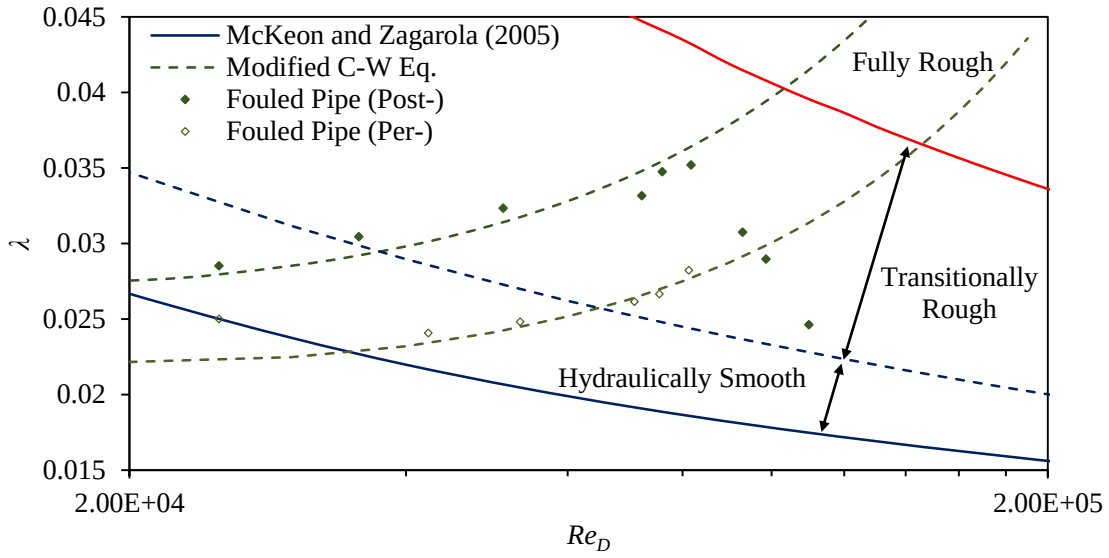

Figure 6.20 λ against Re_D of the fouled pipe for both pre- and post- sediment testing.

It is evident that the frictional characteristics pre- and post- sediment testing were significantly different. In particular, an observed increase in frictional resistance was found post testing. The average value of k_s determined from the modified C-W equation pre testing was 0.119 mm and post- testing was 0.294 mm. Biofilm detachment fostered by sediment abrasion was attributed to the observed differences in the pre- and post- testing conditions. Visual inspections indicated that the biofilm remained reasonably intact post testing, with the exception of the invert side. The sediment was observed to have a tendency to become embedded within the interstitial voids and channels of the biofouled surface. This initial deposition fostered further sediment deposition, until the shear forces acting over the whole area were sufficient to separate the biofilm and sediment from the surface. This type of low level detachment would have given rise to a more heterogeneous roughness distribution along the pipe's invert, and would explain the observed increase in frictional resistance post testing.

The key frictional parameters of interest within the sediment investigation were τ_w and u^*. Regression lines were fitted to both the fouled and non-fouled frictional data, as shown in Appendix D.5 by Figure D.5. For the fouled pipe the regression lines were fitted to both the pre- and post- testing datasets, and as a result the derived relationships represent the average of the respective conditions. The τ_w and u^* for the non-fouled pipe were given by:

$$\tau_w = 1.97 \times 10^{-9} \, {Re_D}^{1.81} \qquad \textit{Equation 6.1}$$

$$u^* = 4.46 \times 10^{-7}\ Re_D + 2.63 \times 10^{-3} \qquad \textit{Equation 6.2}$$

Whereas, the τ_w and u^* for the fouled pipe were given by:

$$\tau_w = 2.08 \times 10^{-10}\ {Re_D}^{2.06} \qquad \textit{Equation 6.3}$$

$$u^* = 6.40 \times 10^{-7}\ Re_D + 9.76 \times 10^{-4} \qquad \textit{Equation 6.4}$$

6.4.2 Self-cleansing velocity and critical shear stress

The results of each of the sediment transport surveys undertaken with and without fouling are presented in Appendix D.4 in Table D.5 and Table D.6. Figure 6.21 and Figure 6.22 summarises the data listed within Table E.6 and Table E.7 In particular, Figure 6.21 and Figure 6.22 illustrate the percentage of sand transported after 60 minutes post injection.

The velocity required to transport at least 90% of a sediment sample within a 60 minute period was defined by Guzmán et al. (2007) as the self-cleansing velocity. It is evident from Figure 6.21 that the presence of the biofilm increase the velocity needed for self-cleansing. The velocity required to transport at least 90% of the sand with fouling was 0.55 ± 0.01 m/s and without fouling was 0.46 ± 0.01 m/s. It is also evident from Figure 6.21 some sediment deposition occured at velocities as high as 0.65m/s, irrespective of the biofilm. The established self-cleansing velocities with and without fouling documented within the current study are consistent with the findings outlined by Guzmán et al. (2007), who found that the self-cleansing velocity of PVC pipes of D = 150-200 mm with fouling was 0.55 m/s and without fouling was 0.45 m/s. Guzmán et al. (2007) also reported some deposition at high velocities (i.e. $\overline{U} \approx 0.86$ m/s). Interestingly, even with fouling the observed self-cleansing velocity for the S-HDPE pipe was found to be lower than the traditionally accepted values, i.e. $\overline{U} > 0.60$ m/s (Fair and Geyer 1954). Furthermore, the observed self-cleansing velocities for the S-HDPE pipe were lower than the values recommended within current UK and US design guidelines, i.e. $\overline{U}$ = 0.75 m/s and $\overline{U}$ = 0.60 m/s, respectively.

Based upon the observations reported within the current study and within the literature (Guzmán et al. 2007) it can be concluded that current design guidelines significantly overestimate the actual requirements needed for self-cleansing. Such overestimations could have considerable financial and environmental consequences, as a result of oversizing. However, it should be stated the observations made within the current study and by Guzmán et al. (2007) are limited to very specific situations and small pipe diameters.

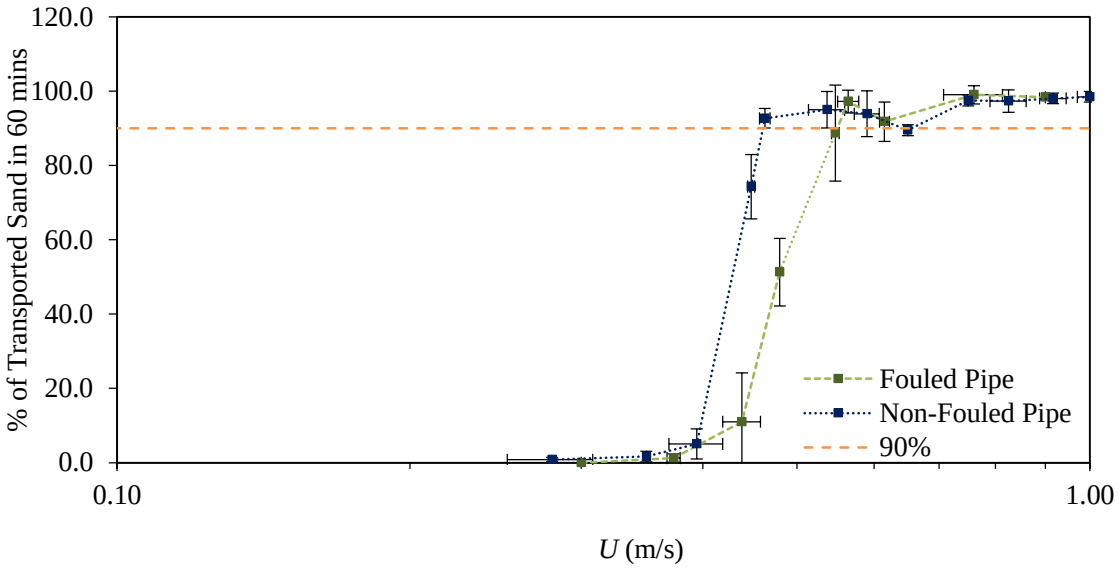

Figure 6.21 Percentage of sand transported after 60 minutes within the pilot-scale pipeline against average freestream velocity.

It is evident from Figure 6.22 that the critical shear stress required to transport at least 90% of the sand (τ_{90}) with fouling was 1.30 ± 0.02 N/m^2 and without fouling was 0.59 ± 0.06 N/m^2. Consequently, in order to ensure a pipe is self-cleansing the shear stress generated by the operating conditions needs to be at least 1.30N/m^2 if a biofilm is present. These values are similar to the findings outlined by Guzmán et al. (2007), who found τ_{90} was between 1.10-1.40 N/m^2 with fouling and was between 0.40-0.55 N/m^2 without fouling.

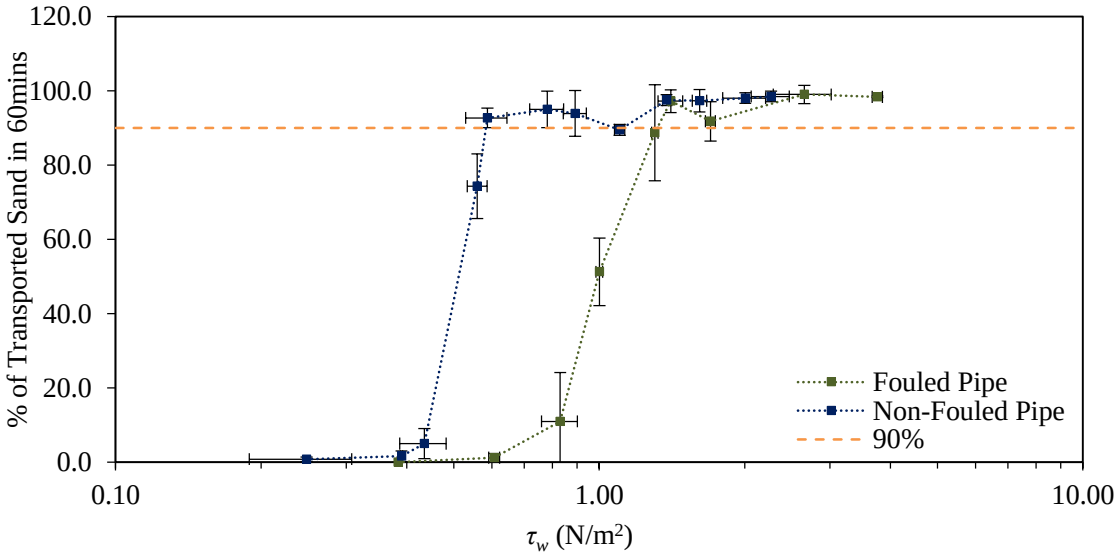

Figure 6.22 Percentage of sand transported after 60 minutes within the pilot-scale pipeline against wall shear stress.

Critical shields parameters were calculated using Equation 3.20. The coefficients were calculated for $d = d_{90} = 0.40$ mm using the experimentally determined values of critical shear stress. The critical shields parameter was 0.20 with fouling and 0.09 without fouling. Again these coefficients are comparable to those found by Guzmán et al. (2007).

6.5 Summary

This chapter has outlined the results of the mature phase aspect of the current study, in which the biofilms incubated within the $Re_D = 5.98x10^4$ and $Re_D = 1.00x10^5$ assays were subject to varying flow conditions. This phase of the study had particular industrial relevance given the highly variable nature of real systems and the relatively short development period of a wastewater biofilm (≈ 180 h, as outlined in Chapter 5). As a mature biofilm would represent the most frequently occurring biofilm state within pipelines.

The results outlined within this chapter have improved the current scientific understanding of the dynamic feed-back relationship that exists between a biofilm and its surroundings. In particular, the impact and response of a biofilm to varying flow regimes has been evaluated and discussed in detail of the first time.

The molecular analysis undertaken within this chapter indicated that a biofilm incubated with synthetic wastewater is a diverse array of bacterial communities and extracellular materials. In particular, the biofilms were dominated by extracellular carbohydrates, which based on the general conditioning of the biofilms within the current study was to be expected (Hunag et al. 1994; Ohashi and Harada 1994; Pratt and Kolter 1999; Tay et al. 2001; Ahimou et al. 2007; Miquletot et al. 2010). Furthermore, the biofilms were dominated by *Bacteroidetes, Actinobacteria, Alphaproteobacteria, Betaproteobacteria* and *Firmicutes*, all of which are also commonly found within real DNs (Santo Domingo et al. 2011). Consequently, the biofilms incubated under artificial conditions within this study can be considered representative to those found within real systems.

The changes in shear conditions imposed by the variations in flow had an influence on the overall bacterial community composition. In particular, members of the *Alphaproteobacteria* and *Actinobacteria* phyla were found to have the highest resistance to an increased shear event, whereas *Betaproteobacteria and Firmicutes* were found to have the lowest resilience of the observed communities. The molecular analysis also indicated that although, the number of cells per unit area on the surface following the incubation phases of the $Re_D = 5.98x10^4$ and $Re_D = 1.00x10^5$ assays was statistically the same, and equal to $1.77x10^7$ Cells/cm^2, their

overall structure differed between the respective assays, as a result of the differences in shear conditioning. In particular, the biofilm conditioned at high shear (i.e. in the $Re_D = 1.00x10^5$ assay) had a more regular structural distribution around the pipe than the biofilm conditioned at low shear (i.e. in the $Re_D = 5.98x10^4$ assay). This supports the findings outlined in Chapter 5 with regards to the observed difference in equivalent roughness distribution between the respective flow assays. For instance, the equivalent roughness distribution for the biofouled surface conditioned at high shear was found to be reasonably uniformly distributed along the pipe's overall length, as indicated by negligible differences in space-averaged conditions. Similarly, the heterogeneous distribution of the global roughness evident within the $Re_D = 5.98x10^4$ assay is consistent with the observed irregularity of the cell distribution on the surface within the respective assay. The negligible difference in the pre shear cell concentration between the two biofilms confirms that the evident differences in structural distribution between the respective biofilms was a result of the variations in mass transfer and shear characteristics imposed by the different flow regimes (as outlined in detail in Chapter 5). In addition, to influencing their overall structure the stress imposed during conditioning was also shown to influence the cell's production and secretion of extracellular material, namely carbohydrates. It should be noted however, that the biofilm sampling undertaken within the current study was limited and bias to one area of the pipe, and it is recommended that in future investigations that multiple pipe locations are sampled and evaluated, to ensure the aforementioned observations were not random chance.

In terms of their frictional behaviour the results have shown that biofouled surfaces do not follow a traditional C-W relationship, as depicted on the Moody Diagram. As a result, the current study is in agreement with the general literature consensus that the traditional C-W equation is not applicable to biofouled surfaces (Schultz and Swain 1999; Schultz 2000; Barton et al. 2004; Barton 2006; Lambert et al. 2008; 2009; Perkins et al. 2013; 2014). In particular, it was evident that the biofouled surface exhibited an extreme inflectional type roughness behaviour, which was illustrated by a pronounced increase in λ with Re_D. This behaviour was fostered by the observed non-universality of κ, which is an integral aspect of the C-W equation, as discussed in Chapter 5. The friction factor continued to increase until a critical point was reached, after which the λ began to decrease with Re_D. The decrease in λ was attributed to the biofilm becoming compressed or sheared under loading, the latter was confirmed by changes in bulk water chemistry and physical appearance. Prior to the critical point, the theoretically determined values of λ derived from the modified C-W equation (proposed by Lambert et al. (2009)) and the case-specific values of κ determined using Equation 5.2, were in strong agreement with the experimentally determined values of λ.

Consequently, the frictional data determined independently from the mean-velocity data (i.e. using the system's PG) is in support of the non-universal values of κ determined from Re_D using Equation 5.2. The observed relationship whereby λ increases before decreasing with Re_D is consistent with the findings of previous biofilm investigations (Lambert et al. 2008; 2009; Perkins et al. 2013; 2014).

The degree of decrease in λ was a function of the incubation conditions, with the greatest decrease occurring for the biofilm incubated at lowest shear (i.e. in the $Re_D = 5.98 \times 10^4$ assay). This was attributed to the structural strength of the respective biofilm and the composition of its EPS. In particular, the same porous and irregular structure, which was responsible for the high frictional resistance imposed by the biofilm conditioned at low shear (see Chapter 5) also contributed to the low overall stability of the respective biofilm. Furthermore, the biofilms extracellular carbohydrate fraction, which has been shown to provide the majority of a biofilm's mechanical stability and cohesion (Korstgens et al. 2001; Wloka et al. 2004; Branda et al. 2005; Flemming and Wingender 2010) was also lower for lower conditioning shear. The implication of this was that more microbial material was removed by a small incremental increase in boundary shear. Whereas, the compact structural distribution induced by the high shear conditioning contributed to a more cohesive and resilient biofilm, as it's discrete extracellular constituents were forced closer together, resulting in stronger bond formation (Stoodley et al. 2002). Furthermore an increase in extracellular carbohydrates was also seemingly fostered by higher conditioning stress. As a result of the increased stability, less microbial material was removed by an increase in boundary stress.

The sediment investigation undertaken within this chapter provides much needed data on the subject of biofilm-sediment interaction within DNs, expanding on the work outlined previously by Guzmán et al. (2007), who evaluated the impact of biofilm development on sediment transport within PVC pipes of D = 150-200 mm.

The nutrient conditions, and in particular the carbon concentrations used by Guzmán et al. (2007) to culture biofilms were far more concentrated than those conditions used within the current study, and expected in typical DNs in Europe (Pons et al. 2004). In particular, Guzmán et al. (2007) used methanol and glucose to generate an average COD concentration of approximately 800 mg/l. This is almost 1.5 times greater than the equivalent concentration used within the current study (i.e. COD = 543 mg/l, see Table 3.3), which was based upon the European average conditions outlined by Pons et al. (2004). It should be stated however, that the investigation outlined by Guzmán et al. (2007) was undertaken in the US, were nutrient conditions may differ from Europe. Nevertheless, a concentration of COD of 800

mg/l within Europe would represent the upper most limit expected within natural DNs (see Table 3.3), and as a consequence, it is less representative of the most frequently occurring operating conditions, which would be reflected in the resultant biofilm's thickness, morphology and equivalent roughness (Melo and Bott 1997; Lambert et al. 2008; 2009). Typically, an increase in nutrient loading fosters thicker biofilm development and a higher equivalent roughness (Melo and Bott 1997; Lambert et al. 2008; 2009), which in theory would affect the system's required self-cleansing velocity through an increase in boundary shear stress. Nevertheless, the results outlined within the current study were equivalent to those outlined by Guzmán et al. (2007). This suggests that the perceived increase in thickness and equivalent roughness encouraged by the high nutrient loading had negligible impact on a pipe's self-cleansing requirements, aside from that caused by the presence of the biofilm itself.

The results of the sediment investigation indicate that the presence of a biofilm can adversely affect a DNs ability to be self-cleansing, by means of an increase in shear stress. In particular, the minimum self-cleansing velocity required of a S-HDPE pipe of D = 102 mm without fouling was 0.46 m/s and with fouling was 0.55 m/s. Similarly, the required shear stress for a S-HDPE pipe to be self-cleansing with without fouling was 0.59 N/m^2 and fouling was 1.30 N/m^2. The self-cleansing criteria outlined within this section can be considered more applicable for use in the design of small-diameter HDPE DNs, than that outlined within the current design standards, as it incorporates the influence of a biofilm. Interestingly, even with a biofilm present the required velocity of a S-HDPE pipe to be self-cleansing is lower than the values recommended within current UK and US design guidelines (i.e. $\overline{U}$ = 0.75 m/s and $\overline{U}$ = 0.60 m/s, respectively). Though, the data presented within this section is much needed, it has its limitation. In particular, it is highly unlikely that sediments and loose deposits found within natural DNs will be non-cohesive in nature. Furthermore, within natural systems the sediment and biofilm will accumulate together, forming a symbiotic relationship. When sediments and biofilms accumulate in this manner, the resultant mass is typically more cohesive (Vignaga 2012). The changes in morphology and cohesiveness will naturally affect the pipe's self-cleansing criteria. These limitations require adequate addressing within future studies before the data can be applied to actual systems. It is also recommended a more diverse range of operating conditions and pipe diameters be assessed in future studies. The impact of low nutrient loading on biofilm development and thus sediment transport may be of particular interest given that the current prevailing data is based upon biofilms incubated under medium to high nutrient conditions. The effect on different operating depths on biofilm development and sediment transport will also be of interest, given nature of typical DNs.

Chapter 7 Drinking water investigation

7.1 Introduction

The environment within a typical DWDS is extremely adverse due to the inherent oligotrophic conditions and the occasional presence of residual disinfectants. Nevertheless, biofouling has a ubiquitous presence within most DWDSs. To assess the impact of biofouling within DWDSs a brief investigation was undertaken as part of the current study. A series of purpose built flow cell styled biofilm reactors were used to simulate the conditions within a typical DWDS; for the purpose of evaluating the combined impacts of different pipe materials and flow regimes on biofilm development. In order to study the influence of different pipe materials on biofilm development, four commonly used materials were selected, namely PVC, Polypropylene (PP), Str-HDPE and S-HDPE. Biofilms were incubated on each of these materials within the flow cell systems at two different representative flow regimes, namely a high and low flow. The purpose of this chapter is to outlined and discuss the results of the drinking water aspect of the current study. The specific details of the flow cell systems are comprehensively outlined within the current chapter. The drinking water biofilms were evaluated by ESEM, bacterial 16S rRNA gene PCR-DGGE and DNA quantification.

7.1 Materials and methods

7.1.1 Experimental facility

A variety of laboratory scale biofilm reactors which are known to be capable of sufficiently simulating the environmental conditions inherent within pipelines have been outlined within the literature. These systems range from simple batch reactors (Manuel et al. 2007) to complex continuous flow systems, such as annular reactors (Lawrence et al. 2000; Gjaltema et al. 2004; Altman et al. 2009; Zhou et al. 2009) and flow cell reactors (Pereira et al. 2000; 2002; Hallam et al. 2001; Manuel et al. 2007; Teodosio et al. 2010). The variations in reactors and systems outlined within the literature could in part explain the highly variable and sometimes conflicting information outlined on the subject of biofilms and biofouling. A flow cell arrangement was used within the current study to emulate the conditions of a pipeline. In total four individual reactors were designed, developed and procured as part of the current

study, although only two were utilised within this part of the study. The flow cells were located within the Characterisation Laboratories for Environmental Engineering Research (CLEER) laboratory, Cardiff University School of Engineering, as shown by Figure 8.1.

The basic design concepts for a flow cell styled reactor were outlined by Teodosio et al. (2010; 2013) and Pereira et al. (2000; 2002). The ability of a flow cell styled reactor to accurately mimic the hydrodynamic conditions within a pipeline have been comprehensively documented through numerical and physical investigations (Teodosio et al. 2010; 2013). The specific hydrodynamic conditions associated with the current study's flow cell arrangement were also simulated by numerical methods using the computational fluid dynamics (CFD) software known as CFX (developed by *Ansys*) (results not shown). The numerical investigation found that the flow cell arrangement used within the current study was capable of adequately emulating pipe flow and satisfying known flow development criteria. Furthermore, when compared against an annular reactor – which is generally considered to be the most effective laboratory scale system currently available – the flow cell reactor produced identical results (Batté et al. 2003; Manuel et al. 2007). A flow cell arrangement is also typically one of the most cost efficient continuous systems currently available, with a complete unit costing under £200.

The flow cell systems utilised within the current study consisted of a 10 l maximum capacity recirculating tank; one vertical positioned flow cell; a clear PVC recirculation tube; a inline turbine flow meter (*RS* 511-4772) and a 0.33 kW centrifugal water pump (*Clarke* CEB102), as shown by Figure 8.1.

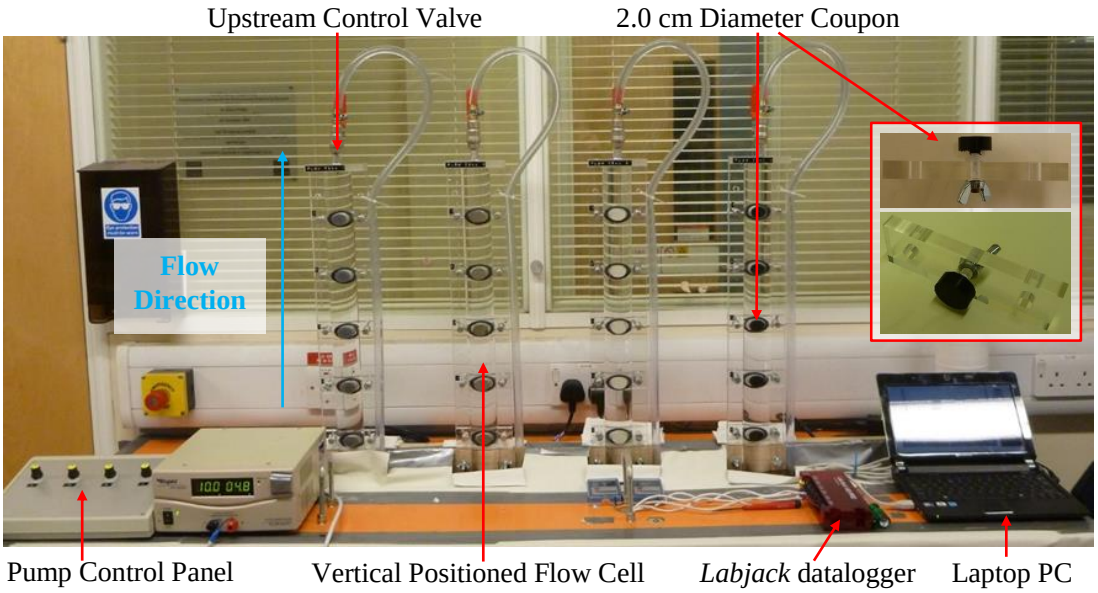

Figure 7.1 A series of flow cell systems in the Characterisation Laboratories for Environmental Engineering Research laboratory at Cardiff University School of Engineering.

The flow cells were positioned vertically within the current study to minimise trapped air within the system.

The flow cell units themselves were 100 cm in length and composed of a 4 cm diameter semi-circular acrylic duct (with an equivalent hydraulic diameter and area of 2.44 cm and 6.28 cm^2, as shown in Table 7.1). Along the planar surface of the flow cell were 5 equally spaced apertures, to fit 5 removable circular adhesion coupons, measuring 20 mm in diameter. The circular nature of the apertures and coupons allowed standard size 'O' ring-type seals to be used to seal the systems. The first aperture was positioned 51.5 cm from the flow cells inlet. The four remaining apertures were positioned every 10 cm from the first. The purpose of this separation was to minimise potential disruptions in boundary shear caused by the respective downstream coupons. The last aperture was located 0.15 m from the flow cells outlet. The CFD evaluation of this studies flow cell arrangement indicated that 0.5 m was a sufficient length of fully development flow to be obtained within the system, for the full range of operating conditions.

Table 7.1 Key Characteristics of the flow cells used in the current study.

Parameter	***Value***
Material	Acrylic
k_s	0.009 mm
Hydraulic Diameter	2.44 cm
Flow Area	6.28 cm^2
Wetted Perimeter	10.28 cm
Hydraulic Radius	0.61 cm
Length	100 cm
Internal Volume	628.3 cm^3 (or 0.63 l)
Volume/Area	100 cm
Biofilm Sampling Points	5
Biofilm Sampling Area	3.14 cm^2

The coupons were fabricated from representative pipe materials, including PVC, Polypropylene (PP), Str-HDPE and S-HDPE. An acrylic (A) coupon was also evaluated, as a control (results not shown). Where possible the discrete coupons were cut from actual pipes. Consequently, the surface finishes inherent to the respective pipe material's fabrication process were accurately assessed. Thus reducing any potential bias. Each of the coupons were

imaged using an Environmental Scanning Electron Microscope (ESEM) before incubation in the bulk water in order to evaluate their respective surface finishes (as outlined in Section 3.2.3.1). The coupons were held in place by a uniquely designed holding bracket. The design of which allowed for independent coupon positional adjustments to be made. This ensured that each coupon was positioned perfectly flush with the internal surface of the flow cell during testing. Any protrusions would have had an adverse effect on the boundary shear conditions and thus, would have introduce considerable bias. It should also be noted, that the design of the flow cell and holding brackets also allowed for individual sampling of the discrete coupons at any given time interval.

The flow rate within each of the discrete systems was independently controlled using two 1/4" ball valves, which were located at the inlet and outlet sides of the respective flow cells. The water temperature within the flow cell systems was regulated using an external cooling unit (*D&D* DC-750) and was measured using a universal temperature probe (*LabJack* EI-1034, as outlined in Section 3.5.1. The external cooling unit was capable of cooling volumes of 200l < V < 600l to within ± 1°C, over the temperature, T range of 4°C < T < 28°C.

The water temperature within the flow cells was maintained at 15.2 ± 1.2ºC, using the external cooling unit. This temperature is representative of the typical temperature expected within DWDSs (in the UK) during the spring and summer months (i.e. 16 ºC) (Douterelo et al. 2013) and as a result, the temperature within the system can be considered accurate for to real system, whilst providing the maximum representative temperature for microbial growth.

A *LabJack* multifunction 24-bit datalogger (Model: U6-Pro) streamed all data recorded by the respective flow cell temperature probes and flowmeters to a laptop PC. A purpose built interface was developed using the DAQfactory (*AzeoTech*) data acquisition software, to manage and export all measurement readings. Appropriate sampling times were derived for the respective measurements using a cumulative average approach (as outlined in Section 3.4).

7.1.2 Pre testing maintenance and sterilisation

The flow cell systems were disinfected using a concentrated chlorine solution prior to any experimental work. An adaptation of the procedure outlined in Section 3.9 for the pilot-scale pipeline was used to sterilise each of the flow cell units. The procedure was essentially the same as that used for the pilot-scale pipeline with the exception that the water in the system was continuously replaced until the chlorine levels were within local drinking water limits. Preliminary testing identified that the average concentration of chlorine within the local DWDS was approximately 0.04 mg/l.

The coupons were independently sterilised prior to testing to remove any residual bacteria and impurities. Each of the coupons was immersed in an 80% ethanol solution for 12 h and then left to dry in a clean fume cupboard for a further 24 h.

7.1.3 Operating conditions

Two separate (steady state) flow regimes were evaluated within two individual flow cells, namely a high and low flow assay. In particular, the two regimes assessed were Re_D = $3.41x10^3$ (i.e. low flow assay) and Re_D = $5.35x10^3$ (i.e. high flow assay). The average freestream velocities within the two flow cells during low and high flow assays were 0.16 and 0.24 m/s, respectively. The shear forces acting on the biofilms within the low flow and high flow assays were 0.13 and 0.24 N/m^2, respectively. These values are based upon the initial conditions (i.e. without fouling) and the principle that the primary shear force acting on the biofilm was the shear force generated by the flow (Stoodley et al. 2002).

Husband et al. (2008) documented that the average values of $\overline{U}$, Re_D and τ_w within DWDSs in the UK are 0.06 m/s, 4200 and 0.28 N/m^2, respectively. Applying this information, Husband et al. (2008), and later Douterelo et al. (2013) cultivated biofilms within a 203 m long pilot-scale pipeline across the range of 0.2 N/m^2 < τ_w < 9.10 N/m^2. Manual et al. (2007) incubated drinking water biofilms within a flow cell reactor at $\overline{U}$ = 0.21 m/s and Re_D = 5000. The shear forces induced by the respective flow regimes employed within the current study are therefore, comparable to equivalent studies and representative of actual systems.

In order to provide representative water chemistry, the flow cells were connected to the local (Cardiff, UK) drinking water distribution system by a trickle feed (and drain). The trickle was set to give an overall system HRT of 12 h. The internal HRT within the high and low assays were 79 s and 109 s, respectively and as a result, both systems were considered to be well mixed (Stoodley and Warwood 2003).

The high and low flow assays were run in parallel for 100 d, in which time the incubated biofilms should have reached a moderately mature state (LeChevallier et al. 1987; 1990; Laurent and Servais 1995; Zhou et al. 2009; Douterelo et al. 2013). It has been suggested that the process of biofilm maturation within DWDSs can take several years (Martiny et al. 2003). However, steady state conditions, based on heterotrophic plate counts have been documented after just 14-22 d (LeChevallier et al. 1987; 1990, Zhou et al. 2009).

During the 100 d incubation period the flow cell systems were shielded from natural light using a high grade blackout material.

7.1.4 Water physico-chemistry

Table 7.2 presents the average local physico-chemical parameters measured directly from the flow cell systems and where possible, the equivalent parameters measured by Welsh Water, as outlined in their independent national database. These values represent the average of 12572 water samples taken across Wales, UK between 02/01/2009-30/08/2013. Also presented in Table 7.2 are the equivalent parameters which have been outlined previously within the literature.

Table 7.2 Physico-chemical properties of drinking water

Parameter	***Local Drinking Water***		***Reported Values***	***Reference***
	Measured in Lab	***Measured by Welsh Water****		
***T* (°C)**	15.20 ± 0.70	-	15.50-25.0	Niquette et al. (2000), Momba and Makala (2004), Manuel et al. (2007), Douterelo et al. (2013)
pH	7.60 ± 0.25	-	6.90-8.96	LeChevallier et al. (1987), Lehtola et al. (2004), Momba and Makala (2004), Teng et al. (2008), Zhou et al. (2009), Wang et al. (2012), Douterelo et al. (2013)
TOC (mg/l)	4.10 ± 0.24	1.21 ± 0.54	1.49-5.10	LeChevallier et al. (1987), Lehtola et al. (2004), Manuel et al. (2007), Zhou et al. (2009), Wang et al. (2012)
DOC (mg/l)	3.50 ± 0.20	1.30 ± 0.56	0.80-19.00	Niquette (2000), Momba and Makala (2004), Manuel (2007), Wang (2012)
COD (mg/l)	1.21 ± 0.48	-	0.36-0.91	Teng et al. (2008), Zhou et al. (2009)
TN (mg/l)	1.78 ± 0.14	1.03 ± 1.23	0.50-2.10	Momba and Makala (2004)
NH_3^- (mg/l)	0.01	0.05 ± 0.70	0.40-1.66	Manuel et al. (2007), Zhou et al. (2009)
NO_3^- (mg/l)	1.27 ± 0.02	1.03 ± 1.22	0.01-2.47	Teng et al. (2008), Manuel et al. (2007), Zhou et al. (2009)
NO_2^- (mg/l)	0.01	0.01 ± 0.06	< 0.01	Manuel et al. (2007)
TP (mg/l)	0.33 ± 0.43	0.53 ± 0.34	0.01-2.00	Lehtola et al. (2004), Manuel et al. (2007)
Cl (mg/l)	0.03 ± 0.01	-	0.05-3.00	Niquette et al. (2000), Lehtola et al. (2004), Manuel et al. (2007), Teng et al. (2008), Zhou et al. (2009), Wang et al. (2012), Douterelo et al. (2013)
Mn (mg/l)	0.02 ± 0.01	-	0.02-0.05	Lehtola et al. (2004), Douterelo et al. (2013)
Fe (mg/l)	< 0.1	-	0.01-0.64	Lehtola et al. (2004), Douterelo et al. (2013)

* Physico-chemical properties of local drinking water as measured by Welsh Water between 02/01/2009 to 30/08/2013

For the first 10 d water samples were measured every 24 h, after this period samples were measured every 5 d. The parameters measured directly from the flow cell systems were established using the protocols outlined in Section 3.5.2, with the exception of COD, which was measured using a low range reagent assay (LCK 500, *Hach-Lange*, detection range of 0 mg/l < COD < 150 mg/l) and a Benchtop Spectrophotometer (DR3900, *Hach-Lange*).

It is evident from Table 7.2 that the pH of the water within the flow cells during incubation was close to neutral (i.e. 7.60 ± 0.25). The temperature ranged from 14.80-15.62°C during incubation and was within the ±1.00°C control specified for the external cooling unit.

The measured parameters were within or very close to the typically local values outlined by Welsh Water and by previous equivalent studies. However, it should be stated, that the measured organic contents were at the upper limit of the expected range during testing, The maximum recorded values of TOC and DOC by Welsh Water were 5.22 and 4.83 mg/l, respectively (Date: 12/06/2010). The current study's equivalent concentrations were 4.10 and 3.30 mg/l, respectively. The chlorine concentration within the system was towards the lower range expected within a DWDS within the UK (Husband et al. 2008; Douterelo et al. 2013). However, this was to be expected, as chlorine decreases with time due to its reactive nature, and therefore it would be naturally lower towards the end of the system.

7.1.5 Biofilm sampling

To investigate the biofilms within the high and low flow assays, biofilm samples were obtained after the 100 d of incubation within the drinking water. In particular, the biofilms were evaluated using ESEM, PCR-DGGE and DNA quantification, using the protocols outlined in Section 3.2.3.1 and Section 3.7.The total cell concentration on each coupon was estimated using the recommendations outlined by McCoy and Olson (2008) and the respective DNA concentrations of the coupons.

After 100 d, the flow within each of the respective flow cells was stopped and the bulk water sealed within them by closing the inlet and outlet valves. The discrete flow cells were then detached from the recirculating system and placed planar side up on a clean table. The coupons were then detached and part of the biofilm (approximate area: 2.4 cm^2 or 75% of total area) was completely removed from each of the coupons using a sterile cotton swab and stored at -80°C for molecular analysis. The remainder (approximate area: 0.8 cm^2) of biofilm was then imaged by ESEM. The relevant extraction and evaluation protocols outlined in Section 3.6 were then used. The biofilm samples were stored at -80°C between extraction and evaluation.

7.2 Results and discussion

7.2.1 Surface finish pre incubation

In order to estimate the physical roughness of the different pipe materials the images captured of them by ESEM were evaluated using the MountainsMaps image analysis software (as outlined in Section 3.4.2). The results of the physical roughness evaluation for the four different materials are presented in Figure 8.2 and Table 8.3. It is evident from Figure 8.2 that the surface micro-geometry of the four coupons are very different when viewed under ESEM. In particular, the surface of the PVC and Str-HDPE coupons appeared to be covered with numerous scratches, grooves and deformation marks. Whereas, the surfaces of the PP coupon was seemingly free from deformations and was extremely smooth. The S-HDPE coupon was in the middle of the two extremes.The roughness parameters listed in Table 8.3 show that the Str-HDPE coupon had the highest roughness of the assessed coupons, with average k_{rms} of 3.70µm. The PP coupon was statistically the smoothest of the five coupons, with an average k_{rms} of 0.59µm. Ranking the respective materials based on their physical roughness yields PP < S-HDPE < PVC < Str-HDPE. Presumably, the increased roughness of the Str-HDPE coupon would aid microbial attachment and biofilm formation, whereas, the relatively smooth nature of the PP coupon would limit biofilm development.

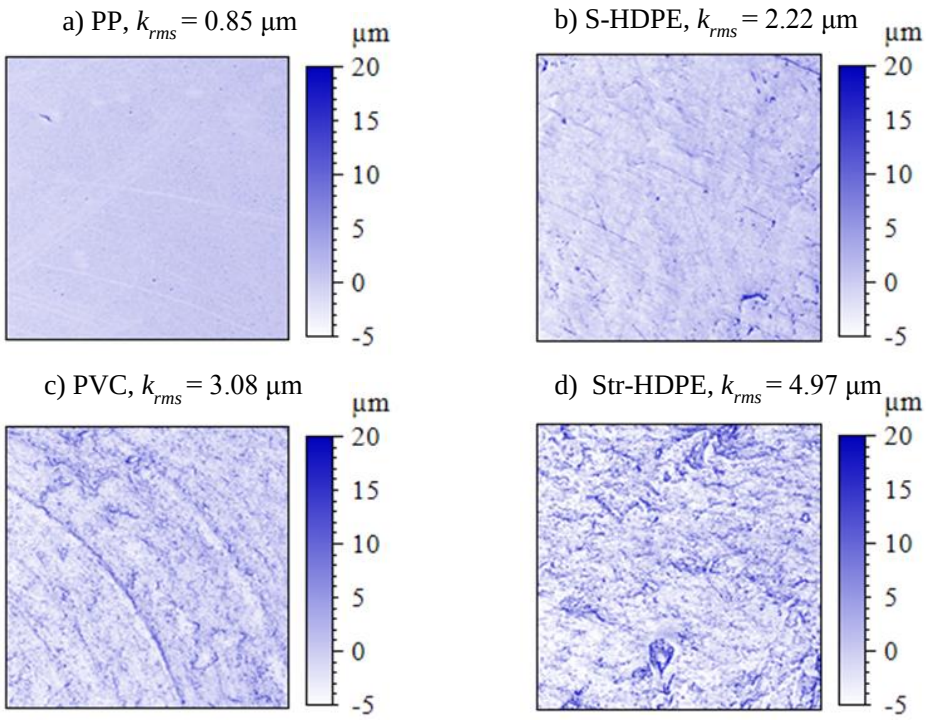

Figure 7.2 2-D Pre incubation micro-topography maps of a) PP b) S-HDPE, c) PVC and d) Str-HDPE coupons (size: 0.5 x 0.5 mm^2 and Mag.: x 200).

Table 7.3 Pre incubation physical roughness paramters of PP, S-HDPE, PVC and Str-HDPE coupons.

Material	k_{av} ***(μm)***	k_t ***(μm)***	k_{rms} ***(μm)***	s_{kl}	k_s ***(μm) (Predicted)****
PP	0.59	24.10	0.85	2.24	2.55
S-HDPE	1.47	23.50	2.22	2.78	6.66
PVC	2.28	28.80	3.08	1.60	9.24
Str-HDPE	3.70	29.40	4.97	1.49	14.91

$k_s \approx 3k_{rms}$ (Zagarola and Smits 1998)

7.2.2 Surface finish post incubation

The ESEM imaging identified the major components of the biofilms incubated with drinking water, which consisted predominantly of sparse populations of rod-shaped colonising bacteria and embedded within Extracellular Polymer Substances (EPS) (see Figure 7.3). Small numbers of filamentous bacteria were also evident when the coupons were used by ESEM, as shown in Figure 7.3e.

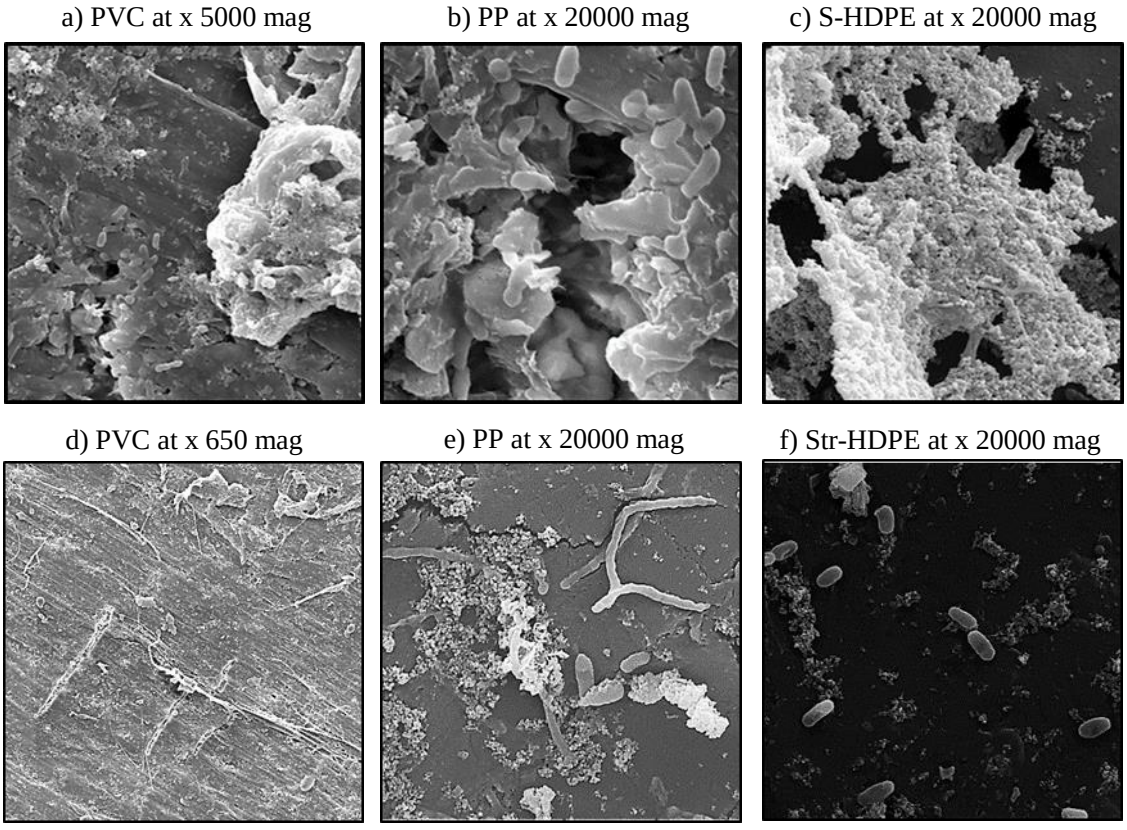

Figure 7.3 Photomicrographs captured by ESEM of the different coupons post incubation, inlcuding the a) PVC at x 5000 x mag. b) PP at x 20000 mag. c) S-HDPE at x 20000 mag. d) PVC at x 650 mag. e) PP at x 20000 mag and f) Str-HDPE at x 20000 mag.

Similar observations were documented by Percival et al. (1999) for biofilms incubated with drinking water when viewed under Scanning Electron Microscope (SEM). Furthermore, the "fibrillar strand" structures of EPS observed by Percival et al. (1999) were also observed within the current study, particularly on the PVC coupons, as shown by Figure 7.3d. However, Percival et al. (1999) also observed Small numbers of fungi, yeast cells and diatoms, none of which were evident within the images captured within the current study.

The captured ESEM images also showed that various amounts of microbial material with very different morphology were present depending on the material and flow hydrodynamic condition, as shown by Figure 7.4 and Figure 7.5.

Relatively, the amount of microbial biomass on the coupons was typically greater within the low flow assay than within the high flow assay, as shown by Figure 7.4. Furthermore, it is evident that the biofilms incubated within the high flow assay were seemingly more isolated than those within the low flow assay.

It is typically expected, that providing the overall shear conditions remain below the critical level, biofilms conditioned at high shear will show more rapid and extensive development than those conditioned at low shear, due to mass transfer and diffusion principles (Percival et al. 1999; Pereria et al. 2002; Lehtola et al. 2005; Manuel et al. 2010). Furthermore, the high mass transfer potentials associated with high shear conditioning will generally induce a less isolated and more uniformly distributed biofilm (Percival et al. 1999). Nevertheless, the inherently low nutrient conditions within drinking water will likely negate the influence of mass transfer and diffusion on biofilm development, due to the overall lack of biological material present (Melo and Bott 1997; Stoodley et al. 1998a; Volk and LeChevallier 1999; Gjaltema et al. 2004). The increased mass transfer and diffusion associated with high shear conditioning will also encourage the influx of disinfectants (if used). However, it should be noted that the observations made by Percival et al. (1999) with regards to the fostered biofilm uniformity at high shear conditioning were for a drinking water system. Notwithstanding, it is evident from the current study that biofilm development within a drinking water environment was inhibited at high shear, which suggests that the overall shear forces imposed by the flow were above the critical levels.

In terms of the discrete materials, the PVC and Str-HDPE coupons showed the largest amounts of microbial biomass, irrespective of the flow conditions (as shown by Figure 7.5). These materials also showed the greatest initial roughness of the four coupons (see Table 7.3). The morphology of the respective biofilms incubated on the PVC and Str-HDPE coupons however, differed considerably between the respective coupons (see Figure 7.5).

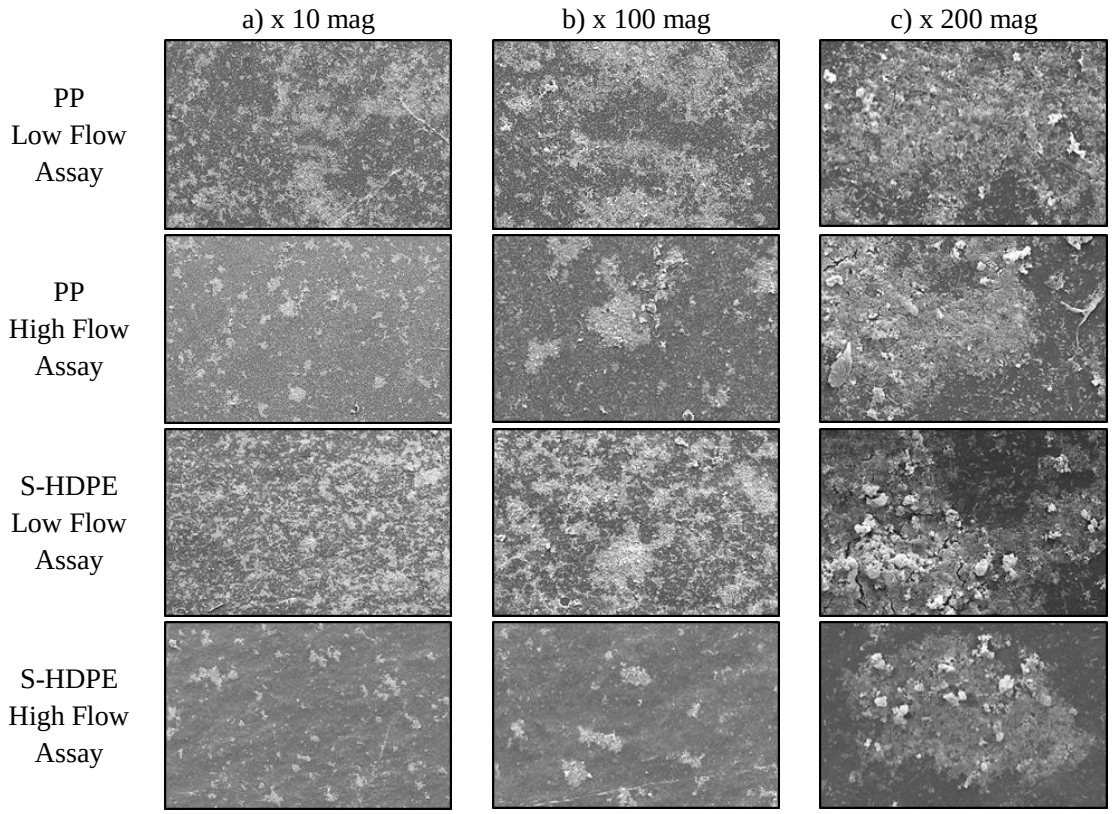

Figure 7.4 Photomicrographs captured by ESEM of the PP and S-HDPE coupons incubated in the low and high flow assays at a) x 10 mag. b) x 100 mag. c) x 200 mag.

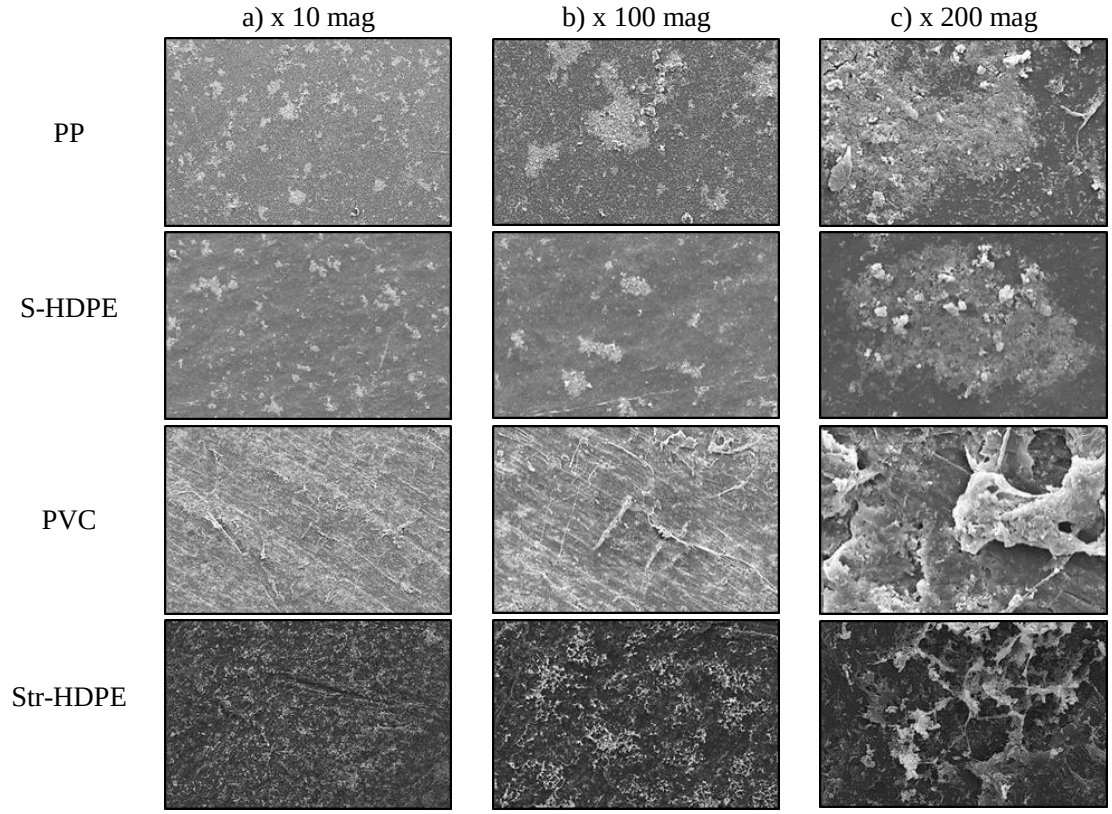

Figure 7.5 Photomicrographs captured by ESEM of the PP, S-HDPE, PVC and Str-HDPE coupons incubated in high flow assay at a) x 10 mag. b) x 100 mag. c) x 200 mag.

The biofilms incubated on the PP and S-HDPE coupons showed similar morphologies and were comprised of similar amounts of microbial material (see Figure 7.5). Yu et al. (2010) suggested based on similar visual observations on biofilms incubated with drinking water on different pipe materials that surface roughness can have a considerable impact on biofilm formation and that materials which are initially rough will foster greater biofilm development.

The images captured by ESEM of the coupons after incubation with drinking water were processed using the MountainsMap software. The results of the physical roughness evaluation of the coupons post incubation are presented in Figure 7.6 and Figure 7.7. A change in roughness was observed within all cases post incubation. The change in physical roughness post incubation is a function of the biofilms structure, and in particular its thickness (Barton 2006; Andrewartha 2010). Typically, an increase in roughness is fostered by an increase in thickness. However, this is not always the case, in some instances biofilms have been known to smoothen an initially rough surface by filling its cavities and grooves (Barton 2006; Andrewartha 2010). Such growth practices are common among low-level fouling systems and it was suggested on this basis (in Chapter 2) that the surface of a DWDS could potentially be smoothened by biofilm development, and as a consequence it could in fact improve the system's hydraulic performance. The smoothening of a surface is typically illustrated by a reduction in the maximum valley or pit height (Barton 2006; Andrewartha 2010). This was not found to be the case for any of the assessed materials incubated with drinking water within the current study. As a result, an increase in physical roughness post incubation was reported for all the materials (shown by Figure 7.6 and Figure 7.7). For instance, k_{rms} for the PP coupon increased from 0.85-5.86 μm following incubation. Similarly, the k_{rms} for the Str-HDPE coupon increased from 4.97-7.39 μm following incubation.Nevertheless, the observed increases in roughness caused by the biofilm would have had negligible effect on a system's hydraulic performance and equivalent roughness. Take for example the Str-HDPE coupon, which showed the greatest amount of microbial growth, and the assumption that the k_s induced by a biofilm is 1.5 times greater than its k_t (Barton 2006; Andrewartha 2010), the k_s imposed by the surface with fouling would have been between 0.048-0.050 mm depending the conditioning shear (i.e. k_t = 32.3-33.6 μm).

The impact of flow hydrodynamics on biofilm thickness has been well documented within the current study and literature (Stoodley et al. 1998a; Percival et al. 1999; Lehtola et al. 2005; Barton 2006; Lambert et al. 2008; 2009; Celmer et al. 2008; Perkins et al. 2013; 2014). Typically, the higher the shear conditioning the thinned the overall biofilm. This was found to be the case within the current study and is illustrated by Figure 7.7 (in terms of physical roughness) although, differences were small.

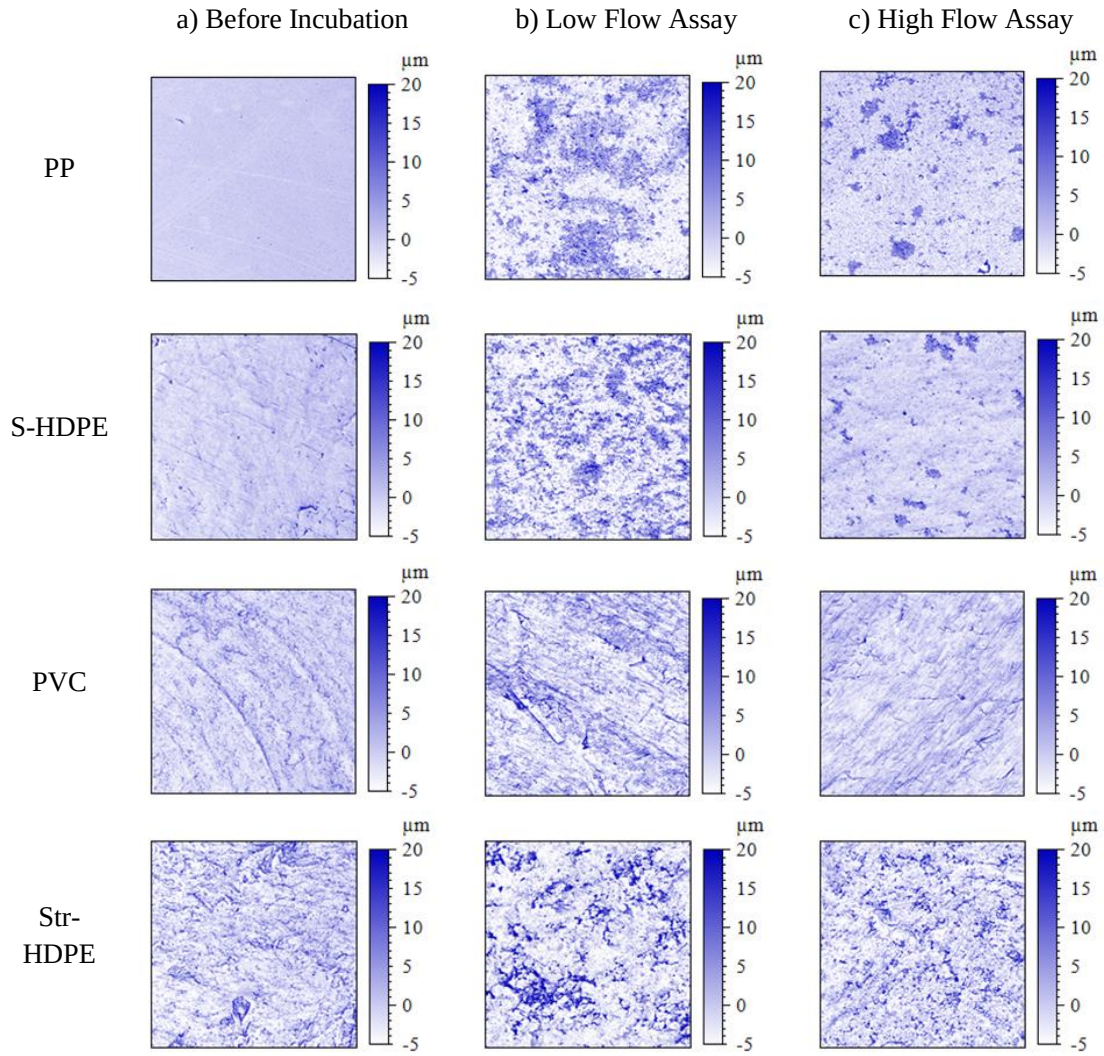

Figure 7.6 Photomicrographs using captured by ESEM of the PP, S-HDPE, PVC and Str-HDPE a) before incuabtion and after incubation within the b)low flow assay c) high flow assay (x 200 mag).

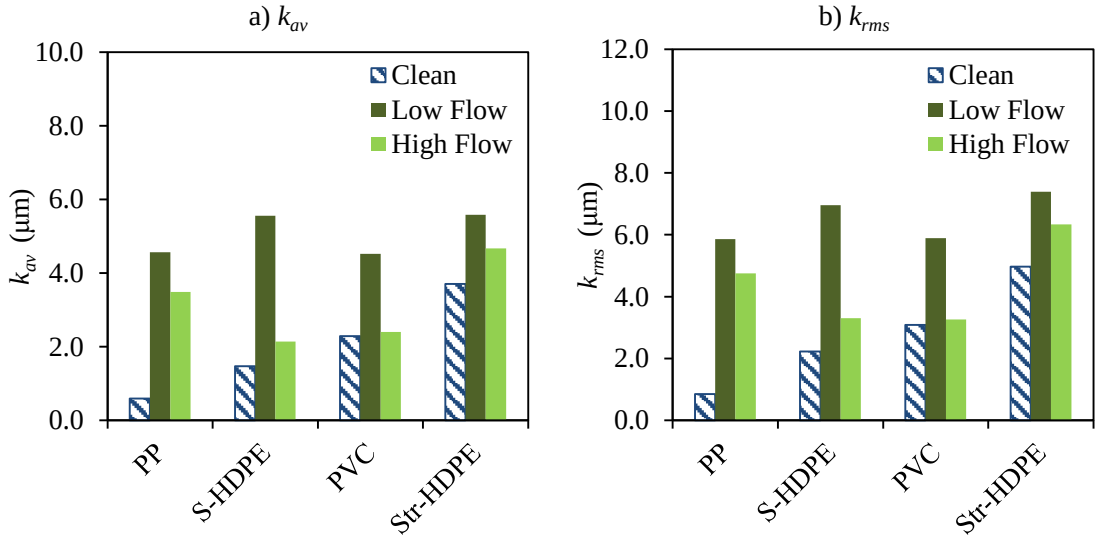

Figure 7.7 Per- and Post- incubation physical roughness paramters for the PP, S-HDPE, PVC and Str-HDPE coupons, incluiding a) k_{av} and b) k_{rms}.

It should be noted, that the potential dehydration caused by the preparation process for ESEM imaging may have reduced the biofilm's water content and ultimately its overall structure, although this effect, if any, would have been the same for all treatments the results should be viewed with caution.

7.2.3 Biofilm DNA concentration

Following incubation with drinking water for 100 d the microbial DNA concentrations extracted from the discrete coupons ranged from 5.28-45.60 ng/cm^2, as shown by Figure 7.8. The estimated cell concentrations on each of the coupons ranged from 4.0x10^5-3.7x10^6 cells/cm^2. This concentration range is similar to that reported by Niquette et al. (2000), who found that the total cell concentration on plastic-based materials (including PE and PVC) when incubated with drinking water with low levels of residual chlorine (i.e. < 0.05 mg/l) ranged from 7.0x10^4-5.0 x10^5 cells/cm^2. Manuel et al. (2007) found that the cell concentration on coupons fabricated from HDPE and PVC when incubated with drinking water under shear conditions in excess of those reported within the current study (i.e. τ_w = 0.80-1.91 N/m^2) ranged from 2.6x10^7-8.7x10^7 cell/cm^2.

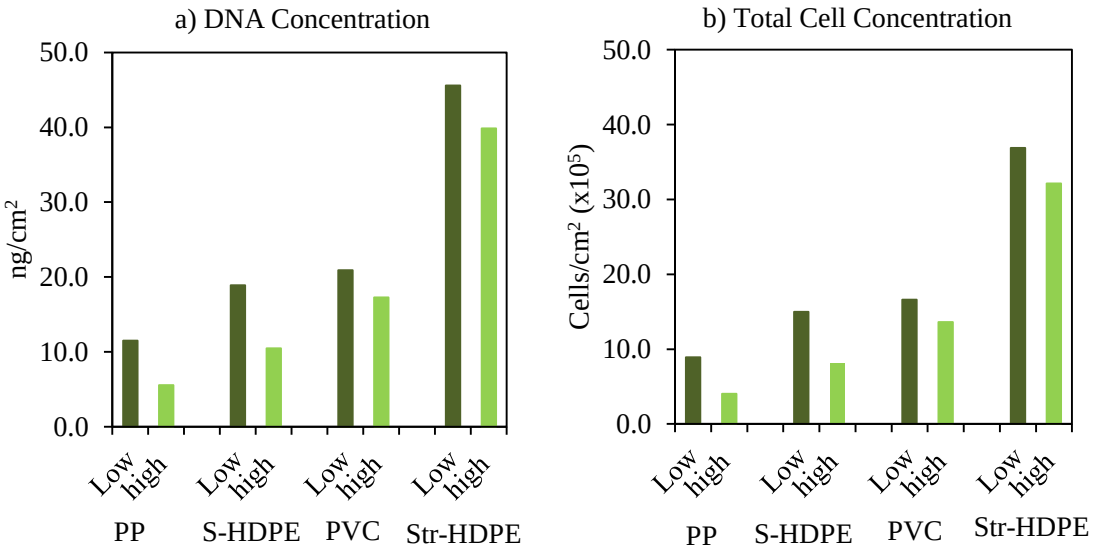

Figure 7.8 Post incubation a) DNA and b) total estimated cell concetrations of the for the PP, S-HDPE, PVC and Str-HDPE coupons (for both high and low flow assays).

The DNA and total estimated cell concentrations were lower within the high flow assay compared to the low flow assay. This supports the visual observations outlined in Section 7.2.2. The magnitude of the difference between the high and low flow assay's DNA concentrations was seemingly dependant on the material. The greatest difference occurred

between the respective DNA and cell concentrations documented for the PP coupon, which was also deemed to be the smoothest assessed material (see Table 7.3). In this instance, the percentage difference between the high and low flow assay was 108%. The lowest difference was found to be 14% and occurred between the respective DNA and cell concentrations documented for the material with the highest initial roughness, i.e. Str-HDPE. These observations were to be expected, as a smooth material will typically induce higher near-wall velocities and provide less protection and attachment areas than a rough material. Consequently, the surface characteristics of the PP coupon would have magnified the impact of the increased shear conditions inherent within the high flow assay and therefore, contribute to the greater difference between the low and high flow assay's biofilms characteristics.

The lowest DNA and cell concentrations were measured on the PP coupon and the highest was measured on the Str-HDPE coupon (which was 4.0-7.2 times higher than those measured on the PP coupon). The S-HDPE and PVC coupons showed intermediate levels of the respective parameters. The DNA concentrations on the S-HDPE coupons were 2.4-3.8 times lower than the equivalent concentrations on the Str-HDPE. The only difference between the respective HDPE materials was thought to be surface roughness (See Table 7.3). This suggests that the initial surface roughness of a material can have a significant influence on microbial adhesion and subsequent colonisation. This was to be expected, as the cavities and grooves which form a material's surface roughness will typically influence the transport and attachment of microbial cells by increasing the mass transfer potential; providing shelter from the adverse shear conditions and increase the attachment area (Geesey and Costerton 1979; Costerton et al. 1987; Percival et al. 1999). Consequently, numerous studies have found that materials initially high in roughness support significant amounts of biofilm development over the short and long term (Niquette et al. 2000; Tsevetanova 2006; Yu et al. 2010). Figure 7.9 and Figure 7.10 illustrates further the impact of initial surface roughness (in terms of k_{av} and k_{rms}) on resultant biofilm development. Strong correlations between k_{av} and k_{rms} with the biofilm DNA concentration are evident from Figure 7.9 and Figure 7.10 ($R^2 > 0.92$).

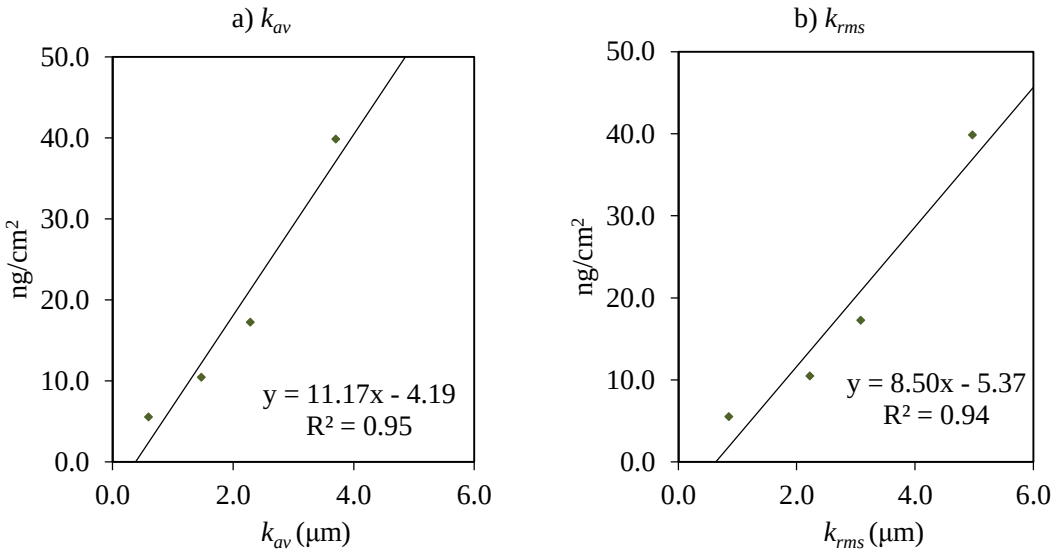

Figure 7.9 DNA concertations post incubation within the low flow assay againsnt a) k_{av} and b) k_{rms}

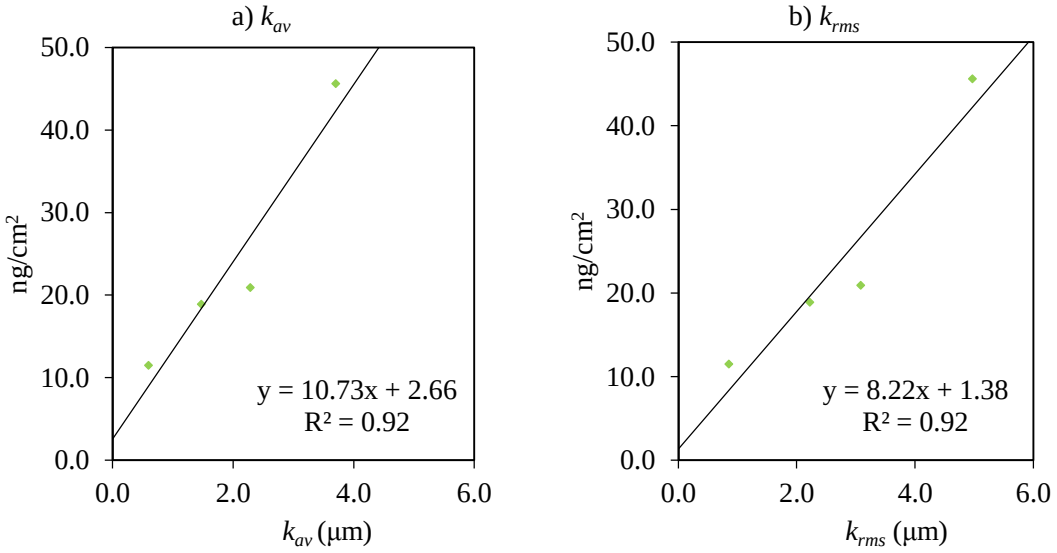

Figure 7.10 DNA concertations post incubation within the high flow assay againsnt a) k_{av} and b) k_{rms}

7.2.4 Biofilm bacterial community structure

The dominant bacterial communities within the biofilms incubated on the different plastic material coupons were identified by 16S rRNA gene PCR-DGGE, using the protocols outlined within Section 3.7.3. The distinguishable bands were excised and sequenced from one DGGE gel (see Figure 7.11). The results of the PCR-DGGE analysis for the biofilms incubated with drinking water on different material coupons within the high and low flow assay are summarised in Figure 7.11 and Table 7.3.

Bacillus sp. was found as a contaminant within the cotton buds used for sampling the biofilm (i.e. control, in Figure 7.11), and therefore, it was not included within the discussions herein.

It is evident from Figure 7.11 that the dominant bacterial phyla within biofilms incubated with drinking water were *Betaproteobacteria*, *Alphaproteobacteria*, *Gammaproteobacteria* and *Firmicutes*. The bacterial phylum of *Cyanobacterium* was also found to be dominant, although only on the S-HDPE coupon under high flow conditions. At the genus level *Pseudomonas sp.*, *Sphingomonas sp.* and *Aquabacterium sp.* were found to be abundant within the biofilms.

It is evident from Figure 7.11, Figure 7.12 and Table 7.4 that the characteristics of the biofilm communities varied significantly depending on the material and hydrodynamic condition. *Alphaproteobacteria* was the predominant bacterial group within the biofilms incubated within the low flow assay and represented on average 30% of the total evaluated bands. *Gammaproteobacteria* (26%) and to a lesser extent *Betaproteobacteria* (18%) and *Firmicutes* (18%) were also abundant within the low flow assay. Within the high flow assay, *Betaproteobacteria* (18%) and *Firmicutes* (18%) were dominate bacterial groups within the biofilms. *Gammaproteobacteria* (10%) and *Alphaproteobacteria* were also evident within the biofilms incubated in the high flow assays. *Betaproteobacteria* have been documented to have a greater ability than other bacterial groups to attach to a surface and form biofilms within DWDSs (Manz et al. 1999). Consequently, *Betaproteobacteria* typically dominate biofilm processes in DWDSs (Manz et al. 1999; Douterelo et al. 2013) and therefore, this could explain its abundance within the biofilms incubated within the current study. The dominance of *Alphaproteobacteria* within the respective biofilms could be explained by their known resilience to commonly used disinfectants, namely chlorine (Douterelo et al. 2013). In particular, *Alphaproteobacteria* have a stronger resistance to known disinfectants than other bacterial groups found within DWDSs and as a result, it is typically found in abundance in both planktonic and biofilm growth phases of such systems, although more commonly within the former (Douterelo et al. 2013).

Sphingomonas sp. and *Pseudomonas sp.* were the predominant pathogens and opportunistic pathogens found in the biofilms incubated within the high and low assays. The abundance of such species confirms the potential of biofilms to act as a reservoir for pathogens and opportunistic pathogens, which if mobilised into the water column could result in health and disease issues for consumers, particularly for the young, elderly and the infirm (Douterelo et al. 2013).

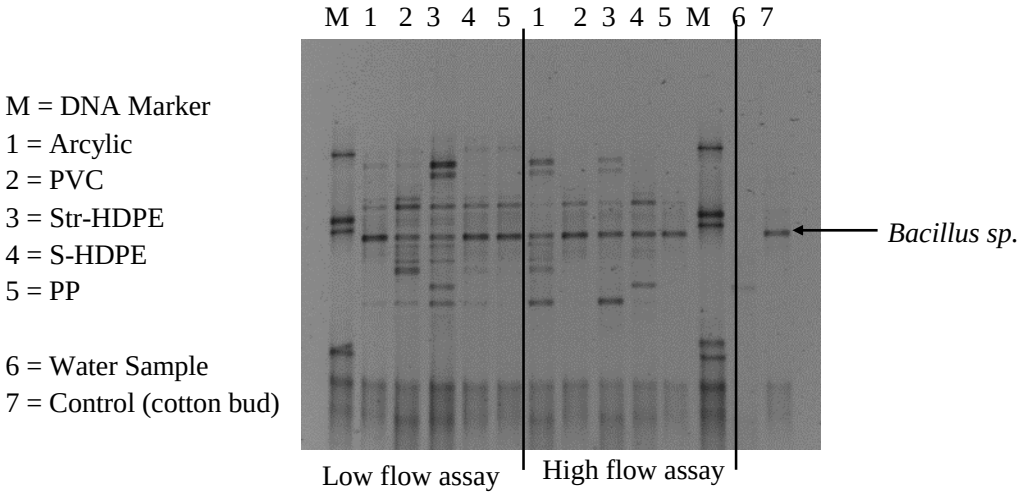

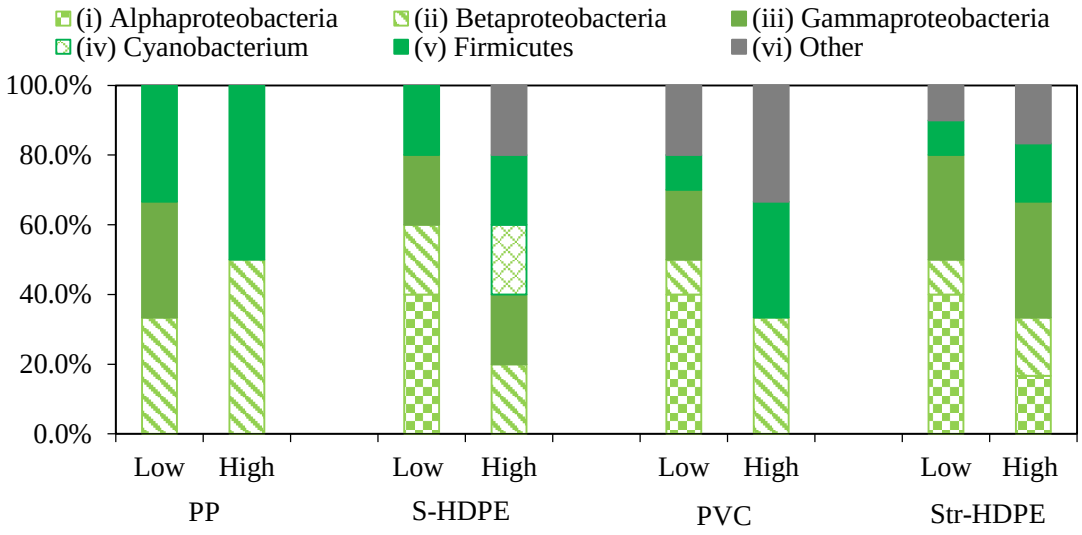

Figure 7.11 PCR-DGGE analysis of bacterial 16S rRNA genes within biofilms on different plastic coupons incubated with drinking water at two different flow regimes

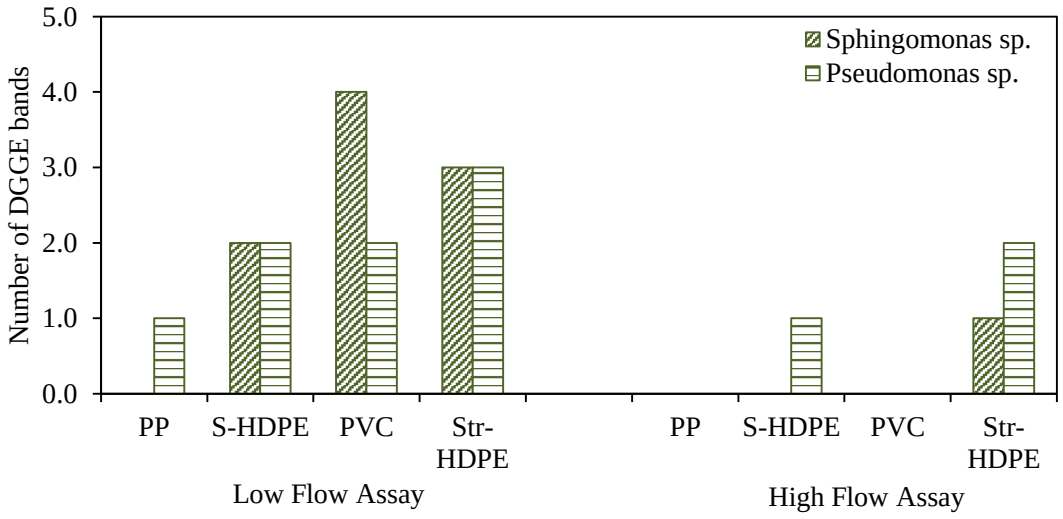

Figure 7.12 Number of Sphingomonas sp. and Pseudomonas sp. bands on each material coupon.

Table 7.4 Summary of the results of the PCR-DGGE analysis of bacterial 16S rRNA genes within biofilms on different plastic coupons incubated with drinking water at two different flow regimes

Genus	***Low Flow Assay***				***High Flow Assay***			
	PP	***S-HDPE***	***PVC***	***Str-HDPE***	***PP***	***S-HDPE***	***PVC***	***Str-HDPE***
Bradyrhizobium sp.		✓	✓	✓				✓
Sphingomonas sp.		✓	✓	✓			✓	
Methylobacterium sp.				✓				
Aquabacterium sp.	✓	✓	✓		✓	✓		✓
Pseudomonas sp.	✓	✓	✓	✓		✓		✓
Nevskia sp.								
Cyanobacteria sp.						✓		

Sphingomonas sp. is typically observed in abundance within DWDSs and is known to have a high ability to form bacterial aggregates and biofilms in order to protect itself from disinfectants (Yu et al. 2010; Douterelo et al. 2013). The dominance of *Pseudomonas sp.* within DWDSs is generally explained by its ability to produce high amounts of cohesive extracellular polymers (Burns and Stach 2002; Bitton 2011), and as a result, they are typically the most abundant bacterial species within DWDSs irrespective of the conditioning (LeChevallier et al. 1987; Percival et al. 1999; Martiny et al. 2005; Douterelo et al. 2013).

Sphingomonas sp. and *Pseudomonas sp.* were found to be particularly dominant within the biofilms incubated within the low flow assay (see Table 7.3 and Figure 7.12). However, in contrast to previous findings, they were rarely found within the biofilms incubated within the high flow assay (Yu et al. 2010; Douterelo et al. 2013). In particular, in the high flow assay, *Sphingomonas sp.* and *Pseudomonas sp.* were only evident within biofilms incubated on the HDPE-based materials. This suggests that these species have a limited ability to propagate within biofilms under high shear conditions (i.e. $\tau_w > 0.24 N/m^2$) without sufficient protection (i.e. roughness). The fact, that these pathogens and opportunistic pathogens were only consistently evident on the HDPE coupons within the high flow assay, potentially suggests that a property inherent within HDPE fostered their development. Douterelo et al. (2013) found that *Pseudomonas sp.* was abundant within biofilms incubated at shear forces in excess of $0.24 N/m^2$. However, the pilot-scale pipeline used by Douterelo et al. (2013) to incubate biofilms was also fabricated from HDPE.

There is conflicting evidence within the literature on whether or not PE-based pipes release biodegradable organic compounds and phosphorus, which could provide nutrients to support biofilm development within DWDS that *Pseudomonas sp.*, particularly could exploit given

their highly metabolically versatile nature (Nanda et al. 2010). It is also highly possible at the *Pseudomonas sp*. itself was caused the release of the compounds due to their enzyme activity, as highlighted by their use in the biodegradation of plastics (Nanda et al. 2010). There is evidence to suggest PE-based materials do release such compounds (Lehtola et al. 2004; Yu et al. 2010) and there is equally compelling evidence to suggest they do not (Tsvetanova 2006; Manuel et al. 2007). The low overall system HRT meant it was not possible to determine if any leaching did occur within the current investigation. It is suggested therefore, that further work is undertaken to investigate the potential of HDPE to harbour greater concentrations of pathogens and opportunistic pathogens compared to other plastics.

7.3 Summary

This chapter has presented the results of the drinking water aspect of the current study and although concise, it has expanded on the current knowledge relating to the impact of surface roughness on biofilm development within DWDSs; with a particular focus on the surface roughness of plastic-based materials.

Surface roughness and flow hydrodynamics are inherently linked by basic boundary layer principles (as outlined in Chapter 2) and as a result, the impacts of these factors on biofilm development are also naturally related to each other. The results outlined within the current chapter have highlighted this inherent relationship.

The results of the DNA and estimated cell counts indicate that the surface properties, namely roughness of different plastic materials can have a considerable impact on microbial attachment and subsequent biofilm colonisation. This is in contrast to previous investigations, which found that plastic-based materials as a whole support similar amounts of fixed biomass (Schwartz et al. 1998; Niquette et al. 2000; Momba and Makala 2004; Manuel et al. 2007). However, these studies, with the exception of Manuel et al. (2007) compared plastic-based materials to traditional pipe materials, such as concrete and iron. The latter typically have considerably high biofilm formation potential, particularly when compared to plastic-based materials (Pedersen 1990; Kerr et al. 1999; Niquette et al. 2000; Chang et al. 2003; Yu et al. 2010). For instance, Niquette et al. (2000) found that the density of fixed biomass on an iron-based material was 10-45 times higher than that measured on plastics (including PVC and PE). Consequently, the small difference between the respective plastics may have been overlooked or deemed relatively insignificant within the respective studies due to the high amounts of biofilm often associated with traditional pipe materials.

The impact of surface roughness on biofilm development (in terms of DNA concentration) was seemingly greater than the impact of flow hydrodynamics, at least for the range of 0.13 $N/m^2 < \tau_w < 0.24\ N/m^2$ and although, this range is relatively small it is representative of typical DWDSs (Husband et al. 2008; Douterelo et al. 2013). Furthermore, the concentrations of bacteria was lower within the high flow assay on the smoother coupons than within the low flow assay on the rougher coupons.

The observations outlined within this chapter therefore, support the argument that material properties can have a considerable influence on biofilm development within DWDSs (Pervival, et al. 1999; Niquette et al. 2000; Schwartz et al. 2003; Cloete et al. 2003; Momba and Makala 2004, Abdel-Monim et al. 2005, Zhou et al. 2009). However, the inherent relationship between surface roughness and flow hydrodynamics should not be ignored. Moreover, it also widely acknowledged that any potential material impact is lessened when high levels of disinfectants are used (Niquette et al. 2000; Tsvetanova 2006; Hallam et al 2001). Therefore, the conclusions drawn within this chapter are limited to the aforementioned shear conditions and areas of low chlorine concentrations (i.e. < 0.04 mgCl/l). Such areas are typical at the end of long pipelines or branches.

It is noteworthy that the biofilms incubated for 100 d with drinking water within the current study were extremely thin (i.e. in the order of 2.14 μm < k_{av} < 5.58 μm). If the observed development is representative of that within actual plastic based systems, then it is likely those system's hydraulic performance will be unaffected by biofilm development

However, as it can take several years for a biofilm to reach a state of maturity (Martiny et al. 2003) it is suggested further long term incubations are performed and ideally within a larger facility, such as the pilot-scale pipeline outlined in Chapter 3 which is capable of measuring small changes in surface roughness.

Chapter 8 Results synthesis, conclusions and recommendations

8.1 Introduction

Biofouling in drainage networks realistically unavoidable. Consequently, the frictional properties of a biofilm, which are characterised by their highly dynamic and case-specific nature, should represent the "true" underlying surface roughness of all pipelines in service. However, such understanding is currently not recognised within conventional design practices, and in the author's opinion, this is to the detrimental of efficient and sustainable operation, especially given:

1. A biofilm's inherent ability to induce an effective roughness which is well in excess of what its physical structure would traditionally suggest;
2. That traditional frictional relationships fail to adequately account for the true nature of a biofouled surface in their current manifestation.

The current study has comprehensively evaluated and discussed biofouling and biofilm development within drainage networks, with the underlying industrial focus of improving pipe design techniques. In particular, the impact and implications of biofouling was established within a purpose built pipeline facility under wastewater conditions. The prevailing conditions within drainage networks are conducive to both significant and rapid growth, and as a consequence, the implications of biofouling on the system's hydraulic performance and effective operation can be considerable. Not only in terms of the biofilm itself but also its capacity to compound the impact of other fouling mechanisms, such as the accumulation of sediments and loose deposits.

A review of the main results obtained and the conclusions derived from the current study are presented within this chapter.

The conclusions drawn from the brief drinking water investigation are presented at the end of this chapter, before the recommendation for future work are outlined.

8.2 Main achievements and contribution to knowledge

The nature of the problem necessitated the need for a multidisciplinary approach, which incorporated both engineering and microbiological techniques. Considering the aims outlined in Chapter 1, the main achievements of the study were:

1. A thorough review of the problem of biofouling and the methods available to measure its influence on turbulent flow within pipelines (Chapter 2). The review fundamentally highlighted the significance of the current study by illustrating the lack of comprehensive information and data on the topic of biofouling within water and wastewater systems, particularly on its influence on hydraulic efficiency. The principal of a sensitivity analysis, centred on controlled laboratory testing seemed the most prudent course of action to establish the impact that discrete factors had on the complex surface dynamics of a biofouled surface.
2. The development of a pilot-scale pipeline facility for the explicit purpose of evaluating the frictional resistance of a HDPE pipe with and without fouling (Chapter 3). This facility was shown experimentally to be capable of measuring to a high degree of certainty all required measurements for a boundary layer and biofouling investigation (Chapter 4). As a result, the pipeline facility indirectly contributed to an improved understanding on biofouling by its capacity to facilitate a biofouling investigation.
3. An extensive series of investigations on the impacts of biofouling on surface roughness, mean-velocity structure and sediment transport under wastewater conditions (Chapter 5 and Chapter 6). A comprehensive approach was used to improve and further the current scientific understanding of these topics. Most notably, the impact of different hydrodynamic conditions on biofilm frictional development was evaluated over time, using a series of enhanced techniques to a level of detail beyond that previously outlined. The culmination of these experiments was the formulation of a novel series of dynamic equivalent roughness parameters, which could form the basis for an improved design framework and result in more efficient pipeline operations.

The main experimental findings of the current study can be classified under two major topics: i) a non-fouled investigation and ii) a fouled wastewater investigation. The main findings of these investigations are outline herein.

8.2.1 Non-fouled investigation

The pilot-scale pipeline facility was evaluated under non-fouled conditions across the range of $3.15 \times 10^4 < Re_D < 1.12 \times 10^5$; for the purpose of validating the suitability of the facility for the intended study. In addition, contributions to knowledge on the topic of turbulent flow in

smooth pipes was also provided. The main observations and conclusions drawn from the evaluation of the non-fouled pipe are outlined herein:

1. The pilot-scale pipeline was shown to be capable of attaining consistent headloss and boundary layer measurements with low experimental uncertainties. The uncertainties in the measured frictional parameters for the non-fouled pipe, using a 95% confidence interval were ±5.15% for λ; ±0.005 mm (± 58%) for k_s; ±6.49% for u^*; ±13.44% for τ_w and ±4.53% for c_f. The uncertainties in the measured local boundary layer profiles were ±3.85% for $y^+ < 50$; ±1.21% for $50 < y^+ < 300$ and ±0.70% for $300 < y^+ < R^+$.
2. The 3.35 m (33 D) run-in length was sufficient to attain fully developed flow within the pipeline, as far as the pressure head distribution in the flow direction was concerned.
3. The respective values of k_s and n for the non-fouled HDPE pipe were 0.009 mm and 0.008. The maximum value of k_s^+ was found to be 0.51 and consequently, the pipe was hydraulically smooth (i.e. $k_s^+ < 5$).
4. The experimentally determined values of λ had a reasonably strong agreement with the smooth pipe relationships outlined within the literature. In particular, the maximum discrepancy between the measured and theoretical values of λ was ±3.97% and was within the experimental uncertainties.
5. Townsend's Wall Similarity Hypothesis was shown to be valid for the non-fouled pipe.
6. The Perry and Li's and Bradshaw's Methods were found to produce consistent localised frictional data with low experimental uncertainties for a non-fouled pipe. Furthermore the established frictional data conformed well with the system's pressure gradient, confirming the validity of the methods to a high degree of certainty (within the experimental error).
7. The linear regression method for determining κ and C was found to produce reliable and repeatable results.
8. The value of κ was shown to have a significant influence on the value of u^* derived from wall similarity techniques, namely the Perry and Li's Method.
9. The results were in support of the existence of a universal Log-Law for the range of $5.23 \times 10^4 < Re_D < 1.13 \times 10^5$. Furthermore, the location of the Log-Law region within the boundary layer was shown conclusively to be $50 < y^+ < 0.2R^+$. The value of the Log-Law constants of κ and C were found to be 0.42 ± 0.01 and 5.59 ± 0.53, respectively.

8.2.2 Fouled wastewater investigation

The frictional resistance imparted by developing and mature biofilms incubated with wastewater on a HDPE pipe was evaluated within a controlled laboratory environment, for

the first time. The molecular structure of the incubated biofilms was also comprehensively evaluated.

Biofilms were incubated with synthetic wastewater under three steady-state flow regimes, namely Re_D = 5.98x10^4 ($\overline{U}$ = 0.58 m/s), Re_D = 7.82x10^4 ($\overline{U}$ = 0.76 m/s) and Re_D = 1.00x10^5 ($\overline{U}$ = 0.96 m/s). The global values of τ_w induced by the respective conditions and therefore, imposed on the potential biofilms were 0.82, 1.37 and 1.95 N/m^2. These values were based on the non-fouled conditions. The synthetic wastewater was purposely designed to represent a medium strength wastewater found within European sewers in the summer. The key physico-chemical properties of the wastewater were COD = 543.4 ± 6.2 mg/l, TN = 50.3 ± 0.9 mg/l, TP = 10.4 ± 0.4 mg/l, pH = 7.95 ± 0.15, T = 21.5 ºC, ν = 9.73 x 10^{-7} m^2/s and ρ = 997.9 kg/m^3.

The biofilms incubated with wastewater, were a diverse system of microbial cells, embedded within an extracellular matrix of which carbohydrate dominated. These microbial systems were dominated by *Bacteria*, and in particular members of the plyla *Alphaproteobacteria*, *Betaproteobacteria*, *Actinobacteria*, *Bacteroidetes* and *Firmicutes*. However, it should be noted that only the kingdom of *Bacteria* was evaluated within the current study. On the macro-scale the pipeline showed various amounts of microbial material, with very different low-form gelatinous morphologies, depending on the conditioning. Filamentous type development was observed but very rarely, with filaments seldom exceeding 10 mm.

The statistically insignificant difference in the overall biofilm biomass recorded per unit area between the Re_D = 5.98x10^4 and Re_D = 1.00x10^5 assays, illustrated that the nutrient loading was reasonably equivalent within the respective assays, by virtue of conservation of mass. On this basis all observations and relationships documented on the biofilms incubated within the current study were primarily explained by the variations in mass transfer and shear characteristics imposed by the different flow regimes.

The main observations and conclusions drawn from the evaluation of the biofouled pipes can be divided into three section, namely i) impact of biofouling ii) nature of biofouling and iii) process of biofouling:

8.2.2.1 Impact of biofouling

1. The presence of a biofilm was found to increase the frictional resistance and the equivalent roughness of the HDPE pipe above the non-fouled value, in a relatively short period of time. In all cases, the observed increase were substantial. For instance, it was found that increase in S_f with fouling was 76% for the Re_D = 5.98x10^4 assay, 58% for

the $Re_D = 7.82x10^4$ assay and 51% for the $Re_D = 1.00x10^5$ assay. Similarly, it was found that λ with fouling was 85% for the $Re_D = 5.98x10^4$ assay, 68% for the $Re_D = 7.82x10^4$ assay and 48% for the $Re_D = 1.00x10^5$ assay. Using the modified Colebrook-White equation previously outlined within the literature and the appropriate values of κ it was shown that the biofilm caused an increase in k_s of up to 0.460 mm. Therefore, the observed increases in frictional resistance would have potentially resulted in a reduction in Q of up to 22%.

2. The presence of a biofilm can affected a HDPE pipe's ability to convey sediment by increasing the velocity and shear stress needed for self-cleansing. The minimum velocity required to transport at least 90% of a representative municipal sediment (i.e. d_{50} = 0.30 mm) within 1 h period was 0.55 m/s with fouling and 0.46 m/s without fouling. Similarly, the minimum shear stress required to transport 90% of sediment within 1 h was 1.30 N/m^2 with fouling and 0.59 N/m^2 without fouling.
3. The biofilm's impact on frictional resistance was further compounded by their influence over the Log-Law constants of κ and B. In particular, the current study has provided conclusive evidence that κ and B for biofouled surfaces are non-universal and dependent on Re_D. Furthermore, it was found that the established values of the respective constants for biofouled surfaces were typically lower than the conventionally accepted values of $\kappa \approx 0.42$ and $B \approx 8.48$. For instance, values of κ as low as 0.32 have been reported within the current study. For low-form gelatinous biofilms κ and B can be related to Re_D using: $\kappa = 9.444x10^{-7}Re_D + 0.302$ ($R^2 = 0.95$) and $B = -1.964x10^{-5}Re_D + 6.001$ ($R^2 = 0.98$). These expressions were shown to be valid for a range of $2.50x10^4 < Re_D < 1.22x10^5$ and were independently verified by the frictional data derived from the system's PG using the modified Colebrook-White equation.
4. As a consequence of the non-universality of κ, the traditional Colebrook-White equation is not applicable for biofouled pipes which is also in agreement with the scientific literature. In particular, it was found that the use of the traditional Colebrook-White equation to predict k_s overestimated the true value by between 49-58%, depending on the biofilms conditioning. This was shown to have considerable implications on Q prediction and thus, pipe sizing.
5. The non-universality of the Log-Law constants was shown to have implications on the local frictional data derived from conventional wall similarity techniques. It was implied that the frictional data was likely to be overestimated by such techniques, when applied in the traditional manner (i.e. using $\kappa \approx 0.42$). However, it was found conclusively that Townsend's Wall-Similarity Hypothesis was valid for biofouled

surfaces and wall similarity could be applied, providing one of the following is known: i) the local value of u^* or ii) the appropriate value of κ.

6. The Boundary layer parameters derived from values of u^* and ε established from the global frictional data showed that the boundary layer structure was statistically unaffected by the presence of the biofilm.

8.2.2.2 Nature of biofouling

7. The structural distribution of a biofilm was shown to play a key role in its overall frictional capacity and strength.
8. The magnitude of the biofilm's impact on frictional resistance and equivalent surface roughness was evidently a function of the shear conditions in which it was incubated. The k_s of a mature biofilm incubated in medium strength wastewater on a HDPE can be predicted based on its conditioning Re_D using $k_{s(E)} = 1.99Re_D^{-3.287}$ ($R^2 = 0.99$).
9. It was conclusively found that the lower the conditioning shear the higher the resultant frictional resistance imparted by a biofilm. This was attributed to two factors:
    a. An increase in maximum thickness potential fostered by the lower boundary shear (although, this could not be measured within the current study);
    b. An increase in heterogeneous coverage fostered by the limited mass transfer and drag.

    The coverage and roughness distribution of the biofilm incubated at low shear (i.e. in the $Re_D = 5.98x10^4$ assay) was comprehensively shown to be highly heterogeneous by a combination of visual observations, variations in frictional data and its molecular composition. The non-uniformity of the biofilm's coverage at low conditioning shear was confirmed by images captured during the respective flow assay, which illustrated isolated patches of microbial material of varying densities. This was quantitatively illustrated by variations in space-averaged equivalent roughness along the 5.0 m test pipe. The statistically significant variations in molecular structure, in terms of biomass (as indicated by DNA concentration) and extracellular material around the circumference of the pipe provided most conclusive evidence for a heterogeneous biofilm at low shear conditioning.
10. At the higher conditioning shear (i.e. in the $Re_D = 1.00x10^5$ assay) the resultant biofilm had a more densely packed and uniform roughness distribution, which was induced by the increased mass transfer, diffusion and drag. The imposed drag also limited the biofilm's maximum thickness potential. The overall lower frictional resistance evident at higher shear conditioning was attributed to the thin and homogeneous nature of the biofilm. The uniformity of the respective biofilm was illustrated by negligible

variations in space-averaged effective roughness and statistically insignificant changes in biomass and extracellular material around the circumference of the pipe.

11. Biofilms conditioned at low shear are less resilient to increases in boundary shear and drag than those conditioned at high shear. This was attributed to the inherent differences in structural distribution and extracellular composition induced by the respective shear conditioning. As a result of the biofilms weak nature, more material was mobilised from the surface following a smaller incremental increase boundary shear. Conversely, far less was material was removed by a similar increase in boundary stress when the biofilm was conditioned at a higher shear stress.
12. Extracellular carbohydrates were found to provide the majority of the biofilm's stability and strength. In particular, the higher the carbohydrate fraction the stronger and more cohesive the biofilm will be.

8.2.2.3 Process of biofouling

13. An initial increase in frictional resistance caused by biofilm development was observed after just 25 h of incubation with wastewater and a statistically steady state was achieved at 180 h. The time at which the biofilms reached a state of equilibrium was found to be independent of the conditioning shear.
14. The biofilms frictional development followed a consistent pattern and comprised of three stages, namely: i) the conditioning stage, ii) the transitional development stage and iii) the equilibrium stages.
15. A novel dynamic k_s parameter based on two sigmoidal expressions was derived to express the biofilms frictional evolution over time, using the modified Colebrook-White equation. The derived expressions had a strong correlation with the experimental data ($R^2 < 0.92$) and was valid for the range $5.98\text{x}10^4 < Re_D < 1.00\text{x}10^5$ and for use with medium strength wastewater (i.e. COD ≈ 550 mg/l, TN ≈ 50 mg/l, TP ≈ 10 mg/l).

8.3 Drinking water investigation

Biofouling within drinking water distribution systems was briefly discussed within the current study although, not explicitly with regards to its impact on hydraulic efficiency. In particular, the influence of commonly used plastic-based pipe materials on biofilm development in drinking water systems was investigated (in Chapter 7). This aspect of the study contributed to an improved understanding of surface roughness characteristics on biofilm development within drinking water systems.

Biofilms were incubated on four different commonly used plastic materials including: PVC, Polypropylene, Structural Wall HDPE and Solid Wall HDPE with drinking water under two different flow regimes (Re_D = 3.41x10^3 and Re_D = 5.35x10^3) for 100 d; for the purpose of establishing the impact of pipe material and flow hydrodynamics on biofilm development.

The main observations and conclusions drawn from the evaluation of the drinking water investigation are outlined herein:

1. Images captured by an Environmental Scanning Electron Microscope showed that the 100 d old biofilms incubated with drinking water were predominantly composed of sparse populations of rod-shaped bacteria embedded within extracellular polymer substances. The captured images also showed that the amount and form of the microbial biomass was dependant on the material and hydrodynamic conditions.
2. More microbial biomass was present on the materials conditioned at the low shear conditionings.
3. PVC and Structural Wall HDPE showed the greatest amounts of microbial biomass, which were also the materials with the highest initial substrate roughness.
4. The different materials and flow regimes affected the composition of the bacterial communities. *Alphaproteobacteria* (30%) and *Gammaproteobacteria* (26%) were found to be the predominant bacterial communities within biofilms conditioned at low shear. Whereas, the biofilms incubated at high shear were dominated by *Betaproteobacteria* (18%) and *Firmicutes* (18%).
5. The results have confirmed the potential for biofilms to act as a reservoir for pathogens and opportunistic pathogens, such as *Sphingomanas sp.* and *Pseudomonas sp*. If such pathogens and opportunistic pathogens became mobilised into the bulk water it could have significant health and safety implications, especially, in the old, young and infirm.
6. *Sphingomanas sp.* and *Pseudomonas sp.* were found to be more abundant within the biofilms incubated at low shear.

8.4 Industrial application of the wastewater study

The incubation conditions used within the current study were purposely designed to be representative of those found within natural HDPE sewer systems, albeit, for those operating at full bore. For instance, the physico-chemical properties of the synthetic wastewater used within this study were equivalent to the properties associated with medium strength wastewater found within European sewers in the summer (i.e. COD = 543.4 ± 6.2 mg/l, TN = 50.3 ± 0.9 mg/l, TP = 10.4 ± 0.4 mg/l, pH = 7.95 ± 0.15, T = 21.5 ºC). Furthermore, the

three conditioning flow regimes assessed are commonly found within DNs in the UK, particularly in rising mains, which generally operate at full bore and within the range of 0.6 m/s < $\bar{U}$ < 1.0 m/s. The incubation conditions were selected based upon literature observations and private conversations with leading members of the water industry, along with practicing engineers. The resultant biofilms incubated and evaluated within this study can therefore be considered equivalent to those found within real systems. This was illustrated on a molecular level by the microbial community composition of the biofilms, which were dominated by bacteria commonly found within real DNs, such as *Bacteroidetes*. Given that the biofilms conditioned in this study were accurate to those found within real systems, their documented interactions with turbulent pipe flow can also be considered realistic for actual wastewater biofilms. Under steady state conditions within DNs operating at full bore the combined Colebrook-White and Darcy-Weisbach equation for fouled pipes is given by;

$$\bar{U} = -\frac{\sqrt{2gDS_f}}{2.84\left(\frac{9.44\bar{U}D}{\nu \times 10^7} + 0.3\right)} \ln\left(\frac{k_{s(t)}}{0.85D} + \frac{2.51\nu}{D\sqrt{2gDS_f}}\right) \qquad \textit{Equation 8.1}$$

where $k_{s(t)}$ is given by the following novel roughness expressions;

for 0 h < t < 145 h

$$k_{s(t)} = \frac{k_{s(C2)}}{1 + e^{\left[\frac{4\mu_{G1}}{k_{s(C2)}}(t_{G1} - t) + 2\right]}}; \qquad \textit{Equation 8.2}$$

for t > 145 h

$$k_{s(t)} = k_{sC2} + \left(\frac{\Delta k_{s(E)}}{1 + e^{\left[\frac{4\mu_{G2}}{\Delta k_{s(E)}}(125 - t) + 2\right]}}\right) \qquad \textit{Equation 8.3}$$

However, wastewater systems with the exception of rising mains are rarely operated at full bore, and DNs as a whole are generally unsteady in nature. Consequently, although the study has provided much needed data on the topic of biofouling within DNs, further research is still required, in order for biofouling to be truly incorporated within pipeline design practices. This study has provided the platform and equipment needed for this to be achieved.

8.5 Reccommendations for further work

It is recommended that further investigations are undertaken to improve the understanding of the complex nature of a biofilm within water and wastewater pipelines. Such investigations should ideally expand on the fundamental ideas and concepts outlined within this study. In particular, it is recommended that biofilm development over time is evaluated for a greater range of conditions, including a broader range of flow regimes, nutrient levels, operating depths and temperatures. Similarly, given the highly variable nature of real systems it seems

prudent to incorporate and evaluate typical daily and seasonal variations in operational and environmental conditions within future studies. In order to validate and broaden the application of the dynamic k_s parameters outlined within the current study. This is essential for the development of more advanced real-time modelling frameworks, which are capable of dealing with the problem of biofouling within modern water management pipelines.

The frictional and structural data relating to the biofouled surfaces within the current study was derived from the assessment of up to 500 h old biofilms and although, this time frame was deemed sufficient for them to reach a state of equilibrium in terms of their frictional behaviour, it is known that the process of biofilm maturation can take several years, and that its mechanical stability and cohesive strength are proportional to its age (Martiny et al. 2003; Ahimou et al. 2007). It is therefore suggested, that long term evaluations are undertaken to determine whether the observations outlined within the current study for 500 h old biofilms are representative of much older biofilms and biofouled surfaces. This would improve the applicability of the findings. As long term incubations are potentially unfeasible for most research projects, particularly if multiple conditions require assessment in multiple incubations, then it is recommended that pipe cut-sections are taken from actual systems and then evaluated within the laboratory pipeline. In a similar manner to that outlined by Perkins et al. (2013; 2014). Provisions for which have already been made within the facility, which is capable of accommodating a foreign 2.0 m long pipe with a D of 0.1 m. This approach naturally has its limitations, particularly in terms of variable control. There is also the financial aspect in acquiring the cut-sections and the need for water authority support.

Notwithstanding, the observations outlined within this study have shown that the lower the shear conditioning, the higher the frictional resistance imparted by the biofilm and the lower the overall resilience of it to increased shear stress. The opposite can be said for biofilms incubated under high shear conditions. This ultimately results in a dilemma for asset holders, on whether to operate at low shear conditions accepting the losses in efficiency for the financial benefit of a less intense maintenance routine (in terms of ease of biofilm removal). In contrast, operating at a lower frictional resistance due to high shear conditions would result in a lower daily operational frictional resistance although, ultimately the requirements for biofilm removal would be adversely affected. It is therefore encouraged that a benefit-cost investigation be undertaken to determine the preferred solution, which ultimately maybe client dependent.

References

Abdel-Monim, Y. K., Ead, S. A. and Shabayek, S. A. (2005). Effect of time on pipe roughness. In Paper Presented to the 17th Canadian Hydrotechnical Conference Edmonton, Alberta, Canada.

Abernethy, R., Benedict, R. and Dowdell, R. (1985). ASME measurement uncertainty. Journal of Fluids engineering, 107(2), pp. 161-164.

Ackers, P., Crickmore, M. J. and Holmes, M. J. (1963). Effects of use on the hydraulic resistance of drainage conduits. ICE Proceedings, 28, pp. 339-360.

Adav, S. S. and Lee, D.-J. (2008). Extraction of extracellular polymeric substances from aerobic granule with compact interior structure. Journal of hazardous materials, 154(1), pp. 1120-1126.

Ahimou, F., Semmens, M. J., Haugstad, G. and Novak, P. J. (2007). Effect of protein, polysaccharide, and oxygen concentration profiles on biofilm cohesiveness. Applied and environmental microbiology, 73(9), pp. 2905-2910.

Allen, J., Shockling, M., Kunkel, G. and Smits, A. (2007). Turbulent flow in smooth and rough pipes. Philosophical Transactions of the Royal Society A: Mathematical, Physical and Engineering Sciences, 365(1852), pp. 699-714.

Allison, D. G., Ruiz, B., SanJose, C., Jaspe, A. and Gilbert, P. (1998). Extracellular products as mediators of the formation and detachment of Pseudomonas fluorescens biofilms. FEMS microbiology letters, 167(2), pp. 179-184.

Altman, S. J., McGrath, L. K., Souza, C. A., Murton, J. K. and Camper, A. K. (2009). Integration and decontamination of Bacillus cereus in Pseudomonas fluorescens biofilms. Journal of applied microbiology, 107(1), pp. 287-299.

Andersson, S., Dalhammar, G. and Kuttuva Rajarao, G. (2011). Influence of microbial interactions and EPS/polysaccharide composition on nutrient removal activity in biofilms

formed by strains found in wastewater treatment systems. Microbiological research, 166(6), pp. 449-457.

Andrewartha, J. M. (2010). The effect of freshwater biofilms on turbulent boundary layers and the implications for hydropower canals. PhD, University of Tasmania.

Andrewartha, J. M. and Sargison, J. (2011). Turbulence and mean-velocity structure of flows over filamentous biofilms. In Paper Presented to the 34th IAHR World Congress, Brisbane, Australia.

Andrewartha, J. M., Sargison, J. E. and Perkins, K. J. (2007). The Effect of Gomphonema and Filamentous Algae Streamers on Hydroelectric Canal Capacity and Turbulent Boundary Layer Structure. In Paper Presented to the 16th Australasian Fluid Mechanics Conference (AFMC).

Andrewartha, J. M., Sargison, J. E. and Perkins, K. J. (2008). The influence of freshwater biofilms on drag in hydroelectric power schemes. WSEAS Transactions on Fluid Mechanics, 3(3), pp. 201-206.

Andrewartha, J. M., Sargison, J. E. and Perkins, K. J. (2011). The Effect of Gomphonema and Filamentous Algae Streamers on Hydroelectric Canal Capacity and Turbulent Boundary Layer Structure. In: School of Engineering, The University of Queensland. pp. 241-246.

Antonia, R. and Krogstad, P.-Å. (2001). Turbulence structure in boundary layers over different types of surface roughness. Fluid Dynamics Research, 28(2), pp. 139-157.

Ashley, R. and Verbanck, M. (1996). Mechanics of sewer sediment erosion and transport. Journal of Hydraulic Research, 34(6), pp. 753-770.

Asséré, A., Oulahal, N. and Carpentier, B. (2008). Comparative evaluation of methods for counting surviving biofilm cells adhering to a polyvinyl chloride surface exposed to chlorine or drying. Journal of applied microbiology, 104(6), pp. 1692-1702.

Astaraie-Imani, M., Kapelan, Z., Fu, G., & Butler, D. (2012). Assessing the combined effects of urbanisation and climate change on the river water quality in an integrated urban wastewater system in the UK. Journal of environmental management, 112, pp. 1-9.

Bailey, S., Hultmark, M., Monty, J., Alfredsson, P. H., Chong, M., Duncan, R., Fransson, J., Hutchins, N., Marusic, I. and McKeon, B. (2013). Obtaining accurate mean-velocity

measurements in high Reynolds number turbulent boundary layers using Pitot tubes. Journal of Fluid Mechanics, 715, pp. 642-670.

Bakken, O. M., Krogstad, P.-Å., Ashrafian, A. and Andersson, H. I. (2005). Reynolds number effects in the outer layer of the turbulent flow in a channel with rough walls. Physics of Fluids (1994-present), 17(6), pp. 065101.

Barr, I. H. (1977). Accurate Explicit Equation For Friction Factor. Journal of Hydraulics Division, 103(3), pp. 334-339.

Barton, A. F. (2006). Friction, roughness and boundary layer characteristics of freshwater biofilms in hydraulic conduits, PhD, University of Tasmania.

Barton, A. F., Sargison, J. E., Brandner, P. and Walker, G. J. (2007). A Force balance to measure the total drag of biofilms on test plates In Paper Presented to the 16th Australasian Fluid Mechanics Conference (AFMC), Gold Coast, Queensland, Australia

Barton, A. F., Sargison, J. E., Osborn, J. E., Perkins, K. and Hallegraeff, G. (2010). Characterizing the roughness of freshwater biofilms using a photogrammetric methodology. Biofouling, 26(4), pp. 439-448.

Barton, A. F., Sargison, J. E., Walker, G. J., Osborn, J. E. and Brandner, P. A. (2005). A baseline study of the effect of freshwater biofilms in hydraulic conduits In Paper Presented to the XXXI IAHR Congress, Seoul, Korea.

Barton, A. F., Sylvester, M. W., Sargison, J. E., Walker, G. J. and Denne, A. B. (2004). Deterioration of conduit efficiency due to biofouling. in 8th National Conference on Hydraulics in Water Engineering,Queensland, Australia. pp. 13-16.

Barton, A. F., Wallis, M. R., Sargison, J. E., Buia, A. and Walker, G. J. (2008). Hydraulic roughness of biofouled pipes, biofilm character, and measured improvements from cleaning. Journal of Hydraulic Engineering, 134, pp. 852.

Batté, M., Appenzeller, B. M. R., Grandjean, D., Fass, S., Gauthier, V., Jorand, F., Mathieu, L., Boualam, M., Saby, S. and Block, J. C. (2003). Biofilms in drinking water distribution systems. Reviews in Environmental Science and Biotechnology, 2(2), pp. 147-168.

Bennett, D. and Glaser, R. (2011). Common Pitfalls in Hydraulic Design of Large Diameter Pipelines: Case Studies and Good Design Practice. in ASCE Pipelines Conference 2011,Seattle, Washington pp. 961-971.

Bertrand-Krajewski, J., Briat, P. and Scrivener, O. (1993). Sewer sediment production and transport modelling: A literature review. Journal of Hydraulic Research, 31(4), pp. 435-460.
Betancourt, F. (2001). Sediment transport in sanitary sewers. MSc, University of New Orleans, New Orleans, La.

Bitton, G. (2005). Wastewater microbiology, John Wiley & Sons.

Bland, C. E. G., Bayley, R. W. and Thomas, E. V. (1975). Some observations on the accumulation of slime in drainage pipes the effect of these accumulations on resistance to flow Public Health Engineering, 13.

Blasius, H. (1913). Das Ähnlichkeitsgesetz bei Reibungsvorgängen in Flüssigkeiten, Springer.

Boe-Hansen, R., Albrechtsen, H. J., Arvin, E. and Jørgensen, C. (2002). Bulk water phase and biofilm growth in drinking water at low nutrient conditions. Water Research, 36(18), pp. 4477-4486.

Bott, T. R. and Miller, P. C. (1983). Mechanisms of biofilm formation on aluminium tubes. Journal of Chemical Technology and Biotechnology. Biotechnology, 33(3), pp. 177-184.

Bott, T. R. and Pinheiro, M. M. V. P. S. (1977). Biological fouling — velocity and temperature effects. The Canadian Journal of Chemical Engineering, 55(4), pp. 473-474.

Bradford, M. M. (1976). A rapid and sensitive method for the quantitation of microgram quantities of protein utilizing the principle of protein-dye binding. Analytical biochemistry, 72(1), pp. 248-254.

Bradshaw, P. (1959). A simple method for determining turbulent skin friction from velocity profiles. 26(841).

Bridier, A., Briandet, R., Thomas, V. and Dubois-Brissonnet, F. (2011). Resistance of bacterial biofilms to disinfectants: a review. Biofouling, 27(9), pp. 1017-1032.

British Standards Institution (2008). BS EN 752:2008: Drain and sewer systems outside buildings. London: BSI.

Brkic, D. (2011). Review of explicit approximations to the Colebrook relation for flow friction. Journal of Petroleum Science and Engineering, 77(1), pp. 34-48.

Brown, M. J. and Lester, J. N. (1980). Comparison of bacterial extracellular polymer extraction methods. Applied and environmental microbiology, 40(2), pp. 179-185.

Bryers, J. and Characklis, W. (1981). Early fouling biofilm formation in a turbulent flow system: overall kinetics. Water Research, 15(4), pp. 483-491.

Burns, R. and Stach, J. (2002). Microbial ecology of soil biofilms: substrate bioavailability, bioremediation and complexity. Developments in Soil Science, 28, pp. 17-42.

Callow, M. E. (1993). A review of fouling in freshwaters. Biofouling, 7(4), pp. 313-327.

Callow, M. E. and Callow, J. A. (2000). Substratum location and zoospore behaviour in the fouling alga Enteromorpha. Biofouling, 15(1-3), pp. 49-56.

Candries, M. (2001). Drag, boundary-layer and roughness characteristics of marine surfaces coated with antifoulings. Unpublished, University of Newcastle upon Tyne Newcastle upon Tyne,, UK.

Celmer, D., Oleszkiewicz, J. and Cicek, N. (2008). Impact of shear force on the biofilm structure and performance of a membrane biofilm reactor for tertiary hydrogen-driven denitrification of municipal wastewater. Water Research, 42(12), pp. 3057-3065.

Chadwick, A., Morfett, J. and Borthwick, M. (2004). Hydraulics in civil and environmental engineering, 4th ed., Spon Press (Taylor and Francis Group).

Chamberlain, A. H. L. (1992). The role of adsorbed layers in bacterial adhesion. Biofilmsscience and technology. Dordrecht: Kluwer, pp. 59-67.

Characklis, W. G. (1981). Bioengineering report: Fouling biofilm development: A process analysis. Biotechnology and Bioengineering, 23(9), pp. 1923-1960.

Chen, N. H. (1979). An Explicit Equation for Friction Faiction Factor in Pipe. Industrial & Engineering Chemistry Fundamentals, 18(3), pp. 296-297.

Christensen, B. A., Locher, F. A. and Swamee, P. K. (2000). Limitations and Proper Use of the Hazen-Williams Equation. Journal of Hydraulic Engineering, 126(2), pp. 167-170.

Christensen, B. E. (1989). The role of extracellular polysaccharides in biofilms. Journal of biotechnology, 10(3), pp. 181-202.

Chue, S. (1975). Pressure probes for fluid measurement. Progress in aerospace sciences, 16(2), pp. 147-223.

Chughtai, F. and Zayed, T. (2008). Infrastructure condition prediction models for sustainable sewer pipelines. Journal of Performance of Constructed Facilities, 22(5), pp. 333-341.

Cipolla, S. S. and Maglionico, M. (2014). Heat recovery from urban wastewater: Analysis of the variability of flow rate and temperature. Energy and Buildings, 69, pp. 122-130.

Clauser, F. H. (1954). Turbulent boundary layers in adverse pressure gradients. Journal of the Aeronautical Sciences (Institute of the Aeronautical Sciences), 21, pp. 91-108.

Cloete, T. E., Westaard, D. and van Vuuren, S. J. (2003). Dynamic response of biofilm to pipe surface and fluid velocity. Water Sci Technol, 47(5), pp. 57-9.

Cochran, W. L., McFeters, G. A. and Stewart, P. S. (2000). Reduced susceptibility of thin Pseudomonas aeruginosa biofilms to hydrogen peroxide and monochloramine. Journal of applied microbiology, 88(1), pp. 22-30.

Colebrook, C. F. (1939). Turbulent Flow in Pipes, with particular reference to the Transition Region between the Smooth and Rough Pipe Laws. Journal of the ICE, 11(4), pp. 133-156.

Colebrook, C. F. and White, C. M. (1937). Experiments with fluid friction in roughened pipes. Proceedings of the Royal Society of London. Series A, Mathematical and Physical Sciences, 161(906), pp. 367-381.

Coles, D. (1956). The law of the wake in the turbulent boundary layer. Journal of Fluid Mechanics, 1(02), pp. 191-226.

Conrad, A., Kontro, M., Keinänen, M. M., Cadoret, A., Faure, P., Mansuy-Huault, L. and Block, J.-C. (2003). Fatty acids of lipid fractions in extracellular polymeric substances of activated sludge flocs. Lipids, 38(10), pp. 1093-1105.

Costerton, J. W., Cheng, K. J., Geesey, G. G., Ladd, T. I., Nickel, J. C., Dasgupta, M. and Marrie, T. J. (1987). Bacterial biofilms in nature and disease. Annual Reviews in Microbiology, 41(1), pp. 435-464.

Costerton, J. W. and Lewandowski, Z. (1995). Microbial biofilms. Annual Reviews Microbiol, 49, pp. 711-45.

Cowle, M.W, Babatunde, A.O, Rauen, W.B, Bockelmann-Evans, B.N and Barton, A.F (2014) Biofilm development in water distribution and drainage systems: dynamics and implications for hydraulic efficiency. Environmental Technology Reviews, 4(1), pp. 31-47.

Cowle, M. W., Vasilios, S. and Rauen, W. B. (2012). A comparative analysis of the carbon footprint of large diameter concrete and HDPE pipes. In Paper Presented to the XVI International Plastic Pipes Conference Barcelona, Spain, Hotel Arts.

Crabtree, R. (1989). Sediments in sewers. Water and Environment Journal, 3(6), pp. 569-578.

Creaco, E. and Bertrand-Krajewski, J.-L. (2009). Numerical simulation of flushing effect on sewer sediments and comparison of four sediment transport formulas. Journal of Hydraulic Research, 47(2), pp. 195-202.

Danish, M., Kumar, S. and Kumar, S. (2011). Approximate explicit analytical expressions of friction factor for flow of Bingham fluids in smooth pipes using Adomian decomposition method. Communications in Nonlinear Science and Numerical Simulation, 16(1), pp. 239-251.

Darcy, H. (1857). Recherches expérimentales relatives au mouvement de l'eau dans les tuyaux, Mallet-Bachelier.

De Beer, D., Stoodley, P., Roe, F. and Lewandowski, Z. (1994). Effects of biofilm structures on oxygen distribution and mass transport. Biotechnology and Bioengineering, 43(11), pp. 1131-1138.

Dean, R. and Bradshaw, P. (1976). Measurements of interacting turbulent shear layers in a duct. Journal of Fluid Mechanics, 78(part 4), pp. 641-676.

Donlan, R. M. and Costerton, J. W. (2002). Biofilms: survival mechanisms of clinically relevant microorganisms. Clinical microbiology reviews, 15(2), pp. 167-193.

Douterelo, I., Sharpe, R. L. and Boxall, J. B. (2013). Influence of hydraulic regimes on bacterial community structure and composition in an experimental drinking water distribution system. Water Research, 47(2), pp. 503-516.

Dumbleton, B. (1995). A question of scale and slime. Water and Waste Treatment, 38(4), pp. 39.

Durand, W. F. (1935). Aerodynamic theory, Springer.

Eisnor, J. and Gagnon, G. (2003). A framework for the implementation and design of pilot-scale distribution systems.

Fair, G. M. and Geyer, J. C. (1954). Water supply and waste water disposal. In Water supply and waste water disposal: John Wiley.

Fang, W., Hu, J. Y. and Ong, S. L. (2009). Influence of phosphorus on biofilm formation in model drinking water distribution systems. Journal of applied microbiology, 106(4), pp. 1328-1335.

Flack, K. A. and Schultz, M. P. (2010). Review of hydraulic roughness scales in the fully rough regime. Journal of Fluids engineering, 132(4), pp. 041203.

Flemming, H. C. and Wingender, J. (2010). The biofilm matrix. Nat Rev Micro, 8(9), pp. 623-633.

Flemming, H. C. (2002). Biofouling in water systems - cases, causes and countermeasures Applied Microbiology and Biotechnology, 59(6), pp. 629-640.

Gaylarde, C. C. and Morton, L. H. G. (1999). Deteriogenic biofilms on buildings and their control: A review. Biofouling, 14(1), pp. 59-74.

Geesey, G. G. and Costerton, J. W. (1979). Microbiology of a northern river: bacterial distribution and relationship to suspended sediment and organic carbon. Canadian journal of microbiology, 25(9), pp. 1058-1062.

George, W. K. (2007). Is there a universal log law for turbulent wall-bounded flows? Philosophical Transactions of the Royal Society A: Mathematical, Physical and Engineering Sciences, 365(1852), pp. 789-806.

Gjaltema, A., Arts, P. A. M., Van Loosdrecht, M. C. M., Kuenen, J. G. and Heijnen, J. J. (2004). Heterogeneity of biofilms in rotating annular reactors: occurrence, structure, and consequences. Biotechnology and Bioengineering, 44(2), pp. 194-204.

Goodwin, J. A. S. and Forster, C. F. (1985). A further examination into the composition of activated sludge surfaces in relation to their settlement characteristics. Water Research, 19(4), pp. 527-533.

Grann-Meyer, E. (2010). Discharge of fluid to water recipients environmental and engineering challenges (Engineering Handbook), Svolvaer, Norway.

Guisasola, A., de Haas, D., Keller, J. and Yuan, Z. (2008). Methane formation in sewer systems. Water Research, 42(6), pp. 1421-1430.

Guo, J. (1998). Turbulent Velocity Profiles in Clear Water and Sediment-Laden Flows. PhD, Colorado State University, Fort Collins, CO.

Guo, J. and Julien, P. Y. (2003). Modified log-wake law for turbulent flow in smooth pipes. Journal of Hydraulic Research, 41(5), pp. 493-501.

Guzman, K., La Motta, E. J., McCorquodale, J. A., Rojas, S. and Ermogenous, M. (2007). Effect of biofilm formation on roughness coefficient and solids deposition in small-diameter PVC sewer pipes. Journal of Environmental Engineering, 133(4), pp. 364-371.

Hallam, N. B., West, J. R., Forster, C. F. and Simms, J. (2001). The potential for biofilm growth in water distribution systems. Water Research, 35(17), pp. 4063-4071.

Hama, F. R. (1954). Boundary-layer characteristics for smooth and rough surfaces. Transactions - The Society of Naval Architects and Marine Engineers, 62, pp. 333-358.

Hoa, P. T., Nair, L. and Visvanathan, C. (2004). The effect of nutrients on extracellular polymeric substance production and its influence on sludge properties. Water SA, 29(4), pp. 437-442.

Hoes, O., Schilperoort, R., Luxemburg, W., Clemens, F. and van de Giesen, N. (2009). Locating illicit connections in storm water sewers using fiber-optic distributed temperature sensing. Water Research, 43(20), pp. 5187-5197.

Horan, N. J. and Eccles, C. R. (1986). Purification and characterization of extracellular polysaccharide from activated sludges. Water Research, 20(11), pp. 1427-1432.

Houghton, J. I. and Quarmby, J. (1999). Biopolymers in wastewater treatment. Current opinion in biotechnology, 10(3), pp. 259-262.

Hunt, S. M., Werner, E. M., Huang, B., Hamilton, M. A. and Stewart, P. S. (2004). Hypothesis for the role of nutrient starvation in biofilm detachment. Applied and environmental microbiology, 70(12), pp. 7418-7425.

Husband, P. S., Boxall, J. B. and Saul, A. J. (2008). Laboratory studies investigating the processes leading to discolouration in water distribution networks. Water Research, 42(16), pp. 4309-4318.

Incropera, F. P. (2011). Fundamentals of heat and mass transfer, John Wiley & Sons.

Jahn, A. and Nielsen, P. H. (1998). Cell biomass and exopolymer composition in sewer biofilms. Water science and technology, 37(1), pp. 17-24.

Jain, A. K. (1976). Accurate Explicit Equation For Friction Factor. Journal of Hydraulics Division, 102(5), pp. 674-677.

Jiao, Y., Cody, G. D., Harding, A. K., Wilmes, P., Schrenk, M., Wheeler, K. E., Banfield, J. F. and Thelen, M. P. (2010). Characterization of extracellular polymeric substances from acidophilic microbial biofilms. Applied and environmental microbiology, 76(9), pp. 2916-2922.

Jiménez, J. (2004). Turbulent flows over rough walls. Annu. Rev. Fluid Mech., 36, pp. 173-196.

Kalmokoff, M. L., Austin, J. W., Wan, X. D., Sanders, G., Banerjee, S. and Farber, J. M. (2001). Adsorption, attachment and biofilm formation among isolates of Listeria monocytogenes using model conditions. Journal of applied microbiology, 91(4), pp. 725-734.

Kerr, C. J., Osborn, K. S., Robson, G. D. and Handley, P. S. (1999). The relationship between pipe material and biofilm formation in a laboratory model system. The Society for Applied Microbiology, 85, pp. 29S-38S.

Kistler, A. L. and Tan, F. C. (1967). Some properties of turbulent separated flows. Physics of Fluids (1958-1988), 10(9), pp. S165-S173.

Kjelleberg, S. and Givskov, M. (2007). The biofilm mode of life: mechanisms and adaptations, Horizon Scientific Press.

Körstgens, V., Flemming, H.-C., Wingender, J. and Borchard, W. (2001). Uniaxial compression measurement device for investigation of the mechanical stability of biofilms. Journal of microbiological methods, 46(1), pp. 9-17.

Kreft, J. U. and Wimpenny, J. W. T. (2001). Effect of EPS on biofilm structure and function as revealed by an individual-based model of biofilm growth. Water science and technology, 43(6), pp. 135-142.

Kuliczkowski, A. and Lubczynska, U. (1999). Determination of Roughness Coefficient for Weholite Spiro Pipes with ID 1000mm Manufactured by KWH Pipe (Poland)., on the Basis of Hydraulic Measurements Talenn in the Pipeline. .

Kurth, J. C. (2008). Mitigating biofilm growth through the modification of concrete design and practice.

Lambert, M. F., Brookes, J. D., Kildea, M., Grantham, T. and McFarlane, B. (2008). Understanding the impact of biofilm growth on pipe roughness. In Paper Presented to the World Environmental and Water Resources Congress 2008, Honolulu, Hawaii.

Lambert, M. F., Edwards, R. W. J., Howie, S. J., De Gilio, B. B. and Quinn, S. P. (2009). The impact of biofilm development on pipe roughness and velocity profile. In Paper Presented to the World Environmental and Water Resources Congress 2009, Kansas City, Missouri.

Lauchlan, C., Forty, J. and May, R. (2005). Flow resistance of wastewater pumping mains. Water management, 158(2), pp. 81-88.

Laufer, J. (1954). The structure of turbulence in fully developed pipe flow, National committee for aeronautics.

Laurent, P. and Servais, P. (1995). Fixed bacterial biomass estimated by potential exoproteolytic activity. Canadian journal of microbiology, 41(8), pp. 749-752.

Lawrence, J. R., Swerhone, G. D. W. and Neu, T. R. (2000). A simple rotating annular reactor for replicated biofilm studies. Journal of microbiological methods, 42(3), pp. 215-224.

LeChevallier, M. W., Babcock, T. M. and Lee, R. G. (1987). Examination and characterization of distribution system biofilms. Applied and environmental microbiology, 53(12), pp. 2714-2724.

LeChevallier, M. W., Cawthon, C. D. and Lee, R. G. (1988). Factors promoting survival of bacteria in chlorinated water supplies. Applied and environmental microbiology, 54(3), pp. 649.

LeChevallier, M. W., Lowry, C. D. and Lee, R. G. (1990). Disinfecting biofilm in a model distribution system. Journal American Water Works Association, 82(7), pp. 87-99.

Lehtola, M. J., Miettinena, I. T., Minna, M., Keinänena, Kekkia, T. K., Laineb, O., Hirvonenc, A., Vartiainenb, T. and Martikainenc, P. J. (2004). Microbiology, chemistry and biofilm development in a pilot drinking water districtionsystem with copper and plastic pipes Water Research, 38(17), pp. 3769-3779.

Lewandowski, Z. and Stoodley, P. (1995). Flow induced vibrations, drag force, and pressure drop in conduits covered with biofilm. Water science and technology, 32(8), pp. 19-26.

Lewkowicz, A. and Das, D. (1986). Turbulent boundary layers on rough surfaces with and without a pliable overlayer: a simulation of marine fouling. International shipbuilding progress, 33(386), pp. 174-186.

Lewthwaite, J., Molland, A. and Thomas, K. (1985). An investigation into the variation of ship skin frictional resistance with fouling. Royal Institution of Naval Architects Transactions, 127.

Ligrani, P. M. and Moffat, R. J. (1986). Structure of transitionally rough and fully rough turbulent boundary layers. Journal of Fluid Mechanics, 162, pp. 69-98.

Liu, Y. and Tay, J. H. (2001). Metabolic response of biofilm to shear stress in fixed-film culture. Journal of applied microbiology, 90(3), pp. 337-342.

Manning, R. (1890). On the Flow of Water in Open Channels and Pipes. Instn of Civil Engineers of Ireland.

Manuel, C. M., Nunes, O. C. and Melo, L. F. (2007). Dynamics of drinking water biofilm in flow/non-flow conditions. Water Research, 41(3), pp. 551-562.

Manz, W., Wendt-Potthoff, K., Neu, T., Szewzyk, U. and Lawrence, J. (1999). Phylogenetic composition, spatial structure, and dynamics of lotic bacterial biofilms investigated by fluorescent in situ hybridization and confocal laser scanning microscopy. Microbial Ecology, 37(4), pp. 225-237.

Martiny, A. C., Jørgensen, T. M., Albrechtsen, H.-J., Arvin, E. and Molin, S. (2003). Long-term succession of structure and diversity of a biofilm formed in a model drinking water distribution system. Applied and environmental microbiology, 69(11), pp. 6899-6907.

Matthew, G. (1990). The Colebrook-White equation-an oft cited result but neglected derivation? In ICE Proceedings: Thomas Telford. pp. 39-45.

McCoy, W. F. and Olson, B. H. (1985). Fluorometric determination of the DNA concentration in municipal drinking water. Applied and environmental microbiology, 49(4), pp. 811-817.

McKeon, B., Swanson, C., Zagarola, M., Donnelly, R. and SMITS, A. J. (2004). Friction factors for smooth pipe flow. Journal of Fluid Mechanics, 511, pp. 41-44.

McKeon, B. J., Jiang, L. I. W., Morrison, J. F. and A.J., S. (2004). Further observations on the mean-velocity distribution in fully developed pipe flow Journal of Fluid Mechanics, 501, pp. 135-147.

McKeon, B. J., Li, J., Jiang, W., Morrison, J. F. and Smits, A. J. (2003). Pitot probe corrections in fully developed turbulent pipe flow. Measurement Science and Technology, 14(8), pp. 1449.

McKeon, B. J. and Smits, A. J. (2002). Static pressure correction in high Reynolds number fully developed turbulent pipe flow. Measurement Science and Technology, 13(10), pp. 1608.

McKeon, B. J. and Zagarola, M. V. (2005). A new firction factor relationship for fully developed pipe flow Journal of Fluid Mechanics, 538, pp. 429-443.

Melo, L. F. and Bott, T. R. (1997). Biofouling in water systems. Experimental Thermal and Fluid Science, 14(4), pp. 375-381.

Mikovits, C., Rauch, W., & Kleidorfer, M. (2014). Dynamics in urban development, population growth and their influences on urban water infrastructure. Procedia Engineering, 70, pp. 1147-1156.

Miller, R. W. (1989). Flow Measurement Engineering Handbook 2nd Edition ed.

Millikan, C. B. (1938). A critical discussion of turbulent flows in channels and circular tubes. in Proc. 5th Int. Congr. Appl. Mech.

Minkus, A. J. (1954). Deterioration of the hydraulic capacity of pipelines. New England Water Works Association, 68(1), pp. 1-10.

Miqueleto, A., Dolosic, C., Pozzi, E., Foresti, E. and Zaiat, M. (2010). Influence of carbon sources and C/N ratio on EPS production in anaerobic sequencing batch biofilm reactors for wastewater treatment. Bioresource technology, 101(4), pp. 1324-1330.

Molobela, I. P. and Ilunga, F. M. (2011). Impact of bacterial biofilms: the importance of quantitative biofilm studies. Annals of Microbiology, pp. 1-7.

Momba, M. N. B. and Makala, N. (2004). Comparing the effect of various pipe materials on biofilm formation in chlorinated and combined chlorine-chloraminated water systems. Water SA, 30(2), pp. 175-182.

Monty, J. P. (2005). Developments in smooth wall turbulent duct flows, University of Melbourne, Department of Mechanical and Manufacturing Engineering.

Moody, L. F. (1944). Friction factors for pipe flow. Trans ASME, 66(8), pp. 671-684.

Morrison, J., McKeon, B., Jiang, W. and Smits, A. (2004). Scaling of the streamwise velocity component in turbulent pipe flow. Journal of Fluid Mechanics, 508, pp. 99-131.

Musker, A. (1990). The hull roughness problem.

Muyzer, G., De Waal, E. C. and Uitterlinden, A. G. (1993). Profiling of complex microbial populations by denaturing gradient gel electrophoresis analysis of polymerase chain reaction-amplified genes coding for 16S rRNA. Applied and environmental microbiology, 59(3), pp. 695-700.

Nagib, H. M. and Chauhan, K. A. (2008). Variations of von Kármán coefficient in canonical flows. Physics of Fluids (1994-present), 20(10).

Nanda, S, Sahu S., and Abraham, J. (2010). Studies on the biodegradation of natural and synthetic polyethylene by Pseudomonas spp. Journal of Applied Sciences and Environmental Management, 14(2).

Nielsen, A. H., Vollertsen, J., Jensen, H. S., Wium-Andersen, T. and Hvitved-Jacobsen, T. (2008). Influence of pipe material and surfaces on sulfide related odor and corrosion in sewers. Water Research, 42(15), pp. 4206-4214.

Nielsen, A. H., Yongsiri, C., Hvitved-Jacobsen, T. and Vollemen, J. (2005). Simulation of sulfide buildup in wastewater and atmosphere of sewer networks. Water science and technology, pp. 201-208.

Nikora, V. (2002). Hydrodynamics of aquatic ecosystems: an interface between ecology, biomechanics and environmental fluid mechanics. River Research and Applications, 26(4), pp. 367-384.

Nikuradse, J. (1933). Laws of flow in rough pipes. Mechanical Engineering Papers, 1292(1), pp. 1-62.

Nowell, A. R. M. and Church, M. (1979). Turbulent flow in a depth-limited boundary layer. Journal of Geophysical research, 84(C8), pp. 4816-4824.

O'Sullivan, L. A., Webster, G., Fry, J. C., Parkes, R. J. and Weightman, A. J. (2008). Modified linker-PCR primers facilitate complete sequencing of DGGE DNA fragments. Journal of microbiological methods, 75(3), pp. 579-581.

Oberlack, M. (2001). A unified approach for symmetries in plane parallel turbulent shear flows. Journal of Fluid Mechanics, 427, pp. 299-328.

OECD (1984). Activated sludge, respiration inhibition test. Organistion for Economic Cooperation and Development (OCED) Guidelines. In Testing Chemicals pp. 1-10.

Ohashi, A. and Harada, H. (1994). Adhesion strength of biofilm developed in an attached-growth reactor. Water science and technology, 29(10), pp. 281-288.

Österlund, J. M., Johansson, A. V., Nagib, H. M. and Hites, M. H. (2000). A note on the overlap region in turbulent boundary layers. Physics of Fluids (1994-present), 12(1), pp. 1-4.
Patel, V. (1965). Calibration of the Preston tube and limitations on its use in pressure gradients. Journal of Fluid Mechanics, 23(01), pp. 185-208.

Pedersen, K. (1990). Biofilm development on stainless steel and PVC surfaces in drinking water. Water Research, 24(2), pp. 239-243.

Percival, S. L., Knapp, J. S., Wales, D. S. and Edyvean, R. G. J. (1999). The effect of turbulent flow and surface roughness on biofilm formation in drinking water. Journal of industrial microbiology & biotechnology, 22(3), pp. 152-159.

Pereira, M. O., Kuehn, M., Wuertz, S., Neu, T. and Melo, L. F. (2002). Effect of flow regime on the architecture of a Pseudomonas fluorescens biofilm. Biotechnology and Bioengineering, 78(2), pp. 164-171.

Pereira, M. O., Vieira, M. J. and Melo, L. F. (2000). A simple flow cell for monitoring biofilm formation in laboratory and industrial conditions. Braga, Portugal: Centro de Engenharia Biológica (IBQF) Universidade do Minho.

Perkins, S., Henderson, A., Walker, J., Sargison, J. and Li, X. (2014). The influence of bacteria-based biofouling on the wall friction and velocity distribution of hydropower pipes. Australian Journal of Mechanical Engineering, 12(1), pp. 77-88.

Perkins, S., Henderson, A. D., Walker, J. M. and Li, X. L. (2013). The influence of bacteria based biofouling on the wall friction and velocity distribution of hydropower pipes. In Paper Presented to the 18th Australasian Fluid Mechanics Conference Launceston, Tasmania.

Perry, A. and Abell, C. (1975). Scaling laws for pipe-flow turbulence. Journal of Fluid Mechanics, 67(02), pp. 257-271.

Perry, A. and Joubert, P. (1963). Rough-wall boundary layers in adverse pressure gradients. Journal of Fluid Mechanics, 17(02), pp. 193-211.

Perry, A. and Li, J. D. (1990). Experimental support for the attached-eddy hypothesis in zero-pressure-gradient turbulent boundary layers. Journal of Fluid Mechanics, 218, pp. 405-438.

Peyton, B. M. (1996). Effects of shear stress and substrate loading rate on< i> Pseudomonas aeruginosa</i> biofilm thickness and density. Water Research, 30(1), pp. 29-36.

Picologlou, B. F., Zelver, N. and Charcklis, W. G. (1980). Biofilm growth and hydraulic performance Journal of Hydraulics Division, 106(5), pp. 733-746

Pons, M., Spanjers, H., Baetens, D., Nowak, O., Gillot, S., Nouwen, J. and Schuttinga, N. (2004). Wastewater characteristics in Europe-A survey. European Water Management Online, 4.

Prakash, B., Veeregowda, B. M. and Krishnappa, G. (2003). Biofilms: A survival strategy of bacteria. Current science, 85(9), pp. 1299-1307.

Pratt, L. A. and Kolter, R. (1999). Genetic analyses of bacterial biofilm formation. Current opinion in microbiology, 2(6), pp. 598-603.

Preston, J. (1954). The determination of turbulent skin friction by means of Pitot tubes. Journal of the Royal Aeronautical Society, 58(518), pp. 109-121.

Qi, X., Gao, J., Sun, D., Liang, W., Wan, Y., Li, C., Xu, X. and Gao, T. (2008). Biofilm formation of the pathogens of fatal bacterial granuloma after trauma: potential mechanism underlying the failure of traditional antibiotic treatments. Scandinavian journal of infectious diseases, 40(3), pp. 221-228.

Rauen, W. B., Lin, B. and Falconer, R. A. (2008). Modelling dynamic bed roughness associated with bed form development. In Paper Presented to the 16th IAHR-APD Congress and 3rd IAHR-ISHS Symposium, Nanjing, China.

Rauen, W. B., Lin, B. and Falconer, R. A. (2009). Modelling ripple development under non-uniform flow and sediment supply-limited conditions in a laboratory flume. Estuarine, Coastal and Shelf Science, 82(3), pp. 452-460.

Reynolds, A. J. (1974). Turbulent flows in engineering, J. Wiley.

Romeo, E., Carlos, R. and Monzon, A. (2001). Improved Explicit Equations for Estimation of Friction Factor in Rough and Smooth Pipes. Chemical Engineering Journal, 86, pp. 369-374.

Rose, L., Jensen, B., Peterson, A., Banerjee, S. N. and Arduino, M. J. (2004). Swab materials and Bacillus anthracis spore recovery from nonporous surfaces. Emerg. Infect. Dis, 10(6), pp. 1023-1029.

Saleh, O. A. B. (2005). Fully developed turbulent smooth and rough channel and pipe flows. PhD, Lehrstuhl für Strömungsmechanik, Universität Erlangen–Nürnberg.

Samaras, V. (2011). The performance analysis of large, structured-wall HDPE pipes. MPhil., University of Swansea, Swansea.

Sand, W. and Bock, E. (1991). Biodeterioration of mineral materials by microorganisms—biogenic sulfuric and nitric acid corrosion of concrete and natural stone. Geomicrobiology Journal, 9(2-3), pp. 129-138.

Santo Domingo, J. W., Revetta, R. P., Iker, B., Gomez-Alvarez, V., Garcia, J., Sullivan, J. and Weast, J. (2011). Molecular survey of concrete sewer biofilm microbial communities. Biofouling, 27(9), pp. 993-1001.

Santos, R., Callow, M. E. and Bott, T. R. (1991). The structure of Pseudomonas fluorescens biofilms in contact with flowing systems. Biofouling, 4(4), pp. 319-336.

Schäfer, H. and Muyzer, G. (2001). Denaturing gradient gel electrophoresis in marine microbial ecology. Methods in microbiology, 30, pp. 425-468.

Schlichting, H. (1979). Boundary Layer Theory New York., New York.: McGraw-Hill.

Schultz, M. and Flack, K. (2005). Outer layer similarity in fully rough turbulent boundary layers. Experiments in fluids, 38(3), pp. 328-340.

Schultz, M. P. (2000). Turbulent boundary layers on surfaces covered with filamentous algae. Transactions of the ASME, Journal of Fluids Engineering, 122(2), pp. 357-363.

Schultz, M. P. and Swain, G. W. (1999). The effect of biofilms on turbulent boundary layers. Journal of Fluids engineering, 121, pp. 1-22.

Schwartz, T., Hoffmann, S. and Obst, U. (1998). Formation and bacterial composition of young, natural biofilms obtained from public bank-filtered drinking water systems. Water Research, 32(9), pp. 2787-2797.

Schwartz, T., Hoffmann, S. and Obst, U. (2003). Formation of natural biofilms during chlorine dioxide and u.v. disinfection in a public drinking water distribution system. Journal of applied microbiology, 95(3), pp. 591-601.

Seifert, L. and Kruger, W. (1950). Unusually high friction factor in a long, water supply line. VDI Z, 92, pp. 189-191.

Servais, P., Laurent, P. and Randon, G. (1995). Comparison of the bacterial dynamics in various French distribution systems. Aqua- Journal of Water Supply: Research and Technology, 44(1), pp. 10-17.

Sharp, B. B. (1954). Examination of the friction in the Morgan-Whyalla pipeline. Prepared for Engineering & Water Supply Department, Adelaide, Australia.

Sharp, W. W. and Walski, T. M. (1988). Predicting internal roughness in water mains. Journal (American Water Works Association), pp. 34-40.

Sharpe, R., Smith, C., Biggs, C. and Boxall, J. (2010). Pilot scale laboratory investigations into the impact of steady state conditioning flow on potable water discolouration. Water Distribution System Analysis, pp. 12-15.

Shaw, R. (1960). The influence of hole dimensions on static pressure measurements. Journal of Fluid Mechanics, 7(04), pp. 550-564.

Shirazi, R. H. S. M., Campisano, C., Modica, P., Willems, J. and Berlamont, J. (2013). Modelling the erosive effects of sewer flushing using different sediment transport formulas. In Paper Presented to the 7th International Conference on Sewer Processes and Networks, SPN7, Sheffield, UK.

Shockling, M. A., Allen, J. J. and Smits, A. J. (2006). Roughness effects in turbulent pipe flow. Journal of Fluid Mechanics, 564, pp. 267-285.

Simes, L. C., Azevedo, N., Pacheco, A., Keevil, C. W. and Vieira, M. J. (2006). Drinking water biofilm assessment of total and culturable bacteria under different operating conditions. Biofouling, 22(2), pp. 91-99.

Simões, L. C., Simões, M. and Vieira, M. J. (2010). Adhesion and biofilm formation on polystyrene by drinking water-isolated bacteria. Antonie van Leeuwenhoek, 98(3), pp. 317-329.

Simões, M., Pereira, M. O., Sillankorva, S., Azeredo, J. and Vieira, M. J. (2007). The effect of hydrodynamic conditions on the phenotype of Pseudomonas fluorescens biofilms. Biofouling, 23(4), pp. 249-258.

Skafel, M. G. (1999). Roughness Coefficients for Weholite Pipes (Tech. Paper, Asset Int. Database)

Smits, A., Monty, J., Hultmark, M., Bailey, S., Hutchins, N. and Marusic, I. (2011). Spatial resolution correction for wall-bounded turbulence measurements. Journal of Fluid Mechanics, 676, pp. 41-53.

Sonnad, J. R. and Goudar, C. T. (2006). Turbulent Flow Friction Factor Calculation Using a Mathematically Exact Alternative to the Colebrook-White Equation Journal of Hydraulic Engineering, 132(8), pp. 863-867.

Soulsby, R. (1997). Dynamics of marine sands: a manual for practical applications, Thomas Telford.

Spalding, D. (1961). A single formula for the "law of the wall". Journal of Applied Mechanics, 28(3), pp. 455-458.

Srinivasan, R., Stewart, P. S., Griebe, T., Chen, C. I. and Xu, X. (1995). Biofilm parameters influencing biocide efficacy. Biotechnology and Bioengineering, 46(6), pp. 553-560.

Stewart, P. S. (2012). Mini-review: convection around biofilms. Biofouling, 28(2), pp. 187-198.

Stoodley, P., Cargo, R., Rupp, C. J., Wilson, S. and Klapper, I. (2002). Biofilm material properties as related to shear-induced deformation and detachment phenomena. Journal of Industrial Microbiology and Biotechnology, 29(6), pp. 361-367.

Stoodley, P., Dodds, I., Boyle, J. D. and Lappin-Scott, H. M. (1998a). Influence of hydrodynamics and nutrients on biofilm structure. Journal of applied microbiology, 85(S1), pp. 19S-28S.

Stoodley, P., Lewandowski, Z., Boyle, J. D. and Lappin-Scott, H. M. (1998b). Oscillation characteristics of biofilm streamers in turbulent flowing water as related to drag and pressure drop. Biotechnology and Bioengineering, 57(5), pp. 536-544.

Stoodley, P. and Warwood, B. (2003). Use of flow cells and annular reactors to study biofilms.

Sutherland, I. W. (2001). Biofilm exopolysaccharides: a strong and sticky framework. Microbiology, 147(1), pp. 3-9.

Tay, J. H., Liu, Q. S. and Liu, Y. (2001). The role of cellular polysaccharides in the formation and stability of aerobic granules. Letters in Applied Microbiology, 33(3), pp. 222-226.

Teng, F., Guan, Y. T. and Zhu, W. P. (2008). Effect of biofilm on cast iron pipe corrosion in drinking water distribution system: Corrosion scales characterization and microbial community structure investigation. Corrosion science, 50(10), pp. 2816-2823.

Teodósio, J., Simões, M., Melo, L. and Mergulhão, F. (2011). Flow cell hydrodynamics and their effects on E. coli biofilm formation under different nutrient conditions and turbulent flow. Biofouling, 27(1), pp. 1-11.

Teodósio, J. S., Simões, M., Melo, L. F. and Mergulhão, F. J. (2010). Flow cell hydrodynamics and their effects on E. coli biofilm formation under different nutrient conditions and turbulent flow. Biofouling, 27(1), pp. 1-11.

Townsend, A. A. (1976). The structure of turbulent shear flow, Cambridge university press.

Tsuneda, S., Aikawa, H., Hayashi, H., Yuasa, A. and Hirata, A. (2003). Extracellular polymeric substances responsible for bacterial adhesion onto solid surface. FEMS microbiology letters, 223(2), pp. 287-292.

Tsvetanova, Z. (2006). Study of biofilm formation on different pipe materials in a model of drinking water distribution system and its impact on microbiological water quality. Chemicals as Intentional and Accidental Global Environmental Threats, pp. 463-468.

Van Der Kooij, D., Vrouwenvelder, H. S. and Veenendaal, H. R. (1995). Density and composition of biofilms in drinking water distribution systems in the Netherlands. In Paper Presented to the AWWA Water Quality Technology Conference New Orleans, LA.

Verran, J., Lees, G. and Shakespeare, A. P. (1991). The effect of surface roughness on the adhesion of Candida albicans to acrylic. Biofouling, 3(3), pp. 183-191.

Vieira, M. J., Melo, L. F. and Pinheiro, M. M. (1993). Biofilm formation: hydrodynamic effects on internal diffusion and structure. Biofouling, 7(1), pp. 67-80.

Vigeant, M. A. S., Ford, R. M., Wagner, M. and Tamm, L. K. (2002). Reversible and irreversible adhesion of motile Escherichia coli cells analyzed by total internal reflection aqueous fluorescence microscopy. Applied and environmental microbiology, 68(6), pp. 2794-2801.

Vignaga, E. (2012). The effect of biofilm colonization on the stability of non-cohesive sediments. PhD, University of Glasgow.

Volk, C. J. and LeChevallier, M. W. (1999). Impacts of the reduction of nutrient levels on bacterial water quality in distribution systems. Applied and environmental microbiology, 65(11), pp. 4957-4966.

Vrouwenvelder, J., Buiter, J., Riviere, M., Van der Meer, W., Van Loosdrecht, M. and Kruithof, J. (2010). Impact of flow regime on pressure drop increase and biomass accumulation and morphology in membrane systems. Water Research, 44(3), pp. 689-702.

Vu, B., Chen, M., Crawford, R. J. and Ivanova, E. P. (2009). Bacterial extracellular polysaccharides involved in biofilm formation. Molecules, 14(7), pp. 2535-2554.

Walker, J., Sargison, J. and Henderson, A. (2013). Turbulent boundary-layer structure of flows over freshwater biofilms. Experiments in fluids, 54(12), pp. 1-17.

Walker, J. M. (2014). The Application of Wall Similarity Techniques to Determine Wall Shear Velocity in Smooth and Rough Wall Turbulent Boundary Layers. Journal of Fluids engineering, 136(5), pp. 051204.

Wallingford, H. R. and Barr, D. I. H. (1994). Tables for the hydraulic design of pipes, sewers and channels, Thomas Telford.

Wang, H., Hu, C., Hu, X., Yang, M. and Qu, J. (2012). Effects of disinfectant and biofilm on the corrosion of cast iron pipes in a reclaimed water distribution system. Water Research, 46(4), pp. 1070-1078.

Water Research Centre (Great Britain) (2006). Sewers for adoption, 6th ed., Swindon: WRc plc.

Webster, G., Embley, T. M. and Prosser, J. I. (2002). Grassland management regimens reduce small-scale heterogeneity and species diversity of β-proteobacterial ammonia oxidizer populations. Applied and environmental microbiology, 68(1), pp. 20-30.

Webster, G., John Parkes, R., Cragg, B. A., Newberry, C. J., Weightman, A. J. and Fry, J. C. (2006). Prokaryotic community composition and biogeochemical processes in deep subseafloor sediments from the Peru Margin. FEMS microbiology ecology, 58(1), pp. 65-85.

Webster, G., Newberry, C. J., Fry, J. C. and Weightman, A. J. (2003). Assessment of bacterial community structure in the deep sub-seafloor biosphere by 16S rDNA-based techniques: a cautionary tale. Journal of microbiological methods, 55(1), pp. 155-164.

Wei, T., Schmidt, R. and McMurtry, P. (2005). Comment on the Clauser chart method for determining the friction velocity. Experiments in fluids, 38(5), pp. 695-699.

Wingender, J., Strathmann, M., Rode, A., Leis, A. and Flemming, H.-C. (2001). Isolation and biochemical characterization of extracellular polymeric substances from< i> Pseudomonas aeruginosa</i>. Methods in enzymology, 336, pp. 302-314.

Winter, K. (1979). An outline of the techniques available for the measurement of skin friction in turbulent boundary layers. Progress in aerospace sciences, 18, pp. 1-57.

Wloka, M., Rehage, H., Flemming, H. C. and Wingender, J. (2004). Rheological properties of viscoelastic biofilm extracellular polymeric substances and comparison to the behavior of calcium alginate gels. Colloid and Polymer Science, 282(10), pp. 1067-1076.

Wosnik, M., Castillo, L. and George, W. K. (2001). A theory for turbulent pipe and channel flows. Journal of Fluid Mechanics, 421, pp. 115-145. pp. 103-217

Wu, Y. and Christensen, K. (2007). Outer-layer similarity in the presence of a practical rough-wall topography. Physics of Fluids (1994-present), 19(8)

Xu, J., Mahowald, M. A., Ley, R. E., Lozupone, C. A., Hamady, M., Martens, E. C., Henrissat, B., Coutinho, P. M., Minx, P. and Latreille, P. (2007). Evolution of symbiotic bacteria in the distal human intestine. PLoS biology, 5(7), pp. e156.

Yu, J., Kim, D. and Lee, T. (2010). Microbial diversity in biofilms on water distribution pipes of different materials. Water science and technology, 11(1), pp. 163.

Zagarola, M. V. (1996). Mean-flow scaling of turbulent pipe flow. PhD, Princeton University, Princeton, NJ.

Zagarola, M. V. and Smits, A. J. (1998). Mean-flow scaling of turbulent pipe flow. Journal of Fluid Mechanics, 373, pp. 33-79.

Zanoun, E.-S., Durst, F., Bayoumy, O. and Al-Salaymeh, A. (2007). Wall skin friction and mean-velocity profiles of fully developed turbulent pipe flows. Experimental Thermal and Fluid Science, 32(1), pp. 249-261.

Zanoun, E.-S., Durst, F. and Nagib, H. (2003). Evaluating the law of the wall in two-dimensional fully developed turbulent channel flows. Physics of Fluids (1994-present), 15(10), pp. 3079-3089.

Zhang, T. C. and Bishop, P. L. (1994). Density, porosity, and pore structure of biofilms. Water Research, 28(11), pp. 2267-2277.

Zhang, X., Bishop, P. L. and Kinkle, B. K. (1999). Comparison of extraction methods for quantifying extracellular polymers in biofilms. Water science and technology, 39(7), pp. 211-218.

Zhou, L., Zhang, Y. and Li, G. (2009). Effect of pipe material and low level disinfectants on biofilm development in a simulated drinking water distribution system. Journal of Zhejiang University-Science A, 10(5), pp. 725-731.

Zigrang, D. J. and Sylvester, N. D. (1982). Explicit Approximations to the Solution of Colebrook's Friction Factor. AIChE Journal, 28(3), pp. 514-515.

Zwietering, M., Jongenburger, I., Rombouts, F. and Van't Riet, K. (1990). Modeling of the bacterial growth curve. Applied and environmental microbiology, 56(6), pp. 1875-1881.

Appendices

A. Supporting data for Chapter 3

A.1 Pump performance

An estimated pump performance plot is represented in Figure A.1. The system curves shown in Figure A.1 represent estimates of the total head, H_L including major (i.e. pipe's frictional resistance) and minor (i.e. bends, valves and contractions) losses, required under non-fouled and fouled conditions, as given by:

$$H_L = H_f + H_m \qquad \textit{Equation A.1}$$

$$H_m = \xi \frac{\bar{U}^2}{2g} \qquad \textit{Equation A.2}$$

where ξ is the minor loss coefficient, which is dependent on the type of component or fitting. For instance, for 90º bend ξ = 0.4 (Chadwick et al. 2004).

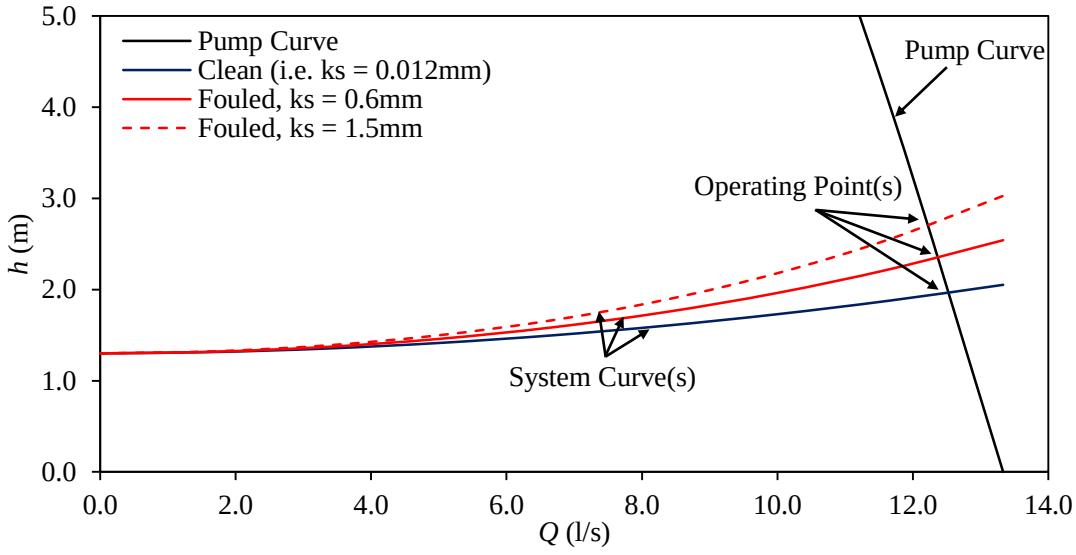

Figure A.1 Estimated pump performance curves for the pilot-scale pipeline with and without fouling

A.2 Physical surface roughness

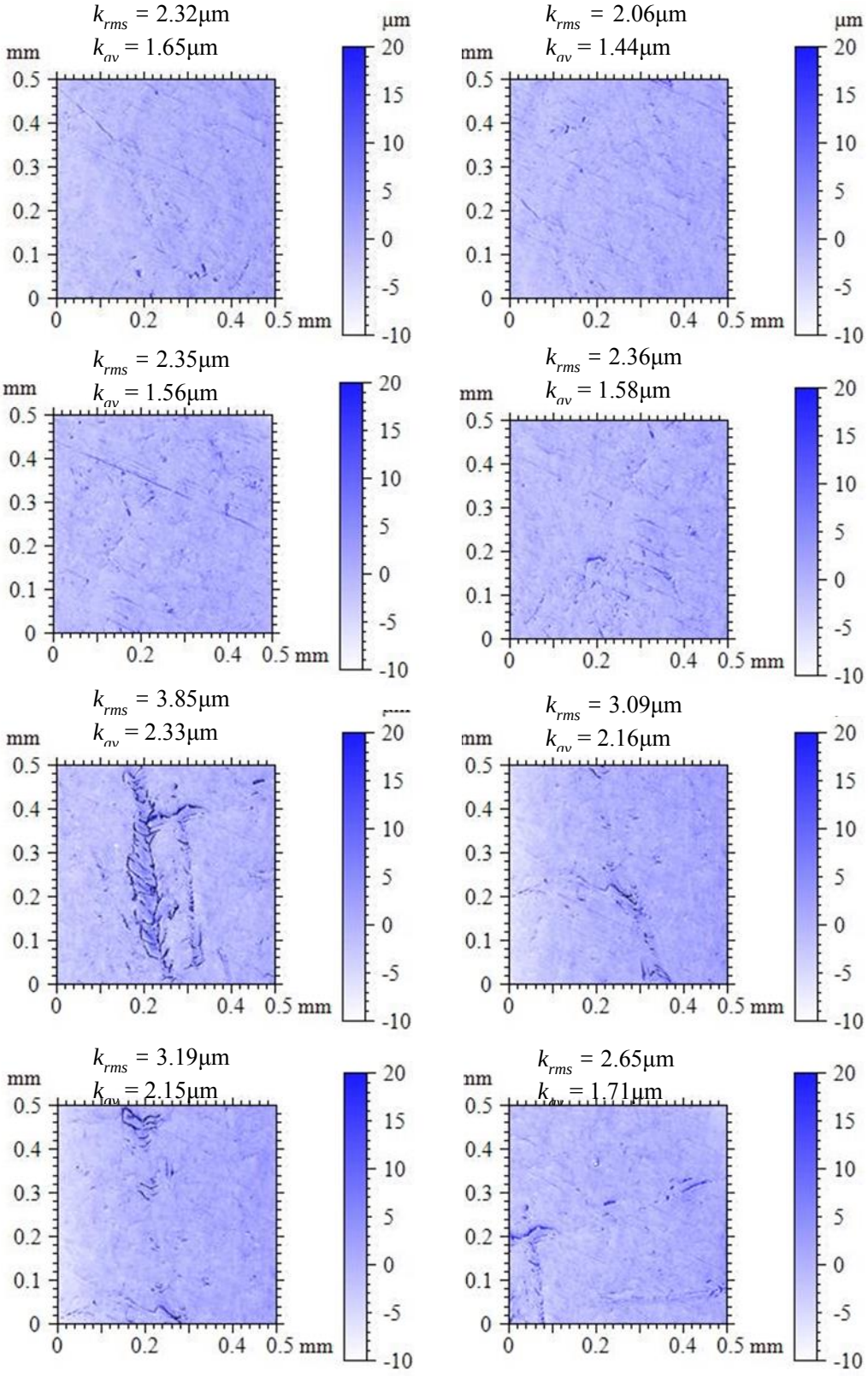

Figure A.2 2-D micro-topography maps of the solid walled HDPE test pipe of the pilot-scale pipeline (Sample Size: 0.5x0.5mm^2, Magnification: x200).

A.3 Roughness similarities

The relative roughness (i.e. k_s/D) determined for the 100 mm internal diameter S-HDPE pipe was compared experimentally to the relative roughness of a 400 mm internal diameter Str-HDPE (referred to as the "400 mm Str-HDPE pipe" herein). Both of these pipes are fabricated from the same resin (i.e. *Carbon Black*), although the fabrication process differs between the respective pipes. For instance, whereas solid wall pipes are generally extruded in large sections over a heated barrel, structured wall pipes are fabricated via the extrusion of a comparatively small hollow box section, continuously wound around a mandrel. The result is two pipes with very different surface finishes, as shown by Figure A.3. The fabrication process for a Str-HDPE results in a pronounced and regularly spaced roughness element along the pipe's length. The roughness element is formed by the welds between the respective box-sections. Aside from the welds the surface finish of a Str-HDPE pipe is extremely smooth. The surface finish of a S-HDPE is also extremely smooth and unlike the Str-HDPE pipe it has no pronounced roughness elements.

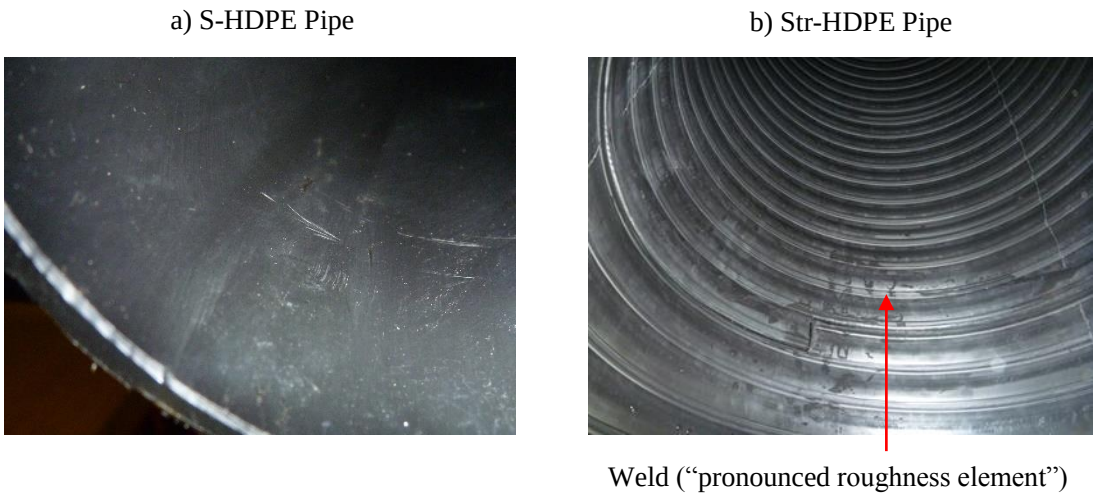

Figure A.3 Surface finishes for a) Solid Wall High Density Polyethylene (S-HDPE) pipe and b) Structural Wall High Density Polyethylene (Str-HDPE) pipe.

A.3.1 Experimental study

The 400 mm Str-HDPE pipe investigation was conducted prior to the development and testing of the pilot-scale pipeline and was undertaken in the summer of 2011. Consequently, the fundamental design principals developed for the 400 mm pipe study were the basis of the 100 mm diameter pilot-scale pipeline facility.

The experimental study was conducted within a 16.8m temporary pipe housed within a high capacity flume located in the Hydraulics laboratory at Cardiff University, School of Engineering, as shown by Figure A.4. The subject of the study was a 400 mm Str-HDPE pipe – commercially known as a *Weholite* large diameter pipe (*Asset* International Ltd.). Four discrete pipe segments, which measured at 1.0, 6.0, 6.0, 6.0 and 3.8 m, respectively were connected by flexible pipe couplings (*Axiflex Teekay*), as shown by Figure A.5. The segments were connected in such a manner to ensure for a smooth transition.

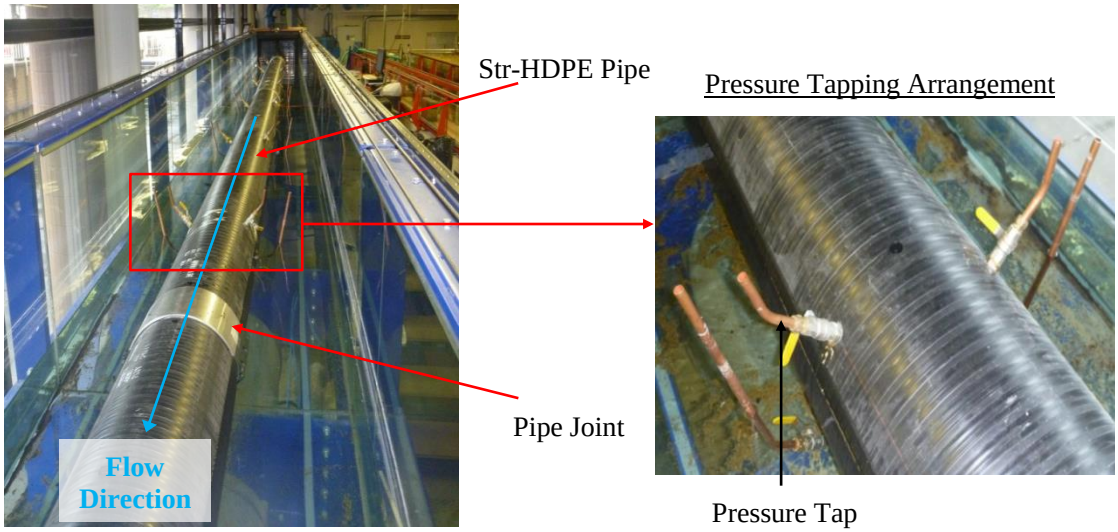

Figure A.4 Experimental arrangement for the 400mm internal diameter Str-HDPE pipeline housed within a high capacity flume (highlighting the pressure tapping arrangement).

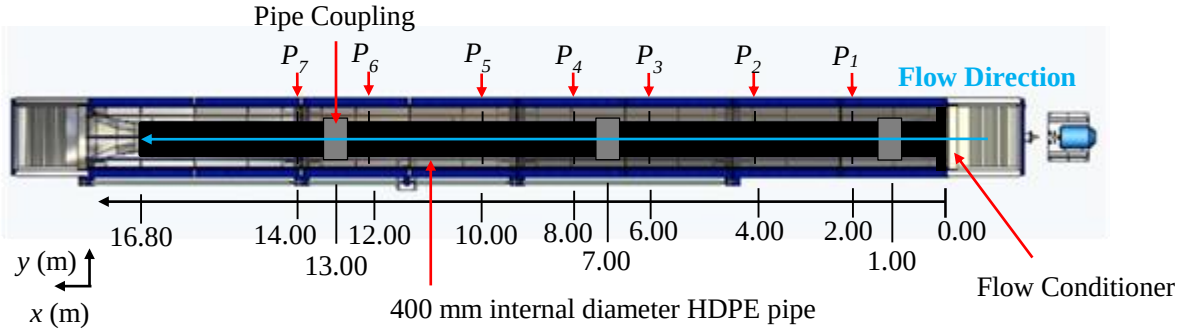

Figure A.5 Schematic of the 400mm internal diameter Str-HDPE pipeline within the high capacity flume, highlighting pressure tapping location(s) (the flow direction is from right to left).

The high capacity flume was a bidirectional, hydraulically tilting and recirculating laboratory flume, capable of generating flows of up to 1 m^3/s. The working section of the flume in spanwise and streamwise directions was 1.2 m and 17.0 m, respectively. The flume had a physical depth of 1.0 m and maximum allowable water depth of 0.8 m. Located directly below the working section was a recirculation pipe, connected to the working section by a series of diffusers and cascade bends. The flume's gradient, which was equal to the pipes (as the pipe was laid parallel to the flume's bed) was controlled by a hydraulic jack. The maximum working gradient was 1:100. A honey comb styled flow conditioner positioned at the pipe inlet was used to encourage flow homogeneity within the pipeline (Miller 1989).

The flow rate within the pipeline was controlled by: i) a hydraulic head (generated by an upstream reservoir); ii) the pipe's gradient and iii) the pump power. A clamp-on transit-time ultrasonic flowmeter (*ABLE*), attached to the recirculation pipe was used to record flow rate within the pipeline. The accuracy of the flowmeter was determined experimentally to be ±5%.

The system's pressure gradient was determined using seven sets of static pressure tappings, positioned at 2.0 m intervals from the pipe inlet. The seven sets of pressure tappings were designated P_1 to P_7, and each consisted of four discrete pressure taps, located at 45º, 135º, 225º and 315º from the pipe's vertical centreline, as shown by Figure A.4. A high accuracy pressure transducer (*Omega* PX409-2-2.5GUSB) was used to record all pressure measurements. The full scale accuracy (including effects of linearity, hysteresis and repeatability) of the transducer was ±0.08%.

A.3.2 Results

The 400 mm Str-HPDE pipe was evaluated across the range of $2.94x10^5 < Re_D < 7.04x10^5$ (or 0.74 m/s < $\overline{U}$< 1.77 m/s). For pipe survey a circumferential average static pressure was determined and recorded at each streamwise measurement location. The frictional data was established using for the systems's PG using the SFM (as outlined in Section 4.3). The measurement locations of P_1 and P_2 were excluded from the regression lines, as the flow had not reached a fully developed state at these locations, as shown for example by Figure A.6, which illustrates a typical static pressure profile (i.e. for $Re_D = 3.50x10^5$). The constant linear PG within the region of 6.0 m < L < 14.0 m presented in Figure A.6, illustrates the fully developed nature of the flow; at least as far as the pressure distribution was concerned.

The frictional data recorded for the 400 mm Str-HDPE pipe are presented within Table A.1.

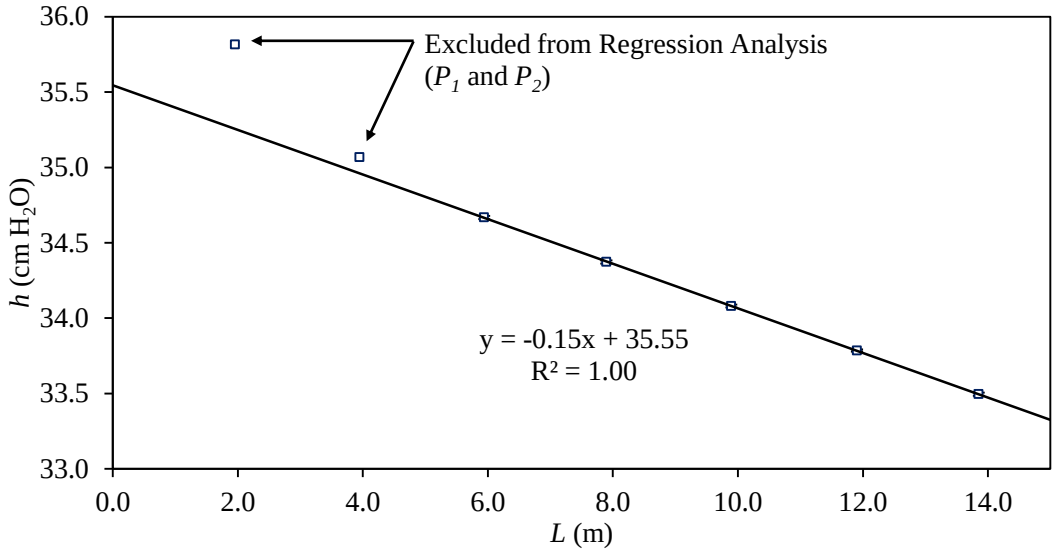

Figure A.6 A typical static pressure profile for the 400 mm internal diameter Str-HDPE pipe (for $Re_D = 3.50x10^5$).

Table A.1 Non-fouled pipe parameters for the 400 mm internal diameter pipe determined using the Slope Fit Method.

Re_D	S_f	λ	u^* (m/s)	τ_w (N/m^2)	k_s (mm)	k_s/D	n	k_s^+
2.94 x 10^5	0.001	0.015	0.032	1.04	0.033	8.23 x 10^{-5}	0.010	1.06
3.50 x 10^5	0.001	0.015	0.038	1.44	0.032	8.00 x 10^{-5}	0.009	1.21
4.09 x 10^5	0.002	0.015	0.044	1.92	0.032	7.90 x 10^{-5}	0.009	1.38
4.74 x 10^5	0.003	0.014	0.050	2.52	0.031	7.75 x 10^{-5}	0.009	1.55
5.65 x 10^5	0.004	0.014	0.060	3.55	0.036	8.90 x 10^{-5}	0.009	2.11
7.04 x 10^5	0.005	0.014	0.073	5.32	0.033	8.21 x 10^{-5}	0.009	2.39
				Average:	**0.033**	8.17 x 10^{-5}	0.009	
				σ	**0.002**	4.03 x 10^{-6}	-	

The k_s and n values for the 400 mm Str-HDPE pipe were found to be 0.033 mm ± 4.93% and 0.009 ± 2.06%, respectively. The relative roughness was found to be 8.17x10^{-5} ± 4.93%. The pipe can be considered hydraulically smooth within the range of $2.94x10^5 < Re_D < 7.04x10^5$ as the established k_s^+ values were less than 5 viscous lengths, as shown by Table A.1.

The average Manning's coefficient determined within the current study for the 400 mm Str-HDPE pipe (i.e. n = 0.009, see Table A.1) was consistent with typical values documented

within the literature for Str-HDPE pipes (Kuliczhowki 1999; Skafel 1999; Grann-Meyer 2010). For instance, Kuliczhowhi (1999) and Skafel (1999) determined that Manning's coefficient for a Str-HDPE pipe was equal to 0.009. The maximum discrepancy between the measured and expected value (i.e. $n = 0.009$) of n was found to be ±5.8%. Kuliczhowhi (1999) and Skafel (1999) determined that the k_s value for a Str-HDPE pipe was 0.030 mm. The average k_s value of 0.033 mm determined within the current study for the 400 mm Str-HDPE pipe was therefore, equivalent to the expected value. The maximum discrepancy between the measured and expected (i.e. $k_s = 0.030$ mm) value of k_s was found to be ±18.65%. Furthermore, the k_s/D determined for the 400 mm Str-HDPE pipe (i.e. $k_s/D = 8.17\text{x}10^5$, see Table A.1) was equivalent to the k_s/D established for the 100 mm diameter pilot-scale pipe, which was found to be $k_s/D = 8.86\text{x}10^5$. This is illustrated by Figure A.7, which shows that the frictional data for the two HDPE pipes followed the same C-W curve (for i.e. $k_s/D = 8.86\text{x}10^5$). Consequently, despite the obvious differences in physical roughness, the two HDPE pipes are similar in a hydraulic sense (i.e. equivalent roughness).

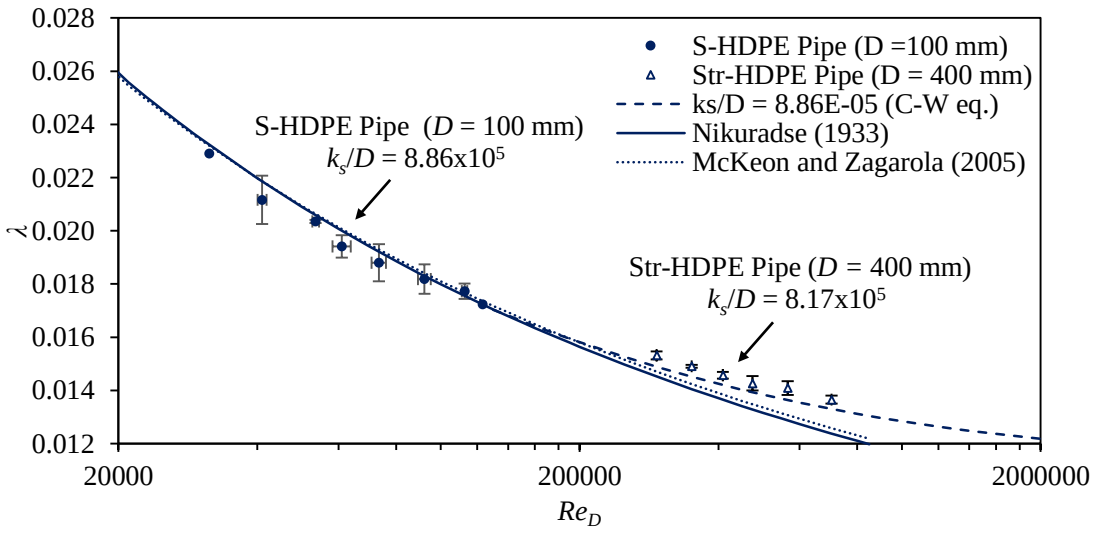

Figure A.7 Moody Diagram illsurating the determined friction factors for the 100 and 400 mm internal diameter HDPE pipes.

A.4 Facility calibration data

Figure A.8 shows a typical set of calibration curves for the three pressure transducers used within this study.

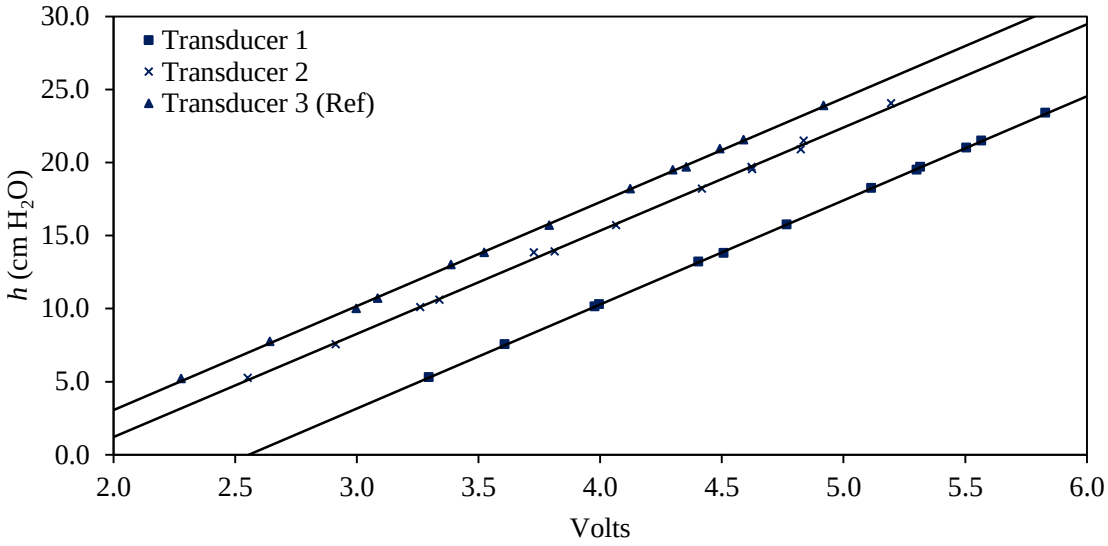

Figure A.8 Typical calibration curves for the three pressure transducer using within the pilot-scale pipeline.

Typical calibration curves for the T_{Pipe} and T_{Tank} temperature probes are presented in Figure A.9. The established calibrations conformed well to that provided within the manufactures specification (i.e. T = 55.56Volts).

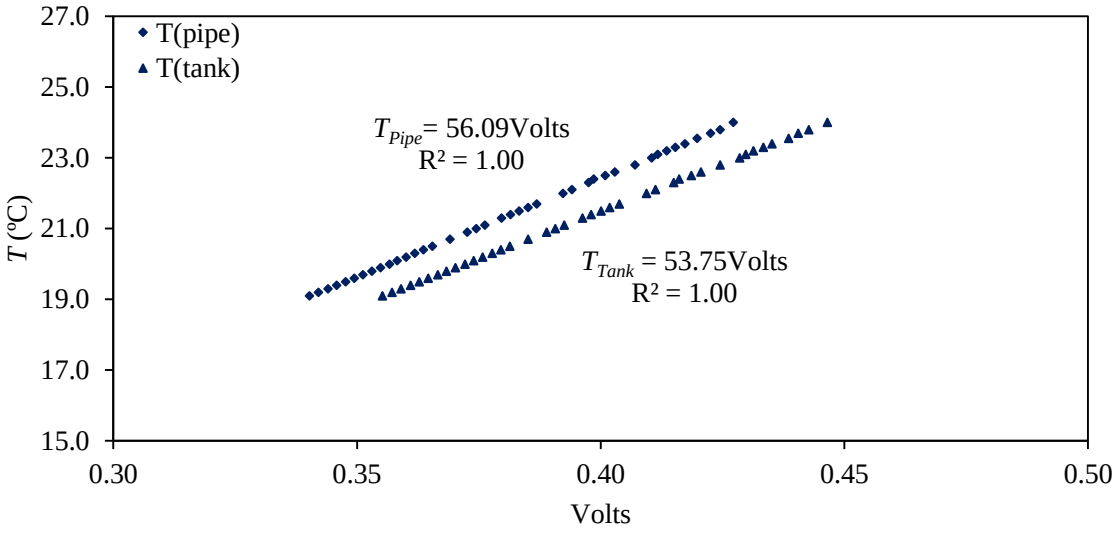

Figure A.9 Typical calibration curves for the tank and pipe temperature probes used within the pilot-scale pipeline.

A.5 Pipeline survey information

Table A.2 Static headloss combinations assessed within each PG assessment within the pilot-scale pipeline in the current study.

Point #	***Headloss Combinations***	***L (m)***
1	P_1-P_5	5.00
2	P_1-P_4	3.30
3	P_1-P_3	3.00
4	P_1-P_2	0.30
5	P_2-P_5	4.70
6	P_2-P_4	3.00
7	P_2-P_3	2.70
8	P_3-P_5	2.00
9	P_3-P_4	0.30
10	P_4-P_5	1.70

Table A.3 Typical wall-normal positions assessed within each velocity profile assessment within the pilot-scale pipeline in the current study.

Point #	***Uncorrected***		***Corrected using the McKeon Method***	
	y-position (mm)	***y/D***	***y-position (mm)***	***y/D***
1	0.00	0.000	0.56	0.005
2	0.10	0.001	0.66	0.006
3	0.15	0.001	0.71	0.007
4	0.20	0.002	0.76	0.007
5	0.25	0.002	0.81	0.008
6	0.50	0.005	1.06	0.010
7	0.75	0.007	1.31	0.013
8	1.00	0.010	1.56	0.015
9	1.50	0.015	2.06	0.020
10	2.00	0.020	2.15	0.021
11	3.01	0.030	3.16	0.031
12	4.00	0.039	4.15	0.041
13	5.00	0.049	5.15	0.050
14	6.00	0.059	6.15	0.060
15	7.00	0.069	7.15	0.070
16	8.00	0.078	8.15	0.080
17	9.00	0.088	9.15	0.090
18	10.00	0.098	10.15	0.099
19	12.00	0.118	12.15	0.119
20	14.00	0.137	14.15	0.139
21	16.00	0.157	16.15	0.158
22	18.00	0.176	18.15	0.178
23	20.00	0.196	20.15	0.197
24	25.00	0.245	25.15	0.246
25	30.00	0.294	30.15	0.295
26	35.00	0.343	35.15	0.344
27	40.00	0.392	40.15	0.393
28	45.00	0.441	45.15	0.442
29	50.00	0.490	50.15	0.491
30	55.00	0.539	55.15	0.540
31	60.00	0.588	60.15	0.589
32	65.00	0.637	65.15	0.638
33	70.00	0.686	70.15	0.687
34	75.00	0.735	75.15	0.736
35	80.00	0.784	80.15	0.785
36	82.00	0.804	82.15	0.805
37	84.00	0.824	84.15	0.824
38	86.00	0.843	86.15	0.844
39	88.00	0.863	88.15	0.864
40	90.00	0.882	90.15	0.883
41	91.00	0.892	91.15	0.893
42	92.00	0.902	92.15	0.903
43	93.00	0.912	93.15	0.913
44	94.00	0.922	94.12	0.922
45	95.00	0.931	95.12	0.932

A.6 TOC and TN analyser calibration data

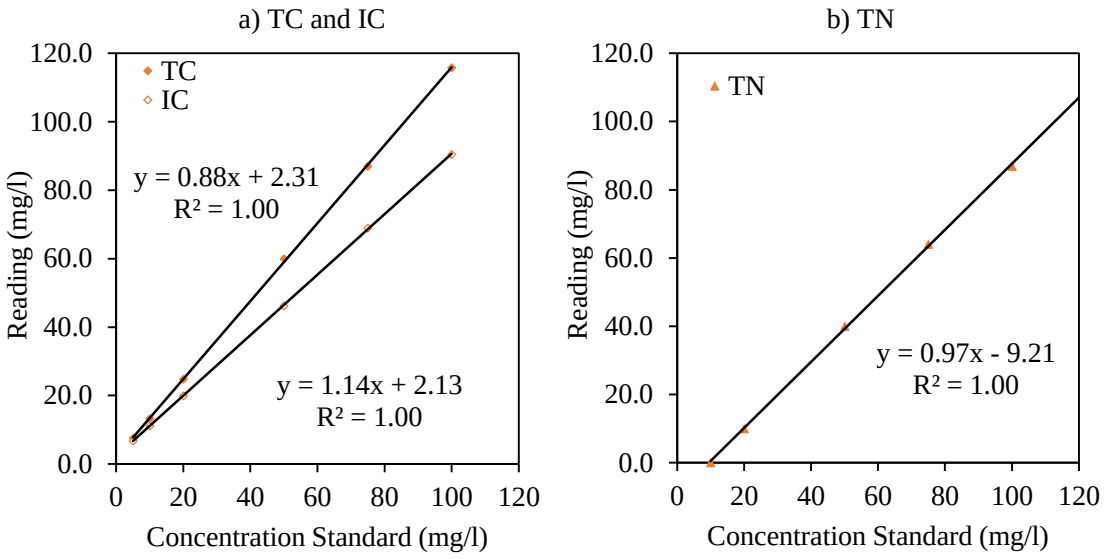

Figure A.10 Typical Calibration Curves for a) TC and IC, and b) TN using the TOC and TN analyser (Shimadzu TOC-V_{CPH}).

A.7 Wastewater evaluation data

Figure A.11 illustrates the results of the OECD wastewater evaluation. The synthetic wastewater strength is relative to standard solution specified by the OECD.

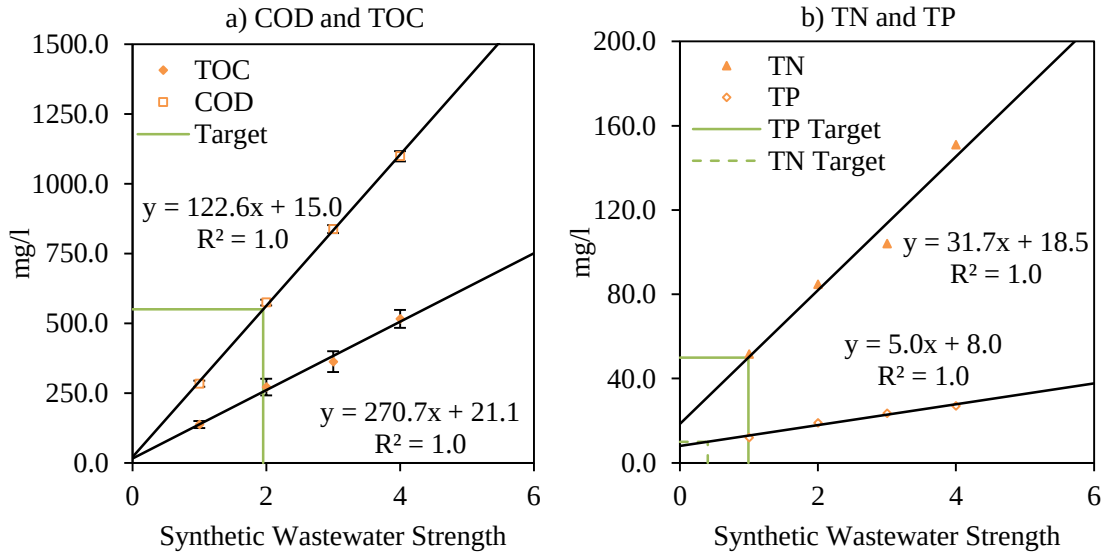

Figure A.11 Synthetic wastewater evaluation for a) COD and TOC, and b) TN and TP concentrations.

The synthetic wastewater specification used throughout this study is listed within Table A.4. The chemicals used to produce synthetic wastewater within this study were supplied by VWR international.

Table A.4 Standard OECD and adjusted specification require to obtain the target values of COD=550mg/l, TN=50mg/l, and TP=10mg/l.

Constituent	***OECD Standard Spec. (mg/l)***	***Adjusted Spec. (mg/l)***
Peptone	160	320
Meat Extract	110	220
Urea	30	30
KH_2PO_4	28	12
NaCl	7	7
$CaCL_2.2H_2O$	4	4
$MgSO_4.7H_2O$	2	2

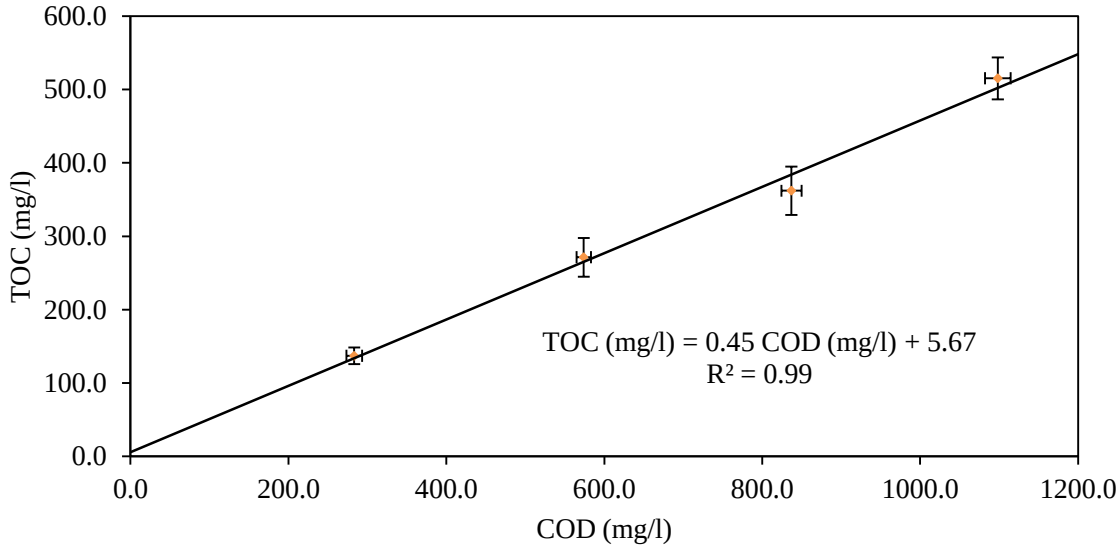

Figure A.12 Correlation between COD and TOC for synthetic wastewater.

A.8 EPS and DNA calibration data

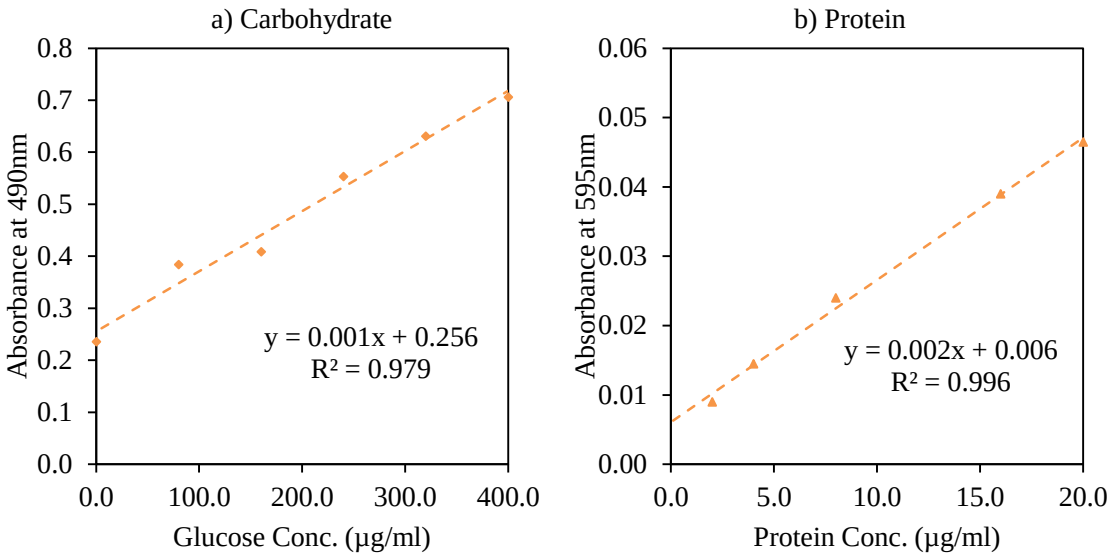

Figure A.13 Typical a) Carbohydrate and b) protein standard curves used the EPS quantification.

Table A.5 Carbohydrate concentration in the cotton bud used in the EPS quantification.

Test No.	***Carbohydrate***	
	µg/ml	*µg/cm²*
B1	222.47	251.79
B2	243.85	275.99
B3	328.95	372.30
B4	325.56	368.46
B5	275.61	311.92
B6	301.85	341.63
B7	257.82	291.80
Av.	**279.45**	**316.27**
σ	**40.98**	**46.38**

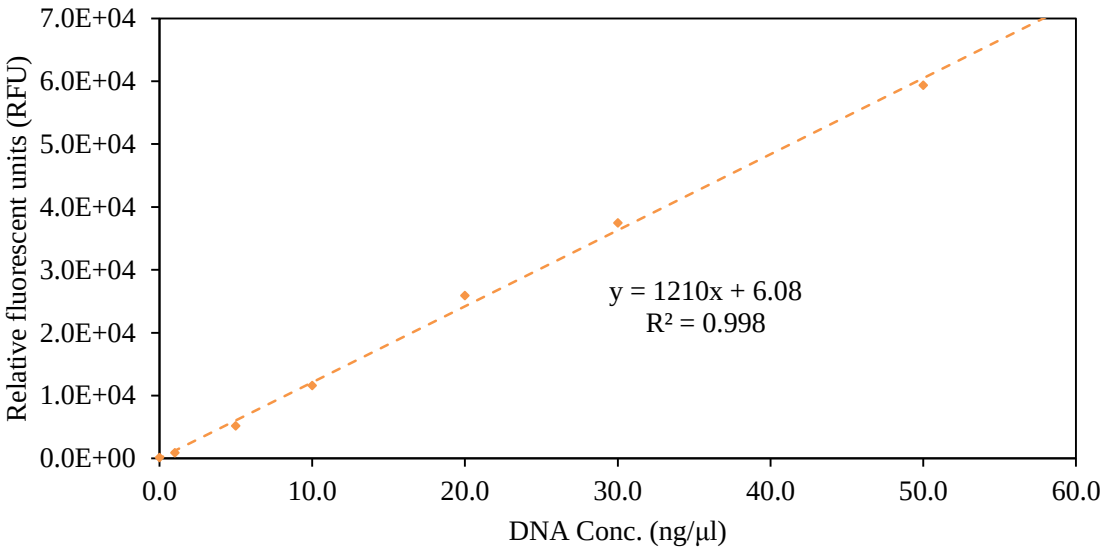

Figure A.14 Typical DNA concentration standard curve.

A.9 Hydraulic retention time data

Table A.6 Hydraulic retention times within each pilot-scale pipe component of the Re = 5.98x10^4, Re =7.82x10^4 and Re = 1.00x10^5 assays.

Component	***Re_D = 5.98x10^4***		***Re_D = 7.82x10^4***		***Re_D = 1.00x10^5***	
	V (l)	***HRT (s)***	***V (l)***	***HRT (s)***	***V (l)***	***HRT (s)***
0.08m ID Recirculating Pipe, 7.6m	34.5	7.6	34.5	5.8	34.5	4.6
0.10m ID Recirculating Pipe, 5.0m	39.3	8.6	39.3	6.6	39.3	5.2
0.10m ID Test Pipe, 5.0m	66.8	14.7	66.8	11.2	66.8	8.9
0.10m ID Visualisation Pipe, 1.7m	13.4	2.9	13.4	2.2	13.4	1.8
0.10m ID Stand Pipe, 0.3m	2.4	0.5	2.4	0.4	2.4	0.3
Recirculating Tank	176.7[1]	38.8	287.2[2]	48.1	397.6[3]	52.7
Whole System	**332.9**	**73.1**	**321.5**	**74.3**	**423.8**	**73.5**

Tank water depth, [1] y_t = 0.4m, [2] y_t = 0.65m, [3] y_t = 0.9m

A.10 Particle size distribution

The results of the particle size distribution of the medium beach sand are presented in Table A.7 and Figure A.15. The initial dry mass, m_i of the sand sample evaluated was 184.06g. It is evident that, during the sieving process, a small amount of sand from the sample was lost. This accounted for approximately 0.4% of the initial dry mass. To account for these losses, a corrected mass retained, m_c was determined using Equation A.3 (BS 1377-2: 1990)

$$m_c = m_R + \left[\left(\frac{m_i - m_T}{m_T}\right) m_R\right] \qquad \textit{Equation A.3}$$

where m_R is the actual retained dry mass and m_T is the total retained dry mass.

Table A.7 Particle size distribution of the medium beach sand used to represent municipal sediment.

Sieve Size (mm)	***Mass Retained (g)***		***% Retained***	***Cumulative % Retained***	***Cumulative % Passing***
	Actual	***Corrected***			
2.000	0.00	0.00	0.00%	0.00%	100.00%
1.180	0.00	0.00	0.00%	0.00%	100.00%
0.600	0.00	0.00	0.00%	0.00%	100.00%
0.425	0.73	0.73	0.40%	0.40%	99.60%
0.300	88.88	88.55	48.11%	48.51%	51.49%
0.212	67.67	67.95	36.92%	85.43%	14.57%
0.150	24.33	24.43	13.27%	98.70%	1.30%
0.063	2.38	2.39	1.30%	100.00%	0.00%
Total	183.29	184.06			

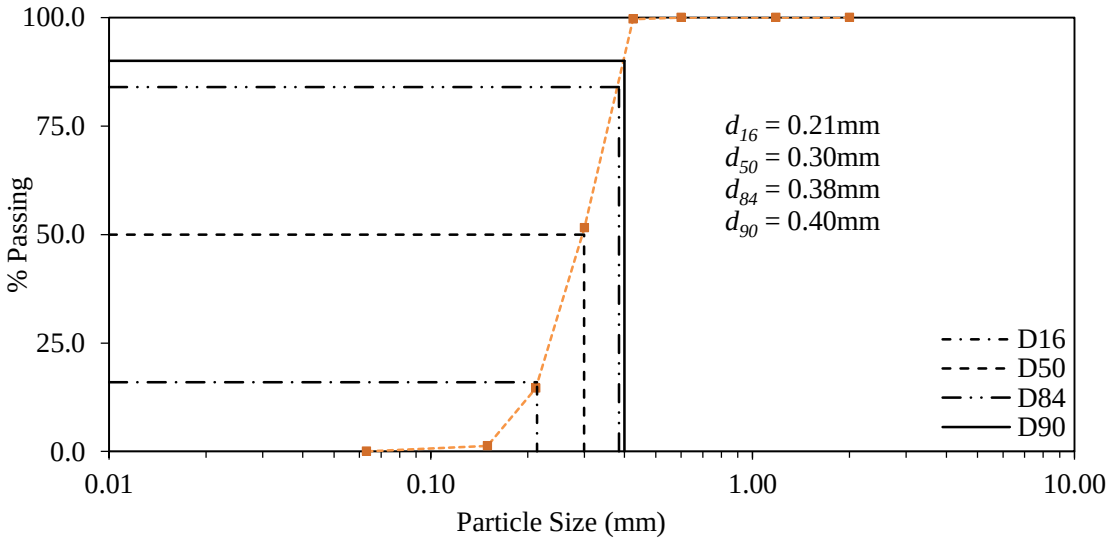

Figure A.15 Particle size distribution of the medium beach sand used to represent municipal sediment.

A.11 Sediment transport characteristics

Table A.8 Key sediment transport parameters for the sediment transport surveys without fouling in the pilot-scale pipeline.

No.	U *(m/s)*	Re **(x10^{-4})**	ρ **(kg/m^3)**	ν **(cm^2/s)**	D^*	d_{50}^+	θ_{cr}	τ_{cr} **(N/m^2)**	u^*_{cr} *(cm/s)*	w_s *(cm/s)*
1	0.40	3.98	998.28	0.010	7.59	8.21	0.037	0.183	1.35	4.49
2	0.45	4.67	997.92	0.010	7.80	10.07	0.037	0.180	1.34	4.58
3	0.45	4.45	998.33	0.010	7.55	9.14	0.038	0.183	1.35	4.48
4	0.46	4.67	998.12	0.010	7.69	9.84	0.037	0.182	1.35	4.53
5	0.57	5.80	998.10	0.010	7.70	12.28	0.037	0.181	1.35	4.54
6	0.60	6.06	998.17	0.010	7.66	12.71	0.037	0.182	1.35	4.52
7	0.42	4.18	998.28	0.010	7.59	8.62	0.037	0.183	1.35	4.49
8	0.65	6.75	997.92	0.010	7.80	14.60	0.037	0.180	1.34	4.58
9	0.45	4.47	998.29	0.010	7.58	9.22	0.037	0.183	1.35	4.49
10	0.40	4.06	998.13	0.010	7.68	8.52	0.037	0.182	1.35	4.53
11	0.51	5.30	997.91	0.010	7.81	11.46	0.037	0.180	1.34	4.58
12	0.45	4.71	997.84	0.010	7.85	10.23	0.037	0.180	1.34	4.59
13	0.45	4.72	997.83	0.010	7.85	10.27	0.037	0.180	1.34	4.59
14	0.55	5.79	997.79	0.010	7.87	12.67	0.037	0.179	1.34	4.60
15	0.46	4.57	998.30	0.010	7.57	9.41	0.037	0.183	1.35	4.49
16	0.90	8.94	998.30	0.010	7.57	18.52	0.037	0.183	1.35	4.49
17	0.85	8.44	998.30	0.010	7.57	17.48	0.037	0.183	1.35	4.49
18	1.00	10.05	998.20	0.010	7.63	21.10	0.037	0.182	1.35	4.51
19	0.75	7.58	998.16	0.010	7.66	15.97	0.037	0.182	1.35	4.52
20	0.90	9.26	998.00	0.010	7.75	19.87	0.037	0.181	1.35	4.56
21	0.95	9.96	997.83	0.010	7.86	21.82	0.037	0.180	1.34	4.59
22	0.30	3.23	997.58	0.009	7.99	7.17	0.036	0.178	1.34	4.65
23	0.35	3.79	997.51	0.009	8.03	8.51	0.036	0.178	1.33	4.66
24	0.35	3.80	997.49	0.009	8.04	8.54	0.036	0.178	1.33	4.66
25	0.35	3.82	997.45	0.009	8.06	8.60	0.036	0.177	1.33	4.67
26	0.36	3.68	998.06	0.010	7.72	7.78	0.037	0.181	1.35	4.54
27	0.45	4.73	997.82	0.010	7.86	10.30	0.037	0.180	1.34	4.60
28	0.40	4.21	997.79	0.010	7.87	9.18	0.037	0.179	1.34	4.60
29	0.36	3.76	997.88	0.010	7.83	8.10	0.037	0.180	1.34	4.58
30	0.47	5.05	997.59	0.009	7.99	11.28	0.036	0.178	1.34	4.64
31	0.26	2.67	998.00	0.010	7.75	5.65	0.037	0.181	1.35	4.56
32	0.44	4.73	997.59	0.009	7.99	10.55	0.036	0.178	1.34	4.64
33	0.44	4.73	997.59	0.009	7.99	10.55	0.036	0.178	1.34	4.64
34	0.80	8.22	998.02	0.010	7.75	17.61	0.037	0.181	1.35	4.55
35	0.75	7.69	998.03	0.010	7.74	16.45	0.037	0.181	1.35	4.55
36	0.60	6.16	998.03	0.010	7.74	13.14	0.037	0.181	1.35	4.55
37	0.55	5.64	998.03	0.010	7.74	12.03	0.037	0.181	1.35	4.55

Table A.9 Key sediment transport parameters for the sediment transport surveys with fouling in the pilot-scale pipeline.

No.	U *(m/s)*	Re **(x10^{-4})**	ρ **(kg/m^3)**	ν **(cm^2/s)**	D^*	d_{50}^+	θ_{cr}	τ_{cr} **(N/m^2)**	u^*_{cr} *(cm/s)*	w_s *(cm/s)*
1	0.37	3.66	998.34	0.010	7.55	5.11	0.038	0.183	1.35	4.48
2	0.58	5.61	998.51	0.010	7.44	7.25	0.038	0.185	1.36	4.43
3	0.55	5.34	998.48	0.010	7.46	6.97	0.038	0.185	1.36	4.44
4	0.45	4.40	998.43	0.010	7.49	5.92	0.038	0.184	1.36	4.45
5	0.48	4.69	998.44	0.010	7.49	6.25	0.038	0.184	1.36	4.45
6	0.62	6.14	998.32	0.010	7.56	8.08	0.037	0.183	1.35	4.48
7	0.3	2.97	998.32	0.010	7.56	4.31	0.037	0.183	1.35	4.48
8	0.55	5.40	998.39	0.010	7.52	7.13	0.038	0.184	1.36	4.46
9	0.55	5.40	998.40	0.010	7.51	7.12	0.038	0.184	1.36	4.46
10	0.57	5.57	998.44	0.010	7.49	7.28	0.038	0.184	1.36	4.45
11	0.45	4.43	998.37	0.010	7.53	6.00	0.038	0.184	1.36	4.47
12	0.41	4.03	998.38	0.010	7.53	5.53	0.038	0.184	1.36	4.47
13	0.54	5.33	998.35	0.010	7.54	7.08	0.038	0.183	1.36	4.47
14	0.45	4.40	998.42	0.010	7.49	5.93	0.038	0.184	1.36	4.46
15	0.45	4.41	998.41	0.010	7.50	5.94	0.038	0.184	1.36	4.46
16	0.38	3.73	998.39	0.010	7.51	5.16	0.038	0.184	1.36	4.46
17	0.45	4.40	998.42	0.010	7.50	5.93	0.038	0.184	1.36	4.46
18	0.55	5.43	998.35	0.010	7.54	7.21	0.038	0.183	1.36	4.48
19	0.56	5.59	998.26	0.010	7.60	7.47	0.037	0.183	1.35	4.50
20	0.59	5.89	998.26	0.010	7.60	7.83	0.037	0.183	1.35	4.50
21	0.37	3.75	998.14	0.010	7.67	5.34	0.037	0.182	1.35	4.52
22	0.57	5.66	998.31	0.010	7.57	7.51	0.037	0.183	1.35	4.48
23	0.55	5.44	998.34	0.010	7.55	7.22	0.038	0.183	1.36	4.48
24	0.44	4.33	998.38	0.010	7.52	5.88	0.038	0.184	1.36	4.47
25	0.48	4.76	998.32	0.010	7.56	6.44	0.037	0.183	1.35	4.48
26	0.61	6.05	998.32	0.010	7.56	7.97	0.037	0.183	1.35	4.48
27	0.30	2.98	998.29	0.010	7.58	4.33	0.037	0.183	1.35	4.49
28	0.55	5.38	998.43	0.010	7.49	7.07	0.038	0.184	1.36	4.45
29	0.48	4.73	998.37	0.010	7.53	6.36	0.038	0.184	1.36	4.47
30	0.56	5.51	998.38	0.010	7.52	7.27	0.038	0.184	1.36	4.47
31	0.45	4.46	998.32	0.010	7.56	6.08	0.037	0.183	1.35	4.48
32	0.40	3.96	998.32	0.010	7.56	5.49	0.037	0.183	1.35	4.48
33	0.70	6.96	998.29	0.010	7.58	12.06	0.037	0.183	1.35	4.49
34	0.90	8.87	998.37	0.010	7.53	15.34	0.038	0.184	1.36	4.47
35	0.80	7.89	998.36	0.010	7.54	13.63	0.038	0.183	1.36	4.47
36	0.78	7.79	998.26	0.010	7.60	13.62	0.037	0.183	1.35	4.50
37	0.90	9.01	998.23	0.010	7.62	15.86	0.037	0.182	1.35	4.50

B. Supporting data for Chapter 4

B.1 Global frictional data

Table B.1 Non-fouled frictional data for the pilot-scale pipe determined using the Slope Fit Method.

Re_D	S_f	*Line Correlation* (R^2)	λ	u^* (m/s)	c_f (x10^{-3})	τ_w (N/m^2)	k_s (mm)	n
3.15 x 10^4	0.001	1.000	0.023	0.017	3.79	0.28	0.015	0.009
4.10 x 10^4	0.002	0.999	0.021	0.021	3.60	0.44	0.013	0.009
5.37 x 10^4	0.003	0.998	0.020	0.027	3.37	0.71	0.011	0.009
6.10 x 10^4	0.004	0.999	0.019	0.030	3.28	0.87	0.001	0.009
7.41 x 10^4	0.005	0.998	0.019	0.035	3.24	1.23	0.004	0.008
9.22 x 10^4	0.008	0.998	0.018	0.044	3.10	1.93	0.009	0.008
1.13 x 10^5	0.011	0.996	0.018	0.053	3.01	2.78	0.014	0.008
1.23 x 10^5	0.013	0.995	0.017	0.057	2.98	3.20	0.010	0.008
						Average:	**0.010**	**0.009**
						σ	**0.005**	**-**

Table B.2 Non-fouled frictional data for the pilot-scale pipe determined using the Combined Average Method.

Re_D	S_f	λ	u^* (m/s)	c_f (x10^{-3})	τ_w (N/m^2)	k_s (mm)	n
3.15 x 10^4	0.001	0.023	0.016	3.76	0.26	0.006	0.009
4.10 x 10^4	0.002	0.022	0.021	3.60	0.44	0.011	0.009
5.37 x 10^4	0.003	0.020	0.027	3.37	0.72	0.016	0.009
6.10 x 10^4	0.004	0.020	0.029	3.28	0.87	0.007	0.008
7.41 x 10^4	0.005	0.019	0.035	3.24	1.22	0.001	0.006
9.22 x 10^4	0.008	0.018	0.043	3.10	1.87	-	0.008
1.13 x 10^5	0.011	0.018	0.051	2.95	2.65	0.010	0.008
1.23 x 10^5	0.013	0.017	0.056	2.90	3.11	-	0.008
					Average:	0.008	0.008
					σ	0.005	0.001

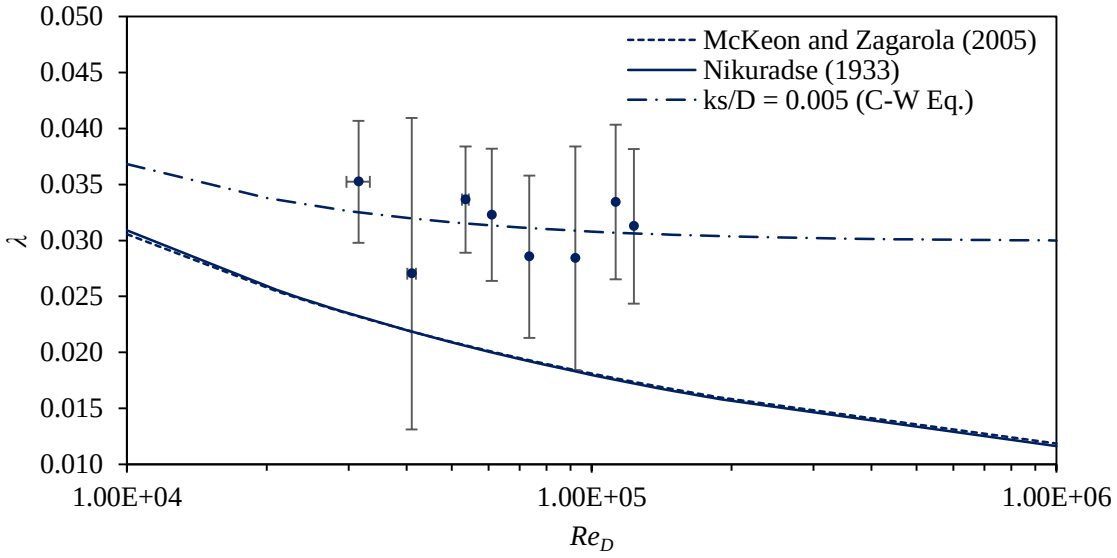

Figure B.1 λ against Re_D, for static headloss combinations P1-P2 and P3-P4 (i.e. for joint 1 and 2, for the range of $2.98x10^4<Re_D<1.12x10^5$).

B.2 Wall similarity data

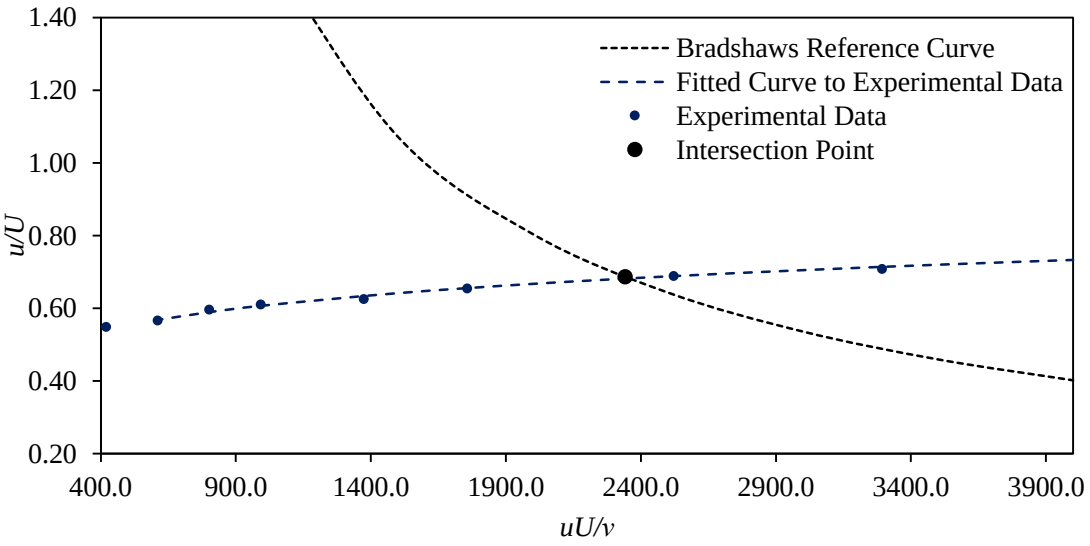

Figure B.2 Example of the Bradshaw Method Plot (for $Re_D = 6.34x10^4$)

Table B.3 Wall origin errors determined from the Pressure Gradient, Preston Probe (PP), Bradshaw (B), Log-Law Slope (LLS) and Perry Li methods

Re_D	ε (mm)				
	PG	**PP**	**B**	**LLS**	**PL**
3.74 x 10^4	0.45±0.09	0.71±0.34	0.85±0.10	0.75±0.36	0.85±0.04
5.53 x 10^4	0.87±0.09	0.57±0.19	0.57±0.19	0.57±0.08	0.99±0.07
6.27 x 10^4	0.85±0.21	0.61±0.16	0.61±0.12	0.65±0.18	0.66±0.06
7.39 x 10^4	0.67±0.04	0.80±0.24	0.80±0.24	0.82±0.21	0.83±0.12
8.60 x 10^4	0.67±0.06	0.65±0.00	0.65±0.00	0.75±0.13	0.67±0.01
9.41 x 10^4	0.45±0.05	0.49±0.07	0.49±0.07	0.73±0.21	0.84±0.05
1.13 x 10^5	0.75±0.18	0.94±0.13	0.94±0.13	0.85±0.08	0.97±0.10

Table B.4 Non-fouled frictional data for the pilot-scale pipe determined using the Preston Probe (PP), Bradshaw (B), Log-Law Slope (LLS) and Perry Li methods.

Re_D	u^* (m/s)				c_f (x 10^{-3})				τ_w (N/m^2)			
	PP	**B**	**LLS**	**PL**	**PP**	**B**	**LLS**	**PL**	**PP**	**B**	**LLS**	**PL**
3.74 x 10^4	0.022	0.020	0.020	0.019	4.73	3.69	3.63	3.62	0.50	0.39	0.38	0.38
5.53 x 10^4	0.030	0.028	0.027	0.027	4.13	3.63	3.31	3.45	0.90	0.79	0.72	0.74
6.27 x 10^4	0.034	0.031	0.031	0.030	3.92	3.37	3.22	3.13	1.13	0.98	0.93	0.91
7.39 x 10^4	0.039	0.036	0.037	0.034	3.92	3.31	3.50	3.10	1.51	1.27	1.34	1.19
8.60 x 10^4	0.045	0.043	0.040	0.041	3.62	3.20	2.86	2.94	2.06	1.82	1.62	1.67
9.41 x 10^4	0.049	0.046	0.045	0.044	3.71	3.29	3.19	3.13	2.36	2.09	2.02	1.96
1.13 x 10^5	0.057	0.052	0.054	0.054	3.45	2.91	3.14	3.13	3.20	2.70	2.91	2.90

C. Supporting data for Chapter 5

C.1 Global frictional data

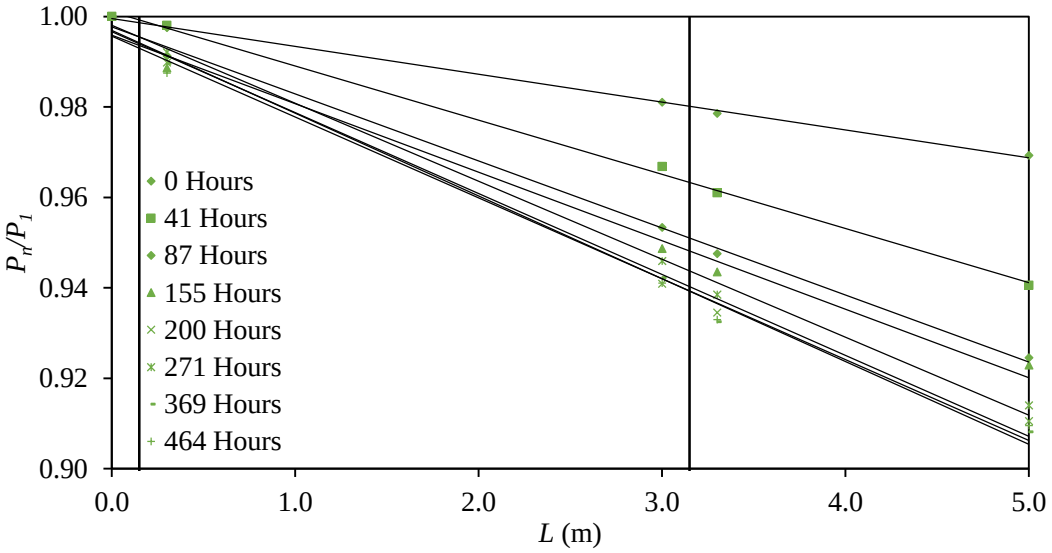

Figure C.1 Normalised static head profiles for the Re = 5.98x10^4 assay.

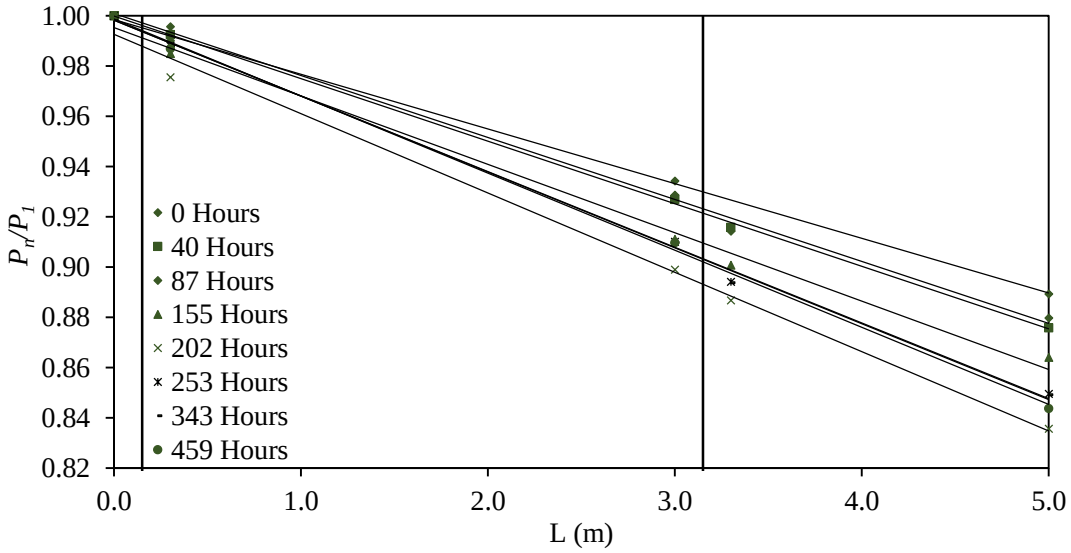

Figure C.2 Normalised static head profiles for the Re = 1.00x10^5 assay.

Table C.1 Frictional data determined using Slope Fit Method, for Re_D = 5.98x10^{4}assay.

Day	*Re* (x10^{-4})	λ	u^* (m/s)	c_f (x10^{-3})	τ_w (N/m^2)	n	k_s (mm)	k_s^+
0	5.98	0.018	0.029	3.24	0.82	0.008	0.013	0.37
1	6.08	0.018	0.029	3.19	0.81	0.008	0.013	0.38
2	6.12	0.022	0.031	3.60	0.97	0.009	0.048	1.52
3	6.01	0.025	0.032	3.86	1.02	0.010	0.139	4.63
4	5.93	0.027	0.034	4.23	1.13	0.010	0.228	7.80
5	5.79	0.027	0.034	4.28	1.14	0.010	0.235	7.90
6	5.68	0.025	0.032	3.95	1.00	0.010	0.141	4.46
7	5.93	0.029	0.034	4.59	1.16	0.010	0.353	12.65
8	5.61	0.034	0.035	5.07	1.25	0.011	0.634	23.16
9	5.90	0.034	0.038	5.35	1.42	0.011	0.605	23.14
10	6.06	0.034	0.038	5.26	1.45	0.011	0.646	25.57
12	5.78	0.034	0.037	5.20	1.36	0.011	0.604	22.64
13	6.06	0.034	0.038	5.25	1.45	0.011	0.642	25.38
14	6.30	0.035	0.039	5.18	1.50	0.011	0.674	27.91
15	6.06	0.034	0.038	5.27	1.45	0.011	0.646	25.61
16	6.26	0.034	0.038	5.29	1.47	0.011	0.658	27.00
18	6.17	0.034	0.038	5.17	1.45	0.011	0.647	26.08
20	5.87	0.035	0.038	5.16	1.41	0.011	0.616	24.00
Av.*	**6.01**	0.034	0.038	**5.22**	1.42	0.011	0.637	25.05
σ*	**0.22**	0.000	**0.001**	**0.08**	0.07	0.000	0.023	1.76

**** Pseudo-equilibrium state average***

Table C.2 Frictional data determined using Slope Fit Method, for Re_D = 7.58x10^{4}assay.

Day	***Re* (x10^{-4})**	***λ***	***u**** **(m/s)**	c_f **(x10^{-3})**	τ_w **(N/m^2)**	***n***	k_s **(mm)**	k_s^+
0	7.55	0.018	0.036	3.11	1.37	0.008	-0.020	-
1	7.63	0.018	0.036	3.10	1.37	0.008	-0.015	-
2	7.84	0.021	0.039	3.48	1.65	0.009	0.055	2.19
3	7.87	0.022	0.040	3.57	1.68	0.009	0.096	3.89
4	7.91	0.023	0.040	3.77	1.71	0.009	0.128	5.31
5	7.73	0.023	0.040	3.81	1.70	0.009	0.123	4.99
6	7.80	0.022	0.039	3.51	1.62	0.009	0.085	3.40
7	7.59	0.026	0.041	4.17	1.75	0.010	0.242	10.34
8	7.69	0.030	0.044	4.65	2.07	0.010	0.447	20.60
9	8.05	0.029	0.046	4.60	2.24	0.010	0.396	18.76
10	7.90	0.030	0.046	4.63	2.16	0.010	0.442	20.92
12	7.68	0.029	0.045	4.65	2.11	0.010	0.437	20.16
13	8.07	0.029	0.045	4.54	2.13	0.010	0.408	19.48
14	8.22	0.029	0.046	4.52	2.18	0.010	0.424	20.69
15	7.78	0.030	0.045	4.68	2.15	0.010	0.454	21.32
16	7.93	0.030	0.046	4.69	2.18	0.010	0.460	22.03
18	7.69	0.030	0.045	4.62	2.12	0.011	0.498	23.35
20	7.58	0.030	0.045	4.59	2.16	0.011	0.482	22.12
Av.*	7.86	0.030	0.045	4.62	2.15	0.010	0.445	20.94
σ*	0.21	0.001	0.001	0.06	0.05	0.000	0.031	1.34

**** Pseudo-equilibrium state average***

Table C.3 Frictional data determined using Slope Fit Method, for Re_D = 1.00x10^{5}assay.

Day	*Re* (x10^{-4})	λ	u^* (m/s)	c_f (x10^{-3})	τ_w (N/m^2)	n	k_s (mm)	k_s^+
0	9.63	0.017	0.044	3.07	1.95	0.008	-0.013	-
1	9.48	0.018	0.044	3.10	1.97	0.008	-0.009	-
2	9.90	0.020	0.049	3.45	2.38	0.009	0.040	2.00
3	10.04	0.020	0.049	3.39	2.40	0.009	0.037	1.86
4	10.33	0.020	0.049	3.43	2.35	0.009	0.033	1.69
5	10.07	0.019	0.048	3.45	2.31	0.008	0.024	1.17
6	10.31	0.019	0.048	3.19	2.29	0.008	0.022	1.09
7	9.60	0.023	0.049	3.87	2.39	0.009	0.119	6.11
8	10.22	0.026	0.054	4.37	2.95	0.010	0.241	14.02
9	10.64	0.025	0.056	3.99	3.13	0.010	0.185	10.95
10	10.13	0.026	0.054	4.13	2.95	0.010	0.226	12.96
11	10.01	0.026	0.054	4.24	2.91	0.010	0.244	13.98
13	10.56	0.025	0.054	3.97	2.87	0.010	0.182	10.66
14	10.56	0.025	0.054	3.99	2.92	0.010	0.185	10.85
15	9.85	0.026	0.054	4.24	2.92	0.010	0.243	13.71
16	9.92	0.026	0.054	4.24	2.95	0.010	0.244	13.85
18	9.57	0.026	0.055	4.15	2.97	0.010	0.239	13.06
20	9.92	0.026	0.054	4.24	2.95	0.010	0.244	13.85
Av.*	10.14	0.026	0.054	4.16	2.95	0.010	0.223	12.79
σ*	0.35	0.001	0.001	0.14	0.07	0.000	0.027	1.41

**** Pseudo-equilibrium state average***

Table C.4 Frictional data determined using Combined Average Method, for Re_D = 5.98x10^{4}assay.

Day	***Re* (x10^{-4})**	***λ***	***u**** **(m/s)**	c_f **(x10^{-3})**	τ_w **(N/m^2)**	***n***	k_s **(mm)**	k_s^+
0	5.98	0.018	0.029	3.25	0.82	0.008	0.013	0.38
1	6.08	0.019	0.029	3.22	0.82	0.008	0.013	0.38
2	6.12	0.022	0.031	3.60	0.99	0.009	0.062	2.01
3	6.01	0.024	0.032	3.81	1.01	0.010	0.145	4.82
4	5.93	0.028	0.034	4.19	1.17	0.010	0.271	9.45
5	5.79	0.026	0.033	4.23	1.12	0.010	0.213	7.09
6	5.68	0.026	0.032	3.98	1.04	0.010	0.180	5.80
7	5.93	0.030	0.035	4.54	1.21	0.010	0.426	15.56
8	5.61	0.035	0.036	5.00	1.28	0.011	0.724	26.67
9	5.90	0.034	0.038	5.24	1.43	0.011	0.642	24.58
10	6.06	0.035	0.039	5.28	1.50	0.011	0.756	30.45
11	5.78	0.035	0.038	5.24	1.42	0.011	0.718	27.39
13	6.06	0.035	0.039	5.27	1.50	0.011	0.754	30.37
14	6.30	0.035	0.039	5.12	1.52	0.011	0.723	30.03
15	6.06	0.035	0.039	5.29	1.51	0.011	0.751	30.27
16	6.26	0.035	0.039	5.30	1.49	0.011	0.723	29.86
18	6.17	0.035	0.039	5.06	1.48	0.011	0.710	28.87
20	5.87	0.037	0.038	5.06	1.46	0.011	0.727	28.81
Av.*	**6.01**	**0.035**	**0.038**	**5.19**	**1.46**	**0.011**	**0.723**	**28.73**
σ*	**0.22**	**0.001**	**0.001**	**0.11**	**0.07**	**0.000**	**0.033**	**1.95**

**** Pseudo-equilibrium state average***

Table C.5 Frictional data determined using Combined Average Method, for Re_D = 7.58x10^{4}assay.

Day	*Re* (x10^{-4})	λ	u^* (m/s)	c_f (x10^{-3})	τ_w (N/m^2)	n	k_s (mm)	k_s^+
0	7.55	0.018	0.036	3.10	1.36	0.008	-0.020	-
1	7.63	0.018	0.036	3.11	1.37	0.008	-0.014	-
2	7.84	0.021	0.040	3.48	1.66	0.009	0.063	2.50
3	7.87	0.022	0.039	3.50	1.65	0.009	0.086	3.45
4	7.91	0.023	0.041	3.75	1.73	0.009	0.144	6.02
5	7.73	0.023	0.040	3.80	1.70	0.009	0.117	4.71
6	7.80	0.022	0.039	3.54	1.64	0.009	0.102	4.12
7	7.59	0.026	0.041	4.09	1.74	0.010	0.254	10.81
8	7.69	0.030	0.044	4.57	2.06	0.010	0.454	20.84
9	8.05	0.029	0.046	4.50	2.21	0.010	0.387	18.19
10	7.90	0.030	0.046	4.59	2.16	0.010	0.464	21.97
12	7.68	0.030	0.045	4.63	2.11	0.010	0.463	21.40
13	8.07	0.029	0.045	4.49	2.11	0.010	0.424	20.18
14	8.22	0.029	0.046	4.49	2.19	0.010	0.435	21.27
15	7.78	0.030	0.046	4.66	2.15	0.010	0.477	22.41
16	7.93	0.030	0.046	4.66	2.16	0.010	0.463	22.13
18	7.69	0.031	0.045	4.55	2.13	0.010	0.529	24.92
20	7.58	0.031	0.045	4.50	2.16	0.010	0.505	23.22
Av.*	7.86	0.030	0.045	4.56	2.14	0.010	0.460	21.65
σ*	0.21	0.001	0.001	0.07	0.04	0.000	0.040	1.80

**** Pseudo-equilibrium state average***

Table C.6 Frictional data determined using Combined Average Method, for Re_D = 1.00x10^{5}assay.

Day	***Re* (x10^{-4})**	***λ***	***u**** **(m/s)**	c_f **(x10^{-3})**	τ_w **(N/m^2)**	***n***	k_s **(mm)**	k_s^+
0	9.63	0.017	0.044	3.04	1.94	0.008	-0.015	-
1	9.48	0.018	0.044	3.08	1.96	0.008	-0.008	-
2	9.90	0.020	0.049	3.46	2.38	0.009	0.045	2.23
3	10.04	0.019	0.048	3.29	2.33	0.008	0.033	1.61
4	10.33	0.020	0.048	3.43	2.35	0.009	0.038	1.95
5	10.07	0.019	0.048	3.48	2.33	0.008	0.030	1.47
6	10.31	0.019	0.048	3.21	2.30	0.008	0.029	1.47
7	9.60	0.022	0.048	3.76	2.32	0.009	0.108	5.44
8	10.22	0.026	0.054	4.27	2.89	0.010	0.242	13.91
9	10.64	0.024	0.055	3.90	3.06	0.009	0.171	9.95
10	10.13	0.025	0.054	4.04	2.88	0.010	0.206	11.71
12	10.01	0.026	0.054	4.16	2.86	0.010	0.226	12.82
13	10.56	0.024	0.053	3.84	2.78	0.009	0.158	9.11
14	10.56	0.025	0.054	3.99	2.93	0.010	0.193	11.32
15	9.85	0.026	0.054	4.16	2.86	0.010	0.225	12.57
16	9.92	0.026	0.054	4.16	2.89	0.010	0.226	12.70
18	9.57	0.026	0.054	4.07	2.91	0.010	0.218	11.80
20	9.92	0.026	0.054	4.16	2.89	0.010	0.226	12.70
Av.*	10.14	0.025	0.054	4.08	2.89	0.010	0.209	11.86
σ*	0.35	0.001	0.001	0.14	0.07	0.000	0.027	1.44

**** Pseudo-equilibrium state average***

Table C.7 Frictional data determined indirectly from the velocity profile using the Perry and Li (PL) method for the Re_D =5.98x10^4 assay

Day	***Re*** **(x10^{-4})**	***u**** **(m/s)**	c_f **(x10^{-3})**	k_s **(mm)**	ε **(mm)**	k_s^+	ε^+	Δu^+
0	6.09	0.029	3.31	0.158	1.40	4.64	40.89	-0.17
1	6.16	0.030	3.61	0.186	1.54	5.79	47.87	0.96
2	6.17	0.031	3.50	0.154	0.89	4.83	28.07	0.67
3	6.13	0.033	4.10	0.389	0.74	13.39	25.52	2.79
4	5.98	0.033	4.00	0.314	1.00	10.47	33.42	2.56
5	5.84	0.033	4.16	0.392	1.40	12.98	46.37	3.09
6	5.70	0.032	4.07	0.317	1.15	10.21	37.05	2.50
7	6.00	0.036	5.18	1.433	1.60	54.51	60.83	6.73
8	5.88	0.043	7.45	3.315	2.92	148.08	130.58	8.87
9	6.34	0.041	6.16	1.341	2.50	55.23	102.95	6.47
10	6.19	0.044	6.95	2.723	2.56	124.13	116.85	8.47
12	5.84	0.042	6.84	2.593	2.54	111.80	109.50	8.19
13	5.38	0.042	6.52	2.103	2.28	92.88	100.57	7.77
14	6.40	0.043	6.30	2.254	1.62	103.06	74.10	8.03
15	6.15	0.042	6.53	2.210	2.29	97.70	101.42	7.90
16	6.39	0.043	6.42	2.268	1.99	103.62	90.94	8.04
18	6.21	0.042	6.20	1.902	1.91	83.83	84.23	7.53
Av.*	6.09	0.04	6.60	2.30	2.29	102.26	101.24	7.91
σ*	0.33	0.00	0.42	0.55	0.40	25.81	16.98	0.67

**** Pseudo-equilibrium state average***

C.2 Local frictional data

Table C.8 Frictional data determined indirectly from the velocity profile using the Perry and Li (PL) for the Re_D =1.00x10^5 assay.

Day	***Re*** **(x10^{-4})**	***u**** **(m/s)**	c_f **(x10^{-3})**	k_s **(mm)**	ε **(mm)**	k_s^+	ε^+	Δu^+
0	9.69	0.044	3.02	0.074	0.83	3.31	37.00	-0.16
1	9.54	0.046	3.31	0.126	0.98	5.80	45.07	0.96
2	9.97	0.047	3.22	0.107	0.84	5.13	39.92	0.89
3	10.11	0.047	3.15	0.111	0.87	5.33	41.86	0.72
4	10.21	0.046	3.14	0.087	1.02	4.26	49.91	0.45
5	9.61	0.045	2.99	0.082	1.07	3.75	48.97	0.14
6	10.40	0.046	2.90	0.069	0.77	3.33	37.53	-0.23
7	9.52	0.043	2.99	0.080	1.19	3.61	53.84	-0.13
8	10.15	0.044	2.82	0.062	0.76	2.91	35.47	-0.65
9	10.58	0.050	3.22	0.091	0.88	4.84	46.64	0.61
10	10.06	0.048	3.29	0.131	1.18	6.71	60.14	1.49
12	9.92	0.049	3.51	0.182	1.39	9.49	72.46	2.34
13	10.54	0.052	3.78	0.255	1.16	14.54	66.17	3.37
14	10.49	0.052	3.71	0.236	1.08	13.34	61.26	3.16
16	9.28	0.052	4.11	0.371	1.01	19.71	53.67	4.09
18	9.86	0.051	3.84	0.289	1.05	15.74	57.01	3.56
19	9.55	0.051	3.66	0.239	1.05	12.31	54.27	2.98
Av.*	10.05	0.05	3.55	0.21	1.06	11.07	56.34	2.33
σ*	0.45	0.00	0.39	0.10	0.18	5.50	10.82	1.56

**** Pseudo-equilibrium state average***

C.2 von Kármán and *B* determination data

Table C.9 Modified κ and B for the biofilms incubated within the Re_D =5.98x10^4 and Re_D =1.00x10^5 assays.

Day	Re_D = 5.98x10^4				Re_D = 1.00x10^5			
	SFM		P_3-P_5		SFM		P_3-P_5	
	κ	B	κ	B	κ	B	κ	B
0	0.40	5.20	0.41	5.10	0.41	5.45	0.41	5.43
1	0.41	5.98	0.42	5.87	0.41	5.33	0.39	5.63
2	0.39	3.51	0.37	2.98	0.38	2.88	0.38	2.98
3	0.36	5.34	0.34	3.20	0.38	2.65	0.35	2.99
4	0.36	6.10	0.37	6.34	0.39	3.29	0.36	3.82
5	0.38	6.12	0.37	5.91	0.41	3.39	0.38	3.82
6	0.37	5.73	0.38	6.12	0.38	3.25	0.38	3.32
7	0.35	5.81	0.33	4.65	0.38	5.99	0.36	1.40
8	0.32	5.36	0.29	2.74	0.39	7.34	0.37	3.93
9	0.32	7.10	0.34	7.47	0.39	6.81	0.39	6.39
10	0.34	6.22	0.32	5.20	0.38	6.83	0.39	7.06
11	0.37	7.11	0.37	6.68	0.39	7.22	0.39	7.20
13	0.35	6.53	0.33	5.57	0.38	6.25	0.39	7.03
14	0.34	5.88	0.31	4.08	0.37	6.27	0.39	7.08
15	0.35	6.48	0.33	5.49	-	-	-	-
16	0.36	6.89	0.33	5.30	-	-	-	-
17	-	-	-	-	0.39	7.08	0.39	7.03
18	0.37	6.88	0.34	5.75	0.40	7.39	0.40	7.47
19	-	-	-	-	0.39	7.19	0.39	7.28
20	0.37	6.78	0.38	7.50	-	-	-	-
Av.*	0.35	6.46	0.34	5.49	0.39	6.84	0.39	6.19
σ*	0.02	0.58	0.03	1.41	0.01	0.50	0.01	1.97

Table C.10 Revised frictional data for the $Re_D = 5.98x10^4$ assay determined from the velocity profile, SFM and P_3-P_5 datasets.

Day	***Re* (x10^{-4})**	***SFM***				***P_3-P_5***			
		ε (mm)	**ΔU^+**	**ε^+**	**k_s^+**	**ε (mm)**	**ΔU^+**	**ε^+**	**k_s^+**
0	5.98	1.19	0.30	24.72	0.19	1.19	0.40	25.03	0.19
1	6.08	0.92	-0.48	26.80	0.26	0.92	-0.37	27.14	0.27
2	6.12	0.98	1.99	31.55	1.55	1.07	2.52	33.88	1.13
3	6.01	0.86	4.45	28.93	4.66	0.86	4.26	27.89	2.33
4	5.93	1.14	4.84	39.16	7.79	1.14	4.49	39.16	8.39
5	5.79	1.70	4.86	57.16	7.92	1.70	4.83	56.61	7.08
6	5.68	1.16	3.80	36.59	12.48	1.16	3.85	37.04	13.23
7	5.93	1.65	6.89	59.56	12.65	1.65	6.82	56.35	7.46
8	5.87	2.19	9.71	81.93	21.69	2.14	9.55	70.89	7.09
9	5.90	1.50	8.29	57.54	23.26	0.60	4.85	21.17	10.39
10	6.06	1.86	8.80	73.84	25.60	1.86	8.81	69.63	15.38
12	5.78	1.34	6.91	50.04	22.73	1.34	5.57	46.80	12.44
13	6.06	1.72	8.13	68.28	25.40	1.72	8.12	64.39	15.26
14	6.30	1.59	9.27	65.99	27.94	1.59	9.35	60.02	12.03
15	6.06	1.76	8.26	69.67	25.63	1.76	8.25	65.65	15.30
16	6.26	1.34	7.76	55.21	27.06	1.34	7.70	50.28	11.72
17	-	-	-	-	-	-	-	-	-
18	6.17	1.45	7.42	58.18	26.00	1.45	7.35	54.07	13.66
19	-	-	-	-	-	-	-	-	-
20	6.17	1.45	7.56	57.24	25.74	1.45	5.73	53.74	18.93
Av. *	**6.06**	**1.62**	**8.21**	**63.79**	**25.10**	**1.52**	**7.53**	**55.66**	**13.22**
σ*	**0.17**	**0.27**	**0.86**	**9.81**	**1.96**	**0.41**	**1.64**	**14.63**	**3.26**

**** Pseudo-equilibrium state average***

Table C.11 Revised frictional data for the Re_D = 1.00x10^5 assay determined from the velocity profile, SFM and P_3-P_5 datasets.

Day	*Re* (x10^{-4})	*SFM*				*P_3-P_5*			
		ε (mm)	ΔU^+	ε^+	k_s^+	ε (mm)	ΔU^+	ε^+	k_s^+
0	9.41	0.62	0.05	27.80	0.40	0.62	0.07	27.88	0.41
1	9.48	0.50	0.17	22.45	0.40	0.50	-0.13	21.57	0.39
2	9.90	0.87	2.62	43.40	2.00	0.87	2.52	42.30	1.44
3	10.04	0.99	2.85	49.24	1.86	0.99	2.51	46.33	0.42
4	10.33	1.66	2.21	84.88	1.69	1.66	1.68	77.88	0.42
5	10.07	1.41	2.11	69.28	1.17	1.41	1.68	64.56	0.41
6	10.40	1.45	2.25	73.90	1.10	1.45	2.18	72.89	0.66
7	9.60	1.84	4.28	94.35	6.07	1.84	4.10	89.15	2.67
8	10.22	1.42	4.84	82.42	14.03	1.42	4.57	76.69	6.03
9	10.64	1.60	4.77	94.66	10.97	1.60	4.70	92.76	8.76
10	10.23	1.80	5.12	103.35	11.88	1.80	5.16	104.75	13.65
12	10.01	1.61	5.02	92.47	14.06	1.61	5.01	92.31	13.81
13	10.59	1.33	5.15	76.56	9.26	1.33	5.27	79.82	14.41
14	10.59	1.45	5.58	84.84	10.84	1.45	5.69	88.95	17.50
15	-	-	-	-	-	-	-	-	-
16	-	-	-	-	-	-	-	-	-
17	9.36	1.72	5.69	95.21	17.61	1.72	5.68	94.86	17.02
18	9.91	1.09	4.87	62.25	15.04	1.09	4.89	62.59	15.86
19	9.57	1.11	4.96	60.93	13.17	1.11	4.97	61.27	13.93
20	-	-	-	-	-	-	-	-	-
Av.*	**10.13**	**1.46**	**5.11**	**83.63**	**12.98**	**1.46**	**5.10**	**83.78**	**13.44**
σ*	**0.46**	**0.25**	**0.32**	**14.78**	**2.54**	**0.25**	**0.39**	**14.85**	**3.76**

**** Pseudo-equilibrium state average***

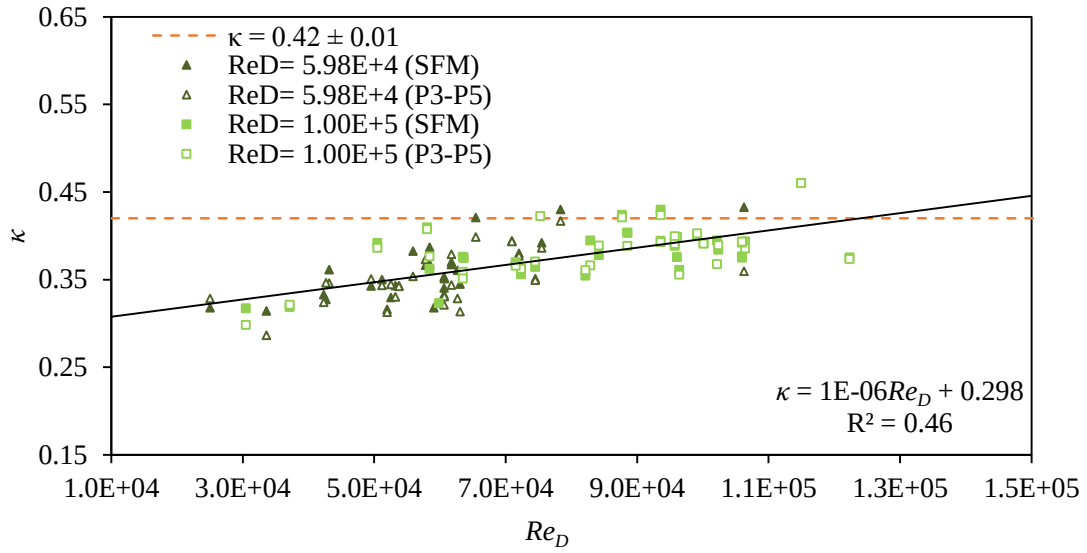

Figure C.3 Influence of Re_D on κ for the Re_D = 5.98x10^4 and Re_D =1.00x10^5 assays.

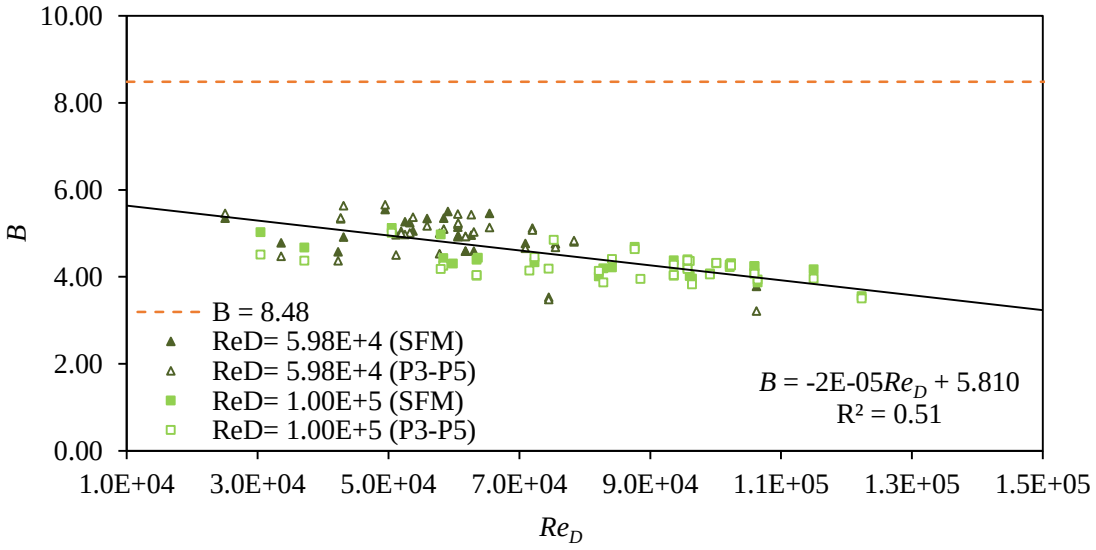

Figure C.4 Influence of Re_D on B for the Re_D = 5.98x10^4 and Re_D =1.00x10^5 assays.

D. Supporting data for Chapter 6

D.1 Global frictional data

Table D.1 Frictional data for the biofilm incubated within the Re_D =5.98x10^4 assay when subjected to the range of 3.36x10^4 < Re_D <1.15x10^5.

***Re* (x10^4)**	***λ***	***u**** **(m/s)**	***τ$_w$*** **(N/m^2)**	***κ***	***Traditional C-W Eq.***		***Modified C-W Eq.***	
					k_s (mm)	k_s^+	k_s (mm)	k_s^+
3.36	0.028	0.023	0.51	0.33	0.268	2.91	0.146	5.34
4.27	0.029	0.027	0.72	0.34	0.257	5.48	0.214	6.58
5.25	0.029	0.032	1.04	0.35	0.233	8.20	0.258	7.40
5.84	0.030	0.036	1.32	0.36	0.230	10.77	0.301	8.24
6.54	0.031	0.042	1.74	0.36	0.239	15.51	0.378	9.82
7.20	0.032	0.047	2.16	0.37	0.232	19.13	0.419	10.58
7.83	0.034	0.052	2.69	0.38	0.246	26.03	0.512	12.51
9.02	0.034	0.060	3.58	0.39	0.210	31.20	0.531	12.35
9.86	0.032	0.064	4.09	0.40	0.156	27.53	0.440	9.73
11.56	0.029	0.071	4.96	0.41	0.081	20.64	0.297	5.61

Table D.2 Frictional data for the biofilm incubated within the Re_D =1.00x10^5 assay when subjected to the range of 3.38x10^4 < Re_D <1.22x10^5.

***Re* (x10^4)**	***λ***	***u**** **(m/s)**	***τ$_w$*** **(N/m^2)**	***κ***	***Traditional C-W Eq.***		***Modified C-W Eq.***	
					k_s (mm)	k_s^+	k_s (mm)	k_s^+
3.38	0.024	0.019	0.36	0.33	-0.015	-0.27	0.142	2.58
4.41	0.024	0.024	0.59	0.34	0.032	0.76	0.125	3.00
5.71	0.025	0.031	0.96	0.36	0.106	3.40	0.126	4.05
6.41	0.026	0.035	1.25	0.36	0.140	5.11	0.124	4.55
7.27	0.025	0.040	1.56	0.37	0.136	5.57	0.101	4.12
8.54	0.026	0.047	2.18	0.38	0.157	7.63	0.084	4.09
9.62	0.027	0.055	2.97	0.39	0.226	12.69	0.090	5.09
10.45	0.025	0.057	3.29	0.40	0.155	9.14	0.056	3.27
11.49	0.025	0.062	3.87	0.41	0.149	9.57	0.043	2.74
12.23	0.025	0.066	4.30	0.42	0.149	10.15	0.036	2.48

D.2 Water chemistry relationships

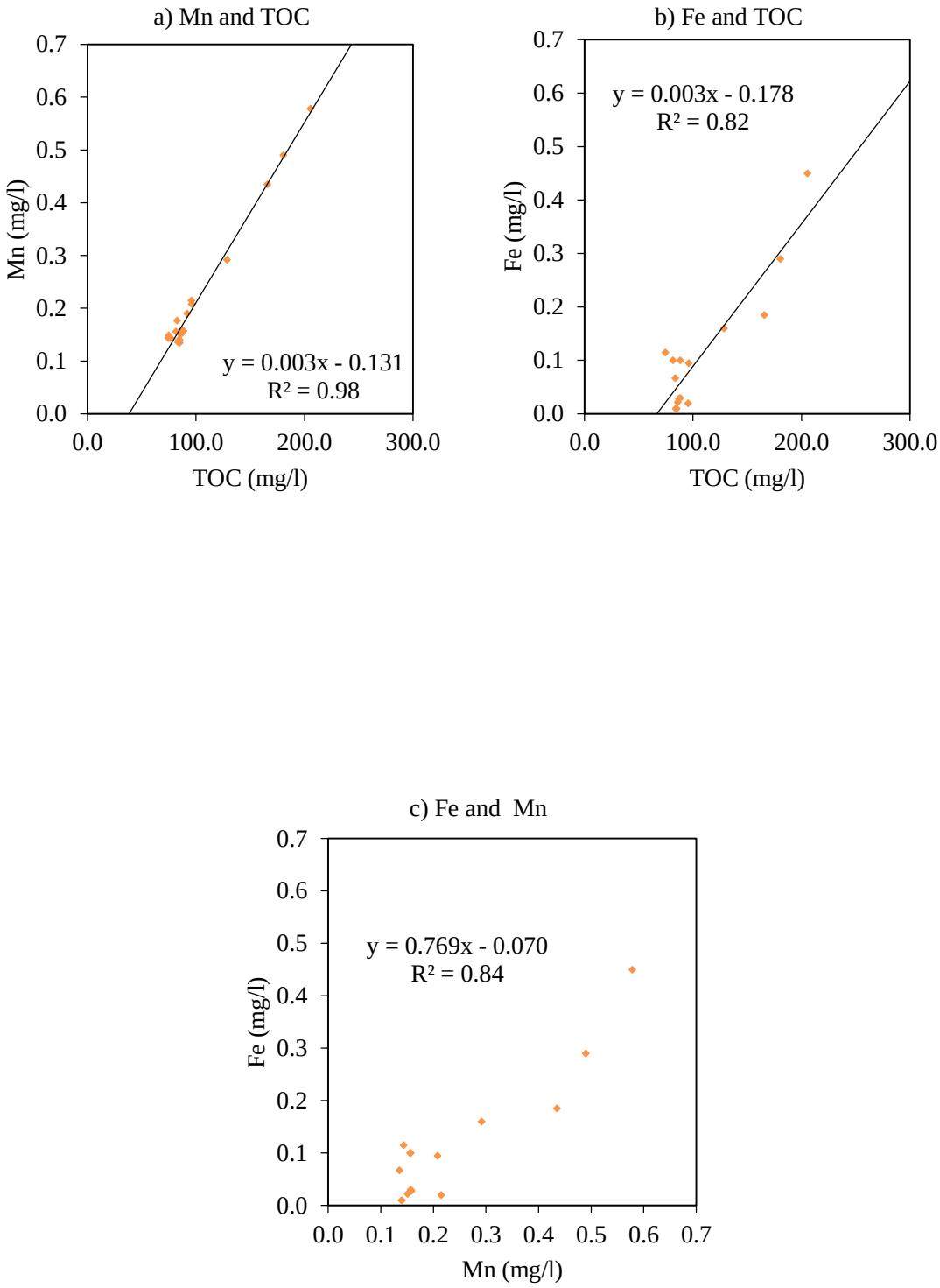

Figure D.1 Relationships between a) Mn and TOC, b) Fe and TOC and c) Fe and Mn.

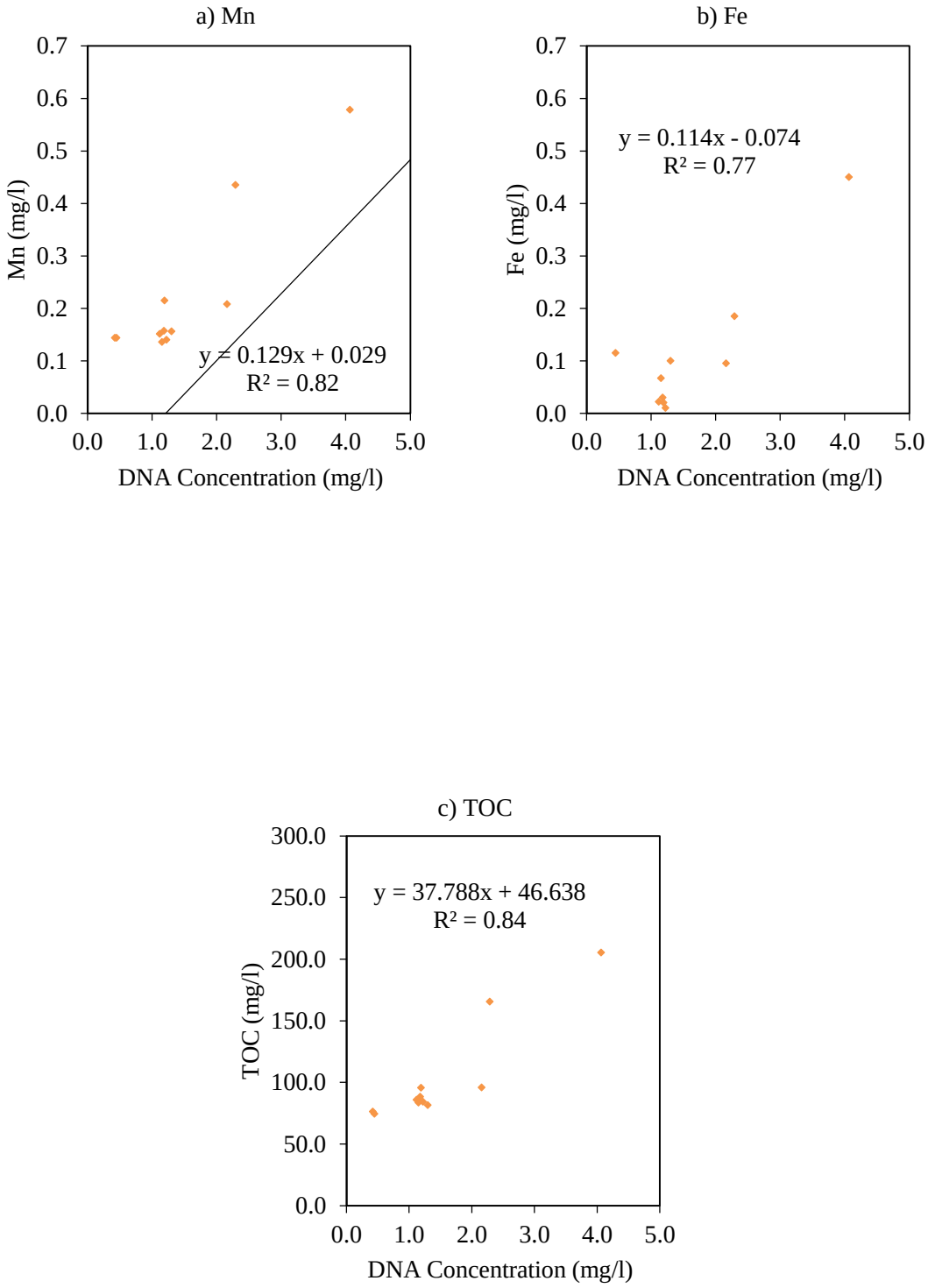

Figure D.2 Relationships between DNA concentration and a) Mn b) Fe and c) TOC.

D.3 PCR products

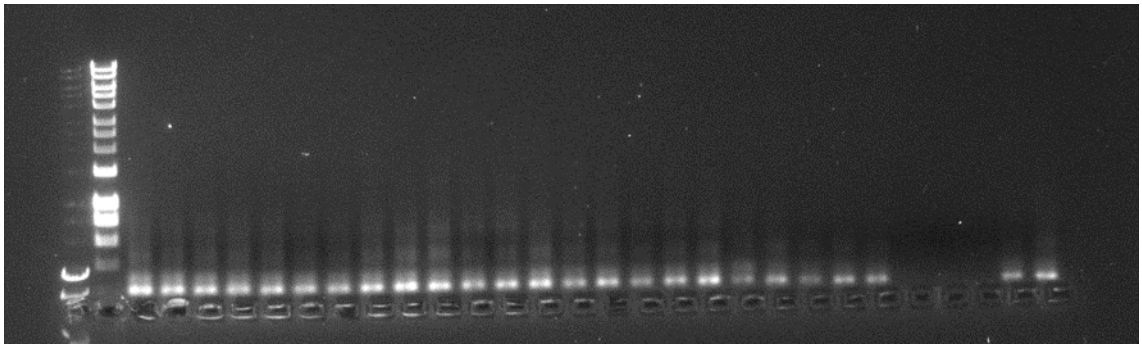

Figure D.3 PCR products for the biofilm samples taken from the Re_D = 5.98x10^4 and Re_D = 1.00x10^5 assays per- and post- shear

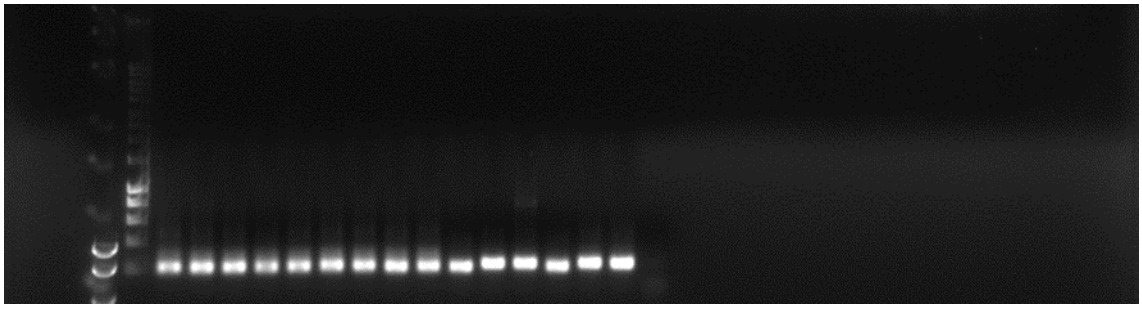

Figure D.4 PCR products for the water samples taken from the Re_D = 5.98x10^4 and Re_D = 1.00x10^5 assays per- and post- shear

D.4 Sediment transport data (with and without fouling)

Table D.3 Frictional data for the fouled pipe determined before the sediment investigations.

***Re* (x10^{-4})**	***λ***	***u**** **(m/s)**	***τ_w*** **(N/m^2)**	***κ***	***Traditional C-W Eq.***		***Modified C-W Eq.***	
					k_s (mm)	k_s^+	k_s (mm)	k_s^+
2.50	0.025	0.014	0.19	0.33	-0.033	-0.46	0.197	2.76
4.23	0.024	0.023	0.53	0.34	0.033	0.76	0.134	3.10
5.32	0.025	0.032	1.00	0.35	0.085	2.53	0.127	3.75
7.09	0.026	0.041	1.64	0.37	0.157	6.37	0.115	4.66
7.55	0.027	0.044	1.90	0.37	0.180	7.85	0.115	4.99
8.13	0.028	0.049	2.36	0.38	0.246	11.85	0.129	6.21

Table D.4 Frictional data for the fouled pipe determined after the sediment investigations.

***Re* (x10^{-4})**	***λ***	***u**** **(m/s)**	***τ_w*** **(N/m^2)**	***κ***	***Traditional C-W Eq.***		***Modified C-W Eq.***	
					k_s (mm)	k_s^+	k_s (mm)	k_s^+
2.50	0.029	0.016	0.26	0.33	0.106	1.58	0.313	4.67
3.55	0.030	0.024	0.56	0.34	0.259	5.66	0.335	7.33
5.10	0.032	0.034	1.18	0.35	0.398	12.90	0.321	10.40
7.22	0.033	0.048	2.28	0.37	0.472	21.94	0.254	11.81
7.60	0.035	0.051	2.58	0.37	0.565	28.29	0.277	13.88
8.17	0.035	0.055	3.03	0.38	0.597	32.37	0.266	14.41
9.30	0.031	0.059	3.45	0.39	0.365	21.01	0.145	8.33
8.86	0.029	0.061	3.71	0.40	0.288	17.08	0.107	6.32
1.10	0.025	0.062	3.90	0.41	0.136	8.29	0.044	2.69

Table D.5 Results of the sediment transport surveys without fouling in the pilot-scale pipeline.

No.	*U (m/s)*	τ_w (N/m^2)	*u** (m/s)	m_0 *(g)*	*Cumulative Mass Trans. (g)*				m_{res} *(g)*	m_{tt} *(g)*	*% Diff Between* m_0 *and* m_{tt}
					m_{15}	m_{30}	m_{45}	m_{60}			
1	0.40	0.69	2.75	100.0	0.0	0.1	0.1	0.2	99.3	99.5	0.55%
2	0.45	0.95	3.23	100.0	0.0	7.8	7.8	67.8	32.9	100.7	0.63%
3	0.45	0.87	3.08	100.0	0.0	20.4	20.4	69.5	30.5	100.0	0.00%
4	0.46	0.95	3.23	100.0	0.0	90.4	90.4	92.3	7.3	99.6	0.40%
5	0.57	1.48	4.02	100.0	0.0	23.0	23.0	66.8	32.8	99.6	0.46%
6	0.60	1.62	4.20	100.0	85.6	87.4	87.4	87.4	13.5	100.9	0.83%
7	0.42	0.76	2.89	100.0	0.0	4.1	4.1	8.8	91.1	99.9	0.14%
8	0.65	2.02	4.69	100.0	87.3	89.5	89.5	89.5	11.0	100.5	0.49%
9	0.45	0.87	3.09	100.0	0.0	28.9	28.9	74.8	24.9	99.8	0.26%
10	0.40	0.72	2.80	100.0	0.0	0.9	0.9	3.1	97.8	100.8	0.80%
11	0.51	1.23	3.67	100.0	0.0	94.2	94.2	97.3	4.0	101.3	1.22%
12	0.45	0.97	3.26	100.0	0.0	24.8	24.8	75.1	25.9	101.0	0.95%
13	0.45	0.97	3.26	100.0	0.0	90.7	90.7	91.6	7.1	98.7	1.34%
14	0.55	1.48	4.01	100.0	88.2	88.2	89.3	89.3	11.2	100.5	0.50%
15	0.46	0.91	3.16	100.0	0.0	0.0	0.0	95.5	4.6	100.1	0.09%
16	0.90	3.57	6.22	100.0	0.0	0.0	0.0	98.6	2.2	100.8	0.78%
17	0.85	3.18	5.87	100.0	0.0	0.0	0.0	99.5	0.2	99.7	0.33%
18	1.00	4.54	7.00	100.0	0.0	0.0	0.0	98.5	1.2	99.7	0.34%
19	0.75	2.55	5.27	100.0	0.0	0.0	0.0	96.5	4.6	101.1	1.05%
20	0.90	3.84	6.44	100.0	0.0	0.0	0.0	99.2	0.3	99.5	0.56%
21	0.95	4.46	6.93	100.0	0.0	0.0	0.0	96.4	4.4	100.8	0.76%
22	0.30	0.45	2.22	100.0	0.0	0.0	0.0	1.2	98.5	99.7	0.28%
23	0.35	0.62	2.62	100.0	0.0	0.0	0.0	2.4	97.2	99.5	0.52%
24	0.35	0.63	2.62	100.0	0.0	0.0	0.0	0.0	98.4	98.4	1.66%
25	0.35	0.63	2.63	100.0	0.0	0.0	0.0	2.6	98.4	100.9	0.92%
26	0.36	0.59	2.54	100.0	0.0	0.0	0.0	2.6	97.2	99.7	0.32%
27	0.45	0.98	3.27	100.0	0.0	10.2	10.2	76.2	22.9	99.1	0.88%
28	0.40	0.77	2.91	100.0	0.0	0.9	0.9	3.1	95.8	98.8	1.19%
29	0.36	0.61	2.59	100.0	0.0	0.0	0.0	5.7	95.6	101.3	1.27%
30	0.47	1.12	3.50	100.0	0.0	0.0	0.0	90.3	8.4	98.6	1.42%
31	0.26	0.31	1.83	100.0	0.0	0.0	0.0	0.4	99.3	99.7	0.34%
32	0.44	0.98	3.27	100.0	0.0	0.0	0.0	65.2	36.2	101.4	1.40%
33	0.80	3.01	5.71	100.0	0.0	0.0	0.0	95.2	5.5	100.7	0.66%
34	0.75	2.63	5.35	100.0	0.0	0.0	0.0	98.5	2.4	100.9	0.87%
35	0.60	1.67	4.27	100.0	0.0	0.0	0.0	97.6	2.3	99.9	0.15%
36	0.55	1.40	3.91	100.0	0.0	0.0	0.0	98.3	1.3	99.5	0.47%
37	0.42	0.83	3.01	100.0	0.0	3.1	3.1	11.8	87.4	99.3	0.76%

Table D.6 Results of the sediment transport surveys with fouling in the pilot-scale pipeline.

No.	*U (m/s)*	τ_w (N/m^2)	*u** (m/s)	m_0 (g)	*Cumulative Mass Trans. (g)*				m_{res} (g)	m_{tt} (g)	*% Diff Between m_0 and m_{tt}*
					m_{15}	m_{30}	m_{45}	m_{60}			
1	0.37	0.59	1.72	100.1	0.0	0.0	0.0	1.3	98.3	99.5	0.54%
2	0.58	1.43	2.50	100.1	0.0	78.9	78.9	99.1	1.3	100.4	0.28%
3	0.55	1.29	2.39	100.0	0.0	55.2	55.2	92.1	7.2	99.3	0.73%
4	0.45	0.86	2.02	100.2	0.0	3.5	3.5	22.8	77.3	100.1	0.13%
5	0.48	0.98	2.13	100.1	0.0	10.6	10.6	51.3	48.8	100.1	0.03%
6	0.62	1.73	2.72	100.6	0.0	88.8	88.8	95.5	5.0	100.6	0.05%
7	0.3	0.38	1.45	100.1	0.0	0.0	0.0	0.0	99.2	99.2	0.90%
8	0.55	1.32	2.42	100.0	12.6	63.8	93.8	94.7	5.7	100.4	0.36%
9	0.55	1.32	2.42	100.0	0.0	23.0	23.0	69.7	29.2	99.0	1.06%
10	0.57	1.41	2.49	100.0	38.3	90.5	91.5	92.0	8.3	100.4	0.35%
11	0.45	0.87	2.03	100.0	1.5	1.5	1.5	3.9	95.9	99.8	0.21%
12	0.41	0.72	1.87	100.0	0.0	0.3	0.3	1.1	100.0	101.2	1.19%
13	0.54	1.28	2.39	100.0	0.0	50.8	50.8	98.3	1.5	99.8	0.19%
14	0.45	0.86	2.02	100.2	0.0	0.4	0.4	1.6	98.7	100.4	0.16%
15	0.45	0.87	2.02	100.0	0.0	0.3	0.3	2.7	96.3	99.0	1.08%
16	0.38	0.61	1.75	100.0	0.0	0.1	0.1	0.1	99.4	99.5	0.53%
17	0.45	0.86	2.02	100.0	0.0	7.0	7.0	32.6	67.4	100.0	0.01%
18	0.55	1.34	2.43	100.0	0.0	95.9	95.9	97.6	2.2	99.9	0.16%
19	0.56	1.42	2.50	100.0	91.6	91.6	95.6	95.6	4.4	100.0	0.01%
20	0.59	1.58	2.62	100.0	0.0	90.6	90.6	93.2	6.7	99.9	0.08%
21	0.37	0.62	1.76	100.1	0.0	0.0	0.0	2.3	98.3	100.6	0.53%
22	0.57	1.45	2.52	100.4	0.0	67.9	67.9	100.1	0.0	100.1	0.32%
23	0.55	1.34	2.43	100.0	0.0	65.2	65.2	99.8	0.0	99.8	0.16%
24	0.44	0.83	1.99	100.2	0.0	3.5	3.5	28.8	72.2	101.0	0.82%
25	0.48	1.02	2.16	100.1	0.0	6.6	6.6	42.2	56.8	99.0	1.03%
26	0.61	1.67	2.68	100.1	0.0	80.1	80.1	88.0	12.3	100.3	0.23%
27	0.30	0.39	1.45	100.1	0.0	0.0	0.0	0.0	99.3	99.3	0.81%
28	0.55	1.31	2.41	100.0	16.6	61.8	96.8	100.3	0.0	100.3	0.31%
29	0.48	1.00	2.15	100.0	0.0	13.7	13.7	60.4	40.6	101.0	0.99%
30	0.56	1.38	2.46	100.0	38.3	90.4	93.5	97.0	3.3	100.3	0.28%
31	0.45	0.89	2.04	100.0	0.0	0.0	0.0	5.6	93.9	99.4	0.58%
32	0.40	0.70	1.85	100.0	0.0	0.0	0.0	0.0	99.6	99.6	0.45%
33	0.70	2.23	4.04	100.0	0.0	55.8	55.8	100.3	0.0	100.3	0.29%
34	0.90	3.69	5.19	100.0	0.0	0.0	0.0	98.5	1.1	99.6	0.45%
35	0.80	2.90	4.60	100.0	0.0	0.0	0.0	100.5	0.0	100.5	0.49%
36	0.78	2.82	4.54	100.2	0.0	0.0	0.0	96.2	4.1	100.3	0.05%
37	0.90	3.82	5.28	100.0	0.0	0.0	0.0	98.2	1.3	99.5	0.54%

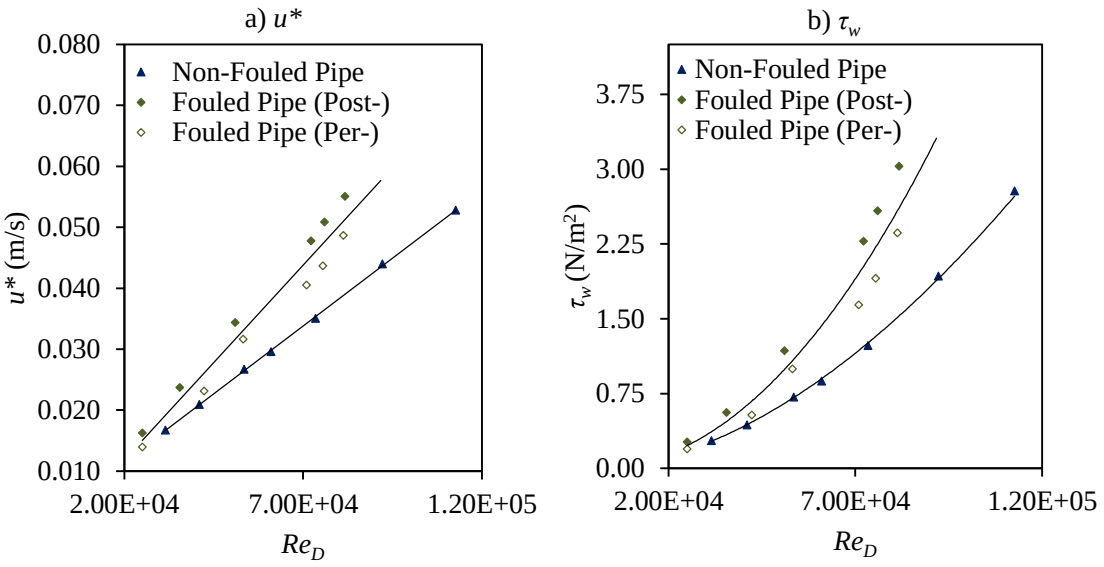

Figure D.5 a) u and b) τ_w for the non-fouled and fouled pipe (both pre- and post- sediment testing time intervals).*